Alma Mater Studiorum · Università di Bologna

Dottorato di ricerca in
Fisica
Ciclo XXX

Settore Concorsuale: 02/A1
Settore Scientifico disciplinare: FIS/01

Measurement of the differential cross section of $t\bar{t}$ production, using data collected by the ATLAS detector at $\sqrt{s} = 13$ TeV

Presentata da: Federica Fabbri

Coordinatore Dottorato:
Prof. Silvia Arcelli

Supervisore:
Prof. Nicola Semprini Cesari

Relatore:
Dott. Matteo Negrini

Esame finale anno 2018

Abstract

The study of the top quark physics covers a large part of the ATLAS experiment physics program and represents an active research field for the theoretical community. In this thesis, the measurement of the differential cross-sections of top quark pair production in proton proton collisions at a centre of mass energy of $\sqrt{s} = 13$ TeV is presented. The measurement is performed in a fiducial phase-space, as a function of top quark and $t\bar{t}$ system kinematic observables, and the data set corresponds to an integrated luminosity of 3.2 fb^{-1}, recorded in 2015 with the ATLAS detector at the CERN Large Hadron Collider. Only events with exactly one electron or muon in the final state are retained and the analysis employs two separate selections and top quark reconstruction techniques, focusing on different regions of the top quark momentum spectra. The measured spectra are corrected for detector effects and are compared to several theoretical Monte Carlo simulations through χ^2 and p-values calculations. The measured spectra provide stringent tests of perturbative QCD and can be used to tune the Monte Carlo simulations and re-interpreted to set limits on the existence of processes beyond the standard model. Finally, new techniques that will improve the sensitivity of future analysis in the region where the top quark is produced with high transverse momentum are presented.

Abstract

Lo studio della fisica del quark top è tuttora uno dei principali ambiti nel programma di ricerca dell'esperimento ATLAS, continuamente in sviluppo anche da parte della comunità teorica. In questa tesi viene presentata la misura della sezione d'urto di produzione di coppie $t\bar{t}$ in collisioni protone protone ad un'energia nel centro di massa di $\sqrt{s} = 13$ TeV. La misura è effettuata in una regione fiduciale, in funzione delle variabili cinematiche del quark top e del sistema $t\bar{t}$ ed i dati utilizzati corrispondono ad una luminosità integrata di 3.2 fb^{-1}, raccolti nel 2015 dall'esperimento ATLAS, situato al Large Hadron Collider del CERN. Nell'analisi presentata sono selezionati solo eventi contenenti esattamente un muone o un elettrone nello stato finale e sono utilizzate due diverse selezioni e tecniche di ricostruzione, focalizzate su regioni diverse dello spettro dell'impulso del top quark. Gli spettri misurati sono corretti per gli effetti indotti dal rivelatore e confrontati con diverse simulazioni teoriche Monte Carlo utilizzando i test statistici χ^2 e p-valori. Gli spettri misurati forniscono prove stringenti dei calcoli di QCD perturbativa, e possono essere utilizzati per la calibrazione dei parametri delle simulazioni Monte Carlo e reinterpretati per estrarre dei limiti sull'esistenza di processi previsti da modelli di nuova fisica. In conclusione sono presentate nuove tecniche atte a migliorare la sensibilità delle analisi future nella regione di spazio delle fasi in cui il quark top è prodotto con un elevato impulso trasverso.

"Good morning, O Deep Thought" said Loonquawl nervously,
"Do you have an answer to Everything? To the great Question of Life, the Universe and Everything?"
"Yes, though I don't think" said Deep Thought, *"that you're going to like it."*
"Doesn't matter!" said Phouchg. *"We must know it! Now!"*
"Alright", said the computer and settled into silence again.
"The Answer to the Great Question of Life, the Universe and Everything is ...Forty-two", said Deep Thought, with infinite majesty and calm.
"Forty-two!", yelled Loonquawl. *"Is that all you've got to show for seven and a half million years' work?"*
"I checked it very thoroughly", said the computer,
"and that quite definitely is the answer. I think the problem, to be quite honest with you, is that you've never actually known what the question is."

"The Hitchhiker's Guide to the Galaxy", Douglas Adams

Contents

Introduction

The top quark, discovered in 1995 at Fermilab, thanks to its peculiar properties still represents one of the most interesting research fields in particle physics and in the ATLAS experiment physics program. The top quark is the fundamental particle with the largest mass observed until now, two order of magnitude heavier than all the other quarks. It is also the only quark which decays before it hadronizes, giving direct access to the property of a "bare" quark through its decay products. Thanks to its properties the top quark has a large coupling with the Higgs boson and it is involved in many theories beyond the standard model. Moreover the measurement of the production cross-section of $t\bar{t}$ represents a stringent test of perturbative QCD.

The large sample of top quarks collected at the Large Hadron Collider (LHC) allows the measurement of the top quark characteristics with high precision. The high instantaneous luminosity of the collider and the center of mass energy of $\sqrt{s} = 13$ TeV, producing a four time increase of the $t\bar{t}$ production cross-section with respect to the one at $\sqrt{s} = 8$ TeV, allow to collect large $t\bar{t}$ samples even in limited data taking periods. The energy and luminosity reached from the LHC allow the acquisition of large amount of data also in kinematic regions never studied before such as the one in which the top quark has a large transverse momentum (p_T), where the application of specific techniques to reconstruct the top quark and the $t\bar{t}$ system is necessary.

In this thesis, the measurement of the $t\bar{t}$ production differential cross-section in proton proton collisions at a center of mass energy of $\sqrt{s} = 13$ TeV at the ATLAS experiment is presented. The differential cross-section is measured in a fiducial phase space, as a function of the kinematic properties of the top quark and the $t\bar{t}$ system. The analysis selects only events with a single lepton in the final state and uses two different approaches, depending on the transverse momentum (p_T) of the top quark, optimized to enhance the reconstruction and identification efficiency of the $t\bar{t}$ system along the full top quark p_T spectra. The results of the analysis are compared with various theoretical predictions to assess the level of accuracy reached from perturbative QCD calculations, a large disagreement with the predictions could indicate the need for additional tuning of Monte Carlo (MC) generator or the presence of new physics processes. In particular, the tuning of MC simulations is of central importance to reduce the $t\bar{t}$ modelling uncertainties both in analyses where the $t\bar{t}$ represents the signal and in measurement of rare processes where the $t\bar{t}$ is among the main background sources. The results presented in this thesis have been published in December 2017 [1].

The structure of the thesis is the following. In Chapter 1 an overview of the Standard Model and of top quark physics is presented, together with the latest experimental results obtained on the measurement of the $t\bar{t}$ production differential cross-section. In Chapter 2 is given an overview of the ATLAS experiment. In Chapter 3 all the steps of the Monte Carlo production and the detector simulation are described, with a particular emphasis on the development of an alternative algorithm for the simulation of the digitization step, explained in detail in Appendix B. The following Chapters cover the full analysis chain, starting from the object calibration, event selection and background determination presented in Chapter 4. In Chapter 5 the determination of the corrections due to the limited acceptance and resolution of the detector are described, together with the unfolding procedure. The systematic uncertainties affecting the measurement, due to the reconstruction of the objects and the $t\bar{t}$ system, the background determination and the modelling, are presented in Chapter 6. The results of the measurement of the $t\bar{t}$ production differential cross-section using data collected by the ATLAS experiment in 2015, corresponding to 3.2 fb^{-1} integrated luminosity are presented in Chapter 7. In conclusion, Chapter 8 presents some prospective and new techniques that will be applied in future measurements to improve the accuracy of the $t\bar{t}$ production cross-section measurements, in the region where the top quark is produced with high transverse momentum. Appendix A shows an example of the re-interpretation of cross-section measurements that can be performed to extract limits on the existence of physics processes beyond the Standard Model.

Chapter 1

Top Quark Physics

The particle physics era began in 1897 with the discovery of electrons by Joseph J. Thomson. In the following fifty years the number of discoveries and related theories increased rapidly and became clear the need for a larger scenario that could describe and order all the different phenomena observed. Finally in the 1960s and 1970s the ideas of gauge symmetries and spontaneous symmetry breaking was developed and the cooperation between theorists and experimentalists laid the foundations of the large experimental-theoretical framework known as Standard Model (SM) of particle physics. The SM included all the known elementary particles and interactions, and foresaw the existence of processes and particles found in the following decades, as the Higgs Boson, discovered in 2012. In the SM all the bricks of matter are contained and organized in three generations of leptons and quarks. Among all the quarks, the top was the latest to be discovered, in 1995 by CDF and DØ experiments [2, 3]. The top is the heaviest quark of the SM and the only one that does not create bound states. These two properties open the possibility to many interesting studies, to understand the basis of the weak and strong interactions, and made top quark physics one of the main area of study in high energy physics.

1.1 The Standard Model of Particle Physics

The SM framework describes all the discovered elementary particles that form the ordinary and unstable matter and the way they interact.

In the following paragraphs a short introduction to the SM will be given.

1.1.1 The Elementary Particles

The basis for the SM were settled in 1964 independently by Murray Gell-Mann and George Zweig [4, 5]. They introduced the idea of nucleons composed by charged particles of spin $\frac{1}{2}$, called quarks. Initially, only three quarks were introduced, as the components of the particles discovered at that time. Many other elementary particles of the SM were predicted in the following years and observed in accelerators experiments afterwards.

The charm quark was discovered in 1974 independently at the Stanford Linear Accelerator Center [6] and the Brookhaven National Laboratory [7] with the observation of the J/ψ resonance, the $c\bar{c}$ bound state. In 1977 at Tevatron (Fermilab) another heavy meson state was observed [8, 9, 10], called Υ, a $b\bar{b}$ bound state. This represented the discovery of the bottom quark. The last quark, the top, was finally observed in 1995 at Tevatron.

The electron, the first charged lepton, was discovered by J.J. Thomson, while the muon and τ were observed respectively in the cosmic rays in 1937 [11] and in the accelerators in 1975 [12].
The first neutrino was postulated by Pauli in 1930, in order to account for the energy and momentum distributions in *Beta-decay*. In the following years many experiments were done to prove their existence and test the properties of these particles.

The leptons and quarks are fermions, particles with half-integer spin, described by the Dirac equation [13]. The equation leads to both positive and negative energy solutions. The negative solutions are interpreted as anti-particles, with the same mass and spin of the respective fermions, but opposite charges.
The quarks and the leptons are divided in three families as shown in Table 1.1.

Quarks:	$\begin{pmatrix} u \\ d \end{pmatrix}$	$\begin{pmatrix} c \\ s \end{pmatrix}$	$\begin{pmatrix} t \\ b \end{pmatrix}$
Leptons:	$\begin{pmatrix} e \\ \nu_e \end{pmatrix}$	$\begin{pmatrix} \mu \\ \nu_\mu \end{pmatrix}$	$\begin{pmatrix} \tau \\ \nu_\tau \end{pmatrix}$

Table 1.1: Elementary particles of the Standard Model.

The quarks have fractional electric charge, $+\frac{2}{3}e$[1] for the ones in the first row in Table 1.1, and $-\frac{1}{3}e$ for the others. The quarks bring several internal charges: the *flavor* (up, down, charm, strange, top, bottom), and the color charge (red, green, blue and anti-red, anti-green, anti-blue for the anti-particles). The interaction through the color charges creates color singlet bound states (hadrons) and only color singlet states can be observed in nature, this property of the color charge is called confinement. The quarks, being fermions, can combine to produce singlet states in only two ways: a quark and an anti-quark (mesons) or three quarks/anti-quarks (baryons). The mesons have integer spin while the baryons have half-integer spin, multiple of $\frac{1}{2}$. As a consequence, the baryons follow the Fermi-Dirac statistics, that determines the properties of the atoms's nuclei, composed by protons and neutrons. These are the only stable hadrons, the neutron is not really stable outside the nucleus but has a long lifetime of about fifteen minutes. The other composite states, that can be formed also by heavier quarks s, b, c, decay rapidly ($\sim 10^{-13}$s) to lighter particles and consequently do not play a role in ordinary matter.

The leptons are e, μ and τ and the three associated neutrinos that complete the families. The leptons bring integer electric charge that is $1e$ for the first row

[1] $e = 1.60217662 \cdot 10^{-19} C$

Interaction	Relative strength	Range (m)	Mediator
Strong	1	10^{-13}	gluons
Electromagnetic	10^{-2}	∞	photons
Weak	10^{-5}	$< 10^{-15}$	$W^{\pm}$, Z
Gravity	10^{-39}	∞	graviton

Table 1.2: Relative strength and range of different interactions [17]. The strength comparison of the four basic forces is determined as the force between two particles placed on a certain distance, it has a meaning only in relative terms. The graviton, indicated as gravity mediator, is a spin 2 *boson* introduced in quantum field theory, but not included yet in the SM.

in Table 1.1 and 0 for the neutrinos. All the leptons bring an internal charge, called leptonic number, that is different for each family (l_e, l_μ, l_τ) and is defined on the basis of the weak interaction properties. The leptonic quantum number is conserved in many interactions, the only phenomena that breaks this conservation is the neutrino oscillation.

1.1.2 Interactions

The SM is a renormalisable field theory, that describes all particles as quanta of an associated field, and includes also the interactions between particles, described in terms of exchange of bosons. Three different fundamental interactions are included: electromagnetic, weak and strong. The electromagnetic and weak forces were unified in 1960s and 1970s, thanks to the work of Glashow, Weinberg, Salam, t'Hooft [14, 15, 16] and others, while the gravity is still not included in the SM framework.
The gravitational interaction is dominant at the scale of the universe, but is the weakest at particle scale, as can be seen in Table 1.2, where the relative strength of different interactions is shown.

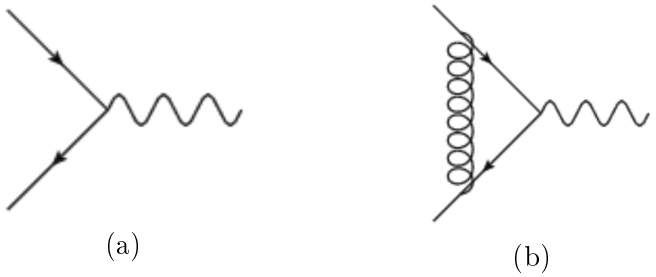

Figure 1.1: Examples of Feynman diagrams of the interaction between two fermions to create a boson, on the left an example of a LO diagram while on the right a higher order diagram with a virtual gluon radiation, in this case the two fermions are a quark and an anti-quark.

In quantum field theory the interaction between two particles is described by the probability of transition between two different states. The common way to visualize the interactions and evaluate this probability is through the Feynman diagrams, an example is given in Figure 1.1.
In Feynman diagrams the time is represented on the horizontal axis, the straight lines represent the fermions while the curved ones the bosons. The fermions (anti-fermions) are represented with arrows toward the positive (negative) time directions. Each vertex represents an interaction, that could be strong or electroweak, depending on the particles involved.
The diagrams are a useful tool to evaluate the matrix element of the interaction, the square of which gives the probability amplitude of a process. The probability of the process qq to $q'q'$, for example, is evaluated considering all the possible diagrams that can represent that process. Every diagram brings a different contribution to the total amplitude. Defining g the characteristic coupling of the interaction, each vertex of a Feynman diagram contributes with a factor $\sqrt{\alpha} \propto g$ to the amplitude. Thus diagrams involving loops and many vertexes are proportional to higher orders of α. In perturbative theory α is smaller than one, consequently, diagrams as 1.1b give a lower contribution to the probability amplitude with respect to diagrams as 1.1a. The considered order of α determines the precision of a perturbative calculation, for example leading-order (LO) means that only diagrams at the lower order of α for a certain process are included in the calculation. The coupling α or g and the mediators are the fundamental characteristics of each interaction.
A brief description of the three SM interactions will be given in the following paragraphs.

Electromagnetic Interaction

The electromagnetic interaction is the most precisely known and is theoretically described by Quantum Electrodynamics (QED). The quantum of the electromagnetic field is the photon (γ), that is a mass-less, charge-less boson of spin 1.

The strength of the electromagnetic interaction is proportional to the inverse of the square of the distance between the particles and to the coupling constant [18]:

$$\alpha = \frac{e^2}{4\pi\hbar c} = \frac{1}{137.036}. \tag{1.1}$$

The vertex of QED interaction is shown in Figure 1.1a, where the straight lines indicate charged fermions while the curved line represents the photon. The field theory does not allow self-interaction vertexes for charge-less particles, consequently the QED does not include this kind of vertex for the γ.

Quantum Chromodynamics

Quantum Chromodynamics (QCD) is the SU(3) gauge field theory that describes the strong interactions between colored quarks and gluons.

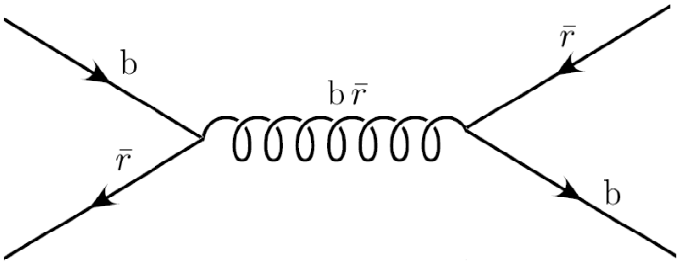

Figure 1.2: Example of color-flow in a QCD diagram, the symbol $\bar{r}$ represents the anti-red color, while the b represents the blue.

The color charge was initially introduced to explain the existence of observed particles as Δ^{++}, which is a three u-quarks bound state of spin $\frac{3}{2}$. The existence of this particle seemed to break the Pauli principle, a state formed by fermions should be anti-symmetric, while this composite state is completely symmetric with 3 quarks of the same *flavor* and spin $\frac{1}{2}$. The introduction of the color charge gives to the quarks an additional degree of freedom, that allows to define anti-symmetric states formed by 3 quarks with the same spin and *flavor*.
The color charge has three possible values, called (green) g, (red) r and (blue) b, and the interaction between quarks are invariant under color interchange. The me-

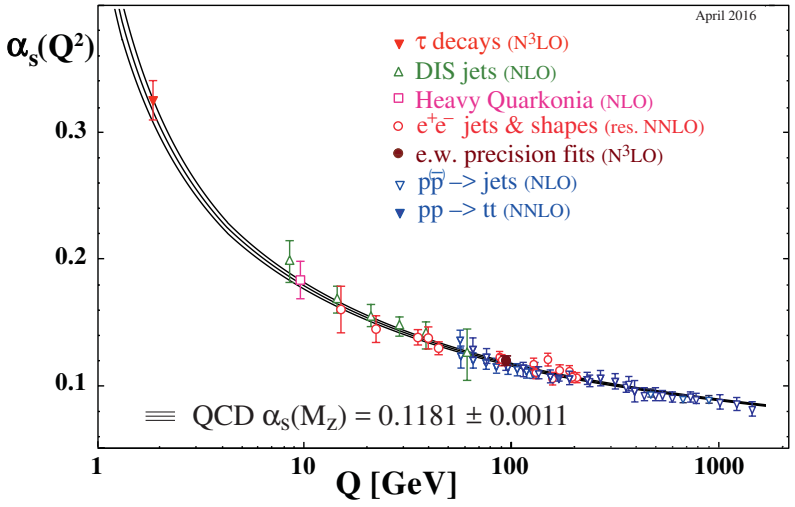

Figure 1.3: Summary of measurements of α_s as a function of the energy scale Q.

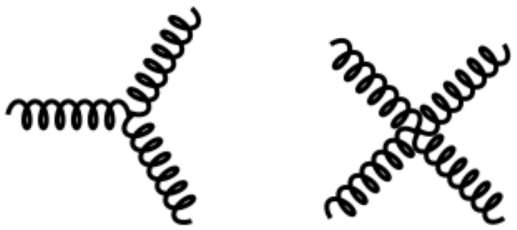

Figure 1.4: Self-coupling gluon vertices.

diators of the interaction are an octet of color-charged bosons, called gluons, each carrying a color and an anti-color. These particles, as the γ, are mass-less and have spin 1.
An example of the interaction is given in Figure 1.2. The main characteristics of the strong interaction are linked to the dependence on the momentum of the strong coupling constant α_S:

$$\alpha_s(q^2) = \frac{\alpha_s(\mu^2)}{1 + \frac{7}{4\pi}\alpha_s(\mu^2)\ln\left(\frac{q^2}{\mu^2}\right)} \tag{1.2}$$

where q^2 indicates the transferred momentum of the interaction and μ^2 is a fixed reference value of q^2. The trend of α_{QCD} as function of the energy scale of the interaction [18] is shown in Figure 1.3. For momentum transfers in the range 100 GeV - 1 TeV $\alpha_s \sim 0.1$ while the QCD is strongly interacting for scales around and below 1 GeV.
From the behaviour of α_s at large distances or low exchanged momentum, ($q^2 \to 0 \implies \alpha_S \to \infty$), derives the property of the QCD interaction called confinement: it is impossible to observe free colored states. The coupling increase with the distance, so the interaction becomes so intense at large ranges ($\sim$ 1 fm) that is impossible to separate a single colored state. This property is observed in high-energy scattering processes when quarks or gluons are pulled out from hadrons. In this case the strong interaction generate a process called *hadronization*, where a bundle of color singlet hadrons are the outcome of the gluon radiation and branching produced by the scattered colored particle. The experimental signature of this "hadron shower" is called *jet*.
At large q^2, the coupling $\alpha_s(q^2)$ tends to zero and the quarks behave as free particles. This feature is called *asymptotic freedom* and is the only condition in which the QCD can be described as a perturbative theory. This phenomena has great impact in high-energy hadron colliders, where the dynamic of the scattering process can be described using point-like and mass-less constituents rather than homogeneous hadrons. This behaviour of the strong coupling constant is due to the not-abelian nature of the interaction, that implies the presence of vertexes of self-interaction among the gluons, shown in Figure 1.4.

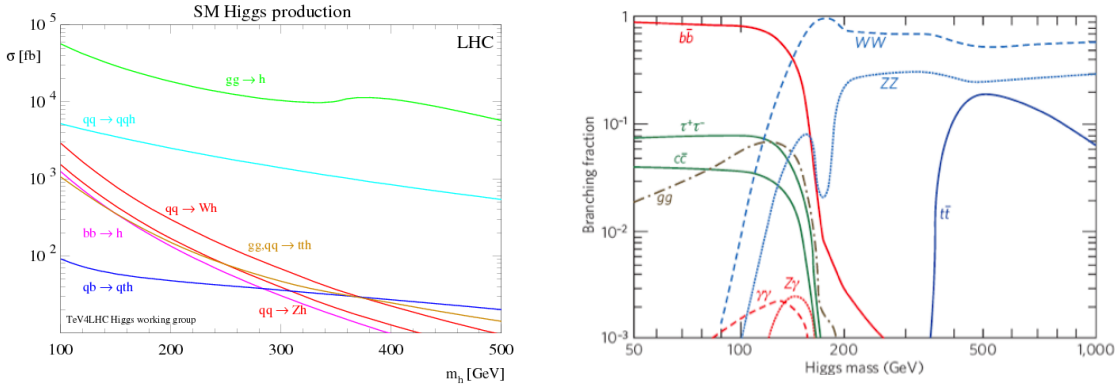

(a) (b)

Figure 1.5: Higgs boson production cross-section in pp collisions at 13 TeV (a) [18] and branching fraction in different channels (b) [21], in dependence of the Higgs mass [18].

Weak Interaction

The first hint of the existence of this interaction was found in the lifetime of the charged pions $\pi^{\pm}$. The neutral pion π^0 decays through electromagnetic interaction with a lifetime $\sim 10^{-17}$s while the charged π have a lifetime of 10 orders of magnitude larger. The $\pi^{\pm}$ is the lightest *meson*, thus there are no possible hadronic final state for its decay. In this case the decay through an interaction weaker than the electromagnetic, usually swamped by other interactions, becomes possible. The weak interaction, indeed, breaks many symmetries that are conserved by the strong and electromagnetic interactions, such as the quark flavor conservation:

$$\pi^{\pm}(ud) \rightarrow \mu\nu_{\mu} \tag{1.3}$$

and it is the only interaction affecting the charge-less and color-less neutrinos. The flavor changing is preferably inside the same family, however also decays across different families are allowed, with lower probability. This mixing between the families happens because the eigenstates of the weak interaction are different with respect to the mass eigenstates.
The mixing is described by the matrix introduced by Cabibbo, Kobayashi, Maskawa (CKM) in [19, 20]:

$$\begin{pmatrix} d' \\ s' \\ b' \end{pmatrix} = \begin{pmatrix} V_{ud} & V_{us} & V_{ub} \\ V_{cd} & V_{cs} & V_{cb} \\ V_{td} & V_{ts} & V_{tb} \end{pmatrix} \begin{pmatrix} d \\ s \\ b \end{pmatrix}$$

The choice of the quark with negative charge as mixed state is only a formalism convention. The weak interaction is mediated by massive, spin 1 bosons: $W^{\pm}$ and Z^0. The mass of these mediators has been introduced in the theory thanks to the unification of electromagnetic and weak theory and the spontaneous symmetry breaking proposed by Anderson, Higgs [22], Englert and Brout [23] in 1964.

They added to the SM Lagrangian a scalar field that permeates the vacuum and interacts with both the material fermion fields and the weak field. Through the spontaneous symmetry breaking of the Lagrangian this field gives mass to W and Z bosons (BEH mechanism) and interacting with material fields also to all the fermions. This scheme furthermore requires a single coupling for the weak and electromagnetic interaction leaving the photon mass-less. The theory includes also a massive, chargeless boson (Higgs boson) that is the quantum of the scalar field introduced. The proof of this theory has been the discovery of the Higgs boson, announced by ATLAS [24] and CMS [25] experiments on 4^{th} of July 2012 at CERN.

In Figure 1.5 are reported the different branching fractions[2] and production cross-section of the Higgs boson as a function of its mass[3], these depend on the coupling of the Higgs boson to other particles, usually expressed as equation (1.4):

$$\lambda_f = \sqrt{2}\frac{m_f}{v}, \lambda_b = 2\sqrt{2}\frac{m_b^2}{v}, \tag{1.4}$$

where v represents the Higgs field expectation value in vacuum, m_f the mass of the fermion and m_b the mass of the boson. The fermion with highest coupling to the Higgs is the top quark, but the decay in $t\bar{t}$ is forbidden because the Higgs mass is well below two top masses. Nevertheless the top quark plays a fundamental role in the main Higgs production mechanism: the gluon-gluon fusion, see Figure 1.6, that involves a loop in which the top-quark gives the main contribution.

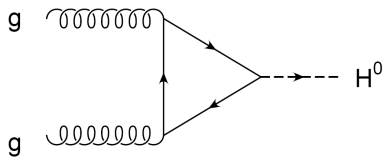

Figure 1.6: Feynman diagram of Higgs production through gluon-gluon fusion.

1.2 Top Quark

The top quark was looked for since the introduction of a third quark family by Kobayashi and Maskawa in 1973 [20] to describe the CP violation in the weak interaction. Due to its large mass, the experimental observation of the top quark required more than two decades and many progresses in particle accelerator technique. The discovery was made by the experiments CDF and DØ at Fermilab's Tevatron, a proton anti-proton collider working at a center of mass energy $\sqrt{s} = 1.96$ TeV.

[2]Probability of a particle to decay in a certain channel.

[3]The Higgs boson mass has been measured by ATLAS and CMS to be $m_H = 125.09 \pm 0.21 \pm 0.11$ [26].

1.2.1 Top Quark Mass

The top quark is the heaviest particle of the SM, its mass is comparable to the mass of a Rhenium atom (atomic number Z=75). This characteristic is fundamental in the study of top quark properties as the large mass drives all its phenomenology. The top is the only quark that can decay to a W boson on-shell, therefore it has a really short lifetime $\tau \sim 10^{-24}$ s, ($\tau = \hbar/\Gamma, \Gamma = 1.41^{+0.19}_{-0.15}$ GeV [18]), an order of magnitude lower than the average time for hadron formation. Consequently, the top quark can be directly reconstructed from its decay products and gives the opportunity to study the properties of a bare quark, including effects due to its spin, which produce angular correlations among its decay products.
There are several techniques to measure the top quark mass (m^t), both direct and indirect. The direct techniques perform the measurement exploiting the kinematic of the decay products of the top quark, while the indirect techniques exploit the theoretical relation between the $t\bar{t}$ cross-section and the top quark mass.

- **Direct Techniques:** the most widespread technique to measure the top mass is the *template method*. An example of a measurement performed using this method by the CDF collaboration can be found in [27]. In this case probability density function (templates) for observable sensible to m^t are defined from the Monte Carlo simulations. Successively the templates are used in a maximum-likelihood fit to the data which allows extract the m^t together with possible additional parameters, used to reduce the experimental uncertainty. Other direct techniques include the *matrix element* [29] and

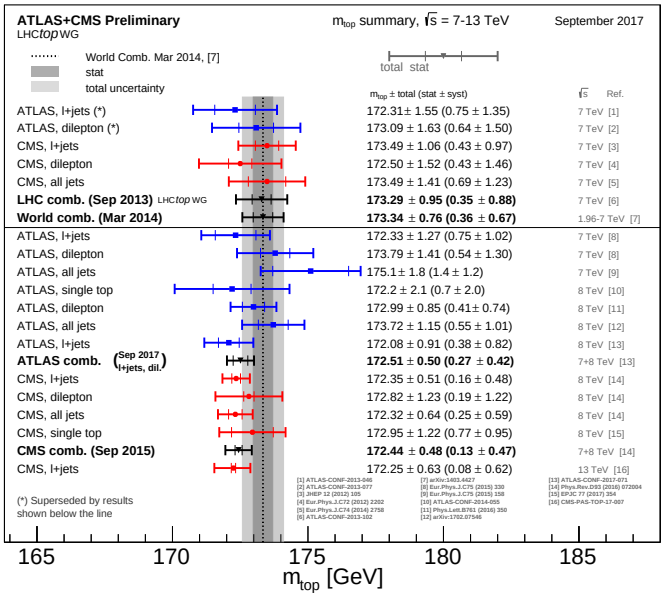

Figure 1.7: Summary of the ATLAS and CMS direct m^t measurements. The figure shows the latest results, as well as previous results that are now superseded. The results are compared with LHC and Tevatron+LHC combination [28].

the *ideogram method* [30]. The first method was introduced to reduce the statistical uncertainty and is based on the likelihood of observing a sample of selected events, obtained as the product of single event likelihood derived from theory. The ideogram method is a combination of the template and matrix element used to extract the maximum amount of information on the top quark mass out of each $t\bar{t}$ candidate event. A summary of the latest direct measurements performed by ATLAS and CMS experiments, is reported in Figure 1.7 [28].

- **Indirect Techniques:** all the indirect methods measure the m^t_{MC}, that is the parameter representing the top quark mass in the MC used to build the templates and not the theoretical definition of the mass m^t_{pole} [31]. This definition requires a defined renormalisation scheme, used to define the parameters in the theoretical prediction. Quantitatively the two masses are expected to differ up to $O(1\text{ GeV})$ [32, 33]. The theoretical dependence of the production cross-section $\sigma_{t\bar{t}}$ from the m^t_{pole} can be exploited, by comparing the measured $\sigma_{t\bar{t}}$ with the corresponding theoretical prediction. The indirect measurements have the disadvantage to reach a lower precision with respect to direct measurements. Results form indirect measurements performed by ATLAS, CMS and DØ are reported in Figure 1.8 [34].

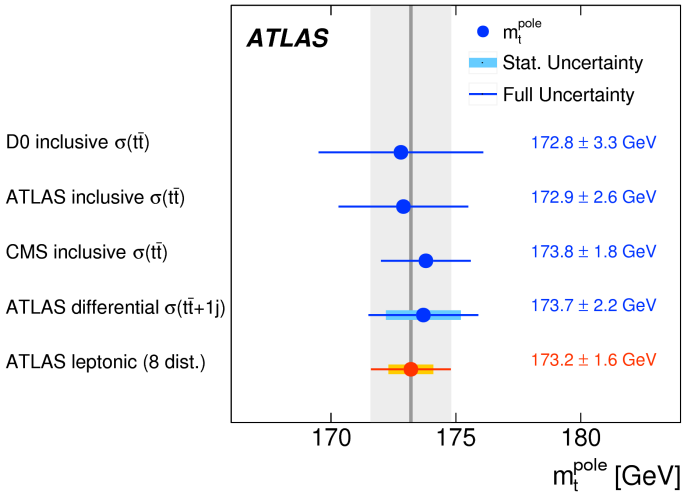

Figure 1.8: Summary of the measurements of the m^t_{pole} [34].

The top quark appears in higher order loop diagrams of the electroweak theory, so m^t is one of the most important parameters of the theory and is highly related to the masses of the W *boson* and of the Higgs *boson*. A comparison between the measurements of these three quantities can be interpreted as a powerful indirect test of the SM electroweak symmetry breaking.

1.3 Top Quark Production in Hadron Colliders

Top quarks are produced through two different mechanism in an hadron collider: generation of $t\bar{t}$ pairs through strong interactions or single top production through weak interaction. The expected rate of top quark production is evaluated through the cross-section calculation [17]:

$$\sigma_{pp\to tX} \propto \int \frac{|M|^2}{v_i} dQ \tag{1.5}$$

where M is the matrix element of the process, v_i is the speed of the incoming particle and dQ is the element of phase space.
In high energy hadron collisions, the matrix element is evaluated considering only the hard scattering between the components of the hadrons and not including the subsequent hadron formation. This factorization is possible due to the specific conditions that are verified in the collisions. At LHC energies, indeed, the partons during the collision behave as free particles and the uncertainty principle allows to separate the time interval of parton scattering, $\tau_{sc} \propto \frac{1}{p_T}$, and the hadronization time, $\tau_{had} \propto p_T$.

1.3.1 Top Quark Pair Production

In hadronic collisions at leading order, top quark pairs can be produced through the strong interaction with two different mechanisms: quark anti-quark annihilation and gluon-gluon fusion, whose Feynman diagrams are shown in Figure 1.9.

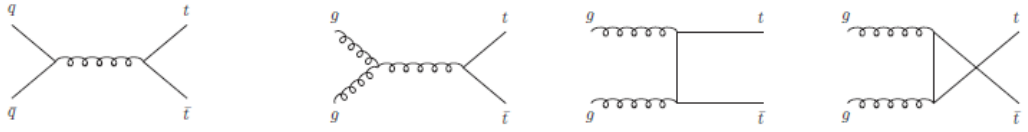

Figure 1.9: Leading order production diagrams of $t\bar{t}$ pairs.

The analytic expressions for the cross-section of the two partonic processes are [35]:

$$\frac{d\hat{\sigma}_{q\bar{q}\to t\bar{t}}}{dz} = \frac{\pi\alpha_S^2}{9s}\beta(2-(1-z^2)\beta) \tag{1.6}$$

$$\frac{d\hat{\sigma}_{gg\to t\bar{t}}}{dz} = \frac{\pi\alpha_S^2}{96s}\beta\frac{7+9z^2\beta^2}{(1-z^2\beta^2)^2}(1+2\beta^2-2z^2\beta^2-2\beta^4+2z^2\beta^4-z^4\beta^4) \tag{1.7}$$

where $s = 4E_{beam}^2$ is the square of the center of mass energy, $\beta = \sqrt{(1-4m_t^2/s)}$ is the top quark speed in the centre of mass system, m^t is the top quark mass, and $z = cos(\theta)$, where θ is the angle between the incoming parton and the outgoing top quark. These expressions are valid for the parton scattering, in order to evaluate

the full hadronic cross-section for top pair production in proton proton collisions is necessary to consider the parton distribution functions (PDF) $f(x)$ of the partons inside the hadron. The PDF $f_1(x_i)$ represents the probability of finding the parton i, inside the hadron 1, with a momentum fraction x of the total hadron momentum. The cross-section for $t\bar{t}$ production in hadron collisions can be written as a convolution of PDF and partonic cross-section $\hat{\sigma}$ [36]:

$$\sigma_{p_1p_2\to t\bar{t}}(s, m^t) = \sum_{i,j=q,\bar{q},g} \int dx_i dx_j f_1(x_i, \mu_f^2) f_2(x_j, \mu_f^2) \cdot \hat{\sigma}_{ij\to t\bar{t}}(\hat{s}, m^t, \mu_f, \mu_r, \alpha_s) \quad (1.8)$$

The sum runs over all partons (quark, anti-quark and gluons), and μ_f and μ_r are the factorization and renormalization scales, that are two cutoff needed to deal with infrared and ultraviolet divergences arising in finite order calculations. The dependence on these two parameters becomes weaker and weaker as higher orders are included in the perturbative calculation.

The relative importance of the two mechanisms of $t\bar{t}$ production depends on the

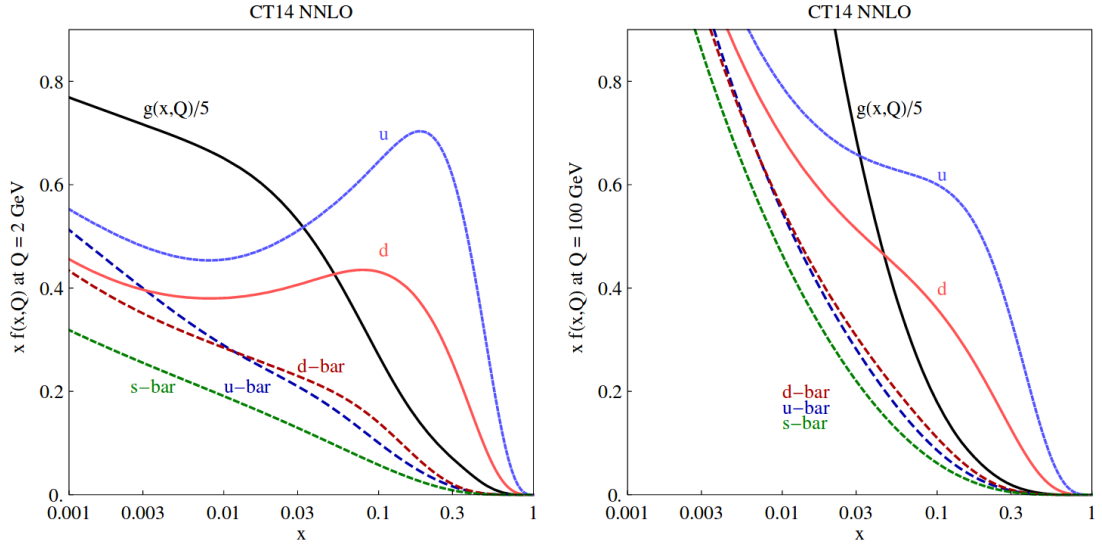

Figure 1.10: The CT14 parton distribution functions at $Q^2 = 2$ GeV and $Q^2 = 100$ GeV for $u, \bar{u}, d, \bar{d}, s$ and g [37].

PDFs inside the hadrons. At Tevatron, a proton anti-proton collider, the quark annihilation was the dominant process while at LHC, where there are two protons beams and the center of mass energy is higher, $\sim 90\%$ of the $t\bar{t}$ pair are produced through gluon-gluon fusion. At LHC most of the production involves sea partons while at Tevatron, due to the proton anti-proton initial state and the much lower centre of mass energy, the production is dominated by valence quark annihilation. Figure 1.10 shows the proton PDFs [37]. Indeed, at the energy of LHC, near the kinematic threshold for the $t\bar{t}$ production ($x \sim \frac{2m^t}{\sqrt{s}} = 0.03$) the gluon PDF is much higher than the one for the anti-quarks, consequently, the gluon fusion process becomes dominant with respect to the quark annihilation.

In $t\bar{t}$ production, higher order diagrams (NLO and NNLO) need to be considered when the theoretical predictions are compared to data since they give sizable contributions to the evaluation of the total production cross-section. This is due both to the relatively high value of α_s ($O(0.1)$) and to the large number of diagrams that enter in the calculations. Some examples of $t\bar{t}$ production diagrams at NLO with a real emission are reported in Figure 1.11.

The latest NNLO calculations for $\sigma_{t\bar{t}}$ at two different center of mass energies are

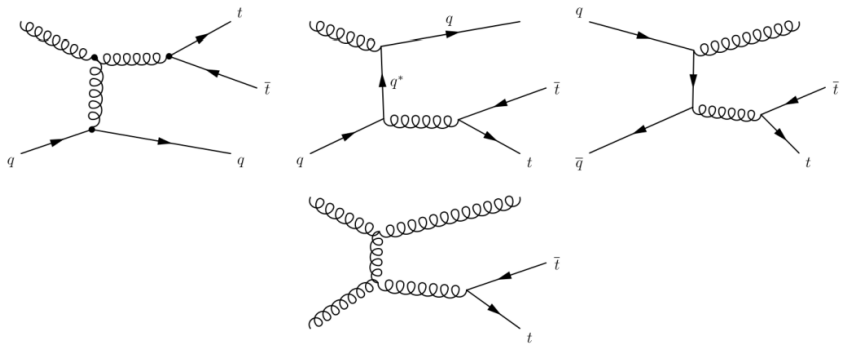

Figure 1.11: Examples of NLO diagrams for $t\bar{t}$ production.

reported in Table 1.3.

$\sqrt{s}$	$\sigma_{t\bar{t}}^{NNLO}$ (pb)	Scale uncertainty (pb)	PDF uncertainty (pb)
8 TeV	252.9	$+6.4$ -8.6	± 11.7
13 TeV	832	$+20$ -29	± 35

Table 1.3: In the table are reported the $\sigma_{t\bar{t}}$ at NNLO in perturbative QCD at two different center of mass energies. The calculation includes soft-gluon resummation to next-to-next-to-leading-log order [38], and assuming a $m^t = 172.5$ GeV. The first uncertainty comes from the independent variation of μ_f and μ_r, while the second one is associated to variations in the PDF and α_S, following the PDF4LHC prescription with the MSTW2008 68% CL NNLO, CT10 NNLO and NNPDF2.3 5f FFN PDF sets [39, 40, 41].

Status of Theoretical Prediction of Differential $t\bar{t}$ Production

Together with the inclusive $\sigma_{t\bar{t}}$, a stringent test of the pQCD is the measurement of the differential distributions of $\sigma_{t\bar{t}}$:

$$d\sigma_{pp\to tX} = \frac{|M|^2}{v_i} dQ \tag{1.9}$$

where the cross-section value $d\sigma_{pp\to tX}$ depends on the specific region of the phase space considered dQ. The precise measurement and calculation of differential cross-section allows to identify, in comparison with data, hints of new physics,

like for instance in the spectra of $\frac{d\sigma_{t\bar{t}}}{dm_{t\bar{t}}}$.
The inclusive $\sigma_{t\bar{t}}$ NNLO calculations agree very well with the measurements, while

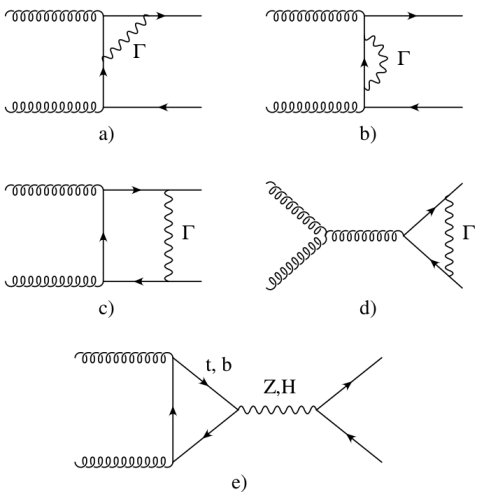

Figure 1.12: Sample diagrams for the virtual electroweak corrections. Γ stands for all contributions from gauge bosons, photons and Higgs exchange [43].

some differential distributions, as $\frac{d\sigma_{t\bar{t}}}{dp_T^t}$, show some tensions with the NLO theoretical predictions. In many searches for new physics, $t\bar{t}$ production represents the main source of background, consequently a discrepancy in the SM description of $t\bar{t}$ could hide the presence of new physics. For this reason, the improvement of the calculation of differential $\sigma_{t\bar{t}}$ has been one of the central theoretical problem in the top quark sector of the last years. Many progresses have been made toward a higher precision in the $\sigma_{t\bar{t}}$ calculation, to understand the reason of possible mis-modelling. One of the first corrections calculated on the NLO predictions are electroweak contributions [43]. Although the weak interactions are suppressed because of the small coupling, diagrams of order up to $\alpha_S^2\alpha_{EW}$ can give a sizable contribution to the total $\sigma_{t\bar{t}}$. The diagrams without a real emission of electroweak particles (virtual) lead to negative contributions, that can be large at high energy, where the gauge bosons Z and W behave as massless particles. Examples of these diagrams in $t\bar{t}$ production through gluon-gluon fusion are given in Figure 1.12.
A large difference between the measurement and the NLO predictions could come from higher order corrections, for this reason a great effort has been done to derive the NNLO predictions on differential distributions [44]. In Figure 1.13 the NNLO predictions are compared to LO and NLO predictions for the $\frac{d\sigma_{t\bar{t}}}{dp_T^t}$. The higher level predictions appears to predict a lower cross-section at high p_T. The error bands represent the uncertainty due to the variation by half and double of μ_r and μ_f, considered equal to m^t and independent from event kinematic. The NNLO predictions improve the agreement with the data, as shown in Figure 1.14a, where NNLO and NLO distributions are compared with $\sqrt{s} = 8$ TeV CMS measurement [45]. In the NNLO predictions there is also a significant reduction of the theoretical

uncertainty, due to the lower dependence on the scale choice.

Another significant improvement on the calculation is obtained with *boosted top resummation*. For top quark pairs with high p_T there are two components that could give a large contribution to the $\sigma_{t\bar{t}}$ and lead to divergences in the calculation: the soft-gluons emission and the gluons emitted nearly parallel to top quark. The formalism developed in [47] allows to parameterize the two effects at the same time, introducing some un-physical scale to the calculation, to remove divergences at a fixed order in perturbation theory. More details on this procedure can be found in [46]. The results of this calculation can be matched to the NLO predictions (NLO+NNLL') and allow to improve the agreement between the data and the theoretical expectations, as shown in Figure 1.15b, where the 8 TeV ATLAS measurement of $\frac{d\sigma_{t\bar{t}}}{dm_{t\bar{t}}}$ [48] is compared with the NLO prediction and with the NLO+NNLL'. This method reduces also the theoretical uncertainty with respect to the NLO predictions, as shown in the Figure 1.15a where ATLAS measurement of $\frac{d\sigma_{t\bar{t}}}{dp_T^t}$ for high p_T top quark [49] is compared with NLO and NLO+NNLL' calculations.

The NLO+NNLL' predictions are available also at $\sqrt{s} = 13$ TeV for $m_{t\bar{t}}$ and p_T^t, Figure 1.16, where the difference with NLO is enhanced with respect to 8 TeV calculations. Consequently, it is a main experimental goal to provide enough precise measurements at high-p_T to discriminate between the two theoretical predictions. The level of agreement with data reached with this resummation method is even better than that obtained using the NNLO corrections, as shown in Figure 1.14b, where the NNLO corrections are compared with the NLO+NNLL' ones and with

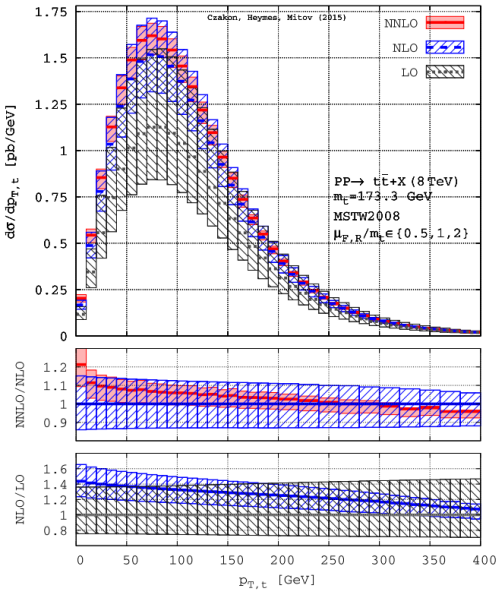

Figure 1.13: Comparison among LO, NLO and NNLO predictions on the $\frac{d\sigma_{t\bar{t}}}{dp_T^t}$. The bands represent the scale uncertainty associated to the three predictions [44].

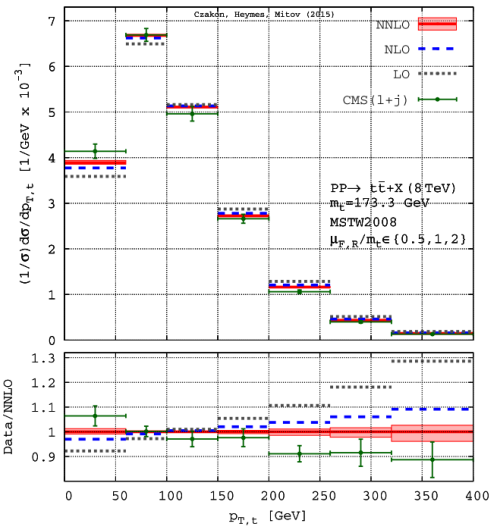

(a)

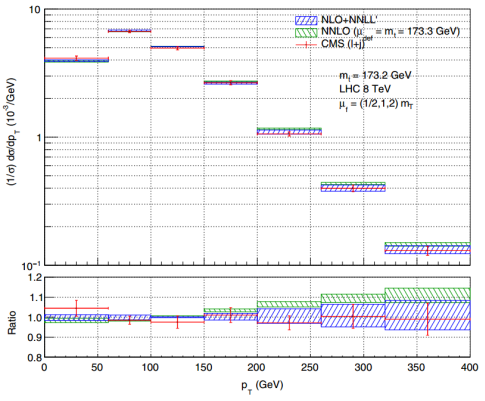

(b)

Figure 1.14: Comparison between boosted top resummation procedure (NLO+NNLL'), NNLO prediction and the measurement performed by CMS at $\sqrt{s} = 8$ TeV [45] on $\frac{d\sigma_{t\bar{t}}}{dp_T^t}$. In (a) the NLO prediction is compared with NNLO and LO [44], but only in the higher order distributions the error on the scale variations are shown. In (b) the NNLO prediction is compared with the NLO+NNLL' [46].

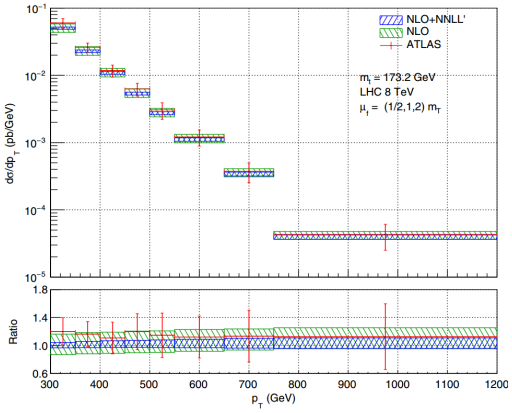

(a)

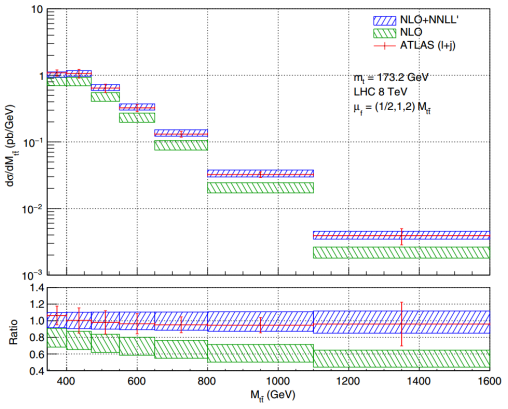

(b)

Figure 1.15: Comparison between *boosted top resummation* procedure (NLO+NNLL') and NLO calculation on $\frac{d\sigma_{t\bar{t}}}{dm_{t\bar{t}}}$ (b) and $\frac{d\sigma_{t\bar{t}}}{dp_T^t}$ (a) measurements performed by the ATLAS experiment at $\sqrt{s} = 8$ TeV [46].

the CMS measurement of $\frac{d\sigma_{t\bar{t}}}{dp_T^t}$ [45]. A significant difference between the two approaches is in the choice of the μ_r and μ_f scales. In the NNLO calculation the scales are fixed to the top mass while in *boosted top resummation* method μ_r and μ_f are dependent on the kinematic of the event (*dynamic scales*), this choice appears to be more suited to reproduce differential distributions, as shown in [50].

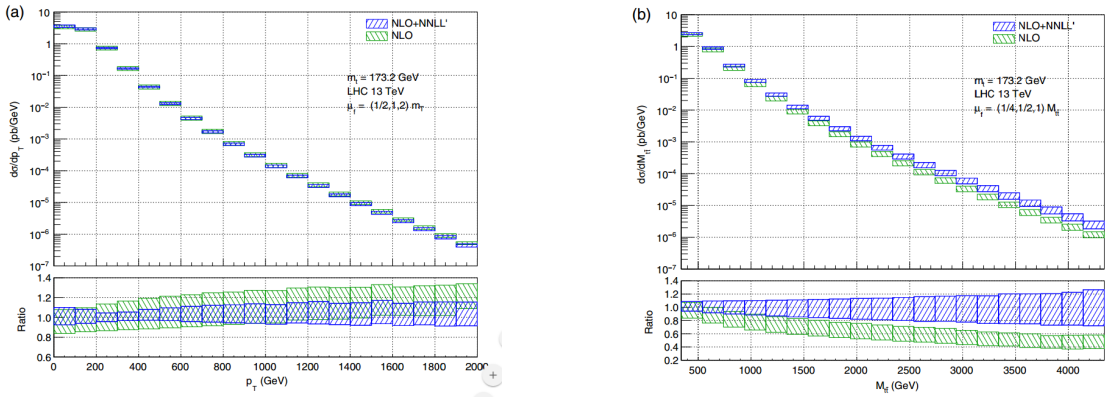

(a) (b)

Figure 1.16: Comparison between *boosted top resummation* procedure (NLO+NNLL') and NLO prediction on $\frac{d\sigma_{t\bar{t}}}{dm_{t\bar{t}}}$ (right) and $\frac{d\sigma_{t\bar{t}}}{dp_T^t}$ (left) at $\sqrt{s} = 13$ TeV [46]

1.3.2 Single Top Production

The single top production is mediated by weak interaction. The production rate of this process is suppressed with respect to pair production by a factor ~ 3, due to the difference between α_S and α_{EW}, partially compensated by the lower production threshold. Leading order Feynman diagrams of single top production are reported in Figure 1.17. The diagram (a) is called t-channel, (b) s-channel, (c) and (d), where the W production is real, are called Wt-channel.

The dominant diagram, both at LHC and Tevatron, is the t-channel. The second

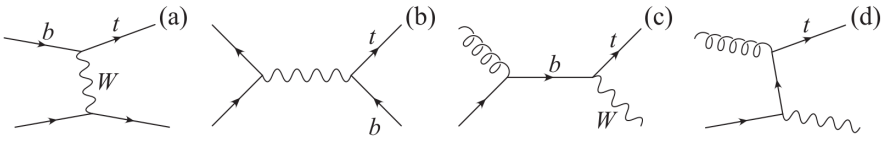

Figure 1.17: LO diagrams of single top quark production

channel, for production rate, at LHC is the Wt-channel, while at Tevatron was the s-channel. The NLO predictions for all single top production channels at $\sqrt{s} = 8$ and $\sqrt{s} = 13$ TeV at LHC are given in Table 1.4.

The single top production in Wt-channel represents one of the most important backgrounds in the measurements of the top pair production cross-section ($\sigma_{t\bar{t}}$), since the final state of this process is similar to the $t\bar{t}$ final state. Moreover, NLO Wt single top production diagrams are identical to LO $t\bar{t}$ production, where a top decayed as: $t\bar{t} \rightarrow \bar{t}Wb$, shown in Figure 1.18. The contribution of these diagrams is relevant in NLO σ_{Wt} calculation and several methods exist [53] to handle the overlap with $\sigma_{t\bar{t}}$, separate the two processes and avoid double counting when evaluating the prediction $pp \rightarrow WbWb$. In diagram removal, the amplitudes

Channel	σ_t at $\sqrt{s} = 8$ TeV	σ_t at $\sqrt{s} = 13$ TeV
t-channel	$84.69^{+3.76}_{-3.23}$ pb	$219.99^{+9.04}_{-7.71}$ pb
s-channel	$5.24^{+0.22}_{-0.20}$ pb	$10.32^{+0.40}_{-0.36}$ pb
Wt	22.37 ± 1.52 pb	71.7 ± 3.84 pb

Table 1.4: In the table are reported the cross-sections for the single top production (σ_t) process computed at NLO at $\sqrt{s} = 8$ and $\sqrt{s} = 13$ TeV calculated with [51, 52]. The calculations have been derived considering a top-quark mass of 172.5 GeV. The uncertainties include the scale and PDF uncertainties.

of doubly-resonant diagrams are set to zero, which also removes the interference term. Another method, called diagram subtraction, preserves the interference but cause an enhancement of the uncertainties related to the theoretical calculation.

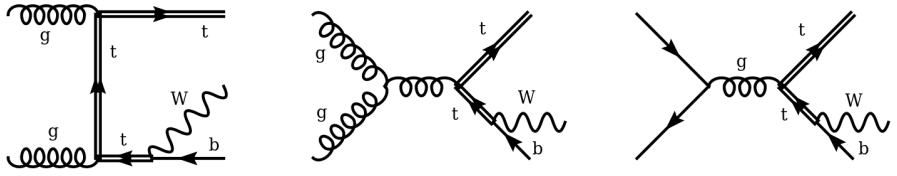

Figure 1.18: Examples of the interference diagrams between the Wt and $t\bar{t}$ production. The doubled line represent the top-quark.

1.4 Top Quark Production Measurements

The cross-section, from an experimental point of view, is defined as:

$$\sigma = \frac{N_{obs}}{\int Ldt \cdot \epsilon} \tag{1.10}$$

where N_{obs} is the number of selected events, L is the luminosity and ϵ is the efficiency of the detector and the selection applied on the collected events. In equation (1.10) the luminosity is integrated over the period of the data acquisition and it is called integrated luminosity. The instantaneous luminosity depends on the features of the collider, as will be described in Chapter 2. The efficiency is determined through Monte Carlo simulations described in Chapter 3.

In the last years, thanks to advanced NNLO or NLO+NNLL calculation techniques, the precision reached on the theoretical predictions is highly increased. Consequently, the measurements of the integrated and differential $t\bar{t}$ production cross-section have acquired a relevant role as test of the level of knowledge on perturbative QCD. Moreover, accurate measurements allow to discriminate between

different predictions and individuate deviations from the expectations. The differential cross-section measurements, in particular, are used to tune the parameters of the Monte Carlo generators at NLO, in order to increase the agreement with the data in particular regions of the phase space and to reduce the uncertainties related to the simulations, that affect many measurements and searches for new physics. The results presented in this thesis have been already used to tune a particular parameter that regulates the amount of radiation emitted from the $t\bar{t}$ system (h_{damp}), as shown in Figure 1.19. Here the measured $d\sigma_{t\bar{t}}/dm^{t\bar{t}}$ is compared with NLO predictions differing for the value of h_{damp}. The value $h_{damp} = 1.5m_{top}$ shows better agreement and is the new nominal value used in ATLAS for MC production. Moreover, the differential distributions can be used to extract QCD parameters as

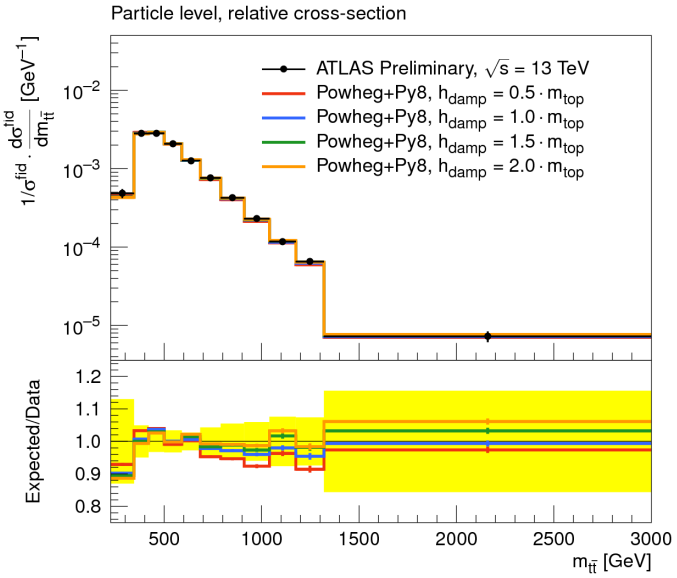

Figure 1.19: Comparison between the $d\sigma_{t\bar{t}}/dm^{t\bar{t}}$ measured from ATLAS collaboration at $\sqrt{s} = 13$ TeV in the semi-leptonic channel and various NLO predictions, differing for the h_{damp} value employed in the simulation [54].

α_S or m^t. The extraction of these parameters is performed comparing the obtained measurement with various predictions at NNLO. The differential distributions of $\sigma_{t\bar{t}}$ are also included in the global fits used to derive the gluon PDFs inside the protons.

1.4.1 Top Pair Production Cross Section Measurements

The top quark has a lifetime of $\sim 10^{-25}$s and consequently can't be directly observed by any detector. The only way to access the information on top quark is detecting its decay products. The top quark decays in 99% of the cases in a W and a b quark, so the detector signature of the $t\bar{t}$ is determined by the decay of the two W in the event ($t\bar{t} \rightarrow bW^+\bar{b}W^-$).

The final states of $t\bar{t}$ decay are divided in three categories:

- **All hadronic**: both the W decay in quark anti-quark pairs ($W \to q\bar{q}'$). The detector signature of these events is composed by 6 jets that derive from the hadronization of the quarks. The branching ratio (BR)[4] of this final state is 45.7% [18]. The disadvantage of this channel is the difficulty to discriminate the $t\bar{t}$ from the overwhelming amount of multi-jet background.

- **Di-leptonic**: both the W decay in leptons ($W \to l\nu$). The detector signature of these events is composed by 2 high energy, isolated leptons, 2 jets coming from b-quark hadronization, and missing energy in the transverse plane due to the presence of 2 neutrinos, that can't be directly detected. The BR of this final state is 10.5% [18]. This channel is easy to identify because the presence of the leptons allows to discriminate the signal from backgrounds.

- **Semi-leptonic**: one W decays in leptons while the other decays in hadrons. The detector signature of these events is composed by 1 high energy, isolated lepton, missing energy in the transverse plane, and 4 jets. The BR of this final state is 43.8% [18]. This is called *golden channel* because the presence of the lepton allows to easily trigger the event and separate the signal from multi-jet background, and at the same time, the statistics is high since almost half of the $t\bar{t}$ pairs decay in this channel. Moreover, the presence of a single neutrino in the event, associated to the missing transverse energy, allows to completely close the kinematic of the event by imposing the W mass constraint to the l, ν pair. Since τ identification and reconstruction is more complicated with respect to e and μ, many analysis consider only final states including these two leptons. This reduce the branching ratio in single lepton channel by $\approx$ 15 %

Integrated Cross Section

The total $t\bar{t}$ production cross-section has been measured using many different channels.

In Figure 1.20a [28] the latest CMS and ATLAS measurements performed at $\sqrt{s} = 13$ TeV in different channels are compared with the NNLO predictions, all the results are in good agreement with the theoretical expectations. In Figure 1.20b [28] is reported a summary of all the measurements performed at Tevatron, ATLAS and CMS at different center of mass energies, also in this case the agreement with the NNLO theoretical calculation is within the error bands.

Differential Cross Section

Once established the agreement of pQCD calculation with the observed cross-section, precise measurements of the differential $d\sigma_{t\bar{t}}/dx$, where x is a kinematic

[4]The *branching ratio* is the fraction of particles which decay through a particular decay mode with respect to the total number of possible decays, it is defined as the ratio between the decay width in a particular channel i and the total width $\Gamma_i / \sum_i \Gamma_i$

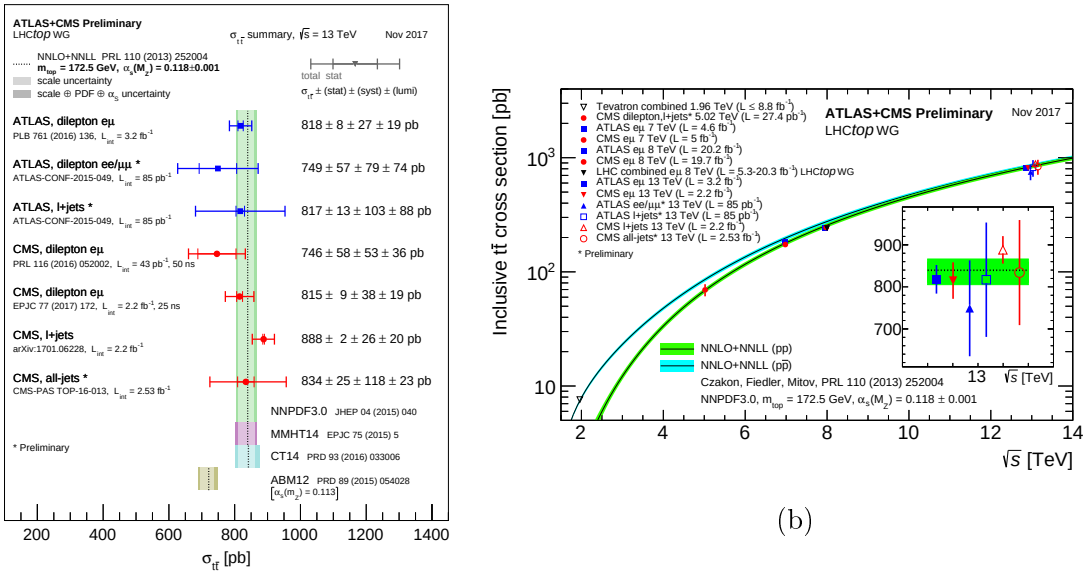

(a) (b)

Figure 1.20: Summary of measurements of $\sigma_{t\bar{t}}$ compared to the exact NNLO QCD calculation. The band on theoretical calculations represents uncertainties due to renormalisation and factorisation scale choice, parton density functions and α_S. In (a) the center of mass energy is $\sqrt{s} = 13$ TeV and the measurement are compared also with predictions using different set of PDFs, while in (b) a summary measurement at different center of mass energy is given [28].

quantity describing the $t\bar{t}$ system, can be used to further constrain pQCD predictions and to identify possible signals of new physics, that could hide in limited regions of the phase space and modify the shape of some kinematic distribution without necessary increase the total $\sigma_{t\bar{t}}$.
The differential cross-section can be expressed as a function of efficiency ϵ_i and of the number of selected events (N^i) in certain interval i of the measured variable x:

$$\frac{d\sigma_{t\bar{t}}}{dx} = \frac{N^i}{\epsilon^i \Delta_x^i \int Ldt}, \tag{1.11}$$

where $\int Ldt$ is the integrated luminosity, the superscript i indicates a bin of the x variable and the Δ^i the bin width.
Both ATLAS and CMS provided an exceptional number of interesting results in measuring $d\sigma_{t\bar{t}}/dx$ for a lot of variables, in many channels, at different center of mass energies and luminosity. Hereafter only the latest measurements in the $l+jets$ channel, the one studied in this thesis, are shown.
The differential cross-section can be measured in the whole phase space (at *parton level)*, or in a fiducial phase space (at *particle level*), where objects analogous to the reconstructed ones are built from stable particles produced by the Monte Carlo generators. The particle level selection is performed applying fiducial cuts that

mimic the requirements applied during the event identification and reconstruction in order to reduce the uncertainty due to the extrapolation in phase-space regions not measured by the detector. A meaningful comparison between ATLAS and CMS measurements can be performed only for *parton level* distributions, because the *particle level* phase-space differ between the two experiments. Both experiments

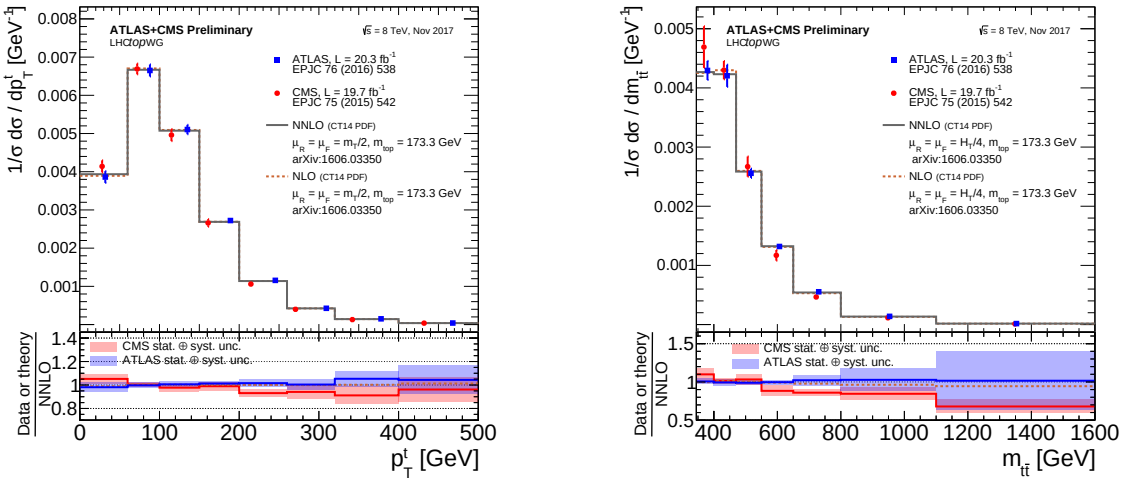

Figure 1.21: Comparison between $\frac{d\sigma_{t\bar{t}}}{dp_T^t}$ (left) and $\frac{d\sigma_{t\bar{t}}}{dm_{t\bar{t}}}$ (right) measured by ATLAS and CMS and the NLO and NNLO predictions [28]. The lower panel shows the ratio of the data measurements and the NLO calculation to the NNLO calculation.

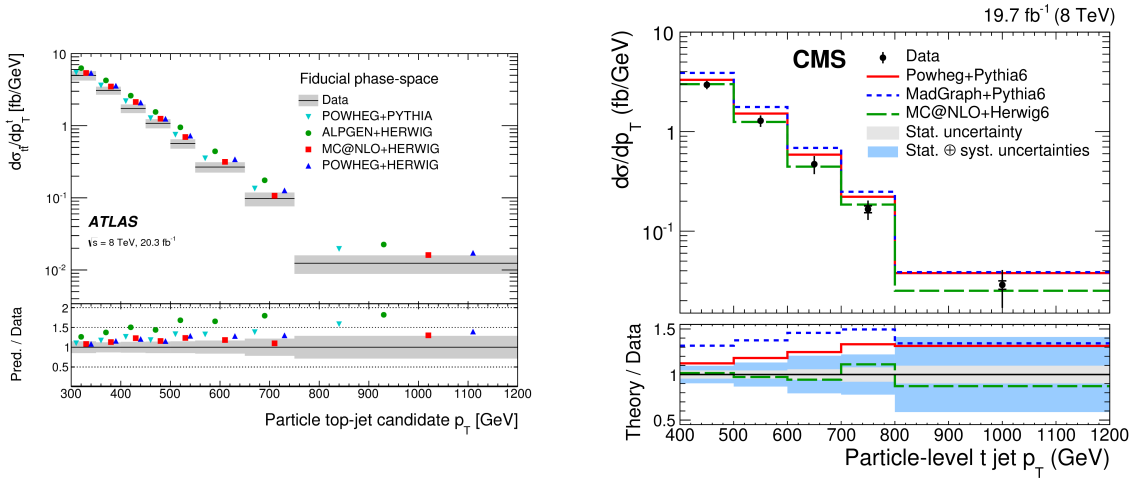

Figure 1.22: *Particle* level measurement of $\frac{d\sigma_{t\bar{t}}}{dp_T^t}$ in *boosted topology* performed by ATLAS [49] (left) and CMS [55] (right) experiment at $\sqrt{s} = 8$ TeV compared with NLO MC generators.

provided *particle* and *parton* level measurements of $d\sigma_{t\bar{t}}$ at $\sqrt{s} = 8$ TeV in $l + jets$ channel [45, 48]. The *parton* level comparison for a couple of variables between the two experiments and the NNLO prediction [28] is shown in Figure 1.21. The

comparison shows a good compatibility between the two measurements and the agreement between theoretical predictions and the ATLAS measurement seems improved by the NNLO calculations, however the large experimental uncertainty prevents a good discrimination between the NLO and NNLO predictions.
ATLAS and CMS experiments also provided measurements at $\sqrt{s} = 8$ TeV in the $l + jets$ channel, optimized to select high-p_T top quarks [49], [55]. In these events, presenting the so called boosted topology, the three jets deriving from the top decaying hadronically are more collimated and may partially overlap, so the top reconstruction and identification techniques need to be modified to increase the selection efficiency in this particular phase space region. In Figure 1.22 the *particle*

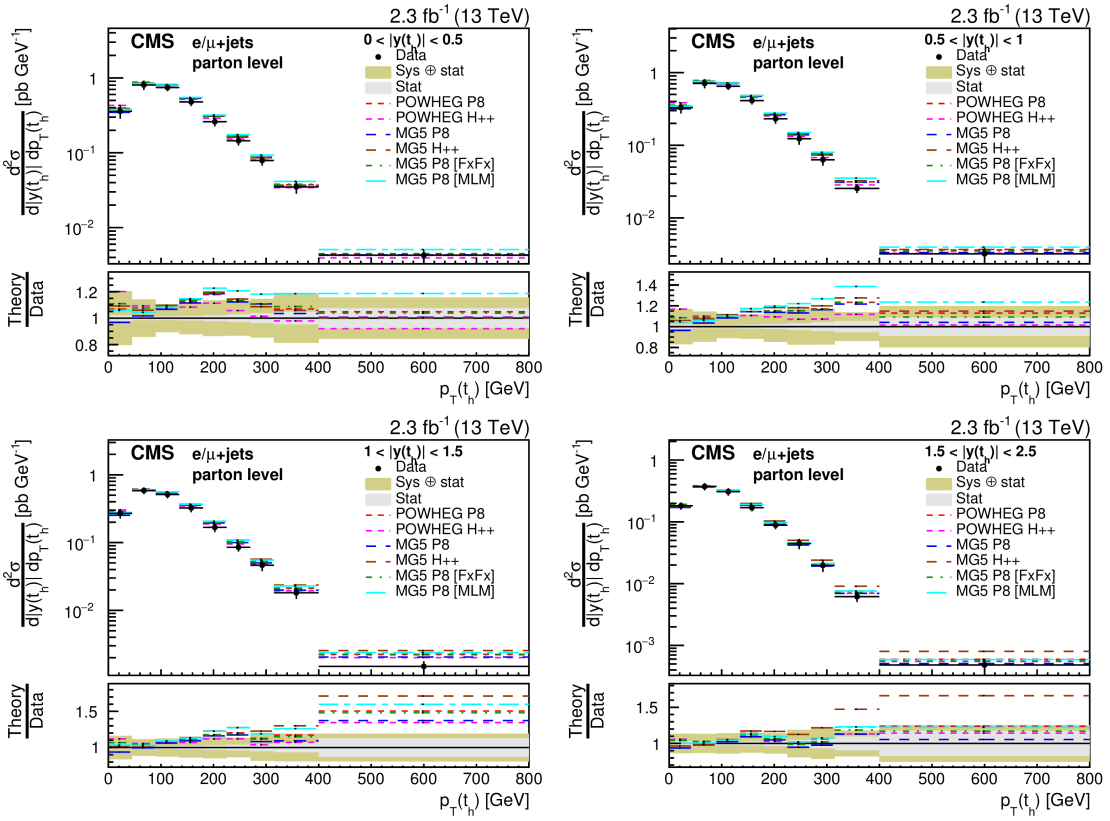

Figure 1.23: Double-differential cross-sections at parton level as a function of $|y^t|$ vs. p_T^t. The measurements are compared to the predictions of POWHEG and MG5-MC@NLO (MG5) combined with PYTHIA8 (P8) or HERWIG++ (H++) and the multi-parton simulations MG5-MC@NLO +PYTHIA8 MLM and MG5-MC@NLO +PYTHIA8 FxFx. The ratios of the predictions to the measured cross-sections are shown at the bottom of each panel together with the statistical and systematic uncertainties of the measurement [56].

level results for the $\frac{d\sigma_{t\bar{t}}}{dp_T^t}$ are shown on the left for the ATLAS measurement and on the right for the CMS one, both the measurements are compared with NLO MC simulations. Both results show a tension between data and theoretical predictions.

The theoretical predictions seem harder than the measured $\sigma_{t\bar{t}}$ at high p_T, but the systematic and statistical uncertainties in this region are still too high to draw any firm conclusion. A better understanding of the level of agreement with the SM expectations and a more stringent comparison with different predictions and employing different PDF sets can be done using double differential distributions. A measurement exploiting these distributions has been presented by CMS using $\sqrt{s} = 13$ TeV data collected in 2015 [56]. The measurement of $\frac{d\sigma^2_{t\bar{t}}}{dp^t_T dy^t_T}$ is reported in Figure 1.23, and compared with several NLO predictions. The agreement between the data and the different MC simulations varies depending on the considered y^t_T region.

1.4.2 Status of Measurement of Single Top Production

The single top production is still a challenging area for experimental measurements, in particular when considering the s-channel, where the production cross-section at $\sqrt{s} = 8$ TeV is ~ 50 times lower than $t\bar{t}$ production, which is one of the largest source of background. A summary of the measurements performed by ATLAS and CMS in all the three single top production channels at $\sqrt{s} = 7, 8, 13$ TeV is reported in Figure 1.24 [28], where the measurements are compared with the latest theoretical predictions.

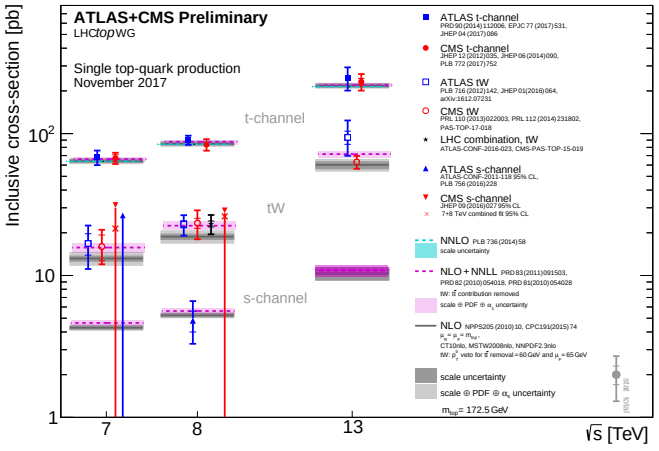

Figure 1.24: Summary of ATLAS and CMS measurements of the single top production cross-sections in the different channels as a function of the center of mass energies. The measurements are compared to theoretical calculations based on: NLO QCD, NLO QCD complemented with NNLL resummation and NNLO QCD (t-channel only) [28].

The measurements result compatible between CMS and ATLAS in all channels and in good agreement with the theoretical expectations.

1.5 Top quark and New Physics Models

In previous sections precise measurements and SM predictions for top production have been presented. A good understanding of the cross-section for $t\bar{t}$ production is fundamental in the search for new physics, both for direct search in the top sector and for a correct background estimation in many searches where the top quark production is the main source of background. After twenty two years from its discovery there are still many open questions raised by the top quark properties, in particular on the reason for its large mass, so different with respect to the other quarks. The large mass implies a high coupling with the Higgs boson and the reason for this bond is another open question that could have implications on the electroweak symmetry breaking mechanism.

There are many models of physics beyond the SM (BSM) that predict a strong interaction with the top quark that could modify the top coupling or the production cross-section. Many of these extensions of the SM predict new resonances decaying mainly in $t\bar{t}$ pair. These new resonances are modeled to have an *Higgs type* coupling, dependent on the mass of the fermions, and consequently coupling mainly with the top quark and decaying with a negligible rate to lighter fermions. Various models exist that predict scalar or pseudoscalar resonances and also color singlets or octets. There are also searches for spin-2 resonances, interpreted as Kaluza-Klein boson, introduced as gravity mediators in models that try to integrate this interaction in the SM. Many analysis have been performed both from ATLAS and CMS spanning on mass ranges from 1 to several TeV and also considering various width for the resonances [57, 58, 59]. The decay products of top deriving from a resonance with mass larger than 1 TeV tend to be collimated, and consequently, techniques developed for this particular phase space are necessary to assess limit on new particles production rate in these boosted regimes. An effect that is not yet studied in detail in these searches is the effect of the interference between the new physics signal and the standard model background. The incoming and outgoing

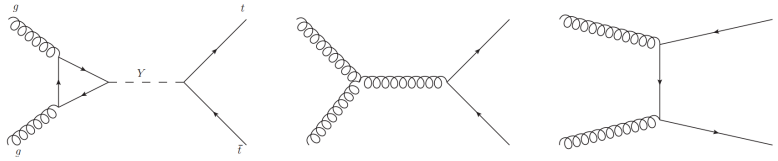

Figure 1.25: Comparison between BSM diagrams where a new resonance is created and SM diagrams.

particles of $t\bar{t}$ creation are the same in BSM and SM feynman diagrams, as shown in Figure 1.25, consequently the two processes are expected to interfere and the total cross-section for $t\bar{t}$ production becomes:

$$\sigma_{t\bar{t}} \propto |S|^2 + |B|^2 - 2\mathrm{Re}(S \cdot B), \tag{1.12}$$

where S and B represent the matrix elements for the signal only and the back-

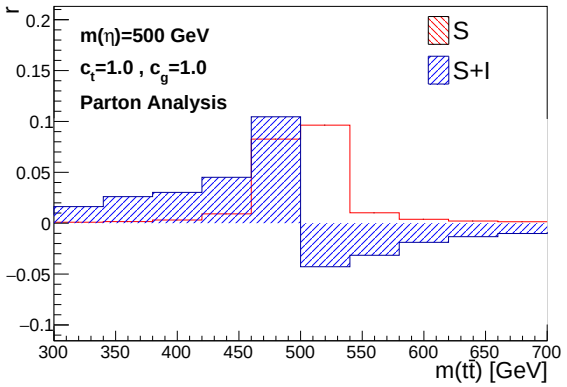

Figure 1.26: Difference in percentage between the only signal hypothesis, the signal plus interference hypothesis and the standard model prediction. In this case the considered signal is a pseudoscalar resonance with mass equal to 500 GeV [60].

ground only hypothesis, while the remaining term represents the interference. The interference component could have a constructive or destructive effect on the total cross-section and the importance of this term depends on the couplings of the model and the width of the resonance. These effects should be considered when deriving limit for new resonances, since including or not the interference term could lead to considerably different excluded regions. An example of the differences between the production cross-section considering or not the interference term in the production of a color singlet, pseudoscalar, resonance with $m = 500$ GeV is reported in Figure 1.26. The difference in percentage with respect to the background only hypothesis is shown. Depending on the mass of the $t\bar{t}$ system the interference can increase or decrease the production cross-section. More details on the effect of interference on the production cross-section for a scalar and pseudoscalar color-singlet resonance and a color octet resonance are reported in Appendix A.

Chapter 2

LHC and the ATLAS detector

The European Organization for Nuclear Research (CERN) is largest center for high energy physics research and is also one of the leading institutions driving the development of new detector technologies and computing facilities.
CERN was initially established in 1954 and is located astride the Franco-Swiss border in the Geneva region. At the moment it includes 25 member states and collaborates with many other nations all around the world. The main target of CERN is to explore the fundamental structure of nature, focusing mainly on the development and maintenance of particle accelerators experiments that allow to investigate a distance scale of 10^{-20} m. The largest accelerator facility actually located at CERN is the Large Hadron Collider (LHC), and the largest experiment located on his ring is the multi-purpose detector ATLAS.

2.1 LHC

The LHC is the latest accelerator built at CERN. With the circumference of 27 km LHC is designed to accelerate colliding proton beams up to a center of mass energy of $\sqrt{s}$ =14 TeV with a peak instantaneous luminosity $L = 10^{34}\text{cm}^{-2}\text{s}^{-1}$.
LHC first became operational in November 2009, and operated till 2012 with $\sqrt{s}$ = 7 and 8 TeV. After a three years upgrade LHC returned in operation in 2015 with the 2 protons beam accelerated up to $\sqrt{s}$ = 6.5 TeV each, and a peak luminosity of approximately $1.2 \cdot 10^{34}\text{cm}^{-2}\text{s}^{-1}$. The accelerating system consists of 16 radiofrequency cavities with a maximum electric field of 5.5 MV/m. The two proton beams are driven, in opposite directions, around the accelerator by a complex magnet system. The required magnetic field is of ≈8 T, and is provided by the 1232 electromagnets that, operating in superconducting state (temperature of 1.9 K), endure a circulating current of 11.85 kA. The focusing system consists of 392 superconducting magnets quadrupoles producing a 6.8 T field.
In the data collected in 2015 and used in this theses, the beams were structured in a maximum of ≈2400 bunches of protons separated in time by 25 ns. The

instantaneous luminosity of a collider can be calculated as [61]:

$$L = F\frac{kN^2 f\gamma}{4\pi\beta^*\epsilon} \tag{2.1}$$

where k is the number of colliding bunch pairs, N the numbers of particles contained in each bunch ($\approx 10^{11}$ protons), $f = 11.25$ kHz is the LHC revolution frequency, ϵ is the normalized emittance (independent from energy), β the amplitude function and γ is the relativistic factor. β^*, ϵ and γ are related to the beam width (σ) by the equation:

$$\sigma = \beta^*\epsilon/\gamma \tag{2.2}$$

. The transverse emittance is strictly related to the beam quality, following the beam preparation phase. A low emittance corresponds to a beam where the particles are confined to a small distance and have nearly the same momentum, for the LHC in 2015 was $\epsilon \approx 3.5\mu$m. The amplitude function is a beam optics quantity and is determined by the accelerator magnet configuration. F in equation (2.1) is a factor that account for geometric luminosity reductions due to the presence of the crossing angle among beams. An illustration of the change in the beam width in correspondence with the collision point, due to the action of the quadrupoles magnets, is shown in Figure 2.1.
An high luminosity has the advantage to increase the production frequency of physics events of interest. However, it has the drawback of increasing also the number of collisions per bunch-crossing, called in-time pile-up. The tracks derived from secondary vertices make more difficult the identification and reconstruction of events originating in interesting vertices. A second source of background derives from the out-of-time pileup, that increases reducing the spacing between different bunch crossing. This is due to the remnants of previous collisions, that remain in the detector because of the finite time required from the particles involved in a collision to develop inside the detector and to the capability of detectors readout.
Before entering in the LHC, the proton beams are accelerated up to 300 GeV by

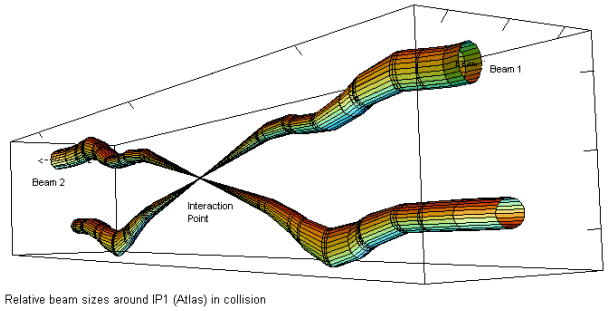

Figure 2.1: Illustration of the proton beams approaching the collision point inside the ATLAS detector. The beam width is reduced in proximity of the collision point to increase the instantaneous luminosity.

a sequence of accelerators: the linear accelerator (Linac2) and three synchrotrons,

Proton Synchrotron Booster (PSB), Proton Synchrotron (PS) and Super Proton Synchrotron (SPS). The accelerating chain of LHC is shown in Figure 2.2. The two

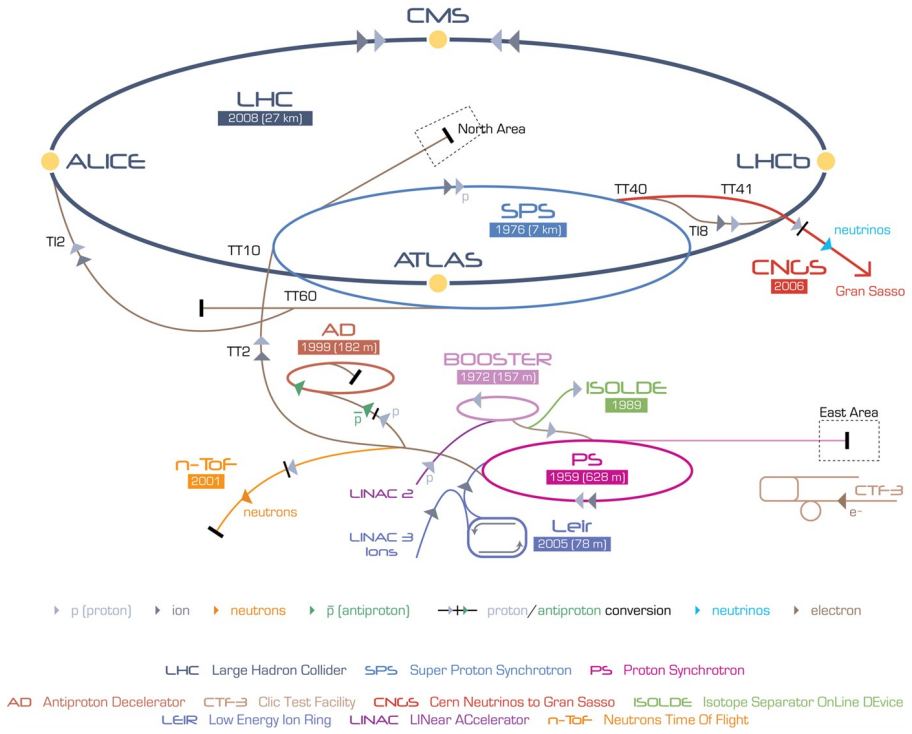

Figure 2.2: Illustration of the various accelerators composing the LHC injection chain. Before entering LHC the beams are accelerated from Linac2, PBS, PS and SPS. The illustration shows also the points where secondary beams are delivered to experiments located outside the LHC ring.

protons beams collide in four interaction points around the LHC ring, in each of this point is located a detector that aims for different physics targets:

- **ATLAS (A Toroidal LHC Apparatus)** is a multipurpose experiment built to perform precise measurements of the building blocks of Standard Model and to discover signature of new physics.

- **CMS (Compact Muon Spectrometer)** is the second multipurpose experiment and pursues the same physics goals as ATLAS, using different and complementary technologies.

- **LHCb,** has a completely different structure with respect to the other experiments and is designed with the main goal to perform accurate measurements on flavor physics of B mesons to explain the source of CP violation observed in nature.

- **ALICE (A Large Ion Collider Experiment)** is dedicated to the study of quark-gluon plasma. This experiment is designed to reconstruct and analyze

the collisions produced in LHC in some special runs were ion-ion or proton-ion beams are used.

2.2 The ATLAS Detector

ATLAS is a general purpose detector [62], that aims to exploit the full discovery potential of LHC, perform precise SM measurements and investigate the characteristics of the recent discovered Higgs boson. With a total length of 42 m, a radius of 11 m and a weight of 7000 tons ATLAS is the largest LHC experiment, shown in Figure 2.3. ATLAS has a cylindrical symmetry and is designed to be totally hermetic and handle high pile-up and luminosity conditions.

ATLAS uses a right-handed coordinate system with its origin at the nominal

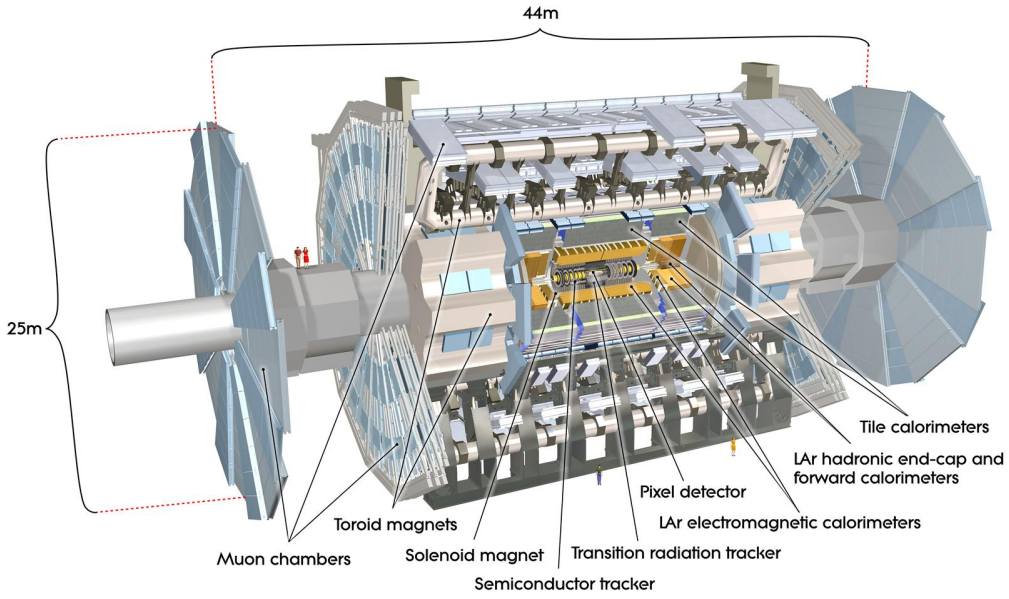

Figure 2.3: Overview of the ATLAS detector.

interaction point (IP) in the centre of the detector and the z-axis along the beam pipe. The x-axis points from the IP to the centre of the LHC ring, and the y-axis points upward. Cylindrical coordinates (r, ϕ) are used in the transverse plane, ϕ being the azimuthal angle around the z-axis. The pseudorapidity (η) is defined in terms of the polar angle θ as $\eta = -\ln\tan(\theta/2)$.

ATLAS is composed by many sub-detectors, that play different roles in the reconstruction of the various particles crossing the detector, as shown in Figure 2.4. The innermost layers compose the inner detector (ID) that serves as tracking system. It is immersed in a magnetic field of 2T generated from a solenoid, and reaches a coverage $|\eta| < 2.5$. The middle section of ATLAS is filled from the calorimetric system, that has an $|\eta|$ coverage up to 4.9. The calorimeters measure the energy of most of the particles and prevent them to enter in the outermost layer, the muon

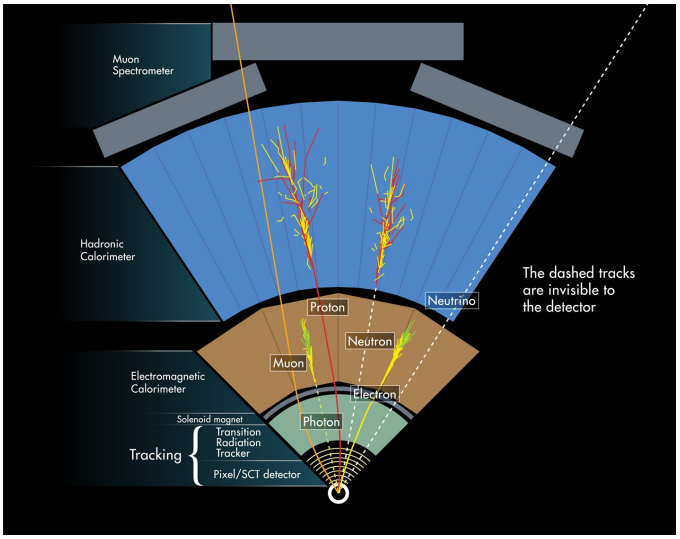

Figure 2.4: Illustration of an ATLAS section showing how each type of particle interact with a different sub-detector.

spectrometer (MS). The MS has a coverage $|\eta| < 2.7$ and is used for the identification and reconstructions of muons. In the following sections will be presented the main features of the ATLAS detector, important to understand the performances in the reconstruction of the complex final state of the semileptonic decay of the $t\bar{t}$ system.

2.2.1 The Inner Detector

The inner detector must be able to identify and reconstruct tracks and vertices in the dense environment of the LHC, where several protons can collide at the same time. The granularity of the inner detector has to be sufficient to discriminate the origin of the tracks and measure the bending of the particles, due to the magnetic field surrounding the ID. The ID is composed by three sub-sections: the silicon pixel detector, the micro-strip detector (SCT) and a straw-tube tracking detector (TRT), Figure 2.5. The detectors with higher granularity (pixels and SCT) are based on silicon technology and arranged on concentric cylinders around the beam axis. In the end-cap regions they are located on disks perpendicular to the beam axis. Figure 2.6 [63] shows the resolution of the inner detector during 2015 data-taking on the reconstructed longitudinal (z_0) and transverse (d_0) impact parameters of minimum bias tracks, as a function of the track p_T. d_0 is defined as the distance of closest approach of the track to the measured beam-line and z_0 as the distance along the beam-line between where d_0 is measured and the beam-spot position.

Pixel Detector

The pixel detector [65], is the nearest to the collision point and measures the particle impact parameters and the decay vertices of short living particles. The

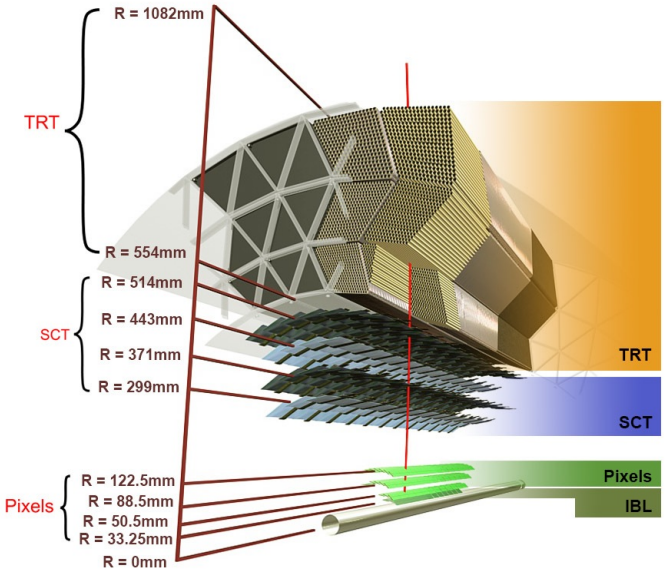

Figure 2.5: Sketch of the ATLAS inner detector showing all its components, including the new insertable B-layer (IBL). The distances to the interaction point are also shown [63].

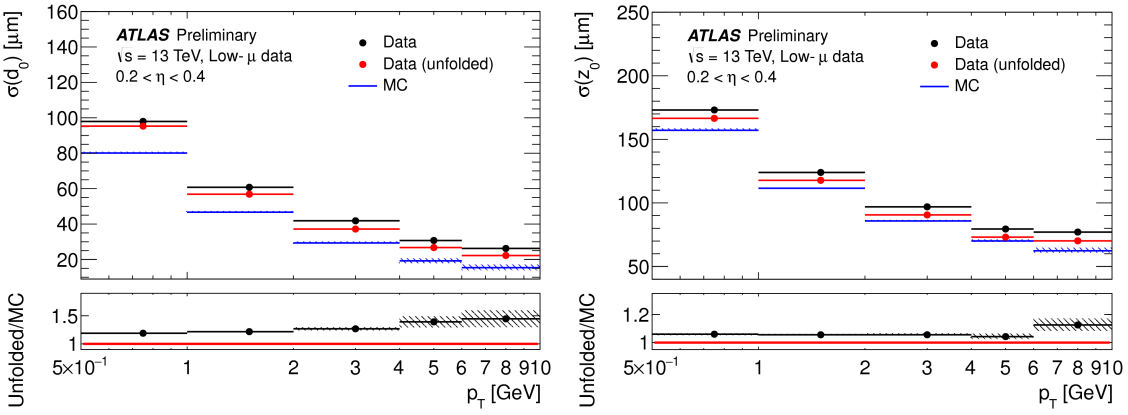

(a) (b)

Figure 2.6: Transverse (a) and longitudinal (b) impact parameter resolution measured in data as a function of p_T compared with the expectations from Monte Carlo simulations. The unfolded line (red) in the plots refers to data deconvoluted from the dependency on η and p_T of its reference point and has been obtained with the procedure described in [64]. The error on Monte Carlo simulation includes the statistical uncertainty and the non-closure of unfolded Monte Carlo data with respect to the true resolution known from simulation. The average number of interactions per bunch crossing for the used data set was about 0.005 [63].

pixel detector consists of 3 layers in the barrel and 3 in each end-cap composed by 1744 pixel modules, containing approximately 80 million pixels. The modules are the building blocks of the pixel detector and contain both the silicon sensors

and the front-end electronics. The size of the pixel sensors are determined by a compromise between physics requirements, that emphasize the R-ϕ resolution (<15 μm per point), and constraints on the electronics layout. This leads to pixels that have a length in R-ϕ direction of 50 μm. The z dimension is determined from the requirement of a resolution of $\approx$ 100 μm and is 400 μm for the larger part of the pixel sensors. The special pixels in the region between integrated circuits on a module have larger dimensions. The sensor parameters are strictly related to the electronics and to the noise threshold applied to consider a signal as coming from a particle crossing the detector. The charge collected from the sensors and the signal are represented by the time over threshold (ToT), that is the amount of time in which a sensor stays over threshold when crossed from a particle. The charge threshold for the pixel sensors is 3000e.

The modules are mounted on mechanical/cooling support called staves in the barrel region and disks in the end-cap. During the ATLAS upgrade between Run1 (2009-2012) and Run2 (2015-2018) a fourth innermost layer has been added, to increase the track and vertex reconstruction performances at the higher luminosity expected during Run2 and to mitigate the impact of radiation damage to the innermost layer of the pixel detector. The insertable B-layer (IBL) [66, 67] and a new beam pipe were installed in place of the original beam pipe inside the previous innermost pixel layer of the ID. The IBL consists of 14 staves instrumented with planar and 3D silicon pixel sensor technology along 332 mm on each side from the center of the ATLAS detector. The staves are arranged in turbine-like fashion, with an overlap in ϕ, and are mounted at an average radius of 35.7 mm. A representation of the ATLAS Pixel detector is shown in Figure 2.7. In Figure 2.7a is represented the ID during Run1, while in Figure 2.7b is shown the IBL inserted inside the innermost layer of Run1.

The charge carriers, liberated by the particles passing within the silicon, drift along the sensor thickness with an angle θ_L (Lorentz angle), determined by the relation $E \times B$ between the electric and magnetic field. The Lorentz effect produces a systematic shift between the position of the signal induced on the electrodes and the position of the track crossing point and needs to be considered during the reconstruction. Since in the end-cap region the electric field is parallel to the magnetic one this effect is significant only in the barrel.

The Micro-strip Detector

The second system composing the ID is the SemiConductor Tracker (SCT), that is designed to contribute to the measurement of the track direction and momentum, impact parameter and vertex position precision measurements in the intermediate radial range. The SCT barrel consists of four concentric layers of microstrip silicon wafers placed at a radius ranging from 30 to 51 cm from the beam axis, with full coverage in the region $|\eta| = 1.5$. Each end-cap region is composed by 9 SCT disks, covering up to $|\eta| = 2.5$. The disks are arranged such that there are always four levels of sensors crossed from particles trajectories. Each SCT module is made of two strip layers, each of which consists of two 6.4 cm long sensors with a strip

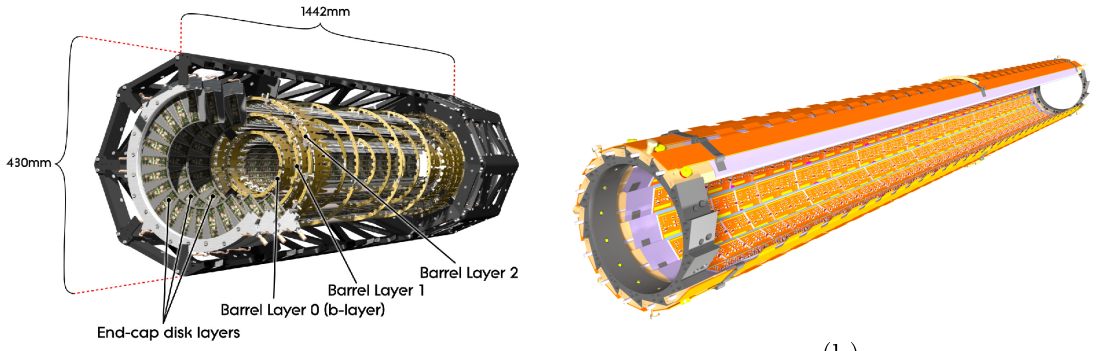

(a) (b)

Figure 2.7: In (a) schematic drawing of the ATLAS Pixel Detector. The detector comprises three concentric barrel layers and two end-caps with three disks each. In (b) Schematic drawing of the ATLAS IBL Detector. The single detector modules are mounted on carbon fibre support structures with incorporated CO_2 cooling circuits. [68]

pitch of 80 μm rotated of 40 mrad with respect to the other. This means that the information of couple of strip sensors are combined in a space point. The accuracies reached from strip sensors are 17 μm in the R-ϕ direction and 580 μm along z.

The Straw-tube Tracking Detector

The Transition Radiation Tracker (TRT) is the outermost system of the ID and combines drift tube chamber tracking capabilities with transition radiation detector power, that allows also electron/pion discrimination. The building blocks of the TRT system are composed by polyimide drift (straw) tubes of 4 mm diameter containing 31 μm diameter tungsten wires plated in gold, which are the anodes and are directly connected to the front-end electronics. The difference in potential between cathode and the anode is kept at 1530V.
The gap between the straw and the wire is filled by a gas mixture composed by 70% Xe, 27% CO_2 and 3% O_2. A charged particle crossing the detector induces by ionization a low energy signal on the anodes. At the same time, some particles with high momentum that transit from the gas to the polypropylene fibers cause the emission of radiations in the X-ray spectrum, absorbed by the Xe present in the gas mixture. This last process leads to an high energy signal that can be distinguished from ionization signal by the amplitude.

Particles crossing the TRT straw tubes originate $\approx$ 36 hits per track up to $|\eta|$ = 2.0, that corresponds to the coverage of this detector. The TRT only provides R - ϕ information with an intrinsic resolution of 130 μm, that is significantly lower with respect to the pixel and SCT detectors. In the barrel region, the straws are parallel to the beam axis and 144 cm long. In the end-cap region, the 37 cm long straws are arranged in wheels positioned, radially with respect to the beam pipe.

2.2.2 Magnetic System

The transverse momenta of the charged particles crossing the ATLAS detector is determined by measuring the track bending caused by a magnetic field. The ATLAS magnet system [69], illustrated in Figure 2.8, is composed by three toroids and a solenoid superconducting magnets that provide a magnetic field covering a volume of 12,000 m^3.

The solenoid is aligned with the beam axis and provides a constant 2T axial mag-

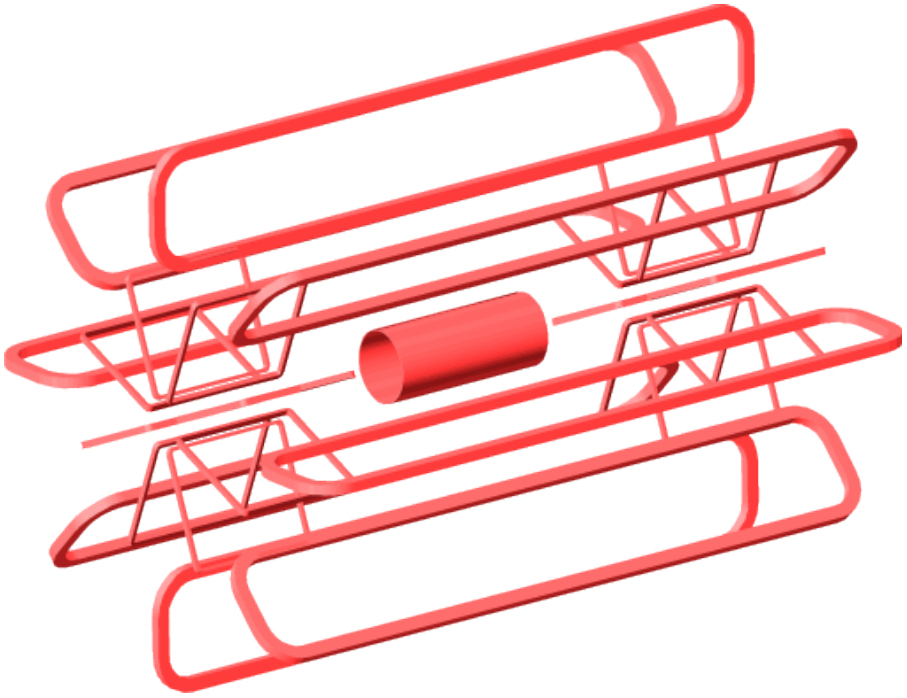

Figure 2.8: Representation of the ATLAS magnet geometry, showing the solenoid and the three toroid magnets.

netic field for the inner detector. The layout was carefully optimized to minimize the amount of material in front of the calorimetric system.

The air-core toroid system provide the magnetic field for the MS, it is composed by eight Barrel Toroids (BT) 25 m long, with an inner core of 9.4 m and an outer diameter of 20.1 m, and two End-Cap Toroids (ECT) 5 m long (inner core 1.64 m, outer diameter 10.7 m). The BT provides the particle bending in the region $|\eta| < 1$, while in $1.4 < |\eta| < 2.7$ charged tracks are bent by the ECTs. In the range $1 < |\eta| < 1.4$, called transition region, the magnetic field derives by a combination of BT and ECTs. This magnets configuration provides overall a $\simeq 3$ T field in the barrel and 6 in the end-cap, mostly orthogonal to the muon trajectories. All coils, to be superconducting, need to be kept at a temperature of $\approx$4K, and are therefore inserted in a vacuum system and cryostats for optimum thermal insulation.

2.2.3 Calorimetric System

The Calorimetric System is designed to trigger and precisely reconstruct all the neutral and charged particles producing a shower: electrons, photons and hadrons. Moreover the calorimeters play an important role in the reconstruction of the neutrinos as missing transverse energy, since they allow the measurement of the visible energy in the event in the plane transverse to the beam pipe.
The interaction of a particle with the material of a calorimeter produces a cascade of particles, called shower. There are two different type of showers, one produced from primary photons and electrons, called Electromagnetic shower, and the other deriving from various hadron sources, called Hadronic shower. The two types of showers are completely different in the composition and the type of interactions involved, this reflects in a different longitudinal and transverse evolution. Consequently two different technologies are needed to reconstruct with high precision the two types of showers. To reflect these differences the Calorimetric System is divided in two different sub-systems, the Hadronic (HC) and Electromagnetic (EC) calorimeter. The calorimeters are located outside the solenoid, and they occupy a large volume of the ATLAS detector. This is important to completely contain the showers, preventing to particles different from the muons to enter in the Muon Spectrometer (MS). The capability to fully contain the showers is a key aspect to perform precise measurements of particles' energy. The calorimeter thickness needed to reach a certain level of shower containment depends on the material and the type of its interaction with impacting particles. The radiation length (X_0) allows to quantify the necessary calorimeter thickness to build an hermetic detector. X_0 is defined as the average distance of material which must be traversed to reduce the energy of an electron to $1/e$ of the starting value. An analogue quantity introduced for the Hadronic shower is the nuclear interaction length defined as the mean length required to reduce the numbers of relativistic charged particles in the shower by the factor $1/e$.
The total thickness of the EC is more than 22 radiation lengths in the barrel and 24 in the end-caps, while the length of the HC is 9.7 interaction lengths (10 in the end-caps), sufficient to provide good resolution also for high-energy jets. The coverage of the calorimetric system reaches $|\eta| < 4.9$ and its structure is shown in Figure 2.9
Both the HC and EC are sampling calorimeters, meaning that they are composed by alternating layers of absorbing and active material. The absorbing material maximize the interaction with the particles, producing the electromagnetic and hadronic showers, while the active layer is used to measure the energy of the original particle. The advantage of the sampling calorimeters is that they provide an excellent shower containment with a limited calorimeter thickness, on the other hand, the precision of this type of detectors is reduced by the amount of energy lost in the absorbing material. The fraction of energy observed is defined as the sampling fraction $f_{scamp} = E_{active}/(E_{active} + E_{passive})$ and quantify the energy loss. The knowledge of the sampling fraction of a calorimeter allows to rescale the measured energy to account for the unobserved contribution. The energy resolution of

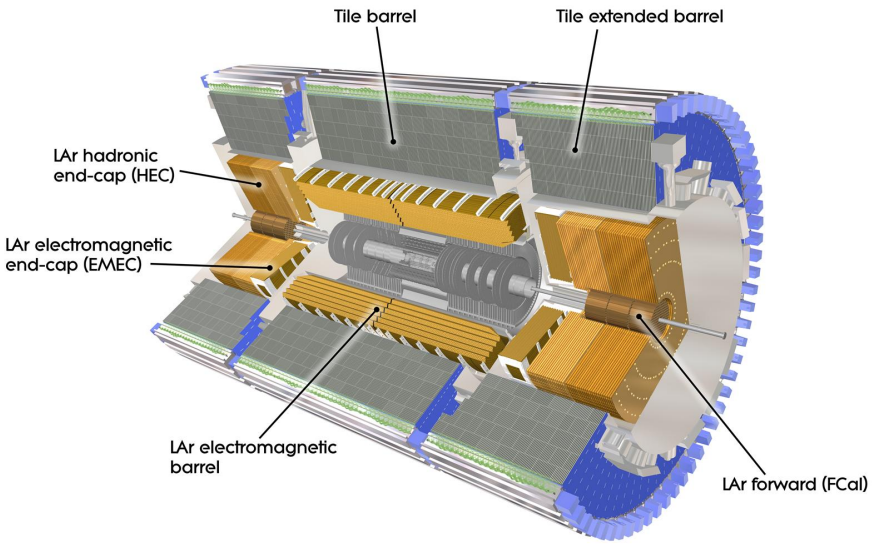

Figure 2.9: Sketch of the ATLAS calorimetric system.

a calorimeter may be calculated as:

$$\frac{\sigma(E)}{E} = \frac{a\%}{\sqrt{E}} \oplus \frac{b}{E} \oplus c\% \tag{2.3}$$

where E is in considered in GeV, a is the sampling term, b the noise term, and c the constant term accounting for local non-uniformities in the response of the calorimeter.

Electromagnetic Calorimeter

The absorbing part of the EC [62] [70] is made of lead, while the active part is liquid argon (LAr), chosen for its uniform nature, stability, and radiation-hardness. It is divided in two sections, the first reaching the $|\eta|$ =3.2 and with accordion geometry and a second with a compact design located in the forward region, described in the following.
The first section is composed by two coaxial wheels in each end-cap and by three active layers in the barrel. The granularity of each active layer is different, to reflect the different reconstruction needs. The first layer is divided in strips that allow a good resolution along η, necessary to resolve two close-by photons originated from a π^0 decay. The outermost layer collects the energy of the final part of the shower and therefore a broad granularity is sufficient.
The peculiar accordion geometry of the EC reduces the number of blind regions of the calorimeter, and provides full ϕ coverage. In the region $|\eta| < 1.8$ the calorimeter is preceded by a pre-sampler that allows to recover the energy lost in the cryostat and superconductive coils located between the ID and the EC. The transition region between the barrel and the endcap ($1.37<|\eta|<1.52$), called crack region, contains

a large amount of material necessary to the inner detector services. This is a source of energy loss that worsen the performance of electron reconstruction in this area. The particles passing through the calorimeter ionize the LAr and the freed electrons drift toward the copper electrodes, in approximately 450 ns. Since 450 ns cover a large number of bunch crossing, a shaping procedure is applied to the signal distributions to create a bipolar pulse signal with a much shorter readout time. A schematic representation of the EC calorimeter, in the barrel, is shown in Figure 2.10.

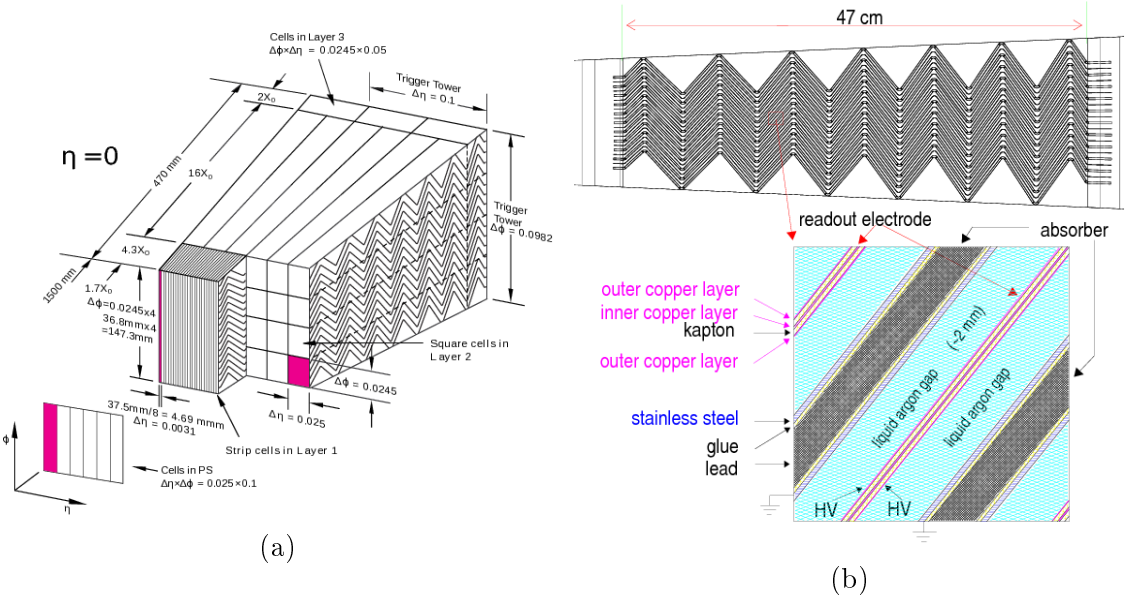

(a) (b)

Figure 2.10: Schematic representation of the EM calorimeter, in the barrel (a) [62] and detail of the accordion geometry in (b) [70]. In (a) is visible the granularity in η and ϕ of the cells of each of the three layers.

Hadronic Calorimeter

The central part of the HC is the tile calorimeter (TILECAL), placed directly outside the EM calorimeter envelope. Overall it covers a range $|\eta| < 1.7$ and it employs iron as absorber material and plastic scintillating tiles as active component. Photons are produced in proportion to the amount of energy deposited from particles crossing the scintillating tiles and the signal is collected by two wavelength-shifting fibres within each calorimeter cell. The tile calorimeter measures jet energies with a resolution $\Delta(E)/E = 40\%/\sqrt{E} \oplus 2.5\% \oplus 5/E\%$.

The Hadronic End-cap Calorimeter (HEC) is located directly behind the EM calorimeter end-caps and reach a coverage of $|\eta| = 3.2$, overlapping with the forward calorimeter. The HEC active medium is the liquid argon while the absorbing layers are made by copper, the detector is structured in two independent wheels for each end-cap.

Forward Calorimeters

The forward calorimeter (FCAL) has a coverage of $3.1 < |\eta| < 4.9$ and consists of three modules in each end-cap. The first is optimized for electromagnetic measurements and the other two, using tungsten as absorber, are useful predominantly for the measurement of the hadronic showers energy. The LAr forward calorimeter is integrated in the end-cap nearby the beam axis with the front face distant ≈ 1.2 m from the EM calorimeter. This calorimeter has to stand extremely high radiation levels and consists of copper rods parallel to the beam axis inside an outer tube filled of liquid Argon.

2.2.4 The Muon Spectrometer

The MS forms the outer part of the ATLAS detector. This is designed to detect charged particles exiting the calorimeters and to measure their momentum in the range $|\eta| < 2.7$.
A part from the shower that are not completely contained in the HC, the only SM particles that can reach the MS are the muons, that release only a small fraction of their energy in the calorimetric system.
For this reason the MS has a central role in the trigger of these particles in the region $|\eta| < 2.4$. The layout of the muon spectrometer is shown in Figure 2.11
The MS is integrated with a series of toroid magnets, placed outside the calorimet-

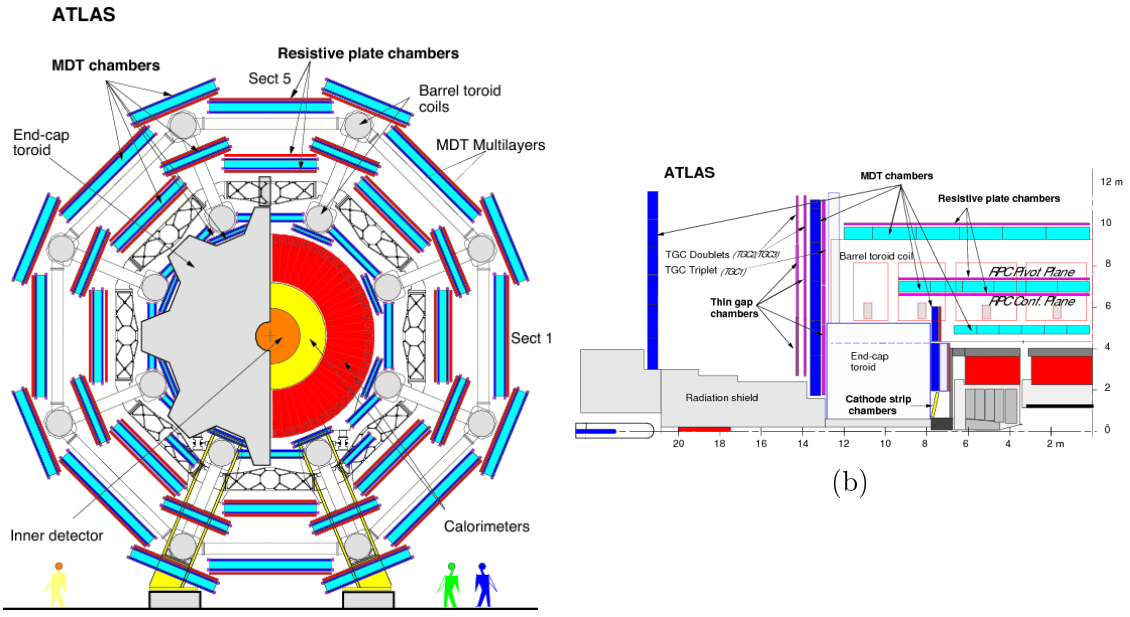

(a) (b)

Figure 2.11: Schematic representation of the muon spectrometer [71], in (a) projection in the $x - y$ direction while in (b) representation in the $z - y$ plane.

ric system, that allow to bend the particle trajectories and measure their momentum. The magnetic field is designed to be mostly orthogonal to the muon direction,

minimizing the multiple scattering, that would imply a degradation of resolution. In the barrel region, tracks are measured in chambers arranged in three cylindrical layers parallel to the beam axis; in the transition and end-cap regions, the chambers are installed in planes perpendicular to the beam.
The MS are composed by various sub-detectors.

- **The Monitored Drift Tubes (MDTs)** are installed on the full η coverage and provide precise measurements of the track coordinates in the principal bending direction of the magnetic field. The 1150 modules are organized into three layers in the barrel and four in the endcap. The maximum time to collect charge in the MDTs is 700ns, for this reason these detectors are suitable for precise measurements but too slow to be used as trigger. The spatial resolution reached by these chambers is 80 μm in the bending plane.

- **The Cathode Strip Chambers (CSCs)** are located in the innermost end-cap layer in the pseudorapidity range $2.0< |\eta| <2.7$ and consist in multiwire proportional chambers with cathodes segmented into strips. These have a smaller maximum collection time to withstand the demanding rate and background conditions and reach a spatial resolution of 60 μm in the bending plane.

- **The Resistive Plate Chambers (RPCs) and Thin Gap Chambers (TGCs)** are the fast muon detectors, providing a signal within 15-25 ns, providing the input to the trigger system. The RPCs are used in the barrel region, while the TGCs in the end-cap regions. The trigger chambers serve three main purposes: provide bunch-crossing identification, provide well-defined p_T thresholds, and measure the muon coordinate in the direction orthogonal to that determined by the MDT. The spatial resolution on the track position (η,ϕ) reached using these detectors is 5-10 mm.

The overall MS resolution for the measurement of the transverse momentum of a single muon varies between 3% and 12%, for p_T values between 10 GeV and 1000 GeV, but the spectrometer can measure muon momenta with adequate momentum resolution and excellent charge identification in the range between $\sim$ 3 GeV and $\sim$ 3 TeV. The coverage and functions of the sub-detectors in the MS are summarized in the Table 2.1 .

2.2.5 The Trigger System

It is impossible to store the huge amount of information contained in all the collisions in the ATLAS detector. The trigger system is designed to perform a fast reconstruction of some quantities of interest in the event, that are used to decide if the event should be rejected or stored for the offline analysis.

Muon Spectrometer	Performance
Monitored drift tubes	
- Coverage	$\|\eta\| < 2.7$ (innermost layer:$\|\eta\| < 2$)
- Function	Precision tracking
Cathode strip chambers	
- Coverage	$2.0 < \|\eta\| < 2.7$
- Function	Precision tracking
Resistive plate chambers	
- Coverage	$\|\eta\| < 1.05$
- Function	Triggering, second coordinate
Thin gap chambers	
- Coverage	$1.05 < \|\eta\| < 2.7$
- Function	Triggering, second coordinate

Table 2.1: Coverage and use of the various components of the MS.

During the Run1 the trigger [62] efficiently operated with an instantaneous luminosity of $8 \cdot 10^{33}$ $\mathrm{cm}^{-2}\mathrm{s}^{-1}$ and an energy in the center of mass varying from 900 GeV to 8 TeV. However, the increased energy and luminosity of Run2 required an upgrade of the trigger system to handle the increased event rate. The trigger system in Run2 is composed by 2 steps, the first is an hardware-based system, called Level-1 trigger, that has a decision time of 2.5 μs. The Level-1 trigger uses information from the MS and the calorimeter layers with coarser granularity to define regions of interest (RoI) in the detector and perform an initial selection on the events, reducing the event rate from ≈30 MHz to ≈100 kHz.
The Level-1 calorimeter trigger uses information both from the HC and EM to quickly reconstruct electrons, photons, taus, jets and missing transverse energy, using simplified techniques with respect to the full offline reconstruction.
The Level-1 muon trigger combine information from TGCs and RPCs to individuate the presence of a muon in the event. The information from the Level-1 trigger pass directly to the software-based high level trigger (HLT). The complex set of algorithms of the HLT analyze the information from the RoI and the full event, applying a reconstruction similar to the offline one in a process time of ≈200 ms. The event rate is reduced by the HLT from ≈100 kHz to ≈1 kHz, increased by more than a factor 2 with respect to the accepted rate in Run1 (400 Hz).
The trigger used to collect the events analyzed in this thesis are single leptons triggers. The HLT selects electrons using a likelihood-based identification which takes as input the electromagnetic shower shape and tracking information, with different working points: loose, medium and tight, with decreasing efficiency but increasing purity, corresponding to the reconstruction efficiency working point that will be described in Chapter 4. Figure 2.12a shows the efficiency of the combined Level-1

and HLT single electron e24_lhmedium_L1EM20VH trigger as a function of the E_T of electron candidates reconstructed offline. This trigger requires an electron candidate with $E_T > 24$ GeV satisfying the medium identification and is seeded by the Level-1 trigger L1_EM20VH, that applies an E_T dependent veto against energy deposited in the HC behind the electron candidates EM cluster. The non-sharp rise of the efficiency curve is due to the difference in the reconstruction applied offline and by the trigger software.
The muons reconstruction is performed at the HLT by combining the ID and MS tracks. The efficiency of the Level-1 L1MU15 trigger and the combination of HLT_mu20_iloose and HLT_mu50 are shown in Figure 2.12b, as a function of the p_T of the offline muon candidates in the barrel region. The L1MU15 trigger requires that a candidate passed the quality requirement of the Level-1 muon trigger system, based on the number of crossed sensors, and a p_T threshold of 15 GeV. The HLT_mu20_iloose and HLT_mu50 triggers are seeded by the L1MU15 and L1MU20, respectively. The first HLT selects only muon candidates that fulfills isolation requirements and has a p_T larger then 20 GeV, while the second one applies a threshold at 50 GeV.

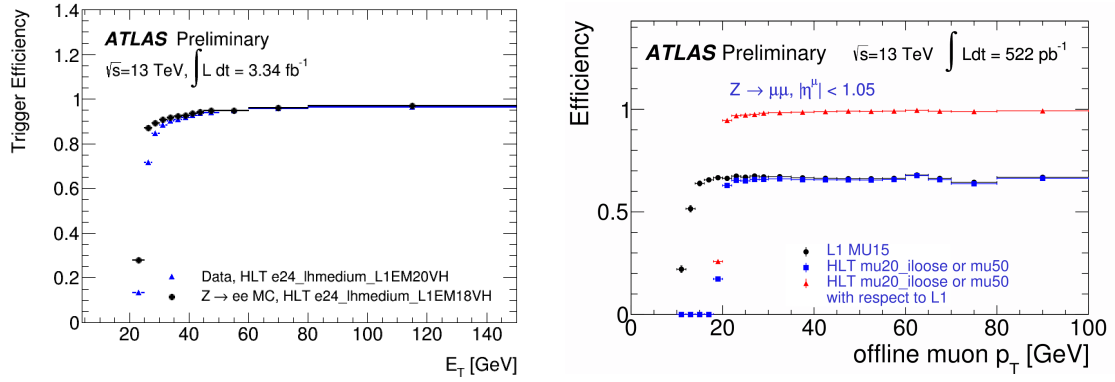

(a) (b)

Figure 2.12: Efficiency for the triggers used in the analysis for the electrons (a) [72], as a function of offline electrons E_T, and muons (b) [73], as a function of the offline p_T^μ. In (a) the efficiencies are obtained by a sample $Z \to ee$ and compared between data (blue) and simulations (black). In (b) the efficiency, calculated in a $Z \to \mu\mu$ is computed with respect to the offline medium muon candidate, defined in Chapter 4.

2.2.6 Luminosity Detectors

The integrated luminosity correlates the cross-section of a certain process with the observed number of events, therefore it has a crucial role in all ATLAS measurements.
In ATLAS there are four detector systems used for the luminosity measurement: LUCID (LUminosity Cherenkov Integrating Detector), BCM (Beam Conditions

Monitor), FCAL, and TILECAL, a redundancy that allows to mutually cross-check luminosity measurements and their stability over time.
In 2015 LUCID [74, 75] has been the preferred detector, used to provide the luminosity measurement.
LUCID is a Cherenkov detector formed by two identical sections, each one composed by 16 aluminum tubes filled with the C_4F_{10} gas and placed at a distance of 17 m from the interaction point. It is located around the beam pipe and covers a pseudorapidity range $5.6 < |\eta| < 6.0$. A charged particle passing through the gas emits photons due to the Cherenkov effect, these are reflected by the tube walls and collected by photomultipliers (PMTs) situated at the end of each tube. Additional Cherenkov photons are produced in the quartz window of the PMT, for a total of about 100 photoelectrons per incident charged particle. From the number of tubes with signal above threshold is possible to evaluate the average number of interactions per bunch crossing and extract the instantaneous luminosity. The BCM detector [76] is composed by two stations of detectors, each formed by four modules, and located symmetrically around the interaction point, at $z = \pm 184$ cm and $r = 55$ mm. The diamond sensors measure the instantaneous rates of collisions and average number of charged particles in the BCM, providing at the same time a luminosity measurement and beam monitoring, necessary to prevent detector damage.

Chapter 3

Data Sample and Monte Carlo Simulation

The measurement described in this thesis is performed on data collected from the ATLAS detector in proton proton collisions. At the same time several simulations are employed to evaluate the acceptance and efficiency of the detector and to estimate the various processes that could mimic the $t\bar{t}$ final state.
The first step of the simulation is the calculation of the expected cross-section for a particular process, that can be signal or background. Then the Monte Carlo (MC) simulation chain proceeds through several steps: the hard scatter simulation, the decay of unstable particles, the showering, the hadronization and the estimate of the underlying events.
While the initial theoretical calculation of the cross-section at a certain fixed perturbative order is unequivocally defined, various approaches and different approximations exist to analytically perform the calculation, generate the particles according to the evaluated cross-section, simulate the evolution of each particle and combine the colored partons to form hadrons. These differences reflect in a large number of Monte Carlo generators. Differences among the generators are used to estimate the impact of the theoretical uncertainties on the final measurement. In the following chapter the main steps of the Monte Carlo simulation will be described, together with the differences among the used generators.
The distributions obtained from the simulations (called truth-level predictions) represent the expected kinematic distributions for a particular process, without considering the effect of the limited resolution and acceptance of the experimental apparatus. To estimate these effects the simulated events are passed through a detailed simulation of the detector, obtained with GEANT4 [77, 78, 79]. The outcome event samples are completely analogous to the collision events recorded with ATLAS detector, and the distributions obtained with these samples after processing them with the same analysis chain used for real data, are called reco level or detector level predictions. The comparison between reco and truth level predictions on the same MC sample allows the calculation of all the identification and reconstruction efficiencies and appropriate scale factors must be applied when the MC is not able to perfectly reproduce effects determined on collisions data.

3.1 Data Sample

The measurement of $t\bar{t}$ production differential cross-section is performed on data collected in 2015 from the ATLAS detector in proton proton collisions at a center of mass energy $\sqrt{s}$ =13 TeV and a bunch spacing of 25 ns. The average number of pp collisions for each bunch crossing ranges approximately between 5 and 25, with an average of 14 interactions. Only data taken under stable beam conditions and with all the relevant sub-detectors fully operational are considered. The collected data correspond to an integrated luminosity of 3.2 fb^{-1}. In Figure 3.1 is shown the luminosity delivered by LHC (in green), collected by ATLAS (in yellow) and in blue are reported the classified good quality data.

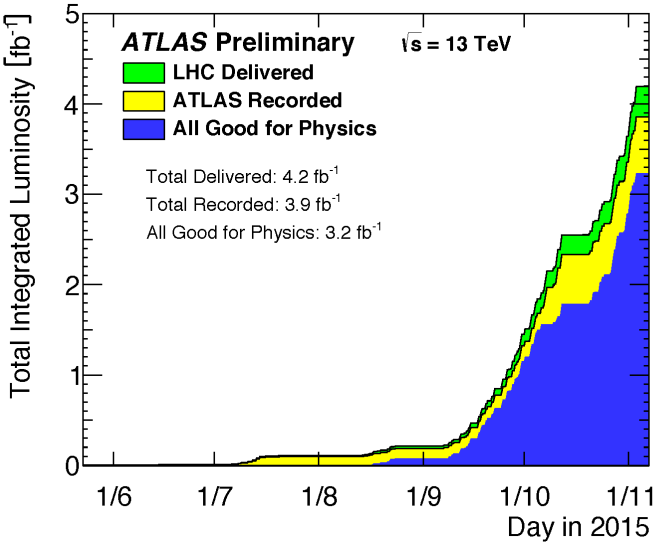

Figure 3.1: Cumulative luminosity versus time delivered to ATLAS (green), recorded by ATLAS (yellow), and certified to be good quality data (blue) during stable beams for pp collisions at 13 TeV centre-of-mass energy in 2015 [80].

The recorded luminosity differs from the delivered due to the DAQ (Data Acquisition System) inefficiency, as well as the inefficiency due to the time required from tracker to reach the optimal working point conditions.

3.2 Monte Carlo Simulation Chain

The expectation value for an observable O in a $pp \to X$ collision can be evaluated solving a complicated integral like:

$$\langle O \rangle = \sum_n \sum_Q \int d^{4n}\mathbf{p} |M_n(\mathbf{Q},\mathbf{p})|^2 O_n(\mathbf{Q},\mathbf{p}) \phi_n(\mathbf{p}), \tag{3.1}$$

where the sum runs on all the n initial partons and quantum numbers $\mathbf{Q}$. In equation (3.1) $\mathbf{p}$ indicates the momenta of the particles, ϕ the phase space density and

M the matrix element for the process calculated perturbatively at a fixed order in QCD (NNLO,NLO,LO).
A technique to solve complicated integrals is to introduce an appropriate probability function. For example calling $f(x)$ the function to integrate on the multi-dimensional dominion Ω is possible to re-write the integral including the function $p_X(x)$ with the property $p_X(x) > 0$ for each x belonging to the dominion Ω and 0 elsewhere:

$$I = \int_\Omega d^n x f(x) = \int_\Omega d^n x \frac{f(x)}{p_X(x)} p_X(x) \tag{3.2}$$

where Ω can be really complicated and $f(x)$ can have peaks and divergences. In equation (3.2) $p_X(x)$ is the probability function of the random variable X such as:

$$P(x^{(j)} < X^{(j)} < x^{(j)} + dx^{(j)}) = p_X(x) \tag{3.3}$$

Saying Y_i a generic random variable and g a function of this variable it is possible to write this relation between the expectation value $\langle g(Y)\rangle$ and the probability function of the random variable Y $p_Y(y)$:

$$\frac{1}{N}\sum_{i=1}^{N} g(Y_i) \sim \langle g(Y)\rangle = \int p_Y(y) g(y) dy \tag{3.4}$$

Consequently using relation (3.2) and (3.4) is possible to write:

$$\langle \frac{f(X)}{p_X(X)} \rangle = \int_\Omega d^n x \frac{f(x)}{p_X(x)} p_X(x) \tag{3.5}$$

and numerically estimate the integral (3.2), extracting N random points X_i and evaluating the average $\frac{f(X)}{p_X(X)}$.

The solution of the integral (3.1) is complicated not only analytically but also using numerical techniques since it is also to be considered that the matrix element can be calculated at high order of precision (NNLO,NLO) just for a limited number of particles, the determination of ϕ_n is not trivial, and to find an appropriate $p_X(x)$ can be really complicated.

The generation is divided in different steps that allow to simulate the full process: hard scattering, showering and hadronization. This splitting procedure, called factorization, can be applied only if the $\sigma_{pp\to X}$ is mainly determined by the hard partonic scattering and the following showering and hadronization happen at softer scales with a negligible effect on the evaluated cross-section.

The MC production chain can be visualized in Figure 3.2 [81]: the hard scatter simulation represents the first step, where the particles are generated according to the cross-section calculated for the partonic scattering. Successively the emissions and evolution of the particles is described in the step called showering; at this stage the remnants of the initial hadrons that did't participate to the hard scattering are included in the simulated event. The final steps are the hadronization, where the colored partons are merged in color singlet hadrons, and the decay of the un-stable hadrons.

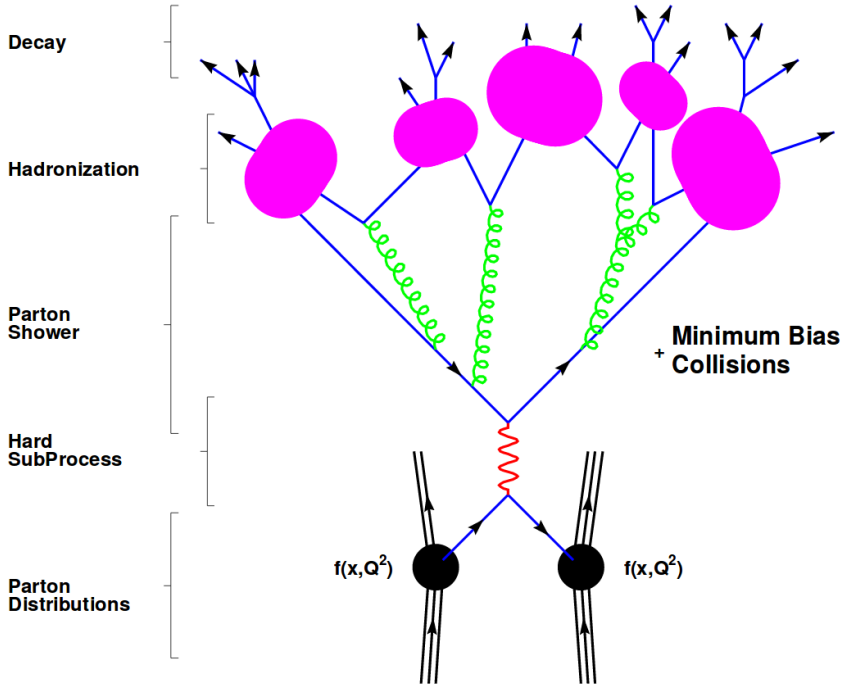

Figure 3.2: Different steps of the Monte Carlo event generation chain.

3.2.1 Hard Process: Matrix Element Generators

The simulation starts from the evaluation of a $2 \to$ n inclusive matrix element.

A certain process can be described from three components at NLO order of perturbation theory:

$$\sigma = \int_n \sigma^B + \int_n \sigma^V + \int_n \sigma^R. \tag{3.6}$$

The born (σ^B) and virtual components (σ^V) contains the diagrams with exactly n particles in the final state, the latter considers also diagrams at higher order in perturbation theory, including loops for example. The third component (σ^R) refers to the contributions of diagrams with a real emission, consequently with n+1 particles in the final state. Since the number of diagrams increases quickly with n, usually only few emissions are considered.

The matrix element calculators can be divided in tree level or NLO, depending on the components of equation (3.6) considered.

- **Tree level:** allows the computation of tree-level matrix elements with a fixed number of legs, virtual contributions are not considered.
- **NLO:** considers all the diagrams contributing to a certain process till a fixed order in α_S, including also the virtual contributions.

For many observables the LO description, that includes only the σ^B component, does not give an accurate description. In Figure 3.3, for example, the p_T^t measured

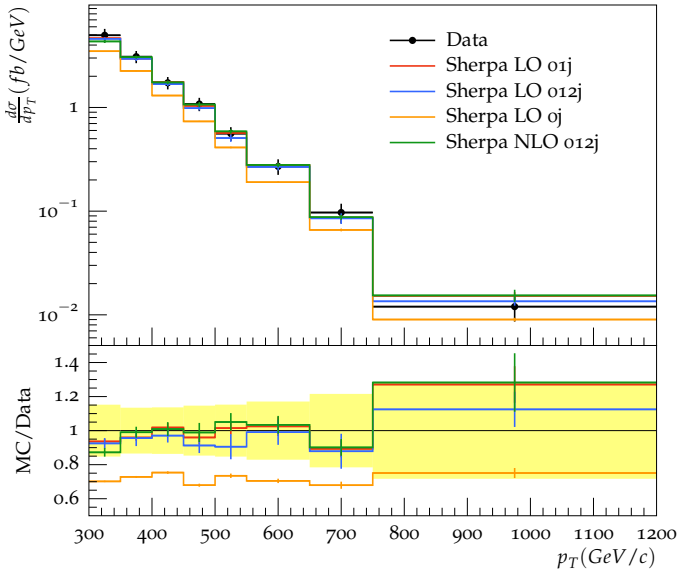

Figure 3.3: Comparison between data measured from the ATLAS experiment and predictions performed with Sherpa at NLO or at LO considering at least 0,1 or 2 extra radiations.

by the ATLAS experiment at $\sqrt{s} = 8$ TeV is compared with predictions obtained using an NLO generator and various tree-level generators, that differ for the number of additional radiations. The LO prediction (in orange), is not sufficient to describe the p_T^t. The calculation of $t\bar{t} + 2j$ is obtained merging different predictions: $t\bar{t}$, $t\bar{t}$+ at least 1 jet and $t\bar{t}$+ at least 2 jets. Since the sample are not exclusive in number of additional jets the merging of these calculations is not simple and requires particular techniques to avoid double counting, since the same diagrams are present in different generations. For example it is possible that a radiation accounted in the matrix element of the process $t\bar{t} + 2j$ is also included in evolution of the $t\bar{t}$+ at least 1 jet process. The basic idea of the merging is introducing a suppression term on the emissions over a certain p_T threshold after a certain number of hard emissions. Recalling the previous example, in the $t\bar{t}$+ at least 1 jet calculation the cutoff is applied after the first hard emission.
The initial momentum of the partons entering in the calculation is assigned following the PDFs (see 1.3.1), that therefore enter in this step of the Monte Carlo generation. Depending on which quarks are considered among the partons that contribute to the cross-section, and are therefore included in the PDF sets, the generators are divided in four and five flavor scheme (FS). The difference is on the role played by the b-quark. In the four FS the b-quark is massive and is excluded from the sea quarks that can be involved in the hard scattering, while diagrams containing the b-quark as initial parton are included in the five FS. A clear difference among the two approaches can be seen in the single top production in t-channel, where the process can happen only at NLO in the four FS, as shown in figure 3.4.

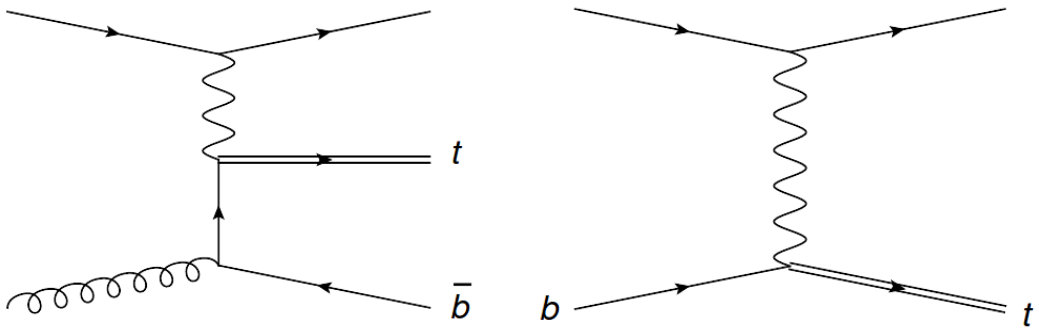

(a) (b)

Figure 3.4: Single top production in t-channel, in (a) using the four flavor scheme and in (b) using the five flavor scheme. In the latter case b-quarks are considered in the sea partons inside the protons.

3.2.2 Parton shower

The aim of this event generation step is to provide a model for QCD radiation, accounting for high multiplicity states and for higher-order corrections, in particular in the phase space where the emissions are soft or collinear. This particular phase space is separated from the one populated by the hard scattering step, to avoid a double counting on the same diagrams. The separation is performed using a matching procedure, that is based on the definition of a threshold on a scale (distance, momentum) of the emissions included by the showering.
The parton shower starts from the external partons (outgoing and incoming) of the hard-process. The showering incorporates higher order QCD effects allowing the split of partons into other partons, (*branching*). In particular the (anti)quarks can branch in a qg pair while a gluon in a $q\bar{q}$ or gg, the resultant partons can successively branch and the result is a shower or cascade of partons.
The showering is a Markov process [82], a random process where the probabilities of future evolution depend on the most recent values of a certain set of variables. In the Markov chain employed in the showering the set of variables contains the Mandelstam variable t[1], the momentum fraction and flavor of the emitted partons. The evolution of the variable t continues until it reaches a cutoff value t_0, at this point the parton can not emit any other particle and is ready for the hadronization step.
The showering is applied both to the final partons of the hard process (*final state radiation*) and in a similar way, to the initial partons of the process (*initial state radiation*). In this latter case the evolution is done backward. It starts at a certain t_{max} scale of the hard process and the evolution is driven by the probability that a parton is unresolved in another parton during a decrease in t.

[1]Saying p_1, p_2 the four momenta of the incoming particles in a scattering and p_3, p_4 there of the outgoing ones, t is defined as the Lorentz invariant expression $t = (p_1 - p_3)^2 = (p_2 - p_4)^2$.

An important difference among the various parton shower generators available is the ordering used in the branching, that can depend on angular variables or be based on p_T.

3.2.3 Underlying Events

The Underlying Events (UE) [83] indicate everything that is present in a hadron-hadron collision, except for the hard scattering part. The UE receives multiple contributions, one is from the beam-beam remnants, that are the left-overs of initial hadrons after the parton hard scattering. Other contributions come from initial and final state radiation and from multiple parton interactions (MPI) that can happen among the two initial hadrons.

The UE populate mainly the forward region of the event but it is possible that, in rare cases, an energetic MPI give a rise to additional jets with high transverse momentum. The physics of the UE contains both perturbative an not perturbative QCD and is consequently hard to describe. For this reason in many generators it is included a tuning of the UE simulation parameters to the data collected in pp collisions.

3.2.4 Hadronization

The hadronization step starts from partons generated from the showering and underlying events and converts these colored states in color singlet hadrons. This process is non-perturbative and starts at the scale where the showering ends.
There are different methods that can be used to model this process:

- **Cluster hadronization:** this method [84] is based on the color pre confinement [85] concept. The quarks and gluons produced in the showering step are organized in finite mass, color singlet clusters. The mass spectrum of these clusters is peaked at low masses with a rapid fall, as shown in figure 3.5b. The first stage of this hadronization technique consists in a $q\bar{q}$ branch of all the remaining gluons after the showering, so the event contains only color connected quarks and anti quarks. The clusters are formed in the second step, grouping the partons. The original clusters momentum is given by the momentum sum of the constituents. Afterwards the clusters with high mass are split into lower masses clusters. As last step, the low masses clusters are decayed isotropically into two hadrons, using weights depending on the phase space. An anisotropic component is included if an heavy quark is present in the cluster. A graphic representation of this hadronization technique is reported in Figure 3.5a.

- **String hadronization:** the string method [86] is based on linear confinement. The basic idea is that in non-perturbative QCD if the quarks of a color connected $q\bar{q}$ pair move apart, they are slowed down by the strong interaction and consequently more and more energy is stored in the color string

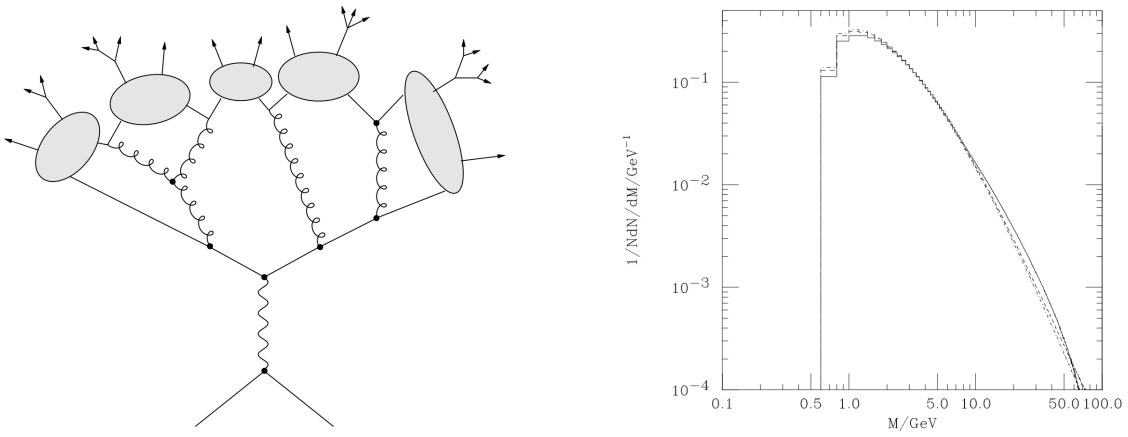

(a) (b)

Figure 3.5: Schematic representation of the clustering hadronization model (a), and distribution of the mass spectrum of the primary clusters (b). The graph in (a) shows how partons after the showering are grouped in massive, singlet color clusters that decay originating the observable hadrons. In plot (b) the solid, dashed and dot-dashed lines correspond at different center-of-mass energy of 100 GeV, 1 TeV and 10 TeV respectively.

connecting them. If the energy is small the pair will form a meson, otherwise a new $q\bar{q}$ pair is created. The method is graphically represented in Figure 3.6. The (anti)quarks or (anti)color triplets are the end of the strings while gluons are the kinks that bring energy and momentum. Consequently a gluon is attached to two strings, one related to its color and the other to the anti-color, and is experiencing a confinement force double than that of a quark. The production of a $q\bar{q}$ pair break the string and a quark can combine with another to create a color singlet meson. The common implementation of this technique in generators is the Lund string model [87, 88].

After the formation, the unstable hadrons are decayed until a set of stable particles is formed. The modelling of this step can vary among different generators, that could have a different set of hadrons included in the simulation or a different definition of decay modes and widths.

3.3 Monte Carlo Generators for Signal and Background

In this analysis several generators are used to simulate the $t\bar{t}$ signal and the various sources of background:

- POWHEG. The Positive Weight Hardest Emission Generator [89, 90, 91] implements NLO calculations for a large number of processes using p_T ordered emissions. To obtain a full event generation POWHEG needs to be interfaced

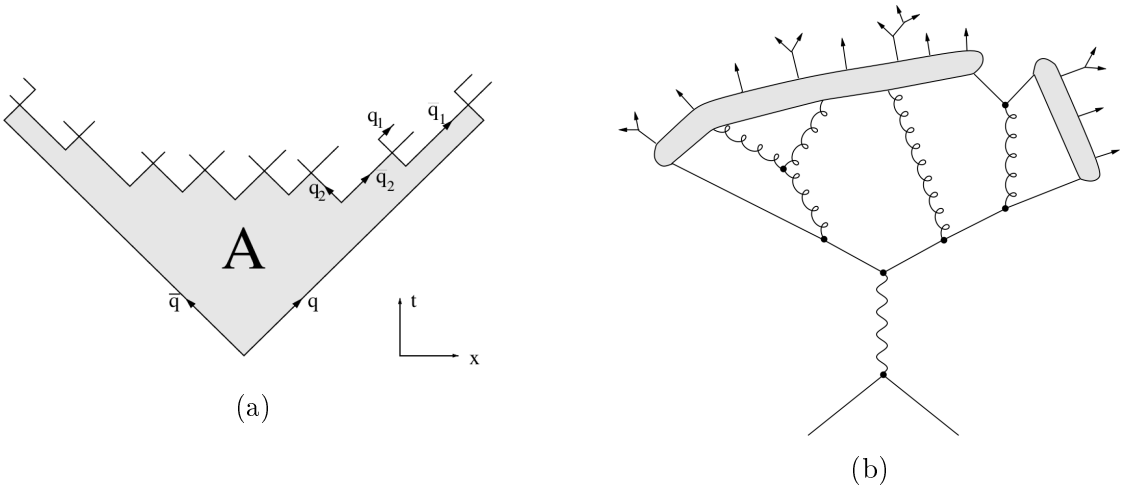

Figure 3.6: Simple illustration of the string hadronization model, where the gluons are represented as kink and the quarks and anti-quarks are at the end of the strings.

with a showering generator. This matching could originate an overlap between the hard emissions and the soft/collinear radiations generated from the showering. For this reason a matching approach, involving various parameters, is used to separate the scales of the emissions and avoid the double counting. The parameter h_{damp} is one of these, it controls the p_T of the first additional emission and effectively regulates the high-p_T radiations and has been extensively studied in top physics modelling for the ATLAS MC tuning.

- MadGraph5_**a**MC@NLO. This generator implements NLO calculations (MADGRAPH) and the following matching with the showering, in an alternative way with respect to Powheg [92]. In the particular procedure followed by MC@NLO is possible that negative weights are assigned to a small fraction of events.

- Pythia. Pythia [93] is a multi-purpose generator that can provide hard scatter simulation for various processes at the LO, or can be interfaced with the output of Powheg or MadGraph5_aMC@NLO to generate the showering, hadronization and decay of the particles. The showering approach used in Pythia follows a p_T ordering, while for the hadronization the Lund string method is used. In the UE simulation MPI events are included. The data tuning used in ATLAS to simulate UE using Pythia is the A2 tune [94].

- Herwig. Herwig [95] is, similarly to Pythia, a multi-purpose generator that can be interfaced with an NLO generator that simulate the hard-scattering step. The showering follows an angular ordering while the hadronization approach is the cluster model.

- Sherpa. The Simulation of High-Energy Reactions of PArticles (Sherpa) is a steering module that handle all the MC generation steps starting from

the NLO calculations and proceeding with the matching with the showering, the showering itself and the hadronization. The different steps are performed by various programs that are initialized and controlled by SHERPA. The hadronization is based on the cluster model and implemented as in HERWIG.

3.3.1 Monte Carlo Generators Employed in the Analysis

The generator used to simulate the $t\bar{t}$ signal and the single top produced in $Wt-$ and $s-$ channel is POWHEG+PYTHIA 6, where the PDF sets CT14 [37] is used for the matrix element calculation, events where both the W decays hadronically are not included in the simulation. This simulation is referred to as nominal prediction. The diagram removal scheme introduced in 1.3.2 is used to remove the overlap between $t\bar{t}$ and single top processes. For the $t-$channel simulation POWHEG+PYTHIA 6 with the PDF set CTEQ6L1 PDF [96] is used, the four flavor scheme is employed in the simulation.

Many alternative generators are used to simulate $t\bar{t}$ signal and evaluate the effects on the measurement of the differences in various simulation steps:

- MADGRAPH5_aMC@NLO+HERWIG++ and POWHEG+HERWIG++ are compared to estimate the impact of the matrix element simulation and the matching to the showering.

- POWHEG+PYTHIA 6 and POWHEG+HERWIG++ are compared to estimate the differences due to showering and hadronization approach

- Two POWHEG+PYTHIA 6 samples with different factorization scale, hadronization scales and h_{damp} parameter tune are used to estimate the impact of differences in the tuning of initial and final state radiation model.

The $t\bar{t}$ samples are normalized to the NNLO prediction $\sigma_{t\bar{t}} = 832^{+46}_{-51}$ pb, where the uncertainty include PDF, μ_r, μ_f and α_S variations [38].

The simulation of W+jets, Z+jets and diboson(WW/ZZ) background is performed using SHERPA, the calculation of NLO for processes with up to 2 partons at LO for processes up to 4 partons.

The $t\bar{t}$ + W/Z processes, where $t\bar{t}$ state is produced in association with electroweak mediators, are simulated using the MADGRAPH5_aMC@NLO generator at LO, interfaced to PYTHIA.

3.4 Detector Simulation

The detailed study of the detector response and efficiencies requires an accurate simulation of the apparatus. The ATLAS collaboration developed a detector simulation that, starting from the event generated as described in the previous section, produces an output equivalent to the data collected from the ATLAS data acquisition system. Consequently, the same triggers and reconstruction algorithms applied

to real data can be used on the simulated samples.
An overview of the various steps followed during the detector simulation is reported in Figure 3.7 [97].

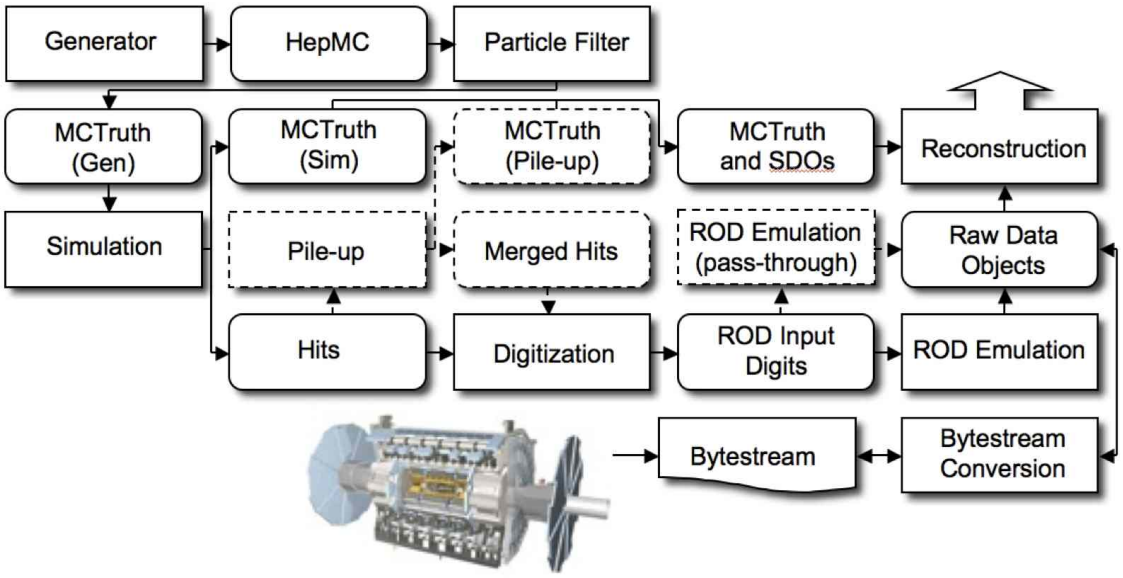

Figure 3.7: Flow-chart of the ATLAS detector simulation from the MC generators to the RAW objects, input to reconstruction algorithms. The algorithms employed are placed in square-cornered boxes, while the data format obtained at each step are placed in rounded-corner boxes [97].

The samples generated in HepMC [98] format from the Monte Carlo generators are passed to the ATLAS detector simulation performed by GEANT4 [77, 78, 79]. The ATLAS geometry is loaded from an external database, that contains also all the information regarding the real detector conditions, as mis-alignment or some sub-detector parts that are not working at the optimal conditions. The simulation performs a detailed description of the interactions between the particles and the various regions of the detector and produces as output the collection of the energy deposited (*hits*) in each sensitive portion of the detector. Information on time, total energy and position of each deposit are recorded in the *hit* file. The digitization step takes as input the *hit* file and emulates the conversion into digital signal operated by the read-out electronic. The digitization output is a Raw Data Object, that can be directly passed through the reconstruction algorithms. During the digitization it is possible to overlay to the events *hits* collections from pile-up events, that are generated separately to save CPU time. These collections are overlaid with a rate optimized to match the real detector conditions. The electronic noise is simulated during the digitization step.

The reconstruction step creates the particles tracks in the detector, this is done by reconstructing the particle trajectories starting from digitized *hits*. The main problem in reconstruction is to identify the *hits* belonging to the same trajectory.

A way to solve this issue is through pattern recognition and the application of ambiguity treatment techniques, used to identify the particles trajectory in the inner tracker dense environment.
During the full detector simulation also the truth information are recorded. In addition a map, that connects the *hits* in the sensitive regions of the detector to the truth particle that generated the deposit, is created during the digitization. The truth information are successively passed to the reconstruction algorithms to quantify the performances of the reconstruction step.

3.4.1 Fast Chain

The amount of data collected by the ATLAS experiment is constantly increasing and a luminosity of 100 fb^{-1} is expected to be collected at the end of 2018. In parallel, also the size of the simulated sample needs to be increased, otherwise analysis could be limited in precision from the generated sample statistical uncertainty.

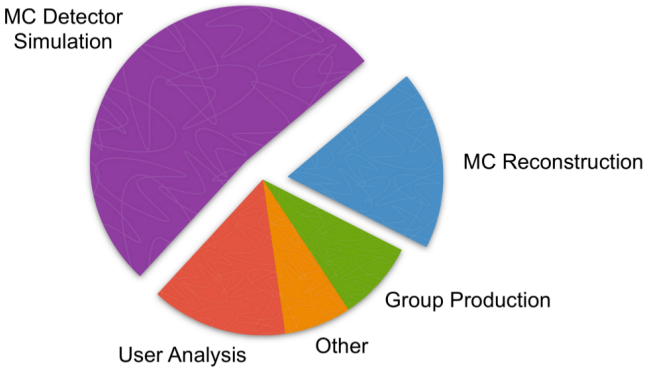

Figure 3.8: Relative CPU grid usage on all ATLAS sites in 2012.

In the current data taking the ATLAS CPU usage is highly dominated by the detector simulation, as shown in Figure 3.8, and the increase of the resources for simulation is not a viable solution. The need for faster, although slightly less accurate, methods to produce simulated samples with a reasonable agreement with full simulation is therefore evident. Several studies have been performed to hasten the detector simulation and find an alternative to an approach fully based on GEANT4. At the moment two different packages exist to simulate different areas of the detector:

- **Fatras:** [99] used to simulate the tracker employing a simplified geometry and interaction model, hastes the simulation of a factor 100 with respect to GEANT4.
- **FastCaloSim:** [100] is a parameterized description of the interaction of the particles with the calorimeter and allows a gain of a factor 20 in CPU time with respect to GEANT4.

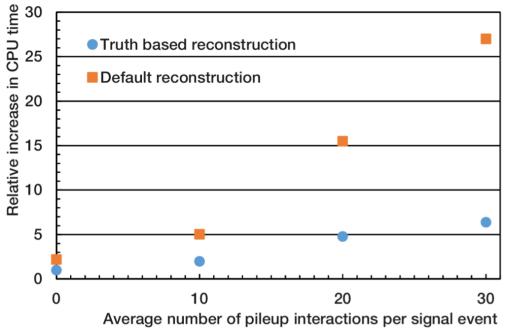

(a)

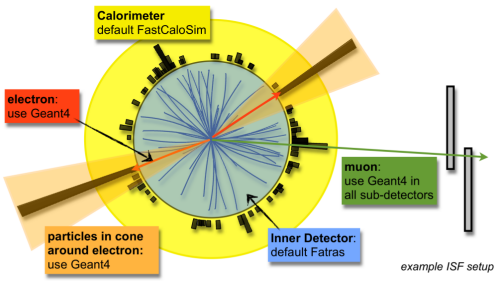

(b)

Figure 3.9: In (a) the increase in CPU time with respect to the average number of pile-up interactions using the default reconstruction approach, based on pattern recognition, and the truth seeded approach is shown. In (b) an example of the maximum flexibility of the ISF is given: the use of different simulators in different regions of the detector for the same event.

However, increasing the speed of the detector simulation is not sufficient. The time required for digitization and reconstruction is comparable with the fast detector simulation. Consequently, in order to speed up the full event simulation chain, it is necessary to develop also a fast digitization and a fast reconstruction. The fast digitization is obtained with a geometric simulation of the charge deposited in each sensor, while the fast reconstruction is achieved skipping all the time consuming pattern recognition techniques in favour of a truth seeded method, that employs the truth information to assign the *hits* to the correct track. In Figure 3.9a is shown the gain in CPU time achieved with the fast reconstruction as a function of the number of pile-up interactions per event.
The combination of fast detector simulation, fast digitization and fast reconstruction is called the fast chain. The fast chain can be combined with the integrated simulation framework ISF, that allows to split the event in different sections that can be simulated with different approaches, depending on the position in sub-detectors or on cones of interest around important particles. A sketch of how an event could be simulated using the ISF is shown in Figure 3.9b. The first application of the fast chain and ISF will be the combination between the full simulation for the hard scattering part of the event with the fast simulation for the pile-up component. This approach allows to avoid an increase in requested CPU time without lack of precision in the interesting regions of the events and will have a central role in the high-luminosity LHC project foreseen for 2023, where the expected number of pile-up events per bunch crossing will be $\sim$200.

Fast Digitization

About 50% of the CPU usage during the digitization step is employed for the inner tracker digitization, hence a faster alternative for the silicon tracker has been developed. The fast silicon digitization approach is based on the relation of pro-

portionality between the segment of the track inside the sensor and the charge collected from it. The algorithm consists in a geometric projection of the track segment on the readout surface. The entrance and exit point of the particle in the detector module, evaluated from the detector simulation, are the input to the fast digitization algorithm. Successively the segment of the track in each crossed sensor is evaluated and the segment is projected on the read-out surface, taking into account the Lorentz angle shift induced by the magnetic field. The path length is

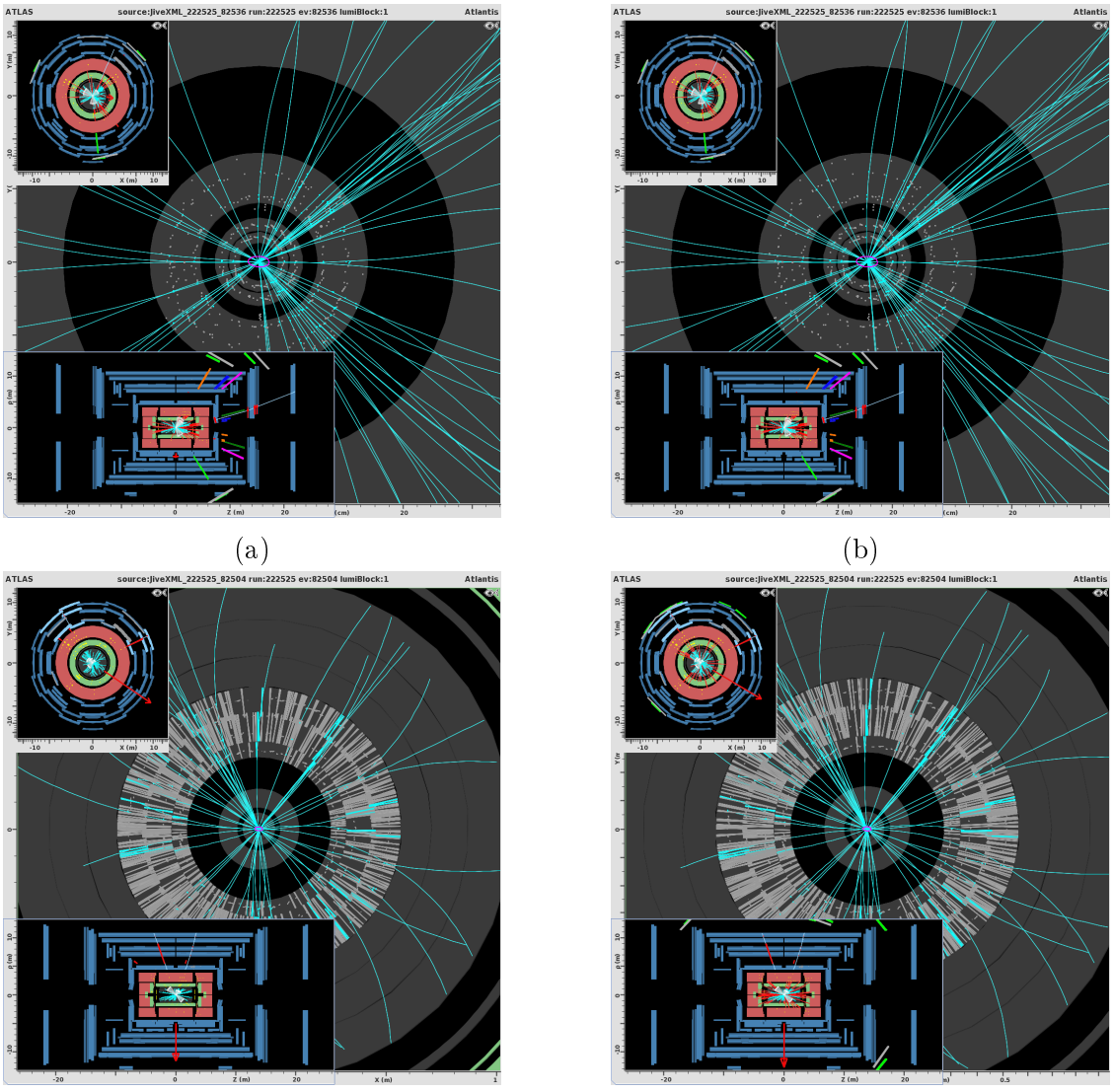

(a) (b)

(c) (d)

Figure 3.10: Comparison of the clusters in the pixel detector (a),(b) and in the strip detector (c),(d) employing the fast digitization (left) and standard digitization and reconstruction (right).

converted in deposited charge employing the proportionality relation between the two. At this point the charged deposits in sensors crossed from the same track are grouped together in a cluster. The output of the algorithm is a collection of

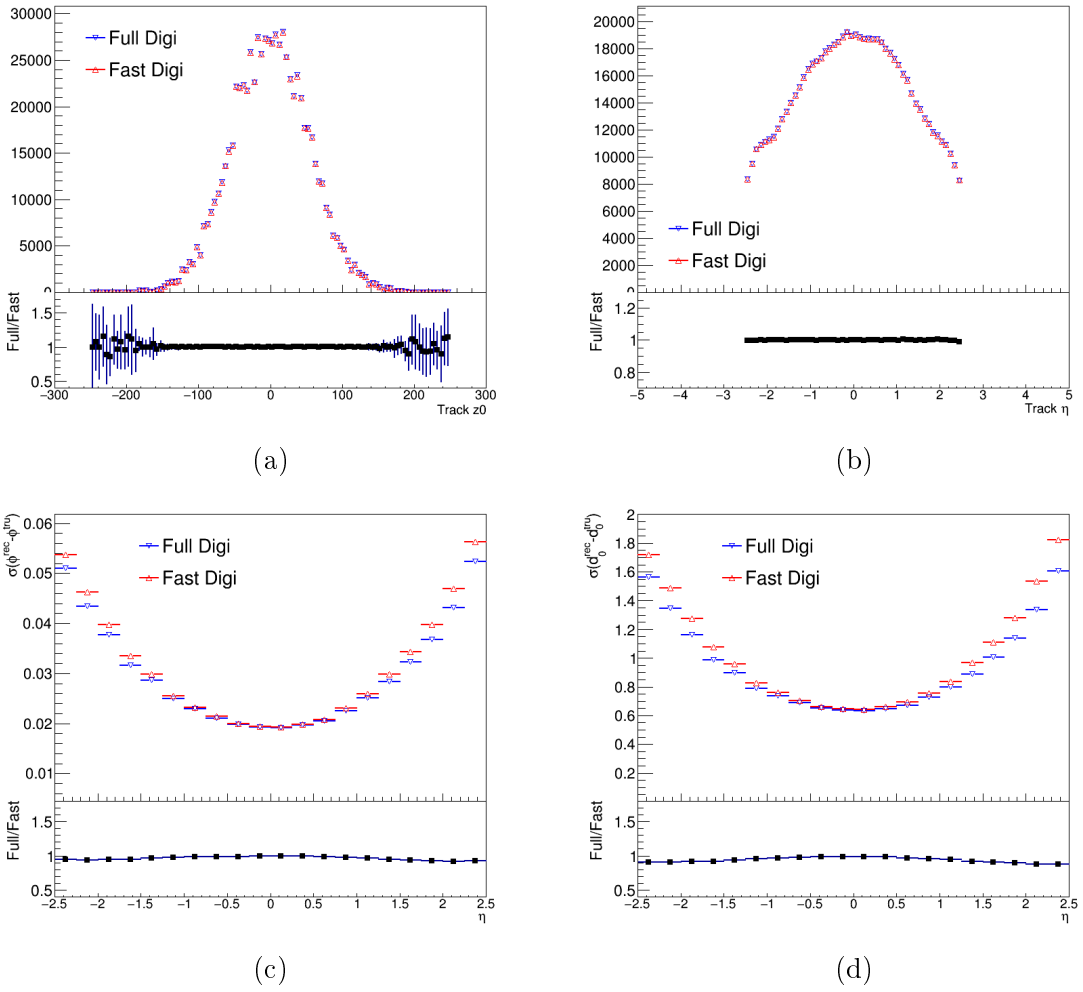

Figure 3.11: Comparison of the reconstructed track parameters (a) z_0, (b) η and track resolution (c) $\sigma(\phi)$, (d) $\sigma(d_0)$, using $t\bar{t}$ events. Events reconstructed with the standard chain are represented in blue while for the red line the fast pixel digitization is employed, together with full detector simulation and reconstruction.

clusters in each module of the pixel and strip tracker, directly used as seeds for the reconstruction. The clusters formed using the two techniques are very similar as visualized in Figure 3.10, that shows, for the same event, a comparison between the clusters formed employing fast digitization and standard digitization, for the pixel detector 3.10a, 3.10b and the strip detector 3.10c, 3.10d. In the standard simulation the cluster formation is performed using sophisticated neural network techniques. The cluster formation performed in the digitization step allows a further gain in CPU usage. The central position of the clusters and the total energy stored in a cluster are smeared in order to emulate diffusion and multiple scattering effects.
A comparison on the track reconstruction parameters obtained using the standard simulation chain and the fast digitization algorithm in each sub-detector separately, is shown in Figure 3.11 and 3.12. The ratio plot shows the good agreement be-

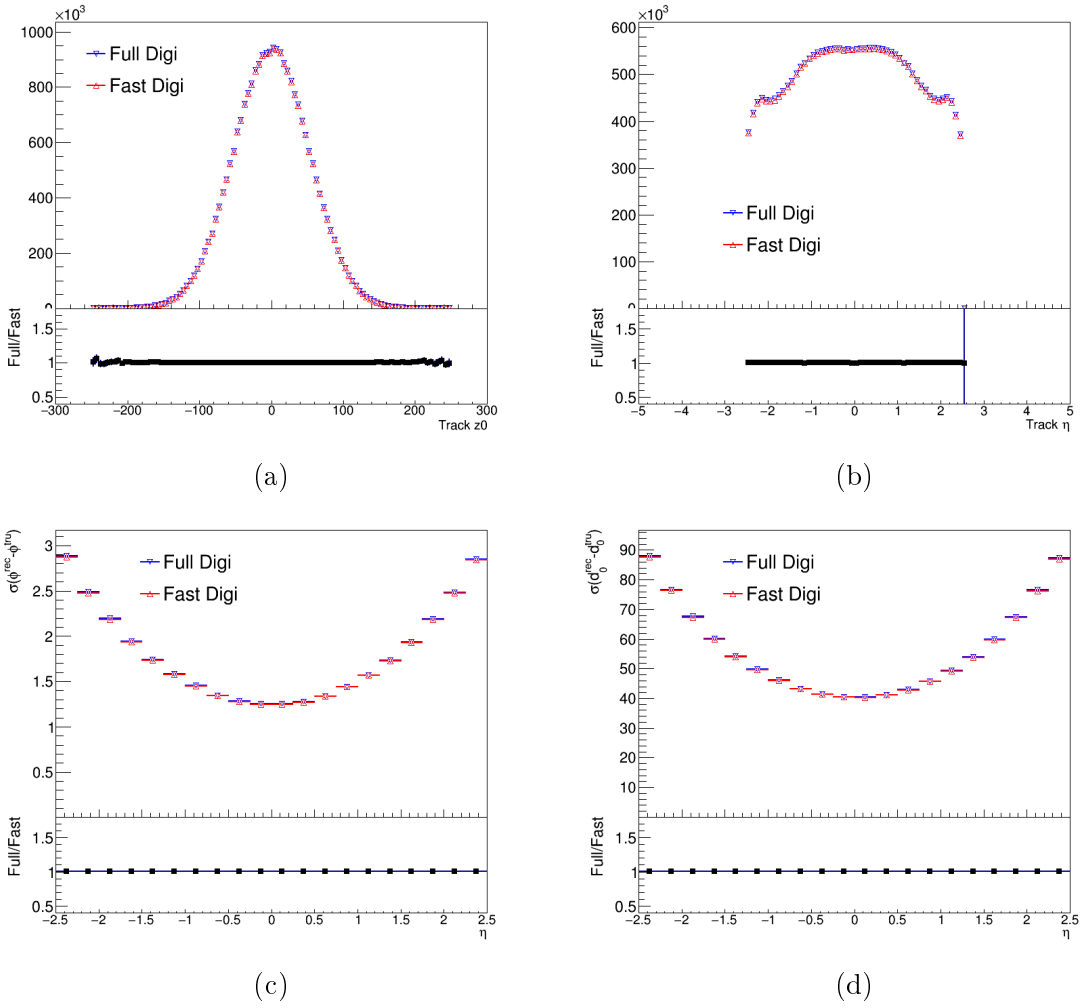

Figure 3.12: Comparison of the reconstructed track parameters (a) z_0, (b) η and track resolution (c) $\sigma(\phi)$, (d) $\sigma(d_0)$, using $Z \to \mu\mu$ sample. Events reconstructed with the standard chain are represented in blue while for the red line the fast strip digitization is employed, together with full detector simulation and reconstruction.

tween the fast digitization and the standard approach on large part of the spectra. Figure 3.13 shows the comparison on track parameters using fast digitization for the whole silicon inner tracker and the standard MC production chain. Also in this case the agreement between the two approaches is good and the largest disagreement is in the tails of the resolution of the impact parameter d_0, where differences up to 10% are visible. A detailed description of the algorithm, the tuning of the parameters and the applications is given in Appendix B.

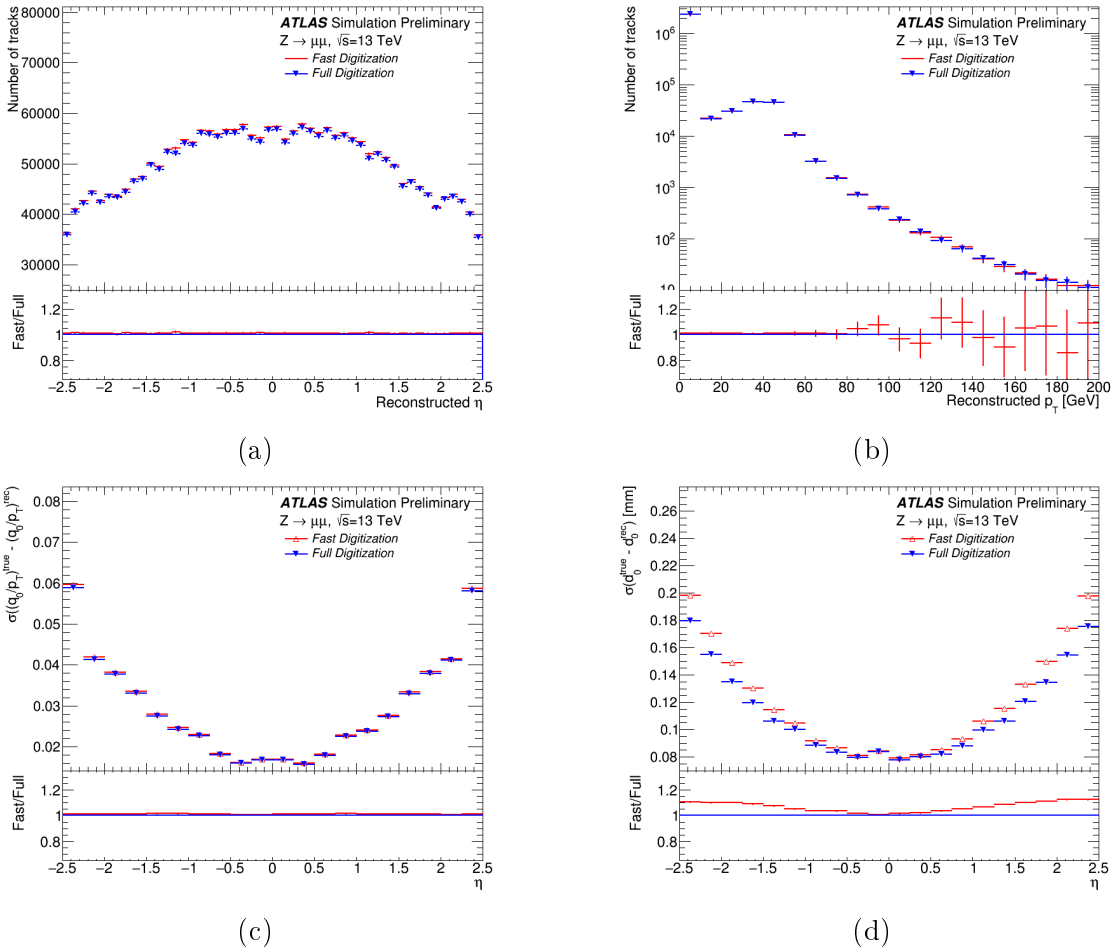

Figure 3.13: Comparison of the reconstructed track parameters (a) η, (b) p_T and track resolution (c) $\sigma(q_0/p_T)$, (d) $\sigma(d_0)$ between two simulations differing just for the digitization used in the silicon tracker: fast digitization (blue) and full digitization (red). The sample used for the comparison is $Z \to \mu\mu$

Chapter 4

Object Definition and Event Selection

The semi-leptonic decay of a $t\bar{t}$ pair leads to a complex final state that contains charged leptons, neutrinos, light and heavy quarks. After subsequent hadronization and decay these particles interact in different sections of the ATLAS detector and are reconstructed using dedicated algorithms. The results of the reconstruction process are called *objects*, and different objects are characterized by specific signatures. The definition of each object is highly related to the detector characteristics, for example the $|\eta|$ range in which an electron is defined depends on the acceptance of the detector.
This chapter will provide an overview of the signature of all the objects employed in the analysis and the event selection applied to individuate $t\bar{t}$ events.

4.1 Physics Objects Definition

The objects are reconstructed starting from the responses of the various subdetectors, that are combined to create tracks and jets. Successively each complex object (muon, electron, ...) is defined by a set of quality criteria and in an appropriate kinematic range, depending on the specific characteristics of the detector.
The charged particles interact in the inner tracker, so it's possible to exploit these information to reconstruct the momentum and the direction of these particles. The tracks reconstructed from the ID are also used to find primary and secondary vertices, fundamental to determine the presence of long-lived particles, as hadrons containing b quarks (b-hadrons).
Electrons, photons and heavier particles loose their energy in the electromagnetic and in the hadronic calorimeter, in case of energetic hadrons. These additional information are used to identify the type of particle and measure its energy.
The muons are less interacting than the electrons, photons and hadrons and pass the calorimeters without losing much energy. These are the only particles that reach the external spectrometer, that allows their complete reconstruction.
ATLAS complete coverage in azimuthal angle allows to detect the presence of

weekly interacting particles as missing energy in the momentum imbalance in the transverse plane, so also the transverse component of the neutrino momenta can be reconstructed.

4.1.1 Track and Vertices Reconstruction

The ATLAS track reconstruction [101] uses information collected by the inner tracker.
The reconstruction proceeds through 3 steps:

- clusters are created from the deposits in Pixel and SCT, a schematic representation is presented in Figure 4.1a, while TRT raw timing information are translated into calibrated drift circles.

- a combination of at least 3 space-points information (3D location of the clusters) from pixel layers and SCT layers is used to create track seeds, that are successively extended in the remaining SCT and pixel layers to form track candidates, using pattern recognition techniques. These candidates are fitted using a global χ^2 and a Kalman-filter, described in [102]. During these procedures ambiguities in cluster-to-track association are resolved and outlier clusters are removed. Fake tracks are identified and removed, applying several quality cuts:

  - $p_T > 400$ MeV, $|\eta| < 2.5$
  - Minimum 7 pixels and SCT clusters,
  - No more than two holes[1] in the combined pixel and SCT detectors,
  - Not more than one hole in the pixel detector,
  - $|d_0^{BL}| < 2.0\ mm$,
  - $|z_0^{BL}| < 3.0\ mm$

  where d_0^{BL} is the transverse impact parameter calculated with respect to the measured beam-line position and z_0^{BL} is the longitudinal difference along the beam line between the point where d_0^{BL} is measured and the primary vertex and θ is the polar angle of the track. During the last step the drift-circle information are added to the tracks and the tracks are refitted. In Figure 4.1b is shown the average number of reconstructed tracks as a function of the number of interactions per bunch crossing (μ) in minimum bias events.

- Once the tracks have been reconstructed, a dedicated vertex finder is employed to find primary and secondary vertices. Only vertices with at least two associated tracks are retained and among all the vertices reconstructed in a bunch crossing, the primary vertex is defined as the one with the highest sum of squared transverse momenta of the associated tracks.

[1] Defined as an active sensor traversed by the track but containing no hits.

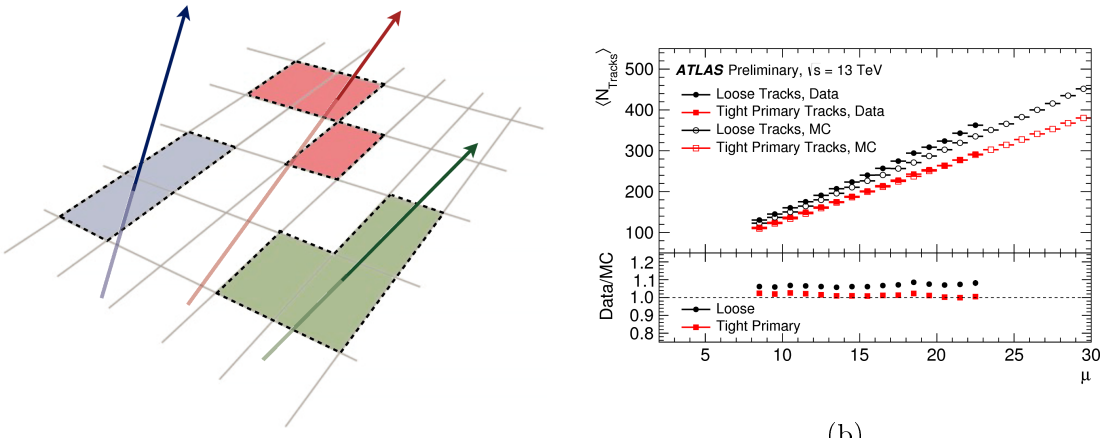

(a) (b)

Figure 4.1: Track reconstruction. In (a) is shown a sketch of the cluster formation (colored pixel groups), starting from the crossed sensors in the pixel layer. [103]. In (b) is shown the number of reconstructed tracks as a function of the average number of interactions per bunch crossing (μ) for data and minimum bias simulation, applying a looser (black) and a tighter (red) requirement on the track quality. [104]

4.1.2 Electrons

The electron reconstruction in ATLAS is performed in the pseudo-rapidity region $|\eta| < 2.47$, excluding the transition region between the barrel and endcap sections of the electromagnetic calorimeter $1.37 < |\eta| < 1.52$, the so called *crack region*. The reconstruction employs information derived from the electromagnetic calorimeter and the inner tracker.
The electron candidate clusters (EM calo electrons) are initially seeded from small group of cells in the electromagnetic calorimeter with global $E_T > 2.5$ GeV and successively expanded with clustering algorithms [105].
The tracks are reconstructed using the techniques described in 4.1.1, but allowing for looser criteria in case of track's seeds formed by 3 space-points and with $p_T > 1$ GeV that can't be successively extended in the other pixel and SCT layers. In this case, if the tracks are matched to an EM calo electron candidate, a pattern recognition approach, that allows for larger energy loss is employed, to take in account possible bremsstrahlung. In the end, in addition to the standard track fit, a Gaussian Sum Filter (GSF) [106] is used, to take into account the effects of a non-linear bremsstrahlung. The reconstruction procedure is ended by the matching between the tracks and the EM calo electrons.
The first quality criteria applied to the electron requires the track to be associated with the primary interaction vertex. This is reached applying two cuts:

- $\Delta z_0 \sin\theta < 0.5$ mm
- $d_0 \sigma_{d_0} < 5$

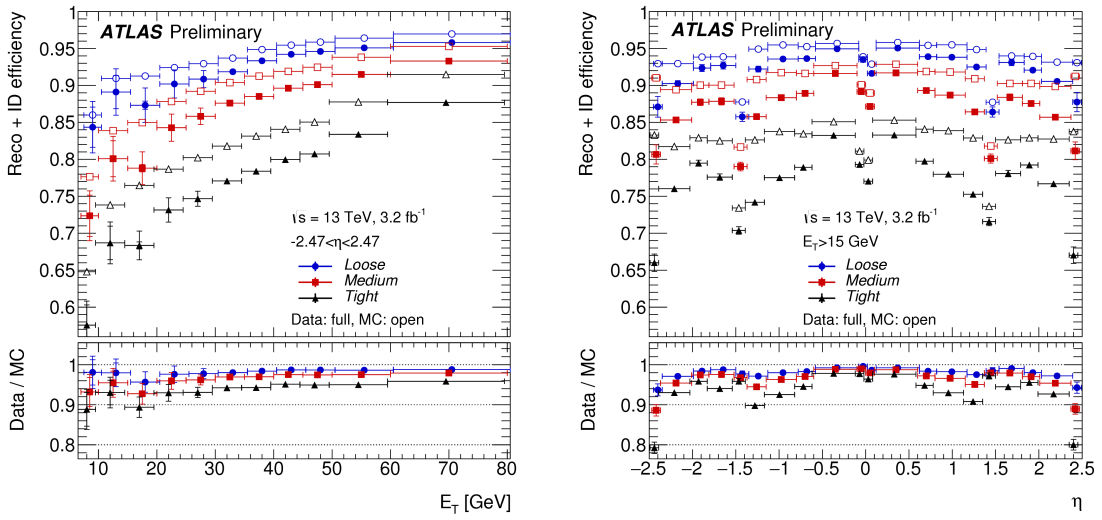

(a) (b)

Figure 4.2: Efficiency of electron reconstruction and identification evaluated in a $Z \to ee$ sample, as a function of E_T (left) and of η (right). The efficiency are shown for the 3 working points defined using the LH method. The ratio plots show the comparison between data and MC events [107].

where d_0 is the transverse impact parameter, σ_{d_0} the associated uncertainty, z_0 is the longitudinal impact parameter and Δz_0 is the distance between the track and the primary vertex. θ is the polar angle of the track.
The separation between real electrons and fakes is reached applying an identification (ID) algorithm that employs a likelihood-based method (LH). This is a multivariate analysis that evaluate simultaneously several properties of the electron and combine them in a discriminant, used to separate signal and background (fake tracks) [107]:

$$d_L = \frac{L_S}{L_S + L_B}, \quad \text{where} \quad L_{S(B)}(x) = \prod_{i=1}^{n} P_{S(B),i}(x_i) \tag{4.1}$$

where x represents all the electron properties used in discrimination and $P_{S(B),i}(x_i)$ is the probability density function that an electron with property x_i is a real(fake) electron. The properties included in the likelihood are related to track quality, EM calorimeter shower shape, track-cluster matching related quantities and information deriving from the TRT. Three different working points (*Tight, Medium* and *Loose*) corresponding at different levels of signal acceptance and background rejection are defined, depending on the cut applied on the discriminant. The electrons used in the analysis are identified using the *Tight* working point.

The comparison between the efficiency of reconstruction and identification in simulated $Z \to ee$ events and data is shown in Figure 4.2 as a function of electron η and E_T. In the analysis presented in this thesis event by event scale factors, derived in $Z \to ee$ samples, are applied to correct for the difference between data

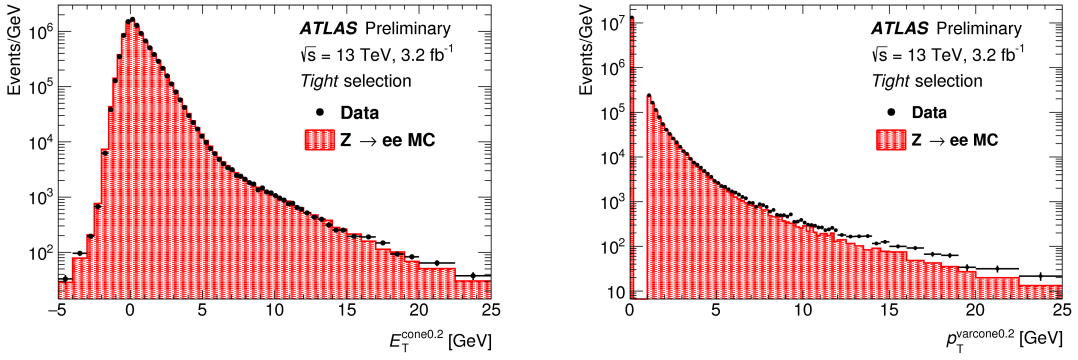

(a) (b)

Figure 4.3: Comparison between data and MC simulation of $E_T^{cone0.2}$ and $p_T^{varcone0.2}$ in a $Z \to ee$ events. The MC distribution is normalized to data. The negative tail in $E_T^{cone0.2}$ is due to the corrections for pile-up and underlying events activity [107].

and MC efficiencies of electron identification and reconstruction.
An isolation requirement is used in addition to the identification criteria to improve the separation from fake. This is based on the definition of two variables:

- $E_T^{cone0.2}$: sum of the transverse energy of EM clusters within a cone $\Delta R = 0.2$ around the electron candidate.
- $p_T^{varcone0.2}$: sum of transverse momenta of all tracks, satisfying specific quality requirements, within a cone of $\Delta R = min(0.2, 10 \text{ GeV}/E_T)$ from the track of the electron candidate and excluding the electron associated tracks. The quality requirement for the tracks are: $E_T > 1$ GeV, $|\Delta z_0 \sin\theta| < 3$ mm and a sufficient number of hits (≥ 7) in the silicon tracker.

The distributions of these two variables are reported in Figure 4.3. Various cuts on these two variables correspond to different isolation efficiencies. The isolation requirement applied in the analysis are depending on electron η and p_T and ensure an efficiency of 90%(99%) for electrons of 25(60) GeV. To correct for the difference between isolation efficiency in data and MC events, an event by event scale factor, calculated in a $Z \to ee$ sample, is applied in the analysis.

4.1.3 Muons

The muon reconstruction is performed in ATLAS combining information deriving from the inner tracker and the muon spectrometer. The reconstruction is performed independently in the two detectors and the information are combined using four techniques, corresponding to different definitions of muon. The track reconstruction in the inner tracker is performed as described in 4.1.1.
In the muon spectrometer the reconstruction starts from the creation of segments in the MDT chambers. A Hough transformation [108] is used to find the hits on a trajectory in the bending plane of the detector, while the hits in RPCs and

TGCs are used to measure the coordinate orthogonal to the bending direction. The tracks are created merging information from different layers and at least two matching segment are required to build a track, with the exception of the transition region between the barrel and endcap, where a single segment can be used. An overlap removal procedure is applied when multiple tracks share the same segment. However, in order to allow high efficiency in close-by muons reconstruction, all tracks with a segment in all the 3 spectrometer layers are kept even if they share segments in the two innermost layers, the only request is the absence of shared hits in the outermost layer.

Four definition of muons are derived combining the information of ID, MS and

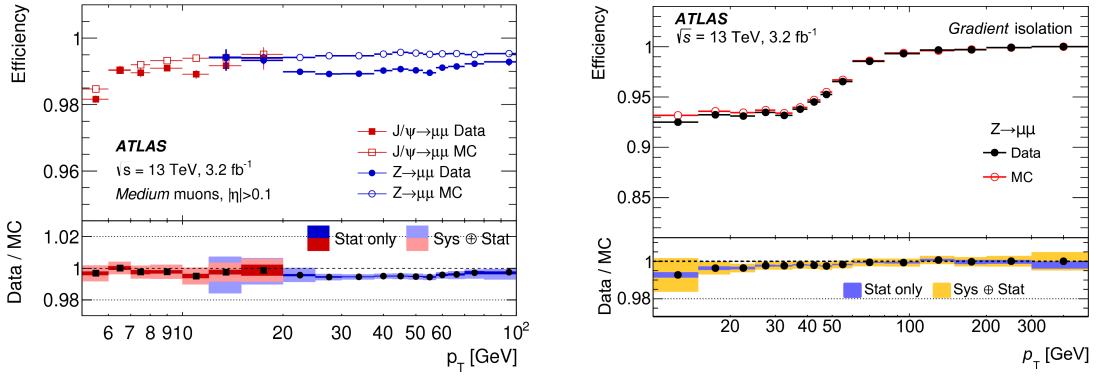

(a) (b)

Figure 4.4: Comparison of reconstruction (a) and isolation (b) efficiency between MC and data. In (a) the reconstruction efficiency for *Medium* muon selection, is shown as a function of the muon p_T in the region $0.1 < |\eta| < 2.5$, obtained using $Z \to \mu\mu$ and $J/Psi \to \mu\mu$ events [109]. In (b) is shown the isolation efficiency in a $Z \to \mu\mu$ sample [109].

calorimeter in various ways, differing for the fake discrimination and the η coverage:

- **Combined muons (CB):** The hits detected in ID and MS are combined in a global fit. The larger part of the muons are reconstructed starting from the MS track and then extrapolated inward and matched to a track in the inner detector. These are defined only in the region $|\eta| < 2.5$.

- **Segment-tagged (ST):** A track reconstructed in the ID is identified as muon if when extrapolated to the MS is associated to at least one segment in the MDT or CSC chambers.

- **Calorimeter tagged (CT):** The ID track's segments are identified as muon if they are matched to a calorimeter deposit compatible with a minimum ionizing particle (MIP). This muon definition has the lowest purity but allows to recover acceptance in the regions of the MS that are only partially instrumented.

- **Extrapolated muons (ME):** The muon trajectory is reconstructed only from MS information. This allows to recover muons in the region ($2.5 < |\eta| < 2.7$) not covered from the inner tracker.

After the muon reconstruction, the muon identification is performed to suppress backgrounds, due mainly to pion and kaon decays. A muon candidate originated from these decays is usually characterized from the presence of a "kink" in the reconstructed track, resulting in a poor fit quality and an incompatibility between the measured p_T in the ID and MS. The identification selection on CB muons, used in the analysis, contains requirements on the q/p significance and on the number of hits in the ID and MS. The q/p significance is defined as the absolute value of the difference between the ratio of the charge and momentum of the muons measured in the ID and MS, divided by the sum in quadrature of the corresponding uncertainties [109].
Different working points can be defined depending on the cuts applied on the number of hits and on q/p significance. In the analysis the working point used, called *Medium*, is the one that minimizes the systematic uncertainties associated with muon reconstruction and calibration. The *Medium* requirements are:

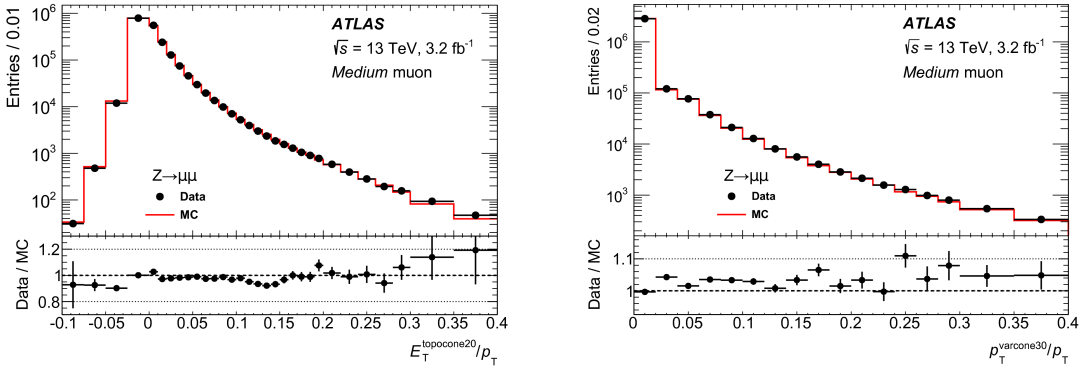

(a) (b)

Figure 4.5: Comparison of the isolation variables $E_T^{cone0.2}$ and $p_T^{varcone0.3}$ between data and a simulated $Z \to \mu\mu$ sample. The ratio plot shows the data over MC ratio [109].

- at least 3 hits in at least two MDT layers, except in $|\eta| < 0.1$ where one MDT layer and no hole are sufficient,
- q/p significance less than 7,
- at least one Pixel hit, five SCT hits and less than 3 Pixel or SCT holes,
- in the region of TRT acceptance $0.1 < |\eta| < 1.9$, at least the 10% of the TRT hits originally assigned to the muon candidate track should be included in the final global re-fit.

The comparison between data and MC efficiency in muon reconstruction, using *Medium* identification, is shown in Figure 4.4a as a function of the muon p_T.
Similarly to the electron case, also for the muon, the isolation requirement is a powerful tool to discriminate signal from background. The variables used to quantify the isolation are the same used for electron isolation, the only difference being the radius of the cone in the track based parameter. In the muon case, it is defined as $\Delta R = min(0.3, 10 \text{ GeV } /p_T^{\mu})$. The distribution of the two isolation variables for a $Z \to \mu\mu$ sample is shown in Figure 4.5. The cuts on $E_T^{cone0.2}$ and $p_T^{varcone0.3}$ applied in the analysis ensure an isolation efficiency equivalent to the electron case, as shown in Figure 4.4b. To account for the difference in muon isolation, reconstruction and identification efficiency between data and MC in the analysis are applied event by event scale factors, derived in $Z \to \mu\mu$ and $J/\Psi \to \mu\mu$ samples.

4.1.4 Small-R Jet Reconstruction and Calibration

The jets are collimated showers of hadrons built to collect all the products of the hadronization of a colored particle.
In ATLAS jets are initially reconstructed using cells in the calorimeter, but the association to the ID tracks is crucial for the calibration and pile-up suppression.
The starting point for the jets reconstruction is a collection of three dimensional, massless, positive-energy topological clusters (topo-clusters). These are built from neighboring calorimeter cells that contain a significant energy above a noise threshold, estimated from pile-up and calorimeter electronic noise simulations. The calorimeter cells energies are measured at the electromagnetic scale (EM), corresponding to the energy deposited by particles interacting electromagnetically.
The topo-clusters form the first collection of proto-jet that are passed to the anti-kt algorithm [110], used to build the jets. Two distances in the $\eta - \phi$ plane are associated to each proto-jet :

$$\rho_{ij} = min(p_{Ti}^{2d}, p_{Tj}^{2d}) \frac{(\Delta R_{ij})^2}{R^2} \tag{4.2}$$

$$\rho_{iB} = p_{Ti}^{2d} \tag{4.3}$$

$$\Delta R_{ij} = \sqrt{(\eta_i - \eta_j)^2 + (\phi_i - \phi_j)^2} \tag{4.4}$$

where ρ_{ij} represents the distance between two proto-jets in the collection and ρ_{iB} represents the distance from the beam pipe. In equation (4.4) ΔR_{ij} is a measure of the opening angle between two proto-jet in the ($\eta - \phi$ plane) and R is the jet radius parameter used to define the final size of the jet. The following step of the algorithm is the comparison between ρ_{ij} and ρ_{iB}:

- if $\rho_{iB} < \rho_{ij}$ the proto-jet i is closer to the beam pipe than to any other proto-jet in the event, it is considered a jet and removed from the proto-jet list,
- if $\rho_{iB} > \rho_{ij}$ the proto-jets i and j are combined in a new proto-jet.

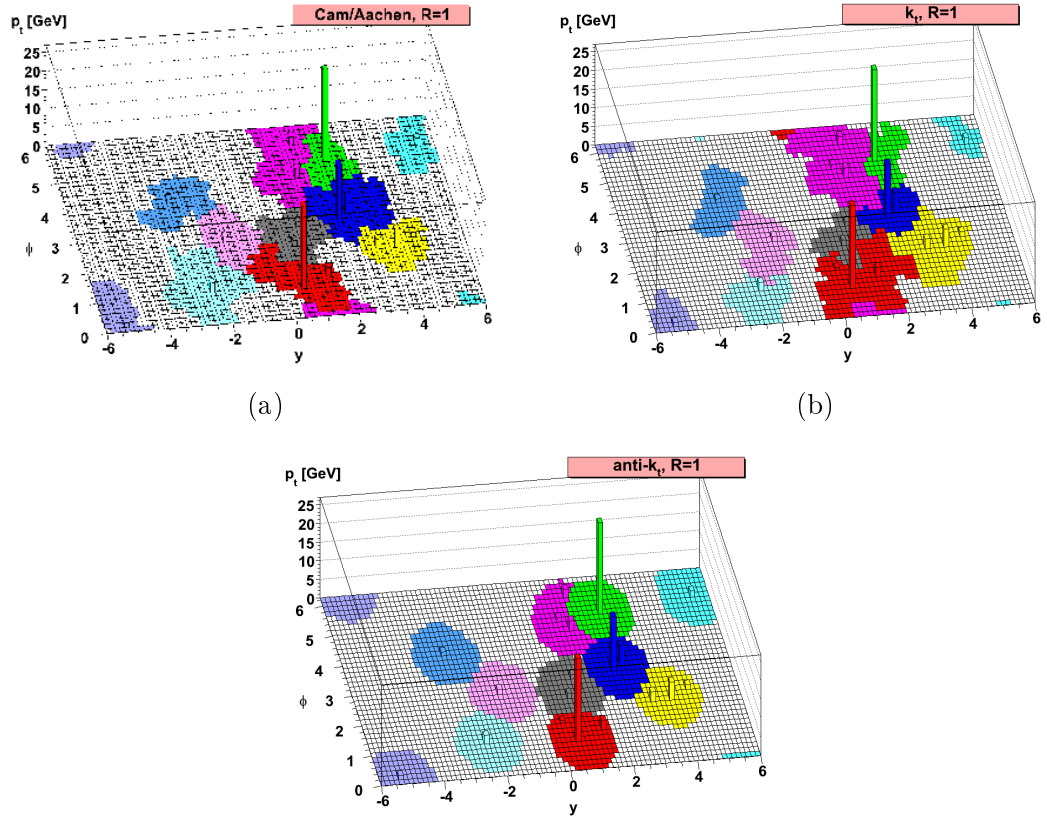

(a) (b)

Figure 4.6: Representation of the final jets obtained in the y-ϕ plane using the C/A, kt and anti-kt algorithms, starting from the same proto-jet collection [111].

The procedure is iterated until the collection of jets with a certain R is created. In ATLAS the parameter chosen to build the jets is 0.4.
The algorithm described allows to define various jet reconstruction strategies, depending on the value of d and consequently on the definition of the distance ρ.
The anti-k_t algorithm sets $d = -1$. The other options are the Cambridge-Achen (C/A), where $d = 0$, and the k_t algorithm, where $d = 1$. All the three algorithms create an infrared and collinear safe collection of jets, meaning that, if an event is modified by a collinear split or a soft emission, the reconstructed collection of jets remains unchanged. Among the three algorithms the anti-k_t provides stable and robust jets, that are defined starting from the hardest proto-jets. In this way the axes of the final jets are fixed after few iterations and the jets tend to be close to circular in the y-ϕ plane, as shown in Figure 4.6. Here the $R = 1.0$ jets obtained with the three algorithms are shown. The disadvantage of the anti-k_t algorithm is that it does not provide information about the substructure of the jets while the other two algorithms allow access to the clustering history, defined as the ordering and structure of the pair-wise recombinations built during the creation of the jets. The jet substructure is useful to discriminate the origin of the hadron shower in case of large-R jets, as it will be described in the next section.

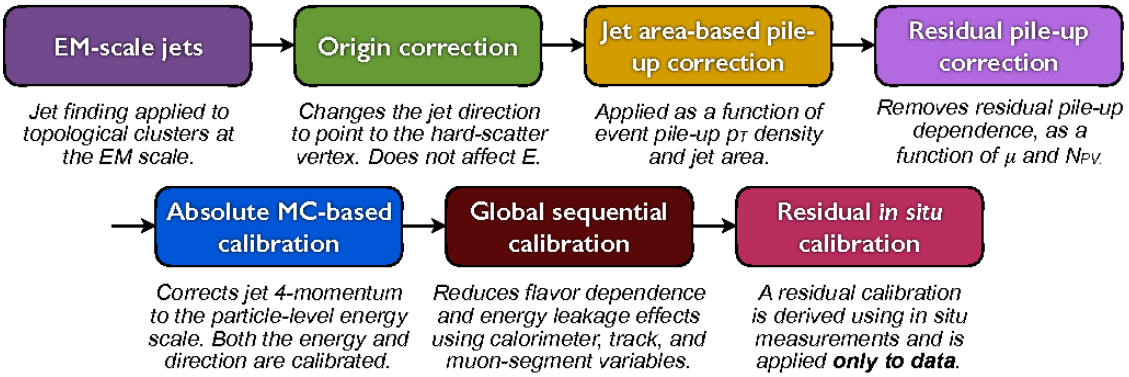

Figure 4.7: Calibration sequence used in ATLAS for the EM-scale jets [112].

The reconstructed jets with $R = 0.4$ are calibrated following the scheme described in Figure 4.7. The first step consists in a correction on the jet direction to point toward the primary vertex. The second and third steps aim to reduce the pile-up contamination of the jets. The jet area-based pile-up correction [113] subtracts the per-event pile-up contribution to the p_T of each jet depending on its area. To define this quantity, particles of infinitesimal momentum are generated uniformly in a solid angle and added to the input of the clustering algorithm. The area is then defined as the fraction of momentum-less particles associated to each jet. The association is obtained through the ghost matching procedure that is the re-clustering of the jets including particles characterized by a direction but infinitesimal momentum, these don't modify the jet four momentum but result as jet constituents. After the area subtraction a residual pile-up correction derived from MC is applied to jets. The fourth step consists in the MC-based calibration of the jets, correcting their energy and direction to the ones of the matched truth-level jets. The truth-level jets are obtained by clustering the stable simulated particles (lifetime $> 10^{-10}$ s) before the interaction with the detector, and these are matched to the reconstructed-level jets requiring a $\Delta R(truth - jet, reco - jet) < 0.3$. The following step in the calibration chain, the Global Sequential Calibration (GSC), aims to reduce the dependence in jet response from the distribution of the energy within the jet and the jet particle composition, which depend on the initial parton that originated the jet. A jet originated from a quark usually includes hadrons with a large fraction of the jet p_T, with respect to gluon-initiated jet that typically contains many softer particles, leading to a lower calorimeter response and a wider transverse profile. This algorithm employs information deriving from the calorimeter, the MS, and tracks. The last step of the calibration accounts for the difference in jets response in MC simulations and data, quantified balancing the p_T of a jet against other well-measured reference objects (photons, Z bosons and calibrated jets). These corrections are applied only on data jets and highly constraint the uncertainties on the jet energy scale.

b-tagging

The signature of a semileptonic decay of a $t\bar{t}$ pair contains two jets deriving from a b-quark. The capability to identify these jets (b-tag) has a fundamental role in the identification of $t\bar{t}$ events and in their discrimination from the background.

The identification of the presence of a hadron containing a b-quark inside the jet

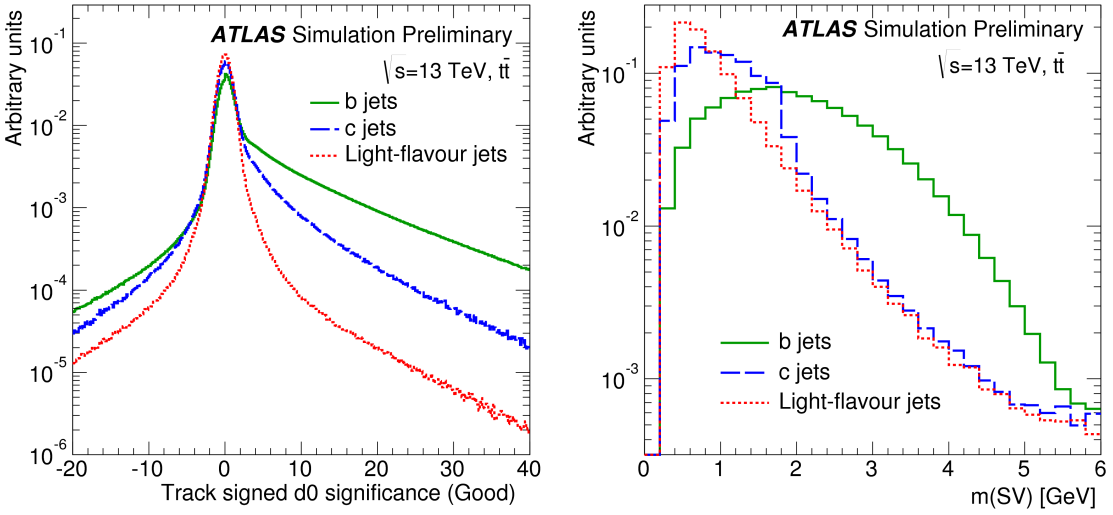

(a) (b)

Figure 4.8: Variables used to discriminate the jet flavour in b-tagging algorithms [114]. In (a) is shown the transverse signed impact parameter significance of tracks in $t\bar{t}$ events associated with b, c and light-flavour jets. In (b) is presented the invariant mass of the reconstructed secondary vertex for b, c and light-flavour jets in $t\bar{t}$ events.

is possible thanks to the long decay time ($\sim$ 1 ps [18]) [2] of these hadrons. This leads to the existence of a secondary vertex that is well separated from the primary one where the b-hadron was created ($1 \cdot 10^{-12} s \text{x} 3 \cdot 10^{8} m/s \approx 0.3$ mm) that can be exploited to b-tag the jets.

In ATLAS three different b-tagging algorithms exist, that employ charged particle tracks information to define variables used to discriminate between different jet flavours. The first algorithm uses the significance of the impact parameter of the tracks matched to the jet, as shown in Figure 4.8a, which represents a very good discriminant among jets with different flavour. The second is based on the reconstruction and identification of the secondary vertex and of its properties. The distributions of the invariant mass of the secondary vertex for jets originated from different sources is shown in Figure 4.8b. The last algorithm exploits the topological structure of b-hadrons and c-hadrons decay inside the jet and try to reconstruct

[2] The b-quark is by far the lightest quark in the third generation, consequently its weak decay to lighter quarks occurs only via generation-changing. Since the CKM matrix, that regulates these decays, is almost diagonal, the off diagonal decays are suppressed and the life time of particles containing b-quarks are longer than for lighter quarks.

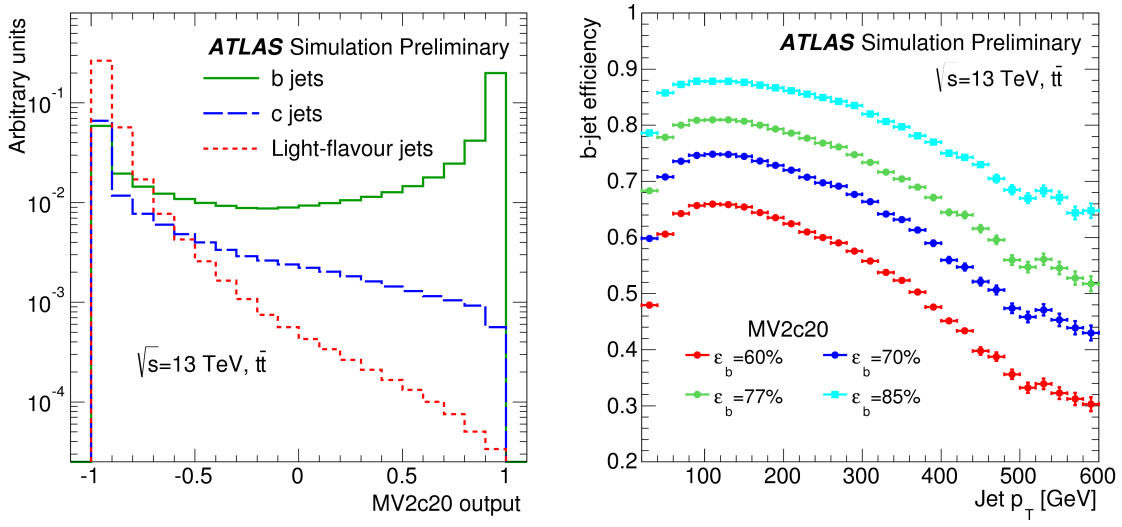

(a) (b)

Figure 4.9: In (a) is shown the output discriminant obtained from the BDT that combines the 3 b-tagging algorithms for b, c and light-flavour jets [114]. In (b) is shown the b-tagging efficiency as a function of the jet p_T at 60, 70, 77, 85% WP, obtained applying various cuts on the discriminant [114].

the full decay chain. The variables built from the three algorithms are successively given as input to a boosted decision tree (BDT) that combines the information in a discriminant used to separate the different jet flavours. The discriminant distribution is shown in Figure 4.9a.
The operating point used in the analysis corresponds to an overall 77% b-tagging efficiency in $t\bar{t}$ events. Figure 4.9b shows the b-tagging efficiency as a function of the jet p_T for the four available working points (WP).

4.1.5 Large-R Jet Reconstruction and Calibration

The high energy and luminosity reached by the LHC collider increases the frequency for the production of heavy objects with high momentum (boosted massive objects). The decay products of these objects are collimated and can't be completely resolved using jets with $R = 0.4$ (small-R jets). The angular separation of the decay products of an heavy particle is approximately:

$$\Delta R \approx \frac{2m}{p_T} \tag{4.5}$$

where m and p_T refer to the the decaying particle. Consequently, when the p_T is sufficiently high the decay products of the heavy particles can be fully contained in a jet with radius 1.0. Figure 4.10 shows the ΔR distributions between the decay products of the top quark as a function of its p_T, the fraction of events where ΔR is smaller than 1 is significant for $p_T > 300$ GeV.

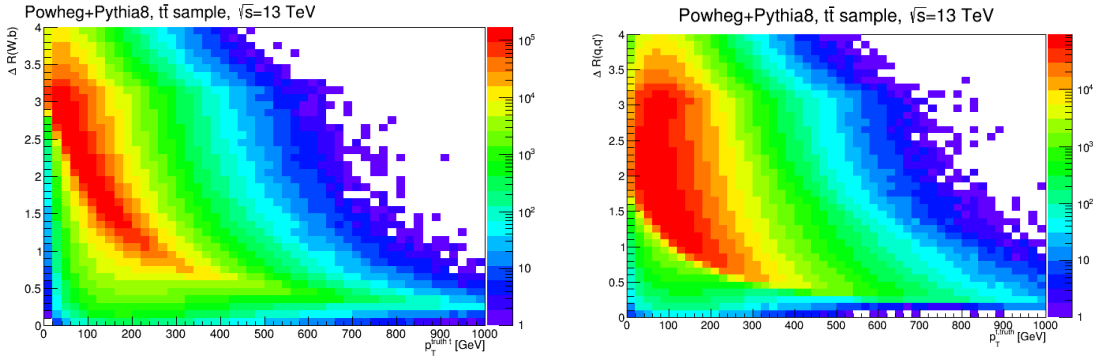

(a) (b)

Figure 4.10: Distance in the $\eta - \phi$ plane between the decay products of the top quark, as a function of its p_T. In (a) is shown the ΔR between the W and b quark originated from the decay of the top quarks, while in (b) is presented the ΔR between the quarks originated from the decay of the W derived from the top quark.

The input used for the large-R jet reconstruction are calorimeter topological clusters, as for the small-R jet case, but with applied energy corrections specifically derived for hadronic case (LCW clusters). Successively the jets are built with the anti-k_t algorithm described in the previous section, but using R=1.0, and calibrated correcting the energy response to the energy of the truth large-R jet.
A single jet containing all the decay products of a single heavy particle has different properties with respect to a jet generated from a single gluon or light quark with the same p_T. The three body decay of the top quark reflects in an hard substructure of the large-R jet, that can be identified and used to discriminate signal from the multi-jet QCD background. The jet substructure is highlighted using the k_t algorithm to re-cluster the anti-k_t large-R jets components and then applying techniques to remove the soft radiation contained in the jets, usually called *grooming techniques*.

Large-R Jet Trimming

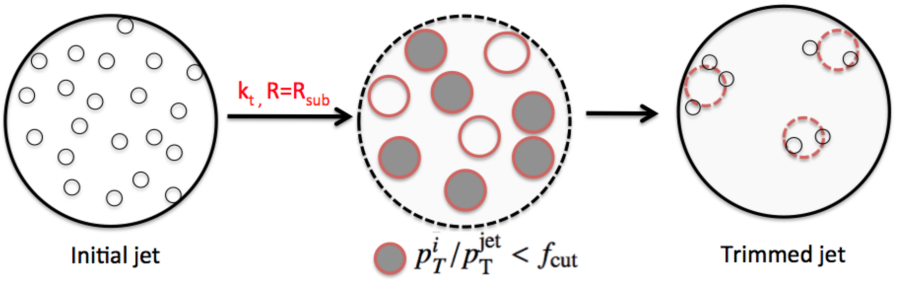

Figure 4.11: Schematic description of the trimming procedure [115].

The standard grooming technique used in ATLAS and in this thesis is the trimming [116]. The idea underlying the trimming procedure is that the contributions to large-R jets deriving from pile-up, initial state radiation and underlying events are much softer than the jets components deriving from the decay of the heavy particles. The removal of these parts is possible because such radiation sources usually contribute creating new topological clusters in the calorimeter, instead of increasing the energy deposited in the clusters of interest, typically much harder in p_T.
The trimming procedure starts with the re-clusterization of the large-R jets components using the k_t algorithm with radius parameter equal to R_{sub}. Afterward all the sub-jets i with $p_{Ti}/p_{Tjet} < f_{cut}$ are removed, here f_{cut} indicates a parameter of the method. The values of R_{sub} and f_{cut} used in the present analysis are 0.2 and 0.05, respectively. An illustration of the procedure is shown in Figure 4.11.
The trimming procedure, as shown in Figure 4.12a, highly reduces the mass of jets originated from light quarks or gluons (30%-50%) while leaving almost unchanged the jets derived from boosted objects. Figure 4.12b shows how the trimming helps to highlight the substructure of the large-R jet, that is used in top-tagging, described in the next section.
The trimming procedure is applied also on truth jets, where the soft components

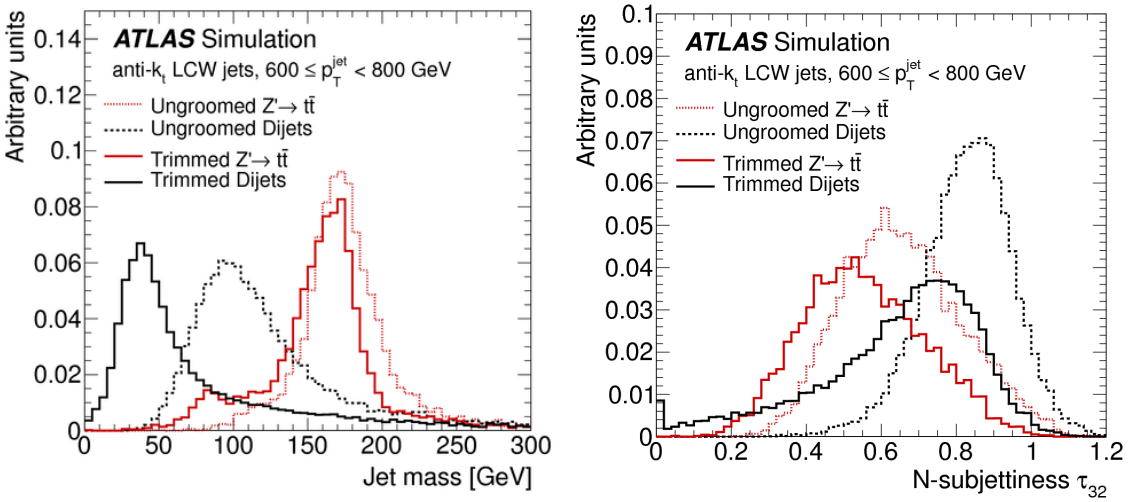

(a) (b)

Figure 4.12: Effect of the trimming on the on the mass (a) and N-subjettiness of large-R jets (b) originated from a top quark and in a dijet sample [115].

derive from the underlying event included in the simulation. The trimming applied on truth jets, shown in Figure 4.13, enhances the top mass peak. In this case the trimming reduces also the difference between the two generators, mitigating the effect on the underlying events, simulated with different approaches in SHERPA and MadGraph+PYTHIA 8.

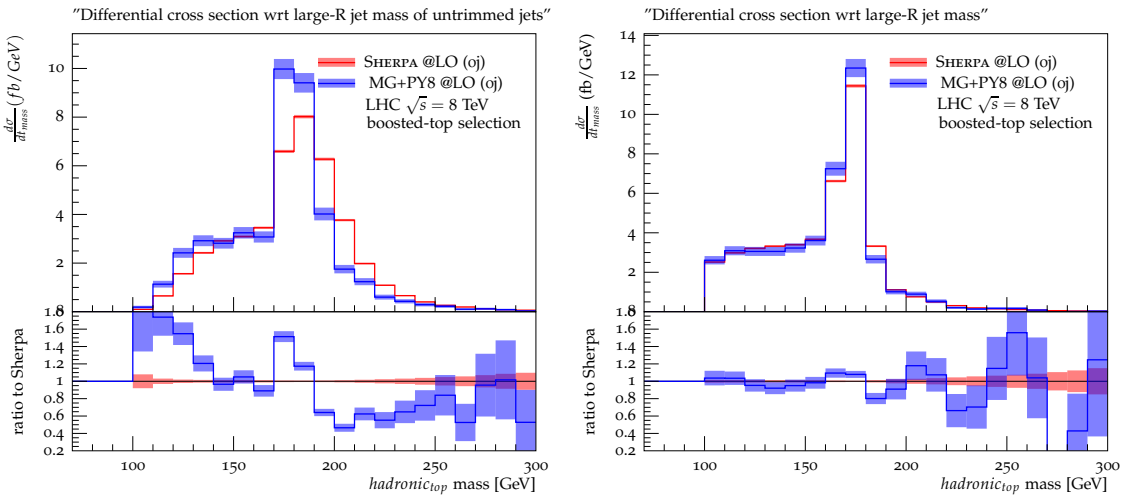

(a) (b)

Figure 4.13: Truth jet mass distribution, before (a) and after (b) the trimming on truth jets is applied. In the ratio plots is compared the distribution obtained using SHERPA and MadGraph+PYTHIA 8. The colored band represents the statistical uncertainty.

Top Tagging

The differences between a large-R jet originated from a heavy quark or from a light quark or a gluon can be exploited to define a set of substructure variables, used in boosted objects tagging:

- m^{jet}**:** the jet mass is calculated from the energies and momenta of its constituents:

$$m_{jet}^2 = (\sum_i E_i)^2 - (\sum_i p_i)^2 \tag{4.6}$$

  where E_i and p_i are the energy and momenta of the i^{th} constituent. In Figure 4.14 is shown the mass distribution of the large-R jet for the samples $t\bar{t}$ and W+jet, where the W boson decays leptonically, as a function of the large-R jet p_T. The peak around the top mass becomes more visible at high p_T where the 3 decay products of the top quark, and their hadronization shower, are fully contained in the large-R jet.

- N**-subjettiness:** the N-subjettiness variable [117, 118] is related to the sub-jet multiplicity. The starting point to define this variable is the usage of the k_t algorithm to re-cluster the k constituents of the large-R jets until N sub-jets are built. Then the N sub-jets are used to define the axes around which the ΔR in equation (4.7) are defined. The N-subjettiness is defined as:

$$\tau_N = \frac{1}{d_0} \sum_k p_{Tk} \times \min(\Delta R_{1k}, \Delta R_{2k}, ..., \Delta R_{Nk}), \text{with} \quad d_0 \equiv \sum_k p_{Tk} \times R \tag{4.7}$$

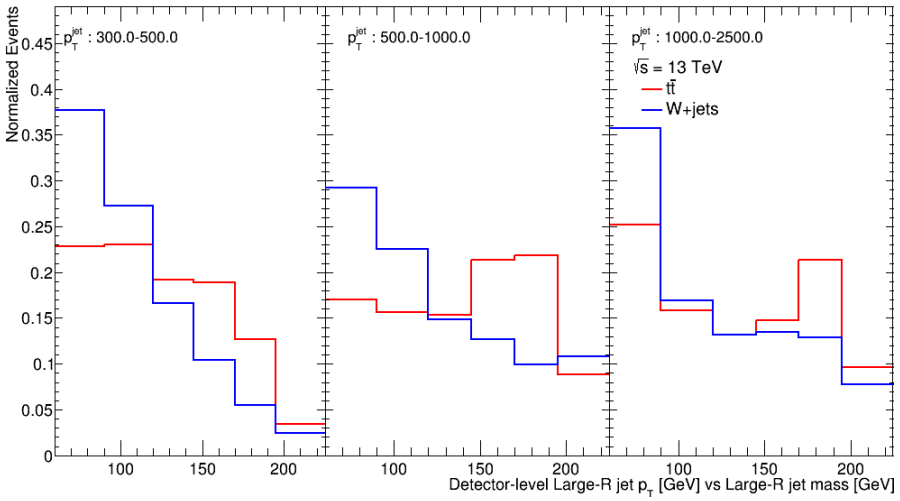

Figure 4.14: Comparison of the large-R jet mass distributions for $t\bar{t}$ and W+jets samples, in different regions of large-R jet p_T. Only events with a single μ or e, $E_T^{miss} > 20$ GeV, $E_T^{miss} + m_T^W > 60$ GeV and containing at least one large-R jet with p_T larger than 200 GeV and a small-R jet with p_T larger than 25 GeV are considered. All large-R jets in the events are included, without applying any jet tagging algorithm.

where R is the radius parameter used to build the initial jet. In order to obtain an observable independent from the recoil of soft radiation inside the jet, the sub-jets are reconstructed with a winner-takes-all (WTA) recombination scheme [119].
The quantity τ_N quantifies the goodness of the description of the large-R jet as formed from N sub-jets, it is small only if all the constituents k are close to one of the N axes corresponding to the sub-jets. Various combinations of τ_N are used as discriminant variables to identify jets originating from top quarks or heavy bosons. In this thesis the tagger used to identify boosted top quarks employs $\tau_{32} = \tau_3/\tau_2$. This quantity is small if a three body hypothesis describes a large-R jet better than a two body one. The distribution of τ_{32} for the signal and the W+jets sample is shown in Figure 4.15, as a function of the p_T of the large-R jet. The discriminating power of the variable decreases at high large-R jet p_T, because the sub-jets are more collimated and the values of τ_N tend to be similar for $N = 2$ and $N = 3$.

In the analysis presented in this thesis, the top tagging algorithm used to identify the hadronically decaying boosted top quarks is based on a combination of requirements on τ_{32} and m^{jet}. The cuts applied on these two variables are defined to obtain a constant 80% selection efficiency on the full p_T^{jet} range. The tagger has been developed using a $Z' \to t\bar{t}$ sample, where both the top quarks decay hadronically, as signal and considering only reconstructed large-R jets matched to the corresponding truth jet ($\Delta R < 0.75$). The signal efficiency is defined as the ratio between the top-tagged jets and all the reconstructed jets. The background

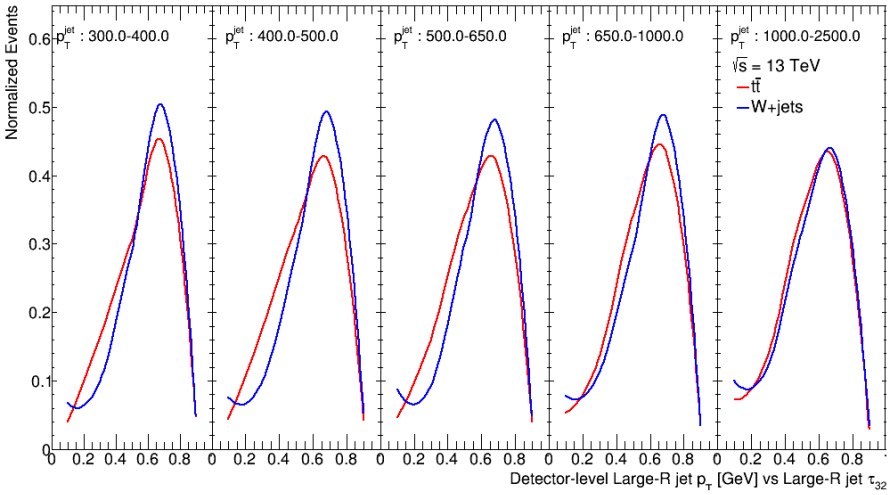

Figure 4.15: Comparison of normalized τ_{32} distribution for $t\bar{t}$ signal and W+jets background, in different regions of large-R jet p_T. The small peak at zero corresponds to jets with less than 3 constituents, afterward discarded from the top tagger. Only events with a single μ or e, $E_T^{miss} > 20$ GeV, $E_T^{miss} + m_T^W > 60$ GeV and containing at least one large-R jet with p_T larger than 200 GeV and a small-R jet with p_T larger than 25 GeV are considered. All large-R jets in the events are included, without applying any jet tagging algorithm.

rejection, instead, is defined as the reciprocal of the fraction of jets from a simulated QCD di-jet sample, matched to a truth-jet, passing the top-tagging algorithm. Figure 4.16 shows the signal efficiency and the background rejection of the tagger as a function of the large-R jet p_T for two different working points, where the efficiency has been fixed to 50% and 80%. The cuts on m^{jet} and τ_{32}^{jet} vary with the large-R jet p_T between the edges requirements shown in Table 4.1. The top tagger is applied

	m^{jet}		τ_{32}^{jet}	
	$p_T^{jet} = 300$ GeV	$p_T^{jet} = 1500$ GeV	$p_T^{jet} = 300$ GeV	$p_T^{jet} = 1500$ GeV
WP 50%	> 85 GeV	>140 GeV	< 0.75	< 0.57
WP 80%	> 70 GeV	>135 GeV	< 0.85	< 0.7

Table 4.1: Edge requirements on the two variables used in the top tagging procedure.

in the present analysis using the 80% WP.
The signal sample used in this thesis is $t\bar{t}$, the cuts applied to select the signal differs from the ones used to derive the tagger and no matching are applied among reconstructed and truth jets, therefore a different efficiency of the tagger with respect to the nominal one is expected. The efficiency observed in the analysis is shown in Figure 4.17.

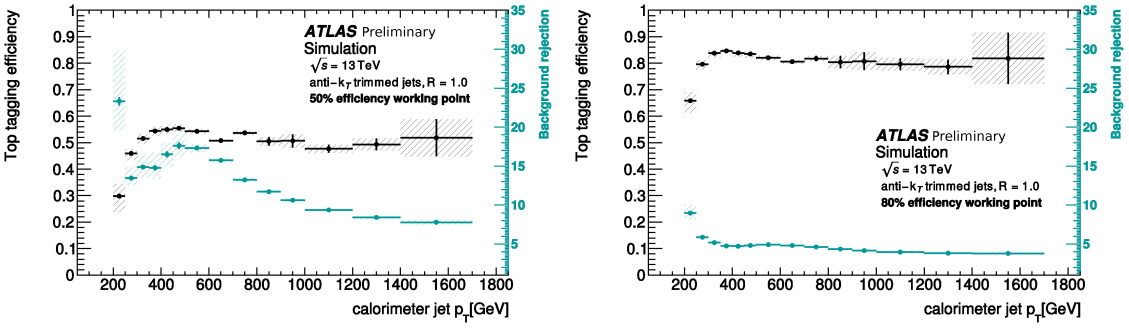

(a) (b)

Figure 4.16: Efficiency and rejection of the top-tagging algorithm versus jet transverse momentum p_T for simulated $Z' \to t\bar{t}$ events and for simulated QCD di-jet production at two different working point 50% (a) and 80% (b) [120].

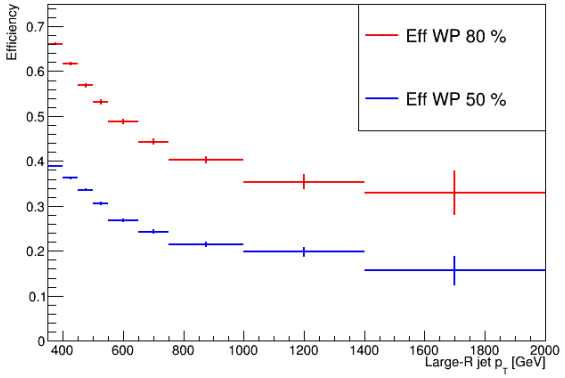

Figure 4.17: Tagging efficiency evaluated using $t\bar{t}$ sample as signal, without any matching to the truth jets and after a pre-selection that contains requirement on the presence of a single lepton and missing transverse energy.

4.1.6 Missing Transverse Energy

The conservation of momentum implies that the total momentum of the collisions products in the plane transverse to the beam pipe should be zero. The ATLAS detector has a complete coverage in the transverse plane and this allows to individuate weakly-interacting particles by computing the momentum imbalance of all the visible transverse momentum, called missing transverse momentum (E_T^{miss}).
The measurement of E_T^{miss} can be affected by the presence of particles not properly reconstructed or falling outside the acceptance of the detector. For these reasons the performance of the reconstruction of this quantity is studied in samples that contain neutrinos as $W \to l\nu$, where an high component of E_T^{miss} is expected, and in $Z \to \mu\mu$, where the expected E_T^{miss} from not interacting particles is zero and its measurement gives an estimate of the detector performance.
The imbalance to determine E_T^{miss} can be written as [121]:

$$E_{x(y)}^{miss} = E_{x(y)}^{miss,e} + E_{x(y)}^{miss,\mu} + E_{x(y)}^{miss,\gamma} + E_{x(y)}^{miss,\tau} + E_{x(y)}^{miss,jets} + E_{x(y)}^{miss,soft} \quad (4.8)$$

where the terms for jets, charged leptons, and photons are the negative vector sum of the momenta of the respective calibrated objects. The soft term can be reconstructed using the calorimeter cells that are not associated to hard objects (*Calorimeter Soft Term*, CST) or using a track based approach (*Track Soft Term*, TST). In this latter case the tracks from the primary vertex, not matched to other objects or ghost associated to jets are considered. Also a third approach completely based on the tracks can be used to determine the E_T^{miss}. In this case it is reconstructed as the negative sum of the momenta of good ID tracks.

The method used to reconstruct the soft term influences the performance of the

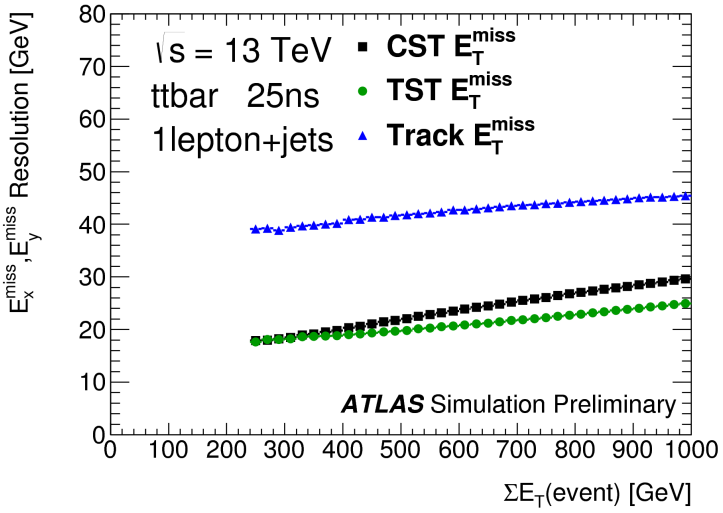

Figure 4.18: Comparison of the performance of TST E_T^{miss} , CST E_T^{miss} and Track E_T^{miss}, quantified by the resolution as a function of E_T in $t\bar{t}$ events [121].

reconstructed E_T^{miss}, as can be seen in Figure 4.18, where the resolution on reconstructed E_T^{miss} in a $t\bar{t}$ sample is compared among the three methods. Here the resolution is presented as a function of $\sum E_T$, defined as the scalar sum of transverse momenta of the objects used to calculate $E_{x(y)}^{miss}$.
In the analysis presented in this thesis the TST method is used to reconstruct the E_T^{miss}.

4.1.7 Overlap Removal

In some cases the object reconstruction, as described in this paragraph, can produce two different objects from the same energy deposit and lead to an energy double counting or to a mis-reconstruction of the objects. To avoid these problems an overlap removal among collections of objects is applied.
If a small-R jet is within a $\Delta R < 0.2$ from a reconstructed electron it is removed from the jets collection. Subsequently, to reduce the impact of non-prompt leptons, electrons in a $\Delta R < 0.4$ from a jet are removed. If a small-R jet has less than three tracks and is within a $\Delta R < 0.4$ from a muon it is removed from the good jet

collection, then the muons separated by $\Delta R < 0.4$ from a small-R jet with at least 3 tracks are removed.

4.2 Event Selection

The objects defined as described in Section 4.1 are used to identify $t\bar{t}$ events and reconstruct the $t\bar{t}$ system. The analysis applies two different not-exclusive selections. One is optimized to reconstruct the $t\bar{t}$ system in the resolved topology, where the 3 jets deriving from the decay of the hadronic top can be resolved by the detector. The other is specifically designed to deal with the collimated decay topology of highly energetic top quarks (boosted topology).
The common requirements applied in both topologies are the presence in the event of a single lepton (μ or e) with $p_T^{\ell} > 25$ GeV, matching the trigger object, and the presence of a primary vertex with two or more associated tracks.
For the resolved selection, each event must also contain at least four small-R jets with $p_T > 25$ GeV and $|\eta| < 2.5$ of which at least two must be tagged as b-jets.
The boosted selection requires events with at least one small-R jet close to the lepton, i.e. with ΔR(small-R jet, lepton) < 2.0, and at least one large-R jet with $p_T > 300$ GeV. Only events with a top tagged large-R jet are retained. The large-R jet must be well separated from the small-R jet associated with the lepton, ΔR(large-R jet, small-R jet) > 1.5 and from the lepton itself, $\Delta\phi$(large-R jet, lepton) > 1.0. This cut, as shown in Figure 4.19a, doesn't have a large discriminating power between signal and background, but helps in rejecting fake large-R jets, seeded by a hard lepton. All the small-R jets that fulfill the angular separation

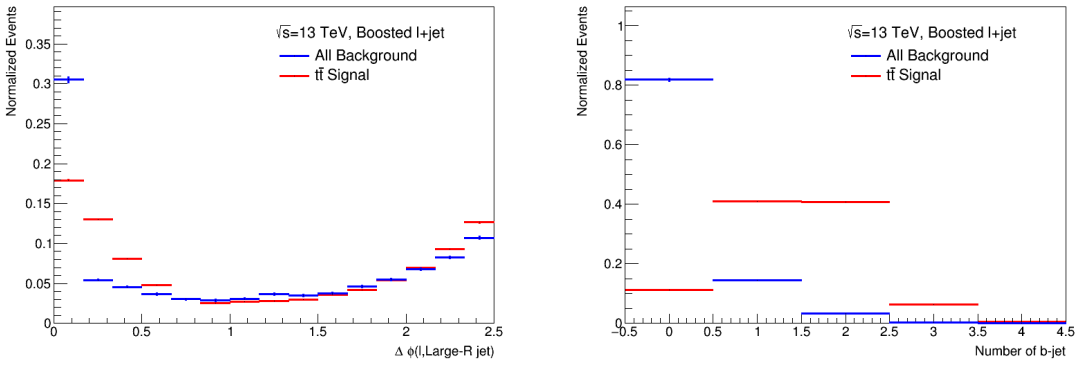

(a) (b)

Figure 4.19: Normalized kinematic distribution in the boosted topology at the detector level: (a) $\Delta\phi$(large-R jet, lepton) > 1.0, (b) b-tagged jets multiplicity. The blue line represent the $t\bar{t}$ signal, while the red line the sum of all the backgrounds. All events passing all the requirement till the fourth row in Table 4.2 are included.

requirement with the lepton and the large-R jet are considered associated to the lepton. In addition, it is required that at least one b-tagged small-R jet fulfills the

following requirements: it is either inside the large-R jet, ΔR(large-R jet, b-tagged jet) < 1.0, or it is associated with the lepton. Since the decay products of the $t\bar{t}$ system always include two b quarks, the presence of b-tagged jets is a very good discriminant to select $t\bar{t}$ events, as shown in Figure 4.19b. However the b-tagging efficiency decreases at high p_T, as shown in Figure 4.9b, and in dense environment as the large-R jets, therefore in the boosted topology only one b-tag is required, to avoid a drop in signal efficiency at high p_T. Finally, in order to suppress the multijet background[3] in the boosted topology the missing transverse momentum must be larger than 20 GeV and the sum of E_T^{miss} and m_{T}^W (transverse mass of the W boson[4]) must be larger than 60 GeV.
In order to reduce the number of small-R jets originated by pile-up contamination, an additional requirement on all the small-R jets with $p_T < 60$ GeV and $|\eta| < 2.4$ based on the Jet Vertex Tagger (JVT) [122] is applied in both boosted and resolved topologies. This quantity is a likelihood discriminant that combines information deriving from tracking and quantifies the match of a jet to the primary vertex.
The event selection is summarized in Table 4.2.

4.2.1 Kinematic Reconstruction of the $t\bar{t}$ System

In the boosted topology, the highest-p_T large-R jet that satisfies the top-tagging requirements is identified as the hadronic top-quark candidate. The number of events with 2 top-tagged large-R jets is $\sim 10\%$ of the total, as shown in Figure 4.20.

In the resolved topology, the pseudo-top algorithm [123] reconstructs the four-

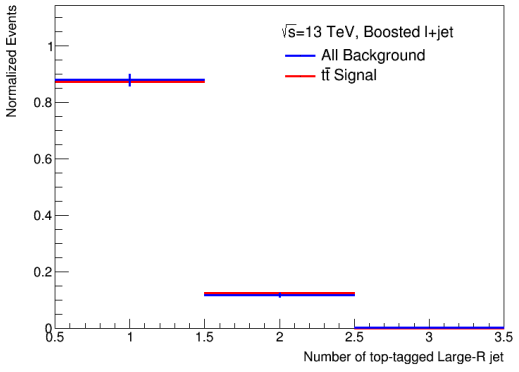

Figure 4.20: Normalized distribution of the number of top-tagged large-R jets present in an event.

momenta of the top quarks and their complete decay chain from final-state objects, namely the charged lepton (electron or muon), missing transverse momentum, and

[3] Also referred to as non-prompt real-leptons and fake-leptons background, as described in Section 4.3.2.

[4] $m_{\mathrm{T}}^W = \sqrt{2p_{\mathrm{T}}^{\ell} E_{\mathrm{T}}^{\mathrm{miss}} (1 - \cos\Delta\phi(\ell, E_{\mathrm{T}}^{\mathrm{miss}}))}$, where ℓ stands for the charged lepton.

Level	Detector	
Topology	Resolved	Boosted
Leptons	$\lvert d_0\rvert/\sigma(d_0) < 5$ and $\lvert z_0 \sin\theta\rvert < 0.5$ mm Track and calorimeter isolation $\lvert\eta\rvert < 1.37$ or $1.52 < \lvert\eta\rvert < 2.47$ (e), $\lvert\eta\rvert < 2.5$ (μ) E_{T} (e), p_{T} (μ) > 25 GeV	
Small-R jets	$\lvert\eta\rvert < 2.5$ $p_{\mathrm{T}} > 25$ GeV JVT cut (if $p_{\mathrm{T}} < 60$ GeV and $\lvert\eta\rvert < 2.4$)	
Num. of small-R jets	≥ 4 jets	≥ 1 jet
E_T^{miss}, m_T^W		$E_T^{miss} > 20$ GeV, $E_T^{miss} + m_T^W > 60$ GeV
Leptonic top	Kinematic top-quark reconstruction	least one small-R jet with $\Delta R(\ell$, small-R jet$) < 2.0$
Hadronic top	Kinematic top-quark reconstruction	The leading-p_{T} trimmed large-R jet has: $\lvert\eta\rvert < 2.0$, 300 GeV $< p_{\mathrm{T}} <$ 1500 GeV, $m > 50$ GeV, Top-tagging at 80% efficiency ΔR(large-R jet, small-R jet associated with lepton) $>$ 1.5, $\Delta\phi(\ell$, large-R jet$) > 1.0$
b-tagging	At least 2 b-tagged jets	At least one of: 1) the leading-p_{T} small-R jet with $\Delta R(\ell$, small-R jet$) < 2.0$ is b-tagged 2) at least one small-R jet with ΔR(large-R jet, small-R jet$) < 1.0$ is b-tagged

Table 4.2: Summary of the requirements for detector-level events, for both the resolved and boosted event selections. The description of the kinematic top-quark reconstruction for the resolved topology is in Section 4.2.1. Leptonic (hadronic) top refers to the top quark that decays into a leptonically (hadronically) decaying W boson.

four jets, two of which are b-tagged. In events with more than two b-tagged jets, only the two with the highest transverse momentum are considered as b-jets.
The algorithm starts with the reconstruction of the neutrino four-momentum.
The x and y components of the neutrino momentum are taken directly from the E_T^{miss}, while the z component is calculated imposing the W boson mass constraint on the invariant mass of the charged-lepton and neutrino system. If the resulting quadratic equation has two real solutions, the one with the smaller value of $|p_z|$ is chosen. If the discriminant is negative, only the real part is considered. The leptonically decaying W boson is reconstructed from the charged lepton and the neutrino. The leptonic top quark is reconstructed from the leptonic W and the b-tagged jet closest in ΔR to the charged lepton. The hadronic W boson is reconstructed from the two non-b-tagged jets whose invariant mass is closest to the mass of the W boson. Finally, the hadronic top quark is reconstructed from the hadronic W boson and the other b-tagged jet.

4.3 Background Determination

Due to the presence of a prompt lepton and the requirements on b-tagging and top-tagging, the fraction of non $t\bar{t}$ events selected in the signal region is small ($\sim 15\%$). However there are various processes that contribute to the background and can be reconstructed as a $t\bar{t}$ event: single top, W+jets, Z+jets, WW or ZW (Diboson) and $t\bar{t}V$.
The single top produced in t-channel and Wt-channel shares a very similar final state with the signal, as shown in Figure 4.21, and represents the main background both in boosted and resolved topology. Also the processes where the W and Z

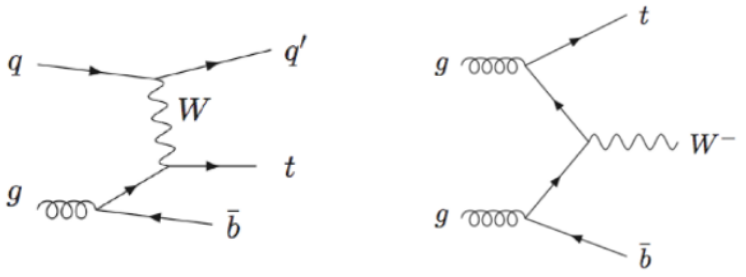

Figure 4.21: Feynman diagram of the single top process in t-channel (a) and Wt-channel (b), that could mimic the $t\bar{t}$ production. The Wt-channel has exactly the same final state of the $t\bar{t}$ decay while in the t-channel is sufficient the presence of an extra jet to mimic perfectly the $t\bar{t}$ decay.

bosons are produced in association with jets and decay leptonically have a final state similar to the semileptonic decay of the $t\bar{t}$ system. These can be reconstructed as signal if one or more of the additional jets derive from an heavy quark or are mis-tagged as a b-jets. The W+jets process has an high production cross-section, two

order of magnitude larger than the $t\bar{t}$ production one, and represents a main source of background in boosted regime, where only one b-jet is required. Analogously also the WW and ZZ events, where one of the bosons decay hadronically and the other leptonically can be reconstructed as signal, if additional jets are radiated in the process. The $t\bar{t}V$ process can be easily reconstructed as $t\bar{t}$, but its cross-section is three order of magnitude lower than $t\bar{t}$ production, consequently it represents a tiny background in both boosted and resolved topologies.
An additional source of background is represented by events with a mis-identified lepton (multijet background), in this case the estimate is performed using a data driven technique.

The contributions of the single top, Z+jets, Diboson, $t\bar{t}V$ is estimated directly through Monte Carlo simulations. The W+jets prediction, instead, is corrected using data driven scale factors.
$t\bar{t}$ events where both top quarks decay leptonically, that pass the selection, are considered signal and contribute to $\sim 5\%$ of the total yield. Semileptonic $t\bar{t}$ decays including a τ are considered signal only if the τ decays leptonically, the events where the τ decays hadronically are accounted for in the multijet background.

4.3.1 W+jets Data-driven Estimation

The initial estimate of the W+jets background is obtained from the SHERPA MC samples described in Section 4.2, but additional data-driven weights are estimated and applied to correct the overall normalization and the flavour composition to match what is observed in data.
The Charge Asymmetry (CA) method is used to obtain the overall normalization. This method exploit the difference in production cross-section for W^+ and W^-, due to the LHC beam composition. The W^+ production is due to the interaction of a u quark with a see quark, while W^- is produced from the interaction of a d quark. Since in pp collisions the number of valence u quarks is higher with respect to d quarks, the production of a W^+ is favoured with respect to W^-.
The cross-section ratio $\frac{(\sigma_{pp\to W^+})}{(\sigma_{pp\to W^-})}$ is predicted [124] with a better precision than the single $W^\pm$ production cross-section and can be used to extract the normalization. The equation used is:

$$N_{Data,W} = N_{W^+} + N_{W^-} = \frac{r_{MC}+1}{r_{MC}-1}(D^+ - D^-) \tag{4.9}$$

where the W charge is determined from the charge of the prompt lepton in the event. In equation (4.9) $D^\pm$ indicates the data, once subtracted the MC estimate of the other processes that could give a contribution to charge asymmetry (single top, $t\bar{t}V$ and WZ events), while r_{MC} represents the $\frac{(\sigma_{pp\to W^+})}{(\sigma_{pp\to W^-})}$ estimated from MC simulations. The CA weight is then extracted as $\frac{N_{Data,W}}{N_{MC,W}}$.
To increase the W+jet sample the scale factors are obtained applying a looser selection with respect to the one indicated in Section 4.2, and no b-tagging requirement is applied. The normalization is extracted in the region where the W is produced

with exactly two jets and then extrapolated to the region with higher jet multiplicity. The normalization weights, obtained applying the CA method, are reported in Table 4.3.

Beside the normalization weights, additional scale factors are derived to correct

Channel	2j ex	3j ex	4j incl
e+jets	0.967 ± 0.033	0.824 ± 0.023	0.959 ± 0.037
μ+jets	1.024 ± 0.020	0.944 ± 0.016	0.925 ± 0.039

Table 4.3: The W+jets scale factors derived via the charge asymmetry method in separate jet multiplicity bins, including their statistical uncertainties.

the flavour composition of the W+jet sample (HF). These weights are extracted at the same time of the normalization weights in an iterative procedure and don't have effects on the normalization of the sample. These weights, as the normalization ones, are extracted in the region where the W is produced with 2 additional jets and then extrapolated to the region of interest for the analysis.
The weights are extracted by solving the following equation:

$$\begin{pmatrix} CA \cdot (N^{bb}_{MC,W^-} + N^{bb}_{MC,W^-}) & CA \cdot N^{c}_{MC,W^-} & CA \cdot N^{ll}_{MC,W^-} \\ (f_{bb} + f_{cc}) & f_c & f_{ll} \\ CA \cdot (N^{bb}_{MC,W^+} + N^{bb}_{MC,W^+}) & CA \cdot N^{c}_{MC,W^+} & CA \cdot N^{ll}_{MC,W^+} \end{pmatrix} \cdot \begin{pmatrix} K_{bb,cc} \\ K_c \\ K_{ll} \end{pmatrix} = \begin{pmatrix} D_{W^-} \\ 1.0 \\ D_{W^+} \end{pmatrix} \quad (4.10)$$

where $D_{W^\pm}$ is the b-tagged yields evaluated after all the non-W+jets events have been subtracted to data:

$$D_{W^\pm} = D^{\pm}_{Data} - N^{\pm}_{\text{otherbkg}}. \quad (4.11)$$

In equation (4.10) $N^{c,bb,ll}_{MC,W^{+(-)}}$ represents the b-tagged W+jets yield with charge $+(-)$ and (c, bb, ll) represents the jet flavour, while the factors f_j represent the fraction of W+jets events for a given flavour $j \in [light, c, bb, cc]$ before the b-tagging is applied (pre-tag):

$$f_i = \frac{N^{j,pre-tag}_{MC,W}}{N^{pre-tag}_{MC,W}}. \quad (4.12)$$

The second equation of (4.10) represents an unitariety constraint. The first and third equation of (4.10) represents the adaption of the MC yields to the data yields, applying the scaling factors. The linear equation system is solved for the vector of scaling factors $(K_{bb,cc}, K_{cc}, K_c)$ in an iterative process, applying the scaling factors to the pre-tag yields after each iteration and recalculating the charge asymmetry normalization CA. The iterative procedure can be described in four steps and starts with $K_i = 1.0$:

1. Apply scaling factors K_i to MC pre-tag yields used for calculation of CA.

2. Calculate charge asymmetry normalization CA.

3. Solve the linear system (4.10).

4. Return to step 1.

The scale factors are applied in the analysis to the events and depend on the jet multiplicity and the lepton flavour. A set of CA and HF scale factors is extracted for each detector level systematic uncertainty, using the MC samples shifted for each systematic source. The effect of the systematic uncertainties enter the procedure as a change in the MC yields subtracted to the data during the extraction of the scale factors. More details on the various systematic sources are reported in Chapter 6. The W+jets estimate is derived in a pre-tag region shared between resolved and boosted and the estimate, being done in bins of jet multiplicity, can be applied to both topologies.
The agreement reached using the CA and HF scale factors is shown in Figure 4.22, where the data are compared with the predictions in a region dominated by the W+jet events. This region is obtained removing the b-tagging and top tagging requirements from the boosted selection, listed in Table 4.2. The agreement is below 10% in all the distributions shown, a part for the large-R jet p_T tail.

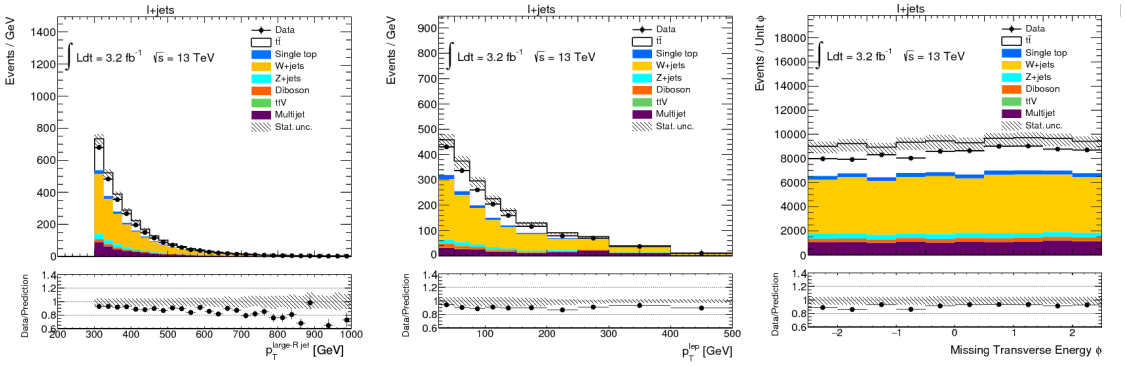

(a) (b) (c)

Figure 4.22: Comparison between data and MC predictions in a phase space region dominated by the W+jet. The selection applied on the events includes the same cuts applied for boosted topology in Table 4.2, a part from the b-tagging and top-tagging requirements. The number of events is presented as a function of the large-R jets p_T (a), the lepton p_T (b) and the $E_T^{miss}\phi$ (c).

4.3.2 Multijet Background Data-driven Estimation

Events with non-prompt leptons or non-leptonic particles identified as leptons, may satisfy the analysis selection criteria giving rise to the so called multijet/fake background. The estimate of this source of background is performed using a data-driven technique, called Matrix Method [125].
The first step of the estimate is the definition of two levels of lepton selection: *tight* and *loose*. The first corresponds to the lepton selection used in the analysis while

the *loose* selection contains less stringent identification and isolation requirements. The two definitions are summarized in Table 4.4.
The inclusive data sample (S) is selected by requiring exactly one *loose* lepton, and at least one jet. The sample S can be divided in two sub-samples, called T and L, based on the presence of a *tight* (T) or a *loose* (L) lepton in the event, or can be divided in a subset of events containing a real lepton (R) or just a fake lepton (F):

$$S = T + L = R + F. \tag{4.13}$$

Background events that enter in the selected data sample are defined by the intersection of T and F.
The matrix method is based on the equation:

$$\begin{pmatrix} \langle n_T \rangle \\ \langle n_L \rangle \end{pmatrix} = \begin{pmatrix} \varepsilon_r & \varepsilon_f \\ \overline{\varepsilon_r} & \overline{\varepsilon_f} \end{pmatrix} \begin{pmatrix} n_R \\ n_F \end{pmatrix} \tag{4.14}$$

which relates the expected number of *tight* and *loose* events, $\langle n_T \rangle$ and $\langle n_L \rangle$, to the unknown number of real and fakes events, n_R and n_F. The coefficient ε_r (ε_f) is defined as the probability of a real (fake) lepton to pass the *tight* selection criteria and it is called the real (fake) efficiency. The coefficients $\overline{\varepsilon_i}$ are defined as $\overline{\varepsilon_i} = 1 - \varepsilon_i$. The real (fake) efficiency is measured in data control regions dominated by real (fake) leptons events.
In order to estimate the number of fake leptons in the *tight* selection ($\varepsilon_f \langle n_T \rangle$) the

	Loose selection	**Tight selection**
Electron	Identification: MediumLH Isolation: None	Identification: TightLH Isolation: Gradient
Muon	Identification: Medium Isolation: None	Identification: Medium Isolation: Gradient

Table 4.4: Summary of differences between *loose* and *tight* lepton selection requirements.

equation is inverted, with the assumption $\varepsilon_r \neq \varepsilon_f$:

$$\begin{pmatrix} n_R \\ n_F \end{pmatrix} = \frac{1}{\varepsilon_r - \varepsilon_f} \begin{pmatrix} \overline{\varepsilon_f} & -\varepsilon_f \\ -\overline{\varepsilon_r} & \varepsilon_r \end{pmatrix} \begin{pmatrix} \langle n_T \rangle \\ \langle n_L \rangle \end{pmatrix} \tag{4.15}$$

and the estimator of n_{TF} can be constructed:

$$\hat{n}_{TF} = \varepsilon_f \hat{n}_F = \frac{\varepsilon_f}{\varepsilon_r - \varepsilon_f} \left(\varepsilon_r (n_T + n_L) - n_T \right). \tag{4.16}$$

and evaluated from the observed numbers of *tight* and *loose* events.
To account for the dependency of the efficiencies ε_r and ε_f on kinematic properties of an event, they are parameterized in the chosen observables and calculated per-event. In practice, the estimation of the background in a certain bin of a distribution is obtained summing all *loose* and *tight* events i in that bin, weighted by:

$$w_i = \frac{\varepsilon_f}{\varepsilon_r - \varepsilon_f}(\varepsilon_r - \delta_{i\in T}) \tag{4.17}$$

where $\delta_{i\in T} = 1$ if the event passes the *tight* selection and 0 otherwise.
The fake efficiency is measured as the ratio of the number of *tight* lepton events to the number of all events in a data control sample, dominated by multijet background, selected requiring:

- exactly one *loose* or *tight* lepton,
- at least one jet,
- in the e+jets channel: $E_T^{miss} < 30$ GeV and $m_{\mathrm{T}}^{\mathrm{W}} < 50$ GeV,
- in the μ+jets channel: muon $|d_0^{\mathrm{sig}}| > 5$,

where d_0^{sig} is the transverse parameter significance defined as d_0/σ_{d_0}. The residual event yields from other processes ($t\bar{t}$, single top, W+jets, Z+jets) are estimated with MC simulation and subtracted separately in the numerator and denominator of the efficiency.
The fake efficiency is parameterized using both one and two dimensional histograms and the final efficiency is obtained combining several parameterizations:

- **electron-channel:**

$$\varepsilon_f = \sqrt[3]{\varepsilon_f^{\mathrm{2D}}(p_T^\ell, N_b)\cdot\varepsilon_f^{\mathrm{2D}}(\Delta\phi,\eta^\ell)\cdot\varepsilon_f^{\mathrm{2D}}(\Delta\phi,p_T^\ell)}. \tag{4.18}$$

- **muon-channel:** in this case two different parameterizations are used for the low and high p_T regions,

$$p_T^{high} : \varepsilon_f^{\mathrm{H}} = \varepsilon_f(p_T^\ell) \tag{4.19}$$

$$p_T^{low} : \varepsilon_f^{\mathrm{L}} = \sqrt{\varepsilon_f^{\mathrm{2D}}(\Delta\phi,p_T^\ell)\cdot\varepsilon_f(E_T^{miss})} \tag{4.20}$$

Here ℓ represents the lepton, N_b the b-tagged jets multiplicity, $\Delta\phi$ the azimuthal angle difference between the lepton and the E_T^{miss}. The two parameterizations are combined as $\varepsilon_f = (1-f)\cdot\varepsilon_f^L + f\cdot\varepsilon_f^H$, where f is the Fermi function defined as:

$$f = f(p_T^\ell) = (1 + e^{-\frac{p_T^\ell - 60GeV}{10GeV}})^{-1}. \tag{4.21}$$

The real efficiency is measured with the tag-and-probe method on a $Z \to \ell\ell$ sample. Events with a pair of same-flavour opposite-sign *loose* or *tight* leptons and

at least one jet are selected, requiring the invariant mass of the dilepton system to be between 60 and 120 GeV. If one of the two leptons passes the *tight* lepton requirements, it is considered a tag and the other lepton is considered a probe. The denominator of the efficiency is the number of all probes, whereas the numerator is the number of probes which pass the *tight* criteria. If both leptons pass the *tight* criteria, the pair serves both as a tag-probe and as a probe-tag pair.
The parameterization used for the real efficiency is:

- **electron-channel:**
$$\varepsilon_r = \varepsilon_r(p_T^\ell) \tag{4.22}$$
- **muon-channel:** two different parameterizations are used for the low and high p_T regions,
$$p_T^{high} : \varepsilon_f^{\mathrm{H}} = \sqrt{\varepsilon_r(\Delta\phi) \cdot \varepsilon_r(p_T^\ell)} \tag{4.23}$$
$$p_T^{low} : \varepsilon_f^{\mathrm{L}} = \varepsilon_r(p_T^\ell). \tag{4.24}$$

The combination of the two parametrization is done in the same way as for the fakes efficiencies.

4.4 Data MC Comparison at Detector Level

The selections described in 4.2 applied on data, simulated signal and all background components, lead to the yields reported in Table 4.5. The purity of the signal is high in both resolved and boosted topology, 87% and 84% respectively.

The two selections overlap in the region where the p_T of the hadronic top is larger than 300 GeV. In this region $\sim 50 - 30\%$ (depending on p_T) of the events passing the boosted selection are selected also by the resolved one, as shown in Figure 4.24. However, on the overlapping events the *pseudo-top* algorithm does not provide a good reconstruction of the $t\bar{t}$ system, as shown in Figure 4.23. Here only events with parton $p_T^{t,had} > 300$ GeV are included, and is shown the pseudo-top reconstruction leads to a large fraction of the reconstructed top not matched with the parton level top, neither angular nor in p_T. In Figure 4.23a, the peak around $\Delta R = 3$ is due to cases where the reconstruction algorithm peaks up the leptonic top, this is possible due to the mis-reconstruction of some objects present in the event.

Figure 4.25 shows the distributions of the E_T^{miss} and the jet multiplicity in the resolved selection. The difference between MC and data, shown in the ratio plot, is covered by the uncertainties.
In Figure 4.26 the distributions of the p_T^μ and m_T^W in boosted events, and the mass and τ_{32} of the hadronic top candidate, are shown. The invariant mass of the reconstructed hadronic top quark has a peak on the W boson mass, indicating that not all of the top-quark decay products are always contained within the jet. The

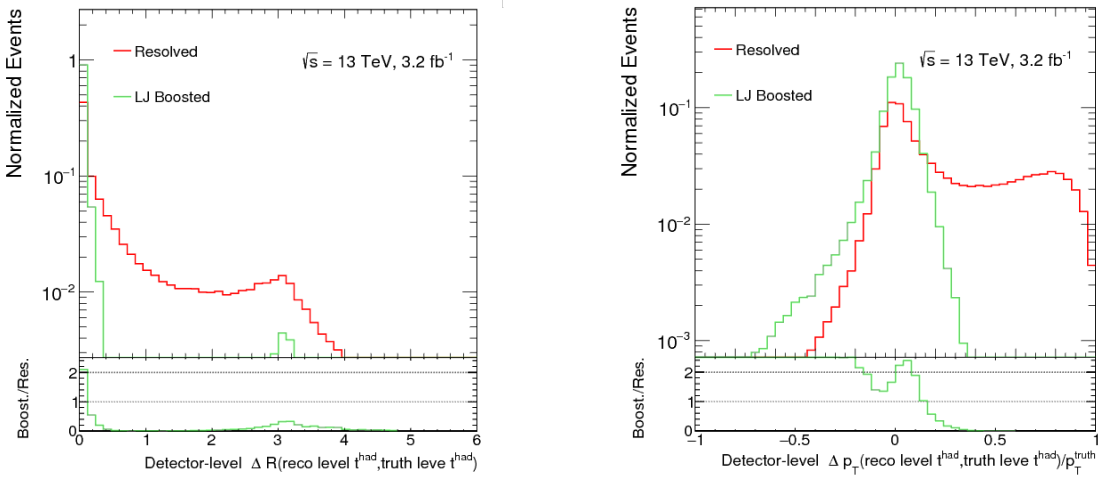

(a) (b)

Figure 4.23: Comparison between the truth hadronic top position in the $y - \phi$ plane (a) and p_T (b) with respect to the reconstructed ones, using resolved (red) and boosted (green) approaches, for events where the p_T^{had} is larger than 300 GeV.

Process	Expected events	
	Resolved	Boosted
$t\bar{t}$	123800 ± 10600	7000 ± 1100
Single top	6300 ± 800	500 ± 80
Multijets	5700 ± 3000	300 ± 80
W+jets	$3600\ ^{+2000}_{-2400}$	500 ± 200
Z+jets	1300 ± 700	60 ± 40
$t\bar{t}V$	400 ± 100	70 ± 10
Diboson	300 ± 200	60 ± 10
Total prediction	$142000\ ^{+11000}_{-12000}$	8300 ± 1300
Data	155593	7368

Table 4.5: Event yields after the resolved and boosted selections. The signal model, denoted $t\bar{t}$ in the table, is generated using POWHEG+PYTHIA6, normalized to the theoretical total NNLO cross-section. The uncertainties include the combined statistical and systematic uncertainties, excluding the systematic uncertainties related to the modelling of the $t\bar{t}$ system [1].

agreement between the data and MC predictions is covered from the systematic uncertainties for all the 4 distributions.

In the resolved topology the data tends to overestimate the predictions, while in the boosted it is the opposite. The reason for this difference is shown in Figure 4.27a, 4.27b where the comparison between data and MC predictions is shown with respect to the $p_T^{t,had}$ in the boosted and resolved topology. The ratio pads show a trend in the data MC agreement, at low p_T the predictions underestimate

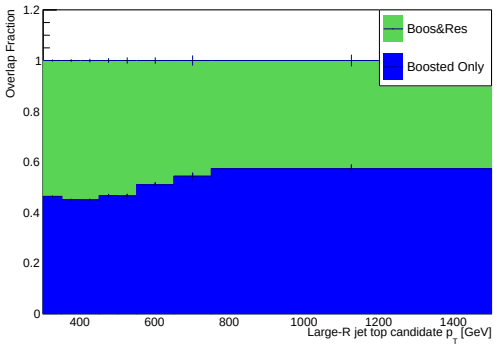

Figure 4.24: Fraction of the boosted events that overlaps with the resolved selection as a function of the large-R jet p_T. In blue is represented the fraction of events that pass only the boosted selection, while in green the fraction that pass both the selections, with respect to all boosted events. The fraction is evaluated using $t\bar{t}$ POWHEG+PYTHIA6 simulation.

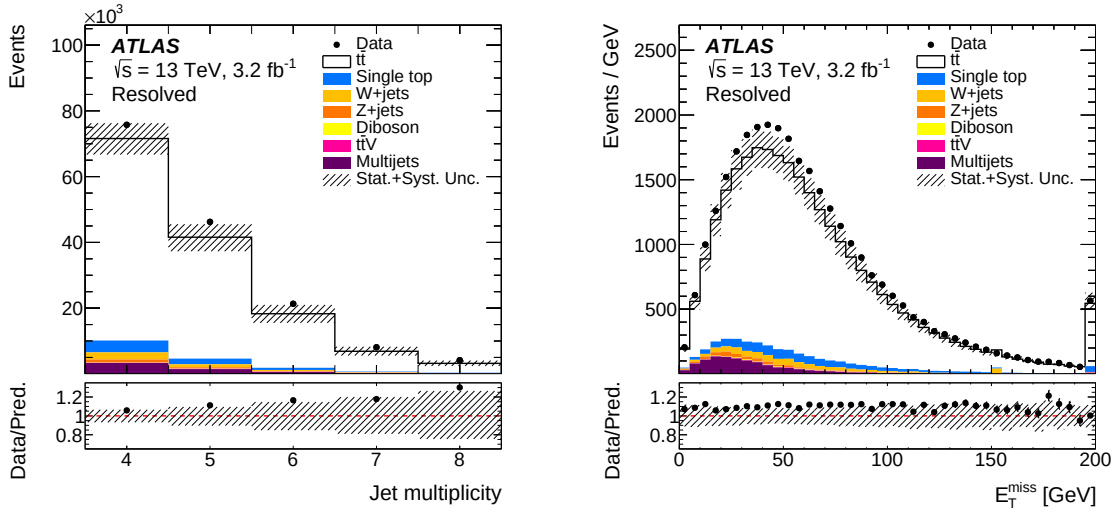

(a) (b)

Figure 4.25: Kinematic distributions in the resolved topology at the detector level: (a) jet multiplicity, (b) E_T^{miss}. The hatched area indicates the combined statistical and systematic uncertainties in the total prediction, excluding systematic uncertainties related to the modelling of the $t\bar{t}$ system. Events beyond the range of the horizontal axis are included in the last bin.

the data while in the boosted regime ($p_T^{t,had} > 300$ GeV) the number of expected events exceeds data. Figures 4.27 and 4.28 show all the observables that will be unfolded to extract the differential cross-section measurement in resolved and boosted regime. In all distributions the difference between MC and data is covered by the uncertainties.

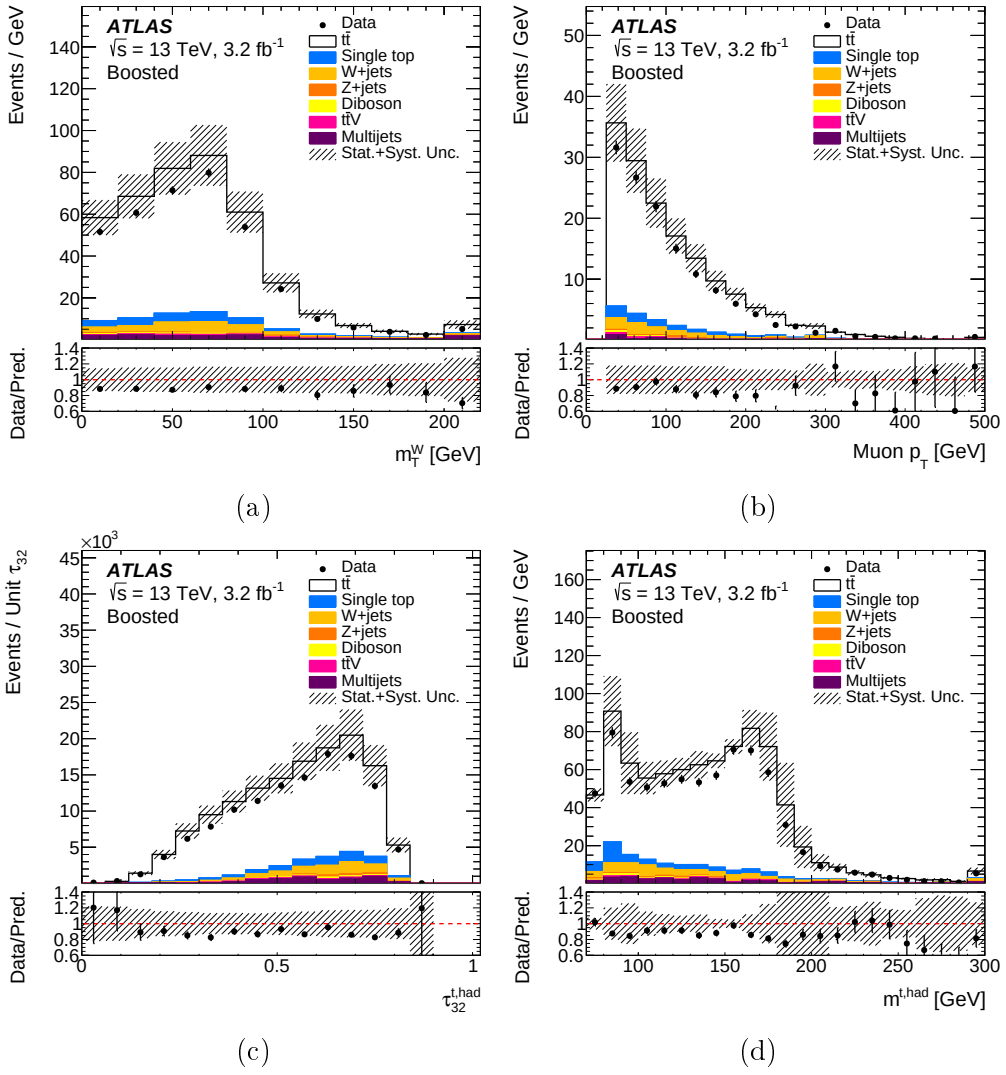

Figure 4.26: Kinematic distributions in the boosted topology at the detector level: (a) m_T^W, (b) p_T^μ, (c) large-R jet τ_{32}, (d) large-R jet mass. The hatched area indicates the combined statistical and systematic uncertainties in the total prediction, excluding systematic uncertainties related to the modelling of the $t\bar{t}$ system. Events beyond the range of the horizontal axis are included in the last bin [1].

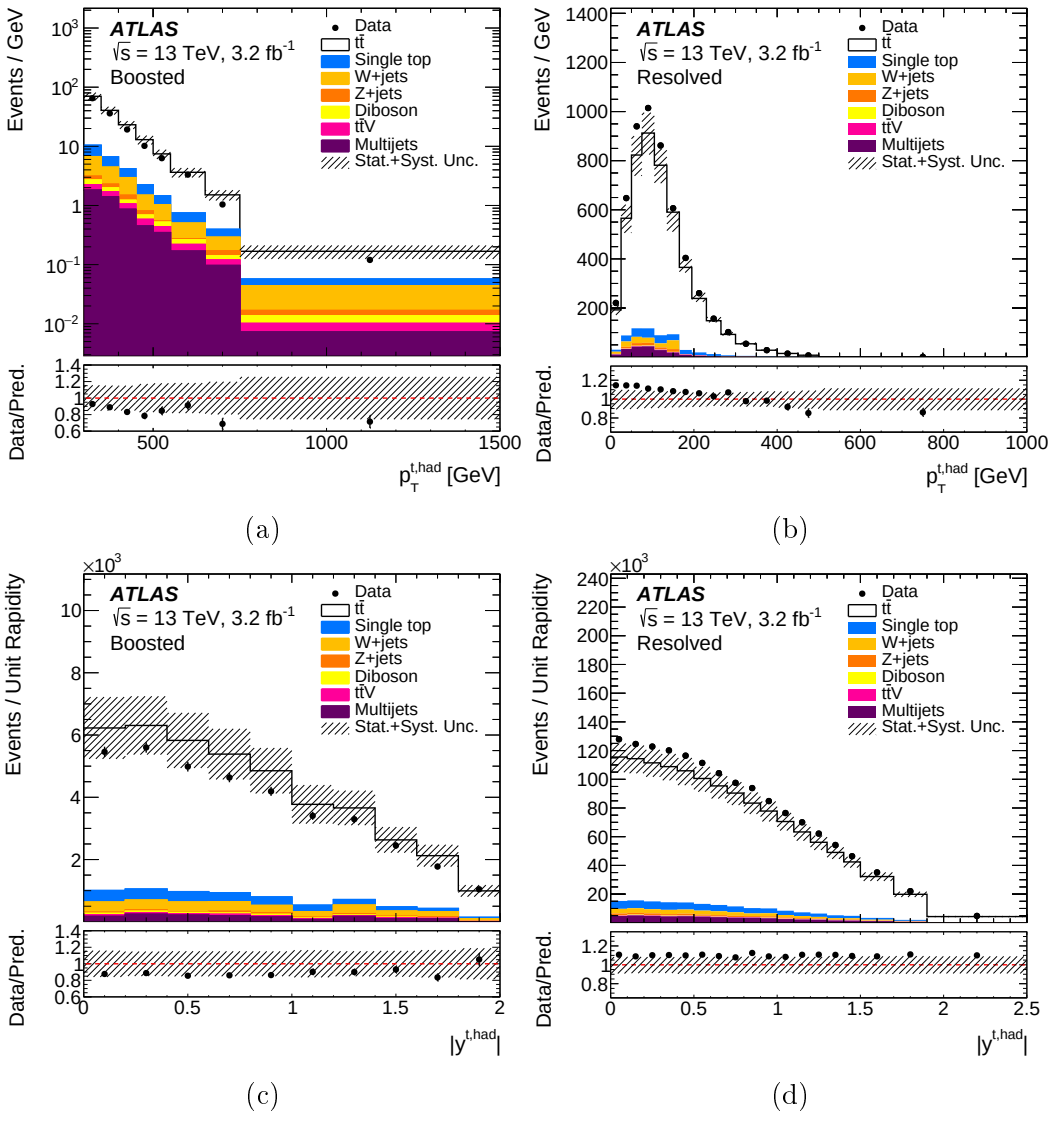

Figure 4.27: Kinematic distributions of $p_T^{t,had}$ (a)(b) and $|y^{t,had}|$ (c)(d) in the boosted (left) and resolved (right) topology at the detector level. The hatched area indicates the combined statistical and systematic uncertainties in the total prediction, excluding systematic uncertainties related to the modelling of the $t\bar{t}$ system. Events beyond the range of the horizontal axis are included in the last bin [1].

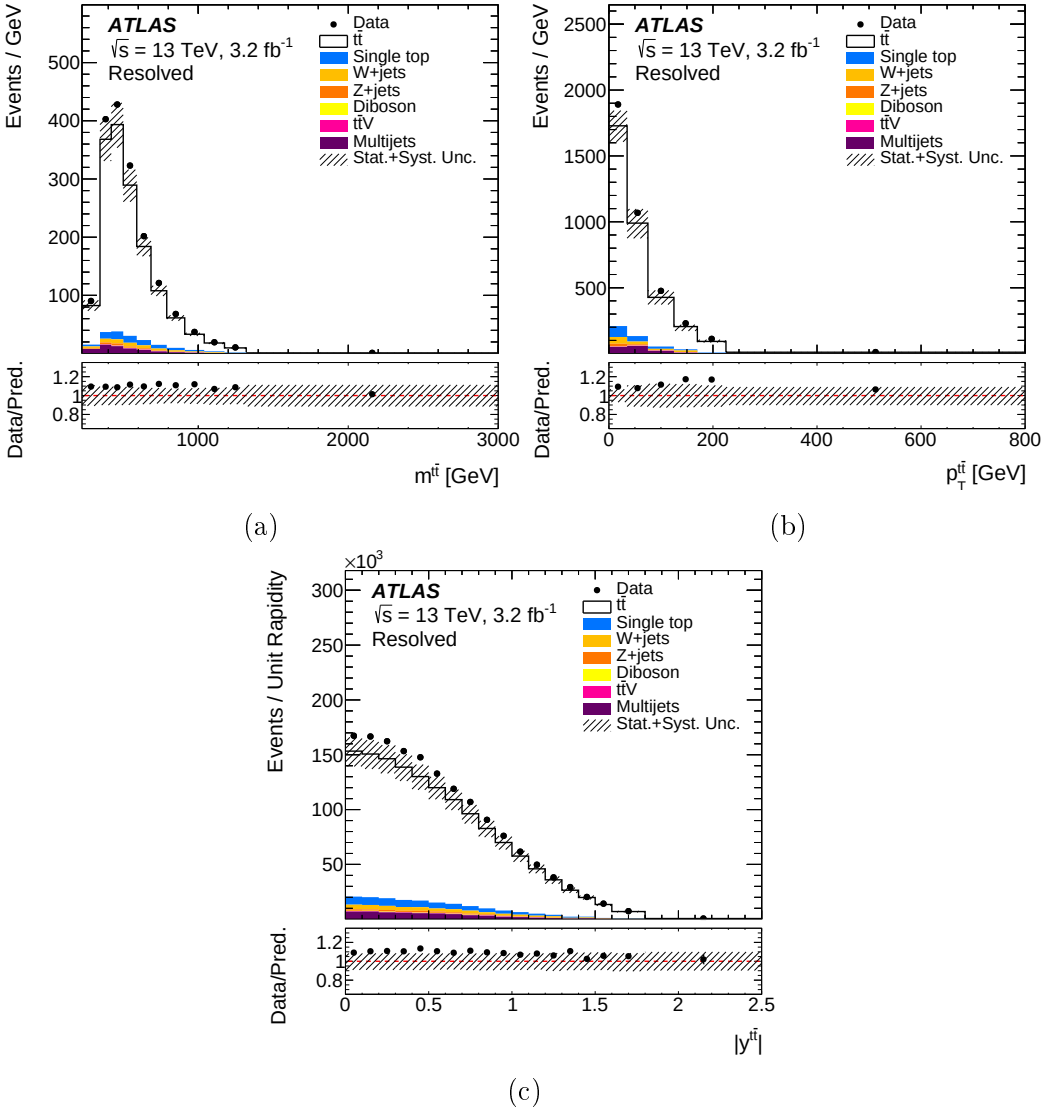

Figure 4.28: Kinematic distributions in the resolved topology at the detector level: (a) $m_{t\bar{t}}$, (b) $p_T^{t\bar{t}}$, (c) $|y^{t\bar{t}}|$. The hatched area indicates the combined statistical and systematic uncertainties in the total prediction, excluding systematic uncertainties related to the modelling of the $t\bar{t}$ system. Events beyond the range of the horizontal axis are included in the last bin [1].

Chapter 5

Cross Section Measurement

The cross-section measurement consists of various steps following the event selection. The first is the combination of the two channels (electron+jets and muon+jets) and the subtraction of the estimated background, the second is the definition of the phase space where the measurement is defined. Afterward the effects of the limited resolution and acceptance of the detector are evaluated using MC simulation. The last step consists in the application of these corrections to the observed distributions (unfolding), to extract the final cross-section. In this chapter all these steps are described.

5.1 Combination of Analysis Channels

The data is collected in two independent samples, depending on the flavor of the lepton that triggers the event, and also the MC simulation and background estimation are done depending on the lepton present in the event. Both the data and MC samples are combined, before the evaluation of the corrections and before the unfolding procedure is applied.
The combination is performed simply by adding the two channels at the reconstructed level. This procedure can be followed only if the relative yield in the two channels is the same in data and in MC, which is the case as shown in Table 5.1 and 5.2.
One advantage of this approach is that it allows to properly account for all the correlations among various sources of uncertainty, since correlated uncertainties will add linearly while uncorrelated uncertainties, as specific lepton scale factors, will enter only through the related channel and will be properly added in quadrature to the other uncertainties.

5.2 Correction Evaluation

Every experimental apparatus is characterized by a specific resolution and acceptance that originate differences between the observed and the original kinematic

Process	Events	Syst
$t\bar{t}$	3577.91	± 572.19
W+jets	254.49	± 181.71
Z+jets	25.88	± 18.48
Diboson	32.3	± 6.15
Single top	242.1	± 43.32
Multijets	251.57	± 82.18
$t\bar{t}V$	37.99	± 7.83
Total prediction	4422.24	± 686.63
Data	4007	
Data/Pred	0.91	

Process	Events	Syst
$t\bar{t}$	3168.6	± 538.60
W+jets	222.32	± 117.89
Z+jets	37.62	± 23.15
Diboson	30.31	± 6.02
Single top	205.43	± 38.9
Multijets	21.24	± 25.46
$t\bar{t}V$	33.63	± 7.58
Total prediction	3719.14	± 634.32
Data	3361	
Data/Pred	0.9	

Table 5.1: Yield in data, signal and estimated background in boosted topology for electron (left) and muon (right) channels. Last row shows also the agreement between data/MC ratio in the two channels.

Process	Events	Syst
$t\bar{t}$	62402.3	$^{+6132.87}_{-6084.75}$
W+jets	1796.175	$^{+1355.735}_{-1617.025}$
Z+jets	941.515	$^{+504.093}_{-492.039}$
Singletop	3200	± 418
Diboson	185.848	$^{+93.61}_{-93.0659}$
$t\bar{t}V$	227.745	$^{+36.64}_{-36.4026}$
Multijet	4199.84	$^{+2256.86}_{-2321.76}$
TotalPrediction	72953.134	$^{+7255.919}_{-7822.765}$
Data	81722	
Data/Pred	1.12	

Process	Events	Syst
$t\bar{t}$	58140.5	$^{+5630.66}_{-5631.18}$
W+jets	1788.565	$^{+729.341}_{-833.865}$
Z+jets	393.965	$^{+206.233}_{-202.076}$
Singletop	2970	± 379
Diboson	162.36	$^{+81.5245}_{-81.9947}$
$t\bar{t}V$	200.47	$^{+32.1778}_{-31.981}$
Multijet	1494.38	$^{+774.662}_{-776.789}$
TotalPrediction	65149.843	$^{+6170.342}_{-6285.657}$
Data	73871	
Data/Pred	1.13	

Table 5.2: Yield in data, signal and estimated background in resolved topology for electron (left) and muon (right) channels. Last row shows also the agreement between data/MC ratio in the two channels.

properties of the particles. The limited detector resolution reflects in a discrepancy between the reconstructed momentum, energy and position with respect to the *true* ones. The limited acceptance cause the loss of some particles that could cross regions of space not covered from the detector. Also the analysis strategy, optimized to separate $t\bar{t}$ events from background, reduces the acceptance of the analysis, since also real $t\bar{t}$ events with all particles in detector acceptance could fail the event selection. The measured $t\bar{t}$ yields in each bin of the considered kinematic variable are corrected for these effects, whose impact is estimated using MC distributions and detector simulation.

The first stage to determine these corrections is the definition of the *truth*, that is the stage where the particles have not interacted with the detector yet. The definition of the *truth* is not trivial, because previous to the interaction with the detector the unstable particles, as the top quark, undergo several processes (radiation, decay, hadronization) and it is necessary to identify at which stage to evaluate the corrections. As described in section 3.2, the radiation and hadronization descriptions differ between different MC event generators. Consequently, to reduce

the dependence on these effects, the *truth* used in this thesis is defined after all these processes, when the top quark already decayed and the hadron formation is concluded. Therefore the *truth* level is defined using objects (jets, leptons), analogous to the ones reconstructed at the detector level.
Afterward a fiducial phase space is defined on the *truth* objects, applying a selection similar to the one presented in section 4.2, to reduce the extrapolation of the measurement in regions not observed from the detector. This definition of the *truth* is called particle level.

5.2.1 Particle Level Objects and Fiducial Phase-space Definition

Particle level objects are defined using only particles with mean lifetime $\tau > 30$ ps, considered stable in the particle level definition.
Only prompt electrons, muons and neutrinos not originate, either directly or through a τ decay, from a hadron are used. Since the particle level is defined using only a $t\bar{t}$ sample, this ensures that the lepton derives from an electroweak decay, without any additional requirement on a direct match to a W boson.
The detector has not sufficient resolution to separate the lepton energy from the almost collinear photons emissions, consequently this is reproduced at particle level by adding to the electrons and muons the four-momenta of all photons within $\Delta R = 0.1$ from the lepton and not originating from hadron decays (lepton dressing). The dressed leptons, considered in the particle level selection, are then required to have $p_T > 25$ GeV and $|\eta| < 2.5$. Electrons in the calorimeter transition region ($1.37 < |\eta| < 1.52$) are rejected at detector level but accepted in the fiducial selection. The acceptance correction described in next sections account for this difference.
Particle level jets are obtained by clustering with the anti-kt algorithm, with radius parameter R =0.4 (small-R) or R =1.0 (large-R), all stable particles with $|\eta| < 4.5$, except for the prompt leptons, their radiated photons, and the prompt neutrinos. The small-R jets are required to have $p_T > 25$ GeV and $|\eta| < 2.5$. The b-tagging is performed using hadrons with $p_T > 5$ GeV containing b-quarks, that are associated to the small-R jets using a ghost-matching technique.
The large-R jets need to satisfy the same momentum and angular requirements of the detector level hadronic top candidate, $300 < p_T < 1500$ GeV and $|\eta| < 2$. The top tagging strategy adopted, on the other hand, is different from the detector level one: the large-R jet is considered top-tagged if $m^{jet} > 100$ GeV and $\tau_{32} < 0.75$. The motivations for this choice are detailed in the section 5.2.3.
No overlap removal criteria are applied to particle level objects.
The particle level missing transverse energy is calculated from the four-vector sum of all the prompt neutrinos.
The event selection applied at detector level follows strictly the reconstructed level selection. Both resolved and boosted selections require the presence of one high p_T lepton. Then, for the two selections:

- **Resolved:** Events are required to contain at least 4 jets, with at least two of them b-tagged.
- **Boosted:** Events must contain at least one top-tagged large-R jet, at least one b-tagged small-R jet fulfilling the same ΔR requirements, described in section 4.2. In addition, the missing transverse momentum must be larger than 20 GeV and the sum $E_T^{miss} + m_T^W > 60$ GeV. Events where both top quarks decay leptonically, passing the described selection, are considered signal.

5.2.2 Unfolding Corrections

There are 3 corrections that are evaluated from MC and applied in the unfolding procedure to extract the differential cross-section:

- **Acceptance correction:** This quantity corrects for the events that are generated outside the fiducial particle level phase space but pass the detector level requirements. It is defined, for each kinematic distribution and for each bin i, as:

$$f_{acc}^i = \frac{N_{reco\&particle}^i}{N_{reco}^i} \tag{5.1}$$

  where $N_{reco\&particle}^i$ are the events passing both the reconstructed and particle level selections in the bin i, while N_{reco}^i is the number of events passing the reconstructed selection. In Figure 5.1 the acceptance distributions for the events selected in the boosted topology are shown, as a function of the $p_T^{t,had}$ and $|y^{t,had}|$. In Figure 5.2 the acceptance of the events in the resolved topology as a function of: $p_T^{t,had}$,$|y^{t,had}|$,$m^{t\bar{t}}$,$p_T^{t\bar{t}}$ and $|y^{t\bar{t}}|$ are shown.

  Both in the resolved and the boosted topology the shape of acceptance is approximately flat over the full spectra. The only exception is the acceptance with respect to the $p_T^{t,had}$ in the boosted regime, that decreases at low p_T, due to the difference between the particle level and detector level top tagging definition, as shown in the next section.

- **Migration matrices:** These corrections map the bin-by-bin migrations between each generated particle level $t\bar{t}$ distribution and the detector level one. The probability for particle level events to remain in the same bin is therefore represented by the elements on the diagonal, while the off-diagonal elements describe the fraction of events that migrate in other bins.

  The migration matrices in the boosted and the resolved topologies are shown in Figure 5.3 and 5.4, respectively. The matrices are quite diagonal and the migrations are low, with more than the 50% of the events always contained in the diagonal for each bin of each distribution. This behavior is due to the binning employed in the analysis that is optimized to reduce the off-diagonal elements, taking into account the resolution of each variable, while maintaining a sufficient statistic in each bin and have stability in the systematic uncertainty propagation through the unfolding machinery.

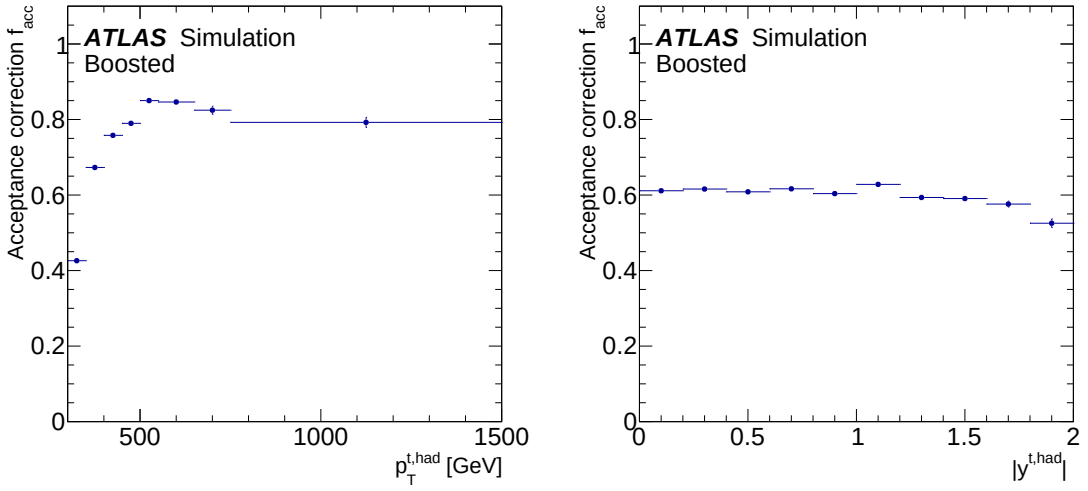

(a) (b)

Figure 5.1: Acceptance in boosted regime as a function of $p_T^{t,had}$ and $|y^{t,had}|$ [1].

- **Efficiency Correction:** this correction quantifies the number of events that pass the particle level selection but are not reconstructed at detector level and is defined as:

$$\epsilon = \frac{N^i_{reco\&particle}}{N^i_{particle}} \tag{5.2}$$

where $N^i_{reco\&particle}$ represent events passing both the particle and reconstruction selection and $N^i_{particle}$ are the events passing the particle level selection. The efficiencies in the resolved and boosted selections, for all the unfolded variables are shown in Figure 5.5 and 5.6.

In the resolved topology the efficiencies with respect to all variables show a flat distribution, a part from the $p_T^{t,had}$, where a decrease at high p_T is observed. This is due to the increasing fraction of events where jets are merged or close and are better reconstructed by the boosted analysis. Also the boosted analysis shows a reduction of the efficiency at high p_T, due to low b-tagging performance in this region or to the too stringent requirements on lepton isolation at high p_T, since the leptonically decaying top quarks could be boosted and the leptons can be produced close to the jets. These events are discarded by the overlap removal at detector level but accepted at particle level and this reflects in a reduction of the efficiency.

In the resolved topology, in order to separate resolution and combinatorial effects leading to events migrating from a particle to various detector level bins, distributions are corrected so that detector and particle level objects forming the pseudo-top quarks are angularly well matched, leading to a better correspondence between the particle and detector levels. This reflects in an additional correction, applied only in the resolved case, the matching correction. The matching is performed using

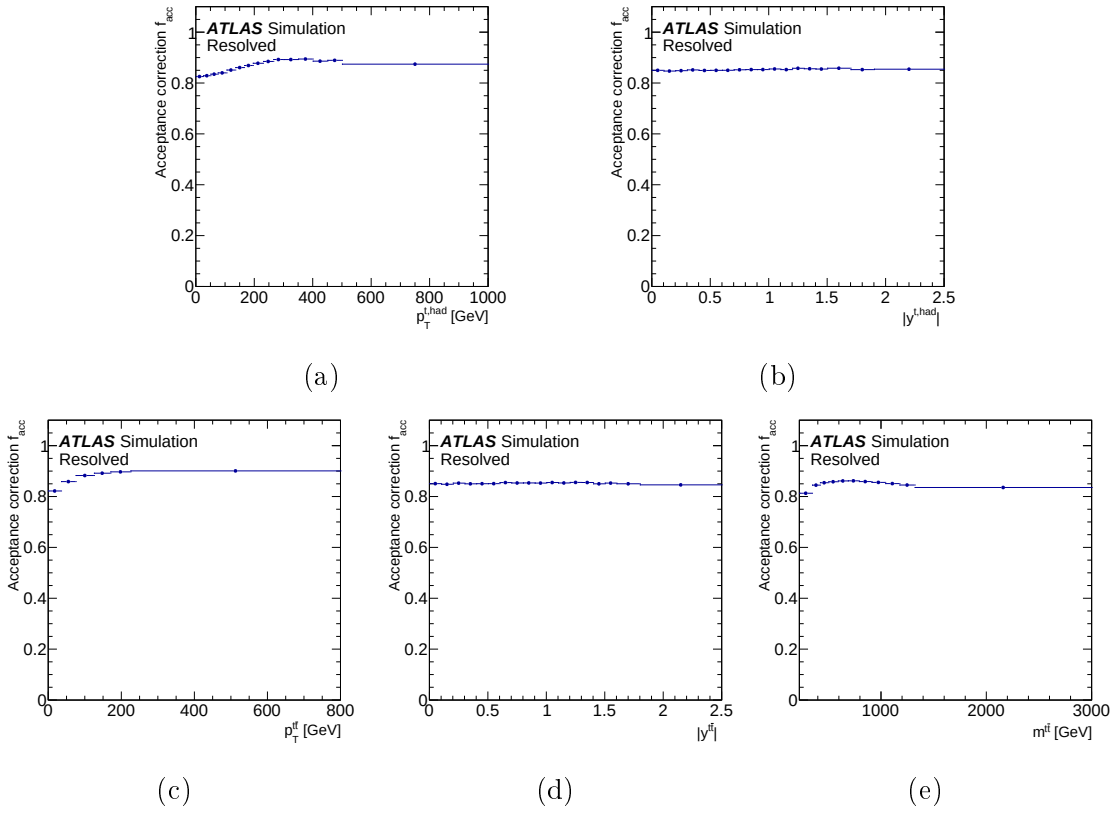

Figure 5.2: Acceptance in resolved regime as a function of $p_T^{t,had}$,$|y^{t,had}|$,$m^{t\bar{t}}$,$p_T^{t\bar{t}}$ and $|y^{t\bar{t}}|$ [1].

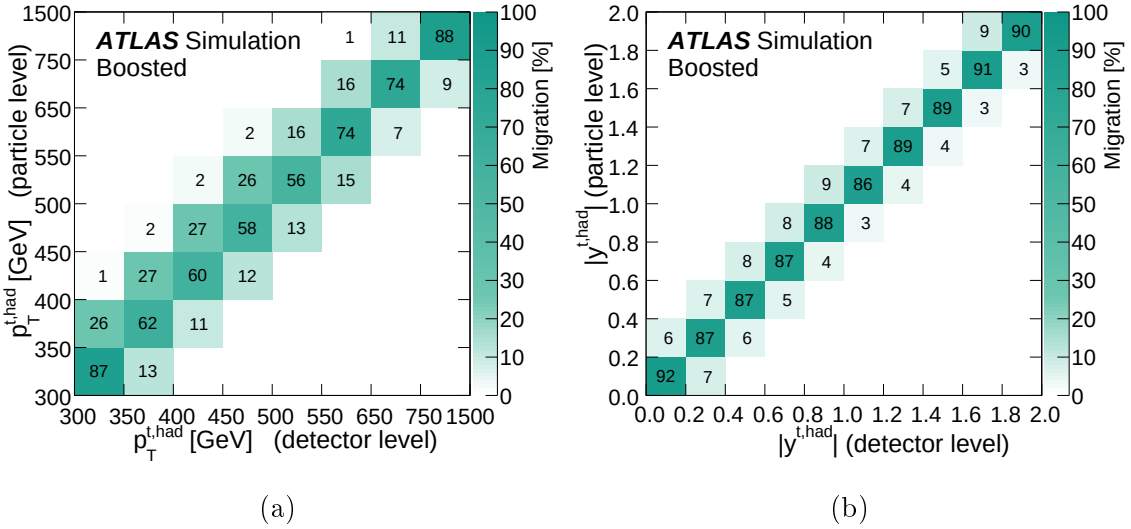

Figure 5.3: Migration matrices in the boosted regime as a function of $p_T^{t,had}$ and $|y^{t,had}|$. Values smaller then 1% are not shown [1].

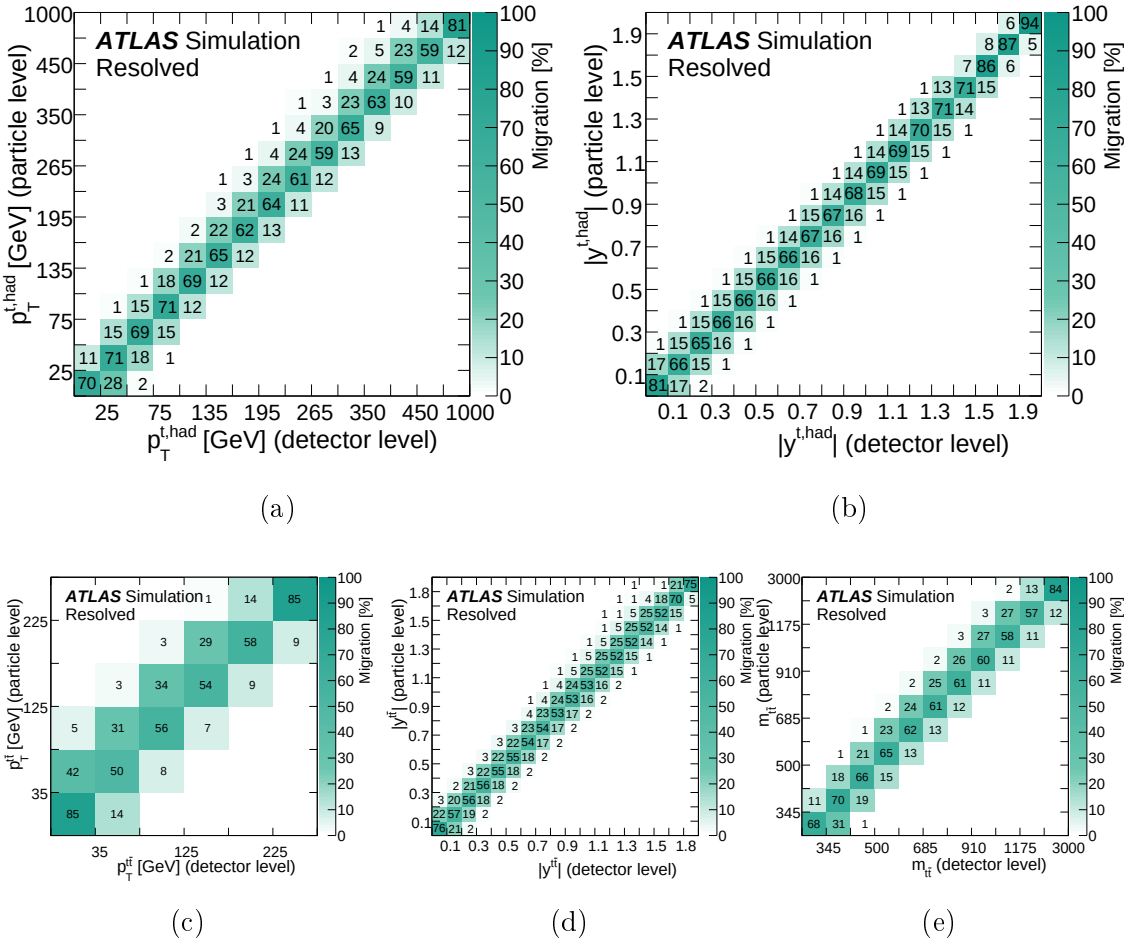

Figure 5.4: Migration matrices in the resolved regime as a function of (a) $p_T^{t,had}$, (b) $|y^{t,had}|$, (c) $m^{t\bar{t}}$, (d) $p_T^{t\bar{t}}$ and (e) $|y^{t\bar{t}}|$. Values smaller then 1% are not shown [1].

geometrical criteria, based on the distance ΔR. Each lepton is matched to the closest detector level one within $\Delta R < 0.02$. Particle level jets forming the pseudo-top quark candidates at the particle level are then required to be geometrically matched to the corresponding jets at the detector level within $\Delta R < 0.35$. An example of the matching correction is shown in Figure 5.7, as a function of the hadronic top $p_T^{t,had}$ and $|y^{t,had}|$.

The evaluation of the corrections provides an additional confirmation to the strategy adopted to combine the electron and muon channels. The efficiencies evaluated are indeed compatible between the two channels, as shown in Figure 5.8 for the boosted and resolved regimes for the case of the $p_T^{t,had}$.

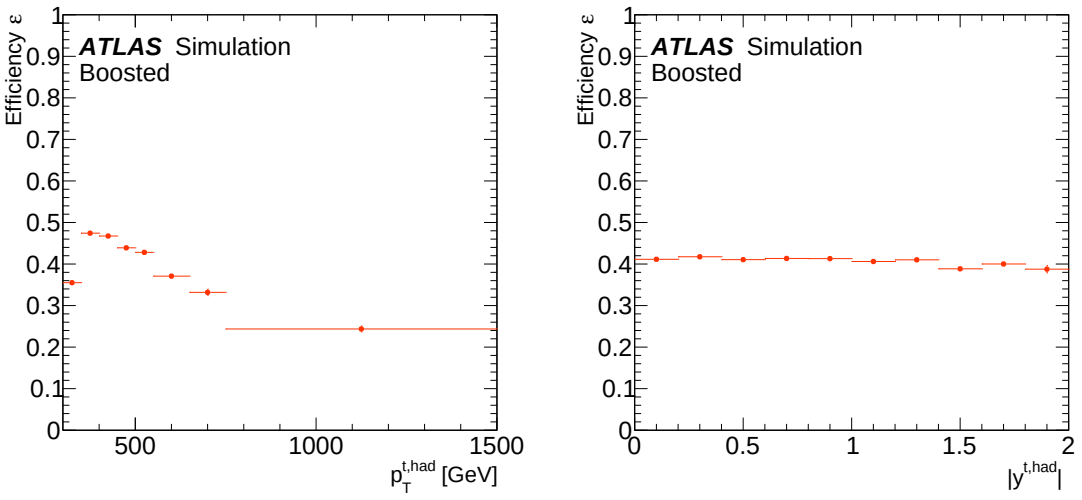

(a) (b)

Figure 5.5: Efficiency in boosted regime as a function of (a) $p_T^{t,had}$ and (b) $|y^{t,had}|$ [1].

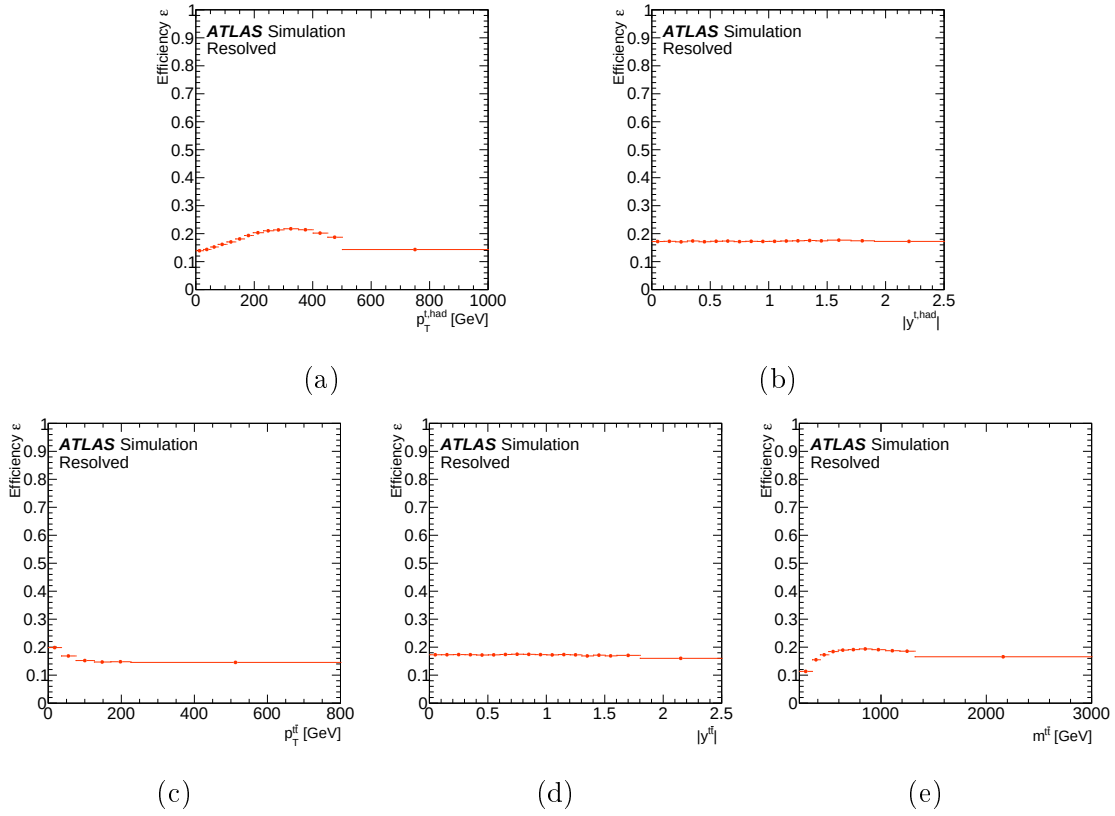

(a) (b)

(c) (d) (e)

Figure 5.6: Efficiency in resolved regime as a function of (a) $p_T^{t,had}$, (b) $|y^{t,had}|$, (c) $m^{t\bar{t}}$, (d) $p_T^{t\bar{t}}$ and (e) $|y^{t\bar{t}}|$ [1].

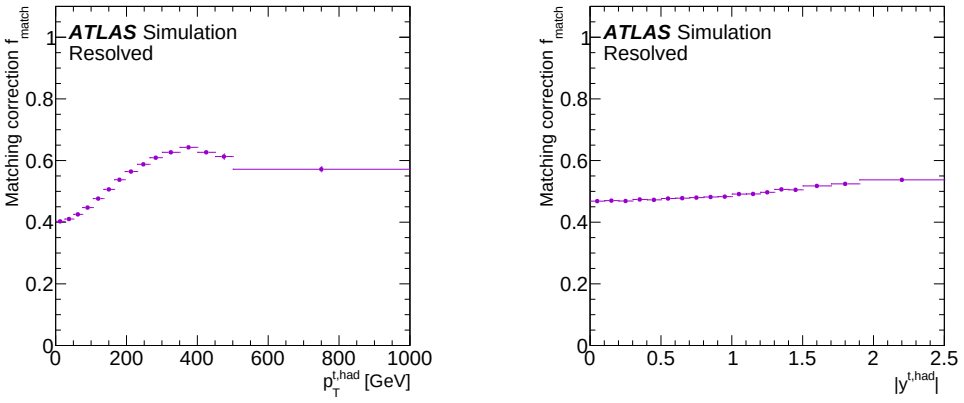

(a) (b)

Figure 5.7: Matching efficiency in resolved regime as a function of (a) $p_T^{t,had}$ and (b) $|y^{t,had}|$ [1].

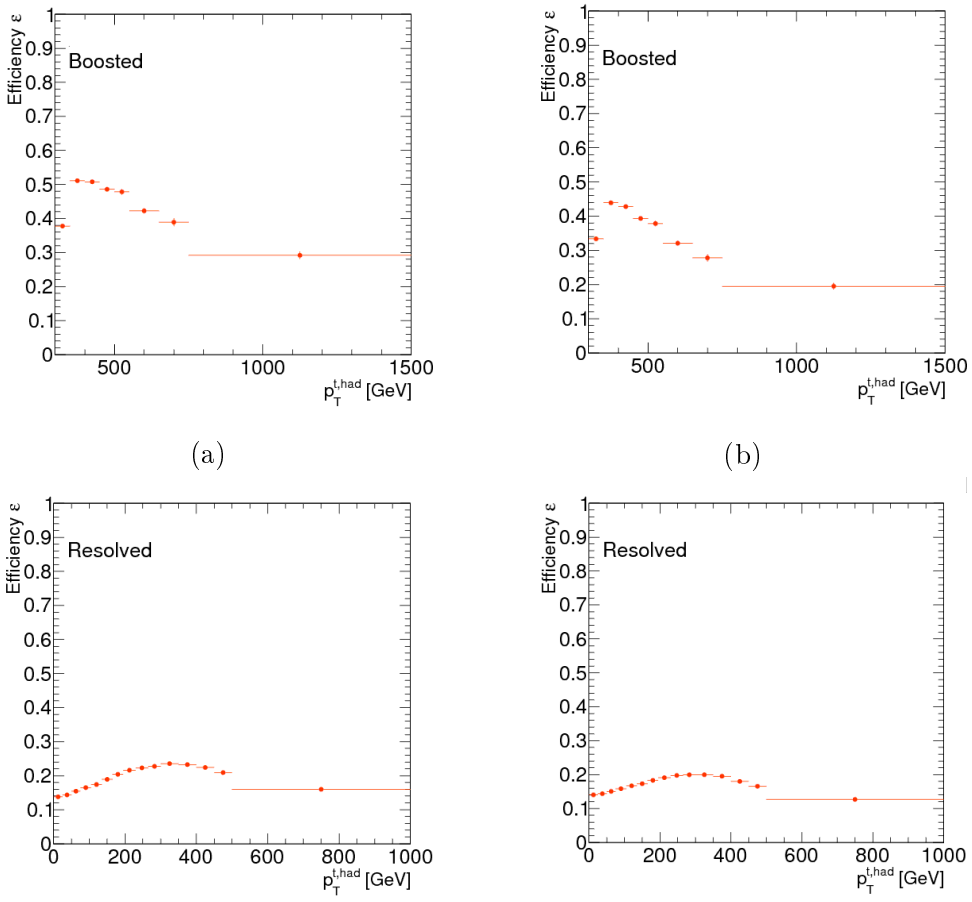

(a) (b)

(c) (d)

Figure 5.8: Efficiency in electron (left) and muon (right) channel as a function of $p_T^{t,had}$ in boosted (top) and resolved (bottom) regimes.

5.2.3 Particle Level Top Tagging

Several top tagging definitions at the particle level are compared, with the aim to keep a simple definition of the particle level phase space as well as maintaining a good correspondence between detector and particle levels. At the same time the top tagging is studied to keep low the number of tagged large-R jets in each event but keeping the top quark selection efficiency high. The additional tagged jets derive from the mis-tagging of jets deriving from W bosons or from extra radiations, present in $t\bar{t}$ events.
The following top tagging definitions are compared:

1. the same p_T-dependent cuts on mass and τ_{32}, as at the detector level;
2. no cuts at the particle level on the mass of the large-R (m^J) jet, nor the subjettiness ratio (τ_{32});
3. fixed cuts of $m^J > 85\,\text{GeV}$ and $\tau_{32} < 0.75$;
4. fixed cuts of $m^J > 100\,\text{GeV}$ and $\tau_{32} < 0.75$;
5. fixed cuts of $m^J > 135\,\text{GeV}$ and $\tau_{32} < 0.70$.

The same definition used at the detector level is shown for comparison but is not applied in the particle level requirements. This definition is p_T-dependent in order to maximize the background rejection, and is strongly motivated by the the actual detector performances, which is to be avoided when defining an ideally detector-independent particle level phase space.
The comparison of the acceptances obtained using different top tagging approaches, as a function of the $p_T^{t,had}$, are shown in Figure 5.9a, while the efficiencies comparison is shown in Figure 5.9b.

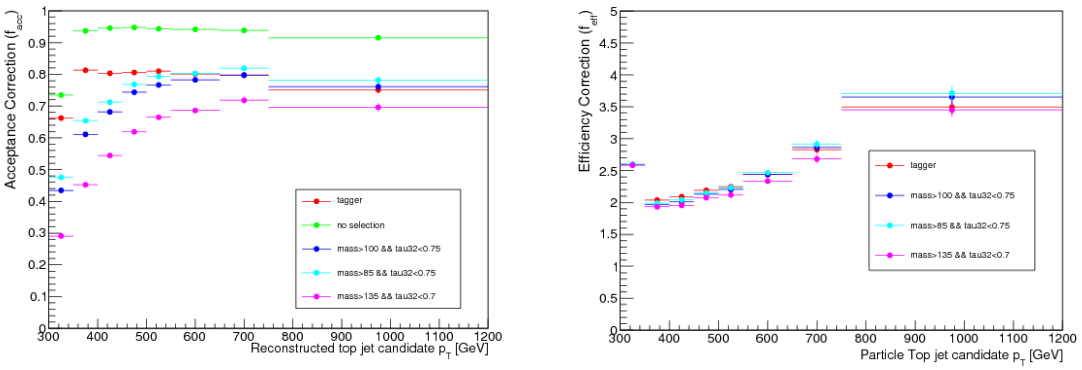

(a) (b)

Figure 5.9: Comparison of the the acceptance correction f^i_{acc} (a) and $f^i_{eff} = \frac{1}{\epsilon}$ (b) as a function of the large-R jet p_T for different operation points of top tagging at the particle level.

The use of different particle level top tagging techniques shows an high impact on the acceptance correction while the efficiency correction is similar for all the compared tagger. The absence of specific particle level top tagging requirements results in a really high acceptance, but at the same time the number of events where 2 jets are top tagged is sensibly larger with to all other strategies investigated, as shown in Figure 5.10, and this could reflect in the mis-identification of the particle level hadronic top. This mis-match between the particle and detector level

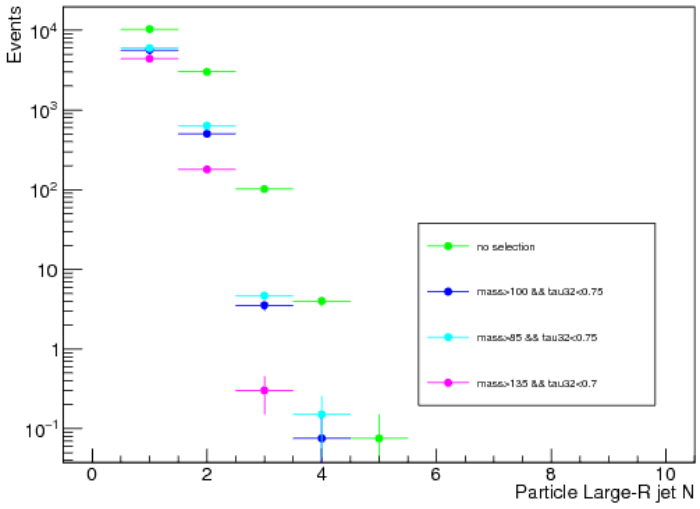

Figure 5.10: Comparison on the number of particle level top-tagged large-R jets with $p_T > 300$ GeV and $|\eta| < 2$. Various top-tagging approaches are compared.

is reflected in an increase of the migrations, observed in Figure 5.11a. All the other top-tagging definitions, a part from the detector level one, produce a shape on the acceptance that decreases at low p_T. In particular the fifth top tagging strategy leads to a very low acceptance, with just the 30% of the events accepted in the first bin. The performances of the third and fourth tagger investigated are similar, but the one with the cut on $m^J > 100$ GeV is chosen in order to remove large-R jets originating from hadronically decaying boosted W bosons.
An additional check on the various particle level top tagging approaches consists in the comparison of the migration matrices, shown in Figure 5.11. In this case the third, fourth and fifth tagger investigated lead to similar performances.

Finally, a detailed comparison between the systematic uncertainties obtained on the unfolded distributions at particle level has been performed between the chosen approach and the one with the p_T dependent tagger, but no significant impact is visible on the total uncertainty.

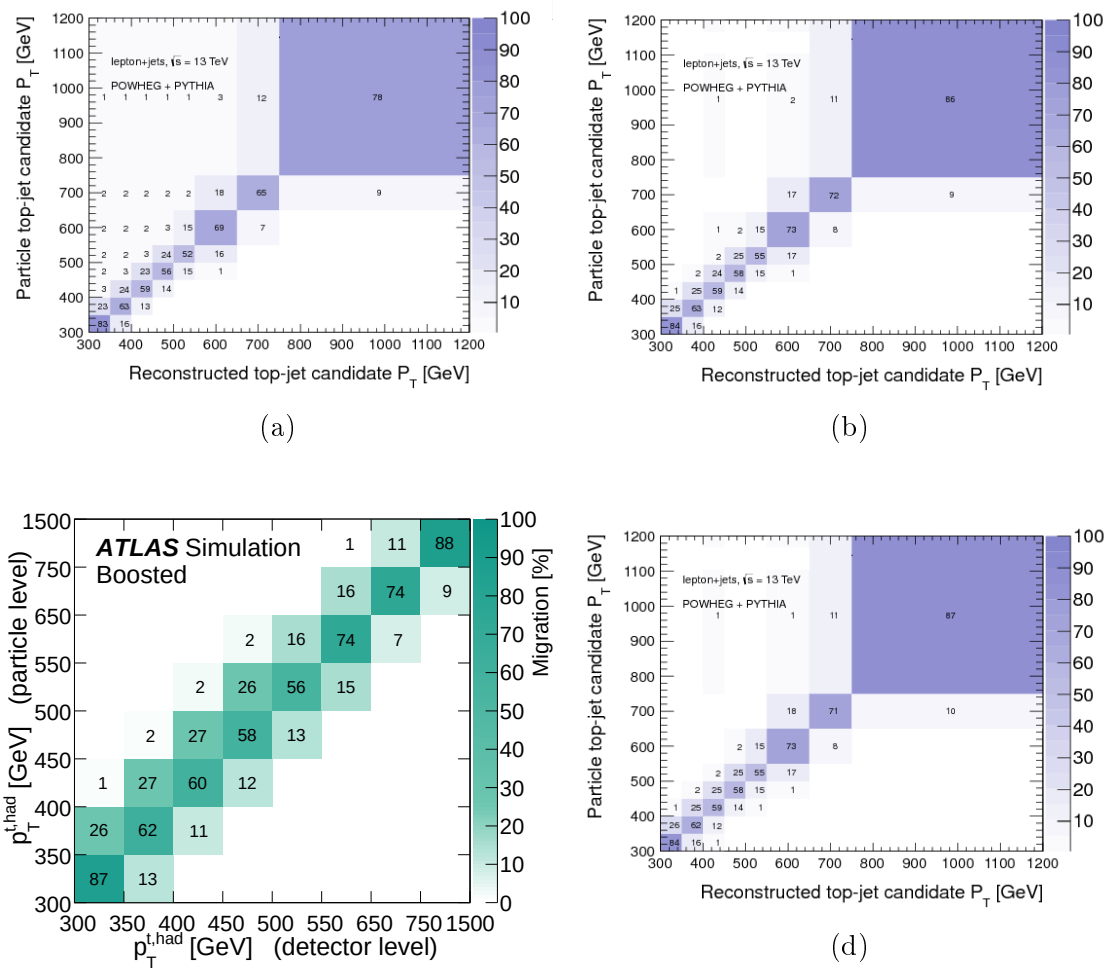

Figure 5.11: Migration matrices obtained applying different particle level tagging strategies: (a) no top-tagging requirement at particle level, (b) $m^J > 85$ GeV and $\tau_{32} < 0.75$, (c) $m^J > 100$ GeV and $\tau_{32} < 0.75$ and (d) $m^J > 135$GeV and $\tau_{32} < 0.70$.

5.3 The Unfolding Procedure

The limited resolution and acceptance of an experimental apparatus leads to a smearing of the true kinematic variable x in the measured quantity y. This relation can be represented by the Fredholm integral [126]:

$$g(y) = \int A(y,x) f(x) dx \tag{5.3}$$

where $g(y)$ represents the measured distribution, $f(x)$ the true one and $A(y,x)$ contains all the detector effects. The unfolding consist in the evaluation of $f(x)$ knowing $g(y)$ and $A(y,x)$.
In the analysis discussed in this thesis the distributions $f(x)$ and $g(y)$ are discrete

so equation (5.3) should be re-written as:

$$g_j = \sum_i A_{j,i} f_i \tag{5.4}$$

where j and i represents the various bins of the distribution at detector and particle level, respectively, and $A_{j,i}$ is the migration matrix. This equation implies that many bins i of the distribution f could contribute to the bin g_j, if the matrix A is not diagonal. The diagonal elements of A, with this convention, represent the the bin by bin reconstruction efficiency, i.e. the number on events generated in the bin i are reconstructed in the bin $j = i$.
The central problem of the unfolding is the inversion of the matrix A. The inversion of a finite system of equations rarely admits an exact solution, and several methods that calculate approximate solutions have been developed. Many of these techniques employ some regularization conditions, based on *a priori* information, that allows the suppression of spurious fluctuations. These information usually consist in the theoretical predictions of the measured distributions. The presence of regularization implies the possibility to bias the results, consequently before applying the unfolding procedure is necessary to perform tests on the stability of the method and monitor the presence of a bias on the final result.

5.3.1 Unfolding Techniques

The unfolding technique employed in this thesis is called Bayesian Unfolding and it is based on a generalization of the Bayes theorem described in [127], as implemented in the RooUnfold [128] framework.
The Bayes theorem is written as:

$$P(C_i|E_j) = \frac{P(E_j|C_i)P(C_i)}{\sum_{l=1}^{n_c} P(E_j|C_l)P(C_l)} \tag{5.5}$$

where the probability of the cause C_i is related to the observed effect E_j through the conditioned probability to get E_j given the cause C_i, multiplied by the probability of C_i and the sum over the number of possible causes n_C. If $n(E_j)$ events are observed from the experiment, the expected number of events assignable to each cause is:

$$\hat{n}(C_i) = \frac{1}{\epsilon_i} \sum_{j=1}^{n_E} n(E_j) P(C_i|E_j) \tag{5.6}$$

where ϵ_i is the efficiency related to the cause i and n_E is the number of possible effects. The same equation can be re-written, using (5.5), as:

$$\hat{n}(C_i) = \sum_{j=1}^{n_E} n(E_j) M_{ij} \tag{5.7}$$

where

$$M_{ij} = \frac{P(E_j|C_i)P_0(C_i)}{[\sum_{l=1}^{n_E} P(E_l|C_i)][\sum_{l=1}^{n_c} P(E_j|C_l)P_0(C_l)]} \tag{5.8}$$

The $P(E_j|C_i)$ terms are estimated from the MC, and represent the elements of the migration matrix, introduced in the previous section, while the $P_0(C_i)$ consists in the initial predictions of the expected number of events in each bin i of the particle level distribution. After the result of the first unfolding iteration has been obtained, using equation (5.7), the total number of true events can be re-evaluated as:

$$N^{\hat{true}} = \sum_{i=1}^{n_c} \hat{n}(C_i) \tag{5.9}$$

and the initial C_i probability can be redefined as:

$$\hat{P}(C_i) = P(C_i|n(E)) = \frac{\hat{n}(C_i)}{\hat{N}_{true}} \tag{5.10}$$

If the initial distribution $P_0(C)$ used *a priori* is not consistent with the observation then $P_0(C)$ and $\hat{P}(C_i)$ will differ and the procedure can be repeated iteratively replacing the $P_0(C)$ with $\hat{P}(C_i)$.
The Bayes method, related uncertainty, and correlations will be compared in Section 6.6.1 with the Thickonov Singular Value Decomposition (SVD) method, used in the measurement of the $t\bar{t}$ differential cross-section in boosted regime at 8 TeV [49]. The SVD method [129] is based on the decomposition of the A migration matrix in three matrices:

$$A = USV^T \tag{5.11}$$

where the three matrices have the following properties:

$$U^T U = UU^T = 1 \tag{5.12}$$
$$V^T V = VV^T = 1 \tag{5.13}$$
$$S_{ij} = \lambda_i \delta_{ij} \text{and} \lambda_i \geq 0 \tag{5.14}$$

This decomposition makes the inversion of the migration matrix A easier, since only the diagonal matrix S must be inverted:

$$(A)^{-1} = (USV^T)^{-1} = (V^T)^{-1}(S)^{-1}(U)^{-1} = VS^{-1}U^T. \tag{5.15}$$

Using this method the statistical fluctuations in the calculation can be suppressed introducing a regularization term, based on some a priori knowledge about the solution. The regularization is technically achieved adding a stabilization term that tends to minimize the curvature of x distribution, assuming that the distribution should be smooth and with small bin-by-bin variations. The amount of regularization depends on the value of the parameter of the method, which must be determined in each specific case that employs SVD technique. More details on the method and on the determination of the regularization parameter can be found in [129].

5.3.2 Unfolding Tests

The unfolding technique employed in this theses is the iterative Bayesian method with four iterations. The reliability and stability of the chosen unfolding technique have been tested to verify the absence of bias on the measurement and investigate the need of additional uncertainties accounting for this.

Closure Test

The first check is a simple closure test, that aims to show that the unfolding technique can completely recover the particle level spectrum from the predicted reconstructed spectra, when the corrections are extracted from the same sample. For this study the MC sample is randomly divided in two sub-samples of equal size $(\text{half}_0, \text{half}_1)$. One sample is then used as pseudo-data, while the other is used to evaluate the unfolding migration matrix. The pseudo-data sample is then unfolded using the other independent sub-sample, without applying efficiency or acceptance corrections. The obtained unfolded pseudo-data are then compared with the corresponding particle level sub-sample, and the two distributions are found to agree within the statistical uncertainty, as shown in Figure 5.12.
Due to the result of the test no non-closure uncertainties are assigned to the measured differential cross-section.

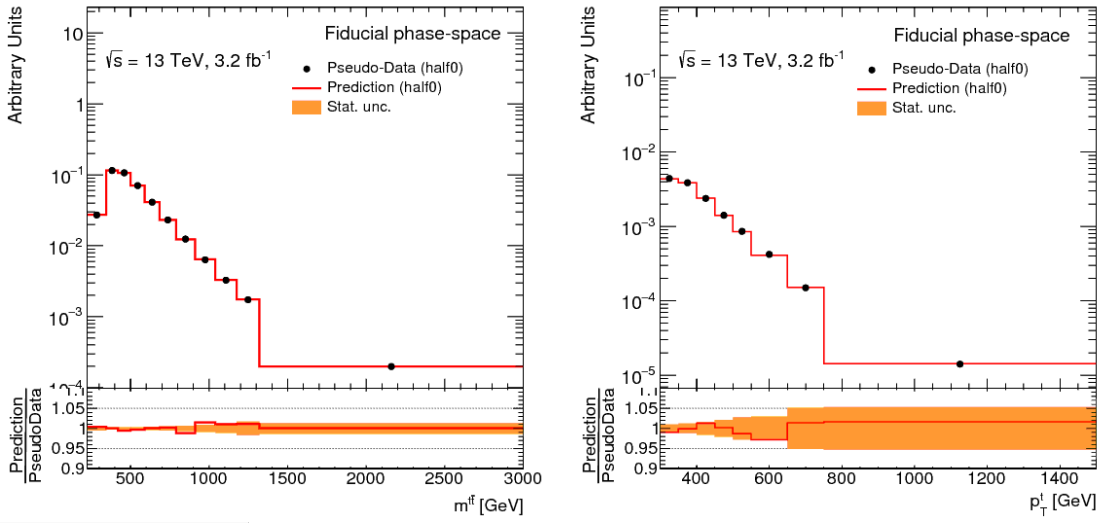

(a) (b)

Figure 5.12: Closure test of the unfolding procedure, the pseudo-data distribution of $m^{t\bar{t}}$ in the resolved topology (a) and of $p_T^{t,had}$ in the boosted topology (b) are unfolded using the migration matrix obtained with an independent MC sample and compared with the particle level distribution corresponding to the pseudo-data. The orange band represents the half_0 statistical uncertainty.

Stress Test

The corrections employed in the unfolding procedure are obtained from MC distributions and moreover the regularized unfolding employs the truth distribution to stabilize the unfolding result. Consequently, is necessary to verify if this procedure introduces a bias on the measured cross-section.
This test is done by re-weighting the MC, both at reconstructed and particle level, in order to change the shapes of the distributions, and use these varied distributions as pseudo-data. The re-weighted sample is then unfolded with the migration matrix obtained with the original prediction (un-weighted), and the unfolding result is compared with the re-weighted particle level. Non-closure would indicate that the unfolding introduces a bias towards the particle level spectrum used to derive the corrections.
Different re-weighting strategies, based on the kinematic of the truth t and $\bar{t}$ quarks, have been used for the different spectra:

- Gaussian re-weighting as a function of the rapidity of the $t\bar{t}$ system are applied on $t\bar{t}$ and hadronic top rapidity spectra, in boosted and resolved topology. The re-weighting function has been chosen as:

$$f(y_{t\bar{t}}) = 1 - k \cdot e^{-\frac{y_{t\bar{t}}^2}{\sigma^2}} \tag{5.16}$$

  where $k = 0.4$ and $\sigma = 0.3$.

- On the hadronic $p_T^{t,had}$ is applied a combined linear re-weighting, function of the p_T of both hadronic and leptonic top quarks, defined as:

$$f(p_T^{t,had}, p_T^{t,lep}) = 1 + \frac{1}{750} \cdot \frac{p_T^{t,had} + p_T^{t,lep}}{2} \tag{5.17}$$

- A *bump* has been added in the $t\bar{t}$ mass spectrum. This has been parameterized as:

$$f(m_{t\bar{t}}) = 1 + k \cdot e^{-\frac{\Delta^2(m_{t\bar{t}})}{\sigma^2}} \tag{5.18}$$

  where k=2, $\Delta(m_{t\bar{t}}) = m_{t\bar{t}} - 800$ GeV and $\sigma = 100$ GeV.

- A linear re-weighting, function of the p_T of the $t\bar{t}$ system, is applied on the $p_T^{t\bar{t}}$. In this case the weight is evaluated as:

$$f(p_T^{t\bar{t}}) = 1 + \frac{1}{600} \cdot p_T^{t\bar{t}} \tag{5.19}$$

Some examples of the result of the stress tests are shown in Figure 5.13, for the boosted topology, and 5.14, for the resolved one, all the other distributions are presented in Appendix E.

The unfolding procedure exhibits a good recovery of the re-weighted particle level spectrum when the re-weighted detector level spectrum is unfolded using un-weighted corrections. The differences are contained in the MC statistic band, consequently no additional systematic uncertainty related to the unfolding bias is added to the final measurement.

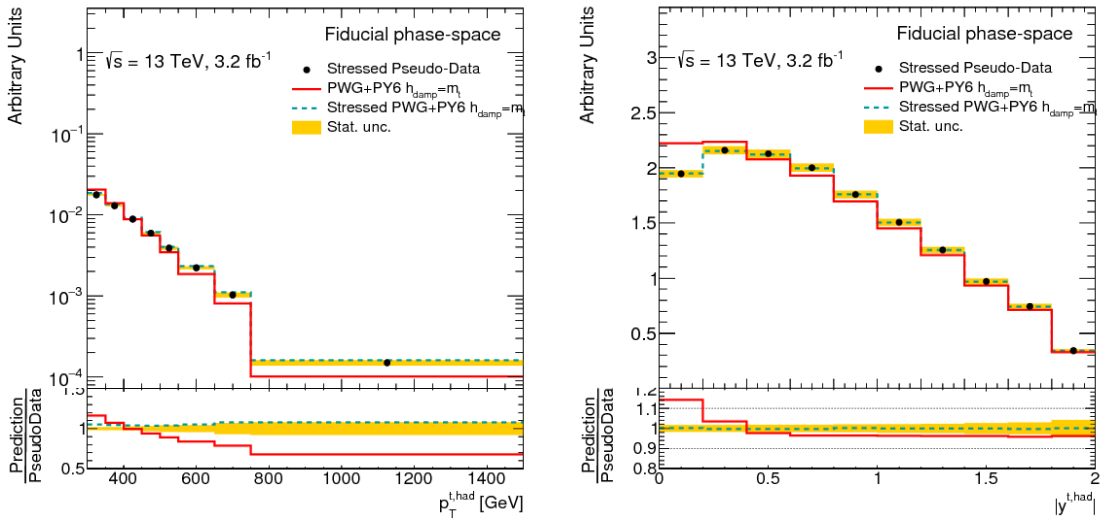

(a) (b)

Figure 5.13: Stress test results in boosted topology. In a(b) is shown the cross-section as a function of $p_T^{t,had}(|y^{t,had}|)$, the green line represents events re-weighted using $f(p_T^{t,had}, p_T^{t,lep})(f(y_{t\bar{t}}))$ and unfolded employing the original migration matrix, while the red line represents the original distribution. The ratio plot shows the ratio with the re-weighted truth and the orange band represents the statistical uncertainty.

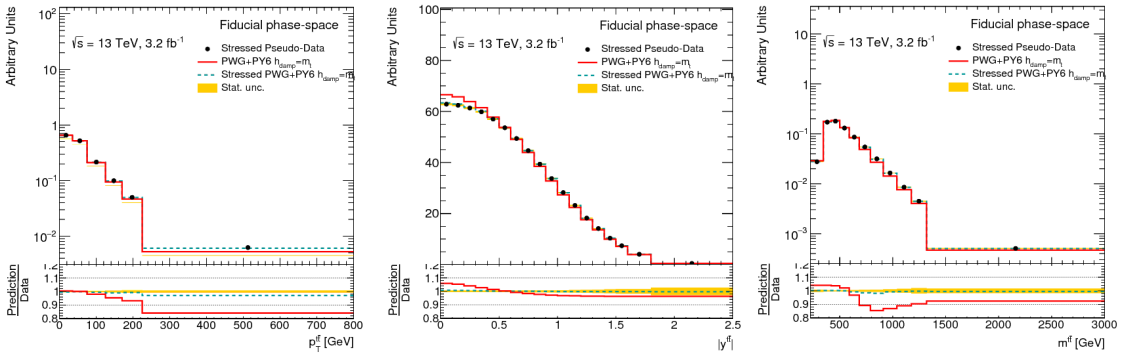

(a) (b) (c)

Figure 5.14: Stress test results in resolved topology. In a(b,c) is shown the cross-section as a function of $p_T^{t\bar{t}}(|y^{t\bar{t}}|, m^{t\bar{t}})$, the green line represents events re-weighted using $f(p_T^{t\bar{t}})(f(y_{t\bar{t}}), f(m_{t\bar{t}}))$ and unfolded employing the original migration matrix, while the red line represents the original distribution. The ratio plot shows the ratio with the re-weighted truth and the orange band represents the statistical uncertainty.

Pull Test

An additional test, called Pull, is performed as additional check on the presence of bias introduced by the unfolding and to verify the correct estimate of the statistical

uncertainty, described in the next chapter.
One thousand pseudo-experiments are built starting from the sum of MC background and signal predictions, varying the original distribution following the statistical uncertainty. The variation is performed extracting, in each bin i of the distributions, 1000 random numbers from a Poisson distribution with mean equals to the number of events expected in that bin. Each replica of the distribution is then passed through the full unfolding procedure and the pull for each pseudo-experiment j, in each bin i, is evaluated as:

$$P_j = \frac{(s_i^j - \hat{s}_i)}{\sigma_i} \tag{5.20}$$

where s_i^j is the unfolded cross-section in bin i for the pseudo-experiment j, $\hat{s}_i$ and σ_i are the cross-section and the statistical uncertainty estimated in the bin i.
The resulting pull distributions for some bins of $p_T^{t,had}$ are shown in Figure 5.15, for the boosted topology. The distributions are fitted to a Gaussian in each bin, and

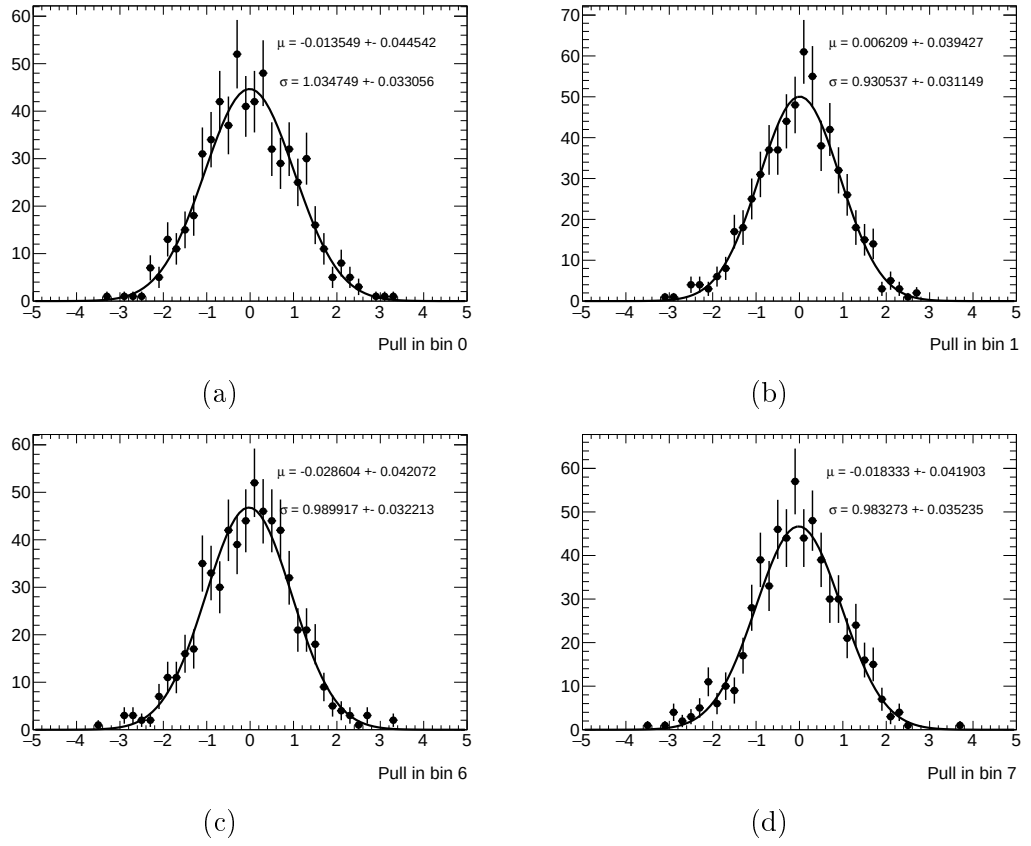

Figure 5.15: Pull distribution in the first two (top) and last two (bottom) bins of $p_T^{t,had}$, in the boosted topology.

the obtained means and widths are summarized in Figure 5.16.
The means are consistent with zero, while the widths with one, indicating no bias in the measurement and the correct assessment of the statistical uncertainties. The

test has been repeated for all the distributions in boosted and resolved topologies and similar conclusions have been drawn.

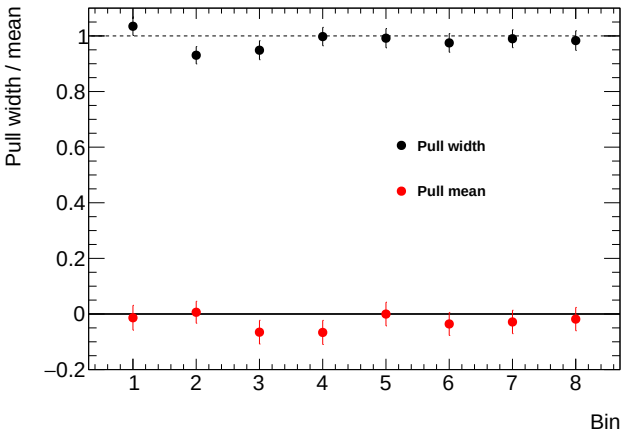

Figure 5.16: Fitted pull widths and means for the $p_T^{t,had}$ distribution in boosted topology. The uncertainties on the fit parameters resulting from the 1000 pseudo-experiments are shown on the dots.

5.3.3 Test on the Number of Iterations

The number of iterations used in the Bayes method is four, both for boosted and resolved analysis. In the previous sections this unfolding technique has been shown to be unbiased but further checks can be done to verify the effects of changing the number of iterations and that the used number is reasonable. It is expected

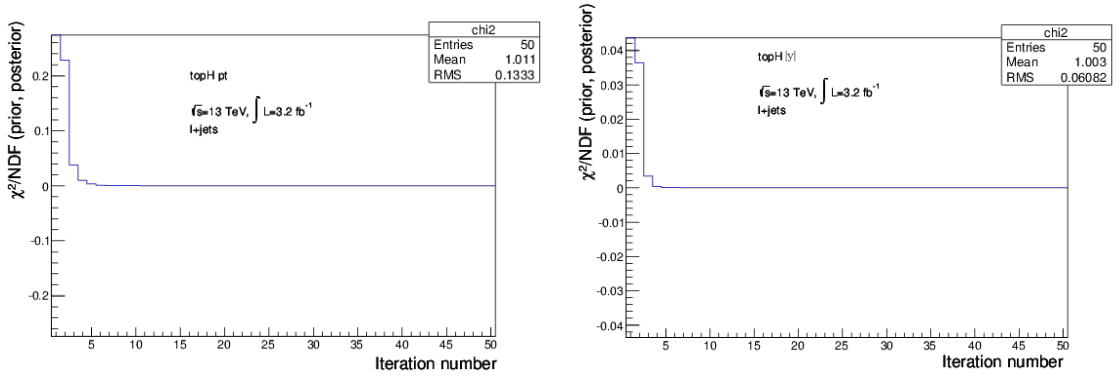

(a) (b)

Figure 5.17: χ^2 between the unfolded result and the prior of the i^{th} iteration of the Bayesian unfolding technique, as a function of the number of iterations. The spectra considered are the $p_T^{t,had}$ (a) and the $|y^{t,had}|$ (b) in the boosted topology

that increasing the number of iterations the χ^2 between the unfolded result of the i^{th} iteration and the prior of the same iteration would decrease, and this is

observed both in the boosted and resolved topologies, as shown in Figure 5.17 and 5.18. An increased number of iterations implies a reduced regularization and

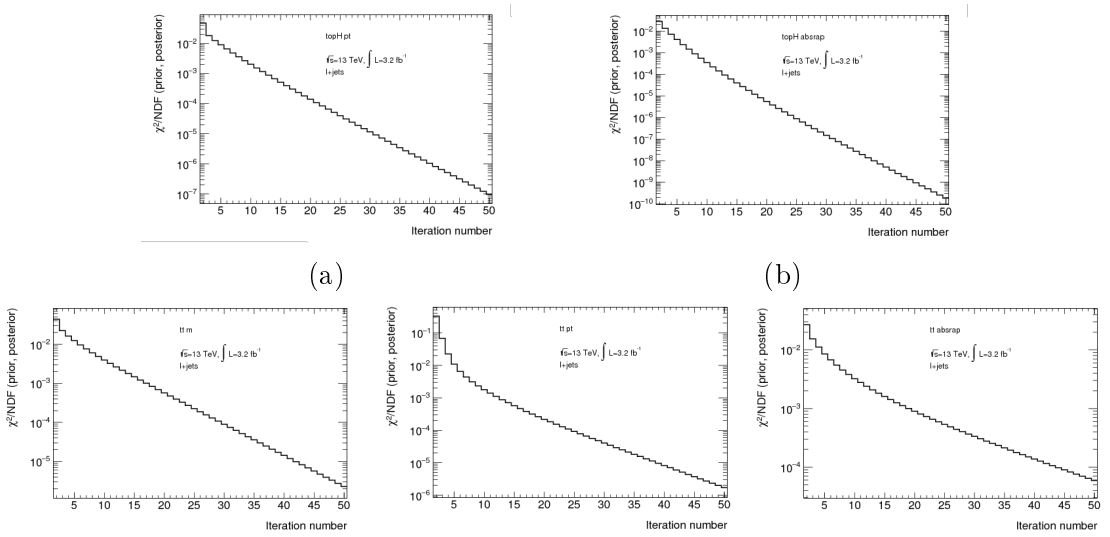

Figure 5.18: χ^2 between the unfolded result and the prior of the i^{th} iteration of the Bayesian unfolding technique, as a function of the number of iterations. The spectra considered are $p_T^{t,had}$ (a), $|y^{t,had}|$ (b), $m^{t\bar{t}}$ (c), $p_T^{t\bar{t}}$ (d) and $|y^{t\bar{t}}|$ (e) in the resolved topology

a corresponding increase in the statistical uncertainty. An example is shown in Figure 5.19 where the dependency of the statistical uncertainty from the number of iterations is represented for two bins of the $p_T^{t,had}$ in boosted topology.

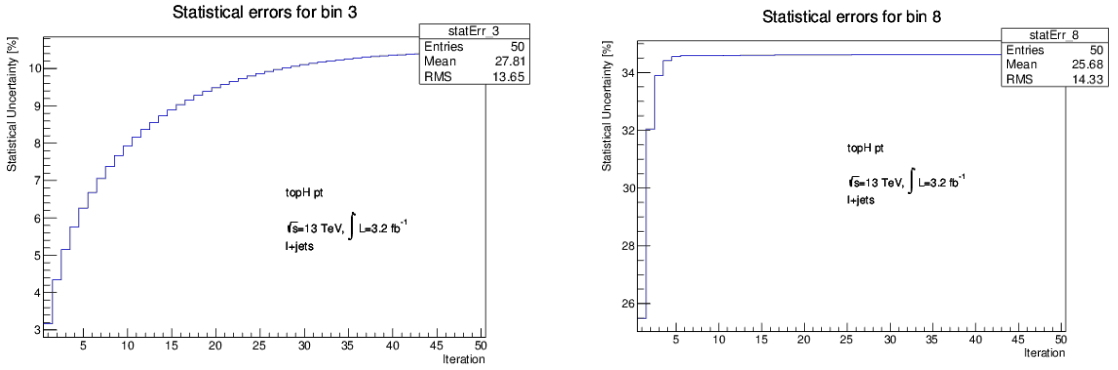

Figure 5.19: Dependency of the statistical uncertainty from the number of iterations in Bayesian unfolding in the third (a) and last (b) bins of the $p_T^{t,had}$ distribution in the boosted topology.

5.4 Cross Section Extraction

The extraction of the cross-section from the reconstructed spectra, applying the corrections and the unfolding procedure can be summarized as:

$$\frac{d\sigma_{fid}}{dX^i} = \frac{1}{L \cdot \Delta X^i} \cdot \frac{1}{\epsilon_i} \cdot \sum_j M_{ij}^{-1} \cdot f_{match}^j \cdot f_{acc}^j \cdot (N_{reco}^j - N_{bkg}^j), \tag{5.21}$$

where $\frac{d\sigma_{fid}}{dX^i}$ represents the measured cross-section, as a function of the kinematic variable X^i in the bin of the particle level distribution i. In 5.21 the $f_{acc(eff,match)}^j$ represents the acceptance (efficiency, matching) correction presented in section 5.2.2. f_{match}^j is applied only in the resolved case. As a first step, the expected background (N_{bkg}) estimated as described in Chapter 4, is subtracted from the selected data sample (N_{reco}). Afterward, the unfolding (M_{ij}^{-1} in the equation) corrects only for the migration effects, because the acceptance and efficiency corrections are factorized out from the matrix and applied to the distribution before and after the Bayesian procedure has been applied.
The last step consists in the division by the total integrated luminosity (L) and bin-width (ΔX^i).

Chapter 6

Systematic Uncertainties

The measurement of the differential cross-section is affected by uncertainties deriving from multiple sources: object reconstruction and calibration, $t\bar{t}$ signal modelling and background estimation.
The impact of each uncertainty is estimated using alternative simulations of the signal or varying the detector level predictions of the signal and backgrounds by one standard deviation for each source of systematic uncertainty, which need to be propagated through the unfolding procedure.
In this chapter all the components contributing to the total uncertainty affecting the measurement and the method employed to propagate them will be presented.

6.1 Detector-level Uncertainties

The impact of the reconstruction level systematic uncertainties is determined by varying the detector level predictions of signal and background, to account for all the uncertainties related to the objects calibration and reconstruction. The varied total predictions, sum of all signal and backgrounds, are used to extract distributions of the differential cross-section for each uncertainty component. The varied cross-sections are evaluated using equation (5.21), where nominal background and corrections are used. Each unfolded distribution is compared with the nominal particle level signal and the relative difference is considered as the uncertainty associated to the cross-section measurement.

Small-R Jet Uncertainties

The uncertainty on the energy scale of the jets (JES) [130, 131, 132] is formed by many components that account for each step of the jet calibration described in 4.1.4. The majority of the components derive from the assumptions made on event topology, MC simulation and sample statistic in the in situ calibrations. Other components account for the potential MC mis-modeling of the pile-up, the calorimeter response to different flavor compositions of the jets, and the mis-modeling in the region $2.0 < |\eta^{jet}| < 2.6$.

The jet energy resolution uncertainty (JER) is obtained with an in situ measurement of the jet response in dijet events [133].
These uncertainties have a significant effect in the resolved measurement, where in all the distributions they range between 7% and 12%, depending on the bin. In the boosted regime this source of uncertainty is sub-dominant.

Large-R Jet Uncertainties

The large-R jet uncertainties are obtained using the in situ R_{trk} method [115]. This technique is based on the ability of the ATLAS detector to provide two independent measurements of the jet kinematic, using the tracker and the calorimeter. The measurements differ due to the presence of neutral particles and the different performances of the two detectors, but their comparison can give indications on the modelling of both. The first step of the R_{trk} technique is the definition of the R_{trk} ratio, that compares tracking ($p_T^{track,jet}$) and calorimeter (p_T^{jet}) jet kinematic in the data and MC predictions:

$$\begin{aligned} \text{Ratio} : r^{p_T}_{track,jet} &= \frac{p_T^{jet}}{p_T^{track,jet}} \\ \text{Double ratio} : R^{p_T}_{trk} &= r^{p_T,data}_{track,jet} / r^{p_T,MC}_{track,jet} \end{aligned}$$

Afterward, various sources of uncertainty are studied and their effect evaluated: the difference between the data and the nominal simulation, the difference between the modelling with two different generators, the uncertainties on the tracks used for the track jet measurements. This technique is used to evaluate the scale uncertainty of mass and p_T, that are considered as completely correlated.
Two additional terms of the large-R jet uncertainties are related to the n-subjettiness ratio τ_{32} [120], considered uncorrelated from mass and p_T. The first component is obtained by applying the R_{trk} method on data collected in 2012 at ATLAS, while the second is a cross-calibration contribution derived by comparing the different conditions of the ATLAS detector at $\sqrt{s} = 8$ TeV and $\sqrt{s} = 13$ TeV in terms of reconstruction, characteristics of the calorimeter topological clusters, beam bunch spacing and modelling of nuclear interactions.
To evaluate the large-R jet mass resolution component (JMR) the jet mass is smeared to account for a degrade of 20% of the jet mass resolution. The resolution map was determined on a $Z' \to t\bar{t}$ sample, as the width of the Gaussian fit to the mass response $R \equiv m^{jet}_{detector}/m^{jet}_{particle}$ and parameterized in terms of large-R jet p_T and m/p_T.
The large-R jet JES uncertainty components represent the dominant uncertainty on the measured cross-section in the boosted topology.

b-tagging Uncertainties

The tagging efficiency of jets deriving from b-quarks, c-quarks and light quarks is corrected in simulations by applying an event by event weight that accounts for

the differences between the data and simulation efficiencies. The scale factors with the associated uncertainty band are derived in $t\bar{t}$ samples.
The systematic uncertainties on the cross-section measurement are derived varying the scale factor for each component forming its uncertainty band.
The impact of this uncertainty is dominant only in the resolved topology, where it reaches the 10% level in the $m^{t\bar{t}}$ and $p^{t,had}$ spectra.

Lepton Uncertainties

The lepton reconstruction, identification and the associated isolation requirement are described in Chapter 4. Scale factors are associated to all these steps, to account for the difference between simulation and data [109, 107]. The lepton uncertainties associated to the final distributions are derived varying the scale factors within their uncertainties.
An additional component is considered to account for the lepton's energy scale and resolution.
The lepton uncertainties on the final measurement are dependent on the lepton flavor, so uncorrelated between the two channels.
These uncertainties are sub-dominant both in boosted and resolved topology.

E_T^{miss} Uncertainties

The uncertainties associated to the E_T^{miss} are derived by propagating the energy scale and resolution uncertainties of the objects used to evaluate this quantity. Also the components related to energy deposits not associated to any reconstructed object are included [134].
The uncertainties related to E_T^{miss} have a small impact on the final measurement in both the topologies.

6.2 Luminosity Uncertainty

The uncertainty on the integrated luminosity is 2.1%, that is a sub-dominant uncertainty for the absolute differential cross-section in both topologies and cancels almost completely for the relative differential cross-section.

6.3 Background Uncertainties

The background estimation is affected by various systematic uncertainties, that can be due to the MC modelling or, in case of the data driven estimate, to the specific method employed. The background uncertainties are propagated through the unfolding procedure by building pseudodata distributions, used as input to the unfolding, as the sum of the varied total background and the nominal signal predictions. The corrections and the background subtracted to the pseudodata are the nominal one. Afterward, the unfolded distributions are compared with the

nominal particle level predictions and the size of the uncertainty is considered as the relative shift between the two.

6.3.1 Data-driven Backgrounds

In the following the components of the systematic uncertainty due to the fake leptons and W+jet estimate are described.

Non-prompt and Fake Lepton

A first component of the uncertainty on the fake leptons background is estimated by changing the definition of the control region where the fake efficiency is derived, as described in Table 6.1. The efficiencies are re-derived in the alternative region, keeping the same parameterization, and the final yield is recalculated. The difference with the original yield is considered as the uncertainty.

	Nominal CR	**Alternative CR**
e+jets	$E_T^{miss} < 30$ GeV and $m_{\mathrm{T}}^{\mathrm{W}} < 50$ GeV	$\frac{1}{2}E_T^{miss} + m_{\mathrm{T}}^{\mathrm{W}} < 60$ GeV
μ+jets	$\lvert d_0^{\mathrm{sig}}\rvert > 5$	$\lvert d_0^{\mathrm{sig}}\rvert > 3$ and $\lvert \Delta z_0 \sin\theta\rvert > 0.5$ mm

Table 6.1: Nominal and alternative fake efficiency control regions definitions.

Another source of uncertainty on the fake efficiency estimate is due to the normalization of the remaining background in the control region. The normalization is varied by ±20% and the efficiencies and final fake yields re-derived. The difference between the two variations and the nominal prediction is taken as two-fold uncertainty.
An additional component derives from the propagation of the statistical uncertainty on the parameterization of the fake and real efficiencies.
In addition to previous components, an extra 50% uncertainty is considered in the resolved topology analysis, to account for the mis-modeling observed in control regions. In the case of the boosted analysis, the mis-modeling of the fake background is found only at values of $m_T^W > 150$ GeV. Consequently, for all the events falling in this category, an extra 100% uncertainty on the fake-leptons background estimate is included.

W+jets Background Estimate

The data-driven charge asymmetry and heavy flavor scale factors were derived as described in Section 4.3.1. For each detector and background normalization uncertainty, the charge asymmetry and heavy flavor scale factors have been re-derived from data.
In the boosted topology an additional component is obtained by changing the normalization of the fake lepton background by 30%, in the procedure to derive

the scale factors.
In the resolved topology the scale factors are re-derived in correlation with the 50% fake variation, described in the previous section. Additional uncertainties has been considered to take into account the statistical uncertainty associated to each scale factor, these are obtained by varying one scale factor at a time and re-deriving the others, using the iterative procedure presented in Section 4.3.1. The overall impact of these additional uncertainties is less than 0.5%.

6.3.2 MC Estimated Backgrounds

The uncertainty associated to the single top quark background is due to its normalization and the overall impact on the measured cross-section is less than 0.5%, for all the distributions.
In the case of Z+jets backgrounds the uncertainty includes a contribution from the cross-section normalization as well as an additional 24% added in quadrature for each reconstructed jet. In the $t\bar{t}V$ and Diboson case the only uncertainty considered is the normalization one.
Details on the normalization uncertainties considered for all samples are shown in Table 6.2.
The total contribution on the final measurement of the $t\bar{t}V$, Z+jets and Diboson

Process	Normalization uncertainty
Single top	uncertainty on cross-section in t-channel [135], Wt-channel [136] and s-channel [137]
Z+jets	50% variation
Diboson	40% variation
$t\bar{t}$V	40% variation

Table 6.2: Summary on the approach used to assign normalization uncertainty to each background sample estimated using MC simulations.

normalization uncertainty is less than 1%, with largest contribution given from the Z+jets background.

6.4 Signal Modelling Uncertainties

The uncertainties on the modelling of the $t\bar{t}$ sample enters in the cross-section measurement through the corrections employed in the unfolding procedure.
Four different sources of uncertainties are considered:

- **Hard scattering:** this uncertainty accounts for the choice of the generator used to simulate the hard scattering step of the $t\bar{t}$ interaction and the following matching to the showering.
  This component is estimated comparing two of the generators described in Section 3.3, keeping the same parton shower in both. In particular MadGraph5_aMC@NLO + Herwig++ is unfolded with the corrections estimated using Powheg + Herwig++, then the unfolded distributions are

compared with the corresponding particle level and the symmetrized relative difference is propagated on the measured cross-section.
The impact of this uncertainty is dependent on the variable considered and reaches a maximum level of 15% at large $p_T^{t,had}$.

- **Parton shower:** this component accounts for the choice of the showering generator and the model used for the hadronization. To evaluate this uncertainty two generators, differing only for the showering, are compared: POWHEG+HERWIG++ and POWHEG+PYTHIA 6. The uncertainty is extracted, as for the hard scattering case, unfolding POWHEG+HERWIG++ with the predictions evaluated with POWHEG+PYTHIA 6.
The impact on the measured distributions ranges between 6(3)% and 9(6)% in boosted(resolved) topology.

- **Initial and final state radiation:** the impact of the modelling of the initial and final state QCD radiations is assessed using POWHEG+PYTHIA 6 $t\bar{t}$ generators, with modified settings of the parameters that regulate the radiation. The upward variation is obtained by multiplying the factorization and hadronization scales by a factor 0.5 and simultaneously increasing the h_{damp} parameter to 2 m_{top}. The downward variation is obtained keeping unchanged the h_{damp} parameter and increasing, at the same time, the factorization and hadronization scales by a factor 2. An additional difference between the two varied sample is in the POWHEG+PYTHIA 6 tuning of the underlying event and showering models.
In this case both the alternative samples are unfolded with the nominal POWHEG+PYTHIA 6 and the results compared with the respective particle level. The relative differences are then propagated to the measured cross-section, keeping separate the up and down shifts without any symmetrization. This uncertainty has an impact of 3–6% for both the resolved and boosted topology.

- **PDF:** the uncertainty related to the choice of the PDF set is assessed using the $t\bar{t}$ sample MADGRAPH5_aMC@NLO + HERWIG++ and a set of re-weighting factors, estimated to emulate the effect of the use of an alternative PDF in the generation. This uncertainty is estimated following the PDF4LHC15PDF prescriptions [138] and has two different components: the intra-PDF and the inter-PDF. The first component is computed re-weighting the central distribution to obtain a set of 30 variations. Each one is then used to re-evaluate the unfolding corrections, shown in Figure 6.1 for the boosted topology. Successively the central MADGRAPH5_aMC@NLO + HERWIG++ is unfolded with each set of corrections and the relative difference with the central particle level distribution is computed. The intra-PDF component is given by the quadrature sum of the relative differences obtained for each variation.
In addition the inter-PDF uncertainty is computed as the hard scattering component, unfolding the central distribution of the PDF4LHC15 set with the

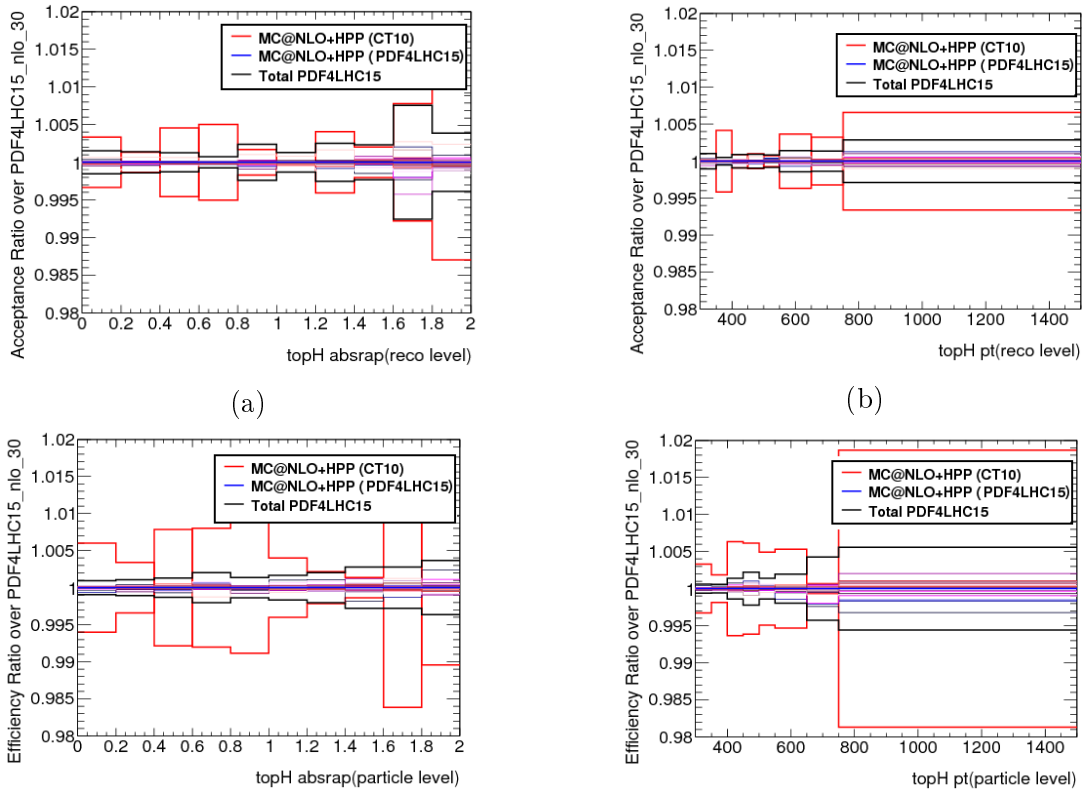

Figure 6.1: Acceptance and efficiencies corrections for the $p_T^{t,had}$ and $|y^{t,had}|$ evaluated using the PDF variations computed to estimate the inter-PDF (red) and the intra-PDF uncertainty in boosted topology. The black line represents the total intra-PDF uncertainty.

corrections obtained from the same generator (MadGraph5_aMC@NLO + Herwig++) but employing the CT10 PDF. The total PDF uncertainty has a small impact on the final measurement, being less than 1% in almost all the spectra, for both topologies.

6.5 Limited Sample Statistic

The uncertainty deriving from the finite size of the simulated samples is obtained using 10000 test distributions, built starting from the sum of all the MC predictions of signal and background. Each bin is varied accordingly to its statistical uncertainty, and the set of varied distributions is unfolded with the nominal corrections. The statistical uncertainty is the RMS of the unfolded spectra.
The effect on the absolute spectra is about 5% in boosted topology, peaking at 12% in the last top quark p_T bins, while in the resolved case the uncertainty reaches at most 1–2%.

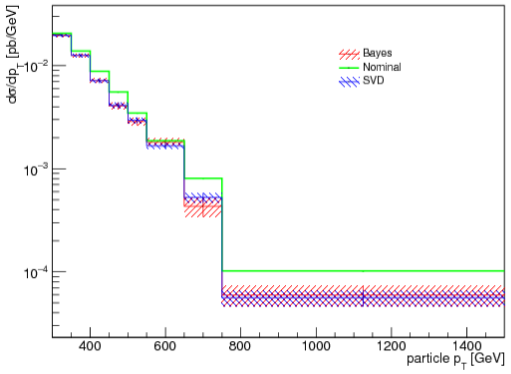

Figure 6.2: Particle level unfolded distributions, as a function of the $p_T^{t,had}$, obtained with two different unfolding technique: SVD with k = 6 (blue) and Bayes with 4 iterations (red). The dashed band represents only statistical uncertainties. The green line represent the particle level POWHEG+PYTHIA 6 Monte Carlo prediction.

6.6 Statistical Uncertainty

The statistical uncertainty is evaluated building 10000 pseudo-experiments, derived from the data distribution before the background subtraction. The pseudo-experiments are derived extracting for each bin a random number from a Poisson distribution, with mean equal to the number of selected events in that bin. Each pseudo-experiment is unfolded with the nominal corrections and the RMS of the unfolded spectra is the statistical uncertainty.

6.6.1 Unfolding Effect on Statistical Uncertainty

In the boosted analysis presented in this thesis an increase of the statistical uncertainty with respect to the similar analysis performed at 8 TeV [49] is observed, although the number of selected events is similar.
Since the unfolding procedure has an impact on the statistical uncertainty and on the bin-by-bin correlations, the method used in this thesis and the method previously used are compared to verify that the difference observed is related to the choice of the unfolding method. The differences on the data distributions unfolded with the two methods, shown in Figure 6.2, is below the statistical uncertainties, as expected since none of the methods showed biases.
The effect on the statistical uncertainties, on the other hand, is sizable, as shown in Figure 6.3, where the uncertainties obtained using the Bayes method, with four iterations, are compared with the ones evaluated using SVD. To this enhancement of the statistical uncertainty corresponds a reduction of the bin-by-bin correlations, shown in Figure 6.4 and 6.5. Here are reported the correlation matrices of the $p_T^{t,had}$ and $|y^{t,had}|$ in boosted topology, obtained with Bayes and SVD. It is shown that the correlations induced from SVD are larger than the ones obtained using the Bayes method with four iterations.

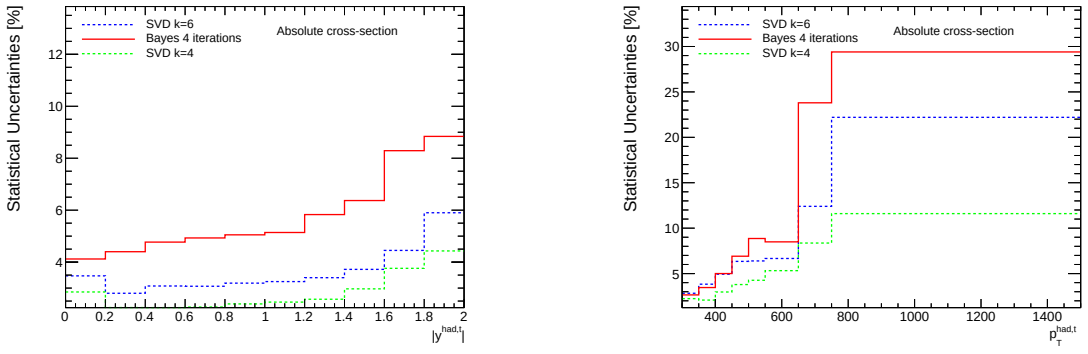

(a) (b)

Figure 6.3: Statistical uncertainty on the particle level unfolded distributions, as a function of the $p_T^{t,had}$ (a) and $|y^{t,had}|$ (b), obtained with three different unfolding techniques: SVD with $k = 6$ (blue), SVD with $k = 4$ (green) and Bayes with 4 iterations (red)

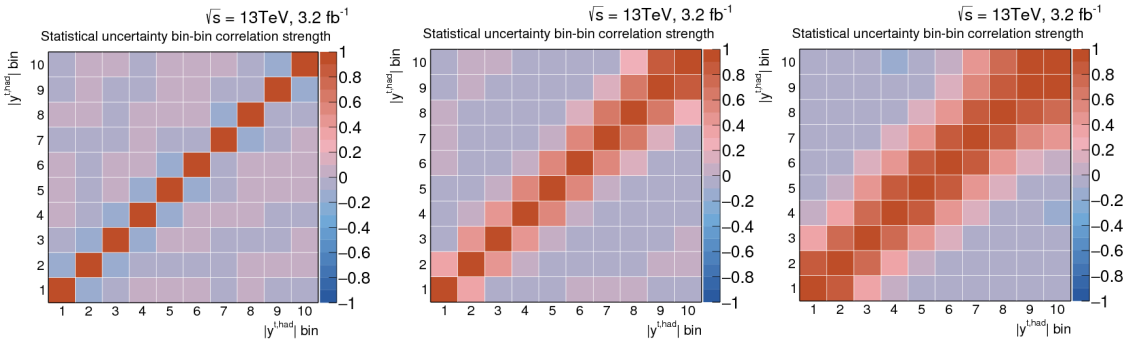

(a) (b) (c)

Figure 6.4: Correlations matrices obtained from data statistical uncertainty evaluation on $|y^{t,had}|$, using Bayes with 4 iterations (a), SVD with $k = 6$ (b) and SVD with $k = 4$.

The statistical uncertainty associated to a measurement is only a diagonal representation of the covariance matrix used in the χ^2 computation. For this reason an additional comparison between the Bayes method and the SVD method is done on the covariance matrices, including data statistics and all detector level systematic uncertainties. The procedure employed to obtain the covariance matrix is described in the next chapter. The ratio obtained between the two correlation matrices for the $p_T^{t,had}$ is reported in Table 6.3, here the diagonal elements represent the ratio between the total uncertainties obtained using the two methods, while the off-diagonal terms are the ratios among the bin-by-bin correlations.

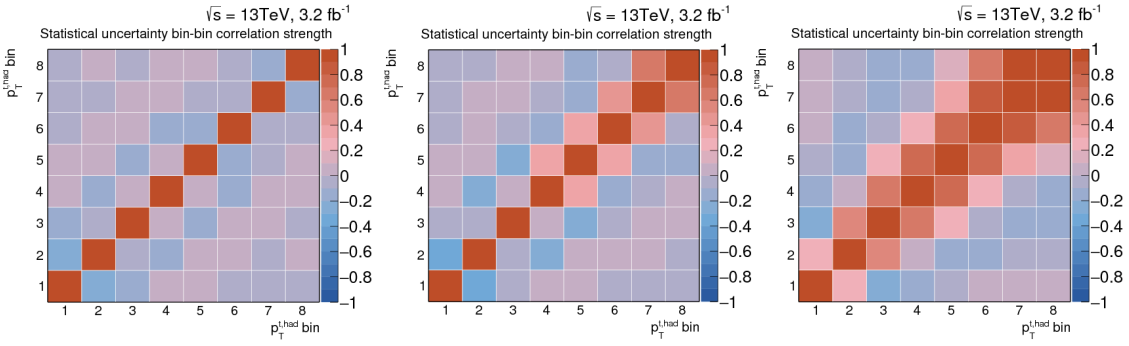

(a) (b) (c)

Figure 6.5: Correlations matrices obtained from data statistical uncertainty evaluation on $|p_T^{t,had}|$, using Bayes with 4 iterations (a), SVD with $k = 6$ (b) and SVD with $k = 4$

	bin 1	bin 2	bin 3	bin 4	bin 5	bin 6	bin 7	bin 8
bin 1	0.989	1.02	0.986	1	0.951	0.97	0.955	0.762
bin 2	1.02	0.978	0.993	1.01	0.944	0.971	0.974	0.748
bin 3	0.986	0.993	0.994	0.992	0.94	0.976	0.948	0.766
bin 4	1	1.01	0.992	0.988	0.945	0.982	0.988	0.777
bin 5	0.951	0.944	0.94	0.945	1.07	0.901	0.935	0.797
bin 6	0.97	0.971	0.976	0.982	0.901	0.975	0.914	0.714
bin 7	0.955	0.974	0.948	0.988	0.935	0.914	0.988	0.563
bin 8	0.762	0.748	0.766	0.777	0.797	0.714	0.563	1.58

Table 6.3: Comparison between the two correlation matrices obtained using the unfolding methods SVD and Bayes, including all detector-level uncertainties. The element on the diagonal are the ratios between the relative uncertainties obtained with the two methods (Bayes/SVD), while the off diagonal terms represent the ratios between the bin-by-bin correlations.

The table shows that the uncertainties obtained with the two methods are similar, but Bayes tends to provide slightly larger uncertainties in some bins. On the other hand the correlations induced from SVD are larger in almost all the bins.

6.7 Uncertainty on the Cross-section Measurement

The detailed results of the evaluation of the systematic uncertainties affecting the particle level differential cross-section measurements are summarized in the Tables reported in Appendix C. In Figure 6.6 and 6.7 is shown the impact of the different uncertainty sources on the absolute and relative measured particle level spectra, evaluated in the boosted topology analysis.
The dominant uncertainties on the absolute spectra in boosted topology are the large-R jet JES components and the statistic, while also the signal modelling uncertainties have a significant impact on the relative spectra. The uncertainty com-

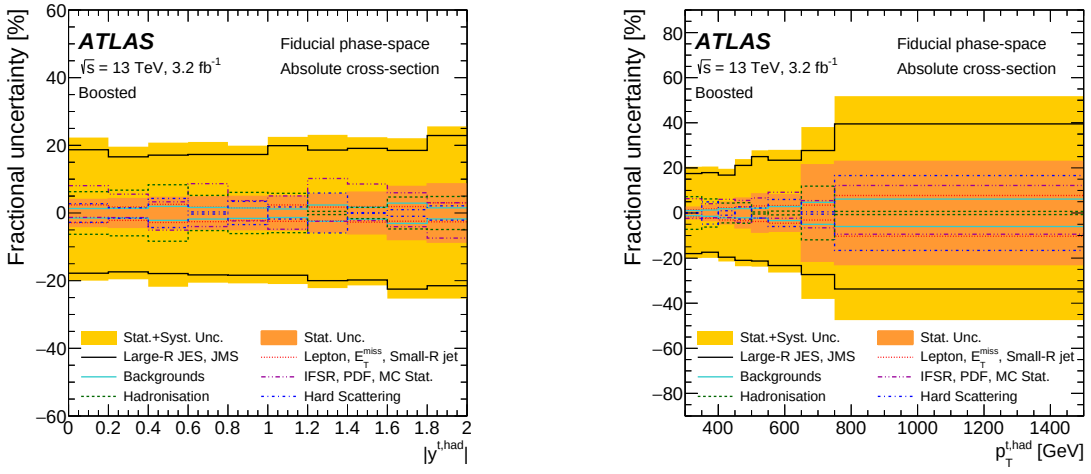

(a) (b)

Figure 6.6: Uncertainties on the particle level distributions as a function of (a) $|y^{t,had}|$ and (b) $p_T^{t,had}$ in the boosted regime [1].

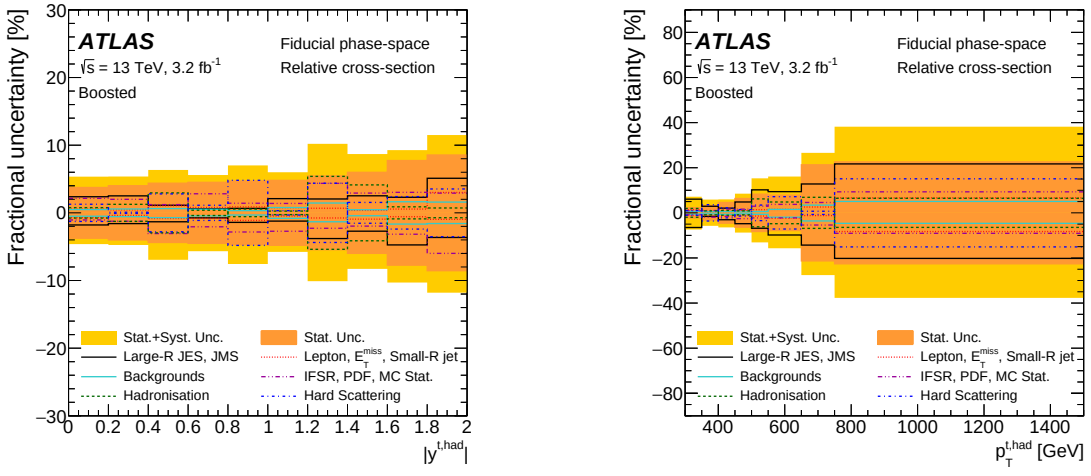

(a) (b)

Figure 6.7: Uncertainties on the relative particle level distributions as a function of (a) $|y^{t,had}|$ and (b) $p_T^{t,had}$ in the boosted regime [1].

position in resolved topology on absolute and relative spectra are shown in Figure 6.8, 6.9, 6.11 and 6.10. The dominant uncertainty in resolved topology depends on the spectra, but the overall main components are the small-R jet JES and the flavor tagging.

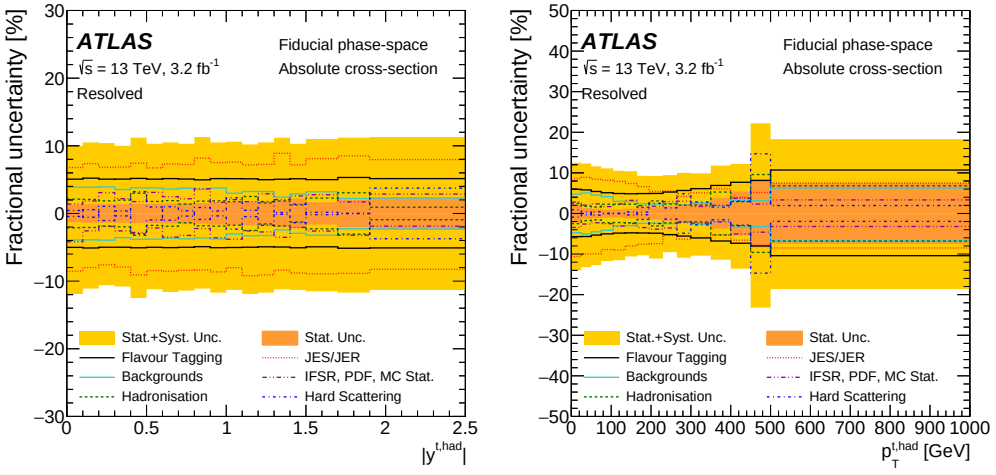

(a) (b)

Figure 6.8: Uncertainties on the relative particle level distributions as a function of (a) $|y^{t,had}|$ and (b) $p_T^{t,had}$ in the resolved regime [1].

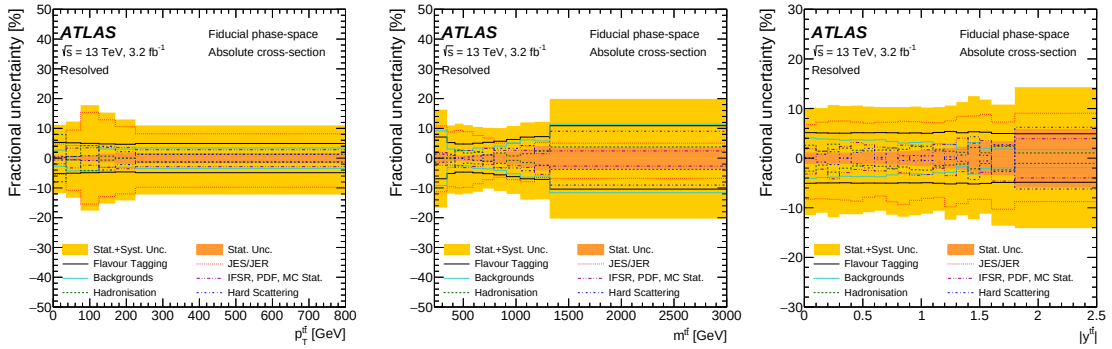

(a) (b) (c)

Figure 6.9: Uncertainties on the particle level distributions as a function of (a) $m^{t\bar{t}}$, (b) $p_T^{t\bar{t}}$ and (c) $|y^{t\bar{t}}|$ in the resolved regime [1].

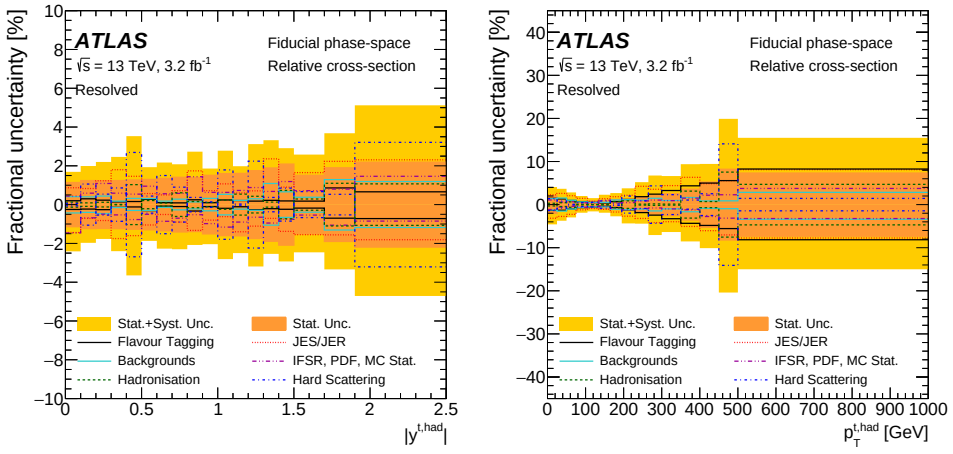

(a) (b)

Figure 6.10: Uncertainties on the relative particle level spectra, as a function of (a) $|y^{t,had}|$ and (b) $p_T^{t,had}$ in the resolved regime [1].

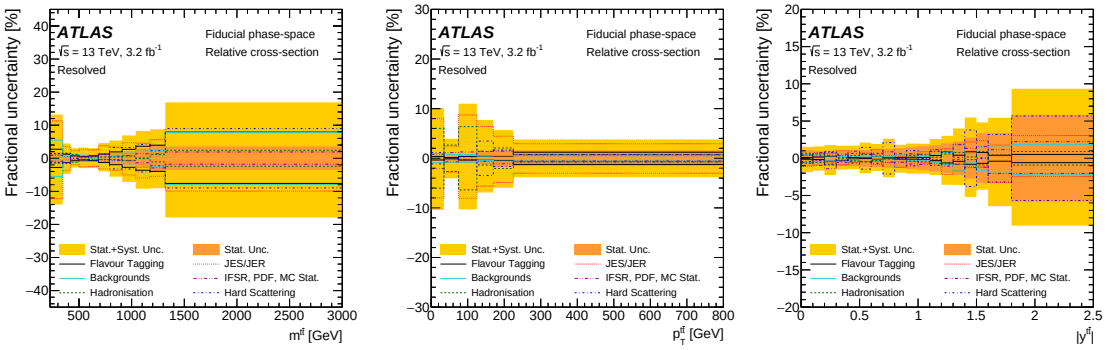

(a) (b) (c)

Figure 6.11: Uncertainties on the relative particle level spectra as a function of (a) $m^{t\bar{t}}$, (b) $p_T^{t\bar{t}}$ and (c) $|y^{t\bar{t}}|$ in the resolved regime [1].

Chapter 7

Results and Interpretation

In this chapter the measured cross-section is compared with several theoretical predictions of the $t\bar{t}$ signal, differing for the matrix element calculation method, the simulation of parton-shower and hadronization. The comparisons are presented both on the absolute and relative cross-sections. While the former are used to compare also the inclusive cross-section with the predictions, the latter are presented in order to exploit the reduction of those systematic uncertainties that are highly correlated across the kinematic bins.
The χ^2 values are also presented, in order to quantify the level of agreement between the measured distributions and the different theoretical predictions.

7.1 Particle Level Differential σ Results

The absolute and relative differential cross-sections, measured in boosted and resolved regimes as a function of the kinematic properties of the hadronic top and $t\bar{t}$ system, are compared with various generators. In particular, every Figure 7.1-7.3 contains three pads reporting MC over data ratios; in the first the nominal prediction POWHEG+PYTHIA6 is compared with the samples used to derive the IFSR uncertainty, presenting a different settings of the parameters that determine the amount of radiation, in the second pad the nominal POWHEG+PYTHIA6 is compared with other predictions employing a different showering and hadronization. In the last one POWHEG+PYTHIA6 and MADGRAPH5_aMC@NLO are compared for the hard scattering calculation technique.

7.1.1 Boosted Topology

Figure 7.1 shows the absolute and relative differential cross-sections as a function of the hadronic top quark transverse momentum and the absolute value of the rapidity in the boosted topology.

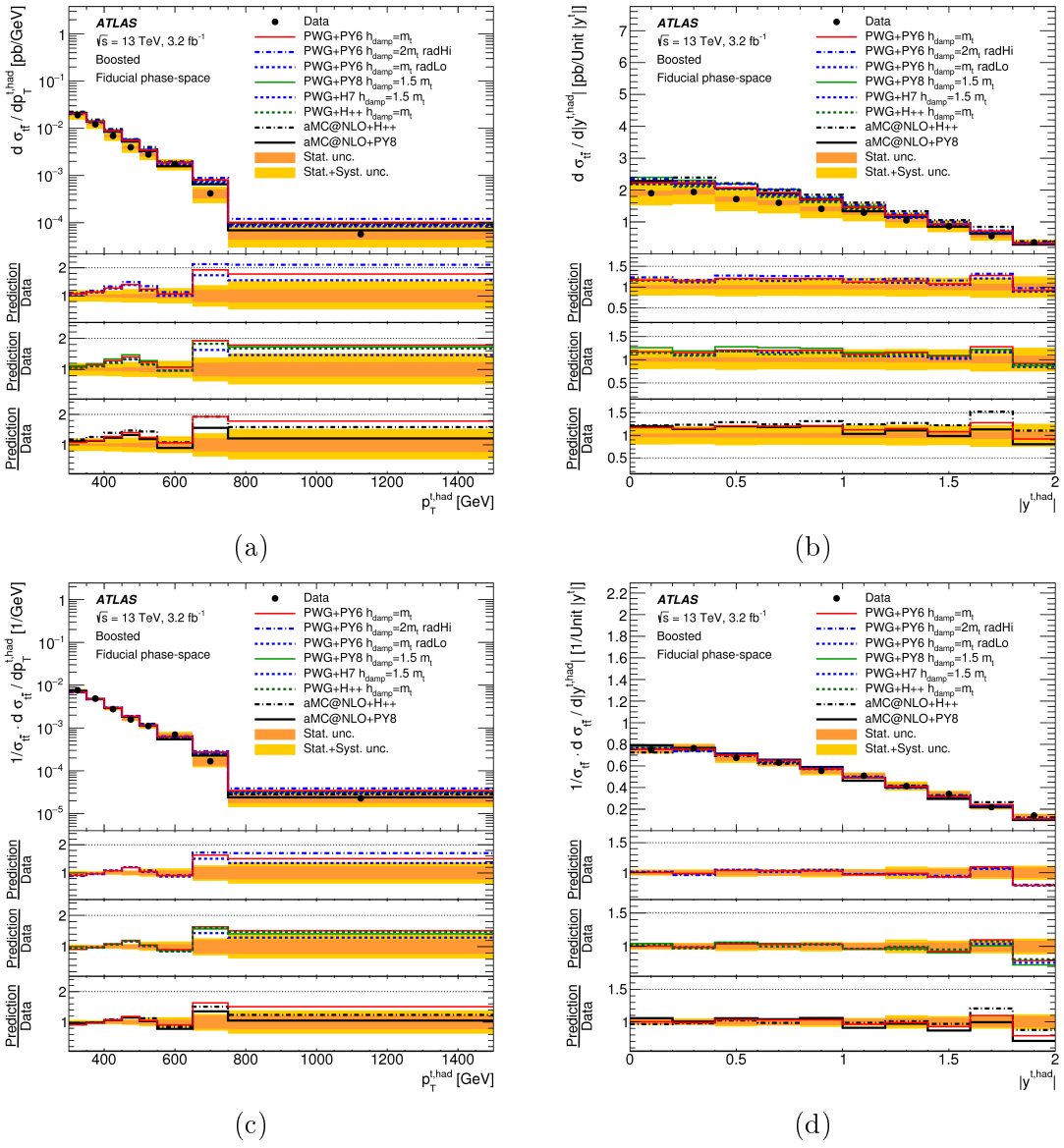

Figure 7.1: Fiducial phase space absolute (first row) and relative (second row) differential cross-sections as a function of the (a,c) transverse momentum $p_T^{t,had}$ and (b,d) the $|y^{t,had}|$ of the hadronic top quark in the boosted topology. The yellow bands indicate the total uncertainty associated to data in each bin, while the orange one is only the statistical component. The lower three panels show the ratio of the predictions to the data [1].

7.1.2 Resolved Topology

Figures 7.2 presents the absolute differential cross-sections in resolved topology as a function of the hadronic top quark transverse momentum and absolute rapidity, and mass, transverse momentum and absolute rapidity of the $t\bar{t}$ system. In Figure 7.3 are shown the corresponding relative distributions.

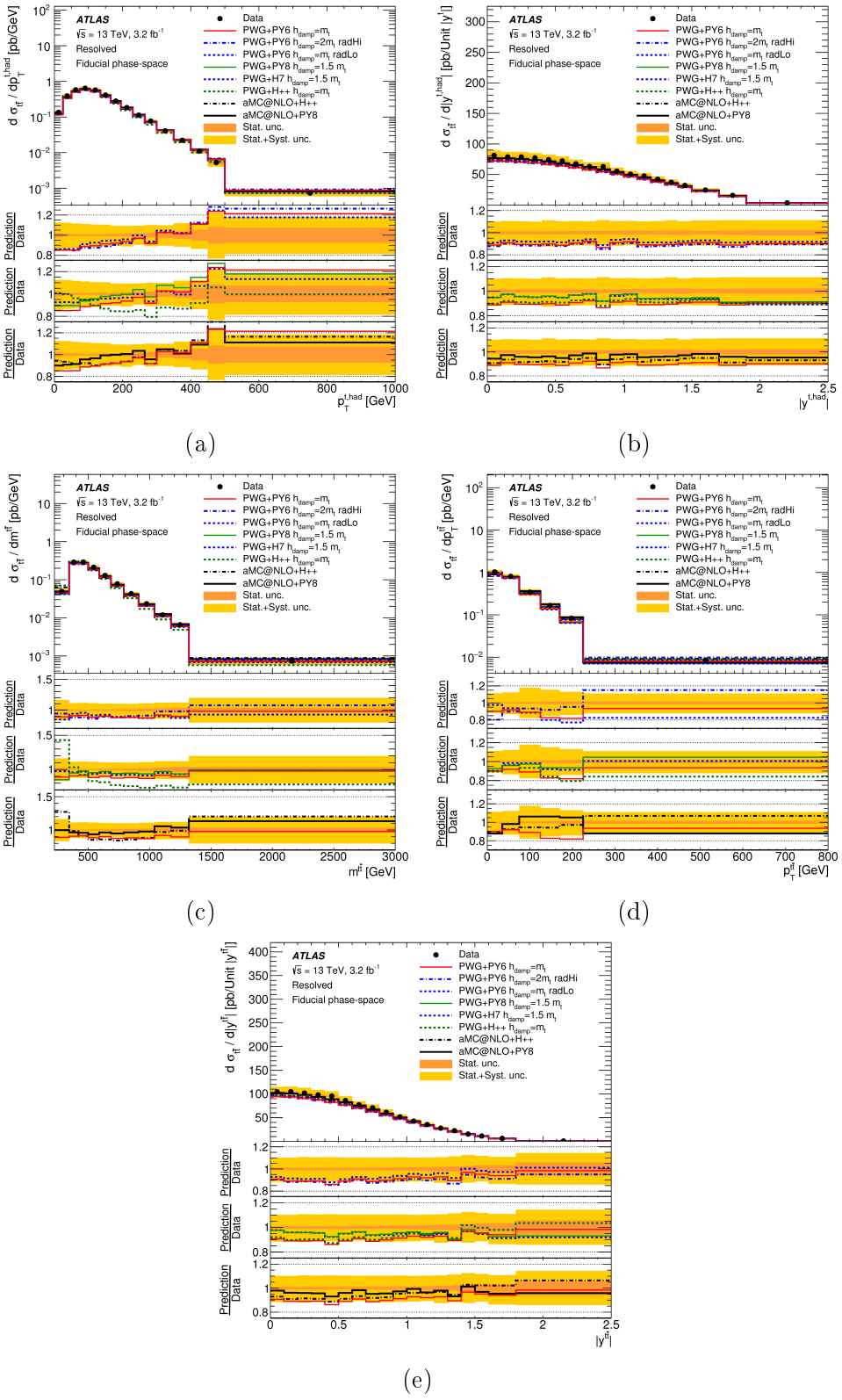

Figure 7.2: Fiducial phase-space absolute differential cross-sections as a function of the (a) $p_T^{t,had}$ and (b) $|y^{t,had}|$ and (c) $m^{t\bar{t}}$, (d) $p_T^{t\bar{t}}$ and (e) $|y^{t\bar{t}}|$ in the resolved topology. The yellow bands indicate the total uncertainty associated to data in each bin, while the orange one is only the statistical component. The lower three panels show the ratio of the predictions to the data [1].

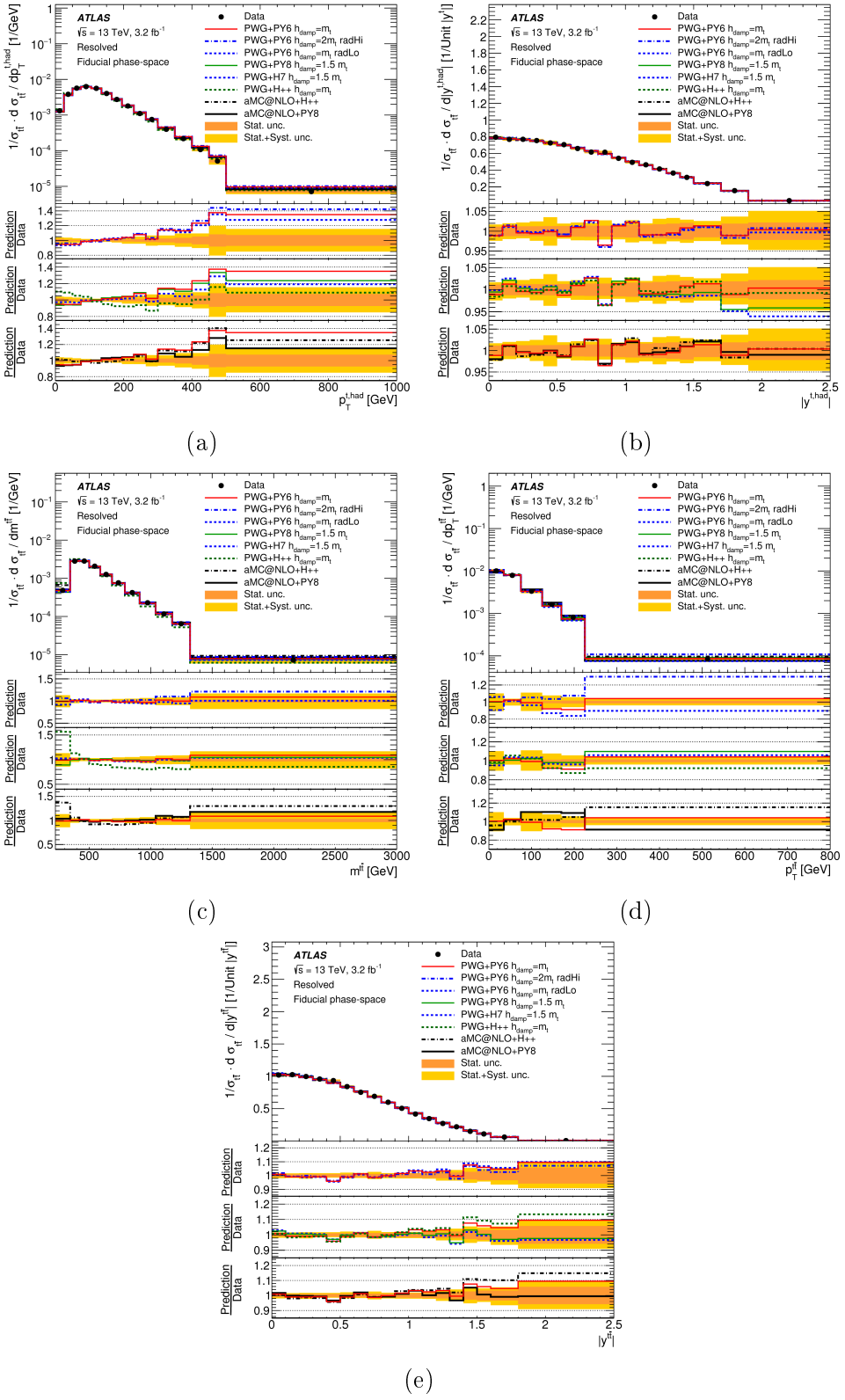

(a) (b)

(c) (d)

(e)

Figure 7.3: Fiducial phase-space relative differential cross-sections as a function of the (a) $p_T^{t,had}$ and (b) $|y^{t,had}|$ and (c) $m^{t\bar{t}}$, (d) $p_T^{t\bar{t}}$ and (e) $|y^{t\bar{t}}|$ in the resolved topology. The yellow bands indicate the total uncertainty associated to data in each bin, while the orange one is only the statistical component. The lower three panels show the ratio of the predictions to the data [1].

7.2 χ^2 Evaluation

A quantitative comparison between the measured cross-section and the various predictions is performed by means of a χ^2 calculation.
The χ^2 is evaluated using the full covariance matrix COV_{NDF}, including all the systematic uncertainties and following the equation:

$$\chi^2 = V_{NDF}^T \cdot COV_{NDF}^{-1} \cdot V_{NDF}, \tag{7.1}$$

where V_{NDF} is the vector of differences between particle level measured cross-section and predictions and NDF is the number of degree of freedoms. The NDF corresponds the number of bins for absolute distributions, but in the relative ones the normalization constraint lowers the NDF by one unit. Consequently it is necessary to remove one row and the corresponding column from the covariance matrix obtained using the relative distributions to keep the matrix rank equal the degrees of freedom. This is necessary to invert the matrix. The removed line corresponds to a bin of the distributions, that is subtracted also from the vector of differences between data and predictions used to compute the χ^2. The χ^2 value does not depend on the choice of row and column discarded.
The full covariance matrix includes the effects of the detector, background and theoretical uncertainties on the measured spectra, while the uncertainties on theoretical predictions are not considered in the χ^2 evaluation.
The χ^2 is then used to extract the probability that repeating the same measurement a value larger or equal to the observed one is obtained (p-value). This is done as illustrated in Figure 7.4, where is represented the χ^2 distribution and p-value extraction for the relative spectra of $p_T^{t,had}$ and $|y^{t,had}|$ in the boosted topology. The p-value is computed by extracting the area under the curve for values that exceeds the observed χ^2.

The covariance matrix is evaluated as a sum of two matrices obtained with two different procedures, the first ($COV^{det.}$) contains all the uncertainties related to the detector calibrations, background modelling and statistical uncertainties while the second ($COV^{theor.}$) the theoretical $t\bar{t}$ modelling uncertainties affecting the corrections applied. The $COV^{det.}$ is obtained using pseudo-experiments derived from pre-unfolding data distributions. In each of the 10000 pseudo-experiments each bin of the data distribution is varied with a Poisson fluctuation. Gaussian-distributed shifts are coherently added for each systematic uncertainty, scaling each Poisson-fluctuated bin with the relative variation due to each systematic uncertainty. The relative systematic variation $\Delta_j^{syst_i}$, due to a certain source $syst_i$ in the bin j, is evaluated starting from the signal (S) and background (B) samples as:

$$\Delta_j^{syst_i} \equiv \frac{S_j^{syst_i} + B_j^{syst_i} - S_j^{nominal} - B_j^{nominal}}{S_j^{nominal} + B_j^{nominal}} \tag{7.2}$$

The number of events N in the bin j of the pseudo-experiment k is evaluated as:

$$N_j^k \equiv P(D_j)[1 + \sum_{syst_i} \lambda_{syst_i} \Delta_j^{syst_i}], \tag{7.3}$$

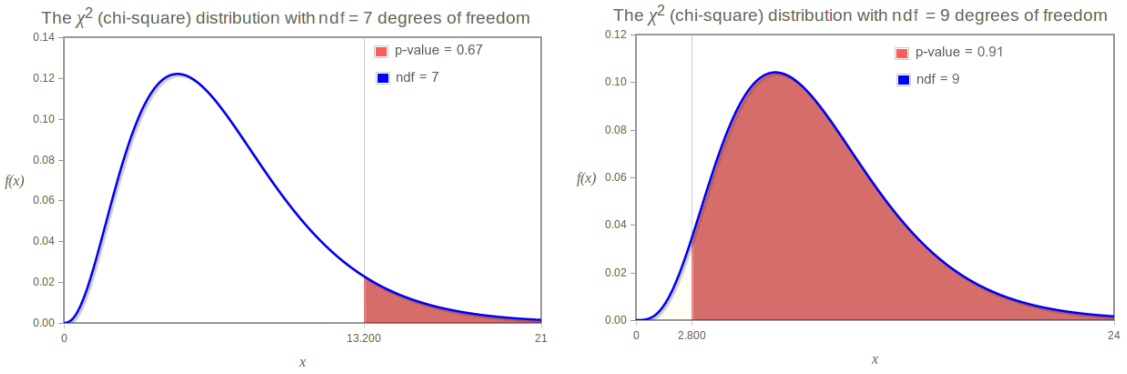

(a) (b)

Figure 7.4: χ^2 distributions corresponding to the degrees of freedom of the relative spectra of (a) $p_T^{t,had}$ and (b) $|y^{t,had}|$ in boosted regime, the red areas correspond to the p-value for the observed χ^2

where $P(D_j)$ is a poissonian rundom number extracted using as average the number D_j of events in bin j of the data distribution and λ_{syst_i} represents a random number drawn from a Gaussian distribution with $\mu = 0$ and $\sigma = 1$. A different λ_{syst_i} is extracted for each source of systematic uncertainty but is applied to all bins, so bin-by-bin variations are fully correlated. In case of asymmetric systematic uncertainties the sign of λ_{syst_i} determines if the upward or downward shift of the systematic is used to derive $\Delta_j^{syst_i}$. After the creation of the pseudo-experiments the expected background is subtracted to each of them and the obtained distributions are passed through the unfolding, computed using the nominal POWHEG+PYTHIA6 corrections. The $COV^{det.}$ in each bin i, j is successively calculated as:

$$COV^{det}(i,j) = \langle (d\sigma_i - \langle d\sigma_i \rangle_N) \cdot (d\sigma_j - \langle d\sigma_j \rangle_N) \rangle_N, \tag{7.4}$$

where dσ represents the differential cross-section and N is the number of pseudo-experiments.
A special modification to the procedure is necessary in bins where the uncertainties are large, such as the p_T distribution in the boosted topology, where the uncertainty in the last two bins is around 40%. In these cases it is possible that, for some pseudo-experiments, the number of extracted signal events is so low that it becomes negative after the background subtraction. This can happen because the uncertainties are completely dominated by one or two components, and consequently a large fluctuation of one of these components may cause a large shift in the number of extracted events. A negative number of events does not have a physical meaning, moreover the iterative Bayesian unfolding interprets the number of events in each bin as a probability, intrinsically defined as positive. For these two reasons the bins where the extracted number of events is negative are set to 0, before passing the distributions to the unfolding. This procedure on negative fluctuations is applied on the 2% of pseudo-experiments on the 7^{th} bin and on the 7% on the last bin of the $p_T^{t,had}$ distribution in *boosted* topology. This approach modifies only the

last two bins of the distributions introducing a slight de-correlation from the others and producing a minimal impact on the covariance evaluation. Other possible approaches, as re-generating the toy if a negative fluctuation is observed, implies a larger impact on the distributions. Indeed in this case, since all the bins are correlated, the large fluctuations would be discarded from all bins of the distributions and a bias toward small and positive fluctations of $P(D_j)$ would be introduced.
The second covariance matrix is obtained by summing four separate covariance matrices corresponding to each $t\bar{t}$ modelling uncertainty: generator, parton shower and hadronisation, ISR/FSR and PDF. The elements of each matrix are determined as:

$$COV^{theor.}_{mod_k}(i,j) = CORR^{theor.}_{mod_k}(i,j) \cdot \sqrt{\Delta\sigma_i^{mod_k} \cdot \Delta\sigma_j^{mod_k}}, \tag{7.5}$$

where $\Delta\sigma_i$ represents the relative uncertainty on the cross-section in the bin i due to a $t\bar{t}$ modelling uncertainty component (mod_k), multiplied by the measured cross-section in the bin i, and $CORR^{theor.}(i,j)$ is correlation among the bins of the distribution. Since the modelling uncertainties are extracted comparing two samples, all the bins are considered as completely correlated ($CORR^{theor.}_{mod_k}(i,j) = 1$). The separate treatment of the signal modelling uncertainties is necessary because these effects cannot be represented by a variation at the detector level, therefore they cannot be included in the pseudo-experiment formalism used to derive the first covariance matrix.

In Table 7.1 are reported as example the covariance matrices for the absolute

bin [GeV]	300-350	350-400	400-450	450-500	500-550	550-650	650-750	750-1500
300-350	1.49e-05	8.83e-06	4.86e-06	3.12e-06	2.04e-06	1.25e-06	4.46e-07	7.02e-08
350-400	8.83e-06	6.27e-06	3.34e-06	2.21e-06	1.52e-06	9.70e-07	3.29e-07	5.88e-08
400-450	4.86e-06	3.34e-06	2.18e-06	1.36e-06	9.56e-07	6.15e-07	2.08e-07	3.65e-08
450-500	3.12e-06	2.21e-06	1.36e-06	1.00e-06	6.79e-07	4.20e-07	1.45e-07	2.57e-08
500-550	2.04e-06	1.52e-06	9.56e-07	6.79e-07	5.89e-07	3.25e-07	1.04e-07	1.99e-08
550-650	1.25e-06	9.70e-07	6.15e-07	4.20e-07	3.25e-07	2.42e-07	6.42e-08	1.27e-08
650-750	4.46e-07	3.29e-07	2.08e-07	1.45e-07	1.04e-07	6.42e-08	3.41e-08	3.84e-09
750-1500	7.02e-08	5.88e-08	3.65e-08	2.57e-08	1.99e-08	1.27e-08	3.84e-09	1.08e-09

bin	0.0-0.2	0.2-0.4	0.4-0.6	0.6-0.8	0.8-1.0	1.0-1.2	1.2-1.4	1.4-1.6	1.6-1.8	1.8-2.0
0.0-0.2	1.65e-01	1.48e-01	1.44e-01	1.28e-01	1.11e-01	1.09e-01	8.73e-02	6.73e-02	4.94e-02	3.21e-02
0.2-0.4	1.48e-01	1.49e-01	1.35e-01	1.21e-01	1.06e-01	1.02e-01	8.00e-02	6.32e-02	4.69e-02	3.03e-02
0.4-0.6	1.44e-01	1.35e-01	1.40e-01	1.14e-01	1.02e-01	9.83e-02	7.87e-02	5.96e-02	4.47e-02	2.91e-02
0.6-0.8	1.28e-01	1.21e-01	1.14e-01	1.15e-01	9.00e-02	8.92e-02	7.43e-02	5.70e-02	4.15e-02	2.66e-02
0.8-1.0	1.11e-01	1.06e-01	1.02e-01	9.00e-02	8.66e-02	7.71e-02	6.31e-02	4.85e-02	3.60e-02	2.33e-02
1.0-1.2	1.09e-01	1.02e-01	9.83e-02	8.92e-02	7.71e-02	8.16e-02	6.15e-02	4.81e-02	3.48e-02	2.26e-02
1.2-1.4	8.73e-02	8.00e-02	7.87e-02	7.43e-02	6.31e-02	6.15e-02	6.42e-02	4.04e-02	2.89e-02	1.86e-02
1.4-1.6	6.73e-02	6.32e-02	5.96e-02	5.70e-02	4.85e-02	4.81e-02	4.04e-02	3.54e-02	2.24e-02	1.44e-02
1.6-1.8	4.94e-02	4.69e-02	4.47e-02	4.15e-02	3.60e-02	3.48e-02	2.89e-02	2.24e-02	1.89e-02	1.03e-02
1.8-2.0	3.21e-02	3.03e-02	2.91e-02	2.66e-02	2.33e-02	2.26e-02	1.86e-02	1.44e-02	1.03e-02	8.03e-03

Table 7.1: Covariance matrices of the absolute cross-section as function of the hadronic top quark $p_T^{t,had}$ (top) and $|y^{t,had}|$ (bottom), accounting for the statistic and all systematic uncertainties in the boosted regime [1].

$p_T^{t,had}$ and $y^{t,had}$ spectra in the boosted topology. Dividing each bin (i,j) of the covariance matrix by the term $\sqrt{COV(i,i) \cdot COV(j,j)}$ it is possible to obtain the correlation matrix, that is a clear illustration of the correlations among the bins of

bin [GeV]	300-350	350-400	400-450	450-500	500-550	550-650	650-750	750-1500
300-350	**1.00**	0.91	0.85	0.81	0.69	0.66	0.62	0.55
350-400	0.91	**1.00**	0.91	0.88	0.79	0.79	0.71	0.71
400-450	0.85	0.91	**1.00**	0.92	0.84	0.85	0.76	0.75
450-500	0.81	0.88	0.92	**1.00**	0.89	0.85	0.78	0.78
500-550	0.69	0.79	0.84	0.89	**1.00**	0.86	0.73	0.79
550-650	0.66	0.79	0.85	0.85	0.86	**1.00**	0.71	0.78
650-750	0.62	0.71	0.76	0.78	0.73	0.71	**1.00**	0.63
750-1500	0.55	0.71	0.75	0.78	0.79	0.78	0.63	**1.00**

bin	0.0-0.2	0.2-0.4	0.4-0.6	0.6-0.8	0.8-1.0	1.0-1.2	1.2-1.4	1.4-1.6	1.6-1.8	1.8-2.0
0.0-0.2	**1.00**	0.94	0.95	0.93	0.93	0.94	0.85	0.88	0.88	0.88
0.2-0.4	0.94	**1.00**	0.93	0.92	0.93	0.93	0.82	0.87	0.88	0.88
0.4-0.6	0.95	0.93	**1.00**	0.90	0.93	0.92	0.83	0.85	0.87	0.87
0.6-0.8	0.93	0.92	0.90	**1.00**	0.90	0.92	0.86	0.89	0.89	0.87
0.8-1.0	0.93	0.93	0.93	0.90	**1.00**	0.92	0.85	0.88	0.89	0.88
1.0-1.2	0.94	0.93	0.92	0.92	0.92	**1.00**	0.85	0.90	0.89	0.88
1.2-1.4	0.85	0.82	0.83	0.86	0.85	0.85	**1.00**	0.85	0.83	0.82
1.4-1.6	0.88	0.87	0.85	0.89	0.88	0.90	0.85	**1.00**	0.87	0.86
1.6-1.8	0.88	0.88	0.87	0.89	0.89	0.89	0.83	0.87	**1.00**	0.84
1.8-2.0	0.88	0.88	0.87	0.87	0.88	0.88	0.82	0.86	0.84	**1.00**

Table 7.2: Correlation matrices of the absolute cross-section as function of the hadronic top quark $p_T^{t,had}$ (top) and $|y^{t,had}|$ (bottom), accounting for the statistic and all systematic uncertainties in the the boosted regime [1].

the distributions. Table 7.2 shows the correlation matrices for the absolute cross-section as a function of $p_T^{t,had}$ and $y^{t,had}$ in the boosted topology. All the other matrices for relative spectra and distributions in resolved topology can be found in Appendix D.

7.2.1 Tests of the Method

The diagonal elements of the covariance matrix represent the RMS squared of the unfolded pseudo-experiments and can be considered as the uncertainties associated to each bin of the measured differential cross-section. The method used to derive these uncertainties is different from the one described in Chapter 6 that allows to quantify the individual contributions of each component, so some differences between the two estimates are expected. In particular, if the up and down shifts of a certain systematic are asymmetric the two methods are intrinsically inconsistent. The asymmetry in systematic shifts will reflect in an asymmetry on the uncertainty evaluated on the measured cross-section while the uncertainty obtained from the covariance diagonal is symmetric by definition. The asymmetry in the upward and downward shifts in the covariance have, on the other side, the effect of moving the mean of the pseudo-experiments with respect to the measured cross-section. Tables 7.3-7.6 present the comparison among the relative uncertainties obtained with the two methods on the relative and absolute spectra of the $p_T^{t,had}$ and $|y^{t,had}|$ in the boosted topology. The row *meas. error* represents the uncertainties obtained in Chapter 6, while the row *cov. error* is obtained as $\sqrt{COV(i,i)}/\mathrm{d}\sigma_i$, where i is the bin of the differential distributions.

In general the uncertainties calculated from the covariance diagonal are compatible with the uncertainties on the measured cross-sections, both for the absolute

cov. error	20.3	20.5	21.09	25	27.4	28.9	44.0	57.3
meas. error	$^{+20.5}_{-20.0}$	$^{+20.6}_{-19.9}$	$^{+19.6}_{-21.5}$	$^{+23.9}_{-23.6}$	$^{+27.8}_{-23.8}$	$^{+28.0}_{-26.4}$	± 38.1	$^{+51.8}_{-47.5}$

Table 7.3: Comparison between the error obtained in each bin of $\mathrm{d}\sigma/\mathrm{d}p_{Ti}$ and the error calculated from the covariance diagonal, in boosted topology.

cov. error	21.4	19.9	21.9	21.2	20.9	22.1	24.1	21.8	24.7	25
meas. error	$^{+22.3}_{-20.0}$	± 19.6	$^{+20.8}_{-21.8}$	$^{+21.0}_{-20.6}$	$^{+19.9}_{-20.8}$	$^{+22.5}_{-21.0}$	$^{+23.1}_{-22.2}$	$^{+22.4}_{-21.4}$	$^{+22.1}_{-25.3}$	$^{+25.6}_{-25.3}$

Table 7.4: Comparison between the error obtained in each bin of $\mathrm{d}\sigma/|y^t|$ and the error calculated from the covariance diagonal, in boosted topology.

cov. error	7.9	5.9	7.0	10.2	15.7	17.3	33.9	47.8
meas. error	$^{+7.15}_{-7.40}$	$^{+5.88}_{-5.76}$	$^{+5.97}_{-6.45}$	$^{+8.50}_{-8.75}$	$^{+15.3}_{-13.1}$	$^{+16.1}_{-15.7}$	$^{+26.6}_{-27.6}$	$^{+38.2}_{-37.7}$

Table 7.5: Comparison between the error obtained in each bin of $1/\sigma \cdot \mathrm{d}\sigma/\mathrm{d}p_{Ti}$ and the error calculated from the covariance diagonal, in boosted topology.

cov. error	5.5	5.6	7.1	5.9	7.5	6.4	10.9	9.04	11.2	12.3
meas. error	$^{+5.35}_{-4.62}$	$^{+5.37}_{-4.75}$	$^{+6.34}_{-6.94}$	$^{+5.59}_{-5.67}$	$^{+7.01}_{-7.56}$	$^{+6.00}_{-5.77}$	$^{+10.2}_{-10.1}$	$^{+8.69}_{-8.28}$	$^{+9.27}_{-10.3}$	$^{+11.5}_{-11.8}$

Table 7.6: Comparison between the error obtained in each bin of $1/\sigma \cdot \mathrm{d}\sigma/\mathrm{d}|y^t|$ and the error calculated from the covariance diagonal, in boosted topology.

and relative spectra, except in the some bins.
A further comparison between the two methods is performed considering just one systematic. This check is done to understand in more details the differences between the two approaches.
Saying U the unfolding operator, R_j the vector of reconstructed events, k a Gaussian random number and δ_j^{reco} the shift associated to a certain uncertainty source, the shifted cross-section (σ) in a certain bin i will be:

$$\sigma_i = U[R_j + k\delta_j^{reco}], \tag{7.6}$$

using the covariance method. Using the method described in Chapter 6, the same relation can be written as:

$$\sigma_i = \sigma_i^{nominal} + k\delta_j^{unfolded} \tag{7.7}$$

where $\sigma_i^{nominal} = U[R_j]$ and $\delta_j^{unfolded} = U[R_j + \delta_j^{reco}] - U[Rj]$. The two equations are the same only if:

$$k(U[R_j + \delta_j^{reco}] - U[R_j]) = U[k\delta_j^{reco}] \tag{7.8}$$

that represents the linearity condition for the operator U.
Since for the regularized unfolding the linearity is not granted, additional comparison on the two methods have been performed, including just few systematics. In

the tests only the $\mathrm{d}\sigma/\mathrm{d}p_T^{t,had}$ distribution in the boosted topology has been considered. The first sanity check, done to verify the implementation of the covariance method, is shown in Table 7.7. Here the *cov. error* has been evaluated from the covariance diagonal where only the Monte Carlo and data sample are considered as uncertainties, the *meas. error* represents the sum in quadrature of the corresponding uncertainties derived as explained in Chapter 6. In this case the two

cov. error	2.6	3.3	4.7	6.5	8.3	8.4	21.8	23.3
meas. error	2.6	3.5	5.0	6.8	8.8	8.4	21.4	23.9

Table 7.7: Comparison between the error obtained in bin of $\mathrm{d}\sigma/\mathrm{d}p_{Ti}$ and the error calculated from the covariance diagonal, considering only data statistics and Monte Carlo sample statistics

approaches bring consistent results in all bins, as expected, since also the statistical uncertainties reported in the tables are obtained using pseudo-experiments.
The same test has been repeated including an additional systematic uncertainties, in particular, the tracking component of the large-R jet JES, that represent the main uncertainty and is highly asymmetric, in Table 7.8, and the small systematic on the electron identification efficiency, in Table 7.9.
Tables 7.8 and 7.9 highlight the differences between the two methods also in cases

cov. error	10.11	12.9	15.8	20.0	23.5	23.2	38.5	49.7
meas. error	$^{+9.1}_{-10.6}$	$^{13.0}_{12.2}$	$^{13.7}_{16.0}$	$^{19.3}_{18.2}$	$^{24.1}_{20.5}$	$^{22.2}_{-21.8}$	$^{+32.1}_{-32.8}$	$^{+43.4}_{-38.1}$

Table 7.8: Comparison between the error obtained in bin of $\mathrm{d}\sigma/\mathrm{d}p_{Ti}$ and the error calculated from the covariance diagonal, considering only data statistics, Monte Carlo sample statistics and the tracking component of the large-R jet JES

cov. error	2.8	3.7	5.3	7.0	9.1	8.8	23.0	26.1
meas. error	2.7	3.5	5.0	6.9	8.8	8.5	21.5	24.9

Table 7.9: Comparison between the error obtained in bin of $\mathrm{d}\sigma/\mathrm{d}p_{Ti}$ and the error calculated from the covariance diagonal, considering only data statistics, Monte Carlo sample statistics and the uncertainty on electron identification efficiency

where only one systematic uncertainty is used.
Despite the intrinsic difference between the two approaches, enhanced in cases of asymmetry in the systematics, the two methods differ by a maximum of $\approx 15\%$ in the last two bins of the p_T^{had}. The advantage of the approach used to extract $COV^{det}(i,j)$ is that all the correlations introduced from the regularized unfolding are considered in the matrix, while the method described in Chapter 6 allows to compute each component of the total uncertainty, with the corresponding sign.

7.2.2 χ^2 results

The χ^2 results in the boosted topology, for absolute and relative spectra, are presented in Tables 7.10 and 7.11, while the resolved results are shown in Table 7.12 and 7.13.

Most predictions do not describe well all the distributions, as also witnessed by

	$p_{\mathrm{T}}^{t,\mathrm{had}}$		$\lvert y^{t,\mathrm{had}}\rvert$	
	χ^2/NDF	p-val	χ^2/NDF	p-val
Powheg+Pythia6	14.7/8	0.06	11.0/10	0.36
Powheg+Pythia6 (radHi)	19.5/8	0.01	12.3/10	0.27
Powheg+Pythia6 (radLo)	15.0/8	0.06	10.0/10	0.44
MadGraph5_aMC@NLO+Herwig++	17.9/8	0.02	12.8/10	0.24
Powheg+Herwig++	14.1/8	0.08	8.0/10	0.63
MadGraph5_aMC@NLO+Pythia8	12.8/8	0.12	20.4/10	0.03
Powheg+Pythia8	16.7/8	0.03	18.4/10	0.05
Powheg+Herwig7	11.9/8	0.15	11.7/10	0.30

Table 7.10: Comparison between the measured fiducial phase-space absolute differential cross-sections and the predictions from several MC generators in the boosted topology in terms of a χ^2/NDF and relative p-values.

	$p_{\mathrm{T}}^{t,\mathrm{had}}$		$\lvert y^{t,\mathrm{had}}\rvert$	
	χ^2/NDF	p-val	χ^2/NDF	p-val
Powheg+Pythia6	10.2/7	0.18	2.9/9	0.97
Powheg+Pythia6 (radHi)	11.3/7	0.12	2.9/9	0.97
Powheg+Pythia6 (radLo)	11.5/7	0.12	2.8/9	0.97
MadGraph5_aMC@NLO+Herwig++	11.1/7	0.13	4.6/9	0.87
Powheg+Herwig++	10.7/7	0.15	2.5/9	0.98
MadGraph5_aMC@NLO+Pythia8	10.9/7	0.14	7.2/9	0.62
Powheg+Pythia8	11.3/7	0.13	4.3/9	0.89
Powheg+Herwig7	9.9/7	0.20	3.6/9	0.94

Table 7.11: Comparison between the measured fiducial phase-space relative differential cross-sections and the predictions from several MC generators in the boosted topology in terms of a χ^2/NDF and relative p-values.

Figures 7.1-7.3.

In general, in boosted topology the absolute spectra show smaller p-values with respect to the relative ones, indicating a difference also in the normalization and not only on the shape of the distributions.

The larger tensions between data and most predictions are observed in the differential cross-sections as a function of the hadronic top quark transverse momentum, in both topologies and for both absolute and relative spectra (Figures 7.1a, 7.1c, 7.2a, 7.3a). For these distributions the Powheg+Herwig 7 generator gives the best χ^2 value and highest p-value.

The differential cross-sections as a function of $|y^{t,had}|$(Figures 7.1d and 7.3b) show a good agreement for all the generators for both the topologies.

As shown in Figures 7.2c and 7.3c, all the predictions agree reasonably well with the measured differential cross-section as a function of $m^{t\bar{t}}$, except for the two HERWIG ++ ones.
The χ^2 values for the $p_T^{t\bar{t}}$ spectrum show, for the case of the absolute differential cross-sections, that none of the predictions agree well with the data, while for the case of the relative differential cross-sections only the POWHEG+PYTHIA 6 with lower radiations and POWHEG+HERWIG ++ predictions disagree with the data. In Figure 7.3e is shown that, in the relative spectrum, the data at high values of $|y^{t\bar{t}}|$ may not be adequately described by many of the generators considered. The POWHEG+HERWIG ++ prediction gives the worst χ^2 value for this observable.
Overall, it can be seen that in the resolved regime POWHEG+HERWIG ++ prediction disagrees the most with data, having a p -value of ≈ 0.01 for four of the five observables studied, while the POWHEG+HERWIG 7 prediction agrees adequately with the data for all five observables.

	$p_{\mathrm{T}}^{t,\mathrm{had}}$		$\lvert y^{t,\mathrm{had}}\rvert$		$m^{t\bar{t}}$		$p_{\mathrm{T}}^{t\bar{t}}$		$\lvert y^{t\bar{t}}\rvert$	
	χ^2/NDF	p-val	χ^2/NDF	p-val	χ^2/NDF	p-val	χ^2/NDF	p-val	χ^2/NDF	p-val
Powheg+Pythia6	19.0/15	0.22	7.8/18	0.98	9.8/11	0.55	14.9/6	0.02	20.0/18	0.33
Powheg+Pythia6 (radHi)	20.9/15	0.14	8.5/18	0.97	8.7/11	0.65	56.1/6	<0.01	17.3/18	0.51
Powheg+Pythia6 (radLo)	20.8/15	0.14	7.4/18	0.99	12.7/11	0.32	22.1/6	<0.01	25.5/18	0.11
MadGraph5_aMC@NLO+Herwig++	23.5/15	0.07	10.7/18	0.91	32.4/11	<0.01	16.4/6	0.01	28.1/18	0.06
Powheg+Herwig++	30.3/15	0.01	7.9/18	0.98	34.8/11	<0.01	28.0/6	<0.01	30.4/18	0.03
MadGraph5_aMC@NLO+Pythia8	19.1/15	0.21	8.4/18	0.97	7.6/11	0.75	19.0/6	<0.01	16.1/18	0.59
Powheg+Pythia8	18.4/15	0.24	10.5/18	0.92	7.7/11	0.74	11.7/6	0.07	12.3/18	0.83
Powheg+Herwig7	13.8/15	0.54	10.9/18	0.90	7.0/11	0.80	11.6/6	0.07	12.8/18	0.80

Table 7.12: Comparison between the measured fiducial phase-space absolute differential cross-sections and the predictions from several MC generators in the resolved topology in terms of a χ^2/NDF and relative p-values [1].

Observable	$p_{\mathrm{T}}^{t,\mathrm{had}}$		$\lvert y^{t,\mathrm{had}}\rvert$		$m^{t\bar{t}}$		$p_{\mathrm{T}}^{t\bar{t}}$		$\lvert y^{t\bar{t}}\rvert$	
	χ^2/NDF	p-val	χ^2/NDF	p-val	χ^2/NDF	p-val	χ^2/NDF	p-val	χ^2/NDF	p-val
Powheg+Pythia6	23.0/14	0.06	8.1/17	0.96	6.3/10	0.79	7.7/5	0.17	22.5/17	0.17
Powheg+Pythia6 (radHi)	23.8/14	0.05	8.5/17	0.95	7.7/10	0.66	5.1/5	0.41	19.3/17	0.31
Powheg+Pythia6 (radLo)	25.9/14	0.03	7.5/17	0.98	8.2/10	0.61	20.4/5	<0.01	28.0/17	0.04
MadGraph5_aMC@NLO+Herwig++	24.4/14	0.04	10.8/17	0.87	23.6/10	<0.01	2.6/5	0.76	30.0/17	0.03
Powheg+Herwig++	24.0/14	0.05	7.4/17	0.98	37.9/10	<0.01	25.0/5	<0.01	32.8/17	0.01
MadGraph5_aMC@NLO+Pythia8	21.8/14	0.08	7.8/17	0.97	6.8/10	0.75	3.3/5	0.66	18.0/17	0.39
Powheg+Pythia8	21.5/14	0.09	9.6/17	0.92	6.5/10	0.77	1.1/5	0.96	14.0/17	0.67
Powheg+Herwig7	15.4/14	0.35	9.3/17	0.93	6.7/10	0.76	5.4/5	0.37	15.1/17	0.59

Table 7.13: Comparison between the measured fiducial phase-space absolute differential cross-sections and the predictions from several MC generators in the resolved topology in terms of a χ^2/NDF and relative p-values [1].

7.3 Compatibility Between the Results.

The fiducial phase-space selected in boosted and resolved regimes are different, as shown in Table 7.14 [1], where the inclusive cross-section measured in the two fiducial regions, including statistical and systematic uncertainties, are reported and compared with several predictions. The boosted analysis investigates a small fraction of the full phase-space and represents just a 2% of the resolved fiducial region.

Sample	Fiducial cross-section [pb]	
	Resolved	Boosted
POWHEG+PYTHIA6	92.0	2.96
POWHEG+PYTHIA radHi	90.9	3.10
POWHEG+PYTHIA radLo	94.2	2.89
aMC@NLO+HERWIG++	94.9	3.19
POWHEG+HERWIG++	93.5	2.84
POWHEG+PYTHIA8	97.5	3.07
POWHEG+HERWIG7	97.2	2.84
aMC@NLO+PYTHIA8	98.5	2.88
Data	110^{+13}_{-14} (stat+syst)	2.54 ± 0.54 (stat+syst)

Table 7.14: Fiducial cross-sections in the resolved and boosted topologies for data and different models. Each model's cross-section is scaled to the NNLO+NNLL value from Refs. [139, 140, 141, 142, 143, 144].

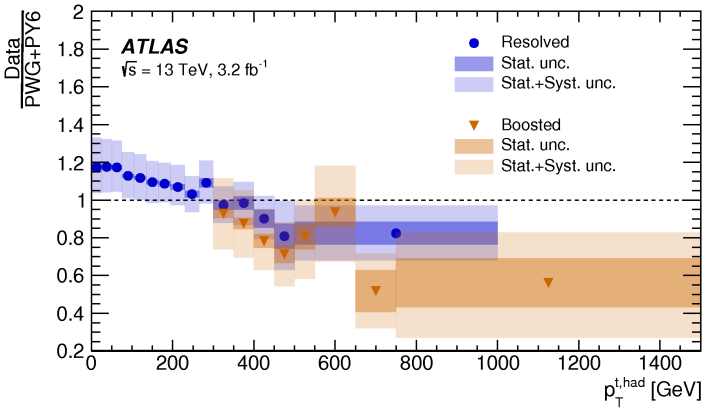

Figure 7.5: Ratio between measured cross-section and POWHEG+PYTHIA 6 prediction, as a function of $p_T^{t,had}$ for the resolved (blue) and the boosted (orange) topologies. The bands represent the sum of systematic and statistical uncertainties [1].

Also in the overlap region of $p_T^{t,had}$ a direct comparison between the two topologies is impossible, since the definition of hadronic top at particle level is different

Resolved particle-level $p_T^{t,had}$ [GeV]	σ in resolved fiducial phase-space [pb]
0–25	$3.37 \pm 0.07 \pm 0.44$
25–50	$9.77 \pm 0.11 \pm 1.22$
50–75	$14.51 \pm 0.14 \pm 1.73$
75–105	$19.26 \pm 0.15 \pm 2.17$
105–135	$17.21 \pm 0.15 \pm 1.88$
135–165	$12.34 \pm 0.12 \pm 1.28$
165–195	$8.40 \pm 0.10 \pm 0.81$
195–230	$6.42 \pm 0.09 \pm 0.65$
230–265	$3.95 \pm 0.07 \pm 0.37$
265–300	$2.69 \pm 0.06 \pm 0.28$
300–350	$2.04 \pm 0.05 \pm 0.21$
350–400	$1.11 \pm 0.04 \pm 0.13$
400–450	$0.55 \pm 0.03 \pm 0.07$
450–500	$0.26 \pm 0.02 \pm 0.06$
500–1000	$0.36 \pm 0.03 \pm 0.07$
Boosted particle-level $p_T^{t,had}$ [GeV]	σ in boosted fiducial phase-space [pb]
300–350	$0.95 \pm 0.02 \pm 0.19$
350–400	$0.61 \pm 0.02 \pm 0.12$
400–450	$0.35 \pm 0.02 \pm 0.07$
450–500	$0.20 \pm 0.01 \pm 0.05$
500–550	$0.14 \pm 0.01 \pm 0.04$
550–650	$0.17 \pm 0.01 \pm 0.05$
650–750	$0.042 \pm 0.009 \pm 0.016$
750–1500	$0.043 \pm 0.010 \pm 0.023$

Table 7.15: Unfolded fiducial phase-space differential cross-section values in bins of $p_T^{t,had}$ for *resolved* (top) and *boosted* (bottom) topologies. The first uncertainty is statistical and the second one is systematic.

and consequently the measured cross-section, as shown in Table 7.15 [1]. However, it can be seen in Figure 7.5 that the ratio of data to prediction is consistent between the two topologies in the overlap region, despite the different definition of the hadronic top candidate. The trend present in Figure 7.5 explains also the difference between the overall data over prediction normalization, that is visible in Table 7.14. Here all the predictions underestimate the resolved cross-section but overestimate the boosted one.

7.4 Rivet Routine

The Rivet toolkit (Robust Independent Validation of Experiment and Theory) [145] is a framework, independent from a specific collaboration, that collects a large number of the particle level analyses, implementing event selection requirements and reconstruction consistent to the ones used in the published results. It is mainly used for validation, development and tuning of Monte Carlo event generators. Rivet allows to preserve analysis code from the LHC and other high-energy colliders for the comparison of the experimental results with BSM theory models, and can be used by phenomenologists to reiterpret the SM measurements with alternative BSM theories (see for example Appendix A). For this reason is important for all particle level analyses to implement a Rivet routine that is added to the database of the analyses after the publication, and can be used for tuning and reinterpretations. The analyses implemented as Rivet routines are only particle level measurements because the smearing of the kinematic observables, due to the detector effects, is not included in the framework, that is designed to handle comparison with measurements corrected at the particle level.
A rivet routine for the $t\bar{t}$ differential cross-section measurement has been developed and validated, by comparing the nominal MC predictions after unfolding with the results obtained using the routine. The validation for all the unfolded variables is shown in Figure 7.6 for the boosted topology, and in Figure 7.7 for the resolved ones.

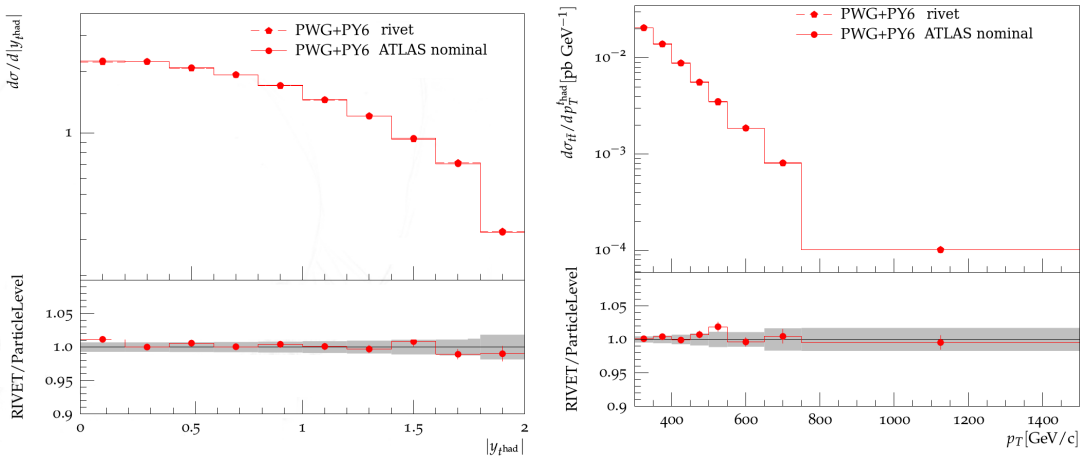

(a)

Figure 7.6: Comparison between the nominal ATLAS particle level POWHEG+PYTHIA MC (dots) and the RIVET predictions (pentagon) for all measured absolute cross-section distributions in the boosted topology. The uncertainty band includes statistical uncertainties of the nominal ATLAS POWHEG+PYTHIA MC.

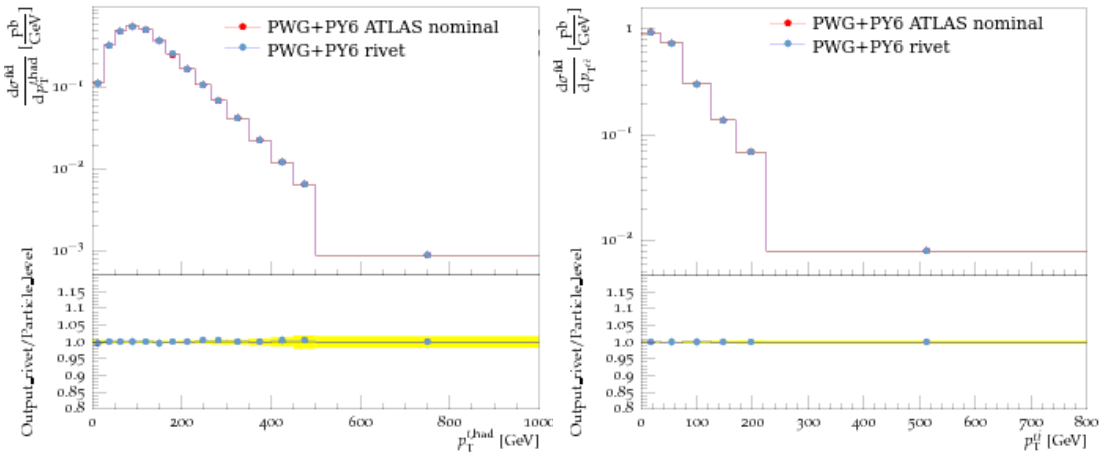

(a)

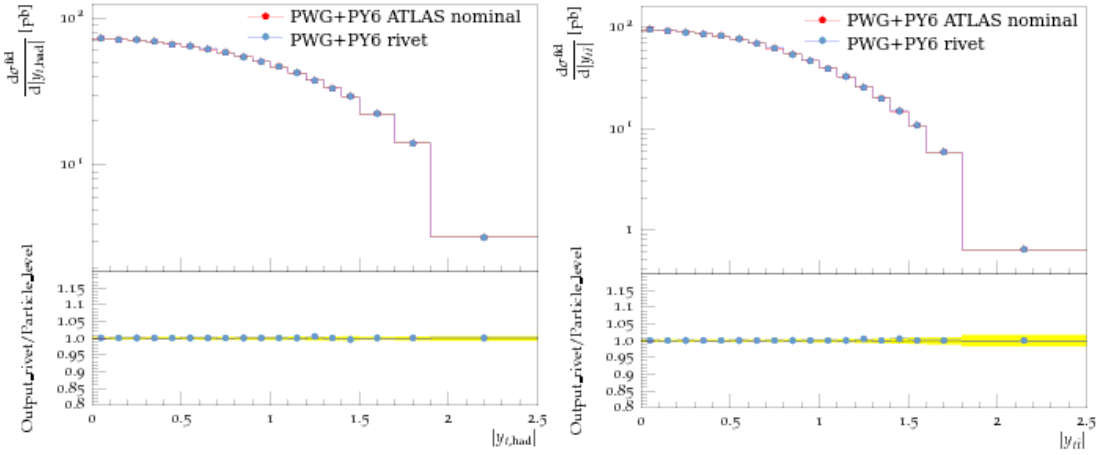

(b) (c)

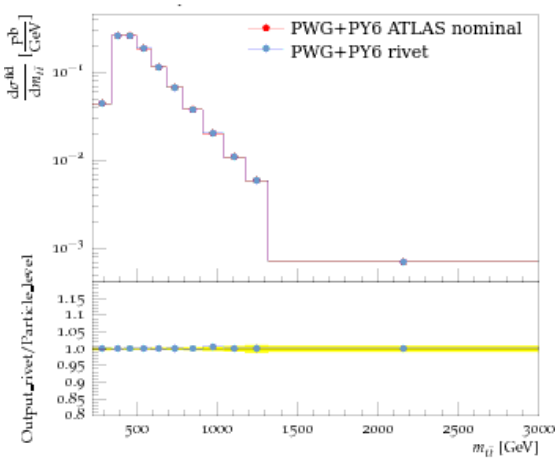

(d)

Figure 7.7: Comparison between the nominal ATLAS particle level POWHEG+PYTHIA MC (red) and the RIVET predictions (blue) for all measured absolute cross-section distributions in the resolved topology. The uncertainty band includes statistical uncertainties of the nominal ATLAS POWHEG+PYTHIA MC.

Chapter 8

Prospective Developments for the Boosted Analysis

The increasing integrated luminosity collected by the ATLAS experiment during the full Run2 data taking will allow to largely reduce the statistical uncertainty also in the studies of highly-boosted massive objects, for which statistical uncertainties at the end of Run1 are still among the dominant uncertainties. However, the uncertainties in the boosted topology, as shown in Figure 6.6, are dominated by systematic sources, in particular by the large-R jet JES. Therefore, an improvement in the statistical uncertainty, is not sufficient to increase the sensitivity of the measurement without a reduction on the systematic one. Improvements in the reconstruction and calibrations of the large-R jets could reduce the JES uncertainties, in particular the in situ calibration of the large-R jets would reduce sizably the JES uncertainty [146].
An approach to derive these calibrations for the 1.0 anti-kt jets is the jet reclustering [147], that allows to directly apply the small-R jet calibrations and uncertainties to the large-R jets.
The larger sensitivity in the *boosted* topology, reached increasing the statistics collected in this phase space region and reducing the systematic uncertainties, makes the measurement of a large number of variables, including $t\bar{t}$ distributions, more important. In particular, the larger sample size allows to increase the number of bins of the distributions and measure for the first time the double differential spectra in the *boosted* regime.
In this chapter an overview of the improvements foreseen for future analyses in *boosted* topology is given.

8.1 Jet Reclustering

The boosted hadronic top is reconstructed, using 1.0 anti-kt jets, obtained clustering calorimeter topo-clusters as described in Chapter 4. An alternative approach, already presented in previous studies [147, 148, 149] but never applied in cross-section measurements, is to use the calibrated small-R jets (R=0.4) as input to the

anti-kt algorithm with R=1.0. This method allows to propagate the well known calibrations and uncertainties derived for small-R jets to reclustered jets (RC).
A recent ATLAS study [150] shows that the calibrations derived with this approach have similar performances to the standard large-R jet calibrations, but the JES uncertainties obtained are smaller and in particular no additional uncertainties are needed specifically for the dense radiation environment present in the *boosted* topology. The calibrations and uncertainties applied to the small-R jets are based on analyses of well-understood, isolated systems of dijet, multijet, γ+jet and Z+jet systems. As these topologies do not contain large amounts of additional hadronic activity near the selected jets, it is necessary to check that calibrations and uncertainties derived using these systems still hold as the amount of radiation near a jet increases. Examples of these studies are shown in Figure 8.1. The effect of a dense environment on the small-R jets calibrations is investigated, in particular the variable f_{Closeby} defines the amount of activity surrounding a probe jet (ref):

$$f_{\text{Closeby}} = \sum_j \frac{\vec{p_j} \cdot \vec{p}_{\text{ref}}}{|\vec{p}_{ref}|^2}, \tag{8.1}$$

where p represents the jet momentum and j indicates all jets with $p_T > 20$ GeV in a radius 1.0 from the reference. A systematic mismodelling of jet kinematics due to large nearby activity could manifest in a dependence of the jet reconstruction performance on f_{Closeby}. The triple ratio $R^{p_T}_{triple}$ is introduced to estimate this effect. $R^{p_T}_{triple}$ compares the ratio between jet p_T measured using tracks (trk) and calorimeter(calo), in MC simulation and data, in different f_{Closeby} regimes:

$$R^{p_T}_{\text{triple}} = \frac{(\{\frac{p_T^{\text{calo}}}{p_T^{\text{trk}}}\}_{f^{low}_{\text{Closeby}}} / \{\frac{p_T^{\text{calo}}}{p_T^{\text{trk}}}\}_{f^{high}_{\text{Closeby}}})_{DATA}}{(\{\frac{p_T^{\text{calo}}}{p_T^{\text{trk}}}\}_{f^{low}_{\text{Closeby}}} / \{\frac{p_T^{\text{calo}}}{p_T^{\text{trk}}}\}_{f^{high}_{\text{Closeby}}})_{MC}} \tag{8.2}$$

where f^{low}_{Closeby} and $f^{high}_{\text{Closeby}}$ are defined as the intervals above and below the median f_{Closeby}, obtained from data in a given slice of p_T and m/p_T. If the dense environment does not introduce any systematic effect on the jet reconstruction $R^{p_T}_{triple}$ is compatible with one, as shown in Figure 8.1, and the calibration derived on isolated systems remain valid also in the *boosted* topology, so no additional uncertainties are needed.

One of the differences between re-clustered jets (RC) and standard large-R jets (LJ) is the technique adopted to remove pile-up components. The technique applied for the large-R jets is the trimming [116], described in Section 4.1.5, the RC relies mainly on the technique and cuts applied to remove the pile-up contribution in the calibration of the small-R jets. A trimming technique is applied also to RC after the jet formation, with the aim to remove soft small-R jets that could be originated entirely from pile-up.
The different techniques used in the formation of LJ and RC reflect in a completely different substructure between the two type of jets. The number of constituents of the RC, in particular, is not usually sufficient to define the substructure variables used to top-tag the large-R jets, as shown in Figure 8.2. Here the number of

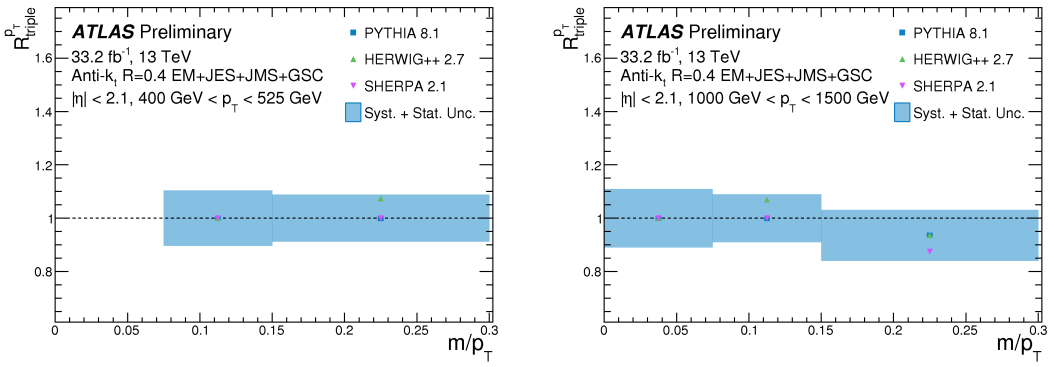

(a) (b)

Figure 8.1: The $R^{p_T}_{\text{triple}}$ (8.2) values of anti-kt R=0.4 probe jets, as a function of m/p_T. Statistical uncertainties and systematic uncertainties related to the JES, JER and JMS uncertainties are shown as a blue band. In (a) only events with jet 400 GeV $< p_T <$ 525 GeV are considered while in (b) only 1000 GeV $< p_T <$ 1500 GeV ones [150].

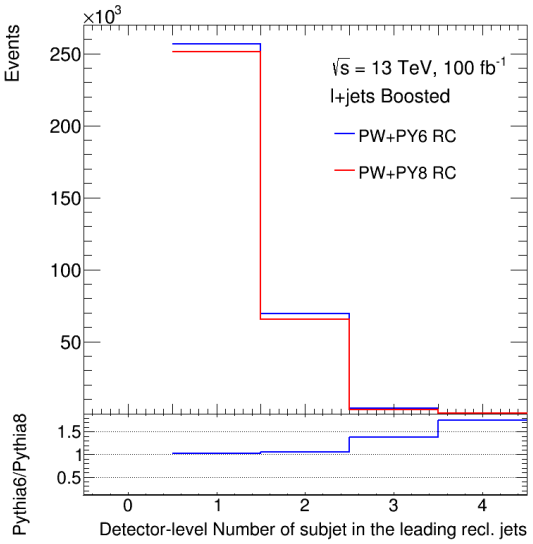

Figure 8.2: Number of constituents of RC jets. The distributions are obtained using the $t\bar{t}$ simulation of POWHEG+PYTHIA 6 and 8 and normalized to 100 $fb^{\cdot 1}$, corresponding to the statistic that is expected to be collected at the end of Run2 by the ATLAS experiment.

re-clustered jets is shown as a function of the number of constituents. The larger part of the re-clustered jets has one or two sub-jets, that can't be used to define many substructure variables, as for example τ_{32}. The substructure variable splitting scale [1], however, is defined at the last step before the large-R jet formation

[1]The first step to define the splitting scale is to apply a k_T re-clustering to the jet constituents, until exactly 2 sub-jet are formed, then it is defined from the two sub-jets as

and only 2 sub-jets are considered in its definition. This variable, consequently, could be evaluated also for the re-clustered jet with at least 2 sub-jets, but the comparison between RC and LJ $\sqrt{d_{12}}$ distribution, shown in Figure 8.3, shows that also for this variable the shape differs between the two jet collections. The re-clustered jets distribution has a large peak at 0, corresponding to jets with only one constituent.
Since the strategy adopted to reconstruct the two types of jets is different, and

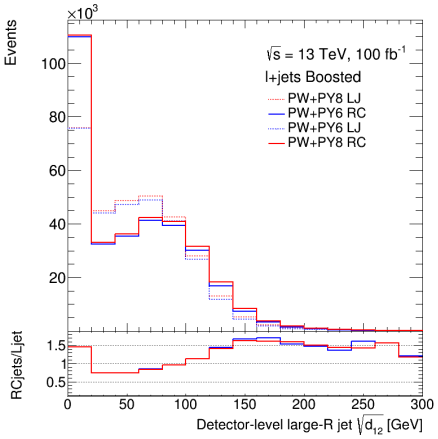

Figure 8.3: Number of re-clustered jets (RC) and standard 1.0 large-R jets (LJ), as a function of $\sqrt{d_{12}}$. The peak at zero for RC indicates the jets with less than 2 constituents.

consequently also the jet properties and substructure, a comparison between the kinematic distributions is necessary before using the RC in a measurement.

8.1.1 Large-R Jet and Re-clustered Jet Comparison

In this section a comparison between standard large-R jets (LJ) and re-clustered jets (RC) is performed on two aspects: kinematic distributions and response. The comparison is done using two $t\bar{t}$ MC samples, POWHEG+PYTHIA 6 and 8, and based on the expected full Run2 data set, with an integrated luminosity of 100 fb^{-1}.
The samples used for the study passed the pre-selection requirements, summarized in Table 8.1. The LJ are calibrated using combined mass, that is a combination of calorimetric and track-based measurement of the jet mass, that improves the mass resolution on the full LJ p_T spectrum with respect to only calorimetric measurement. The RC jets are built starting from calibrated small-R jets, where also the mass is calibrated.
Both LJ and RC are trimmed using two different approaches:

$\sqrt{d_{12}} = \sqrt{\min(p_{T1}, p_{T2}) \cdot \Delta R(1,2)}$.

Preselection
Only one lepton(μ or e) $p_T > 27$ GeV
$E_T^{\text{miss}} > 20$ GeV
$m_T^W > 60$ GeV
At least one RC or LJ $p_T > 350$ GeV
At least two small-R jet, $p_T > 25$ GeV

Table 8.1: Preselection applied to all the events considered in the comparison

- after the formation of an LJ all the constituents of the jet are re-clustered using the kt algorithm with radius parameter equal to 0.2, then all the sub-jets with a fraction of large-R jet p_T below 0.05 are removed from the LJ;
- after the formation of an RC all the small-R jets with a fraction of jet p_T below 0.05 are removed from the RC.

In Figure 8.4 the comparison between LJ and RC jets, as a function of m^{jet}, p_T^{jet}, η^{jet} and ϕ^{jet}, is shown. Only jets with $p_T > 350$ GeV are considered for the study. The p_T, η and ϕ distributions of LJ and RC are very similar, as shown in figure Figures 8.4 (a),(b),(d). The m^{jet} shows, instead, a difference among the LJ and the RC: the RC distribution is more peaked around the top mass of ~ 173 GeV.
An additional comparison between LJ and RC is shown on response with respect to the *parton* level hadronic top, defined here at the stage where the top quark is going to decay in Wb, after all the radiations emission.
For a given kinematic variable X the jet the definition of response is:

$$Response = \frac{X^{jet}}{X^{t,had}} \tag{8.3}$$

Figure 8.5 shows the responses with respect to $m^{t,had}$ and $p_T^{t,had}$ for the RC and LJ that passed the pre-selection and including only jets with $p_T > 350$ GeV. Only jets matched in a $\Delta R(jet, t^{had}) < 0.75$ to the hadronic top are considered. Using both the RC and LJ the hadronic top p_T is correctly reconstructed at detector level for a large part of the events, while some tails are present in mass response for both the reconstruction techniques. The response on $m^{t,had}$ seems more peaked at one for RC jets.
The capability of the RC to properly reconstruct the mass of the hadronic top suggests that an efficient way to top tag the jets is simply by using a mass window cut on the jets.
To verify the effect of this simple tagger, the kinematic distributions of the RC and LC, both top-tagged, are compared in Figure 8.6. The top-tagging approaches employed are:

- LJ top-tagging: variable cuts on m and τ_{32}, optimized to keep tagging efficiency constant to 80%;

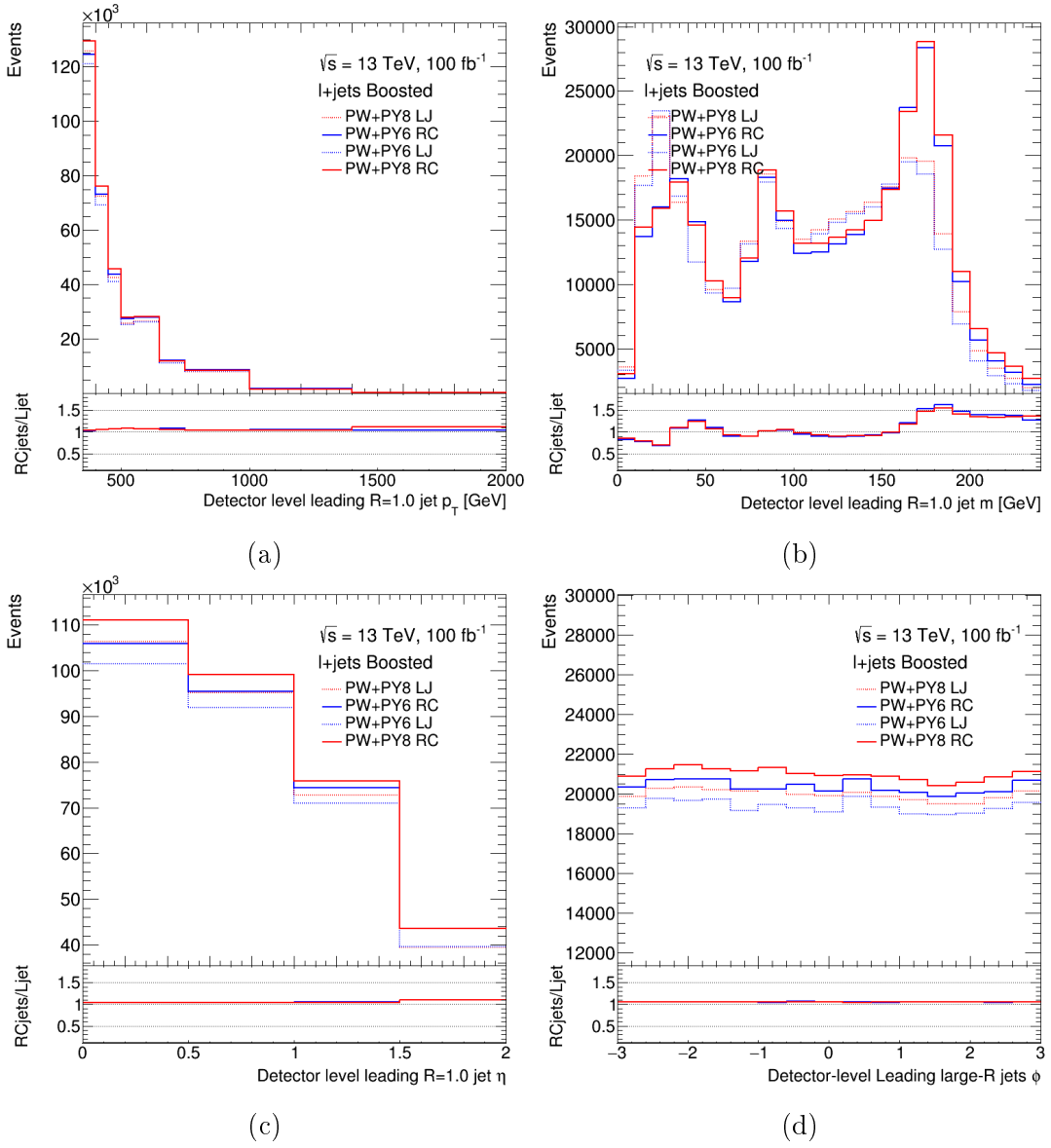

Figure 8.4: Comparison of LJ and RC kinematic distributions, (a) p_T^{jet}, (b) m^{jet}, (c) η^{jet} and (d) ϕ^{jet}. Only events passing the pre-selection in Table 8.1 are considered, and only jets with $p_T > 350$ GeV.

- RC top-tagging: mass window cut 120 GeV $< m^{jet} <$ 220 GeV.

The number of jets selected from the LJ tagger is higher with respect to the ones selected from the mass window cut, consequently the normalization of RC and LJ sample is different. All the kinematic distributions, however, continue to agree in shape between RC and LJ, the only exceptions are the jet mass, that is still more peaked for the RC distribution, and the high p_T tail, where some events are lost for the RC.
A further motivation to define a RC jet top tagger based on mass is in the mass resolution, that appears to be better for the RC jets with respect to the LJ, as shown

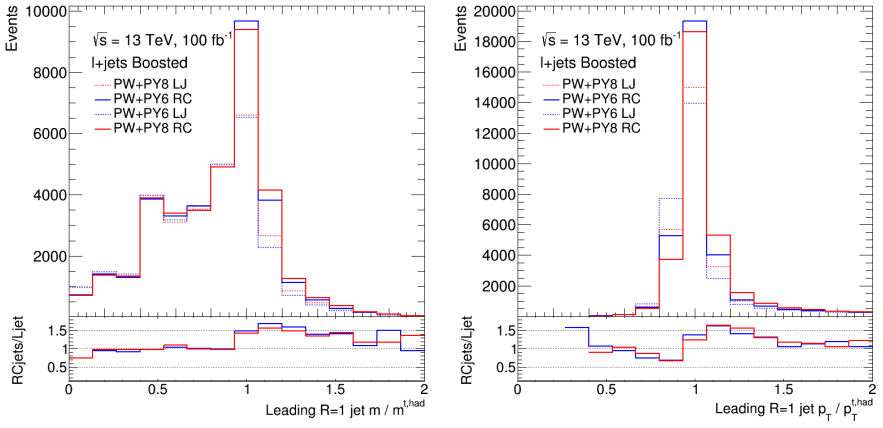

(a) (b)

Figure 8.5: Comparison between RC and LJ response with the hadronic top m (a) and p_T (b), considering only jets in a $\Delta R < 0.75$ from the hadronic top. Only events passing the pre-selection in Table 8.1 are considered, and only jets with $p_T > 350$ GeV.

in Figure 8.7. Here the resolution is obtained as the RMS of the distributions of the difference between reconstructed and particle level jets, both top-tagged, in bins of particle level m^{jet}. The re-clustered particle level jets are obtained with the anti-kt algorithm, with R=1.0, applied on collection of the truth small-R jets, and then using the same trimming procedure employed at detector level. The top-tagging approach for the RC jets is completely consistent between particle and detector levels.

8.1.2 Re-clustering in Differential Measurements

The kinematic distributions of the re-clustered jets have been shown to be similar to the distributions of the standard large-R jets, and in principle they can be used to measure differential cross-sections in the boosted regime, but it should be observed whether this reconstruction technique produces a reduction of the systematic uncertainties on the measurements. This study is performed by applying the same selection described in Section 4.2 on the re-clustered and standard large-R jets. The comparison of the efficiency of each requirement applied on the $t\bar{t}$ signal sample using re-clustering and standard large-R jets reconstruction is shown in Table 8.2. The top tagging efficiency is lower in the re-clustered jets case but the difference is recovered in the cut on the $\Delta\phi(\ell$, R=1.0 jet) and the final difference on the size of the selected signal sample is 1%.
To test the effect of the re-clustering also on topology different from $t\bar{t}$ and test the data/MC agreement and purity reached with the two reconstruction approaches, the two selections are applied on data collected by ATLAS in 2016 and 2015 and on the various MC background samples. Table 8.3 shows the yields of the selected sample components, using the re-clustering technique the purity of the signal seems

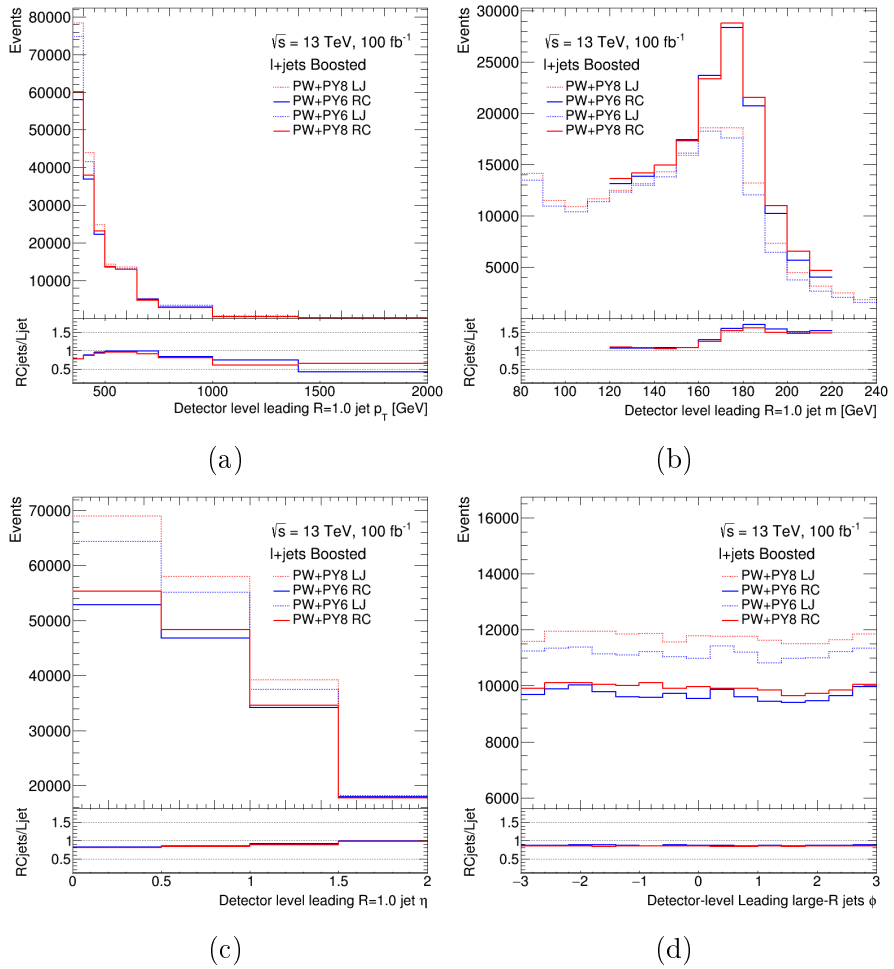

Figure 8.6: Comparison of LJ and RC kinematic distributions, only the top-tagged jets are retained in the distributions.

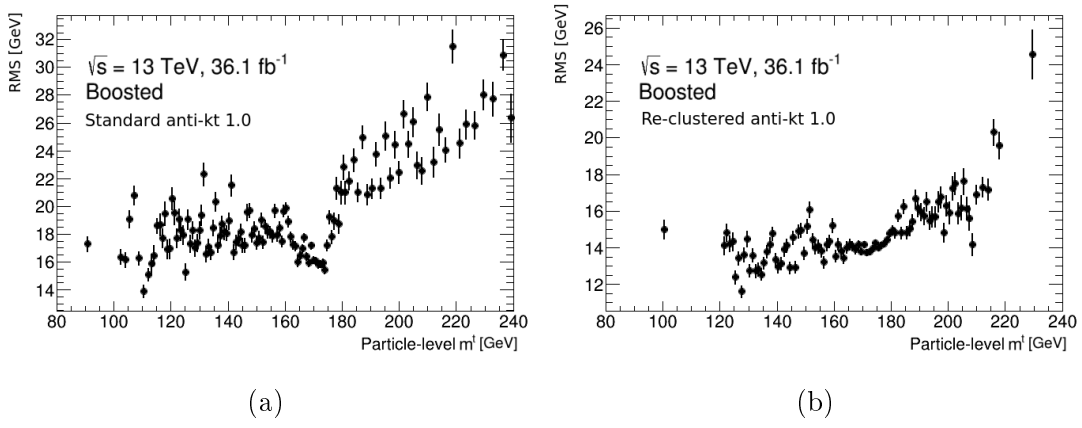

Figure 8.7: Resolution obtained comparing top tagged LJ (a) and RC (b) jets with the corresponding particle level jets.

Requirement	Efficiency, RC	Efficiency, LJ
Single lepton (27 GeV) E_T^{miss} >20 GeV, $m_T^W > 60$GeV		
Leading-p_{T} R=1.0 jet $\lvert\eta\rvert < 2.0$ $p_T > 350$ GeV	8%	8%
R=1.0 jet top tagged	47%	63%
$\Delta\phi(\ell$, R=1.0 jet$) > 1.0$	92%	74%
ΔR(R=1.0 jet, small-R jet associated with lepton) > 1.5 ΔR(lep, small-R jet associated with lepton) < 2.0	91%	92%
Small-R jet associated with lepton b-tagged (WP 70%) or R=1.0 jet b-tagged	91%	90%

Table 8.2: Comparison on the efficiency of the requirements applied in the analysis using the re-clustered jets, in the second column, and the standard large-R jets, in the third one. The top tagging approaches followed in the two cases are described in Section 8.1.1. The b-tagging of the re-clustered jet is fulfilled if one of its small-R jets constituent is b-tagged. The standard large-R jet is considered b-tagged if it matches in a $\Delta R < 1.0$ with a b-tagged small-R jet.

slightly better, as well the agreement between data and MC predictions.

The selected samples are used to derive the distributions shown in Figure 8.8, where the number of events is presented as a function of the $p^{t,had}$. Here the plot on the right contains events reconstructed and selected using the re-clustering, while the one on the left is obtained using standard large-R jet reconstruction. The ratio pad show that the agreement between MC and data improves using the re-clustering approach, and at the same time the uncertainties are smaller by approximately 50% along the full spectra, except in the last bin of the distribution, where the statistical component is dominant. The motivation is shown in Figure 8.9, where the uncertainties due only to the large-R jet JES are compared, on the $t\bar{t}$ sample, using the standard large-R jets and the re-clustering approach. Here is visible that the re-clustering reduces this uncertainty by $\approx 50\%$, thanks to the use of the well calibrated small-R jets.

The different approach used at the detector level to reconstruct the R=1.0 anti-kt jets is also implemented at the particle level, in order to follow the detector level selection as closely as possible. Since the re-clustering has never been used in a particle level measurement it is important to verify that the migrations between

Sample	RC selection	LJ selection
$t\bar{t}$	46823	48446
Single top	2213	3126
W+jets	3758	4945
Z+jets	611	707
$t\bar{t}V$	464	573
Diboson	257	417
Total prediction	54126	58214
Data	50757	50142
Data/Total Predictions	0.94	0.86
S/(S+B)	0.87	0.83

Table 8.3: Yield obtained applying the selection described in Section 4.2, with the changes reported in Table 8.2, on the $t\bar{t}$ signal and all background sources estimated using MC and the data sample corresponding to an integrated luminosity of 36.1 fb^{-1}, collected by ATLAS in 2015 and 2016. The standard large-R jets are used in the third column, while in the second one the re-clustering is employed.

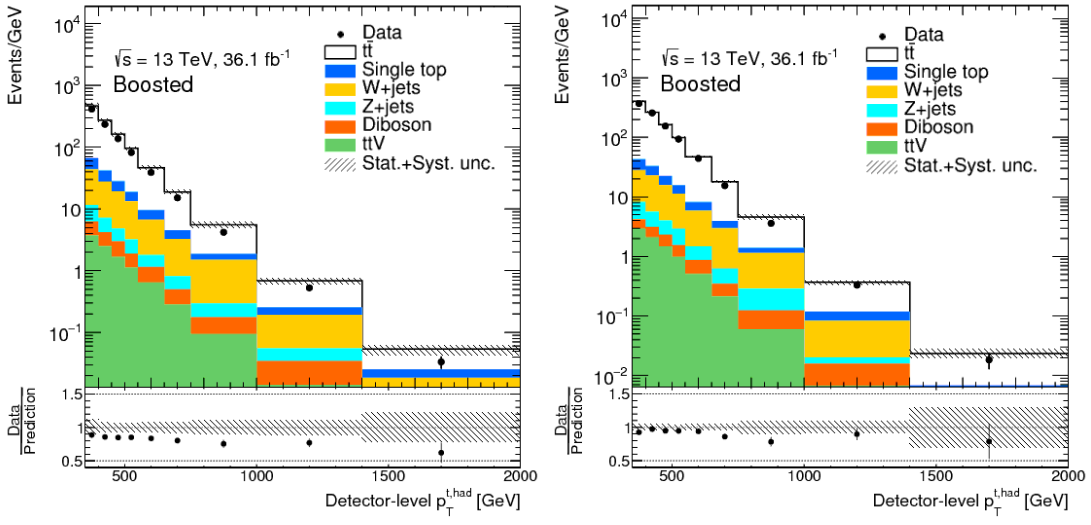

(a) (b)

Figure 8.8: Kinematic distributions of $p_T^{t,had}$ at the detector level. The hatched area indicates all detector level systematic uncertainties on the total prediction, excluding systematic uncertainties related to the modelling of the $t\bar{t}$ system. In (a) the standard large-R jets are used, while in (b) the R=1.0 anti-kt jets are reconstructed using the re-clustering.

the detector and particle level are at least comparable with the migrations obtained using the standard reconstruction. This is shown in Figure 8.10, where the migration matrices obtained with the standard large-R jet reconstruction, on the left, are compared with the one obtained using the re-clustering, right.

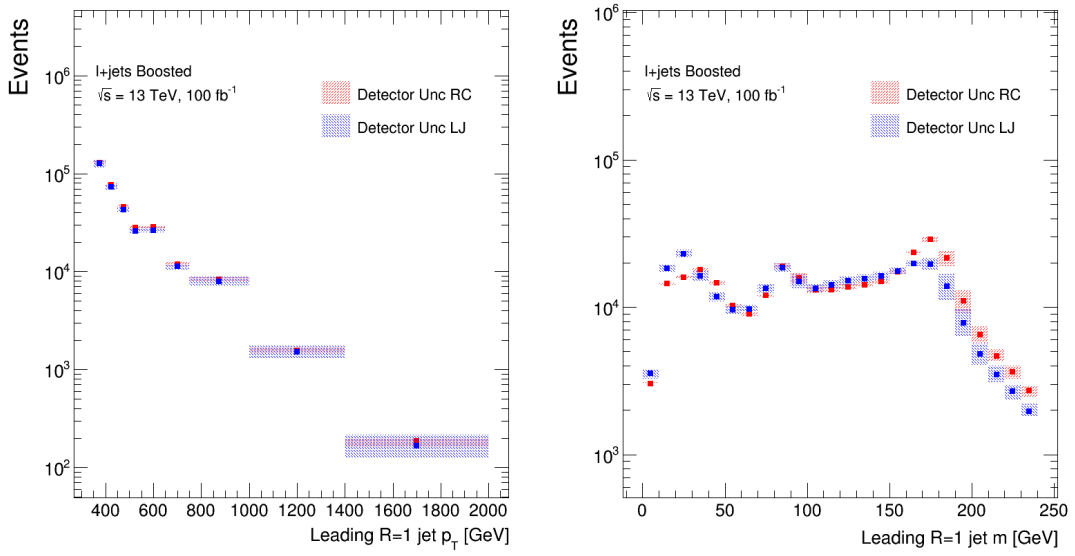

(a) (b)

Figure 8.9: Comparison of the large-R jet JES uncertainties, between two alternative approaches to reconstruct the 1.0 anti-kt jets, the standard (blue) and the re-clustering (red). The sample used is the $t\bar{t}$ POWHEG+PYTHIA 8 simulation, normalized to a luminosity of 100 fb^{-1}. In (a) the events are represented as a function of large-R jet p_T, while in (b) with respect to the large-R jet m.

In conclusion, the use of the re-clustering approach in *boosted* topology for differential measurements highly reduces one of the dominant uncertainties, improves the resolution on the large-R jet masses, and keeps the migrations to particle level compatible with the standard approach. For this reason the re-clustering is the approach selected for the future measurement of the $t\bar{t}$ differential cross-section in the boosted topology in the l+jet channel, that will exploit the full data sample collected by the ATLAS experiment in 2015 and 2016, corresponding to an integrated luminosity of 36.1 fb^{-1}

8.2 Additional Kinematic Variables in the Boosted Topology

In all the published ATLAS measurement of $t\bar{t}$ differential cross-section using the boosted topology, only the hadronic top p_T and $|\eta|$ have been measured, to emphasize the quantities that are strictly correlated with the large-R jet reconstruction. However, additional kinematic variables have the potential to increase the discriminating power of the measurement among various predictions and consequently the importance of the measurement in MC tuning. The larger sample statistics and the reduction of the uncertainties in the boosted topology increases the sensitivity

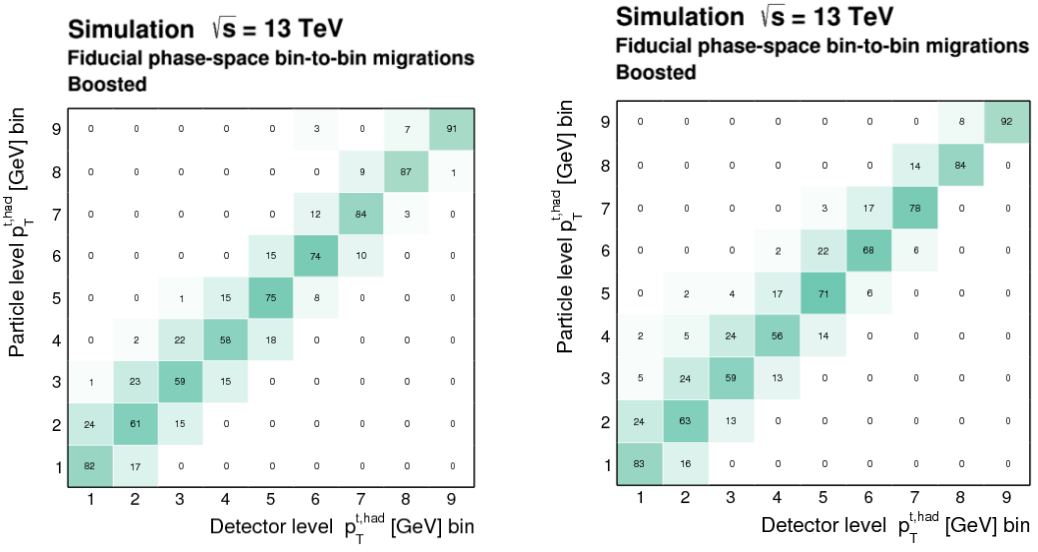

(a) (b)

Figure 8.10: Migration matrices between the detector and particle level $p_T^{t,had}$ using the standard large-R jet (a) and the re-clustering (b) to reconstruct the boosted hadronic top.

of the measurement of the differential cross-section and makes more important the measurement of additional variables in this topology. Moreover, the measurement of the $t\bar{t}$ system in the boosted topology allows to investigate in detail the region of the phase space where the top is produced at high p_T, sensitive to the production of possible massive resonances decaying in $t\bar{t}$ [60, 57], predicted by many new physics models.

8.2.1 Reconstruction of the $t\bar{t}$ System in Boosted Topology

The reconstruction of the leptonic top in the *boosted* regime starts from the set of small-R jets associated to the lepton obtained from the selection described in Section 4.2, which have the following properties:

- ΔR(Top-jet (1.0) candidate, small-R jet) > 1.5;
- ΔR(lepton, small-R jet) < 2.0.

Then, the jet chosen from this group to reconstruct the leptonic top is the b-tagged jet with highest p_T or, in case no one of these jets is b-tagged, the jet with highest p_T is selected. The next step is the reconstruction of the leptonic W from the charged lepton and the neutrino, that is done by imposing the W mass constraint as in the resolved topology, as described in Section 4.2.1. Then the leptonic top quark is obtained as a vector sum of the W and the selected jet. The kinematic distributions of the leptonic top are shown in Figure 8.11. Here the MC predictions of signal and background are compared with the data collected by ATLAS in

2015 and 2016, corresponding to an integrated luminosity of 36.1 fb^{-1}. The same

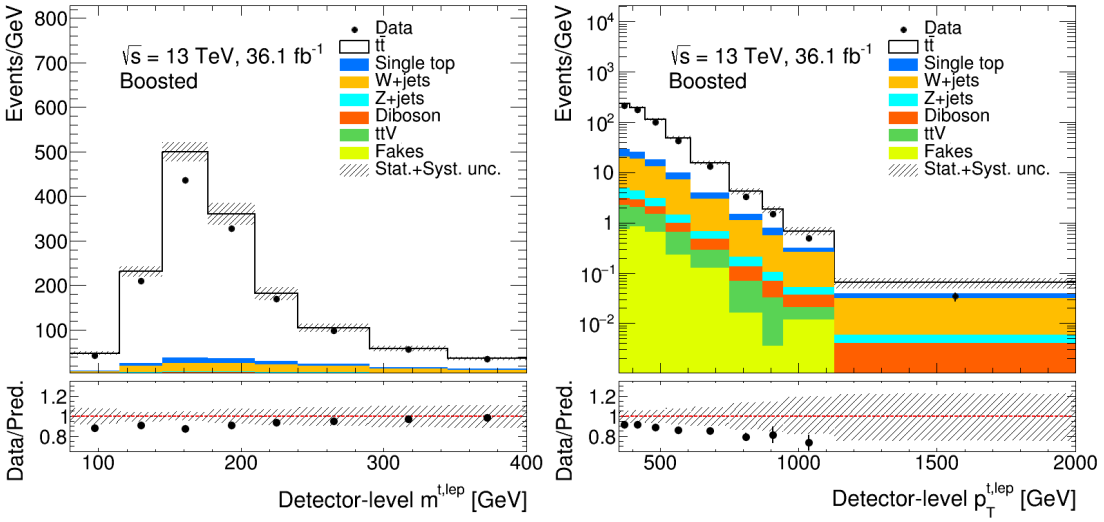

(a) (b)

Figure 8.11: Number of events as a function of leptonic top mass (a) and p_T (b). The data collected by ATLAS in 2015 and 2016 are compared with the MC background and signal simulations. The ratio pad show the data MC agreement

algorithm applied at detector level to reconstruct the leptonic top is employed also at particle level. The migrations between detector and particle level, with respect to the leptonic top p_T, are presented in Figure 8.12b. The matrix is diagonal and the migrations are only slightly larger of the ones shown in Figure 8.12a, relative to the hadronic top p_T.

The reconstruction of the leptonic top allows also to evaluate kinematic distributions of the $t\bar{t}$ system, such as those shown in Figure 8.13.

8.2.2 Double-differential Cross-sections

A way to further increase the capability of the measurement to discriminate among various MC simulation, necessary to test in more details the description of the perturbative QCD reached from the theoretical predictions, is the combination of the kinematic variables to measure double differential cross-sections. This kind of measurements has been published by CMS [56, 151], but, due to statistical limitations, they have never been measured in the boosted topology. The choice of the variables to combine is driven by the sensitivity to some aspect of the MC production that can be probed, for example the combination of $|y^{t\bar{t}}|, m^{t\bar{t}}$ and $|y^{t}|, m^{t\bar{t}}$ lead to a strong constraint of the gluon PDF [151].

Other combinations could be used for further application, such as the extraction of the top pole mass.

A general criteria used to define the combination of variables to measure is the

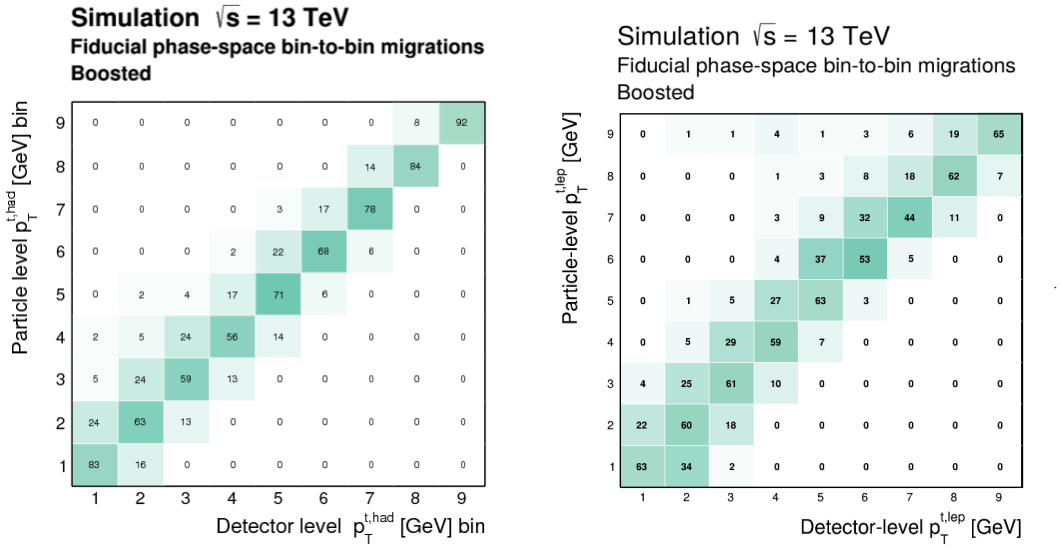

(a) (b)

Figure 8.12: Migration matrices between the detector and particle level $p_T^{t,had}$ (a) and $p_T^{t,lep}$ (b).

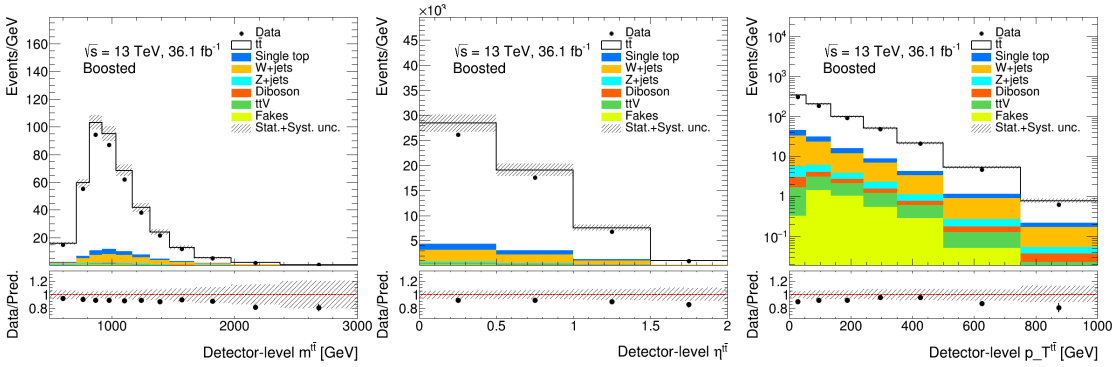

(a) (b) (c)

Figure 8.13: Kinematic distributions in the boosted topology at the detector level: (a) $m_{t\bar{t}}$, (b) $|\eta^{t\bar{t}}|$, (c) $p_T^{t\bar{t}}$. The hatched area indicates the combined statistical and systematic uncertainties in the total prediction, excluding systematic uncertainties related to the modelling of the $t\bar{t}$ system.

correlation among them, a low correlation indicates that the combination of the two variables provide larger sensitivity, with respect to spectra measured considering just one variable at a time.
Examples of variables with small correlations are shown in Figure 8.14, and in Figure 8.15 the corresponding double differential spectra at detector level, using the data collected by ATLAS in 2015 and 2016. All the detector level uncertainties due to object reconstruction are included, together with data and MC statistical uncertainty. The uncertainty obtained is below 15% in all bins of the distributions and the data MC agreement shown in the ratio pad is fair along the full spectra.

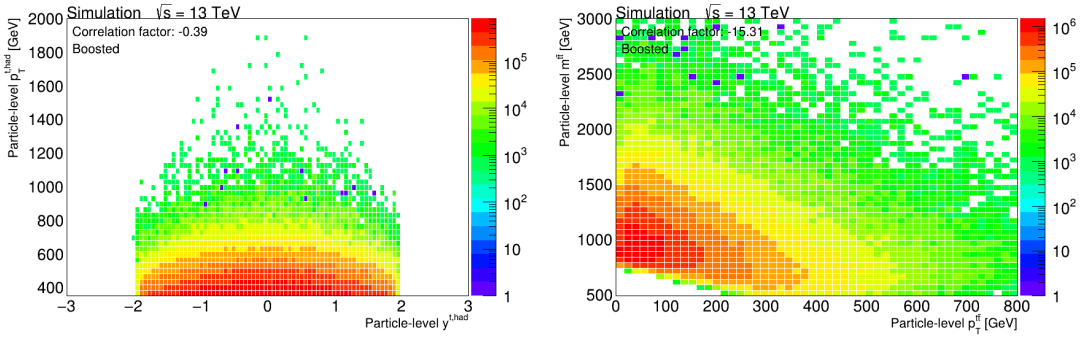

(a) (b)

Figure 8.14: Correlations between particle level $|y^{t,had}|, p_T^{t,had}$ (a) and $m^{t\bar{t}}, p_T^{t\bar{t}}$ (b). The correlation factor are indicated in the upper left part of the plots.

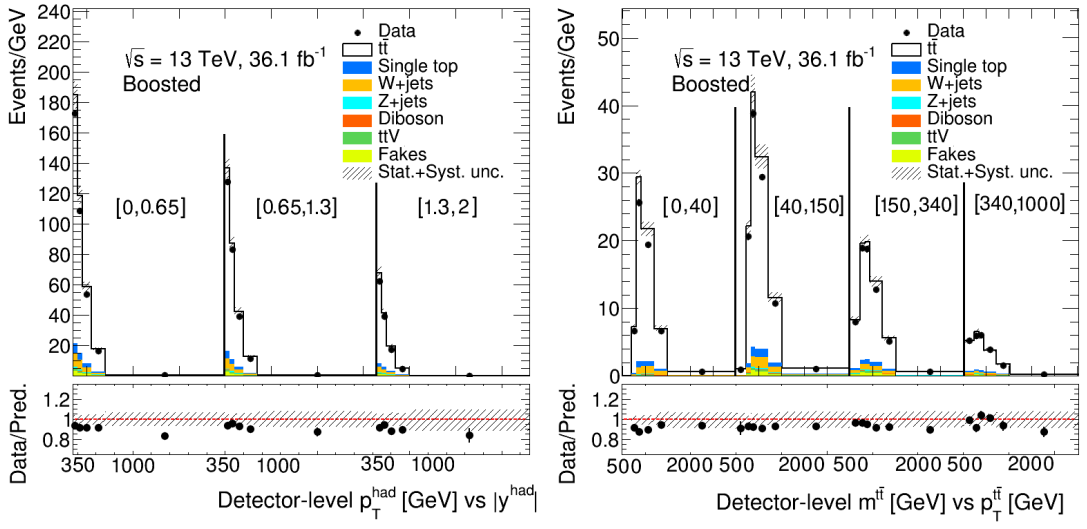

(a) (b)

Figure 8.15: Kinematic distributions in the boosted topology at the detector level: (a) $p_T^{t,had}$ in bins of $|y^{t,had}|$, while in (b) $m_{t\bar{t}}$ in bins of $p_T^{t\bar{t}}$. The hatched area indicates the combined statistical and systematic uncertainties in the total prediction, excluding systematic uncertainties related to the modelling of the $t\bar{t}$ system.

In conclusion, the measurement of the differential cross-section of $t\bar{t}$ production in the boosted topology is a key test for $t\bar{t}$ production models that can be produced in regions of the phase space never investigated before. The importance of this channel will also further increase with the statistics collected by the ATLAS experiment and applying innovative reconstruction techniques, as the re-clustering, that allow to highly improve the sensitivity of this channel and explore for the first time double differential distributions.

Conclusions

The measurement of the $t\bar{t}$ production differential cross-section obtained with data collected by the ATLAS detector in 2015, corresponding to a luminosity of $3.2\,\text{fb}^{-1}$ [1] is presented.

The selected sample contains only $t\bar{t}$ pairs in which one top quark decays hadronically and the other leptonically. Two different strategies are applied in the analysis to identify the events of interest and reconstruct the top quarks, depending on the transverse momentum of the hadronically decaying top. The resolved analysis is optimized to reconstruct the $t\bar{t}$ system in events containing at least four jets, originated by the hadronization of the top quarks decay products. The boosted analysis employs techniques specifically designed to reconstruct the hadronic top produced with high transverse momentum ($p_T > 300$ GeV), whose decay products are more collimated and tend to overlap due to the large Lorentz boost.

Both relative and differential cross-sections are measured in a fiducial phase-space, after the application of the corrections for all the effects of the limited resolution and acceptance of the detector.

The cross-section is presented as a function of the transverse momentum and absolute rapidity of the hadronic top in both the resolved and boosted topologies and as a function of the invariant mass, absolute rapidity and transverse momentum of the $t\bar{t}$ system in the resolved one.

In general, the Monte Carlo predictions agree with the data over a wide kinematic region, but it is observed that the shape of the transverse momentum distribution of hadronically decaying top quarks is poorly modelled by all the NLO predictions. This behaviour is consistent between the resolved and boosted topologies and a trend can be identified by looking at the data-MC agreement along the full transverse momentum spectra.

The measured kinematic distributions show high sensitivity to the differences among the various generators, indicating that the data have sufficient discriminating power to allow the tuning of the $t\bar{t}$ production models.

The use of a specific approach for the boosted topology allows to extend the measurement to the new kinematic regions where the top quark is produced with very high transverse momentum, up to 1.5 TeV. A set of studies also shows how to improve the sensitivity of the analysis to further constrain the tuning of the MC and to possible new physics signals in future analysis. In particular, it is shown that the application of the re-clustering technique reduces the dominant systematic uncertainties by a factor two, and that a larger sample of data allows

to define double differential distributions also in the boosted topology.

The top quark, due to its high mass, it is involved in many models of new physics that could be individuated comparing the $t\bar{t}$ differential distributions with the standard model expectations. For this reason it is possible to re-interpret the measured cross-section to extract limits on the existence of new resonances. In particular, a possible re-interpretation of the measurement of the $\frac{d\sigma}{dm^{t\bar{t}}}$ in the boosted topology, that allows to set limits on the existence of a scalar and a pseudo-scalar color singlet resonance and a pseudo-scalar color octect one, is reported [60].

The analysis presented depends on many MC simulations to estimate backgrounds, systematic uncertainties, and to quantify the corrections due to detector effects. With the increasing data samples collected by the ATLAS experiment also the corresponding need for large simulated samples is growing. The available computing resources are not sufficient to fulfill these requests for future runs with higher luminosity and pile-up or for the foreseen upgrade of the ATLAS detector. For these reasons, ATLAS is developing an alternative approach to speed up the simulation of the pile-up component of the events, without loosing accuracy on the interesting part of the events. The algorithm for the fast digitization of the silicon detector has a central role in this project and the first results on the performances, in comparison with the standard digitization, have been reported.

Appendix A

Constraining Scalar Resonances Using Top-quark Pair Production at the LHC

The top quark, thanks to its large mass, is strictly connected to the Higgs Boson and could play a significant role in the electroweak symmetry breaking mechanism, moreover it plays a crucial role in many new physics models (NPM). Many NPM predict the existence of new resonances decaying to $t\bar{t}$, that could be observed as a modification of the $t\bar{t}$ production cross-section with respect to the SM expectations. A general scalar extension of the SM includes resonances with the same coupling and quantum numbers of the Higgs model, whose coupling to fermions are proportional to the fermion masses. In this case the main production channel at the LHC would be through loops of colored particles, and in case of heavy resonances ($m > 2m_t$) the decay in lighter fermions would be suppressed with respect to the one in $t\bar{t}$ pair. Under these assumptions it is possible to write the Lagrangian for the scalar interactions relevant for $t\bar{t}$ production [60]:

$$\begin{aligned}
\mathcal{L}_\phi &= ic_t^\eta \frac{m_t}{v}\bar{t}\gamma_5 t\eta + c_t^\sigma \frac{m_t}{v}\bar{t}t\sigma + ic_t^{\tilde{\eta}} \frac{m_t}{v}\bar{t}\gamma_5 \frac{\lambda^a}{2} t\tilde{\eta}^a \\
&+ c_g^\sigma \frac{\alpha_S}{12\pi v}\sigma G^a_{\mu\nu} G^{a\mu\nu} - c_g^\eta \frac{\alpha_S}{8\pi v}\eta G^a_{\mu\nu}\widetilde{G}^{a\mu\nu} \\
&- c_g^{\tilde{\eta}} \frac{\alpha_S}{8\pi v}\tilde{\eta}^a d^{abc}\widetilde{G}^{a\mu\nu} G^{b\rho\sigma}. \qquad \text{(A.1)}
\end{aligned}$$

The lagrangian (A.1) contains a CP-odd and a CP-even scalar singlet (η,σ) and a CP-odd color octet ($\widetilde{\eta}$). $G^{\mu\nu}$ is the gluon field strength tensor, $\widetilde{G}^{\mu\nu} = \frac{1}{2}\epsilon^{\mu\nu ro\sigma} G_{ro\sigma}$, λ^a are the $SU(3)$ generators and $d^{abc} = \frac{1}{4}Tr[\lambda^a\lambda^b, \lambda^c]$ is the fully symmetric SU(3) tensor. Using this generic model, differential cross-section measurements can be used to extract limits on the existence of new physics, scanning a wide phase-space of the model parameters (c_t,c_g and the resonance mass) [60].

A.1 Simulation and Analysis Strategy

The signal simulation for the range of interest of the parameters is done through a re-weighting technique. The SM $t\bar{t}$ sample is simulated using the SHERPA [152, 153] generator and the NPM signal is obtained applying an event by event weight defined as:

$$w = \frac{\overline{\mathcal{M}_{SM} + \mathcal{M}_{\phi}}^2}{\overline{\mathcal{M}_{SM}}^2} \tag{A.2}$$

where $\mathcal{M}_{SM}$ and $\mathcal{M}_{\phi}$ are the amplitudes for the SM and new physics contributions from a new resonance derived from (A.1), respectively, and the lines above indicate that the amplitude squared is summed and averaged over colors and spins. Since the considered NPM and the SM $t\bar{t}$ production mechanism have the same initial and final states the two processes interfere and the full amplitude of the new physics production can be evaluated as:

$$|\mathcal{M}_{\mathrm{SM}} + \mathcal{M}_{\phi}|^2 = |\mathcal{M}_{\mathrm{SM}}|^2 + |\mathcal{M}_{\phi}|^2 + 2\mathrm{Re}\,\mathcal{M}^*_{\mathrm{SM}}\mathcal{M}_{\phi} \equiv B_{\mathcal{M}} + S_{\mathcal{M}} + I_{\mathcal{M}}\,. \tag{A.3}$$

where the three terms indicate the background term (B_M), the pure signal (S_M) and the interference term (I_M).
The weights (w) are evaluated using MADGRAPH [154] simulations, taking as input the kinematic of the partons of each event simulated with SHERPA. This approach is chosen because, at the moment, the implementation of the amplitude and vertices derived from the Lagrangian (A.1) are possible only in MADGRAPH. The SM $t\bar{t}$ background simulation is performed with SHERPA, because it shows a very good agreement with the ATLAS measurements, even without detailed studies on MC parameter tuning. This agreement is checked by comparing the simulation with the results of the $t\bar{t}$ differential cross-section in l+jet channel at $\sqrt{s} = 8$ TeV in the boosted regime [49], shown in Figure A.1. Here (a) and (b) differ for the QCD order used in the calculation: in Figure A.1(a) the LO approximation with one extra radiation is used while in Figure A.1(b) the NLO one is applied. The LO approximation in this case is sufficient to describe the data, but the scale uncertainty is quite large, approximately double with respect to the NLO calculation case. In Figure A.2 the differences between NLO and LO predictions obtained with a separate treatment of the of extra radiation allowed in the ME calculation are shown on the distributions of $m^{t\bar{t}}$ and $p_T^{t\bar{t}}$ in the boosted regime, for which ATLAS data are not available. The LO description with at least one additional radiation shows a reasonable agreement with the NLO prediction and will be used in this chapter. This approach is chosen for consistency with the perturbative order used in the description of the the SM $t\bar{t}$ and of the NPM signal, that can be simulated only using LO approximation.

The reinterpretation of the measurements is done exploiting the RIVET framework [145], that allows to reproduce the published ATLAS analysis [49] on particle level simulations. The particle level selection used in this analysis is similar to the boosted measurement presented in Section 5.2.1, the only differences being on the cuts applied to identify the hadronic top and on the distance between the objects

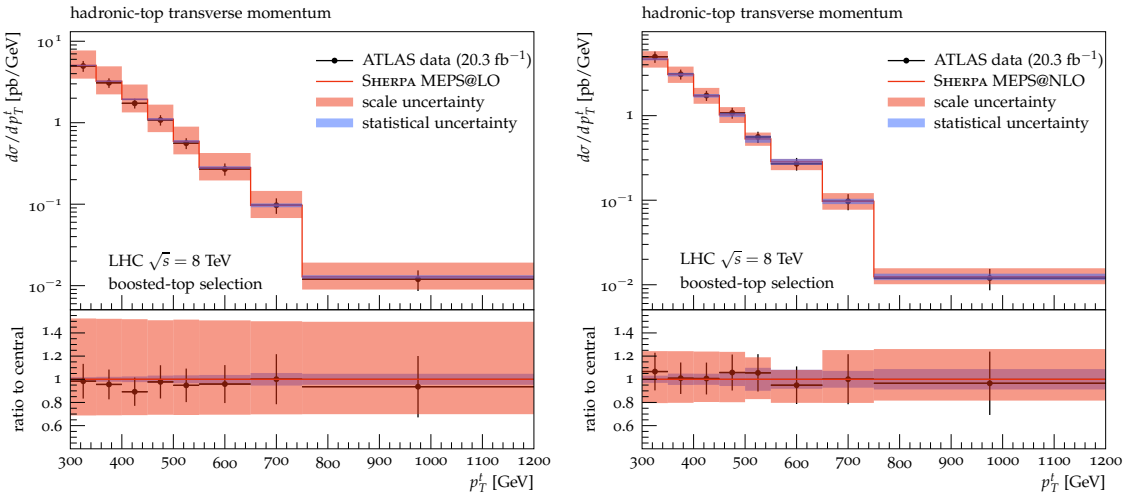

(a) (b)

Figure A.1: Comparison of predictions obtained with SHERPA MEPS@LO simulations of the $p_T^{t,had}$ with the measurement by the ATLAS experiment [49]: in (a) LO prediction, (b) NLO prediction [60].

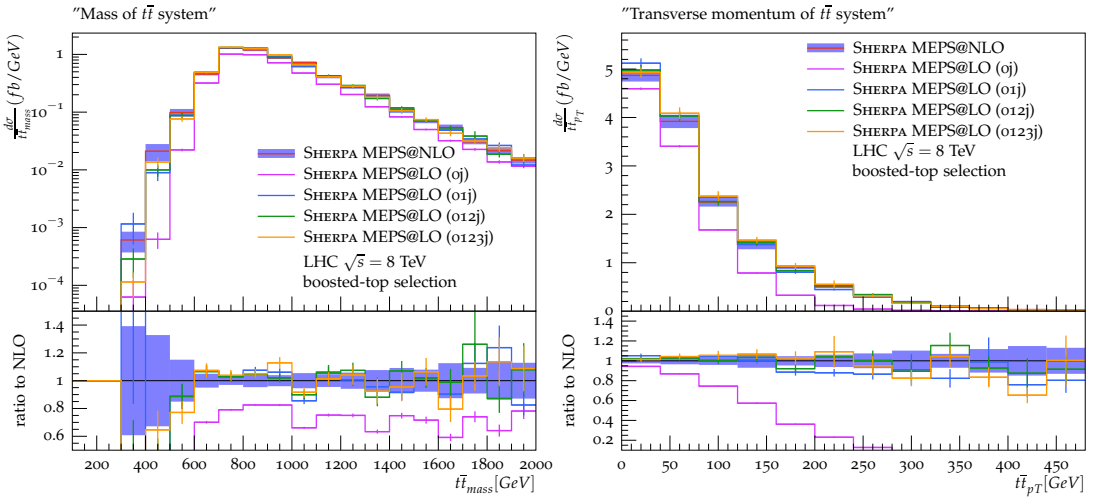

(a) (b)

Figure A.2: Comparison of MEPS@LO predictions based on different maximal parton-multiplicity matrix elements and the MEPS@NLO calculation for the boosted event selection: (a) $m^{t\bar{t}}$, (b) transverse momentum of the $t\bar{t}$ system.

used to define the $t\bar{t}$ system ($\Delta\phi$(large-R jet,ℓ)$>$ 2.3, ΔR(small-R jet,ℓ) $<$ 1.0). The top tagging in the $\sqrt{s} = 8$ TeV measurement is done applying a cut on the large-R jet mass ($m_{jet} > 100$ GeV) and on the splitting scale ($\sqrt{d_{12}} > 40$ GeV). The routine has been modified to add the reconstruction of the $t\bar{t}$ system in the boosted regime and the re-weighting algorithms employed to derive signal distributions.
The analysis performed in the boosted regime is preferred with respect to the re-

solved one because it is sensitive to resonances with mass in the multi-TeV range, not yet excluded by the experimental results.
In the following, the importance of including the interference term in the signal simulation, to derive the exclusion limits on NPM, will be also shown. The interference could completely change the line-shape of the resonance from a pure peak to a peak-dip or a dip-peak structure, or could also enhance or reduce the peak [155, 156, 157, 158, 159, 160].
To verify the impact of the interference on the $t\bar{t}$ differential distributions, before any smearing due to the reconstruction, a simple analysis called *parton* analysis is introduced. This performs the reconstruction of the $t\bar{t}$ system using parton level top quarks, individuated using truth information provided by the MC generator.
Since the $m^{t\bar{t}}$ in the boosted regime has not been measured from the ATLAS collaboration yet, the SHERPA simulation of the SM $t\bar{t}$ sample at $\sqrt{s} = 13$ TeV is used as pseudo-data to test the technique that allows to reinterpret differential measurements for the extraction of limits on new physics models.
Consequently, in the following, it is assumed that the SM perfectly describes the data, in order to derive the exclusion limits corresponding to the sensitivity that can be reached from this type of reinterpretation using differential cross-section $d\sigma/dm^{t\bar{t}}$.

A.2 Statistical Analysis

The approach used to set limits on the existence of new physics is a χ^2 calculation, applied to the differential cross-section ratio r, defined as:

$$r(H) \equiv \frac{d\sigma_H/dm}{d\sigma_{SM}/dm} \tag{A.4}$$

where the $d\sigma_H$ is the cross-section for $t\bar{t}$ production, after the subtraction of the standard model expectation, and can contain the pure signal (S) or the sum of signal and interference (S+I), depending on the cases. The advantage of using r is that the theoretical uncertainty simplify between numerator and denominator.
The χ^2 calculation is performed in a mass window of 400 GeV around the mass of the resonance and is defined as:

$$\chi^2_N = \sum_{i=1}^{N} \frac{r_i(H)^2}{\epsilon_i^2} \tag{A.5}$$

where N is the number of bins of the distribution in the mass window considered. The ϵ^2 is the variance of r in the bins i obtained, for each bin, as:

$$\epsilon^2 = \frac{1}{B}\left(1 + \frac{H^2}{B^2}\right) + \epsilon^2_{\mathrm{SYS}}\left(1 + \frac{H^2}{B^2}\right) + \epsilon^2_{\mathrm{TH}}\frac{(H+B)^2}{B^2}\,. \tag{A.6}$$

The first term of (A.6) represents the statistical uncertainty, where B is the SM $t\bar{t}$ sample representing the background in this analysis and H the signal only or

signal plus interference sample. In the second term ϵ^2_{SYS} represents the relative experimental uncertainties while ϵ^2_{TH} in the third term is the relative theoretical uncertainty.
This formula has been derived using the error propagation formula, for each uncorrelated component of ϵ:

$$\epsilon_i = \sqrt{(|\frac{dr}{dH}|\Delta^i_H)^2 + (|\frac{dr}{dB}|\Delta^i_B)^2 + 2\frac{dr}{dH}\frac{dr}{dB}\Delta^i_B\Delta^i_H\rho_{HB}} \tag{A.7}$$

where i represents the uncertainty component, Δ represents the absolute uncertainty on B or H and ρ_{HB} is the correlation among H and B. The theory uncertainty is considered to affect only the numerator, while for the statistical component the related uncertainties due to the reweighing are neglected and $\Delta = \sqrt{B}$ is assigned both to H and to B.
ϵ_{TH} is assumed flat and equal to 1% for both S and $S + I$ hypothesis. For the experimental uncertainty (ϵ_{SYS}) three different scenarios are taken into consideration:

- The first is a realistic estimate of ϵ_{SYS}, ϵ_{SYS}=10−15%. This is consistent with the experimental systematic that can be reached by detectors with samples of 36 fb^{-1}, as shown in Section 8.2.

- The second scenario is optimistic and consider uncertainties in a range 5% − 10%, that is still realistic considering normalized distributions.

- The last scenario assumes ϵ_{SYS}=1 − 2%. This level of experimental uncertainty could be reached in the future, after introducing new techniques to calibrate the objects and improving the modelling and detector uncertainties.

Another important piece in the determination of the χ^2 is the resolution on $m^{t\bar{t}}$, that determines the number of bins. A small resolution allows to exploit the information of the cross-section line-shape and increases the difference due to the inclusion of the interference term. In the following two scenarios are considered, one where the resolution is 400 GeV and a single bin covers all the mass window around the resonance mass and the other where bins of 40 GeV are used.
The exclusion limits are derived requiring $\chi^2 \geq 2$.

A.3 Results

In this section three different scenarios are investigated to extract the limits on the parameters (resonance mass,c_g,c_t), using the approach described in previous section.

A.3.1 Pseudo-scalar Color Octet

The first scenario considers the presence of a color octet pseudoscalar resonance ($\widetilde{\eta}$). Figure A.3 shows the r ratio obtained using the *parton* analysis for a resonance of 500 GeV and with $c_t = 1$, with $c_g = 1$ on the left and $c_g = -1$ on the right.

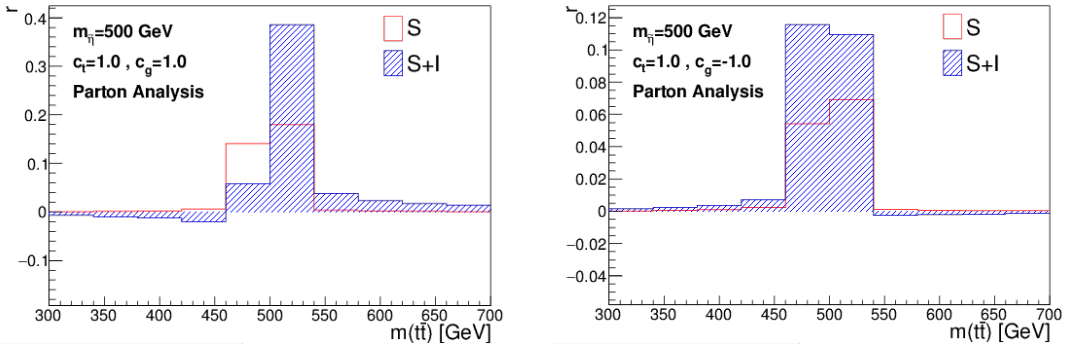

(a) (b)

Figure A.3: Distribution ratio ($r \equiv \frac{d\sigma/dm}{d\sigma_{\mathrm{SM}}/dm}$) as a function of $m^{t\bar{t}}$, for a pseudo-scalar color octet resonance with $m_{\widetilde{\eta}} = 500\,\mathrm{GeV}$, $c_t = 1$ assuming (a) $c_g = 1$ and (b) $c_g = -1$, using the *parton* analysis. Signal plus interference (S+I) is in blue and pure signal (S) in red [60].

The effect of the interference term is visible comparing the blue histogram with the red line, where only the pure signal component is used to obtain the distribution. Similarly to Figure A.3, Figure A.4 shows the r ratio for a resonance with mass 1700 GeV, reconstructed with the the boosted analysis.

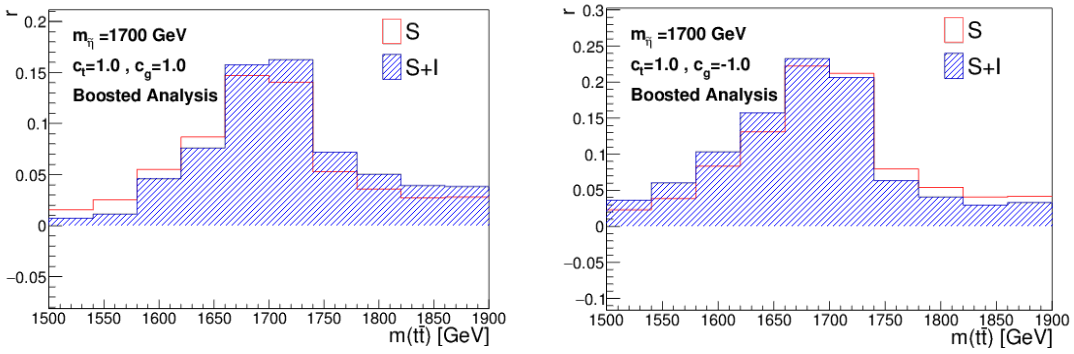

(a) (b)

Figure A.4: Distribution ratio as a function of $m^{t\bar{t}}$ reconstructed with the boosted analysis for a pseudo-scalar color octet resonance with $m_{\widetilde{\eta}} = 1700\,\mathrm{GeV}$, $c_t = 1$ assuming (a) $c_g = 1$ and (b) $c_g = -1$. The color scheme is the same as in Fig. A.3 [60].

Here the impact of the interference term is still visible but the effect is diluted by the reconstruction. The limits corresponding to these distributions are shown

in Figure A.5, where the region of the parameter space $(m_{\tilde{\eta}}, c_g)$ delimited by the colored bands is the one that is not excluded.

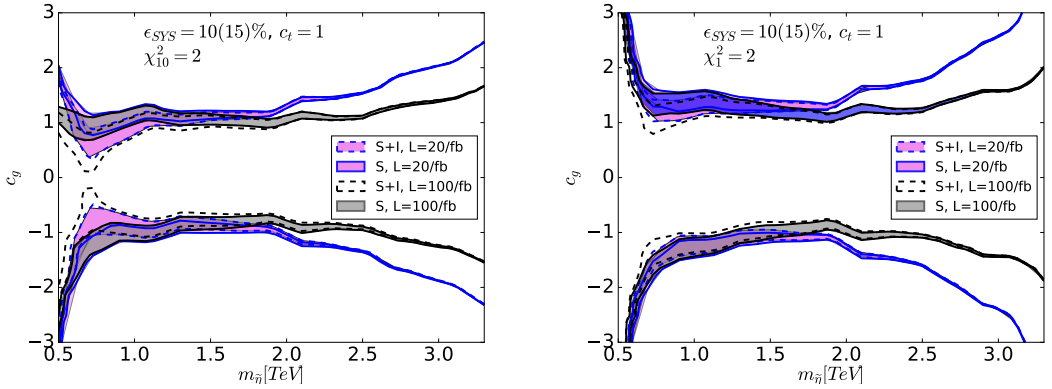

(a) (b)

Figure A.5: Exclusion limits ($\chi^2 = 2$) in $(m_{\tilde{\eta}}, c_g)$ parameter space for a pseudo-scalar color octet assuming $c_t = 1$. The band represents the different assumptions for the systematic uncertainty, varying from 10% to 15%. Integrated luminosities are L =20 fb^{-1} (blue line) and L =100 fb^{-1} (black), as well as considering interference (dashed line) and neglecting it (solid line) [60]. In (a) the limits are extracted using 40 GeV resolution, while in (b) 400 GeV.

Since the excess with respect to the only SM hypothesis overcome the 10% the scenario with the uncertainties ϵ_{SYS}=$5 - 10\%$ would already have the potential to exclude the full parameter phase-space, consequently the uncertainties are assumed to be ϵ_{SYS}=$10 - 15\%$, and represents the colored band in Figure A.5. Both the exclusion limits obtained with luminosity equal to 20 and 100 fb^{-1}, and using the S and $S + I$ hypotheses, are shown. The inclusion of the interference term modifies the excluded parameter range in the low $m_{\tilde{\eta}}$ region. The importance of a good resolution for this line-shape analysis can be seen comparing (a), where is assumed a resolution of 40 GeV, and (b), where 400 GeV resolution is considered. A luminosity of 100 fb^{-1} allows to exclude a large range of parameter space $(m_{\tilde{\eta}}, c_g)$ also in the high mass region, where the dominant uncertainty is statistical.

A.3.2 Pseudo-scalar Color Singlet

The second scenario considers the presence of a color singlet CP-odd resonance. Figure A.6 shows the r ratio obtained with the *parton* analysis considering a resonance with $m_\eta = 500$ GeV, $c_g = 1$ and $c_t = 1$(a) or $c_t = -1$(b). Here the effect of the interference is clearly visible.

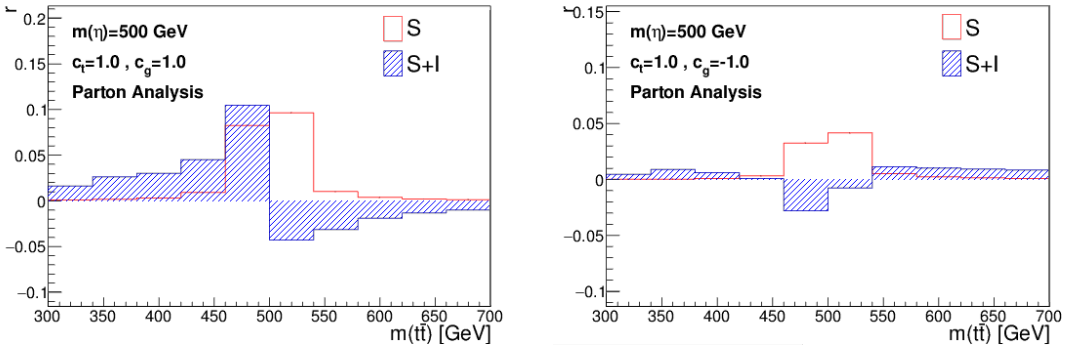

(a) (b)

Figure A.6: Distribution ratio as a function of $m^{t\bar{t}}$ in the range $m^{t\bar{t}} = [300, 700]$ GeV, for a pseudo-scalar signal ($m_\eta = 500$ GeV) in the *parton* analysis [60], assuming only signal (S) and signal plus interference hypotheses (S+I). $c_t = 1$ in both pads, while in (a) $c_g = 1$ and in (b) $c_g = -1$.

The reconstruction partially smears the signal shape and consequently the effect is less visible in Figure A.7, where the $t\bar{t}$ system obtained with the simulation of a resonance with $m_{(\eta)}$ is reconstructed using the boosted analysis.

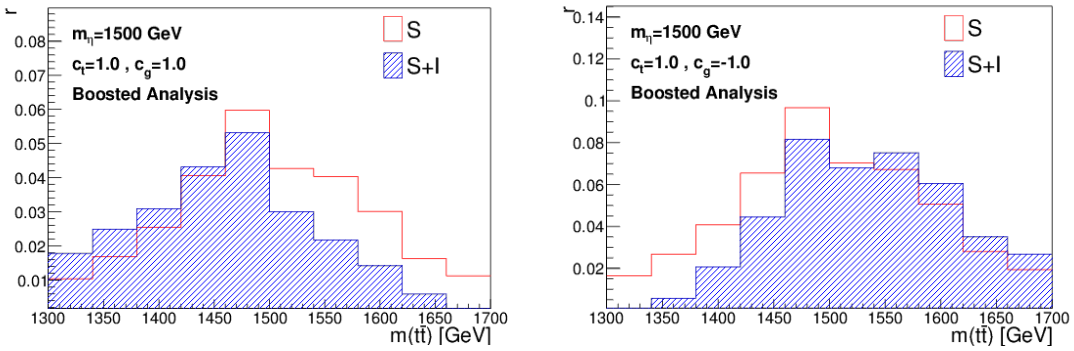

(a) (b)

Figure A.7: Distribution ratio as a function of $m^{t\bar{t}}$ in the range $m^{t\bar{t}} = [1300, 1700]$ GeV for a pseudo-scalar color singlet resonance with $m_\eta = 1500\,\text{GeV}$, $c_t = 1$ and (a) $c_g = 1$, (b) $c_g = -1$, reconstructed with the boosted analysis. The color-scheme is the same as in Fig. A.3 [60].

The exclusion limits in the parameter plane (m_η, c_g) are shown in Figure A.8, for resonance with $c_t = 1$. In this case the scenario ϵ_{SYS}=5 − 10% is used. The interference effect is noticeable for low masses $m_\eta \leq 1.2$ TeV, where also systematic uncertainties have a huge impact on the exclusion power.

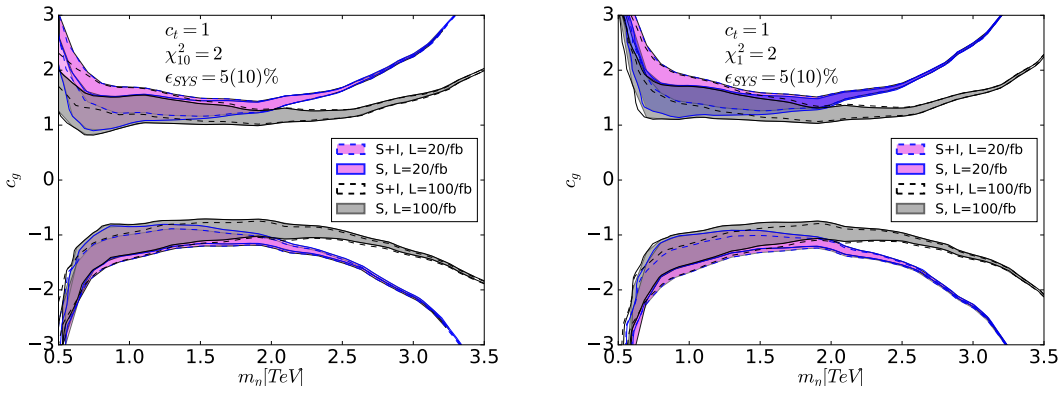

(a) (b)

Figure A.8: Exclusion limits ($\chi^2 = 2$) in (m_η, c_g) parameter space and $c_t = 1$ for a pseudo-scalar color singlet. The band represent the different assumptions for the systematic uncertainty, varying from 5% to 10%. The color and style scheme for the lines are the same as in Fig. A.5 [60]. In (a) the limits are extracted using 40 GeV resolution, while in (b) 400 GeV.

A.3.3 CP-even Color Singlet

The last scenario considers the presence of a color singlet CP-even resonance (σ) with a width much broader with respect to the other resonances investigated, in particular $\Gamma_\sigma = 0.2 m_\sigma$ is assumed. This particular scenario has a tiny cross-section with respect to the scalar case and the very optimistic scenario ϵ_{SYS}=1 − 2% is necessary to exclude part of the (m_σ, c_g) phase space, together with a really high integrated luminosity, $L = 300$ fb^{-1}. The exclusion limits are shown in Figure A.9. The large width of the resonance increases the impact of the interference on the evaluated exclusion limits. Indeed, as it is clearly visible from Figure A.9 the inclusion of the interference term substantial contributes to improve the limits.

A.4 Conclusions

This appendix presents an approach to reinterpret the differential cross-section measurements using the information provided from each analysis in format of RIVET routines [145]. The particle level measurements can be compared with theoretical predictions obtained from new physics models to extract exclusion limits on the existence of new resonances. In particular the sensitivity of differential cross-section measurements of $t\bar{t}$ production in the boosted topology is investigated. Pseudo-data obtained with the SHERPA simulation are processed with the ATLAS event selection performed at 8 TeV in the l+jet channel [49] to set limits on the existence of a CP-odd, a CP-even scalar and a CP-odd color octect resonances. In order to study the sensitivity of this type of reinterpretation, that can be applied to future LHC measurements, various systematic uncertainty scenarios are investigated together

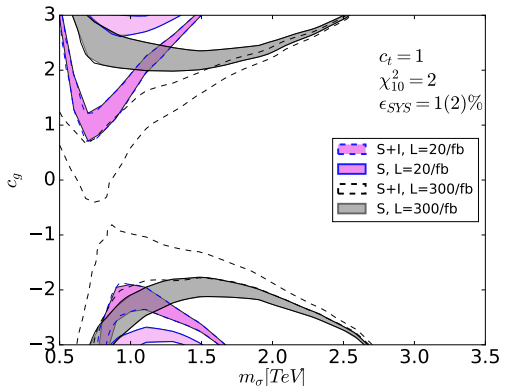

Figure A.9: Exclusion limit ($\chi^2 = 2$) in the (m_σ, c_g) parameter space and $c_t = 1$ for such scalar state. The color scheme is the same as in Fig. A.8, the boosted analysis is adopted [60].

with various resolutions and different integrated luminosity values. The effect of the interference between the standard model background and the new physics contributions are also investigated. In particular the inclusion of the interference term has been observed to have a not negligible impact on the signal sensitivity. The results presented in this appendix are included in a paper under publication [60].

Appendix B

Fast Simulation of the Silicon Detector Digitization

The larger part of ATLAS computing resources is used for the generation of the MC samples, used in physics analyses and for objects calibration, as shown in Figure 3.8.
The increasing amount of data collected by ATLAS implies a corresponding increase in the size of the MC samples, that must be larger than the data samples, to avoid situations where the precision of a measurement is limited by the MC sample statistics.
In order to increase the number of events collected during the data taking, the de-

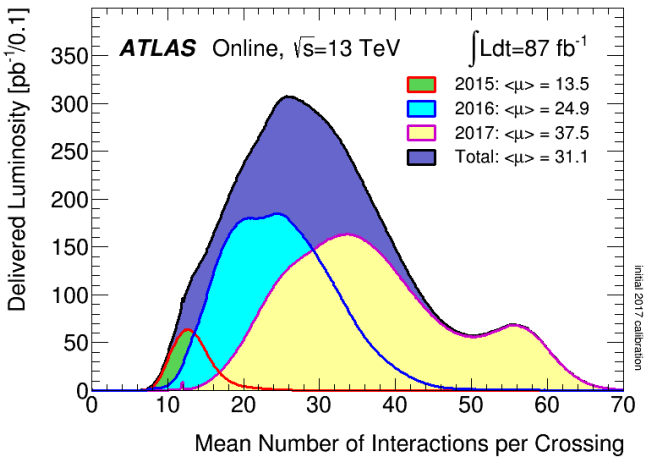

Figure B.1: Luminosity-weighted distributions of the mean number of interactions per crossing for the 2015, 2016 and 2017 proton-proton collisions data at $\sqrt{s} = 13$ TeV. All data delivered to ATLAS during stable beams is shown [80].

tector instantaneous luminosity has been increased during Run2 by approximately a factor 5 in 2016 and 10 in 2017, and is expected to further increase in the future detector upgrade foreseen in 2023 (HL-LHC).The drawback of the luminosity increase is the corresponding growth of the number of interactions per bunch-crossing

(pile-up), that is constantly increasing from 2015 to 2017 data taking, as shown in Figure B.1. A larger pile-up implies a larger number of energy deposits in the sensors and tracks to reconstruct, and an increased complexity in reconstructing the particle's trajectory and correctly assign the hits of a particle to the proper track. This reflects in a larger CPU time required for the digitization and recon-

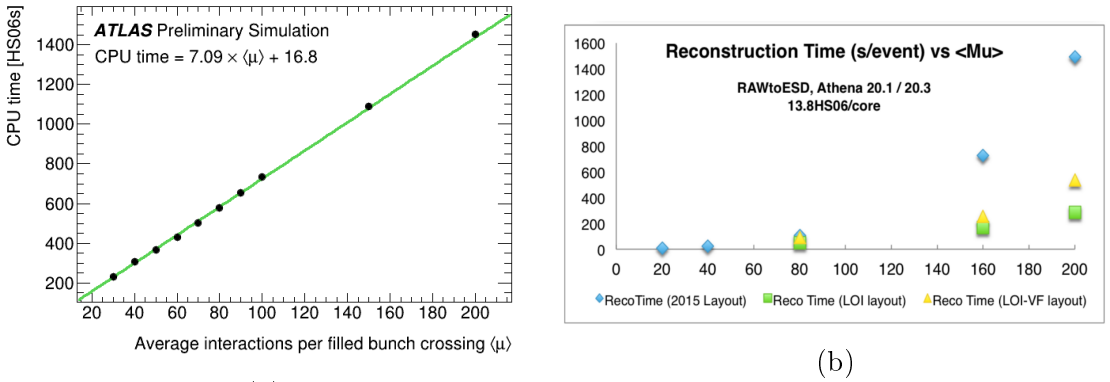

(a) (b)

Figure B.2: CPU time required for the digitization (a) and reconstruction (b) of a single event, as a function of the average number of interactions per bunch crossing [161].

struction steps, as shown in Figure B.2, where is illustrated the dependence of the CPU time for the simulation of a single event from the average interactions per filled bunch crossing. With the current computing model, the foreseen share of the computing resources, shown in Figure B.3, will be dominated by these two steps of the MC production, grouped as MC reconstruction in the chart. To sustain the

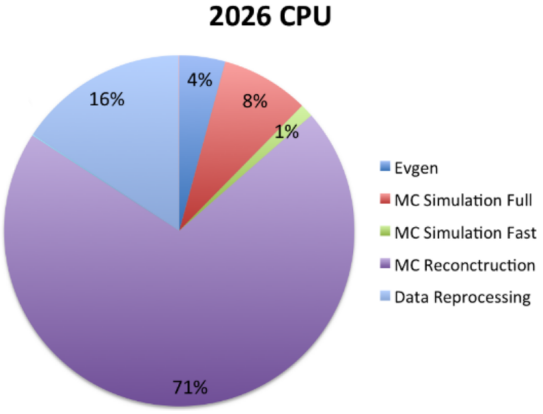

Figure B.3: Foreseen share of the computing resources in 2026 with the current computing model, obtained with an extrapolation of 2016 computing model [162].

large demand of MC samples, with large pile-up, ATLAS is now developing the fast simulation chain, described in Section 3.4.1, that aims to speed up all the steps of

the MC production using a faster, although less accurate, approach to simulate the pile-up component of each event.
One of the main components of the fast chain is the fast digitization of the silicon detector, that is a parametric simulation of the conversion in digital signal of the energy deposited in each sensor of the pixel and strip detectors. This algorithm will replace the standard digitization of the inner detector in the FastChain, where the detailed propagation of charges or light into the active material is simulated together with the the precise response of the readout electronics, taking also in consideration the design and detector conditions.

B.1 Algorithm

The input to the digitization of the silicon tracker are the locations of the energy deposits produced by the GEANT4 [77, 78, 79] simulation of the detector, that consists in a set of 2D entry and exit positions in each module of the silicon detectors and the corresponding amount of energy deposited by the charged particles crossing the module.
The fast digitization starts with a loop on all the detector elements. For each detector element a digitization module is built, with the characteristics that match the readout design of the specific module: number of sensors, dimensions and geometric arrangement of the sensors and Lorentz angle in the region of ATLAS where the module is mounted. While the geometry of the surface, where the charge is collected, is the same between a detector module and a digitization module the geometry of the internal surfaces is different to take into account the Lorentz angle. The Lorentz angle, introduced in Section 2.2.1, corresponds to the drift direction of the charge inside the module and determines where a charge originated from a particle crossing the detector is deposited. A graphic example of a digitization module is shown in Figure B.4. Each module has a local coordinate system that has the origin in the center of the module, the local X corresponds to the $r-\phi$ direction in the global ATLAS geometry, while the local Y corresponds to η. The sensor surfaces are tilted along the local X direction to be parallel to the Lorentz drift direction, this is convenient for the subsequent steps of the algorithm. In this way each detector module is composed by a series of cells with the advantage that all the charge deposited in a single cell can be directly projected on the surface, as illustrated in Figure B.5. Each cell surface corresponds to an element of the module readout, and is therefore straightforward to individuate the appropriate channel to store the information on the digital signal.
After the creation of the digitization module, the algorithm proceeds with a loop on all the hits generated by the GEANT4 simulation inside the detector element. For each hit, the cells in the detector module crossed by the trajectory connecting the local entry and exit positions are individuated. This information is then used to calculate the step of the trajectory, DigiTrackStep (DTS), in each cell of the digitization module. The length of the DTS is considered directly proportional to the charge deposited in each sensor, and so to the signal's time over threshold.

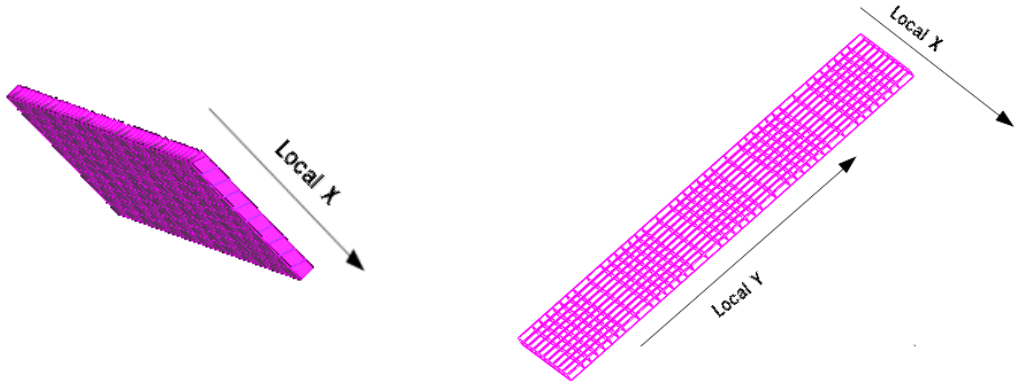

(a) (b)

Figure B.4: Schematic representation of a digitization module built by the fast digitization algorithm. The module is built following the characteristics of each detector element. In particular the Lorentz angle is visible in the tilt applied in the surface in (a) while the particular scheme of the sensors with variable dimensions, depending on the position in the module is visible in (b).

If the local entry or exit of the hit in the detector element are outside the sensitive area of the module the valid entry or exit is calculated as the intersection of the trajectory with the module border. This usually happens if the track enters from another module of the same layer. To include the effect of the multiple scattering the DTS is smeared according to a Landau distribution.
The following step of the algorithm is dedicated to the cluster formation. Each DTS is considered only if its length is larger than a certain threshold, optimized as discussed in the next section. All the DTS over-threshold formed from the same hit are merged to form a cluster, as shown in Figure B.6. The creation of the clusters at this stage allow to furthermore speed up the full Monte Carlo production, avoiding the time consuming algorithms employed in the standard cluster creation, that happens during the reconstruction step. The advantage of creating clusters at this stage is that it is possible to use directly the information provided by GEANT4 of which sensors are crossed from a single particle, while in the standard approach the clusters are created by CPU intensive patter recognition algorithms, used to individuate hits created from the same particle without using MC information.
The resulting clusters are completely consistent with the standard ones and can be used as input for tracking. At the end of the creation of each cluster, all the other ones already formed in the same detector element are checked to verify the presence of clusters adjacent to the newly created one. The rules to define if two clusters should be merged are inherited from the standard reconstruction.
Beside the reconstructed clusters also the information on the truth particles associated to each cluster is stored. This information is used by the tracking algorithms to evaluate the performance of the cluster formation and tracking.

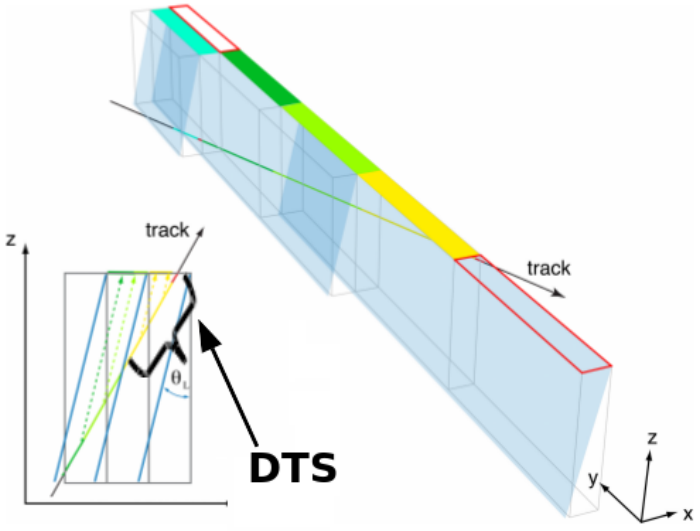

Figure B.5: Sketch of the fast digitization algorithm approach. In the bottom is shown that using surfaces tilted along the Lorentz angle direction allows to take directly into account the Lorentz drift in the DTS evaluation [163].

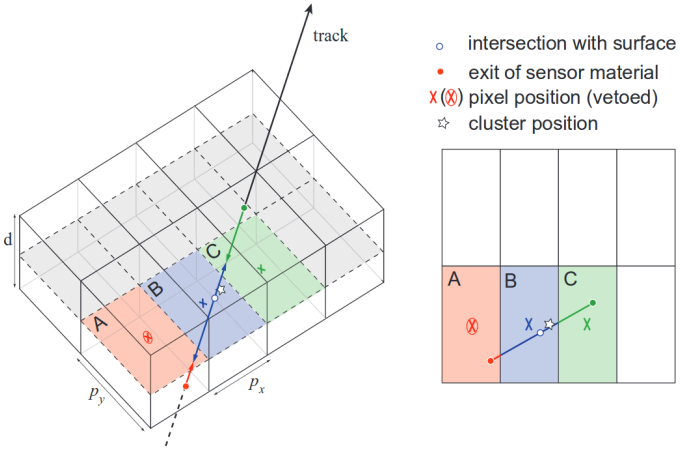

Figure B.6: Example of cluster creation approach followed by fast digitization [164]. The cells A,B,C are crossed by the same particle but the cell A is not included in the cluster because under threshold.

B.2 Tuning of the Parameters

The primary aim of the Fast Digitization is the inclusion in the fast chain to speed-up the simulation of the pile-up contribution. The performance of the fast digitization is not expected to be as precise as the standard one, but since the fast

digitization simulation is a parametric algorithm, it is possible to adjust some of the parameters to increase the agreement with the standard digitization. While most of the distributions are well described from the fast digitization, as shown in Section 3.4.1, some show a disagreement between the two algorithms, and some tuning of the simulation parameters is necessary.
One of the parameters that needs to be tuned is the threshold applied to cut on the DTS. This quantity is present also in the standard digitization, to remove the

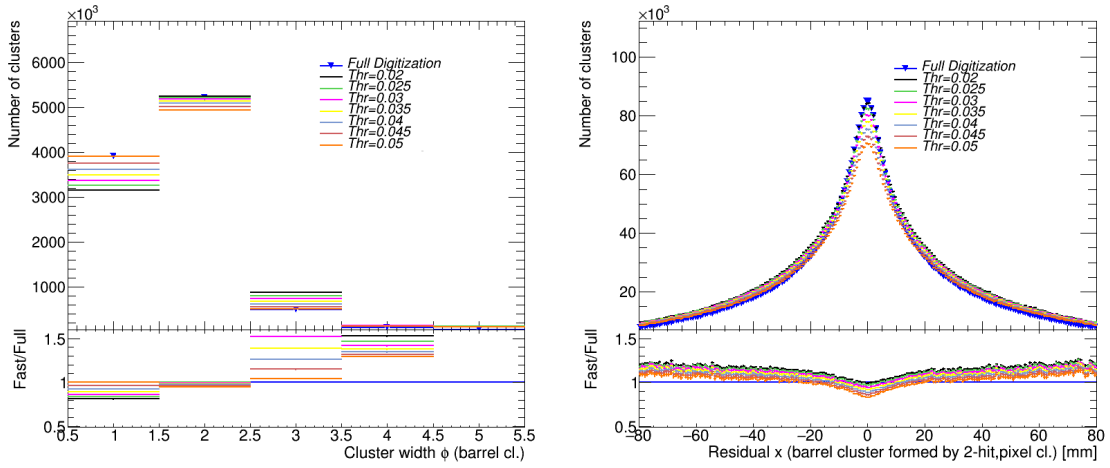

(a) (b)

Figure B.7: Tuning of the threshold applied in the fast pixel digitization on the path step in each sensor, obtained using a sample $Z \to \mu\mu$. The optimization is done comparing the sample obtained using the standard simulation and the one obtained changing only the pixel digitization with the fast approach. In (a) the comparison is shown as a function of the number of pixel composing the clusters along the local X direction in the barrel, while in (b) on the residual distribution for barrel clusters that contain at least two cells.

detector noise and is expressed in terms of electrons freed in each sensor, instead of in term of a length, as is done in the fast approach. The threshold influences the cluster dimensions, so it has an impact on all the parameters of the reconstructed tracks. The effect of the variation of the fast digitization threshold on the cluster dimensions and on the residuals[1] in the pixel detector can be seen in Figure B.7 for the barrel and B.8 for the endcap. The residuals shown are only for clusters formed by at least two cells, that are a large fraction of the total barrel clusters ($\approx 50\%$) but just a 9% of all clusters in the endcap, where there is no Lorentz shift and the tracks impact mostly perpendicularly to the detector. The tuning shows that in the barrel the initial threshold value of 0.02 mm seems to provide a good agreement with respect to the standard simulation, on the other hand in the endcap a larger value of the threshold seems to provide a better description of the cluster dimensions. The same studies made on the SCT clusters in the barrel are shown in

[1]Difference between the cluster center position and the position of the reconstructed track.

Figure B.9, here the threshold 0.09 mm seems to provide a better agreement with the standard digitization. Another effect that needs to be considered in the fast digitization is that some sensors adjacent to ones above threshold could register a signal also if not directly crossed from the track. This happens in the real detector and is simulated in the standard approach. The simulation of this phenomena

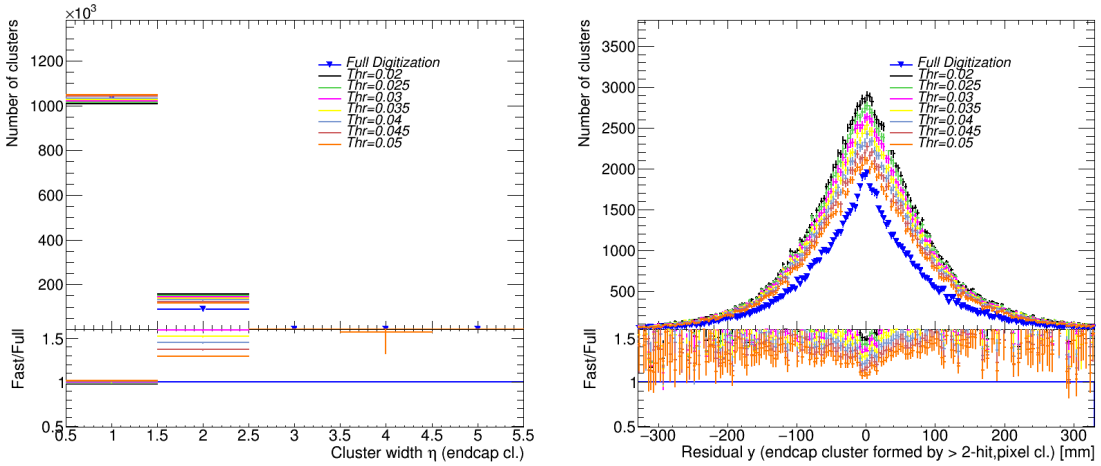

(a) (b)

Figure B.8: Tuning of the threshold applied in the fast pixel digitization on the path step in each sensor, obtained using a sample $Z \to \mu\mu$. The optimization is done comparing the sample obtained using the standard simulation and the one obtained changing only the pixel digitization with the fast approach. In (a) the comparison is shown as a function of the number of pixel composing the clusters along the local Y direction in the endcap, while in (b) on the residual distribution for endcap clusters that contain at least two cells.

in the fast digitization is obtained by applying a smearing of the local entry and exit position of a track in a detector module, producing a smearing in the cluster dimension if additional cells became over threshold. In this approach the parameter that can be tuned is the length of the shift applied to the hit ends. The results of this tuning are shown in Figure B.10 for the pixel clusters in the endcap and in Figure B.11 for the SCT clusters, in the barrel. In both pixel and strip clusters a shift of 0.004 mm results in an overall improvement of the agreement between the fast and standard digitization.
All the studies performed in this Section are obtained using a $Z \to \mu\mu$ sample and selecting one fast algorithm at a time, to disentangle the effects due to the fast pixel and SCT digitization. The optimized parameters have been used to produce the public plots shown in Section 3.4.1.

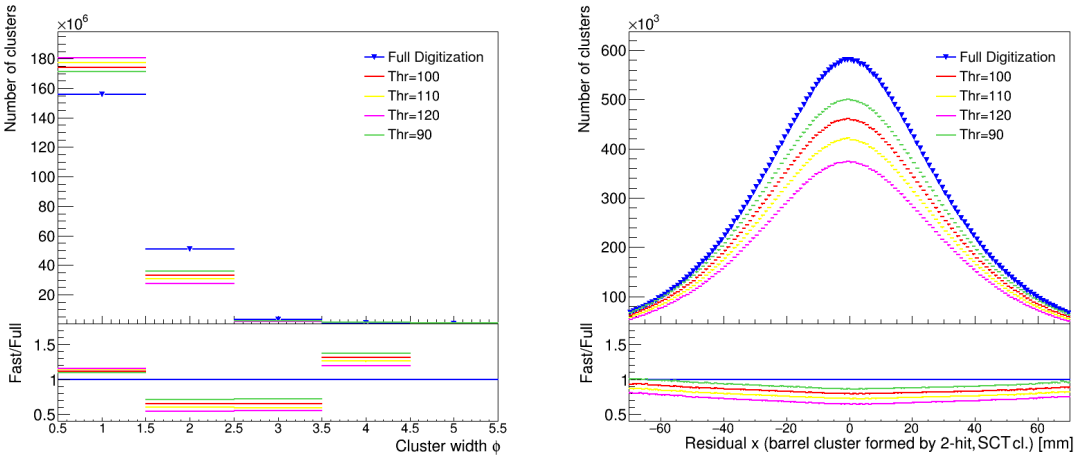

(a) (b)

Figure B.9: Tuning of the threshold applied in the fast SCT digitization on the path step in each sensor, obtained using a sample $Z \to \mu\mu$. The optimization is done comparing the sample obtained using the standard simulation and the one obtained changing only the SCT digitization with the fast approach. In (a) the comparison is shown as a function of the number of strip composing the clusters along the local X direction in the barrel, while in (b) on the residual distribution for barrel clusters that contain at least two strips.

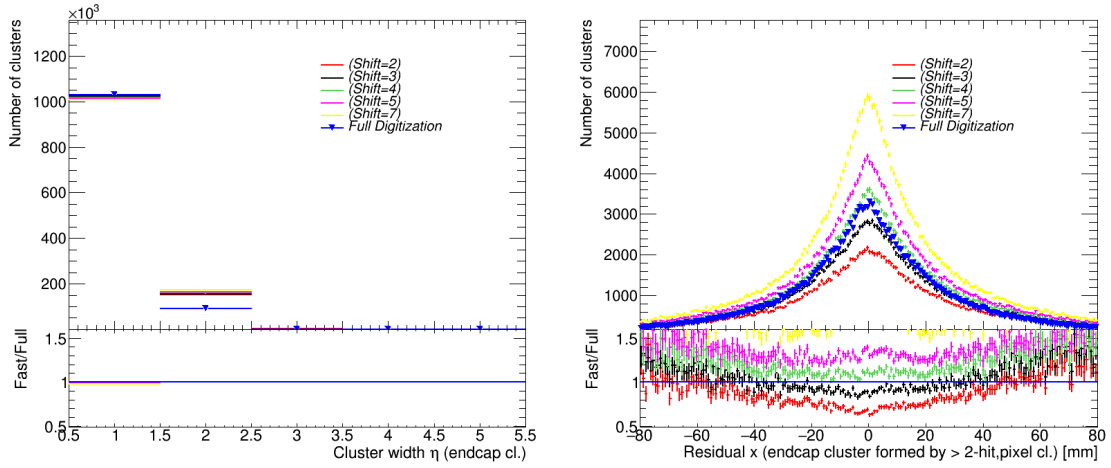

(a) (b)

Figure B.10: Optimization of the smearing parameter applied to the entry and exit positions of the hits in the detector element. The optimization is done comparing the standard digitization (blue) with simulations that differ only for the pixel digitization. The sample employed is $Z \to \mu\mu$. In (a) the comparison is shown as a function of the number of pixel composing the clusters along the local X direction, while in (b) on the residual distribution for the end cap clusters that contain at least two pixels.

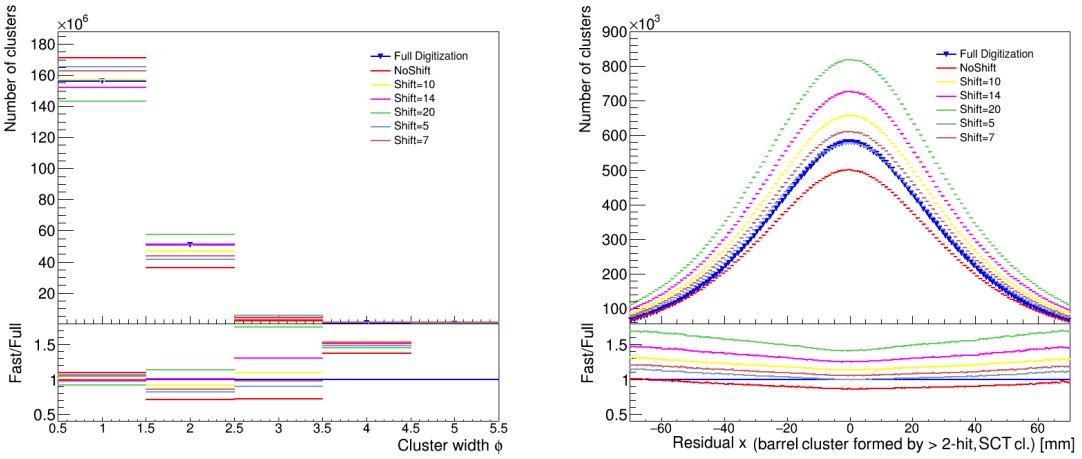

(a) (b)

Figure B.11: Optimization of the smearing parameter applied to the entry and exit positions of the hits in the detector element. The optimization is done comparing the standard digitization (blue) with simulations that differ only for the SCT digitization. The sample employed is $Z \to \mu\mu$. In (a) the comparison is shown as a function of the number of strip composing the clusters along the local X direction, while in (b) on the residual distribution for the barrel clusters that contain at least two strip.

B.3 Detector Studies for the ATLAS Upgrade

The fast pixel digitization can be employed also in the design of a new tracking system for the ATLAS upgrade, to easily compare the performances of the detector using different pixel technologies, pitch dimensions and sensor thicknesses. The

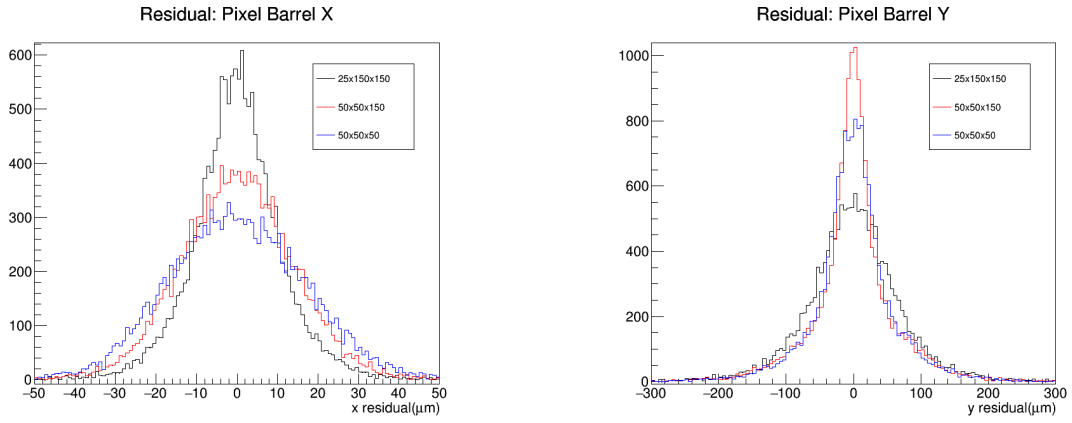

(a) (b)

Figure B.12: Effect on the residuals of different dimensions and thickness of the pixel sensors along $r\phi$ direction and along η direction.

algorithm takes as input only the information on the entrance and exit positions

of a track in the module, but no information on the energy deposition is required. Changes in the sensor parameters can be consequently handled from the fast digitization without the need to rerun the detector simulation, but simply changing the digitization module to reproduce a custom geometry under study. There are, anyway, some limitations to this approach: for example the active area of the detector cannot be varied in order to reuse the hits evaluated by the detector simulation with a different geometry.
An example of the effect of the change of the pitch dimensions on the track residuals is shown in Figure B.12, where the parameters of the sensors, reported in Table B.1, are compared. Figure B.12 shows that a longer side of the pixels corresponds to

(X,Y,Thickness) [μm]	Starting point	Alternative pitch	Alternative thickness
Barrel, Local X	25x150x150	50x50x150	50x50x150
Barrel, Local Y	25x150x150	50x50x150	50x50x150

Table B.1: Example of different geometries of pixels pitch.

worst residuals. Also the detector thickness plays an important role: a thinner detector implies lower charge deposited in each cell, and consequently a different cluster dimension and a reduction in the total number of clusters. To mitigate the impact of the volume variation is necessary to modify the threshold applied on the DTS length accordingly.
This type of studies are useful to explore the performance of alternative sensors, with different dimensions or alternative technology. In particular, the algorithm has been used for the results presented in the ATLAS pixel detector TDR for the upgrade foreseen in 2023. One of the proposed layout for the barrel part of the

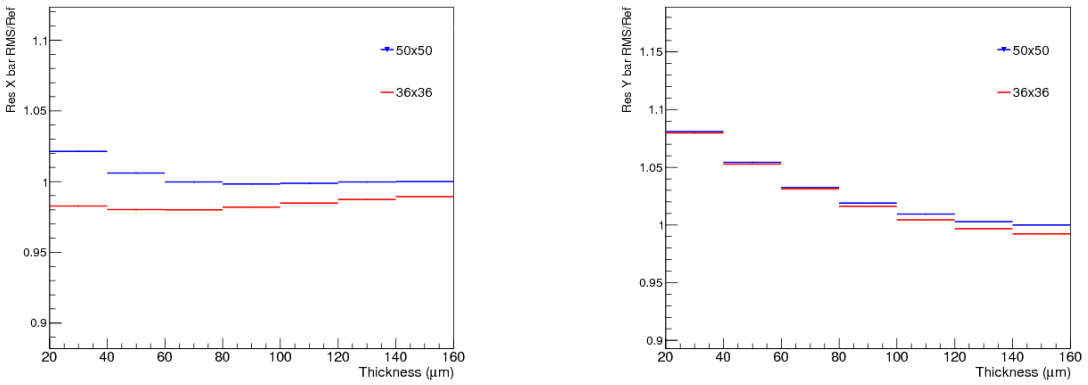

(a) (b)

Figure B.13: Track residuals in the fourth layer of the pixel tracker along local X (a) and Y (b) directions.

fourth layer of the pixel inner tracker is based on monolithic sensors that integrate

readout electronics with the silicon sensors. The thickness and pitch of these sensors are different from the planar pixels employed at the moment in ATLAS. In this context the fast digitization algorithm has been used to investigate the differences on detector performance due to the different sensor geometry. In Figure B.13 the residuals obtained employing sensors with two different surfaces (50 μm x 50 μm and 36 μm x 36 μm) are compared, as a function of the sensors thickness. The threshold on DTS length applied in the algorithm is re-scaled proportionally to the pixel area. The plots show that the residuals along local X are sensitive to the sensor area, while the sensor thickness has a larger impact on the residuals along local Y.

Appendix C

Tables with Systematic Uncertainties Breakdown

In this appendix are shown the tables with the breakdown of the systematic uncertainties affecting the particle level differential cross-section measurements, propagated as described in Chapter 6. Tables C.1, C.2 show the systematic components on the absoulte $p_T^{t,had}$, $|y^{t,had}|$ spectra in the boosted regime, while the uncertainties on relative spectra are shown in Tables C.3, C.4. The breakdown of uncertainties components on the $p_T^{t,had}$, $|y^{t,had}|$, $m^{t\bar{t}}$, $p_T^{t\bar{t}}$ and $|y^{t\bar{t}}|$ measured in the resolved topology are shown in Tables C.5- C.9 for the absolute spectra and in Tables C.10- C.14 for the relative ones. The values shown in this appendix are obtained by propagating the individual uncertainties to the measured cross-sections, while the covariance matrices are evaluated using pseudo-experiments as described in Chapter 7.

Bins [GeV]	300–350	350–400	400–450	450–500	500–550	550–650	650–750	750–1500
$d\sigma$ / $d\hat{p}_T^t$ [pb/GeV]	$1.91 \cdot 10^{-2}$	$1.22 \cdot 10^{-2}$	$6.92 \cdot 10^{-3}$	$3.97 \cdot 10^{-3}$	$2.79 \cdot 10^{-3}$	$1.75 \cdot 10^{-3}$	$4.19 \cdot 10^{-4}$	$5.72 \cdot 10^{-5}$
Total uncertainty [%]	$^{+20.5}_{-20.0}$	$^{+20.6}_{-19.9}$	$^{+19.6}_{-21.5}$	$^{+23.9}_{-23.6}$	$^{+27.8}_{-23.8}$	$^{+28.0}_{-26.4}$	± 38.1	$^{+37.8}_{-47.5}$
Statistical uncertainty [%]	± 2.5	± 3.3	± 4.7	± 6.6	± 8.5	± 8.1	$\pm 21.$	$\pm 22.$
Systematic uncertainty [%]	$^{+20.3}_{-19.8}$	$^{+20.3}_{-19.6}$	$^{+18.9}_{-20.9}$	$^{+22.9}_{-22.6}$	$^{+26.4}_{-22.1}$	$^{+26.7}_{-25.0}$	± 31.1	$^{+46.5}_{-40.5}$
Large-R jet Baseline (JES) [%]	$^{+13.0}_{-13.0}$	$^{+10.4}_{-9.53}$	$^{+7.76}_{-7.01}$	$^{+7.30}_{-7.02}$	$^{+7.08}_{-6.88}$	$^{+4.01}_{-5.01}$	$^{+8.39}_{-6.78}$	$^{+8.47}_{-6.43}$
Large-R jet Tracking (JES) [%]	$^{+6.70}_{-10.2}$	$^{+12.3}_{-11.7}$	$^{+12.8}_{-15.2}$	$^{+16.7}_{-16.0}$	$^{+22.1}_{-18.3}$	$^{+20.6}_{-20.1}$	$^{+25.9}_{-24.8}$	$^{+36.3}_{-29.7}$
Large-R jet Modelling (JES) [%]	$^{+7.90}_{-7.03}$	$^{+6.53}_{-6.47}$	$^{+4.52}_{-3.12}$	$^{+4.70}_{-3.37}$	$^{+3.88}_{-2.46}$	$^{+2.95}_{-3.98}$	$^{+3.03}_{-3.76}$	$^{+3.74}_{-2.90}$
Large-R jet CrossCalib r32 (JES) [%]	$^{+1.17}_{+0.38}$	$^{+1.50}_{+1.14}$	$^{+2.02}_{+1.62}$	$^{+2.02}_{+1.89}$	$^{+2.02}_{+1.82}$	$^{+3.13}_{+2.13}$	$^{+2.04}_{+2.82}$	$^{+4.07}_{+1.06}$
Large-R jet Run 1 r32 (JES) [%]	$^{+1.02}_{\mp 0.28}$	$^{+3.24}_{\mp 0.81}$	$^{+5.16}_{\mp 1.01}$	$^{+6.25}_{\mp 0.33}$	$^{+7.58}_{\mp 0.24}$	$^{+9.20}_{\mp 0.24}$	$^{+12.7}_{\mp 0.44}$	$^{+11.6}_{\mp 0.98}$
Large-R jet JMR [%]	-	-	-	-	-	$^{+0.19}_{-0.14}$	$^{+0.11}_{-0.11}$	$^{-0.41}_{-1.83}$
b-Tagged jet energy scale (JES) [%]	-	-	-	-	-	-	-	-
Effective detector NP set 1 (JES) [%]	$^{+0.67}_{+0.52}$	$^{+0.92}_{+0.28}$	$^{+0.88}_{+0.58}$	$^{+1.08}_{+0.46}$	$^{+1.20}_{+0.74}$	$^{+1.51}_{+0.59}$	$^{+0.38}_{+1.04}$	$^{+1.60}_{+0.71}$
Effective detector NP set 2 (JES) [%]	-0.22	$^{-0.57}_{-0.35}$	$^{-0.74}_{-0.25}$	-0.61	$^{-0.62}_{-0.27}$	$^{-0.85}_{-0.36}$	$^{-0.93}_{-0.41}$	-1.50
Effective detector NP set 3 (JES) [%]	∓ 0.10	∓ 0.12	∓ 0.10	∓ 0.14	∓ 0.12	∓ 0.14	∓ 0.33	∓ 0.33
Effective detector NP set 4 (JES) [%]	-0.14	-	-	-	-	-0.24	-	-0.50
Effective detector NP set 5 (JES) [%]	-	-	-	-	-	-	$^{+0.34}_{-0.21}$	$^{-0.50}_{-0.19}$
Effective detector NP set 6 restTerm (JES) [%]	-	-	-	-	-	-	$^{+0.21}_{-0.20}$	-
η intercalibration model (JES) [%]	-	$^{-0.94}_{-0.59}$	$^{+0.13}_{-0.55}$	-0.38	$^{+0.54}_{-0.37}$	$^{-0.78}_{+0.65}$	$^{+0.67}_{-0.23}$	$^{-2.60}_{+1.40}$
η intercalibration total stat (JES) [%]	∓ 0.12	∓ 0.23	$^{+0.45}_{-0.97}$	$^{+0.32}_{-0.95}$	$^{+0.59}_{-1.33}$	$^{+1.02}_{+0.63}$	$^{-0.82}_{+1.02}$	$^{-0.94}_{+0.96}$
Flavour composition (JES) [%]	-0.26	-0.53	$^{+0.16}_{+0.13}$	$+0.29$	$^{+0.48}_{+0.39}$	-1.20	$^{+0.39}_{+0.39}$	$^{-4.16}_{+1.81}$
Flavour response (JES) [%]	-	$^{-0.42}_{+0.24}$	$^{-0.89}_{+0.22}$	$^{-0.78}_{+0.29}$	$^{-0.77}_{+0.30}$	$^{-1.79}_{+0.45}$	$^{+0.59}_{+0.31}$	$^{-2.29}_{+0.48}$
Pile-up offset μ (JES) [%]	-	$^{+0.24}_{+0.16}$	$^{+0.22}_{+0.22}$	$^{+0.39}_{+0.29}$	$^{+0.30}_{\pm 0.14}$	$^{+0.24}_{-0.15}$	$^{+0.31}_{-0.13}$	$^{+0.37}_{-0.74}$
Pile-up offset N_{PV} (JES) [%]	-	-	$^{+0.10}_{-0.11}$	-	-	$^{-0.16}_{+0.16}$	$^{-0.13}_{+0.13}$	$^{-0.52}_{+0.52}$
Pile-up offset p_T (JES) [%]	-	-	$+0.12$	-	$^{-0.88}$	$^{+0.19}_{-0.19}$	$^{+0.21}_{-0.20}$	$^{+0.12}_{-0.12}$
Pile-up offset ρ topology (JES) [%]	-0.28	-0.66	-1.05	-0.90	-	-1.58	$^{+0.19}_{+0.21}$	$+0.95$
Punch-through (JES) [%]	-	-	-	-	-	-	-	-0.21
Single particle high-p_T (JES) [%]	-	-	-	-	-	-	-	-
Jet energy resolution [%]	∓ 0.82	∓ 1.24	∓ 1.74	∓ 2.23	∓ 2.41	∓ 2.80	∓ 2.02	∓ 5.32
Jet vertex fraction [%]	$^{+0.58}_{-0.54}$	$^{+0.55}_{-0.54}$	$^{+0.28}_{-0.97}$	$^{+0.75}_{-0.58}$	$^{+0.92}_{-0.86}$	$^{+0.24}_{-0.99}$	$^{+0.44}_{-1.04}$	$^{+0.45}_{-0.91}$
b-Quark tagging efficiency (eigenvector 0) [%]	$^{+0.94}_{-1.01}$	$^{+0.90}_{-1.19}$	$^{+0.94}_{-1.26}$	$^{+0.94}_{-1.22}$	$^{+0.82}_{-1.17}$	$^{+0.95}_{-1.37}$	$^{+1.01}_{-1.31}$	$^{+0.88}_{-1.48}$
b-Quark tagging efficiency (eigenvector 1) [%]	$+1.01$	$+1.08$	$+1.22$	$^{+1.09}_{-1.10}$	$+1.12$	$^{+1.27}_{-1.25}$	$^{+1.22}_{-1.22}$	$+1.36$
b-Quark tagging efficiency (eigenvector 2) [%]	-	∓ 0.12	∓ 0.14	∓ 0.12	∓ 0.18	∓ 0.21	∓ 0.14	∓ 0.20
b-Quark tagging efficiency (eigenvector 3) [%]	-	-0.33	-0.22	-0.28	-	-0.43	-0.57	-0.99
b-Quark tagging efficiency (eigenvector 4) [%]	-	-	-	-	-	-	-	-
c-Quark tagging efficiency (eigenvector 0) [%]	-0.52	-0.70	-0.55	-0.43	-0.57	-0.43	-0.43	-1.20
c-Quark tagging efficiency (eigenvector 1) [%]	∓ 0.12	∓ 0.15	∓ 0.20	-	∓ 0.10	∓ 0.10	∓ 0.23	$^{+0.59}_{-0.23}$
c-Quark tagging efficiency (eigenvector 2) [%]	-	-	-	-	-	-	-	∓ 0.22
c-Quark tagging efficiency (eigenvector 3) [%]	-	-	-	-	-	-	-	-
Light-jet tagging efficiency (eigenvector 0) [%]	-0.88	-0.59	-1.90	-1.10	-1.26	-0.74	-1.45	-7.21
Light-jet tagging efficiency (eigenvector 1) [%]	$+0.91$	$+0.62$	$+1.95$	$+1.09$	$+1.22$	$^{+0.73}_{-0.73}$	$+1.99$	$+7.14$
Light-jet tagging efficiency (eigenvector 2) [%]	-	-	∓ 0.11	∓ 0.10	-	-0.13	-	∓ 0.61
Light-jet tagging efficiency (eigenvector 3) [%]	-	-	∓ 0.11	-	-	-	-	∓ 0.25
Light-jet tagging efficiency (eigenvector 4) [%]	-	-	-	-	-	-	-	∓ 0.35
Light-jet tagging efficiency (eigenvector 5) [%]	-	-	-	-	-	-	-	∓ 0.38
Light-jet tagging efficiency (eigenvector 6) [%]	-	-	-	-	-	-	-	∓ 0.50
Light-jet tagging efficiency (eigenvector 7) [%]	-	-	-	-	-	-	-	∓ 0.19
Light-jet tagging efficiency (eigenvector 8) [%]	-	-	-	-	-	-	-	∓ 0.26
Light-jet tagging efficiency (eigenvector 9) [%]	-	-	-	-	-	-	-	-
Light-jet tagging efficiency (eigenvector 10) [%]	-	-	-	-	-	-	-	-
Light-jet tagging efficiency (eigenvector 11) [%]	-	-	-	-	-	-	-	-
b-Quark tagging extrapolation [%]	$^{+0.61}_{-0.62}$	$^{+0.88}_{-0.91}$	$^{+1.13}_{-1.16}$	$^{+1.12}_{-1.17}$	$^{+1.24}_{-1.29}$	$^{+1.34}_{-1.44}$	$^{+1.00}_{-1.09}$	$^{+3.71}_{-3.98}$
b-Quark tagging extrapolation from c-Quark [%]	-	-	-	-	-	-	-	∓ 0.14
Electron energy resolution [%]	-	-	-0.24	-	-0.28	$^{-0.44}_{-0.30}$	$^{-0.16}_{+0.14}$	$^{-1.75}_{-0.37}$
Electron energy scale [%]	-	-	-	-	-	-	∓ 0.42	-1.29
Electron trigger efficiency [%]	± 0.30	± 0.31	± 0.33	± 0.34	± 0.35	± 0.35	± 0.35	± 0.39
Electron reconstruction efficiency [%]	± 0.23	± 0.24	± 0.26	± 0.27	± 0.28	± 0.29	± 0.30	± 0.35
Electron identification efficiency [%]	± 0.61	± 0.68	± 0.76	± 0.80	± 0.88	± 0.92	± 1.00	± 1.18
Electron isolation efficiency [%]	± 0.31	± 0.39	± 0.47	± 0.51	± 0.57	± 0.61	± 0.70	± 0.84
Muon energy scale [%]	-	-	-	-	-	-	-	-
Muon (MS) momentum resolution [%]	-	-	-	-	-	-	-	-
Muon (ID) momentum resolution [%]	-	-	-	-	-	-	-	-
Muon trigger efficiency stat [%]	-	-	-	-	-	-	-	-
Muon trigger efficiency syst [%]	± 0.26	± 0.26	± 0.26	$^{+0.26}_{-0.25}$	± 0.25	± 0.25	± 0.27	± 0.26
Muon identification stat [%]	-	-	-	-	-	-	-	-
Muon identification syst [%]	± 0.28	± 0.33	± 0.36	± 0.39	± 0.38	± 0.41	± 0.47	$^{+0.48}_{-0.47}$
Muon isolation efficiency stat [%]	-	-	-	-	-	-	-	-
Muon isolation efficiency syst [%]	± 0.11	± 0.11	± 0.12	± 0.11	± 0.12	± 0.14	± 0.23	± 0.25
Muon TTVA efficiency stat [%]	-	-	-	-	-	-	-	-
Muon TTVA efficiency syst [%]	-	-	-	-	-	-	-	-
E_T^{miss} Soft jet resolution para [%]	-	-	-	-	-	± 0.13	± 0.41	∓ 2.23
E_T^{miss} Soft jet resolution perp [%]	∓ 0.37	∓ 0.42	∓ 0.32	∓ 0.28	∓ 0.32	∓ 0.63	∓ 0.79	∓ 0.85
E_T^{miss} Soft jet scale [%]	$^{-0.29}_{+0.10}$	$^{-0.23}_{+0.10}$	-	-	$^{-0.13}$	$^{-0.35}$	$^{-0.53}$	$^{-0.98}$
Luminosity [%]	∓ 2.05	∓ 2.05	∓ 2.05	∓ 2.05	∓ 2.05	∓ 2.05	∓ 2.05	∓ 2.05
W+jets CA_{Rscr} stat error [%]	-	-	-	-	-	-	-	-
W+jets CA_{Rscr} stat error [%]	-	-	-	-	-	-	-	-
W+jets CA_{Mmcf} stat error [%]	± 0.17	± 0.16	± 0.20	± 0.20	± 0.26	± 0.23	± 0.30	± 0.90
W+jets Fcc stat error [%]	-	-	-	-0.16	-	$^{+0.50}_{-0.85}$	$^{+0.47}_{-0.79}$	$^{-1.70}_{+2.88}$
W+jets Flight stat error [%]	-	-	-	-	-	-	-	-
W+jets Fc error [%]	-	-	-	-	-	$^{+0.11}_{-0.12}$	-	$^{+0.48}_{-0.53}$
QCD norm. impact on W+jets [%]	$^{+0.56}_{-0.61}$	$^{+0.71}_{-0.78}$	$^{+1.13}_{-1.24}$	$^{+0.97}_{-1.07}$	$^{+1.04}_{-1.14}$	$^{+1.90}_{-2.09}$	$^{+1.72}_{-1.87}$	$^{+1.48}_{-1.55}$
Single top cross-section [%]	± 0.32	± 0.33	± 0.33	± 0.36	± 0.37	± 0.45	± 0.49	± 0.63
Z+jets cross-section [%]	± 0.23	± 0.29	± 0.61	± 0.50	± 0.12	± 0.23	± 1.23	± 1.51
Diboson cross-section [%]	± 0.25	± 0.28	± 0.29	± 0.32	± 0.49	± 0.50	± 0.64	± 1.16
$t\bar{t}V$ cross-section [%]	± 0.10	± 0.13	± 0.15	± 0.18	± 0.22	± 0.26	± 0.31	± 0.40
Monte Carlo sample statistics [%]	± 0.81	± 1.06	± 1.61	± 1.65	± 2.26	± 2.23	± 4.37	± 9.25
ISR/FSR + scale [%]	$^{-2.27}_{+6.31}$	$^{-1.86}_{+3.98}$	$^{-1.18}_{+5.81}$	$^{-3.80}_{+5.29}$	$^{+6.27}$	$^{+8.89}$	$^{-4.61}_{+2.86}$	$^{-1.43}_{+7.92}$
Alternate hard-scattering model [%]	± 0.17	± 4.92	± 0.99	± 2.70	∓ 2.24	∓ 6.00	± 0.53	± 16.6
Alternate parton-shower model [%]	∓ 7.25	∓ 6.24	∓ 4.40	∓ 4.56	∓ 0.44	∓ 0.84	∓ 11.9	± 0.70
Inter PDF [%]	-	-	∓ 0.14	± 0.20	± 0.15	± 0.12	± 1.54	± 0.61
Intra PDF [%]	± 0.10	± 0.12	± 0.43	± 0.47	± 0.16	± 0.68	± 0.66	± 0.65
Real lepton efficiency stat [%]	$^{+0.24}_{-0.24}$	$^{+0.28}_{-0.28}$	$^{+0.40}_{-0.40}$	$^{+0.31}_{-0.31}$	$^{+0.53}_{-0.53}$	$^{+0.78}_{-0.78}$	$^{+0.73}_{-0.73}$	$^{+0.93}_{-0.93}$
Fake lepton efficiency MC scale [%]	$^{-0.63}_{+0.53}$	$^{-0.87}_{+0.72}$	$^{-1.22}_{+1.01}$	$^{-1.14}_{+1.02}$	$^{-0.99}_{+0.98}$	$^{-0.95}_{+0.82}$	$^{-1.28}_{+1.24}$	$^{-1.03}_{+1.05}$
Fake lepton efficiency alternate CR [%]	-	± 0.24	-	± 0.39	± 0.44	± 1.01	± 2.19	± 1.09
Poor MTW Modelling in QCD [%]	∓ 0.46	∓ 0.39	∓ 0.40	∓ 0.86	∓ 1.01	∓ 1.15	∓ 3.74	∓ 4.24

Table C.1: Table of systematic uncertainties for the absolute differential cross-section at particle level for the top quark transverse momentum in the boosted regime.

Bins / Unit $[\|y^t\|]$	0–0.20	0.20–0.40	0.40–0.60	0.60–0.80	0.80–1	1–1.20	1.20–1.40	1.40–1.60	1.60–1.80	1.80–2
$d\sigma$ / $d\|y^t\|$ $\cdot b$ / Unit $[\|y^t\|]$	$1.90 \cdot 10^{0}$	$1.94 \cdot 10^{0}$	$1.71 \cdot 10^{0}$	$1.60 \cdot 10^{0}$	$1.41 \cdot 10^{0}$	$1.29 \cdot 10^{0}$	$1.05 \cdot 10^{0}$	$8.63 \cdot 10^{-1}$	$5.56 \cdot 10^{-1}$	$3.58 \cdot 10^{-1}$
Total uncertainty [%]	$^{+22.3}_{-20.0}$	±19.6	$^{+20.8}_{-21.8}$	$^{+21.0}_{-20.6}$	$^{+19.9}_{-20.8}$	$^{+22.5}_{-21.0}$	$^{+23.1}_{-22.2}$	$^{+22.4}_{-21.4}$	$^{+22.1}_{-25.3}$	$^{+26.8}_{-25.3}$
Statistical uncertainty [%]	±4.0	±4.2	±4.6	±4.7	±4.9	±5.0	±5.6	±6.1	±7.8	±8.6
Systematic uncertainty [%]	$^{+21.9}_{-19.6}$	±19.1	$^{+20.2}_{-21.3}$	$^{+20.3}_{-20.0}$	$^{+19.2}_{-20.2}$	$^{+21.9}_{-20.3}$	$^{+22.3}_{-21.4}$	$^{+21.5}_{-20.4}$	$^{+20.3}_{-23.9}$	$^{+24.0}_{-23.6}$
Large-R jet Baseline (JES) [%]	$^{+9.9}_{-9.53}$	$^{+10.5}_{-9.92}$	$^{+9.83}_{-9.48}$	$^{+10.0}_{-9.26}$	$^{+9.68}_{-9.10}$	$^{+11.1}_{-9.39}$	$^{+10.6}_{-9.87}$	$^{+10.5}_{-9.76}$	$^{+11.3}_{-11.1}$	$^{+11.4}_{-10.4}$
Large-R jet Tracking (JES) [%]	$^{+15.4}_{-15.1}$	$^{+11.8}_{-13.6}$	$^{+12.3}_{-13.7}$	$^{+12.7}_{-13.5}$	$^{+12.6}_{-13.0}$	$^{+14.1}_{-13.7}$	±13.0	$^{+13.0}_{-13.9}$	$^{+12.1}_{-16.0}$	$^{+17.4}_{-15.6}$
Large-R jet Modelling (JES) [%]	$^{+6.85}_{-6.09}$	$^{+5.99}_{-6.20}$	$^{+6.22}_{-6.40}$	$^{+6.29}_{-5.89}$	$^{+5.68}_{-6.21}$	$^{+6.79}_{-6.48}$	$^{+6.29}_{-6.29}$	$^{+6.87}_{-6.13}$	$^{+6.56}_{-7.17}$	$^{+6.26}_{-6.78}$
Large-R jet CrossCalib τ32 (JES) [%]	$^{+1.91}_{+6.95}$	$^{+1.96}_{+9.74}$	$^{+1.87}_{+9.86}$	$^{+2.10}_{+1.46}$	$^{+1.67}_{+1.93}$	$^{+2.10}_{+1.83}$	$^{+1.27}_{+1.90}$	$^{+2.46}_{+1.71}$	$^{+3.60}_{+1.98}$	$^{+1.88}_{+2.95}$
Large-R jet Run1 τ32 (JES) [%]	$^{+6.95}_{+1.88}$	$^{+9.74}_{+2.49}$	$^{+9.86}_{+2.46}$	$^{+1.46}_{+3.26}$	$^{+1.93}_{+3.95}$	$^{+1.83}_{+5.09}$	$^{+1.90}_{+5.59}$	$^{+1.71}_{+5.98}$	$^{+1.98}_{+5.95}$	$^{+2.95}_{+6.06}$
Large-R jet JMR [%]	$^{+0.53}_{-0.53}$	$^{+0.45}_{-0.45}$	$^{+0.61}_{-0.61}$	$^{+0.40}_{-0.40}$	$^{+0.44}_{-0.44}$	$^{+1.01}_{-1.01}$	$^{+0.82}_{-0.82}$	±0.21	$^{+0.60}_{-0.60}$	$^{+1.16}_{-1.16}$
b-Tagged jet energy scale (JES) [%]	-	-	$^{+0.20}_{-0.20}$	-	-	-	$^{+0.19}_{-0.19}$	-	-	$^{+0.26}_{-0.26}$
Effective detector NP set 1 (JES) [%]	$^{-0.74}_{+0.36}$	$^{+0.65}_{+0.33}$	$^{-0.59}_{+0.40}$	$^{-0.91}_{+0.50}$	$^{-1.09}_{+0.35}$	$^{-0.86}_{+0.59}$	$^{-0.29}_{+0.44}$	$^{-0.99}_{+0.17}$	$^{-0.62}_{+0.38}$	$^{-0.77}_{+0.51}$
Effective detector NP set 2 (JES) [%]	$^{-0.44}_{+0.23}$	$^{-0.53}_{+0.22}$	$^{-0.33}_{+0.26}$	$^{-0.71}_{+0.23}$	$^{-0.50}_{+0.25}$	$^{-0.45}_{-}$	$^{-0.71}_{+0.43}$	$^{-0.40}_{+0.35}$	$^{-0.44}_{+0.22}$	$^{+0.61}_{-}$
Effective detector NP set 3 (JES) [%]	±0.20	$^{+0.13}_{-}$	$^{+0.20}_{-0.20}$	$^{+0.14}_{-}$	-	-	-	-	$^{+0.13}_{-}$	-
Effective detector NP set 4 (JES) [%]	$^{-0.18}_{-}$	-	$^{+0.12}_{-0.12}$	-	-	-	$^{-0.20}_{-}$	-	-	-
Effective detector NP set 5 (JES) [%]	-	-	-	-	-	-	-	-	-	-
Effective detector NP set 6 restTerm (JES) [%]	-	-	-	-	-	-	-	-	-	-
η intercalibration model (JES) [%]	$^{-0.62}_{-0.44}$	$^{-0.47}_{-0.24}$	$^{-0.38}_{-0.34}$	$^{+0.53}_{+0.10}$	$^{-0.29}_{-0.24}$	$^{+0.17}_{+0.30}$	$^{-0.26}_{-0.60}$	$^{-0.36}_{-0.32}$	$^{-0.32}_{-0.39}$	$^{+0.85}_{+0.30}$
η intercalibration total stat (JES) [%]	$^{+0.28}_{-}$	$^{+0.33}_{-0.33}$	$^{+0.31}_{-}$	$^{+0.27}_{-0.75}$	$^{+0.12}_{-}$	$^{+0.55}_{-0.63}$	$^{+0.21}_{-0.63}$	$^{-}$	$^{+0.36}_{-0.87}$	$^{+0.48}_{+0.31}$
Flavour composition (JES) [%]	$^{-0.66}_{-}$	$^{-}$	$^{-0.48}_{+0.20}$	$^{+0.24}_{-}$	$^{-0.51}_{-}$	$^{+0.24}_{-}$	$^{+0.22}_{+0.11}$	$^{-1.02}_{-}$	$^{-}$	$^{+0.44}_{-}$
Flavour response (JES) [%]	$^{-0.54}_{+0.26}$	$^{-0.40}_{+0.17}$	$^{-0.51}_{+0.25}$	$^{-0.79}_{+0.25}$	$^{-0.42}_{+0.19}$	$^{-0.36}_{-0.13}$	$^{-0.51}_{-0.35}$	$^{-0.85}_{-0.21}$	$^{-0.22}_{-0.20}$	$^{-0.11}_{+0.78}$
Pile-up offset μ (JES) [%]	$^{+0.26}_{+0.15}$	$^{+0.17}_{+0.24}$	$^{+0.25}_{+0.19}$	$^{+0.25}_{\pm 0.15}$	$^{+0.19}_{+0.16}$	$^{-0.13}_{+0.20}$	$^{-0.35}_{-}$	$^{+0.18}_{-0.22}$	$^{-}$	$^{+0.79}_{-}$
Pile-up offset N_{PV} (JES) [%]	$^{-0.10}_{+0.12}$	$^{-}$	$^{-0.11}_{-}$	$^{-}$	$^{-}$	$^{-}$	$^{-}$	$^{-}$	$^{-}$	$^{-0.50}_{+0.10}$
Pile-up offset p_T (JES) [%]	-	-	$^{-0.70}_{-}$	-	-	$^{-0.53}_{-}$	-	-	-	$^{+0.10}_{-}$
Pile-up offset ρ topology (JES) [%]	$^{-0.71}_{-}$	$^{-0.62}_{-}$	$^{-}$	$^{-0.87}_{-}$	$^{-0.61}_{-}$	$^{-}$	$^{-0.57}_{-}$	$^{-0.73}_{-}$	$^{-0.95}_{-}$	$^{-0.31}_{-}$
Punch-through (JES) [%]	-	-	-	-	-	-	-	-	-	-
Single particle high-p_T (JES) [%]	-	-	-	-	-	-	-	-	-	-
Jet energy resolution [%]	$^{+1.88}_{+0.76}$	$^{+1.11}_{+0.56}$	$^{+2.13}_{+0.27}$	$^{+1.02}_{+0.43}$	$^{+0.72}_{+0.48}$	$^{+1.77}_{\pm 0.65}$	$^{+1.00}_{+0.70}$	$^{+1.46}_{+0.42}$	$^{+1.34}_{+0.52}$	$^{+2.06}_{+0.44}$
Jet vertex fraction [%]	$^{-0.70}_{-0.97}$	$^{-0.52}_{-0.84}$	$^{-0.88}_{-}$	$^{-0.34}_{-0.96}$	$^{-0.47}_{-0.92}$	$^{-0.91}_{-0.91}$	$^{-0.63}_{-1.08}$	$^{-0.39}_{-1.06}$	$^{-0.48}_{-1.03}$	$^{-0.35}_{-1.10}$
b-Quark tagging efficiency (eigenvector 0) [%]	$^{+0.94}_{-1.15}$	$^{+0.80}_{-1.09}$	$^{+0.85}_{-1.14}$	$^{+0.92}_{-1.22}$	$^{+0.88}_{-1.13}$	$^{+0.88}_{-1.14}$	$^{+1.04}_{-1.16}$	$^{+1.03}_{-1.29}$	$^{+1.01}_{-1.13}$	$^{+1.06}_{-1.37}$
b-Quark tagging efficiency (eigenvector 1) [%]	$^{+1.06}_{-}$	$^{+1.01}_{-}$	$^{+1.07}_{-}$	$^{+1.15}_{-}$	$^{+1.04}_{-}$	$^{+1.07}_{-}$	$^{+1.03}_{-}$	$^{+1.22}_{-}$	$^{+1.05}_{-}$	$^{+1.33}_{-}$
b-Quark tagging efficiency (eigenvector 2) [%]	-	-	±0.11	±0.11	-	-	-	±0.15	-	±0.15
b-Quark tagging efficiency (eigenvector 3) [%]	$^{-0.21}_{-}$	$^{-0.36}_{-}$	$^{-0.33}_{-}$	-	$^{-0.33}_{-}$	$^{-0.30}_{-}$	-	-	-	-
b-Quark tagging efficiency (eigenvector 4) [%]	-	-	-	-	-	-	-	-	-	-
c-Quark tagging efficiency (eigenvector 0) [%]	$^{-0.53}_{+0.15}$	$^{-0.65}_{+0.30}$	$^{-0.62}_{+0.31}$	$^{-0.62}_{+0.30}$	$^{-0.50}_{+0.16}$	$^{-0.45}_{+0.14}$	$^{-0.69}_{+0.42}$	$^{-0.49}_{+0.18}$	$^{-0.48}_{+0.15}$	$^{-0.66}_{+0.27}$
c-Quark tagging efficiency (eigenvector 1) [%]	-	∓0.18	∓0.17	∓0.20	-	∓0.16	-	∓0.10	∓0.13	∓0.24
c-Quark tagging efficiency (eigenvector 2) [%]	-	-	-	-	-	-	-	-	-	-
c-Quark tagging efficiency (eigenvector 3) [%]	-	-	-	-	-	-	-	-	-	-
Light-jet tagging efficiency (eigenvector 0) [%]	$^{-1.02}_{+0.99}$	$^{-0.54}_{+0.60}$	$^{-0.83}_{+0.87}$	$^{-1.40}_{+1.44}$	$^{-0.93}_{+0.95}$	$^{-0.56}_{+0.55}$	$^{-1.23}_{+1.22}$	$^{-1.89}_{+2.19}$	$^{-2.51}_{+2.47}$	$^{-1.24}_{+1.26}$
Light-jet tagging efficiency (eigenvector 1) [%]	±0.21	±0.10	±0.14	-	±0.14	-	-	-	∓0.22	∓0.14
Light-jet tagging efficiency (eigenvector 2) [%]	-	-	-	-	-	-	-	-	∓0.20	-
Light-jet tagging efficiency (eigenvector 3) [%]	-	-	-	-	-	-	-	-	-	-
Light-jet tagging efficiency (eigenvector 4) [%]	-	-	-	-	-	-	-	-	-	-
Light-jet tagging efficiency (eigenvector 5) [%]	-	-	-	-	-	-	-	-	-	-
Light-jet tagging efficiency (eigenvector 6) [%]	-	-	-	-	-	-	-	-	-	-
Light-jet tagging efficiency (eigenvector 7) [%]	-	-	-	-	-	-	-	-	-	-
Light-jet tagging efficiency (eigenvector 8) [%]	-	-	-	-	-	-	-	-	-	-
Light-jet tagging efficiency (eigenvector 9) [%]	-	-	-	-	-	-	-	-	-	-
Light-jet tagging efficiency (eigenvector 10) [%]	-	-	-	-	-	-	-	-	-	-
Light-jet tagging efficiency (eigenvector 11) [%]	-	-	-	-	-	-	-	-	-	-
b-Quark tagging extrapolation [%]	$^{+0.95}_{-0.98}$	$^{+0.88}_{-0.92}$	$^{+0.97}_{-1.00}$	$^{+0.91}_{-0.94}$	$^{+0.76}_{-0.80}$	$^{+0.98}_{-1.02}$	$^{+0.86}_{-0.88}$	$^{+0.99}_{-1.02}$	$^{+0.70}_{-0.72}$	$^{+1.19}_{-1.22}$
b-Quark tagging extrapolation from c-Quark [%]	-	-	-	-	-	-	-	-	-	-
Electron energy resolution [%]	$^{-0.23}_{-}$	-	-	$^{-0.32}_{-}$	-	-	$^{-0.36}_{-}$	$^{+0.17}_{-}$	-	$^{-0.20}_{-0.21}$
Electron energy scale [%]	-	-	-	-	-	-	-	-	-	-
Electron trigger efficiency [%]	±0.31	±0.31	±0.31	±0.32	±0.32	±0.31	±0.32	±0.34	±0.35	±0.34
Electron reconstruction efficiency [%]	±0.24	±0.25	±0.25	±0.25	±0.25	±0.24	±0.24	±0.26	±0.26	±0.25
Electron identification efficiency [%]	±0.70	±0.71	±0.70	±0.71	±0.71	±0.69	±0.69	±0.74	±0.71	±0.70
Electron isolation efficiency [%]	±0.41	±0.41	±0.41	±0.42	±0.42	±0.40	±0.40	±0.43	±0.40	±0.39
Muon energy scale [%]	-	-	-	-	-	-	-	-	-	-
Muon (MS) momentum resolution [%]	-	-	-	-	-	-	-	-	-	-
Muon (ID) momentum resolution [%]	-	-	-	-	-	-	-	-	-	-
Muon trigger efficiency stat [%]	-	-	-	-	-	-	-	-	-	-
Muon trigger efficiency syst [%]	±0.26	±0.26	±0.26	±0.26	±0.26	±0.25	$^{+0.28}_{-0.27}$	±0.25	±0.26	±0.25
Muon identification stat [%]	-	-	-	-	-	-	-	-	-	-
Muon identification syst [%]	±0.33	$^{+0.33}_{-0.32}$	±0.33	±0.33	±0.33	±0.32	±0.35	±0.31	±0.37	±0.32
Muon isolation efficiency stat [%]	-	-	-	-	-	-	-	-	-	-
Muon isolation efficiency syst [%]	±0.12	±0.12	±0.12	±0.12	±0.12	±0.11	±0.12	±0.11	±0.12	±0.11
Muon TTVA efficiency stat [%]	-	-	-	-	-	-	-	-	-	-
Muon TTVA efficiency syst [%]	-	-	-	-	-	-	-	-	-	-
E_T^{miss} Soft jet resolution para [%]	±0.12	-	-	-	∓0.27	-	-	-	-	±0.13
E_T^{miss} Soft jet resolution perp [%]	±0.48	∓0.31	∓0.52	∓0.34	∓0.49	∓0.43	∓0.30	∓0.18	∓0.22	∓0.40
E_T^{miss} Soft jet scale [%]	$^{-0.22}_{+0.10}$	$^{-0.22}_{+0.14}$	$^{-0.20}_{-}$	$^{-0.26}_{-}$	$^{-0.36}_{-}$	$^{-0.35}_{-}$	$^{-0.17}_{-}$	$^{-0.31}_{-}$	$^{-}$	$^{-}$
Luminosity [%]	∓2.05	∓2.05	∓2.05	∓2.05	∓2.05	∓2.05	∓2.05	∓2.05	∓2.05	∓2.05
W+jets CA_{bcr} stat error [%]	-	-	-	-	-	-	-	-	-	-
W+jets CA_{tcr} stat error [%]	-	-	-	-	-	-	-	-	-	-
W+jets CA_{tmcf} stat error [%]	±0.18	±0.17	±0.19	±0.23	±0.16	±0.17	±0.21	±0.22	±0.24	±0.20
W+jets Fcc stat error [%]	$^{-}_{-0.13}$	$^{+0.10}_{-0.18}$	$^{+0.16}_{-0.27}$	$^{-0.12}_{+0.20}$	$^{-}_{-}$	$^{+0.19}_{-0.33}$	$^{-0.52}_{+0.87}$	$^{-0.12}_{+0.21}$	$^{-0.11}_{+0.20}$	$^{-0.14}_{+0.24}$
W+jets Flight stat error [%]	-	-	-	-	-	-	-	-	-	-
W+jets Fc error [%]	-	-	-	-	-	-	$^{+0.10}_{-0.16}$	-	$^{+0.11}_{+0.17}$	$^{+0.12}_{+0.13}$
QCD norm. impact on W+jets [%]	$^{+0.94}_{-1.04}$	$^{+0.79}_{-0.77}$	$^{+1.04}_{-1.15}$	$^{+0.80}_{-0.87}$	$^{+0.61}_{-0.66}$	$^{+0.91}_{-1.00}$	$^{+0.44}_{-0.44}$	$^{+0.97}_{-1.08}$	$^{+1.37}_{-1.50}$	$^{+0.63}_{-0.73}$
Single top cross-section [%]	±0.37	±0.35	±0.36	±0.33	±0.35	±0.33	±0.31	±0.32	±0.33	±0.31
Z+jets cross-section [%]	±0.20	±0.33	±0.18	±0.31	±0.52	±0.17	±0.43	±0.47	±0.78	±0.11
Diboson cross-section [%]	±0.30	±0.29	±0.28	±0.29	±0.34	±0.32	±0.26	±0.40	±0.33	±0.34
$t\bar{t}V$ cross-section [%]	±0.15	±0.14	±0.14	±0.14	±0.14	±0.14	±0.14	±0.14	±0.13	±0.12
Monte Carlo sample statistics [%]	$^{+1.09}_{-0.62}$	$^{+1.14}_{-0.68}$	$^{+1.26}_{-0.90}$	$^{+1.69}_{-3.60}$	$^{+1.39}_{-1.86}$	$^{+1.40}_{-4.58}$	$^{+2.41}_{+9.95}$	$^{+1.92}_{-0.74}$	$^{+3.10}_{-2.48}$	$^{+2.79}_{-6.78}$
ISR/FSR τ scale [%]	$^{+8.00}_{-}$	$^{+5.43}_{-}$	$^{+3.03}_{-}$	$^{+8.49}_{-}$	$^{+3.36}_{-}$	$^{+4.84}_{-}$	$^{-}$	$^{+8.30}_{-}$	$^{+5.06}_{-}$	$^{+0.46}_{-}$
Alternate hard-scattering model [%]	±2.75	±1.55	±4.30	±0.31	±3.43	±1.79	±5.90	±0.11	±0.98	±2.12
Alternate parton-shower model [%]	±6.30	±6.75	±8.35	±5.20	±6.09	±3.82	±0.47	±1.66	±4.72	±4.88
Inter PDF [%]	±0.32	-	±0.20	±0.39	±0.22	-	±0.36	±0.82	±0.24	-
Intra PDF [%]	±0.22	±0.26	±0.15	±0.29	±0.21	±0.29	±0.35	±0.38	±0.71	±1.10
Real lepton efficiency stat [%]	$^{+0.34}_{-0.34}$	$^{+0.36}_{-0.36}$	$^{+0.32}_{-0.32}$	$^{+0.35}_{-0.35}$	$^{+0.34}_{-0.34}$	$^{+0.31}_{-0.31}$	$^{+0.29}_{-0.29}$	$^{+0.34}_{-0.34}$	$^{+0.27}_{-0.27}$	$^{+0.51}_{-0.51}$
Fake lepton efficiency MC scale [%]	$^{-0.62}_{+0.53}$	$^{-0.78}_{+0.68}$	$^{-1.03}_{+0.84}$	$^{-1.01}_{+0.86}$	$^{-0.80}_{+0.70}$	$^{-0.36}_{+0.24}$	$^{-1.78}_{+1.56}$	$^{-1.88}_{+0.84}$	$^{-1.19}_{+0.97}$	$^{-0.16}_{-0.14}$
Fake lepton efficiency alternate CR [%]	±0.17	±0.21	±0.29	±0.17	±0.18	±0.16	±0.62	±0.41	±0.23	±1.02
Poor MTW Modelling in QCD [%]	±0.31	∓0.28	∓1.13	∓0.46	∓0.64	∓0.30	∓0.87	∓0.40	∓2.03	∓0.44

Table C.2: Table of systematic uncertainties for the absolute differential cross-section at particle level for the absolute value of the top quark rapidity in the boosted regime.

Bins [GeV]	300–350	350–400	400–450	450–500	500–550	550–650	650–750	750–1500
$1/\sigma \cdot d\sigma \,/\, dp_T^t$	$7.60 \cdot 10^{-3}$	$4.86 \cdot 10^{-3}$	$2.76 \cdot 10^{-3}$	$1.58 \cdot 10^{-3}$	$1.12 \cdot 10^{-3}$	$6.98 \cdot 10^{-4}$	$1.67 \cdot 10^{-4}$	$2.28 \cdot 10^{-5}$
Total uncertainty [%]	$^{+7.15}_{-7.40}$	$^{+5.88}_{-5.76}$	$^{+5.97}_{-6.45}$	$^{+8.50}_{-8.75}$	$^{+15.3}_{-13.1}$	$^{+16.1}_{-15.7}$	$^{+26.6}_{-27.6}$	$^{+38.2}_{-37.7}$
Statistical uncertainty [%]	± 2.2	± 3.2	± 4.5	± 6.3	± 8.2	± 7.8	$\pm 21.$	$\pm 22.$
Systematic uncertainty [%]	$^{+6.73}_{-6.99}$	$^{+4.83}_{-4.67}$	$^{+3.50}_{-4.26}$	$^{+5.40}_{-5.79}$	$^{+12.7}_{-9.97}$	$^{+13.9}_{-13.4}$	$^{+15.4}_{-17.0}$	$^{+29.3}_{-28.7}$
Large-R jet Baseline (JES) [%]	$^{+2.89}_{-3.05}$	$^{+0.28}_{-0.90}$	$^{+1.38}_{+1.47}$	$^{-2.00}_{+1.90}$	$^{-2.52}_{+1.81}$	$^{+1.71}_{+1.67}$	$^{-5.09}_{+2.72}$	$^{-7.24}_{+3.19}$
Large-R jet Tracking (JES) [%]	$^{-3.48}_{+1.26}$	$^{-1.12}_{+2.70}$	$^{-1.45}$	$^{+3.83}_{-3.42}$	$^{+7.58}_{-5.31}$	$^{+6.65}_{-7.10}$	$^{+8.69}_{-15.5}$	$^{+10.8}_{-18.3}$
Large-R jet Modelling (JES) [%]	$^{+1.69}_{-1.72}$	$^{+0.40}_{-0.48}$	$^{-0.73}_{+0.94}$	$^{-1.32}_{+0.70}$	$^{-2.09}_{+3.77}$	$^{-2.97}_{+2.19}$	$^{-2.90}_{+2.39}$	$^{-2.22}_{+3.90}$
Large-R jet CrossCalib r32 (JES) [%]	$^{+0.82}_{+2.93}$	$^{+0.48}_{-2.16}$	$^{-0.79}_{+0.31}$	$^{-0.75}_{+0.57}$	$^{-0.63}_{+9.59}$	$^{-1.17}_{+1.49}$	$^{-0.97}_{+2.47}$	$^{-2.65}_{+7.12}$
Large-R jet Run1 r32 (JES) [%]	$^{-3.00}$	$^{-0.87}$	$^{+0.97}$	$^{+2.01}$	$^{+3.29}$	$^{+4.84}$	$^{+8.24}$	$^{+7.23}$
Large-R jet JMR [%]	± 0.25	∓ 0.28	∓ 0.47	± 0.20	± 0.29	± 0.29	± 0.10	∓ 0.44
b-Tagged jet energy scale (JES) [%]	-	-	-	-	-	$^{+0.18}$	$^{-0.16}_{+0.24}$	$^{-0.42}$
Effective detector NP set 1 (JES) [%]	$^{+0.56}_{-0.21}$	$^{+0.29}_{-0.47}$	$^{-0.22}_{+0.37}$	$^{-0.44}_{+0.39}$	$^{-0.63}_{+0.36}$	$^{-0.87}$	$^{+0.24}_{+0.62}$	$^{+1.22}_{+2.12}$
Effective detector NP set 2 (JES) [%]	$^{-0.10}_{+0.31}$	-	$^{+0.16}_{-0.20}$	-	$^{+0.31}$	$^{-0.32}$	$^{+0.24}_{-0.40}$	$^{+0.24}_{-0.97}$
Effective detector NP set 3 (JES) [%]	-	-	-	-	-	-	$^{-0.18}_{+0.21}$	$^{-0.23}$
Effective detector NP set 4 (JES) [%]	-	-	-	-	-	-	-	$^{-0.49}$
Effective detector NP set 5 (JES) [%]	-	-	-	-	-	-	$^{+0.26}$	$^{-0.26}$
Effective detector NP set 6 restTerm (JES) [%]	-	-	-	-	-	-	$^{+0.24}$	-
η intercalibration model (JES) [%]	$^{+0.28}_{-0.34}$	-	$^{-0.23}_{+0.14}$	-	$^{-0.16}_{+0.20}$	$^{-0.44}_{-0.41}$	$^{+1.08}_{-0.27}$	$^{-2.30}_{+1.51}$
η intercalibration total stat (JES) [%]	$^{+0.20}_{-0.27}$	$^{+0.12}$	$^{+0.12}_{-0.35}$	$^{-0.29}$	$^{-0.67}$	$^{+0.32}$	$^{+0.70}_{-1.06}$	$^{+0.62}_{-3.52}$
Flavour composition (JES) [%]	$^{-0.29}_{-0.14}$	$^{-0.31}$	$^{+0.14}$	$^{+0.26}$	$^{+0.45}_{+0.34}$	$^{-0.54}$	$^{+0.93}$	$^{+1.78}_{+1.17}$
Flavour response (JES) [%]	$^{+0.35}$	-	$^{-0.35}$	$^{-0.24}$	$^{-0.22}$	$^{-0.66}$	$^{+0.48}$	$^{+1.85}$
Pile-up offset μ (JES) [%]	$^{+0.15}$	-	-	-	-	$^{-0.23}$	$^{+0.55}$	$^{+1.45}_{-0.26}$
Pile-up offset N_{PV} (JES) [%]	-	-	-	-	-	-	$^{+0.12}_{-0.64}$	$^{+0.72}$
Pile-up offset p_T (JES) [%]	-	-	-	-	-	$^{-0.20}_{+0.11}$	-	$^{-0.23}$
Pile-up offset ρ topology (JES) [%]	$^{+0.44}_{-0.14}$	-	$^{-0.32}$	-	$^{-0.16}_{+0.19}$	$^{-0.86}$	$^{+0.36}_{+0.21}$	$^{-1.76}_{+1.08}$
Punch-through (JES) [%]	-	-	-	-	-	-	-	$^{-0.20}$
Single particle high-p_T (JES) [%]	-	-	-	-	-	-	-	-
Jet energy resolution [%]	± 0.74	± 0.32	∓ 0.18	∓ 0.68	∓ 0.86	∓ 1.26	∓ 0.47	∓ 3.81
Jet vertex fraction [%]	-	-	$^{-0.24}_{+0.23}$	$^{+0.22}_{-0.27}$	$^{+0.39}_{-0.38}$	$^{-0.48}_{+0.68}$	-	$^{+0.13}$
b-Quark tagging efficiency (eigenvector 0) [%]	-	-	-	-	-	-	-	-
b-Quark tagging efficiency (eigenvector 1) [%]	-	-	-	-	-	$^{-0.17}_{+0.18}$	$^{-0.14}_{+0.12}$	$^{-0.31}_{+0.26}$
b-Quark tagging efficiency (eigenvector 2) [%]	-	-	-	-	-	∓ 0.11	-	∓ 0.10
b-Quark tagging efficiency (eigenvector 3) [%]	-	-	-	-	$^{+0.26}$	$^{-0.20}$	$^{-0.34}$	$^{-0.76}$
b-Quark tagging efficiency (eigenvector 4) [%]	-	-	-	-	-	-	-	-
c-Quark tagging efficiency (eigenvector 0) [%]	-	$^{-0.12}_{+0.13}$	-	$^{+0.14}_{-0.27}$	-	$^{+0.13}_{-0.23}$	$^{+0.14}_{-0.41}$	$^{-0.62}_{+0.36}$
c-Quark tagging efficiency (eigenvector 1) [%]	-	-	-	-	-	-	-	-
c-Quark tagging efficiency (eigenvector 2) [%]	-	-	-	-	-	-	-	-
c-Quark tagging efficiency (eigenvector 3) [%]	-	-	-	-	-	-	-	-
Light-jet tagging efficiency (eigenvector 0) [%]	± 0.30	$^{+0.59}_{-0.58}$	$^{-0.73}_{+0.72}$	$^{-0.12}$	-	$^{+0.44}_{-0.45}$	$^{-0.27}_{+0.77}$	$^{-6.10}_{+5.85}$
Light-jet tagging efficiency (eigenvector 1) [%]	-	-	-	-	-	-	-	± 0.52
Light-jet tagging efficiency (eigenvector 2) [%]	-	-	-	-	-	-	-	∓ 0.19
Light-jet tagging efficiency (eigenvector 3) [%]	-	-	-	-	-	-	-	∓ 0.36
Light-jet tagging efficiency (eigenvector 4) [%]	-	-	-	-	-	-	-	∓ 0.38
Light-jet tagging efficiency (eigenvector 5) [%]	-	-	-	-	-	-	-	∓ 0.48
Light-jet tagging efficiency (eigenvector 6) [%]	-	-	-	-	-	-	-	± 0.19
Light-jet tagging efficiency (eigenvector 7) [%]	-	-	-	-	-	-	-	∓ 0.26
Light-jet tagging efficiency (eigenvector 8) [%]	-	-	-	-	-	-	-	-
Light-jet tagging efficiency (eigenvector 9) [%]	-	-	-	-	-	-	-	-
Light-jet tagging efficiency (eigenvector 10) [%]	-	-	-	-	-	-	-	-
Light-jet tagging efficiency (eigenvector 11) [%]	-	-	-	-	-	-	-	-
b-Quark tagging extrapolation [%]	$^{-0.36}_{+0.39}$	-	± 0.15	$^{+0.14}_{-0.16}$	$^{+0.26}_{-0.27}$	$^{+0.36}_{-0.43}$	-	$^{+2.71}_{-2.99}$
b-Quark tagging extrapolation from c-Quark [%]	-	-	-	-	-	-	-	± 0.10
Electron energy resolution [%]	-	-	-	-	-	$^{-0.25}$	-	$^{-1.56}$
Electron energy scale [%]	-	-	-	-	-	$^{-0.25}$	$^{-0.32}_{+0.40}$	$^{-1.32}$
Electron trigger efficiency [%]	-	-	-	-	-	-	-	-
Electron reconstruction efficiency [%]	-	-	-	-	-	-	-	-
Electron identification efficiency [%]	$^{-0.11}_{+0.12}$	-	-	-	± 0.15	± 0.19	± 0.27	± 0.45
Electron isolation efficiency [%]	∓ 0.11	-	-	-	± 0.14	± 0.18	$^{+0.26}_{-0.27}$	$^{+0.40}_{-0.41}$
Muon energy scale [%]	-	-	-	-	-	-	-	-
Muon (MS) momentum resolution [%]	-	-	-	-	-	-	-	-
Muon (ID) momentum resolution [%]	-	-	-	-	-	-	-	-
Muon trigger efficiency stat [%]	-	-	-	-	-	-	-	-
Muon trigger efficiency syst [%]	-	-	-	-	-	-	-	-
Muon identification stat [%]	-	-	-	-	-	-	-	-
Muon identification syst [%]	-	-	-	-	-	-	± 0.13	$^{+0.14}_{-0.13}$
Muon isolation efficiency stat [%]	-	-	-	-	-	-	-	-
Muon isolation efficiency syst [%]	-	-	-	-	-	-	± 0.10	± 0.12
Muon TTVA efficiency stat [%]	-	-	-	-	-	-	-	-
Muon TTVA efficiency syst [%]	-	-	-	-	-	-	-	-
E_T^{miss} Soft jet resolution para [%]	-	-	-	-	-	± 0.18	± 0.45	∓ 2.19
E_T^{miss} Soft jet resolution perp [%]	-	-	-	± 0.12	-	∓ 0.22	∓ 0.38	∓ 0.45
E_T^{miss} Soft jet scale [%]	-	-	-	-	-	-	$^{-0.26}$	$^{-0.71}$
Luminosity [%]	-	-	-	-	-	-	-	-
W+jets CA_{bcr} stat error [%]	-	-	-	-	-	-	-	-
W+jets CA_{tcr} stat error [%]	-	-	-	-	-	-	-	-
W+jets CA_{bmcl} stat error [%]	-	-	-	-	-	-	-	± 0.69
W+jets Fcc stat error [%]	-	-	-	$^{+0.10}_{-0.17}$	-	$^{+0.51}_{-0.86}$	$^{+0.48}_{-0.81}$	$^{-1.69}_{+2.86}$
W+jets Flight stat error [%]	-	-	-	-	-	-	-	-
W+jets Fc error [%]	-	-	-	-	-	$^{+0.10}_{-0.11}$	-	$^{+0.47}_{-0.47}$
QCD norm. impact on W+jets [%]	$^{-0.32}_{+0.36}$	$^{-0.17}_{+0.19}$	$^{+0.23}_{-0.27}$	-	$^{+0.15}_{-0.16}$	$^{+1.03}_{-1.13}$	$^{+0.82}_{-0.90}$	$^{+0.59}_{-0.58}$
Single top cross-section [%]	-	-	-	-	-	-	± 0.13	± 0.27
Z+jets cross-section [%]	∓ 0.15	-	± 0.23	± 0.12	∓ 0.25	∓ 0.15	± 0.84	± 1.12
Diboson cross-section [%]	-	-	-	-	± 0.15	± 0.17	± 0.30	± 0.82
$t\bar{t}V$ cross-section [%]	-	-	-	-	-	± 0.11	± 0.15	± 0.24
Monte Carlo sample statistics [%]	± 0.75	± 1.02	± 1.50	± 1.61	± 2.22	± 2.20	± 4.34	± 9.04
ISR/FSR + scale [%]	$^{-0.43}_{+0.57}$	$^{-1.63}$	$^{+0.68}_{-1.99}$	$^{-}$	$^{+1.90}_{-}$	$^{+3.01}_{-}$	$^{-2.81}$	$^{+2.10}_{-}$
Alternate hard-scattering model [%]	∓ 1.06	± 3.62	∓ 2.22	± 1.43	∓ 3.45	∓ 7.17	± 0.71	± 15.1
Alternate parton-shower model [%]	∓ 1.95	∓ 0.88	± 1.05	± 0.88	± 6.18	± 4.81	∓ 6.89	± 6.45
Inter PDF [%]	-	-	∓ 0.21	± 0.13	-	-	± 1.47	∓ 0.67
Intra PDF [%]	∓ 0.15	∓ 0.13	± 0.17	± 0.20	-	± 0.42	± 0.39	± 0.39
Real lepton efficiency stat [%]	$^{-0.12}_{+0.13}$	$^{+6.19}$	-	-	$^{+0.16}_{-0.29}$	$^{+0.41}_{-0.88}$	$^{+0.36}_{-0.42}$	$^{+0.56}_{-0.55}$
Fake lepton efficiency MC scale [%]	$^{+0.26}_{-0.23}$	-	$^{-0.33}_{+0.23}$	$^{-0.25}_{+0.24}$	$^{+0.20}$	-	$^{-0.40}_{+0.46}$	$^{-0.13}_{+0.27}$
Fake lepton efficiency alternate CR [%]	∓ 0.20	-	∓ 0.22	± 0.18	± 0.24	± 0.80	∓ 0.39	± 0.89
Poor MTW Modelling in QCD [%]	± 0.27	± 0.35	± 0.33	∓ 0.12	∓ 0.27	∓ 0.42	∓ 3.03	∓ 3.52

Table C.3: Table of systematic uncertainties for the relative differential cross-section at particle level for the top quark transverse momentum in the boosted regime.

Bins $\lvert$ Unit $\lvert y^t \rvert$ $\lvert$	0–0.20	0.20–0.40	0.40–0.60	0.60–0.80	0.80–1	1–1.20	1.20–1.40	1.40–1.60	1.60–1.80	1.80–2
$1/\sigma \cdot d\sigma / d\lvert y^t \rvert$	$7.50 \cdot 10^{-1}$	$7.64 \cdot 10^{-1}$	$6.76 \cdot 10^{-1}$	$6.31 \cdot 10^{-1}$	$5.56 \cdot 10^{-1}$	$5.09 \cdot 10^{-1}$	$4.14 \cdot 10^{-1}$	$3.40 \cdot 10^{-1}$	$2.19 \cdot 10^{-1}$	$1.41 \cdot 10^{-1}$
Total uncertainty [%]	$^{+5.35}_{-4.62}$	$^{+5.37}_{-4.75}$	$^{+6.34}_{-6.94}$	$^{+5.59}_{-5.67}$	$^{+7.01}_{-7.56}$	$^{+6.00}_{-5.77}$	$^{+10.2}_{-10.1}$	$^{+8.69}_{-8.28}$	$^{+9.27}_{-10.3}$	$^{+11.5}_{-11.8}$
Statistical uncertainty [%]	±3.7	±4.0	±4.3	±4.5	±4.7	±4.8	±5.4	±5.9	±7.7	±8.5
Systematic uncertainty [%]	$^{+3.68}_{-3.50}$	$^{+3.39}_{-3.29}$	$^{+4.42}_{-4.84}$	$^{+3.90}_{-3.95}$	$^{+5.02}_{-5.76}$	$^{+3.32}_{-3.30}$	$^{+8.31}_{-8.25}$	$^{+6.00}_{-5.98}$	$^{+4.13}_{-4.25}$	$^{+7.28}_{-7.27}$
Large-R jet Baseline (JES) [%]	$^{-}_{-}$	$^{-}_{-}$	$^{-}_{-}$	$^{-}_{-}$	$^{-}_{-}$	$^{-}_{-}$	$^{-}_{-}$	$^{-}_{-}$	$^{-}_{-}$	$^{-}_{-}$
Large-R jet Tracking (JES) [%]	$^{+0.55}_{-}$	$^{-}_{-0.87}$	$^{-}_{-0.45}$	$^{+0.33}_{-0.61}$	$^{+0.51}_{-0.28}$	$^{-}_{+1.10}$	$^{-0.33}_{-}$	$^{-0.22}_{+0.17}$	$^{-1.73}_{-}$	$^{-0.94}_{+1.26}$
Large-R jet Modelling (JES) [%]	$^{+0.47}_{-}$	$^{+0.65}_{-0.53}$	$^{+0.54}_{-}$	$^{-}_{-}$	$^{+0.24}_{-0.63}$	$^{-}_{+0.41}$	$^{-}_{-}$	$^{-0.48}_{+0.49}$	$^{-3.23}_{+0.19}$	$^{-2.73}_{-}$
Large-R jet CrossCalib τ32 (JES) [%]	$^{+0.54}_{-}$	$^{+0.55}_{-}$	$^{+0.33}_{-}$	$^{+0.36}_{-}$	$^{-}_{-0.26}$	$^{-}_{+0.32}$	$^{-1.45}_{+0.73}$	$^{-0.57}_{+0.58}$	$^{-1.18}_{+0.34}$	$^{-0.57}_{+0.88}$
Large-R jet Run1 τ32 (JES) [%]	$^{+0.77}_{-}$	$^{+0.44}_{-}$	$^{+0.39}_{-}$	$^{+0.27}_{-0.36}$	$^{+0.44}_{+0.30}$	$^{-}_{-1.13}$	$^{+0.73}_{+1.88}$	$^{+0.58}_{+2.26}$	$^{+0.34}_{+2.23}$	$^{+0.88}_{-}$
Large-R jet JMR [%]	$^{+1.69}_{-}$	$^{-1.10}_{-}$	$^{-1.13}_{-}$	$^{-}_{\pm 0.14}$	$^{-}_{-}$	$^{+1.40}_{\mp 0.46}$	$^{+1.88}_{\mp 0.28}$	$^{+2.26}_{\pm 0.76}$	$^{+2.23}_{-}$	$^{+2.34}_{\mp 0.61}$
b-Tagged jet energy scale (JES) [%]	$^{-}_{-}$	$^{-}_{-}$	$^{+0.19}_{-}$	$^{-}_{-}$	$^{-}_{-}$	$^{-}_{-}$	$^{+0.16}_{-}$	$^{-}_{-}$	$^{-}_{-}$	$^{+0.24}_{-0.11}$
Effective detector NP set 1 (JES) [%]	$^{-}_{-0.22}$	$^{-0.12}_{+0.11}$	$^{+0.14}_{-}$	$^{-0.38}_{+0.34}$	$^{+0.29}_{+0.37}$	$^{+0.23}_{-}$	$^{+0.29}_{-}$	$^{-}_{-0.39}$	$^{-}_{-}$	$^{+0.26}_{+0.26}$
Effective detector NP set 2 (JES) [%]	$^{-}_{-}$	$^{-}_{-}$	$^{-}_{-}$	$^{-}_{-0.21}$	$^{-}_{-}$	$^{-}_{-}$	$^{-}_{-0.20}$	$^{-}_{-0.22}$	$^{-}_{-}$	$^{+0.91}_{-}$
Effective detector NP set 3 (JES) [%]	$^{-}_{-}$	$^{-}_{-}$	$^{-}_{-}$	$^{-}_{-}$	$^{-}_{-}$	$^{-}_{-}$	$^{-}_{-0.20}$	$^{-}_{-}$	$^{-}_{-}$	$^{+0.84}_{-}$
Effective detector NP set 4 (JES) [%]	$^{-}_{-}$	$^{-}_{-}$	$^{+0.21}_{-}$	$^{-}_{-}$	$^{-}_{-}$	$^{-0.13}_{-}$	$^{-}_{-}$	$^{-}_{-}$	$^{-}_{-}$	$^{-}_{-}$
Effective detector NP set 5 (JES) [%]	$^{-}_{-}$	$^{-}_{-}$	$^{-}_{-}$	$^{-}_{-}$	$^{-}_{-}$	$^{-}_{-}$	$^{-}_{-}$	$^{-}_{-}$	$^{-}_{-}$	$^{-}_{-}$
Effective detector NP set 6 restTerm (JES) [%]	$^{-}_{-}$	$^{-}_{-}$	$^{-}_{-}$	$^{-}_{-}$	$^{-}_{-}$	$^{-}_{-}$	$^{-}_{-}$	$^{-}_{-}$	$^{-}_{-}$	$^{+0.14}_{-0.10}$
η intercalibration model (JES) [%]	$^{-}_{-0.25}$	$^{-}_{-}$	$^{-}_{-}$	$^{-0.16}_{+0.14}$	$^{-}_{-0.14}$	$^{+0.21}_{-}$	$^{-}_{-}$	$^{-}_{-0.28}$	$^{+0.31}_{-0.27}$	$^{+1.21}_{-0.28}$
η intercalibration total stat (JES) [%]	$^{-}_{-}$	$^{-}_{-}$	$^{-}_{-}$	$^{-}_{-}$	$^{+0.45}_{-0.16}$	$^{+0.26}_{-}$	$^{-0.25}_{-}$	$^{-0.21}_{-}$	$^{-}_{-}$	$^{+0.90}_{-}$
Flavour composition (JES) [%]	$^{-}_{-}$	$^{-}_{-}$	$^{-}_{-0.23}$	$^{-0.17}_{+0.31}$	$^{+0.28}_{-0.45}$	$^{+0.31}_{+0.20}$	$^{+0.28}_{-}$	$^{-0.43}_{-}$	$^{-0.29}_{+0.10}$	$^{+0.90}_{+0.95}$
Flavour response (JES) [%]	$^{-}_{-}$	$^{-}_{-}$	$^{-}_{-}$	$^{-0.30}_{-}$	$^{-0.18}_{-}$	$^{+0.20}_{-}$	$^{-}_{-}$	$^{-0.35}_{-}$	$^{+0.27}_{-}$	$^{-}_{-}$
Pile-up offset μ (JES) [%]	$^{-}_{-}$	$^{-}_{-}$	$^{-}_{-}$	$^{-}_{-}$	$^{-}_{-}$	$^{-}_{-}$	$^{-}_{-}$	$^{-}_{-}$	$^{-}_{-}$	$^{-0.21}_{+0.99}$
Pile-up offset N_{PV} (JES) [%]	$^{-}_{-}$	$^{-}_{-}$	$^{-}_{-}$	$^{-}_{-}$	$^{-}_{-}$	$^{-}_{-}$	$^{-}_{-}$	$^{-}_{-}$	$^{-}_{-}$	$^{+0.92}_{-}$
Pile-up offset p_T (JES) [%]	$^{-}_{-}$	$^{-}_{-}$	$^{-}_{-}$	$^{-}_{-}$	$^{-}_{-}$	$^{-}_{-}$	$^{-0.24}_{-}$	$^{-}_{-}$	$^{-}_{-}$	$^{-0.41}_{-}$
Pile-up offset ρ topology (JES) [%]	$^{-}_{-}$	$^{-}_{-}$	$^{-}_{-}$	$^{-0.20}_{+0.12}$	$^{-}_{-}$	$^{+0.21}_{-}$	$^{-}_{-}$	$^{-}_{-0.24}$	$^{-}_{-0.29}$	$^{+0.85}_{-0.15}$
Punch-through (JES) [%]	$^{-}_{-}$	$^{-}_{-}$	$^{-}_{-}$	$^{-}_{-}$	$^{-}_{-}$	$^{-}_{-}$	$^{-}_{-}$	$^{-}_{-}$	$^{-}_{-}$	$^{-}_{-}$
Single particle high-p_T (JES) [%]	$^{-}_{-}$	$^{-}_{-}$	$^{-}_{-}$	$^{-}_{-}$	$^{-}_{-}$	$^{-}_{-}$	$^{-}_{-}$	$^{-}_{-}$	$^{-}_{-}$	$^{-}_{-}$
Jet energy resolution [%]	∓ 0.45	± 0.31	∓ 0.72	± 0.41	± 0.71	∓ 0.35	± 0.42	$^{-}_{-}$	$^{-}_{-}$	∓ 0.64
Jet vertex fraction [%]	$^{+0.22}_{-0.25}$	$^{-}_{-}$	$^{-0.25}_{+0.48}$	∓ 0.10	$^{-}_{-}$	$^{+0.11}_{-0.20}$	± 0.17	$^{-}_{-}$	$^{-}_{-}$	$^{-}_{-}$
b-Quark tagging efficiency (eigenvector 0) [%]	$^{-}_{-}$	± 0.10	$^{-}_{-}$	$^{-}_{-}$	$^{-}_{-}$	$^{-}_{-}$	∓ 0.13	∓ 0.11	$^{-}_{-}$	∓ 0.15
b-Quark tagging efficiency (eigenvector 1) [%]	$^{-}_{-}$	$^{-}_{-}$	$^{-}_{-}$	$^{-}_{-}$	$^{-}_{-}$	$^{-}_{-}$	$^{-}_{-}$	$^{-0.11}_{+0.13}$	$^{-}_{-}$	$^{-0.21}_{+0.24}$
b-Quark tagging efficiency (eigenvector 2) [%]	$^{-}_{-}$	$^{-}_{-}$	$^{-}_{-}$	$^{-}_{-}$	$^{-}_{-}$	$^{-}_{-}$	$^{-}_{-}$	$^{-}_{-}$	$^{-}_{-}$	$^{-}_{-}$
b-Quark tagging efficiency (eigenvector 3) [%]	$^{-}_{-}$	$^{-}_{-}$	$^{-}_{-}$	$^{+0.33}_{-}$	$^{-}_{-}$	$^{-}_{-}$	$^{+0.19}_{-}$	$^{-}_{-}$	$^{-}_{-}$	$^{-}_{-}$
b-Quark tagging efficiency (eigenvector 4) [%]	$^{-}_{-}$	$^{-}_{-}$	$^{-}_{-}$	$^{-}_{-}$	$^{-}_{-}$	$^{-}_{-}$	$^{-}_{-}$	$^{-}_{-}$	$^{-}_{-}$	$^{-}_{-}$
c-Quark tagging efficiency (eigenvector 0) [%]	$^{-}_{-}$	$^{-}_{-}$	$^{-}_{-}$	$^{-}_{-}$	$^{-}_{-}$	$^{+0.11}_{-0.10}$	$^{-0.11}_{+0.17}$	$^{-}_{-}$	$^{-}_{-}$	$^{-}_{-}$
c-Quark tagging efficiency (eigenvector 1) [%]	$^{-}_{-}$	$^{-}_{-}$	$^{-}_{-}$	$^{-}_{-}$	$^{-}_{-}$	$^{-}_{-}$	± 0.10	$^{-}_{-}$	$^{-}_{-}$	∓ 0.10
c-Quark tagging efficiency (eigenvector 2) [%]	$^{-}_{-}$	$^{-}_{-}$	$^{-}_{-}$	$^{-}_{-}$	$^{-}_{-}$	$^{-}_{-}$	$^{-}_{-}$	$^{-}_{-}$	$^{-}_{-}$	$^{-}_{-}$
c-Quark tagging efficiency (eigenvector 3) [%]	$^{-}_{-}$	$^{-}_{-}$	$^{-}_{-}$	$^{-}_{-}$	$^{-}_{-}$	$^{-}_{-}$	$^{-}_{-}$	$^{-}_{-}$	$^{-}_{-}$	$^{-}_{-}$
Light-jet tagging efficiency (eigenvector 0) [%]	$^{-}_{-}$	$^{+0.52}_{-0.49}$	$^{+0.24}_{-0.22}$	$^{-0.33}_{+0.34}$	$^{+0.13}_{-0.14}$	$^{+0.50}_{-0.54}$	$^{-0.17}_{+0.12}$	$^{-0.83}_{+1.08}$	$^{-1.45}_{+1.36}$	$^{-0.17}_{+0.16}$
Light-jet tagging efficiency (eigenvector 1) [%]	± 0.14	$^{-}_{-}$	$^{-}_{-}$	$^{-}_{-}$	$^{-}_{-}$	$^{-}_{-}$	$^{-}_{-}$	∓ 0.16	∓ 0.20	∓ 0.22
Light-jet tagging efficiency (eigenvector 2) [%]	$^{-}_{-}$	$^{-}_{-}$	$^{-}_{-}$	$^{-}_{-}$	$^{-}_{-}$	$^{-}_{-}$	$^{-}_{-}$	$^{-}_{-}$	∓ 0.15	$^{-}_{-}$
Light-jet tagging efficiency (eigenvector 3) [%]	$^{-}_{-}$	$^{-}_{-}$	$^{-}_{-}$	$^{-}_{-}$	$^{-}_{-}$	$^{-}_{-}$	$^{-}_{-}$	$^{-}_{-}$	$^{-}_{-}$	$^{-}_{-}$
Light-jet tagging efficiency (eigenvector 4) [%]	$^{-}_{-}$	$^{-}_{-}$	$^{-}_{-}$	$^{-}_{-}$	$^{-}_{-}$	$^{-}_{-}$	$^{-}_{-}$	$^{-}_{-}$	$^{-}_{-}$	$^{-}_{-}$
Light-jet tagging efficiency (eigenvector 5) [%]	$^{-}_{-}$	$^{-}_{-}$	$^{-}_{-}$	$^{-}_{-}$	$^{-}_{-}$	$^{-}_{-}$	$^{-}_{-}$	$^{-}_{-}$	$^{-}_{-}$	$^{-}_{-}$
Light-jet tagging efficiency (eigenvector 6) [%]	$^{-}_{-}$	$^{-}_{-}$	$^{-}_{-}$	$^{-}_{-}$	$^{-}_{-}$	$^{-}_{-}$	$^{-}_{-}$	$^{-}_{-}$	$^{-}_{-}$	$^{-}_{-}$
Light-jet tagging efficiency (eigenvector 7) [%]	$^{-}_{-}$	$^{-}_{-}$	$^{-}_{-}$	$^{-}_{-}$	$^{-}_{-}$	$^{-}_{-}$	$^{-}_{-}$	$^{-}_{-}$	$^{-}_{-}$	$^{-}_{-}$
Light-jet tagging efficiency (eigenvector 8) [%]	$^{-}_{-}$	$^{-}_{-}$	$^{-}_{-}$	$^{-}_{-}$	$^{-}_{-}$	$^{-}_{-}$	$^{-}_{-}$	$^{-}_{-}$	$^{-}_{-}$	$^{-}_{-}$
Light-jet tagging efficiency (eigenvector 9) [%]	$^{-}_{-}$	$^{-}_{-}$	$^{-}_{-}$	$^{-}_{-}$	$^{-}_{-}$	$^{-}_{-}$	$^{-}_{-}$	$^{-}_{-}$	$^{-}_{-}$	$^{-}_{-}$
Light-jet tagging efficiency (eigenvector 10) [%]	$^{-}_{-}$	$^{-}_{-}$	$^{-}_{-}$	$^{-}_{-}$	$^{-}_{-}$	$^{-}_{-}$	$^{-}_{-}$	$^{-}_{-}$	$^{-}_{-}$	$^{-}_{-}$
Light-jet tagging efficiency (eigenvector 11) [%]	$^{-}_{-}$	$^{-}_{-}$	$^{-}_{-}$	$^{-}_{-}$	$^{-}_{-}$	$^{-}_{-}$	$^{-}_{-}$	$^{-}_{-}$	$^{-}_{-}$	$^{-}_{-}$
b-Quark tagging extrapolation [%]	$^{-}_{-}$	$^{-}_{-}$	$^{-}_{-}$	$^{-}_{-}$	$^{-0.14}_{+0.13}$	$^{-}_{-}$	$^{-}_{-}$	$^{-}_{-}$	$^{-0.21}_{+0.22}$	$^{+0.28}_{-0.27}$
b-Quark tagging extrapolation from c-Quark [%]	$^{-}_{-}$	$^{-}_{-}$	$^{-}_{-}$	$^{-}_{-}$	$^{-}_{-}$	$^{-}_{-}$	$^{-}_{-}$	$^{-}_{-}$	$^{-}_{-}$	$^{-}_{-}$
Electron energy resolution [%]	$^{-}_{-}$	$^{-}_{-}$	$^{-}_{-}$	$^{-}_{-}$	$^{-}_{-}$	$^{-}_{-}$	$^{-0.21}_{-}$	$^{-}_{-}$	$^{-}_{-}$	$^{-}_{-}$
Electron energy scale [%]	$^{-}_{-}$	$^{-}_{-}$	$^{+0.21}_{-}$	$^{-}_{-}$	$^{-}_{-}$	$^{-}_{-}$	$^{-}_{-}$	$^{+0.21}_{-}$	$^{-}_{-}$	$^{-0.17}_{-}$
Electron trigger efficiency [%]	$^{-}_{-}$	$^{-}_{-}$	$^{-}_{-}$	$^{-}_{-}$	$^{-}_{-}$	$^{-}_{-}$	$^{-}_{-}$	$^{-}_{-}$	$^{-}_{-}$	$^{-}_{-}$
Electron reconstruction efficiency [%]	$^{-}_{-}$	$^{-}_{-}$	$^{-}_{-}$	$^{-}_{-}$	$^{-}_{-}$	$^{-}_{-}$	$^{-}_{-}$	$^{-}_{-}$	$^{-}_{-}$	$^{-}_{-}$
Electron identification efficiency [%]	$^{-}_{-}$	$^{-}_{-}$	$^{-}_{-}$	$^{-}_{-}$	$^{-}_{-}$	$^{-}_{-}$	$^{-}_{-}$	$^{-}_{-}$	$^{-}_{-}$	$^{-}_{-}$
Electron isolation efficiency [%]	$^{-}_{-}$	$^{-}_{-}$	$^{-}_{-}$	$^{-}_{-}$	$^{-}_{-}$	$^{-}_{-}$	$^{-}_{-}$	$^{-}_{-}$	$^{-}_{-}$	$^{-}_{-}$
Muon energy scale [%]	$^{-}_{-}$	$^{-}_{-}$	$^{-}_{-}$	$^{-}_{-}$	$^{-}_{-}$	$^{-}_{-}$	$^{-}_{-}$	$^{-}_{-}$	$^{-}_{-}$	$^{-}_{-}$
Muon (MS) momentum resolution [%]	$^{-}_{-}$	$^{-}_{-}$	$^{-}_{-}$	$^{-}_{-}$	$^{-}_{-}$	$^{-}_{-}$	$^{-}_{-}$	$^{-}_{-}$	$^{-}_{-}$	$^{-}_{-}$
Muon (ID) momentum resolution [%]	$^{-}_{-}$	$^{-}_{-}$	$^{-}_{-}$	$^{-}_{-}$	$^{-}_{-}$	$^{-}_{-}$	$^{-}_{-}$	$^{-}_{-}$	$^{-}_{-}$	$^{-}_{-}$
Muon trigger efficiency stat [%]	$^{-}_{-}$	$^{-}_{-}$	$^{-}_{-}$	$^{-}_{-}$	$^{-}_{-}$	$^{-}_{-}$	$^{-}_{-}$	$^{-}_{-}$	$^{-}_{-}$	$^{-}_{-}$
Muon trigger efficiency syst [%]	$^{-}_{-}$	$^{-}_{-}$	$^{-}_{-}$	$^{-}_{-}$	$^{-}_{-}$	$^{-}_{-}$	$^{-}_{-}$	$^{-}_{-}$	$^{-}_{-}$	$^{-}_{-}$
Muon identification stat [%]	$^{-}_{-}$	$^{-}_{-}$	$^{-}_{-}$	$^{-}_{-}$	$^{-}_{-}$	$^{-}_{-}$	$^{-}_{-}$	$^{-}_{-}$	$^{-}_{-}$	$^{-}_{-}$
Muon identification syst [%]	$^{-}_{-}$	$^{-}_{-}$	$^{-}_{-}$	$^{-}_{-}$	$^{-}_{-}$	$^{-}_{-}$	$^{-}_{-}$	$^{-}_{-}$	$^{-}_{-}$	$^{-}_{-}$
Muon isolation efficiency stat [%]	$^{-}_{-}$	$^{-}_{-}$	$^{-}_{-}$	$^{-}_{-}$	$^{-}_{-}$	$^{-}_{-}$	$^{-}_{-}$	$^{-}_{-}$	$^{-}_{-}$	$^{-}_{-}$
Muon isolation efficiency syst [%]	$^{-}_{-}$	$^{-}_{-}$	$^{-}_{-}$	$^{-}_{-}$	$^{-}_{-}$	$^{-}_{-}$	$^{-}_{-}$	$^{-}_{-}$	$^{-}_{-}$	$^{-}_{-}$
Muon TTVA efficiency stat [%]	$^{-}_{-}$	$^{-}_{-}$	$^{-}_{-}$	$^{-}_{-}$	$^{-}_{-}$	$^{-}_{-}$	$^{-}_{-}$	$^{-}_{-}$	$^{-}_{-}$	$^{-}_{-}$
Muon TTVA efficiency syst [%]	$^{-}_{-}$	$^{-}_{-}$	$^{-}_{-}$	$^{-}_{-}$	$^{-}_{-}$	$^{-}_{-}$	$^{-}_{-}$	$^{-}_{-}$	$^{-}_{-}$	$^{-}_{-}$
E_T^{miss} Soft jet resolution para [%]	± 0.14	$^{-}_{-}$	$^{-}_{-}$	$^{-}_{-}$	∓ 0.25	$^{-}_{-}$	$^{-}_{-}$	$^{-}_{-}$	$^{-}_{-}$	± 0.15
E_T^{miss} Soft jet resolution perp [%]	$^{-}_{-}$	$^{-}_{-}$	∓ 0.12	$^{-}_{-}$	∓ 0.10	$^{-}_{-}$	$^{-}_{-}$	± 0.21	± 0.16	$^{-}_{-}$
E_T^{miss} Soft jet scale [%]	$^{-}_{-}$	$^{-}_{-}$	$^{-}_{-}$	$^{-}_{-}$	$^{-}_{-}$	$^{-}_{-}$	$^{-}_{-}$	$^{-}_{-}$	$^{-}_{-}$	$^{-}_{-}$
Luminosity [%]	$^{-}_{-}$	$^{-}_{-}$	$^{-}_{-}$	$^{-}_{-}$	$^{-}_{-}$	$^{-}_{-}$	$^{-}_{-}$	$^{-}_{-}$	$^{-}_{-}$	$^{-}_{-}$
W+jets $CA_{bc\tau}$ stat error [%]	$^{-}_{-}$	$^{-}_{-}$	$^{-}_{-}$	$^{-}_{-}$	$^{-}_{-}$	$^{-}_{-}$	$^{-}_{-}$	$^{-}_{-}$	$^{-}_{-}$	$^{-}_{-}$
W+jets $CA_{bc\mu}$ stat error [%]	$^{-}_{-}$	$^{-}_{-}$	$^{-}_{-}$	$^{-}_{-}$	$^{-}_{-}$	$^{-}_{-}$	$^{-}_{-}$	$^{-}_{-}$	$^{-}_{-}$	$^{-}_{-}$
W+jets CA_{dmd} stat error [%]	$^{-}_{-}$	$^{-}_{-}$	$^{-}_{-}$	$^{-}_{-}$	$^{-}_{-}$	$^{-}_{-}$	$^{-}_{-}$	$^{-}_{-}$	$^{-}_{-}$	$^{-}_{-}$
W+jets Fcc stat error [%]	$^{-}_{-}$	$^{+0.10}_{-0.17}$	$^{+0.15}_{-0.26}$	$^{-0.12}_{+0.21}$	$^{-}_{-}$	$^{+0.19}_{-0.33}$	$^{-0.52}_{+0.88}$	$^{-0.13}_{+0.22}$	$^{-0.12}_{+0.20}$	$^{-0.15}_{+0.25}$
W+jets Flight stat error [%]	$^{-}_{-}$	$^{-}_{-}$	$^{-}_{-}$	$^{-}_{-}$	$^{-}_{-}$	$^{-}_{-}$	$^{-}_{-}$	$^{-}_{-}$	$^{-}_{-}$	$^{-}_{-}$
W+jets Fc error [%]	$^{-}_{-}$	$^{-}_{-}$	$^{-}_{-}$	$^{-}_{-}$	$^{-}_{-}$	$^{-}_{-}$	$^{+0.10}_{-0.11}$	$^{-}_{-}$	$^{-0.11}_{+0.13}$	$^{+0.12}_{-0.14}$
QCD norm. impact on W+jets [%]	$^{+0.10}_{-0.12}$	$^{-0.12}_{+0.14}$	$^{+0.20}_{-0.23}$	$^{-}_{-}$	$^{-0.21}_{+0.25}$	$^{-}_{-}$	$^{-}_{+0.47}$	$^{+0.13}_{-0.16}$	$^{+0.13}_{-0.59}$	$^{-0.19}_{+0.18}$
Single top cross-section [%]	$^{-}_{-}$	$^{-}_{-}$	$^{-}_{-}$	$^{-}_{-}$	$^{-}_{-}$	$^{-}_{-}$	$^{-}_{-}$	$^{-}_{-}$	$^{-}_{-}$	$^{-}_{-}$
Z+jets cross-section [%]	∓ 0.15	$^{-}_{-}$	∓ 0.17	± 0.15	± 0.16	∓ 0.18	$^{-}_{-}$	± 0.11	± 0.42	∓ 0.24
Diboson cross-section [%]	$^{-}_{-}$	$^{-}_{-}$	$^{-}_{-}$	$^{-}_{-}$	$^{-}_{-}$	$^{-}_{-}$	$^{-}_{-}$	$^{-}_{-}$	$^{-}_{-}$	$^{-}_{-}$
$t\bar{t}V$ cross-section [%]	$^{-}_{-}$	$^{-}_{-}$	$^{-}_{-}$	$^{-}_{-}$	$^{-}_{-}$	$^{-}_{-}$	$^{-}_{-}$	$^{-}_{-}$	$^{-}_{-}$	$^{-}_{-}$
Monte Carlo sample statistics [%]	± 1.04	± 1.10	± 1.21	± 1.57	± 1.34	± 1.38	± 2.28	± 1.88	± 3.00	± 2.78
ISR/FSR + scale [%]	$^{+1.88}_{-}$	$^{+1.65}_{-0.54}$	$^{-}_{-2.80}$	$^{-1.33}_{+2.33}$	$^{+0.45}_{-2.49}$	$^{-}_{-2.33}$	$^{+3.72}_{-}$	$^{+2.16}_{-}$	$^{-}_{-0.89}$	$^{-}_{-5.23}$
Alternate hard-scattering model [%]	± 1.27	$^{-}_{-}$	± 2.80	∓ 1.12	± 4.81	± 0.32	± 4.38	∓ 1.54	∓ 2.40	∓ 3.53
Alternate parton-shower model [%]	∓ 0.77	∓ 1.26	∓ 2.95	± 0.39	∓ 0.56	∓ 0.26	± 5.39	± 4.13	± 0.89	∓ 0.72
Inter PDF [%]	$^{-}_{-}$	∓ 0.17	$^{-}_{-}$	± 0.12	$^{-}_{-}$	∓ 0.19	$^{-}_{-}$	± 0.55	$^{-}_{-}$	∓ 0.31
Intra PDF [%]	$^{-}_{-}$	$^{-}_{-}$	∓ 0.14	$^{-}_{-}$	$^{-}_{-}$	$^{-}_{-}$	$^{-}_{-}$	$^{-}_{-}$	± 0.41	± 0.80
Real lepton efficiency stat [%]	$^{-}_{-}$	$^{-}_{-}$	$^{-}_{-}$	$^{-}_{-}$	$^{-}_{-}$	$^{-}_{-}$	$^{-}_{-}$	$^{-}_{-}$	$^{-}_{-}$	$^{+0.17}_{-0.22}$
Fake lepton efficiency MC scale [%]	$^{+0.24}_{-0.21}$	$^{-}_{-}$	$^{-0.15}_{-}$	$^{-0.14}_{+0.10}$	$^{-}_{-}$	$^{+0.51}_{-0.50}$	$^{-0.92}_{+0.86}$	$^{-}_{-}$	$^{-0.32}_{+0.22}$	$^{+1.04}_{-0.89}$
Fake lepton efficiency alternate CR [%]	$^{-}_{-}$	∓ 0.37	± 0.12	± 0.33	$^{-}_{-}$	$^{-}_{-}$	± 0.46	± 0.25	$^{-}_{-}$	± 0.85
Poor MTW Modelling in QCD [%]	± 0.30	± 0.33	∓ 0.31	± 0.15	$^{-}_{-}$	± 0.32	∓ 0.25	± 0.21	∓ 1.42	± 0.17

Table C.4: Table of systematic uncertainties for the relative differential cross-section at particle level for the absolute value of the top quark rapidity in the boosted regime.

Bins [GeV]	0–25	25–50	50–75	75–105	105–135	135–165	165–195	195–230	230–265	265–300	300–350	350–400	400–450	450–500	500–1000.00
$d\sigma$ / $d p_T^t$ [pb/GeV]	$1.35 \cdot 10^{-1}$	$3.91 \cdot 10^{-1}$	$5.80 \cdot 10^{-1}$	$6.42 \cdot 10^{-1}$	$5.74 \cdot 10^{-1}$	$4.11 \cdot 10^{-1}$	$2.80 \cdot 10^{-1}$	$1.84 \cdot 10^{-1}$	$1.13 \cdot 10^{-1}$	$7.69 \cdot 10^{-2}$	$4.08 \cdot 10^{-2}$	$2.23 \cdot 10^{-2}$	$1.10 \cdot 10^{-2}$	$5.24 \cdot 10^{-3}$	$7.30 \cdot 10^{-4}$
Total uncertainty [%]	$^{+12.5}_{-14.0}$	$^{+12.3}_{-13.2}$	$^{+11.6}_{-12.7}$	$^{+11.1}_{-11.7}$	$^{+10.5}_{-11.5}$	$^{+10.4}_{-10.6}$	$^{+9.27}_{-10.3}$	$^{+9.24}_{-11.1}$	$^{+9.44}_{-9.53}$	$^{+10.0}_{-10.9}$	$^{+9.87}_{-10.4}$	$^{+11.8}_{-11.4}$	$^{+12.2}_{-13.6}$	$^{+22.2}_{-23.2}$	$^{+18.3}_{-18.6}$
Statistical uncertainty [%]	±2.0	±1.1	±0.9	±0.7	±0.8	±1.0	±1.2	±1.3	±1.7	±2.1	±2.5	±3.5	±5.2	±8.2	±7.3
Systematic uncertainty [%]	$^{+12.2}_{-13.8}$	$^{+12.2}_{-13.2}$	$^{+11.6}_{-12.7}$	$^{+11.1}_{-11.7}$	$^{+10.5}_{-11.5}$	$^{+10.3}_{-10.5}$	$^{+9.18}_{-10.3}$	$^{+9.12}_{-11.0}$	$^{+9.26}_{-9.34}$	$^{+9.78}_{-10.6}$	$^{+9.49}_{-10.0}$	$^{+11.2}_{-10.8}$	$^{+10.8}_{-12.3}$	$^{+20.5}_{-21.6}$	$^{+16.7}_{-17.0}$
b-Tagged jet energy scale (JES) [%]	$^{+0.28}_{-}$	$^{-}_{-}$	$^{+0.25}_{-0.22}$	$^{+0.38}_{-0.33}$	$^{+0.73}_{-0.85}$	$^{+0.83}_{-0.79}$	$^{+0.81}_{-0.62}$	$^{+0.79}_{-0.84}$	$^{+0.78}_{-0.99}$	$^{+0.72}_{-0.50}$	$^{+0.82}_{-0.91}$	$^{+0.68}_{-0.51}$	$^{+0.42}_{-0.94}$	$^{+0.99}_{-1.27}$	$^{+0.64}_{-0.51}$
Effective detector NP set 1 (JES) [%]	$^{+4.90}_{-6.46}$	$^{+5.00}_{-6.12}$	$^{+4.95}_{-6.28}$	$^{+5.31}_{-5.86}$	$^{+5.30}_{-6.00}$	$^{+5.06}_{-5.48}$	$^{+4.58}_{-5.23}$	$^{+3.59}_{-5.00}$	$^{+3.78}_{-3.80}$	$^{+2.56}_{-3.94}$	$^{+3.15}_{-3.74}$	$^{+3.44}_{-3.00}$	$^{+2.17}_{-4.00}$	$^{+2.53}_{-4.20}$	$^{+1.70}_{-4.40}$
Effective detector NP set 2 (JES) [%]	$^{-1.80}_{+1.32}$	$^{-2.02}_{+1.89}$	$^{-1.81}_{+1.77}$	$^{-1.35}_{+1.48}$	$^{-1.00}_{+0.84}$	$^{-0.27}_{+0.38}$	$^{-}_{-}$	$^{+0.18}_{-0.97}$	$^{+1.19}_{-0.91}$	$^{+0.92}_{-1.44}$	$^{+1.51}_{-1.50}$	$^{+3.02}_{-2.76}$	$^{+1.78}_{-2.55}$	$^{+2.80}_{-3.14}$	$^{+5.58}_{-3.05}$
Effective detector NP set 3 (JES) [%]	$^{+0.52}_{-0.96}$	$^{+0.87}_{-0.94}$	$^{\pm 0.73}$	$^{+0.68}_{-0.68}$	$^{-0.24}$	$^{-}_{+0.10}$	$^{-0.39}_{+0.31}$	$^{-0.76}_{+0.40}$	$^{-1.08}_{+1.03}$	$^{-1.03}_{+0.79}$	$^{-1.03}_{+1.24}$	$^{-1.07}_{+1.69}$	$^{-1.53}_{+0.95}$	$^{-2.17}_{+1.91}$	$^{-2.09}_{+2.56}$
Effective detector NP set 4 (JES) [%]	$^{+0.70}_{+0.23}$	$^{+0.49}_{-}$	$^{-0.49}_{+0.35}$	$^{-0.39}_{+0.33}$	$^{-}_{-0.10}$	$^{+0.10}_{-0.14}$	$^{+0.35}_{-0.18}$	$^{+0.27}_{-0.46}$	$^{+0.33}_{-0.42}$	$^{+0.29}_{-0.44}$	$^{+0.39}_{-0.39}$	$^{+0.14}_{+0.37}$	$^{-0.29}_{-}$	$^{+0.23}_{-0.23}$	$^{+0.46}_{+0.43}$
Effective detector NP set 5 (JES) [%]	$^{-}_{-0.15}$	$^{-}_{-0.11}$	$^{-}_{-}$	$^{-}_{-}$	$^{+0.11}_{+0.11}$	$^{-0.14}_{+0.11}$	$^{-}_{-}$	$^{-}_{-}$	$^{-}_{+0.14}$	$^{-}_{-}$	$^{\pm 0.34}_{+0.22}$	$^{-}_{+0.18}$	$^{-0.51}_{+0.35}$	$^{-0.73}_{+0.47}$	$^{-0.81}_{+0.61}$
Effective detector NP set 6 restTerm (JES) [%]	$^{-}_{+0.83}$	$^{+0.16}_{+1.04}$	$^{-}_{+1.04}$	$^{-}_{+1.27}$	$^{-}_{+1.48}$	$^{-}_{+1.70}$	$^{-}_{+1.35}$	$^{-0.17}_{+1.12}$	$^{-0.11}_{+1.23}$	$^{-}_{+0.94}$	$^{-0.34}_{+1.08}$	$^{-0.18}_{+1.32}$	$^{-0.31}_{+0.51}$	$^{-0.69}_{+0.89}$	$^{-0.52}_{+1.97}$
η intercalibration model (JES) [%]	$^{-1.51}_{-}$	$^{-1.36}_{+0.48}$	$^{-1.73}_{+0.64}$	$^{-1.57}_{+0.59}$	$^{-1.86}_{+0.68}$	$^{-1.66}_{+0.79}$	$^{-1.88}_{+0.75}$	$^{-1.78}_{+0.71}$	$^{-1.99}_{+0.72}$	$^{-1.78}_{+0.52}$	$^{-1.55}_{+0.99}$	$^{-1.13}_{+0.88}$	$^{-1.65}_{+0.64}$	$^{-1.38}_{+1.05}$	$^{-2.18}_{+1.14}$
η intercalibration total stat (JES) [%]	$^{-0.39}_{+0.67}$	$^{+0.42}_{-0.42}$	$^{+0.37}_{-0.37}$	$^{+0.40}_{-0.40}$	$^{+0.42}_{-0.42}$	$^{+0.49}_{-0.49}$	$^{+0.51}_{-0.51}$	$^{+0.64}_{-0.64}$	$^{+0.48}_{-0.48}$	$^{+1.05}_{-1.05}$	$^{+0.57}_{-0.57}$	$^{+0.83}_{-0.83}$	$^{-0.89}_{+1.23}$	$^{+0.99}_{-0.99}$	$^{+0.72}_{-0.72}$
Flavour composition (JES) [%]	$^{-5.10}_{-1.47}$	$^{-4.33}_{-0.97}$	$^{-4.23}_{-1.04}$	$^{-3.95}_{-0.79}$	$^{-4.19}_{-1.34}$	$^{-4.01}_{-1.13}$	$^{-3.78}_{-1.38}$	$^{-3.69}_{-1.28}$	$^{-2.61}_{-0.71}$	$^{-2.70}_{-1.39}$	$^{-2.73}_{-1.16}$	$^{-2.13}_{-1.00}$	$^{-2.40}_{-}$	$^{-2.70}_{-1.56}$	$^{-3.19}_{-0.30}$
Flavour response (JES) [%]	$^{+0.35}_{-}$	$^{+0.26}_{-0.26}$	$^{+0.34}_{-0.38}$	$^{+0.71}_{-0.71}$	$^{+0.83}_{-0.59}$	$^{+0.92}_{-0.92}$	$^{+0.99}_{-0.71}$	$^{+0.75}_{-0.27}$	$^{+0.82}_{-}$	$^{+0.52}_{-}$	$^{+0.89}_{-0.17}$	$^{+0.86}_{-}$	$^{-1.02}_{-}$	$^{+0.70}_{-}$	$^{+0.41}_{-0.24}$
Pile-up offset μ (JES) [%]	$^{-}_{-}$	$^{+0.20}_{-}$	$^{+0.18}_{-}$	$^{+0.10}_{-}$	$^{+0.20}_{-}$	$^{\mp 0.20}_{-}$	$^{+0.18}_{-}$	$^{+0.10}_{-}$	$^{-}_{-}$	$^{-}_{-}$	$^{+0.13}_{-0.39}$	$^{-}_{-0.14}$	$^{-0.25}_{-}$	$^{-}_{-0.23}$	$^{-0.49}_{+0.43}$
Pile-up offset N_{PV} (JES) [%]	$^{-}_{-0.20}$	$^{-}_{-}$	$^{-}_{-}$	$^{-}_{-}$	$^{-}_{-}$	$^{-}_{-}$	$^{-}_{-}$	$^{-}_{-}$	$^{-}_{-}$	$^{-}_{-}$	$^{-}_{-}$	$^{+0.22}_{-}$	$^{-}_{-0.47}$	$^{-}_{-0.24}$	$^{-}_{-0.45}$
Pile-up offset p_T (JES) [%]	$^{-0.23}_{+0.42}$	$^{-0.33}_{+0.39}$	$^{-0.20}_{+0.26}$	$^{\mp 0.13}_{-}$	$^{-}_{-}$	$^{-}_{-}$	$^{-}_{-}$	$^{-}_{-}$	$^{+0.20}_{-}$	$^{+0.18}_{-}$	$^{-}_{-}$	$^{+0.34}_{-}$	$^{+0.10}_{-0.59}$	$^{-}_{-}$	$^{+0.32}_{-}$
Pile-up offset ρ topology (JES) [%]	$^{+0.42}_{-2.30}$	$^{+0.39}_{-1.97}$	$^{+0.36}_{-2.16}$	$^{+1.34}_{-1.76}$	$^{+1.62}_{-2.18}$	$^{+1.59}_{-1.99}$	$^{+1.25}_{-1.84}$	$^{+0.93}_{-1.77}$	$^{+0.89}_{-1.25}$	$^{+0.47}_{-1.65}$	$^{+0.22}_{-1.45}$	$^{+0.75}_{-0.98}$	$^{-0.43}_{-1.34}$	$^{-}_{-1.86}$	$^{+0.45}_{-1.20}$
Punch-through (JES) [%]	$^{-}_{-}$	$^{-}_{-}$	$^{-}_{-}$	$^{-}_{-}$	$^{-}_{-}$	$^{-}_{-}$	$^{-}_{-}$	$^{-}_{-}$	$^{-}_{-}$	$^{-}_{-}$	$^{-}_{-}$	$^{-}_{-}$	$^{-}_{-}$	$^{-}_{-0.28}$	$^{+0.17}_{-}$
Single particle high-p_T (JES) [%]	$^{-}_{-}$	$^{-}_{-}$	$^{-}_{-}$	$^{-}_{-}$	$^{-}_{-}$	$^{-}_{-}$	$^{-}_{-}$	$^{-}_{-}$	$^{-}_{-}$	$^{-}_{-}$	$^{-}_{-}$	$^{-}_{-}$	$^{-}_{-}$	$^{-}_{-}$	$^{-}_{-}$
Jet energy resolution [%]	∓2.08	∓2.41	∓2.16	∓1.80	∓1.55	∓0.91	∓0.86	∓1.58	∓0.16	∓1.47	∓1.23	-	∓2.18	∓2.71	∓2.12
Jet vertex fraction [%]	$^{+5.31}_{-5.23}$	$^{+5.34}_{-5.43}$	$^{+4.95}_{-4.82}$	$^{+4.18}_{-4.12}$	$^{+3.50}_{-3.46}$	$^{+2.75}_{-2.85}$	$^{+2.23}_{-2.20}$	±1.78	$^{+1.46}_{-1.52}$	±1.47	$^{+1.05}_{-1.74}$	±0.83	$^{+0.39}_{-0.65}$	$^{+0.89}_{-0.81}$	$^{+0.27}_{-1.10}$
b-Quark tagging efficiency (eigenvector 0) [%]	∓4.81	∓4.69	∓4.46	$^{+4.18}_{+4.12}$	∓4.02	$^{+3.92}_{+3.77}$	$^{+3.86}_{+3.73}$	$^{+3.80}_{+3.63}$	$^{+3.78}_{+3.71}$	$^{+3.78}_{+3.73}$	$^{+3.80}_{+3.77}$	$^{+3.88}_{+3.77}$	$^{+3.74}_{+4.25}$	$^{+3.88}_{+4.36}$	$^{+4.16}_{+4.60}$
b-Quark tagging efficiency (eigenvector 1) [%]	∓0.88	∓0.93	$^{+1.02}_{+1.46}$	$^{+1.19}_{+1.38}$	∓1.40	$^{+1.73}_{+1.05}$	$^{+2.12}_{+0.81}$	$^{+2.56}_{+0.54}$	$^{+3.09}_{+0.24}$	$^{+3.40}_{-}$	$^{+3.77}_{+0.14}$	$^{+4.25}_{+0.39}$	$^{+4.36}_{+0.54}$	$^{+4.60}_{+0.69}$	$^{+5.26}_{+0.91}$
b-Quark tagging efficiency (eigenvector 2) [%]	$^{+1.47}_{-1.46}$	$^{+1.49}_{-1.48}$	$^{+1.45}_{-1.45}$	$^{+1.25}_{-1.37}$	$^{+1.25}_{-1.04}$	$^{+0.89}_{-0.89}$	$^{+0.59}_{-0.79}$	$^{+0.54}_{-}$	$^{+0.24}_{-}$	$^{-}_{-}$	$^{+0.14}_{+0.18}$	$^{+0.39}_{+0.28}$	$^{+0.54}_{+0.35}$	$^{+0.69}_{-0.42}$	$^{+0.91}_{+0.57}$
b-Quark tagging efficiency (eigenvector 3) [%]	$^{-}_{-}$	$^{-}_{-}$	$^{-}_{-}$	$^{-}_{-}$	$^{+0.16}_{-0.15}$	$^{\mp 0.19}_{-}$	$^{-}_{-0.18}$	$^{\mp 0.13}_{-}$	$^{-}_{-}$	$^{-}_{-}$	$^{\mp 0.18}_{-}$	$^{\mp 0.28}_{-}$	$^{\mp 0.35}_{+0.43}$	$^{-}_{+0.43}$	$^{-}_{-}$
b-Quark tagging efficiency (eigenvector 4) [%]	$^{-}_{-}$	$^{-}_{-}$	$^{-}_{-}$	$^{-}_{-}$	$^{-}_{-}$	$^{-}_{-}$	$^{-}_{-}$	$^{-}_{-}$	$^{-}_{-}$	$^{-}_{-}$	$^{\mp 0.10}_{-}$	$^{\mp 0.14}_{-}$	$^{\mp 0.16}_{+0.16}$	$^{\mp 0.19}_{+0.19}$	$^{\mp 0.24}_{-}$
c-Quark tagging efficiency (eigenvector 0) [%]	$^{-1.74}_{+1.76}$	$^{-1.74}_{+1.75}$	$^{-1.81}_{+1.82}$	$^{-1.67}_{+1.68}$	$^{-1.51}_{+1.52}$	$^{-1.41}_{+1.42}$	$^{-1.19}_{+1.20}$	∓1.06	$^{-1.05}_{+1.06}$	∓0.98	$^{-0.87}_{+0.88}$	∓0.87	$^{-0.91}_{+0.92}$	∓1.05	$^{-1.34}_{+1.36}$
c-Quark tagging efficiency (eigenvector 1) [%]	±0.36	±0.34	±0.31	±0.24	±0.16	-	-	-	-	∓0.14	∓0.18	∓0.15	∓0.14	∓0.21	∓0.27
c-Quark tagging efficiency (eigenvector 2) [%]	±0.16	±0.18	±0.21	±0.24	±0.23	±0.18	±0.13	-	-	-	-	-	-	-	-
c-Quark tagging efficiency (eigenvector 3) [%]	∓0.11	∓0.11	-	-	-	-	-	-	-	-	-	-	-	-	-
Light-jet tagging efficiency (eigenvector 0) [%]	$^{-2.05}_{+2.41}$	$^{-2.16}_{+2.30}$	$^{-1.60}_{+1.67}$	$^{-1.43}_{+1.47}$	$^{-1.32}_{+1.36}$	$^{-1.35}_{+1.38}$	$^{-1.42}_{+1.54}$	$^{-1.25}_{+1.28}$	$^{-1.32}_{+1.35}$	$^{-1.58}_{+1.63}$	$^{-1.40}_{+1.39}$	$^{-1.15}_{+1.21}$	$^{-2.54}_{+3.16}$	∓2.71	$^{-3.81}_{+4.06}$
Light-jet tagging efficiency (eigenvector 1) [%]	-	-	-	-	-	-	-	-	-	-	-	-	$^{+0.20}_{-0.18}$	-	∓0.11
Light-jet tagging efficiency (eigenvector 2) [%]	±0.21	$^{+0.21}_{-0.22}$	±0.13	±0.10	-	-	-	-	-	-	-	-	∓0.11	∓0.10	∓0.14
Light-jet tagging efficiency (eigenvector 3) [%]	-	-	-	-	-	-	-	-	-	-	-	-	-	-	-
Light-jet tagging efficiency (eigenvector 4) [%]	-	-	-	-	-	-	-	-	-	-	-	-	-	-	∓0.18
Light-jet tagging efficiency (eigenvector 5) [%]	-	-	-	-	-	-	-	-	-	-	-	-	-	-	-
Light-jet tagging efficiency (eigenvector 6) [%]	-	-	-	-	-	-	-	-	-	-	-	-	-	-	-
Light-jet tagging efficiency (eigenvector 7) [%]	-	-	-	-	-	-	-	-	-	-	-	-	-	-	-
Light-jet tagging efficiency (eigenvector 8) [%]	-	-	-	-	-	-	-	-	-	-	-	-	-	-	-
Light-jet tagging efficiency (eigenvector 9) [%]	-	-	-	-	-	-	-	-	-	-	-	-	-	-	-
Light-jet tagging efficiency (eigenvector 10) [%]	-	-	-	-	-	-	-	-	-	-	-	-	-	-	-
Light-jet tagging efficiency (eigenvector 11) [%]	-	-	-	-	-	-	-	-	-	-	-	-	-	-	-
b-Quark tagging extrapolation [%]	-	-	-	-	-	∓0.10	$^{+0.20}_{-0.22}$	±0.41	±0.97	$^{+1.58}_{-1.57}$	$^{+2.41}_{-2.39}$	$^{+3.44}_{-3.40}$	$^{+3.84}_{-3.76}$	$^{+4.55}_{-4.48}$	$^{+7.08}_{-6.94}$
b-Quark tagging extrapolation from c-Quark [%]	±0.12	$^{+0.12}_{-0.13}$	±0.14	±0.13	±0.11	-	-	-	-	-	-	-	-	-	-
Electron energy resolution [%]	-	-	-	-	-	-	-	-	-	-	-	-	-	-	-
Electron energy scale [%]	-	-	-	-	-	-	-	-	-	-	-	-	-	-	-
Electron trigger efficiency [%]	±0.25	±0.25	±0.24	±0.24	±0.25	±0.26	±0.27	±0.29	±0.29	±0.30	±0.31	±0.31	±0.31	±0.34	±0.37
Electron reconstruction efficiency [%]	±0.15	±0.16	±0.16	±0.16	±0.17	±0.19	±0.20	±0.21	±0.22	±0.23	±0.24	±0.25	±0.25	±0.27	±0.30
Electron identification efficiency [%]	±0.39	±0.39	±0.39	±0.39	±0.41	±0.43	±0.46	±0.51	±0.55	±0.59	±0.65	±0.71	±0.75	±0.84	±0.99
Electron isolation efficiency [%]	±0.12	±0.12	±0.12	±0.13	±0.14	±0.15	±0.18	±0.21	±0.25	±0.29	±0.35	±0.41	±0.47	±0.54	±0.69
Muon energy scale [%]	-	-	-	-	-	-	-	-	-	-	-	-	-	-	-
Muon (MS) momentum resolution [%]	-	-	-	-	-	-	-	-	-	-	-	-	-	-	-
Muon (ID) momentum resolution [%]	$^{-0.21}_{-}$	$^{-}_{-}$	$^{-}_{-}$	$^{-}_{-}$	$^{-}_{-}$	$^{-}_{-}$	$^{-}_{-}$	$^{-}_{-}$	$^{-}_{-}$	$^{-}_{-}$	$^{-}_{-}$	$^{-}_{-}$	$^{-}_{-}$	$^{-}_{-}$	$^{-}_{-}$
Muon trigger efficiency stat [%]	$^{+0.61}_{-0.63}$	$^{+0.59}_{-0.60}$	$^{+0.58}_{-0.60}$	$^{+0.57}_{-0.58}$	$^{+0.56}_{-0.58}$	$^{+0.56}_{-0.57}$	$^{+0.55}_{-0.57}$	$^{+0.55}_{-0.57}$	$^{+0.56}_{-0.57}$	$^{+0.55}_{-0.57}$	$^{+0.55}_{-0.56}$	$^{+0.55}_{-0.57}$	$^{+0.57}_{-0.59}$	$^{+0.57}_{-0.59}$	$^{+0.56}_{-0.58}$
Muon trigger efficiency syst [%]	$^{+0.26}_{-0.25}$	±0.25	±0.25	$^{+0.25}_{-0.24}$	±0.24	±0.24	±0.24	±0.24	±0.24	$^{+0.24}_{-0.23}$	$^{+0.24}_{-0.23}$	$^{+0.24}_{-0.23}$	±0.25	±0.24	$^{+0.26}_{-0.25}$
Muon identification stat [%]	-	-	-	-	-	-	-	-	-	-	-	-	-	-	-
Muon identification syst [%]	±0.17	±0.16	±0.16	±0.16	±0.16	±0.17	±0.18	±0.20	±0.22	±0.24	±0.26	±0.29	$^{+0.34}_{-0.33}$	±0.36	±0.44
Muon isolation efficiency stat [%]	-	-	-	-	-	-	-	-	-	-	-	-	-	-	-
Muon isolation efficiency syst [%]	±0.11	±0.11	±0.11	±0.10	±0.10	±0.10	±0.10	±0.10	±0.10	±0.10	±0.10	±0.10	±0.11	±0.10	±0.16
Muon TTVA efficiency stat [%]	-	-	-	-	-	-	-	-	-	-	-	-	-	-	-
Muon TTVA efficiency syst [%]	-	-	-	-	-	-	-	-	-	-	-	-	-	-	-
E_T^{miss} Soft jet resolution para [%]	±0.12	±0.11	-	-	-	-	-	-	-	-	-	-	-	±0.10	±0.17
E_T^{miss} Soft jet resolution perp [%]	-	±0.12	±0.13	-	-	-	-	-	-	-	-	∓0.11	-	-	±0.19
E_T^{miss} Soft jet scale [%]	-	-	-	-	-	-	-	-	-	-	-	-	-	-	-
Luminosity [%]	∓2.06	∓2.06	∓2.06	∓2.06	∓2.06	∓2.06	∓2.06	∓2.06	∓2.06	∓2.06	∓2.06	∓2.06	∓2.06	∓2.06	∓2.06
Single top cross-section [%]	±0.26	±0.26	±0.25	±0.24	±0.24	±0.25	±0.27	±0.27	±0.29	±0.30	±0.33	±0.36	±0.39	±0.44	±0.69
Z+jets cross-section [%]	±0.59	±0.70	±0.88	±0.68	±0.57	±0.43	±0.45	±0.38	±0.39	±0.38	±0.33	±0.39	±0.28	±0.43	±0.94
Diboson cross-section [%]	±0.18	±0.14	±0.13	±0.12	±0.11	±0.12	±0.13	±0.14	±0.17	±0.17	±0.24	±0.22	±0.38	±0.46	±0.83
$t\bar{t}V$ cross-section [%]	-	-	-	-	-	-	-	-	-	-	-	-	±0.10	-	±0.21
Monte Carlo sample statistics [%]	±1.04	±0.52	±0.41	±0.32	±0.33	±0.36	±0.44	±0.48	±0.55	±0.78	±0.75	±1.09	±1.96	±2.26	±1.94
ISR/FSR + scale [%]	$^{-3.28}_{+2.58}$	$^{-2.54}_{+1.96}$	$^{-2.26}_{+2.33}$	$^{-2.49}_{+1.65}$	$^{-3.08}_{+2.33}$	$^{-2.44}_{+3.21}$	$^{-3.45}_{+1.86}$	$^{-3.85}_{+1.73}$	$^{-3.52}_{+2.87}$	$^{-2.13}_{+2.93}$	$^{-2.26}_{+1.55}$	$^{-1.77}_{+1.66}$	$^{-4.67}_{+3.16}$	$^{-4.00}_{-}$	$^{-0.67}_{+1.13}$
Alternate hard-scattering model [%]	∓0.90	∓0.33	∓0.41	-	-	∓0.35	∓0.32	∓2.49	∓1.38	±4.87	±2.82	±1.57	±3.04	±14.7	±1.95
Alternate parton-shower model [%]	∓2.52	∓1.77	∓1.58	∓2.28	∓2.24	∓2.28	∓1.50	±3.08	∓2.32	∓2.03	∓2.09	±5.27	∓2.90	±9.59	±6.81
Inter PDF [%]	-	±0.13	-	-	-	-	-	±0.11	-	-	±0.14	±0.18	-	±0.17	±1.93
Intra PDF [%]	-	±0.15	-	-	-	-	-	-	±0.11	-	-	±0.13	±0.28	±0.31	±1.52
Real lepton efficiency stat [%]	∓0.11	∓0.12	$^{-0.13}_{+0.12}$	$^{-0.13}_{+0.12}$	$^{-0.15}_{+0.14}$	$^{-0.16}_{+0.15}$	$^{-0.19}_{+0.15}$	$^{-0.21}_{+0.15}$	$^{-0.25}_{+0.27}$	$^{-0.27}_{+0.43}$	$^{-0.32}_{+0.62}$	$^{-0.39}_{+0.52}$	$^{-0.38}_{+0.59}$	$^{-0.55}_{+0.77}$	$^{-1.09}_{+0.93}$
Fake lepton efficiency MC scale [%]	$^{+0.67}_{-0.74}$	$^{+0.80}_{-0.86}$	$^{+0.47}_{-0.77}$	$^{+0.47}_{-0.84}$	$^{+0.43}_{-0.68}$	$^{+0.49}_{-0.75}$	$^{+0.51}_{-0.58}$	$^{+0.49}_{-0.68}$	$^{+0.27}_{-0.68}$	$^{+0.43}_{-0.34}$	$^{+0.62}_{-0.64}$	$^{+0.52}_{-0.39}$	$^{+0.59}_{-1.11}$	$^{+0.77}_{-1.19}$	$^{+0.93}_{-1.23}$
Fake lepton efficiency alternate CR [%]	±0.27	±0.39	±0.40	±0.45	±0.27	±0.30	±0.20	±0.34	±0.17	±0.14	±0.31	±0.44	±0.18	±0.20	±0.15
Fake overall normalisation [%]	±4.59	±4.88	±4.33	±3.96	±2.83	±2.82	±2.26	±2.18	±2.31	±1.90	±2.41	±1.70	±3.00	±2.76	±6.06
W+jets $CA_{4\text{incl}}$ stat error [%]	±0.20	±0.18	±0.14	-	-	-	-	-	-	-	-	-	±0.15	±0.12	±0.18
W+jets Fc stat error [%]	-	-	-	-	-	-	-	-	-	-	-	-	-	-	-
W+jets Fcc stat error [%]	$^{+0.62}_{-0.30}$	$^{+0.20}_{-0.10}$	-	-	-	-	-	-	-	-	$^{-0.17}_{-}$	-	$^{+0.65}_{-0.31}$	-	$^{-0.42}_{+0.20}$
W+jets Flight stat error [%]	-	-	-	-	-	-	-	-	-	-	-	-	-	-	-

Table C.5: Table of systematic uncertainties for the absolute differential cross-section at particle level for the top quark transverse momentum in the resolved regime.

Bins $\lvert$ Unit $\lvert y^t \rvert \rvert$	0-0.10	0.10-0.20	0.20-0.30	0.30-0.40	0.40-0.50	0.50-0.60	0.60-0.70	0.70-0.80	0.80-0.90	0.90-1	1-1.10	1.10-1.20	1.20-1.30	1.30-1.40	1.40-1.50	1.50-1.70	1.70-1.90	1.90-2.50
$d\sigma$ / $d\lvert y^t \rvert$ [pb / Unit $\lvert y^t \rvert$]	$8.13 \cdot 10^{1}$	$7.87 \cdot 10^{1}$	$7.88 \cdot 10^{1}$	$7.73 \cdot 10^{1}$	$7.43 \cdot 10^{1}$	$7.22 \cdot 10^{1}$	$6.75 \cdot 10^{1}$	$6.31 \cdot 10^{1}$	$6.29 \cdot 10^{1}$	$5.55 \cdot 10^{1}$	$5.06 \cdot 10^{1}$	$4.76 \cdot 10^{1}$	$4.24 \cdot 10^{1}$	$3.74 \cdot 10^{1}$	$3.21 \cdot 10^{1}$	$2.45 \cdot 10^{1}$	$1.58 \cdot 10^{1}$	$3.59 \cdot 10^{0}$
Total uncertainty [%]	+10.9 −11.9	+10.5 −11.1	+10.4 −10.6	+10.9 −10.8	+11.2 −12.5	+10.3 −11.2	+10.5 −11.6	+10.3 −11.4	+11.3 −11.1	+10.5 −11.7	+10.8 −11.3	+10.2 −11.9	+10.5 −11.7	±11.2	+10.3 −11.3	+11.0 −11.5	+11.2 −11.7	±11.3
Statistical uncertainty [%]	±1.1	±1.2	±1.2	±1.2	±1.3	±1.3	±1.3	±1.4	±1.4	±1.5	±1.6	±1.6	±1.7	±1.9	±2.1	±1.5	±1.9	±2.2
Systematic uncertainty [%]	+9.93 −11.8	+10.4 −11.0	+10.3 −10.5	+9.95 −10.7	+11.1 −12.4	+10.2 −11.1	+10.4 −11.5	+10.2 −11.3	+11.2 −11.0	+10.4 −11.6	+10.4 −11.2	+10.1 −11.8	+10.3 −11.6	±11.0	+10.0 −11.1	+10.9 −11.4	+11.0 −11.5	±11.0
b-Tagged jet energy scale (JES) [%]	+0.51 −0.60	+0.59 −0.40	+0.37 −0.69	+0.09 −0.52	+0.36 −0.51	+0.46 −0.42	±0.59	+0.54 −0.48	+0.33 −0.51	+0.56 −0.61	+0.58 −0.45	+0.29 −0.70	+0.59 −0.42	+0.83 −0.32	+0.59 −0.46	+0.74 −0.55	+0.41 −0.45	+0.42 −0.37
Effective detector NP set 1 (JES) [%]	+4.33 −5.73	+4.86 −5.93	+4.62 −5.19	+4.54 −5.57	+4.64 −5.93	+4.36 −5.68	+4.78 −5.85	+4.75 −5.89	−5.51 −5.85	+4.99 −5.88	+4.69 −5.04	+4.53 −5.09	+4.44 −5.70	+4.54 −5.49	+4.75 −5.78	+5.14 −5.66	+5.74 −5.94	+4.84 −5.59
Effective detector NP set 2 (JES) [%]	−0.88	−0.74	−0.47	−0.84	−0.74	−0.80	−0.82	−0.77	−0.92	−0.68	−0.69	−1.05	−0.91	−0.76	−0.65	−0.72	−0.74	−0.97
Effective detector NP set 3 (JES) [%]	+0.42 −0.20	+0.63 −0.19	+0.59 −0.13	+0.75 −0.26	+0.87 −0.37	+0.73 −0.19	+0.64 −0.20	+0.44 −	+0.85 −0.30	+0.84 −	+0.80 −0.15	+0.64 −0.28	+0.55 −0.10	+1.25 −0.21	+0.62 −0.21	+0.88 −0.15	+0.83 −0.17	+0.47 −
Effective detector NP set 4 (JES) [%]	-	-	-	−0.16	−0.12	-	-	−0.30 −0.14	−0.30 -	-	-	-	-	−0.11 +0.15	-	-	-	-
Effective detector NP set 5 (JES) [%]	-	-	-	+0.11	-	-	-	-	−0.24	-	-	-	-	-	-	-	-	-
Effective detector NP set 6 restTerm (JES) [%]	-	-	-	-	-	-	-	-	-	-	-	-	-	-	-	-	-	-
η intercalibration model (JES) [%]	+0.37 −1.09	+0.66 −1.02	+0.68 −0.89	+0.38 −0.78	+0.69 −1.20	+0.79 −1.24	+1.08 −1.57	+0.89 −1.50	+1.58 −1.75	+1.61 −1.98	+1.70 −1.83	+1.87 −2.53	+1.97 −2.39	+2.65 −2.13	+1.99 −2.81	+2.86 −3.19	+3.23 −3.42	+3.27 −3.27
η intercalibration total stat (JES) [%]	+0.27 −0.96	+0.69 −0.70	+0.59 −0.77	+0.58 −0.61	+0.67 −0.49	+0.58 −0.78	±0.58 +3.39	+0.39 −0.79	+0.89 −0.73	+0.75 −0.79	+0.74 −0.73	+0.60 −0.99	+0.77 −0.86	+1.14 −0.80	±0.63 −0.80	+0.87 −0.97	+1.02 −0.96	±0.92 −0.63
Flavour composition (JES) [%]	−2.03	−2.03	−2.03	−2.03	−2.00	−2.01	−3.39	−3.02	−3.09	−3.09	−3.09	−3.03	−3.01	−4.03	−2.98	−3.03	−3.03	−3.03
Flavour response (JES) [%]	−1.34 +0.18	−1.55 +0.72	−1.35 +0.56	−1.43 +0.62	−1.40 +0.57	−1.34 +0.78	−1.02 +0.44	−1.02 +0.34	−1.74 +1.13	−1.39 +0.56	−1.40 +0.83	−1.43 +0.77	−1.46 +0.77	−1.55 +1.63	−1.55 +0.49	−1.39 +0.60	−1.32 +1.40	−1.36 +1.05
Pile-up offset μ (JES) [%]	-	−0.56 +0.18	−0.56 -	-	-	+0.52 +0.20	+0.16 +0.21	-	+0.48 +0.20	+0.29 +0.15	+0.24 +0.26	−0.26 +0.13	+0.26 +0.16	+0.54 +0.29	+0.13 +0.20	+0.31 +0.19	+0.32 +0.39	+0.43 +0.31
Pile-up offset N_{PV} (JES) [%]	-	-	-	-	-	-	-	-	-	-	-	-	-	+0.25	-	-	-	−0.17
Pile-up offset p_{T} (JES) [%]	-	-	−0.13	-	−0.10	-	-	-	-	−0.12	-	-	-	-	-	-	-	-
Pile-up offset ρ topology (JES) [%]	+0.96	+1.20	+1.27	+1.25	+0.13 +1.33	+1.33	+1.27	+1.12	+1.75	+1.18	+1.37	+1.37	+1.18	+2.26	+1.03	+1.42	+1.64	+1.47
Punch-through (JES) [%]	−2.22	−1.78	−1.68	−1.99	−2.00	−1.94	−1.78	−1.91	−2.10	−1.98	−1.70	−2.24	−2.26	−1.63	−1.87	−1.67	−1.77	−1.74
Single particle high-p_{T} (JES) [%]	-	-	-	-	-	-	-	-	-	-	-	-	-	-	-	-	-	-
Jet energy resolution [%]	∓2.13	∓1.84	∓1.65	∓0.11	∓2.89	∓1.89	∓1.39	∓2.19	∓0.32	∓1.03	∓2.14	∓1.39	∓1.58	∓1.11	∓1.03	∓1.71	∓1.75	∓1.19
Jet vertex fraction [%]	+3.40 −4.08	+3.48 −4.06	+3.42 −4.06	+3.46 −4.09	+3.47 −4.06	+3.52 −4.08	+3.61 −4.11	+3.49 −4.08	+3.50 −4.05	+3.52 −4.05	+3.60 −4.13	+3.57 −4.04	+3.58 −4.04	+3.56 −4.04	+3.54 −4.04	+3.45 −4.11	+3.37 −4.01	+3.04 −3.99
b-Quark tagging efficiency (eigenvector 0) [%]	+4.13 −1.65	+4.13 −1.63	+4.16 −1.65	+4.13 −1.67	+4.15 −1.66	+4.18 −1.65	+4.15 −1.65	+4.13 −1.63	+4.12 −1.65	+4.20 −1.66	+4.11 −1.66	+4.11 −1.64	+4.11 −1.64	+4.11 −1.63	+4.11 −1.63	+4.19 −1.65	+4.08 −1.67	+4.06 −1.75
b-Quark tagging efficiency (eigenvector 1) [%]	+1.09 −1.07	+1.09 −1.07	+1.07 −1.08	+1.09 −1.06	+1.07 −1.08	+1.08 −1.08	+1.07 ±1.07	+1.04 −1.08	+1.08 −1.08	+1.08 −1.08	+1.06 −1.08	+1.06 ±1.08	+1.05 −1.09	+1.05 −1.09	+1.06 −1.10	+1.06 ±1.11	+1.08 −1.10	+1.70 −1.66
b-Quark tagging efficiency (eigenvector 2) [%]	−1.06	−1.06	−1.08	-	−1.07	−1.07	-	−1.07	−1.07	−1.08	−1.08	-	−1.09	−1.09	-	−1.09	−1.08	−1.06
b-Quark tagging efficiency (eigenvector 3) [%]	-	-	-	-	-	-	-	-	-	-	-	-	-	-	-	-	-	±0.10
b-Quark tagging efficiency (eigenvector 4) [%]	-	-	-	-	-	-	-	-	-	-	-	-	-	-	-	-	-	-
c-Quark tagging efficiency (eigenvector 0) [%]	−1.61 ±1.62	−1.56 ±1.58	−1.54 ±1.55	−1.52 ±1.53	−1.52 ±1.53	−1.57 ±1.58	−1.53 ±1.54	−1.56 ±1.57	∓1.43	∓1.43	∓1.42	∓1.42	−1.44 ±1.45	−1.31 ±1.32	∓1.35	−1.38 ±1.39	∓1.27	∓1.15
c-Quark tagging efficiency (eigenvector 1) [%]	±0.17	±0.16	±0.14	±0.16	±0.15	±0.17	±0.17	±0.15	±0.14	±0.15	±0.15	±0.14	±0.15	±0.14	±0.13	±0.14	±0.15	-
c-Quark tagging efficiency (eigenvector 2) [%]	±0.19	±0.19	±0.18	±0.18	±0.18	±0.18	±0.18	±0.18	±0.17	±0.17	±0.16	±0.17	±0.18	±0.17	±0.17	±0.16	±0.15	±0.13
c-Quark tagging efficiency (eigenvector 3) [%]	-	-	-	-	-	-	-	-	-	-	-	-	-	-	-	-	-	-
Light-jet tagging efficiency (eigenvector 0) [%]	∓1.38	−1.72 ∓1.87	−1.31 ∓1.33	−1.39 ∓1.47	−1.62 ∓1.74	−1.27 ∓1.28	−1.54 ∓1.65	−1.47 ∓1.53	−1.27 ∓1.26	−1.54 ∓1.63	−1.69 ∓1.82	−1.57 ∓1.77	−1.35 ∓1.33	−1.69 ∓1.69	−1.68 ∓1.66	−1.49 ∓1.51	−2.15 ∓2.42	−2.08 ∓2.07
Light-jet tagging efficiency (eigenvector 1) [%]	-	-	∓0.11 −0.10	-	-	-	-	-	-	-	-	-	-	-	-	-	∓0.12	∓0.20
Light-jet tagging efficiency (eigenvector 2) [%]	-	±0.12	-	-	±0.11	-	-	-	-	-	±0.11	-	-	-	±0.10	-	±0.11	-
Light-jet tagging efficiency (eigenvector 3) [%]	-	-	-	-	-	-	-	-	-	-	-	-	-	-	-	-	-	-
Light-jet tagging efficiency (eigenvector 4) [%]	-	-	-	-	-	-	-	-	-	-	-	-	-	-	-	-	-	-
Light-jet tagging efficiency (eigenvector 5) [%]	-	-	-	-	-	-	-	-	-	-	-	-	-	-	-	-	-	-
Light-jet tagging efficiency (eigenvector 6) [%]	-	-	-	-	-	-	-	-	-	-	-	-	-	-	-	-	-	-
Light-jet tagging efficiency (eigenvector 7) [%]	-	-	-	-	-	-	-	-	-	-	-	-	-	-	-	-	-	-
Light-jet tagging efficiency (eigenvector 8) [%]	-	-	-	-	-	-	-	-	-	-	-	-	-	-	-	-	-	-
Light-jet tagging efficiency (eigenvector 9) [%]	-	-	-	-	-	-	-	-	-	-	-	-	-	-	-	-	-	-
Light-jet tagging efficiency (eigenvector 10) [%]	-	-	-	-	-	-	-	-	-	-	-	-	-	-	-	-	-	-
Light-jet tagging efficiency (eigenvector 11) [%]	-	-	-	-	-	-	-	-	-	-	-	-	-	-	-	-	-	-
b-Quark tagging extrapolation [%]	+0.32 −0.33	±0.31	+0.32 −0.31	±0.33	+0.32 −0.31	+0.32 −0.31	±0.32	+0.30 −0.31	±0.31	±0.30	+0.31 −0.31	±0.29	±0.28	±0.28	±0.27	±0.27	±0.26	±0.28
b-Quark tagging extrapolation from c-Quark [%]	+0.10 −0.12	±0.12	+0.11 −0.10	+0.12 −0.13	±0.12	-	±0.11	+0.11 −0.12	-	±0.10	+0.12 −0.13	-	±0.10	-	-	±0.10	-	-
Electron energy resolution [%]	-	-	-	-	-	-	-	-	-	-	-	-	-	+0.15 −	-	-	-	-
Electron energy scale [%]	-	-	-	-	-	-	-	-	-	-	-	-	-	-	-	-	-	-
Electron trigger efficiency [%]	±0.26	±0.25	±0.26	±0.26	±0.26	±0.26	±0.26	±0.26	±0.25	±0.27	±0.26	±0.26	±0.26	±0.26	±0.27	±0.26	±0.27	±0.27
Electron reconstruction efficiency [%]	±0.18	±0.18	±0.18	±0.18	±0.18	±0.18	±0.18	±0.18	±0.18	±0.18	±0.18	±0.18	±0.18	±0.18	±0.18	±0.18	±0.18	±0.18
Electron identification efficiency [%]	±0.44	±0.43	±0.44	±0.44	±0.44	±0.44	±0.44	±0.45	±0.43	±0.45	±0.44	±0.44	±0.43	±0.43	±0.45	±0.43	±0.44	±0.43
Electron isolation efficiency [%]	±0.17	±0.16	±0.17	±0.16	±0.17	±0.17	±0.16	±0.16	±0.16	±0.17	±0.16	±0.16	±0.16	±0.16	±0.16	±0.16	±0.17	±0.16
Muon energy scale [%]	-	-	-	-	-	-	-	-	-	-	-	-	-	-	-	-	-	-
Muon (MS) momentum resolution [%]	-	-	-	-	-	-	-	-	-	-	-	-	-	-	-	-	-	-
Muon (ID) momentum resolution [%]	-	-	-	-	-	-	-	-	−0.18	-	-	-	-	-	-	-	-	-
Muon trigger efficiency stat [%]	+0.57 −0.58	+0.58 −0.59	+0.57 −0.60	+0.58 −0.60	+0.57 −0.59	+0.56 −0.59	+0.57 −0.59	+0.56 −0.58	+0.56 −0.58	+0.58 −0.59	+0.56 −0.58	+0.56 −0.57	+0.56 −0.58	+0.56 −0.57	+0.56 −0.58	+0.56 −0.57	+0.55 −0.57	+0.55 −0.57
Muon trigger efficiency syst [%]	+0.25 −0.24	+0.25 −0.25	+0.25 −0.24	+0.25 −0.25	+0.25 −0.24	±0.24	+0.25 −0.24	±0.24	±0.24	+0.25 −0.24	±0.24	±0.24	±0.24	±0.24	±0.24	±0.24	±0.24	+0.24 −0.23
Muon identification stat [%]	-	-	-	-	-	-	-	-	-	-	-	-	-	-	-	-	-	-
Muon identification syst [%]	±0.18	±0.18	+0.18 −0.17	±0.18	±0.18	+0.18 −0.17	±0.18	+0.18 −0.17	±0.17	±0.18	±0.18	+0.18 −0.17	±0.18	±0.18	+0.18 −0.17	±0.18	±0.18	±0.18
Muon isolation efficiency stat [%]	-	-	-	-	-	-	-	-	-	-	-	-	-	-	-	-	-	-
Muon isolation efficiency syst [%]	±0.10	±0.10	±0.10	±0.10	±0.10	±0.10	±0.10	±0.10	±0.10	±0.10	±0.10	±0.10	±0.10	±0.10	±0.10	±0.10	±0.10	±0.10
Muon TTVA efficiency stat [%]	-	-	-	-	-	-	-	-	-	-	-	-	-	-	-	-	-	-
Muon TTVA efficiency syst [%]	-	-	-	-	-	-	-	-	-	-	-	-	-	-	-	-	-	-
$E_{\mathrm{T}}^{\mathrm{miss}}$ Soft jet resolution para [%]	±0.10	-	-	-	-	-	-	-	-	-	-	-	-	-	-	-	-	-
$E_{\mathrm{T}}^{\mathrm{miss}}$ Soft jet resolution perp [%]	∓0.10	∓0.10	∓0.10	-	-	-	-	-	-	∓0.12	-	-	-	-	-	-	-	-
$E_{\mathrm{T}}^{\mathrm{miss}}$ Soft jet scale [%]	-	-	-	-	-	-	-	-	-	-	-	-	-	-	-	-	-	-
Luminosity [%]	∓2.06	∓2.06	∓2.06	∓2.06	∓2.06	∓2.06	∓2.06	∓2.06	∓2.06	∓2.06	∓2.06	∓2.06	∓2.06	∓2.06	∓2.06	∓2.06	∓2.06	∓2.06
Single top cross-section [%]	±0.28	±0.28	±0.29	±0.29	±0.27	±0.27	±0.27	±0.26	±0.26	±0.25	±0.24	±0.24	±0.24	±0.23	±0.23	±0.22	±0.20	±0.21
Z+jets cross-section [%]	±0.66	±0.61	±0.66	±0.55	±0.67	±0.56	±0.57	±0.58	±0.50	±0.82	±0.60	±0.53	±0.47	±0.36	±0.74	±0.35	±0.62	±0.40
Diboson cross-section [%]	±0.14	±0.14	±0.15	±0.14	±0.14	±0.15	±0.14	±0.12	±0.14	±0.15	±0.13	±0.13	±0.16	±0.12	±0.14	±0.13	±0.12	±0.11
$t\bar{t}V$ cross-section [%]	-	-	-	-	-	-	-	-	-	-	-	-	-	-	-	-	-	-
Monte Carlo sample statistics [%]	±0.45	±0.52	±0.50	±0.53	±0.55	±0.49	±0.54	±0.59	±0.52	±0.64	±0.64	±0.66	±0.66	±0.67	±0.76	±0.54	±0.80	±0.83
ISR/FSR + scale [%]	−4.16 +1.31	−2.52 +1.77	−1.85 +3.04	−2.52 +2.12	−2.75 +1.66	−2.08 +3.06	−3.46 +2.42	−3.19 +2.98	−2.17 +3.61	−3.53 +1.53	−3.76 +1.93	−2.49 +1.61	−2.65 +2.84	−3.45 +1.93	−1.91 +2.47	−2.53 +2.71	−3.11 +1.50	−1.05 +2.71
Alternate hard-scattering model [%]	±0.44	±0.56	±1.05	±0.36	±3.21	±0.95	±1.00	±0.39	±0.88	±0.36	±2.31	±0.47	±1.75	±0.13	±1.36	±0.17	-	±3.74
Alternate parton-shower model [%]	∓2.11	∓2.07	∓1.86	∓1.97	∓2.99	∓1.77	∓1.89	∓1.37	∓1.82	∓1.87	∓1.74	∓2.51	∓1.55	∓1.84	∓1.26	∓2.27	∓3.06	∓0.92
Inter PDF [%]	-	-	-	-	-	±0.12	-	-	-	-	-	-	-	±0.15	-	±0.13	-	±0.19
Intra PDF [%]	-	-	-	-	-	±0.19	-	-	-	-	-	-	-	-	±0.11	±0.13	±0.17	±0.25
Real lepton efficiency stat [%]	−0.17	−0.16	−0.16	−0.18	−0.16	−0.18	−0.16	−0.16	−0.17	−0.17	−0.17	−0.17	−0.16	−0.17	−0.16	−0.17	−0.17	−0.18
Fake lepton efficiency MC scale [%]	±0.15 −0.74	±0.15 −0.92	±0.15 −0.76	±0.15 −0.84	±0.15 −0.84	±0.15 −0.80	±0.15 −0.76	±0.15 −0.66	±0.15 −0.87	±0.15 −0.70	±0.15 −0.69	±0.15 −0.72	±0.15 −0.56	±0.15 −0.39	±0.15 −0.74	±0.15 −0.60	±0.13 −0.56	±0.18 −0.43
Fake lepton efficiency alternate CR [%]	±0.31	±0.36	±0.32	±0.40	±0.35	±0.30	±0.33	±0.29	±0.35	±0.39	±0.40	±0.28	±0.29	±0.29	±0.35	±0.42	-	±0.35
Fake overall normalisation [%]	±3.74	±3.68	±3.76	±3.37	±3.61	±3.62	±3.46	±3.61	±3.41	±3.54	±2.83	±3.12	±3.12	±2.31	±2.68	±3.08	±2.07	±2.16
W+jets CA_{dmat} stat error [%]	∓0.12	∓0.12	∓0.11	∓0.11	∓0.12	∓0.11	∓0.12	∓0.11	-	∓0.11	∓0.10	∓0.10	-	-	-	-	-	-
W+jets Fc stat error [%]	-	-	-	-	-	-	-	-	-	-	+0.19 −	-	-	+0.15 −	-	+0.14 −	-	-
W+jets Fcc stat error [%]	-	-	−0.18 -	-	-	-	-	-	-	-	-	-	-	-	-	-	-	-
W+jets Flight stat error [%]	-	-	-	-	-	-	-	-	-	-	-	-	-	-	-	-	-	-

Table C.6: Table of systematic uncertainties for the absolute differential cross-section at particle level for the absolute value of the top quark rapidity in the resolved regime.

Bins [GeV]	0–35	35–75	75–125	125–170	170–225	225–800
$d\sigma$ / dp_{T}^{tt} [pb / GeV]	$1.03 \cdot 10^{0}$	$8.08 \cdot 10^{-1}$	$3.42 \cdot 10^{-1}$	$1.67 \cdot 10^{-1}$	$8.33 \cdot 10^{-2}$	$8.56 \cdot 10^{-3}$
Total uncertainty [%]	$^{+11.2}_{-11.7}$	$^{+12.3}_{-13.3}$	$^{+17.8}_{-17.6}$	$^{+15.3}_{-15.2}$	$^{+13.0}_{-14.2}$	$^{+11.6}_{-12.2}$
Statistical uncertainty [%]	± 0.5	± 0.5	± 0.8	± 1.2	± 1.6	± 1.5
Systematic uncertainty [%]	$^{+11.2}_{-11.7}$	$^{+12.3}_{-13.3}$	$^{+17.8}_{-17.6}$	$^{+15.3}_{-15.1}$	$^{+12.9}_{-14.0}$	$^{+10.9}_{-12.1}$
b-Tagged jet energy scale (JES) [%]	$^{+0.51}_{-0.46}$	$^{+0.55}_{-0.52}$	$^{+0.58}_{-0.62}$	$^{+0.56}_{-0.57}$	$^{+0.63}_{-0.71}$	$^{+0.34}_{-0.25}$
Effective detector NP set 1 (JES) [%]	-1.29	$^{+6.38}_{-7.32}$	$^{+10.2}_{-10.0}$	$^{+8.22}_{-8.32}$	$^{+6.66}_{-7.46}$	$^{+5.00}_{-5.24}$
Effective detector NP set 2 (JES) [%]	-	$^{+1.48}_{+0.50}$	$^{+1.52}_{+0.34}$	$^{+0.47}_{-0.27}$	$^{+0.42}_{+0.20}$	$^{+1.07}_{\mp 0.86}$
Effective detector NP set 3 (JES) [%]	-	$^{-0.56}_{-0.30}$	$^{-0.40}_{+0.23}$	$^{+0.17}_{+0.14}$	$^{+0.16}_{-0.26}$	-
Effective detector NP set 4 (JES) [%]	-	-	-	-	$^{+0.12}_{-0.20}$	$^{+0.30}_{-0.19}$
Effective detector NP set 5 (JES) [%]	-	-	$^{+0.13}_{-0.16}$	-	$^{+0.11}_{-0.14}$	$^{+0.19}_{-0.20}$
Effective detector NP set 6 restTerm (JES) [%]	-	-	-	-	$^{+2.54}_{-2.41}$	$^{+2.04}_{-2.01}$
η intercalibration model (JES) [%]	-1.54	$+2.35$	$+4.17$	$+2.98$	-3.13	-2.54
η intercalibration total stat (JES) [%]	$^{+0.98}_{-0.25}$	$^{-2.71}_{+0.98}$	$^{-4.21}_{+1.46}$	$^{-3.08}_{+1.24}$	$^{+1.29}_{-1.55}$	$^{+1.00}_{-1.03}$
Flavour composition (JES) [%]	$^{+0.28}_{-1.84}$	$^{-1.05}_{+4.36}$	$^{-1.63}_{+9.17}$	$^{-1.13}_{+8.00}$	$^{+6.60}_{-5.95}$	$^{+4.69}_{-5.46}$
Flavour response (JES) [%]	$^{+0.42}_{-0.99}$	$^{-5.33}_{+1.13}$	$^{-9.04}_{+2.30}$	$^{-7.59}_{+2.09}$	$^{+5.93}_{+1.72}$	$^{+5.46}_{+1.41}$
Pile-up offset μ (JES) [%]	$^{+0.18}_{-0.21}$	$^{-0.36}_{+0.28}$	$^{-0.58}_{+0.56}$	$^{-0.37}_{+0.29}$	$^{-0.48}_{+0.32}$	$^{-0.15}_{+0.13}$
Pile-up offset N_{PV} (JES) [%]	$^{+0.20}_{-}$	$^{-}_{-0.20}$	$^{+0.17}_{-}$	$^{-}_{+0.10}$	$^{-}_{-}$	$^{-}_{-}$
Pile-up offset p_{T} (JES) [%]	-	$^{+0.19}_{+2.03}$	-	$^{-0.14}_{+2.52}$	$^{-0.22}_{+1.87}$	-
Pile-up offset ρ topology (JES) [%]	-0.46	-2.46	$+2.96$ -3.39	-2.81	-3.12	$+1.09$ -1.99
Punch-through (JES) [%]	-	-	-	-	-	-
Single particle high-p_{T} (JES) [%]	-	-	-	-	-	-
Jet energy resolution [%]	∓ 3.09	∓ 1.28	± 0.12	± 0.14	-	∓ 1.59
Jet vertex fraction [%]	$^{+3.28}_{-3.24}$	$^{+3.65}_{-3.58}$	$^{+3.85}_{-3.73}$	$^{+3.65}_{-3.59}$	$^{+3.38}_{-3.31}$	$^{+2.62}_{-2.54}$
b-Quark tagging efficiency (eigenvector 0) [%]	$^{-4.30}_{+4.38}$	$^{-4.09}_{+4.16}$	$^{-3.85}_{+3.90}$	$^{-3.74}_{+3.80}$	$^{-3.69}_{+3.74}$	$^{-3.62}_{+3.67}$
b-Quark tagging efficiency (eigenvector 1) [%]	$^{-1.62}_{+1.63}$	$^{-1.62}_{+1.64}$	$^{-1.61}_{+1.63}$	$^{-1.59}_{+1.60}$	∓ 1.60	$^{-2.38}_{+2.40}$
b-Quark tagging efficiency (eigenvector 2) [%]	$^{+1.23}_{-1.22}$	$^{+1.13}_{-1.12}$	± 0.95	$^{+0.90}_{-0.89}$	± 0.91	± 0.48
b-Quark tagging efficiency (eigenvector 3) [%]	-	-	-	-	-	-
b-Quark tagging efficiency (eigenvector 4) [%]	-	-	-	-	-	-
c-Quark tagging efficiency (eigenvector 0) [%]	$^{-1.50}_{+1.51}$	$^{-1.49}_{+1.50}$	∓ 1.50	$^{-1.48}_{+1.49}$	∓ 1.41	∓ 1.34
c-Quark tagging efficiency (eigenvector 1) [%]	± 0.17	± 0.14	± 0.13	± 0.16	± 0.16	± 0.13
c-Quark tagging efficiency (eigenvector 2) [%]	± 0.19	± 0.18	± 0.14	± 0.15	± 0.18	± 0.18
c-Quark tagging efficiency (eigenvector 3) [%]	-	-	-	-	-	-
Light-jet tagging efficiency (eigenvector 0) [%]	$^{-1.32}_{+1.40}$	$^{-1.60}_{+1.69}$	$^{-1.77}_{+1.83}$	∓ 1.59	∓ 1.48	$^{-1.42}_{+1.46}$
Light-jet tagging efficiency (eigenvector 1) [%]	-	-	-	-	-	-
Light-jet tagging efficiency (eigenvector 2) [%]	-	-	-	-	-	± 0.10
Light-jet tagging efficiency (eigenvector 3) [%]	-	-	-	-	-	-
Light-jet tagging efficiency (eigenvector 4) [%]	-	-	-	-	-	-
Light-jet tagging efficiency (eigenvector 5) [%]	-	-	-	-	-	-
Light-jet tagging efficiency (eigenvector 6) [%]	-	-	-	-	-	-
Light-jet tagging efficiency (eigenvector 7) [%]	-	-	-	-	-	-
Light-jet tagging efficiency (eigenvector 8) [%]	-	-	-	-	-	-
Light-jet tagging efficiency (eigenvector 9) [%]	-	-	-	-	-	-
Light-jet tagging efficiency (eigenvector 10) [%]	-	-	-	-	-	-
Light-jet tagging efficiency (eigenvector 11) [%]	-	-	-	-	-	-
b-Quark tagging extrapolation [%]	± 0.22	± 0.25	$^{+0.34}_{-0.33}$	$^{+0.42}_{-0.43}$	± 0.38	$^{+0.92}_{-0.93}$
b-Quark tagging extrapolation from c-Quark [%]	± 0.12	± 0.10	-	-	-	± 0.11
Electron energy resolution [%]	-	-	-	-	-	-
Electron energy scale [%]	-	-	-	-	-	-
Electron trigger efficiency [%]	± 0.26	± 0.25	± 0.26	± 0.27	± 0.28	± 0.30
Electron reconstruction efficiency [%]	± 0.18	± 0.17	± 0.18	± 0.19	± 0.20	± 0.23
Electron identification efficiency [%]	± 0.43	± 0.42	± 0.43	± 0.46	± 0.49	± 0.60
Electron isolation efficiency [%]	± 0.15	± 0.15	± 0.16	± 0.18	± 0.20	± 0.31
Muon energy scale [%]	-	-	-	-	-	-
Muon (MS) momentum resolution [%]	-	-	-	-	-	-
Muon (ID) momentum resolution [%]	-	-	-	-	-	-
Muon trigger efficiency stat [%]	$^{+0.56}_{-0.58}$	$^{+0.57}_{-0.59}$	$^{+0.57}_{-0.58}$	$^{+0.56}_{-0.58}$	$^{+0.56}_{-0.58}$	$^{+0.56}_{-0.57}$
Muon trigger efficiency syst [%]	± 0.24	$^{+0.25}_{-0.24}$	± 0.24	± 0.24	± 0.24	± 0.24
Muon identification stat [%]	-	-	-	-	-	-
Muon identification syst [%]	± 0.17	± 0.17	± 0.18	± 0.18	± 0.19	± 0.24
Muon isolation efficiency stat [%]	-	-	-	-	-	-
Muon isolation efficiency syst [%]	± 0.10	± 0.10	± 0.10	± 0.10	± 0.10	$^{+0.11}_{-0.10}$
Muon TTVA efficiency stat [%]	-	-	-	-	-	-
Muon TTVA efficiency syst [%]	-	-	-	-	-	-
$E_{\mathrm{T}}^{\mathrm{miss}}$ Soft jet resolution para [%]	∓ 0.12	± 0.23	± 0.28	∓ 0.10	± 0.12	± 0.13
$E_{\mathrm{T}}^{\mathrm{miss}}$ Soft jet resolution perp [%]	∓ 0.36	± 0.14	± 0.11	∓ 0.15	∓ 0.15	∓ 0.12
$E_{\mathrm{T}}^{\mathrm{miss}}$ Soft jet scale [%]	-	-	-	-	-	-
Luminosity [%]	∓ 2.06	∓ 2.06	∓ 2.06	∓ 2.06	∓ 2.06	∓ 2.06
Single top cross-section [%]	± 0.29	± 0.25	± 0.23	± 0.24	± 0.25	± 0.26
Z+jets cross-section [%]	± 0.67	± 0.54	± 0.54	± 0.52	± 0.48	± 0.56
Diboson cross-section [%]	± 0.11	± 0.10	± 0.14	± 0.19	± 0.24	± 0.47
$t\bar{t}V$ cross-section [%]	∓ 0.10	-	-	-	-	-
Monte Carlo sample statistics [%]	± 0.22	± 0.20	± 0.31	± 0.44	± 0.58	± 0.49
ISR/FSR + scale [%]	-1.84	-3.27	-2.36	-3.01	-3.50	-2.80
Alternate hard-scattering model [%]	∓ 0.64	± 0.55	± 0.82	± 3.99	± 2.17	± 1.26
Alternate parton-shower model [%]	∓ 7.92	± 0.59	± 4.22	∓ 0.66	-	∓ 1.34
Inter PDF [%]	-	-	-	± 0.10	-	± 0.16
Intra PDF [%]	-	-	± 0.11	-	-	-
Real lepton efficiency stat [%]	$^{+0.15}_{+0.14}$	$^{+0.14}_{+0.14}$	$^{+0.16}_{+0.15}$	$^{+0.20}_{+0.18}$	$^{-0.21}_{+0.19}$	$^{+0.36}_{+0.28}$
Fake lepton efficiency MC scale [%]	$^{+0.20}_{-0.24}$	$^{+0.91}_{-1.14}$	$^{+0.34}_{-1.22}$	$^{+0.46}_{-0.58}$	$^{+0.46}_{-0.57}$	$^{+0.53}_{-0.48}$
Fake lepton efficiency alternate CR [%]	± 0.24	± 0.45	± 0.41	± 0.29	± 0.13	± 0.17
Fake overall normalisation [%]	± 2.58	± 4.04	± 3.98	± 2.95	± 2.89	± 3.25
W+jets CA_{fixed} stat error [%]	∓ 0.13	-	-	∓ 0.10	∓ 0.11	∓ 0.13
W+jets Fc stat error [%]	-	-	-	-	-	-
W+jets Fcc stat error [%]	-	-	-	-0.16	$^{-0.23}_{+0.11}$	$^{-0.28}_{+0.13}$
W+jets Flight stat error [%]	-	-	-	-	-	-

Table C.7: Table of systematic uncertainties for the absolute differential cross-section at particle level for the $t\bar{t}$ system transverse momentum in the resolved regime.

Bins [Unit $\|y^{t\bar{t}}\|$]	0-0.10	0.10-0.20	0.20-0.30	0.30-0.40	0.40-0.50	0.50-0.60	0.60-0.70	0.70-0.80	0.80-0.90	0.90-1	1-1.10	1.10-1.20	1.20-1.30	1.30-1.40	1.40-1.50	1.50-1.60	1.60-1.80	1.80-2.50
$d\sigma$ / $d\|y^{t\bar{t}}\|$ [pb/ Unit $\|y^{t\bar{t}}\|$]	$1.04 \cdot 10^2$	$1.05 \cdot 10^2$	$1.02 \cdot 10^2$	$9.80 \cdot 10^1$	$9.56 \cdot 10^1$	$8.61 \cdot 10^1$	$7.71 \cdot 10^1$	$7.07 \cdot 10^1$	$6.13 \cdot 10^1$	$5.17 \cdot 10^1$	$4.27 \cdot 10^1$	$3.54 \cdot 10^1$	$2.78 \cdot 10^1$	$2.25 \cdot 10^1$	$1.53 \cdot 10^1$	$1.12 \cdot 10^1$	$6.20 \cdot 10^0$	$6.32 \cdot 10^{-1}$
Total uncertainty [%]	$^{+10.2}_{-11.5}$	$^{+10.1}_{-11.0}$	$^{+10.7}_{-11.9}$	$^{+10.5}_{-11.3}$	$^{+10.6}_{-11.3}$	$^{+10.4}_{-10.9}$	$^{+10.3}_{-10.6}$	$^{+10.3}_{-11.4}$	$^{+10.3}_{-11.8}$	$^{+10.4}_{-11.5}$	$^{+10.2}_{-11.2}$	$^{+10.3}_{-10.6}$	$^{+10.6}_{-12.4}$	$^{+11.3}_{-11.5}$	$^{+12.5}_{-12.3}$	$^{+11.8}_{-11.2}$	$^{+10.8}_{-13.6}$	$^{+14.3}_{-14.1}$
Statistical uncertainty [%]	± 1.0	± 0.9	± 1.0	± 1.0	± 1.0	± 1.1	± 1.1	± 1.2	± 1.2	± 1.4	± 1.5	± 1.7	± 1.9	± 2.2	± 2.7	± 3.2	± 3.3	± 5.7
Systematic uncertainty [%]	$^{+10.1}_{-11.5}$	$^{+10.0}_{-11.0}$	$^{+10.6}_{-11.9}$	$^{+10.4}_{-11.2}$	$^{+10.5}_{-11.3}$	$^{+10.3}_{-10.8}$	$^{+10.2}_{-10.5}$	$^{+10.3}_{-11.4}$	$^{+10.2}_{-11.3}$	$^{+10.3}_{-11.5}$	$^{+10.2}_{-11.1}$	$^{+10.2}_{-10.5}$	$^{+10.3}_{-12.3}$	$^{+11.1}_{-11.2}$	$^{+12.1}_{-11.9}$	$^{+11.2}_{-10.6}$	$^{+10.7}_{-13.1}$	$^{+12.7}_{-12.7}$
b-Tagged jet energy scale (JES) [%]	± 0.48	$^{+0.99}_{-0.90}$	$^{+0.98}_{-0.90}$	$^{+0.98}_{-0.89}$	$^{+0.98}_{-0.93}$	$^{+0.96}_{-0.86}$	$^{+0.95}_{-0.89}$	$^{+0.93}_{-0.91}$	$^{+0.93}_{-0.91}$	$^{+0.94}_{-0.94}$	$^{+0.96}_{-0.99}$	$^{+0.96}_{-0.98}$	$^{+0.97}_{-0.94}$	$^{+0.97}_{-0.94}$	$^{+0.97}_{-0.99}$	$^{+0.98}_{-0.94}$	$^{+0.98}_{-0.93}$	$^{+0.97}_{-0.92}$
Effective detector NP set 1 (JES) [%]	$^{+4.42}_{-5.54}$	$^{+4.72}_{-5.93}$	$^{+4.94}_{-5.53}$	$^{+5.17}_{-5.79}$	$^{+4.83}_{-5.84}$	$^{+4.65}_{-5.84}$	$^{+4.73}_{-5.93}$	$^{+4.69}_{-5.87}$	$^{+4.98}_{-6.25}$	$^{+4.75}_{-5.48}$	$^{+4.46}_{-5.90}$	$^{+4.43}_{-5.30}$	$^{+4.59}_{-6.08}$	$^{+5.16}_{-5.23}$	$^{+5.21}_{-5.23}$	$^{+5.42}_{-5.42}$	$^{+4.58}_{-6.10}$	$^{+5.27}_{-4.90}$
Effective detector NP set 2 (JES) [%]	$^{+0.60}_{+0.71}$	$^{+0.62}_{+0.82}$	$^{+0.62}_{+0.55}$	$^{+0.67}_{+0.78}$	$^{+0.62}_{+0.65}$	$^{+0.70}_{+0.64}$	$^{+0.67}_{+0.92}$	$^{+0.64}_{+0.79}$	$^{+0.66}_{+0.59}$	$^{+0.62}_{+0.72}$	$^{+0.77}_{+0.34}$	$^{+0.72}_{+0.77}$	$^{+0.82}_{+0.70}$	$^{+0.58}_{+0.67}$	$^{+0.58}_{+0.67}$	$^{+0.58}_{+1.46}$	$^{+0.58}_{-1.18}$	$^{+0.59}_{+0.51}$
Effective detector NP set 3 (JES) [%]	$^{+0.11}_{-0.16}$	$^{+0.14}_{-0.16}$	$^{+0.15}_{-0.20}$	$^{+0.19}$	-0.21	$^{+0.12}_{-0.17}$	$^{+0.26}_{-0.33}$	$^{+0.21}$	-0.27	$^{+0.23}$	-	$^{+0.19}$	-	-	-	$^{+0.93}_{+0.32}$	-0.31	-
Effective detector NP set 4 (JES) [%]	-	-	-	-	-0.20	-	$^{+0.10}$	-	-	-	-	-	-	-	$^{+0.14}$	-0.18	-0.26	$^{+0.13}_{-0.23}$
Effective detector NP set 5 (JES) [%]	-	-	-	-	-	-	-	-	-	-	-	-	-	-	-	$^{+0.26}$	-	$^{+0.22}_{-0.29}$
Effective detector NP set 6 restTerm (JES) [%]	-	-	-	-	-	-	-	-	-	-	-	-	-	-	-	$^{+0.28}$	-	-
η intercalibration model (JES) [%]	$^{+0.38}_{-1.39}$	$^{+1.04}_{-1.42}$	$^{+1.05}_{-1.32}$	$^{+1.30}_{-1.28}$	$^{+1.01}_{-1.09}$	$^{+0.92}_{-1.26}$	$^{+1.50}_{-1.40}$	$^{+1.27}_{-1.99}$	$^{+1.45}_{-2.95}$	$^{+1.60}_{-1.98}$	$^{+0.89}_{-1.85}$	$^{+1.67}_{-1.90}$	$^{+1.75}_{-3.07}$	$^{+2.71}_{-2.69}$	$^{+5.10}_{-7.55}$	$^{+2.58}_{-2.80}$	$^{+2.93}_{-4.03}$	$^{+3.94}_{-2.21}$
η intercalibration total stat (JES) [%]	$^{+0.54}_{-0.63}$	$^{+0.70}_{-0.61}$	$^{+0.72}_{-0.53}$	$^{+0.57}_{-0.64}$	$^{+0.57}_{-0.87}$	$^{\pm 0.60}$	$^{+0.78}_{-0.46}$	$^{+0.54}_{-0.67}$	$^{+0.72}_{-1.06}$	$^{+0.75}_{-0.65}$	$^{+0.52}_{-0.84}$	$^{+0.94}_{-0.56}$	$^{+0.72}_{-0.77}$	$^{+0.93}_{-1.00}$	$^{+1.00}_{-0.75}$	$^{+1.16}_{-0.53}$	$^{+0.32}_{-1.40}$	$^{+0.96}_{-0.80}$
Flavour composition (JES) [%]	$^{+2.81}_{-3.70}$	$^{+3.27}_{-3.85}$	$^{+3.40}_{-3.96}$	$^{+3.30}_{-3.95}$	$^{+3.32}_{-4.04}$	$^{+2.99}_{-3.64}$	$^{+3.13}_{-3.93}$	$^{+3.21}_{-4.18}$	$^{+3.24}_{-4.39}$	$^{+3.15}_{-4.13}$	$^{+3.43}_{-4.34}$	$^{+3.13}_{-3.94}$	$^{+2.94}_{-4.00}$	$^{+3.65}_{-4.04}$	$^{+3.39}_{-4.34}$	$^{+3.99}_{-4.17}$	$^{+2.88}_{-3.22}$	$^{+4.21}_{-4.13}$
Flavour response (JES) [%]	$^{+0.61}_{-0.84}$	$^{+0.63}_{-0.92}$	$^{+0.59}$	$^{+0.83}_{-0.89}$	$^{+0.61}_{-0.94}$	$^{+0.58}_{-0.85}$	$^{+0.78}_{-0.79}$	$^{+0.65}$	$^{+0.76}_{-0.91}$	$^{+0.51}_{-0.93}$	$^{+0.62}_{-0.91}$	$^{+1.09}_{-0.77}$	$^{+0.69}_{-0.98}$	$^{+0.88}_{-0.93}$	$^{+1.10}_{-0.89}$	$^{+0.98}_{-0.93}$	$^{+0.93}_{-0.93}$	$^{+1.39}_{-0.92}$
Pile-up offset μ (JES) [%]	$^{+0.10}$	$^{+0.16}$	-	$^{+0.10}$	-	$^{+0.22}$	$^{+0.15}$	-	$^{+0.23}$	$^{+0.19}$	-	$^{+0.30}_{+0.27}$	$^{+0.14}$	$^{+0.32}$	$^{+0.37}_{+0.33}$	$^{+0.96}_{+0.73}$	-	$^{+0.15}$
Pile-up offset N_{PV} (JES) [%]	-	-	-	-	-	-	-	-	-	-	-	-	-	-0.26	-	-	-0.34	-0.20
Pile-up offset p_{T} (JES) [%]	$^{+0.14}$	-	-	-	$^{-0.16}_{+0.11}$	-	$^{+0.15}_{+0.14}$	-	-	-	-	-	$^{-0.20}$	$^{+0.18}_{-0.14}$	-	$^{+0.49}$	-0.23	$^{+0.19}_{+0.26}$
Pile-up offset ρ topology (JES) [%]	$^{+1.09}_{-1.99}$	$^{+1.31}_{-1.76}$	$^{+1.26}_{-1.82}$	$^{+1.53}_{-2.06}$	$^{+1.33}_{-2.15}$	$^{+1.23}_{-1.75}$	$^{+1.27}_{-1.78}$	$^{+1.16}_{-1.93}$	$^{+1.28}_{-2.24}$	$^{+1.31}_{-1.89}$	$^{+1.14}_{-1.91}$	$^{+1.34}_{-1.71}$	$^{+1.29}_{-1.79}$	$^{+1.63}_{-1.86}$	$^{+1.82}_{-1.71}$	$^{+1.68}_{-1.96}$	$^{+0.97}_{-2.47}$	$^{+1.37}_{-1.56}$
Punch-through (JES) [%]	-	-	-	-	-	-	-	-	-	-	-	-	-	-	-	-	-	-
Single particle high-p_{T} (JES) [%]	-	-	-	-	-	-	-	-	-	-	-	-	-	-	-	-	-	-
Jet energy resolution [%]	∓ 1.77	∓ 1.42	∓ 1.95	∓ 0.78	∓ 1.53	∓ 1.53	∓ 0.75	∓ 1.79	∓ 1.62	∓ 1.75	∓ 1.65	∓ 1.46	∓ 2.72	∓ 2.49	∓ 2.21	∓ 1.46	∓ 2.20	∓ 3.22
Jet vertex fraction [%]	$^{+3.50}_{-3.43}$	$^{+3.54}_{-3.69}$	$^{+3.49}_{-3.69}$	$^{+3.45}_{-3.59}$	$^{+3.49}_{-3.80}$	$^{+3.52}_{-3.62}$	$^{+3.52}_{-3.68}$	$^{+3.49}_{-3.65}$	$^{+3.43}_{-3.66}$	$^{+3.52}_{-3.63}$	$^{+3.41}_{-3.62}$	$^{+3.43}_{-3.66}$	$^{+3.57}_{-3.95}$	$^{+3.47}_{-3.60}$	$^{+3.57}_{-3.62}$	$^{+3.38}_{-3.92}$	$^{+3.28}_{-3.27}$	$^{+3.12}_{-3.09}$
b-Quark tagging efficiency (eigenvector 0) [%]	$^{+4.20}_{-4.03}$	$^{+4.16}_{-4.04}$	$^{+4.16}_{-4.05}$	$^{+4.13}_{-4.13}$	$^{+4.19}_{-4.05}$	$^{+4.15}_{-4.04}$	$^{+4.12}_{-4.06}$	$^{+4.12}_{-4.05}$	$^{+4.12}_{-4.05}$	$^{+4.09}_{-4.03}$	$^{+4.09}_{-4.06}$	$^{+4.06}_{-4.09}$	$^{+4.08}_{-4.09}$	$^{+4.09}_{-4.09}$	$^{+3.98}_{-4.05}$	$^{+3.99}_{-4.08}$	$^{+3.94}_{-3.75}$	$^{+4.10}_{-3.81}$
b-Quark tagging efficiency (eigenvector 1) [%]	$^{+1.63}_{-1.08}$	$^{+1.65}_{-1.09}$	$^{+1.67}_{-1.08}$	$^{+1.64}_{-1.08}$	$^{+1.67}_{-1.08}$	$^{+1.66}_{-1.08}$	$^{+1.67}_{-1.09}$	$^{+1.66}_{-1.09}$	$^{+1.67}_{-1.08}$	$^{+1.67}_{-1.08}$	$^{+1.68}_{-1.09}$	$^{+1.74}_{-1.07}$	$^{+1.71}_{-1.08}$	$^{+1.69}_{-1.07}$	$^{+1.71}_{-1.06}$	$^{+1.70}_{-1.06}$	$^{+1.75}_{-1.04}$	$^{+1.83}_{-1.00}$
b-Quark tagging efficiency (eigenvector 2) [%]	-1.07	-1.08	-1.07	-1.07	-1.08	-1.07	-1.08	-1.08	-1.07	$^{+1.08}$	-1.09	-1.06	-1.07	-1.06	-	-	± 1.05	± 1.00
b-Quark tagging efficiency (eigenvector 3) [%]	-	-	-	-	-	-	-	-	-	-	-	-	-	-	-	± 0.10	± 0.11	± 0.11
b-Quark tagging efficiency (eigenvector 4) [%]	-	-	-	-	-	-	-	-	-	-	-	-	-	-	-	-	-	-
c-Quark tagging efficiency (eigenvector 0) [%]	-1.52	-1.53	-1.55	-1.53	-1.49	-1.44	-1.42	-1.50	-1.46	-1.44	∓ 1.43	-1.45	-1.45	-1.45	∓ 1.49	∓ 1.33	-1.30	∓ 1.24
c-Quark tagging efficiency (eigenvector 1) [%]	± 0.16	± 0.15	± 0.16	± 0.16	± 0.15	± 0.13	± 0.14	± 0.17	± 0.16	± 0.14	± 0.14	± 0.15	± 0.13	± 0.14	± 0.14	± 0.18	$^{+1.31}_{-0.16}$	± 0.13
c-Quark tagging efficiency (eigenvector 2) [%]	± 0.17	± 0.18	± 0.17	± 0.17	± 0.18	± 0.17	± 0.17	± 0.18	± 0.17	± 0.19	± 0.18	± 0.17	± 0.17	± 0.17	± 0.17	± 0.17	± 0.17	± 0.15
c-Quark tagging efficiency (eigenvector 3) [%]	-	-	-	-	-	-	-	-	-	-	-	-	-	-	-	-	-	-
Light-jet tagging efficiency (eigenvector 0) [%]	-1.49	-1.38	-1.27	-1.30	-1.43	-1.54	-1.65	-1.61	-1.43	-1.59	∓ 1.45	-1.82	-2.13	-1.88	-2.29	-2.13	-1.72	-1.16
Light-jet tagging efficiency (eigenvector 1) [%]	$^{+1.53}$	$^{+1.44}$	$^{+1.23}$	$^{+1.31}$	$^{+1.52}$	$^{+1.66}$	$^{+1.81}$	$^{+1.66}$	$^{+1.49}$	$^{+1.69}$	-	$^{+1.95}$	$^{+2.42}$	$^{+1.96}$	$^{+2.45}$	$^{+2.33}$	$^{+1.77}$	$^{+1.13}$
Light-jet tagging efficiency (eigenvector 2) [%]	-	-	-	-	-	-	± 0.11	± 0.11	-	-	-	± 0.10	± 0.14	-	± 0.12	∓ 0.11	∓ 0.16	∓ 0.17	∓ 0.16
Light-jet tagging efficiency (eigenvector 3) [%]	-	-	-	-	-	-	-	-	-	-	-	-	-	-	-	-	-	-
Light-jet tagging efficiency (eigenvector 4) [%]	-	-	-	-	-	-	-	-	-	-	-	-	-	-	-	-	-	-
Light-jet tagging efficiency (eigenvector 5) [%]	-	-	-	-	-	-	-	-	-	-	-	-	-	-	-	-	-	-
Light-jet tagging efficiency (eigenvector 6) [%]	-	-	-	-	-	-	-	-	-	-	-	-	-	-	-	-	-	-
Light-jet tagging efficiency (eigenvector 7) [%]	-	-	-	-	-	-	-	-	-	-	-	-	-	-	-	-	-	-
Light-jet tagging efficiency (eigenvector 8) [%]	-	-	-	-	-	-	-	-	-	-	-	-	-	-	-	-	-	-
Light-jet tagging efficiency (eigenvector 9) [%]	-	-	-	-	-	-	-	-	-	-	-	-	-	-	-	-	-	-
Light-jet tagging efficiency (eigenvector 10) [%]	-	-	-	-	-	-	-	-	-	-	-	-	-	-	-	-	-	-
Light-jet tagging efficiency (eigenvector 11) [%]	-	-	-	-	-	-	-	-	-	-	-	-	-	-	-	-	-	-
b-Quark tagging extrapolation [%]	$^{+0.31}_{-0.32}$	$^{+0.32}_{-0.31}$	$^{+0.31}_{-0.32}$	$^{+0.30}_{-0.31}$	$^{+0.32}_{-0.31}$	$^{+0.32}_{-0.31}$	$^{+0.31}_{-0.30}$	$^{+0.30}_{-0.29}$	± 0.29	$^{+0.29}_{-0.28}$	± 0.30	± 0.31	± 0.28	± 0.27	± 0.27	± 0.29	± 0.26	± 0.29
b-Quark tagging extrapolation from c-Quark [%]	$^{+0.10}_{-0.12}$	$^{+0.13}_{-0.12}$	$^{+0.11}_{-0.19}$	$^{+0.10}_{-0.11}$	± 0.11	± 0.11	± 0.11	-	-	± 0.10	± 0.10	± 0.12	-	-	-	-	-	-
Electron energy resolution [%]	-	-	-	-	-	-	-	-	-0.22	-	-	$+0.23$	-0.35	$^{+0.21}_{+0.33}$	$+0.25$	$^{+0.17}_{-0.16}$	-0.50	$^{+0.78}_{-1.05}$
Electron energy scale [%]	-	-	-	-	-	-	-	-	-	$^{+0.19}$	-	-	-0.34	$^{+0.28}_{-0.39}$	-	$^{+0.28}_{-0.39}$	-	-0.14
Electron trigger efficiency [%]	± 0.22	± 0.22	± 0.22	± 0.22	± 0.23	± 0.24	± 0.25	± 0.26	± 0.27	± 0.28	± 0.30	± 0.33	± 0.35	± 0.39	± 0.45	± 0.49	± 0.55	± 0.66
Electron reconstruction efficiency [%]	± 0.18	± 0.18	± 0.18	± 0.17	± 0.18	± 0.18	± 0.18	± 0.18	± 0.18	± 0.18	± 0.18	± 0.18	± 0.19	± 0.19	± 0.20	± 0.21	± 0.21	± 0.23
Electron identification efficiency [%]	± 0.43	± 0.43	± 0.43	± 0.43	± 0.43	± 0.43	± 0.43	± 0.43	± 0.43	± 0.43	± 0.44	± 0.45	± 0.46	± 0.47	± 0.52	± 0.55	± 0.58	± 0.72
Electron isolation efficiency [%]	± 0.17	± 0.17	± 0.16	± 0.16	± 0.16	± 0.16	± 0.16	± 0.16	± 0.16	± 0.16	± 0.16	± 0.16	± 0.16	± 0.16	± 0.17	± 0.18	± 0.19	± 0.22
Muon energy scale [%]	-	-	-	-	-	-	-	-	-	-	-	-	-	-	-	-	-	-0.23
Muon (MS) momentum resolution [%]	-	-	-	-	-	-	-	-	-	-	-	-	-	-	-	-	-	$+0.25$
Muon (ID) momentum resolution [%]	-	-	-	-	-	-	-	-	-	-	-	-	-	$^{+0.20}_{-0.22}$	$+0.23$	$^{-0.10}_{+0.12}$	$+0.33$	$+0.58$
Muon trigger efficiency stat [%]	$^{+0.58}_{-0.59}$	$^{+0.58}_{-0.59}$	$^{+0.57}_{-0.59}$	$^{+0.57}_{-0.59}$	$^{+0.57}_{-0.59}$	$^{+0.57}_{-0.58}$	$^{+0.57}_{-0.59}$	$^{+0.56}_{-0.58}$	$^{+0.56}_{-0.58}$	$^{+0.57}_{-0.58}$	$^{+0.56}_{-0.58}$	$^{+0.57}_{-0.58}$	$^{+0.57}_{-0.55}$	$^{+0.53}_{-0.53}$	$^{+0.51}_{-0.53}$	$^{+0.52}_{-0.51}$	$^{+0.50}_{-0.52}$	$^{+0.58}_{-0.59}$
Muon trigger efficiency syst [%]	$^{+0.26}_{-0.25}$	± 0.25	± 0.25	± 0.25	$^{+0.25}_{-0.24}$	$^{+0.25}_{-0.24}$	$^{+0.25}_{-0.24}$	± 0.24	± 0.24	$^{+0.24}_{-0.23}$	± 0.23	± 0.23	$^{+0.23}_{-0.22}$	$^{+0.23}_{-0.21}$	± 0.21	$^{+0.21}_{-0.20}$	± 0.20	± 0.20
Muon identification stat [%]	-	-	-	-	-	-	-	-	-	-	-	-	-	-	-	-	-	-
Muon identification syst [%]	± 0.16	± 0.16	± 0.17	± 0.17	± 0.17	± 0.17	± 0.18	± 0.18	± 0.18	± 0.19	$^{+0.20}_{-0.19}$	± 0.20	± 0.21	± 0.21	± 0.22	± 0.22	± 0.22	± 0.23
Muon isolation efficiency stat [%]	-	-	-	-	-	-	-	-	-	-	-	-	-	-	-	-	-	-
Muon isolation efficiency syst [%]	± 0.10	± 0.10	± 0.10	± 0.10	± 0.10	± 0.10	± 0.10	± 0.10	± 0.11	± 0.11	± 0.11	± 0.11	± 0.11	$^{+0.12}_{-0.11}$	± 0.12	$^{+0.12}_{-0.11}$	± 0.11	± 0.11
Muon TTVA efficiency stat [%]	-	-	-	-	-	-	-	-	-	-	-	-	-	-	-	-	-	-
Muon TTVA efficiency syst [%]	-	-	-	-	-	-	-	-	-	-	-	-	-	-	-	-	-	-
$E_{\mathrm{T}}^{\mathrm{miss}}$ Soft jet resolution para [%]	-	-	-	-	-	-	± 0.10	± 0.20	∓ 0.11	± 0.20	-	∓ 0.13	± 0.29	± 0.42	-	± 0.43	± 0.34	± 0.26
$E_{\mathrm{T}}^{\mathrm{miss}}$ Soft jet resolution perp [%]	-	∓ 0.17	∓ 0.17	∓ 0.14	-	-	∓ 0.13	∓ 0.11	-	-	∓ 0.17	∓ 0.12	∓ 0.13	± 0.19	± 0.21	± 0.28	∓ 0.12	± 0.45
$E_{\mathrm{T}}^{\mathrm{miss}}$ Soft jet scale [%]	-	-	-	-	-	-	-	-	-	-	-	-	-	-	± 0.29	± 0.14	± 0.21	± 0.36
Luminosity [%]	∓ 2.06	∓ 2.06	∓ 2.06	∓ 2.06	∓ 2.06	∓ 2.06	∓ 2.06	∓ 2.06	∓ 2.06	∓ 2.06	∓ 2.06	∓ 2.06	∓ 2.06	∓ 2.06	∓ 2.06	-0.27 -0.12	-0.52 ∓ 2.06	∓ 2.06
Single top cross-section [%]	± 0.28	± 0.28	± 0.28	± 0.28	± 0.27	± 0.27	± 0.26	± 0.25	± 0.25	± 0.24	± 0.24	± 0.23	± 0.22	± 0.21	± 0.21	± 0.20	± 0.18	± 0.17
Z+jets cross-section [%]	± 0.58	± 0.51	± 0.58	± 0.51	± 0.69	± 0.67	± 0.64	± 0.63	± 0.61	± 0.51	± 0.53	± 0.60	± 0.71	± 0.43	± 0.61	± 0.57	± 0.42	± 0.11
Diboson cross-section [%]	± 0.12	± 0.13	± 0.12	± 0.13	± 0.14	± 0.13	± 0.13	± 0.14	± 0.15	± 0.16	± 0.15	± 0.15	± 0.16	± 0.16	± 0.15	± 0.17	± 0.15	± 0.27
$t\bar{t}V$ cross-section [%]	-	-	-	-	-	-	-	-	-	-	-	-	-	-	-	-	-	-
Monte Carlo sample statistics [%]	± 0.41	± 0.38	± 0.41	± 0.37	± 0.42	± 0.45	± 0.47	± 0.47	± 0.54	± 0.54	± 0.55	± 0.73	± 0.85	± 0.77	± 1.26	± 2.20	± 1.09	± 1.79
ISR/FSR $+$ scale [%]	$^{-3.17}_{+1.86}$	$^{-2.18}_{+1.34}$	$^{-4.14}_{+1.72}$	$^{-2.90}_{+2.33}$	$^{-2.24}_{+3.13}$	$^{-2.42}_{+2.63}$	$^{-2.53}_{+2.15}$	$^{-2.12}_{+2.02}$	$^{-2.90}_{+2.56}$	$^{-3.39}_{+2.55}$	$^{-3.25}_{+0.59}$	$^{-1.92}_{+2.64}$	$^{-3.40}_{+2.58}$	$^{-2.57}_{+3.94}$	$^{+3.72}$	$^{-2.57}_{+3.31}$	$^{-4.46}_{+2.31}$	$^{-3.47}_{+3.41}$
Alternate hard-scattering model [%]	-	± 0.80	± 1.29	-	± 1.16	± 1.97	∓ 0.17	∓ 1.61	± 0.48	± 0.53	± 0.46	± 1.46	∓ 0.27	± 0.63	± 4.31	± 0.56	∓ 2.70	± 6.22
Alternate parton-shower model [%]	∓ 2.61	∓ 1.40	∓ 2.82	∓ 2.02	∓ 1.59	∓ 1.46	∓ 1.64	∓ 2.04	∓ 1.79	∓ 2.35	∓ 2.41	∓ 1.80	∓ 1.40	∓ 1.18	∓ 2.14	∓ 1.07	∓ 2.38	∓ 1.05
Inter PDF [%]	-	-	-	-	-	-	-	-	-	-	-	-	-	± 0.31	-	-	± 0.16	∓ 0.47
Intra PDF [%]	-	-	-	-	-	∓ 0.12	-	-	-	-	-	-	∓ 0.29	± 0.14	-	∓ 0.21	± 0.42	± 0.56
Real lepton efficiency stat [%]	-0.17	-0.16	-0.16	-0.16	-0.16	-0.16	-0.16	-0.17	-0.17	-0.17	-0.18	-0.18	-0.18	-0.19	-0.17	-0.20	-0.19	-0.23
Fake lepton efficiency MC scale [%]	$^{+0.15}_{-0.71}$	$^{+0.15}_{-0.90}$	$^{+0.15}_{-0.82}$	$^{+0.14}_{-0.79}$	$^{+0.17}_{-0.76}$	$^{+0.13}_{-0.83}$	$^{+0.15}_{-0.82}$	$^{+0.12}_{-0.70}$	$^{+0.19}_{-0.72}$	$^{+0.13}_{-0.63}$	$^{+0.16}_{-0.72}$	$^{+0.19}_{-0.57}$	$^{+0.17}_{-0.41}$	$^{+0.17}_{-0.26}$	$^{+0.16}_{-0.59}$	$^{+0.18}_{-0.57}$	$^{+0.18}_{-0.61}$	$^{+0.21}_{-0.57}$
Fake lepton efficiency alternate CR [%]	± 0.31	± 0.39	± 0.33	± 0.46	± 0.40	± 0.30	± 0.39	± 0.31	± 0.18	± 0.31	± 0.42	± 0.30	± 0.11	± 0.19	-	-	± 0.30	± 0.54
Fake overall normalisation [%]	± 3.90	± 3.71	± 3.64	± 3.46	± 3.54	± 3.45	± 3.53	± 3.19	± 2.91	± 3.01	± 3.12	± 2.78	± 2.68	± 1.61	± 3.03	± 1.85	± 1.73	± 1.57
W+jets CA_{dmat} stat error [%]	∓ 0.12	∓ 0.11	∓ 0.11	∓ 0.10	∓ 0.11	-	∓ 0.11	∓ 0.12	∓ 0.10	∓ 0.10	-	∓ 0.11	∓ 0.13	∓ 0.10	∓ 0.11	-	-	-
W+jets Fc stat error [%]	-	-	-	-	-	-	-	-	-	-	-	-	-	-	-	-	-	-
W+jets Fcc stat error [%]	-	-	-0.14	-	-	-	-	-	-	-	-	-	-	-	$+0.41$ -0.19	$+0.16$	-0.17	-
W+jets Flight stat error [%]	-	-	-	-	-	-	-	-	-	-	-	-	-	-	-	-	-	-

Table C.8: Table of systematic uncertainties for the absolute differential cross-section at particle level for the absolute value of the $t\bar{t}$ system rapidity in the resolved regime.

Bins [GeV]	225–345	345–420	420–500	500–590	590–685	685–790	790–910	910–1040	1040–1175	1175–1320	1320–3000
$d\sigma$ / $dm^{t\bar{t}}$ [pb/GeV]	$4.95 \cdot 10^{-2}$	$2.89 \cdot 10^{-1}$	$2.90 \cdot 10^{-1}$	$2.12 \cdot 10^{-1}$	$1.29 \cdot 10^{-1}$	$7.80 \cdot 10^{-2}$	$4.33 \cdot 10^{-2}$	$2.34 \cdot 10^{-2}$	$1.19 \cdot 10^{-2}$	$6.60 \cdot 10^{-3}$	$7.33 \cdot 10^{-4}$
Total uncertainty [%]	$^{+16.3}_{-16.6}$	$^{+11.0}_{-11.9}$	$^{+11.6}_{-12.2}$	$^{+11.1}_{-11.9}$	$^{+10.5}_{-11.3}$	± 10.2	$^{+10.1}_{-11.0}$	$^{+10.8}_{-12.0}$	$^{+12.0}_{-13.9}$	$^{+12.2}_{-13.8}$	$^{+19.9}_{-20.3}$
Statistical uncertainty [%]	± 1.6	± 0.7	± 0.7	± 0.7	± 0.9	± 1.2	± 1.5	± 2.0	± 2.7	± 3.9	± 3.4
Systematic uncertainty [%]	$^{+16.2}_{-16.5}$	$^{+11.0}_{-11.9}$	$^{+11.5}_{-12.2}$	$^{+11.0}_{-11.9}$	$^{+10.4}_{-11.2}$	± 10.2	$^{+9.99}_{-10.8}$	$^{+10.6}_{-11.8}$	$^{+11.6}_{-13.6}$	$^{+11.4}_{-13.2}$	$^{+19.5}_{-19.9}$
b-Tagged jet energy scale (JES) [%]	$^{-2.89}_{+2.93}$	$^{-0.26}_{+0.13}$	$^{+0.86}_{-0.79}$	$^{+1.03}_{-1.01}$	$^{+1.07}_{-1.11}$	$^{+1.31}_{-0.95}$	$^{+0.80}_{-0.90}$	$^{+1.01}_{-0.89}$	$^{+0.79}_{-0.85}$	$^{+0.97}_{-0.77}$	$^{+0.85}_{-0.54}$
Effective detector NP set 1 (JES) [%]	$^{-2.66}_{+0.12}$	$^{+4.08}_{-5.02}$	$^{+6.48}_{-6.88}$	$^{+6.39}_{-6.87}$	$^{+5.44}_{-6.00}$	$^{+4.55}_{-5.16}$	$^{+3.59}_{-4.41}$	$^{+2.91}_{-4.66}$	$^{+1.96}_{-5.45}$	$^{+2.18}_{-3.74}$	$^{-}_{-2.46}$
Effective detector NP set 2 (JES) [%]	$^{-3.50}_{+3.37}$	$^{-2.30}_{+2.19}$	$^{-1.19}_{+1.26}$	$^{-0.67}_{+0.50}$	$^{+0.22}_{-0.25}$	$^{+0.97}_{-0.62}$	$^{+0.41}_{-1.02}$	$^{+2.06}_{-2.10}$	$^{+3.00}_{-2.17}$	$^{+2.43}_{-2.37}$	$^{+3.68}_{-4.24}$
Effective detector NP set 3 (JES) [%]	± 2.37	$^{+1.10}_{-1.16}$	$^{+0.34}_{-0.36}$	-	$^{-0.55}_{+0.46}$	$^{-0.69}_{+0.93}$	$^{-0.88}_{+0.49}$	$^{-1.23}_{+1.34}$	$^{-1.42}_{+1.44}$	$^{-1.53}_{+1.39}$	$^{-2.09}_{+1.94}$
Effective detector NP set 4 (JES) [%]	$^{-1.92}_{+1.80}$	$^{-0.71}_{+0.64}$	-	$^{+0.11}_{-0.26}$	$^{+0.35}_{-0.37}$	$^{+0.46}_{-0.44}$	$^{+0.14}_{-0.50}$	$^{+0.38}_{-0.47}$	$^{+0.48}_{-0.64}$	$^{+0.26}_{-0.56}$	$^{-}_{-0.39}$
Effective detector NP set 5 (JES) [%]	$^{+0.78}_{-0.74}$	-	-	-	$^{-0.10}_{+0.16}$	-	-	$^{+0.22}_{-0.10}$	-	$^{+0.14}_{-0.17}$	$^{+0.28}_{-0.10}$
Effective detector NP set 6 restTerm (JES) [%]	$^{-0.52}_{+0.51}$	$^{-0.15}_{+0.10}$	$^{+0.14}_{-}$	-	$^{+0.13}_{-0.14}$	$^{+0.18}_{-0.15}$	-	$^{+0.20}_{-0.24}$	-	$^{+0.31}_{-0.28}$	$^{+0.19}_{-0.26}$
η intercalibration model (JES) [%]	$^{-2.49}_{+2.14}$	$^{+0.27}_{-0.75}$	$^{+1.50}_{-1.84}$	$^{+2.10}_{-2.19}$	$^{+1.99}_{-2.44}$	$^{+1.91}_{-2.27}$	$^{+1.65}_{-2.10}$	$^{+1.81}_{-2.76}$	$^{+1.79}_{-2.63}$	$^{+1.74}_{-2.14}$	$^{+1.08}_{-2.08}$
η intercalibration total stat (JES) [%]	$^{-1.62}_{+1.14}$	$^{+0.29}_{-0.41}$	$^{+0.90}_{-0.82}$	$^{+1.04}_{-1.08}$	$^{+0.99}_{-0.96}$	$^{+1.11}_{-0.81}$	$^{+0.35}_{-0.75}$	$^{+0.71}_{-0.70}$	$^{+0.31}_{-0.69}$	$^{+0.72}_{-0.43}$	$^{-0.43}_{+0.12}$
Flavour composition (JES) [%]	-	$^{+3.05}_{-3.71}$	$^{+4.19}_{-4.91}$	$^{+4.17}_{-4.87}$	$^{+3.66}_{-4.05}$	$^{+2.93}_{-3.22}$	$^{+2.44}_{-2.80}$	$^{+1.79}_{-3.07}$	$^{+0.73}_{-3.39}$	$^{+1.87}_{-1.83}$	$^{-}_{-1.09}$
Flavour response (JES) [%]	$^{-1.31}_{+0.61}$	$^{-0.82}_{+0.55}$	$^{-1.29}_{+0.95}$	$^{-1.51}_{+1.13}$	$^{-1.37}_{+0.90}$	$^{-1.02}_{+0.98}$	$^{-0.99}_{+0.15}$	$^{-1.33}_{+0.36}$	$^{-}_{-1.07}$	$^{-1.40}_{+0.44}$	$^{-}_{-1.48}$
Pile-up offset μ [JES] [%]	$^{+0.13}_{-0.33}$	$^{+0.16}_{+0.17}$	$^{-0.26}_{+0.21}$	$^{-0.33}_{+0.24}$	$^{-0.23}_{+0.21}$	$^{-0.16}_{+0.27}$	-	-	-	-	$^{+0.38}_{-0.66}$
Pile-up offset N_{PV} [JES] [%]	$^{+0.20}_{-0.41}$	-	-	-	-	$^{+0.21}_{-}$	$^{+0.16}_{-0.20}$	-	$^{-0.27}_{+0.23}$	$^{+0.28}_{-0.19}$	$^{+0.59}_{-0.47}$
Pile-up offset p_{T} [JES] [%]	$^{-0.78}_{+0.83}$	$^{-0.30}_{+0.28}$	-	-	$^{+0.11}_{-0.14}$	-	-	$^{+0.20}_{-0.19}$	$^{+0.27}_{-}$	$^{+0.13}_{-0.18}$	-
Pile-up offset ρ topology (JES) [%]	$^{-1.29}_{+0.56}$	$^{+1.18}_{-1.74}$	$^{+1.89}_{-2.27}$	$^{+2.01}_{-2.45}$	$^{+1.44}_{-2.25}$	$^{+1.61}_{-1.67}$	$^{+0.32}_{-1.55}$	$^{+0.43}_{-1.71}$	-	$^{+0.48}_{-1.69}$	-
Punch-through (JES) [%]	-	-	-	-	-	-	-	-	$^{-1.73}_{-}$	-	$^{-1.75}_{-}$
Single particle high-p_{T} (JES) [%]	-	-	-	-	-	-	-	-	-	-	-
Jet energy resolution [%]	∓ 4.57	∓ 3.74	∓ 1.53	∓ 0.39	∓ 0.49	± 0.38	∓ 0.75	∓ 0.18	∓ 1.00	∓ 2.38	∓ 2.35
Jet vertex fraction [%]	$^{+7.71}_{-7.39}$	$^{+5.38}_{-5.24}$	$^{+3.82}_{-3.77}$	$^{+2.93}_{-2.91}$	$^{+2.30}_{-2.29}$	$^{+1.82}_{-1.81}$	$^{+1.35}_{-1.31}$	$^{+1.07}_{-1.05}$	$^{+0.82}_{-0.72}$	$^{+0.69}_{-0.66}$	$^{+0.18}_{-}$
b-Quark tagging efficiency (eigenvector 0) [%]	$^{-6.09}_{+6.24}$	$^{-4.51}_{+4.60}$	$^{-3.93}_{+4.00}$	$^{-3.79}_{+3.84}$	$^{-3.72}_{+3.78}$	$^{-3.67}_{+3.73}$	$^{-3.66}_{+3.71}$	$^{-3.76}_{+3.81}$	$^{-3.83}_{+3.88}$	$^{-3.78}_{+3.82}$	$^{-4.11}_{+4.17}$
b-Quark tagging efficiency (eigenvector 1) [%]	∓ 0.17	∓ 0.81	∓ 1.27	$^{-1.70}_{+1.72}$	$^{-2.13}_{+2.17}$	$^{-2.51}_{+2.54}$	$^{-2.91}_{+2.95}$	$^{-3.27}_{+3.31}$	$^{-3.60}_{+3.65}$	$^{-3.76}_{+3.81}$	$^{-4.40}_{+4.46}$
b-Quark tagging efficiency (eigenvector 2) [%]	$^{+1.49}_{-1.48}$	$^{+1.55}_{-1.54}$	$^{+1.37}_{-1.36}$	± 1.08	± 0.81	± 0.58	± 0.36	± 0.18	-	-	∓ 0.37
b-Quark tagging efficiency (eigenvector 3) [%]	∓ 0.37	-	± 0.16	± 0.21	± 0.16	-	-	-	∓ 0.12	∓ 0.16	∓ 0.28
b-Quark tagging efficiency (eigenvector 4) [%]	-	-	-	-	-	-	-	-	-	∓ 0.11	∓ 0.15
c-Quark tagging efficiency (eigenvector 0) [%]	$^{-2.04}_{+2.07}$	$^{-1.39}_{+1.40}$	∓ 1.28	$^{-1.39}_{+1.40}$	$^{-1.50}_{+1.51}$	∓ 1.55	$^{-1.75}_{+1.77}$	$^{-1.82}_{+1.83}$	$^{-1.92}_{+1.93}$	$^{-1.96}_{+1.97}$	$^{-2.45}_{+2.48}$
c-Quark tagging efficiency (eigenvector 1) [%]	± 0.58	± 0.31	± 0.20	± 0.14	-	-	-	∓ 0.17	∓ 0.27	∓ 0.30	∓ 0.55
c-Quark tagging efficiency (eigenvector 2) [%]	-	± 0.15	± 0.19	± 0.22	± 0.21	± 0.19	± 0.17	± 0.14	± 0.12	-	-
c-Quark tagging efficiency (eigenvector 3) [%]	∓ 0.22	∓ 0.11	-	-	-	-	-	-	-	-	-
Light-jet tagging efficiency (eigenvector 0) [%]	$^{-1.95}_{+2.09}$	$^{-0.99}_{+1.02}$	$^{-1.11}_{+1.15}$	$^{-1.18}_{+1.23}$	$^{-1.63}_{+1.75}$	$^{-2.01}_{+2.15}$	$^{-2.20}_{+2.23}$	$^{-2.68}_{+2.71}$	$^{-3.39}_{+3.53}$	$^{-3.41}_{+3.51}$	$^{-6.94}_{+7.57}$
Light-jet tagging efficiency (eigenvector 1) [%]	-	-	-	-	-	-	-	-	-	∓ 0.11	$^{-0.37}_{+0.38}$
Light-jet tagging efficiency (eigenvector 2) [%]	± 0.23	± 0.10	-	-	$^{-}_{-0.11}$	-	-	-	-	∓ 0.10	∓ 0.29
Light-jet tagging efficiency (eigenvector 3) [%]	∓ 0.12	-	-	-	-	-	-	-	-	-	-
Light-jet tagging efficiency (eigenvector 4) [%]	-	-	-	-	-	-	-	-	-	-	-
Light-jet tagging efficiency (eigenvector 5) [%]	-	-	-	-	-	-	-	-	-	-	-
Light-jet tagging efficiency (eigenvector 6) [%]	-	-	-	-	-	-	-	-	-	-	-
Light-jet tagging efficiency (eigenvector 7) [%]	-	-	-	-	-	-	-	-	-	-	-
Light-jet tagging efficiency (eigenvector 8) [%]	-	-	-	-	-	-	-	-	-	-	-
Light-jet tagging efficiency (eigenvector 9) [%]	-	-	-	-	-	-	-	-	-	-	-
Light-jet tagging efficiency (eigenvector 10) [%]	-	-	-	-	-	-	-	-	-	-	-
Light-jet tagging efficiency (eigenvector 11) [%]	-	-	-	-	-	-	-	-	-	-	-
b-Quark tagging extrapolation [%]	-	-	-	-	$^{+0.23}_{-0.25}$	$^{+0.63}_{-0.62}$	$^{+1.20}_{-1.19}$	$^{+1.76}_{-1.75}$	$^{+2.27}_{-2.25}$	$^{+2.61}_{-2.59}$	$^{+4.30}_{-4.24}$
b-Quark tagging extrapolation from c-Quark [%]	± 0.15	-	-	± 0.10	$^{+0.11}_{-0.13}$	$^{+0.13}_{-0.12}$	± 0.13	$^{+0.13}_{-0.14}$	± 0.15	± 0.14	± 0.21
Electron energy resolution [%]	-	-	-	-	-	-	-	$^{-0.12}_{+0.10}$	$^{-0.25}_{+0.14}$	$^{-}_{-0.37}$	$^{-0.35}_{+0.10}$
Electron energy scale [%]	$^{-0.19}_{+0.18}$	-	-	-	± 0.11	$^{+0.25}_{-}$	-	$^{+0.28}_{-0.15}$	$^{+0.21}_{-0.12}$	-	$^{+0.28}_{-0.17}$
Electron trigger efficiency [%]	± 0.23	± 0.22	± 0.23	± 0.25	± 0.28	± 0.30	± 0.32	± 0.36	± 0.38	± 0.40	± 0.51
Electron reconstruction efficiency [%]	± 0.14	± 0.15	± 0.16	± 0.18	± 0.20	± 0.21	± 0.22	± 0.24	± 0.26	± 0.27	± 0.32
Electron identification efficiency [%]	± 0.36	± 0.35	± 0.38	± 0.42	± 0.47	± 0.53	± 0.58	± 0.64	± 0.71	± 0.74	± 0.92
Electron isolation efficiency [%]	± 0.11	± 0.11	± 0.12	± 0.15	± 0.18	± 0.23	± 0.27	± 0.32	± 0.37	± 0.39	± 0.52
Muon energy scale [%]	-	-	-	-	-	-	-	-	-	-	-
Muon (MS) momentum resolution [%]	-	-	-	-	-	-	-	-	-	-	-
Muon (ID) momentum resolution [%]	-	-	-	-	-	$^{-}_{-0.14}$	-	-	-	-	-
Muon trigger efficiency stat [%]	$^{+0.60}_{-0.62}$	$^{+0.56}_{-0.57}$	$^{+0.56}_{-0.58}$	$^{+0.56}_{-0.58}$	$^{+0.57}_{-0.58}$	$^{+0.57}_{-0.58}$	$^{+0.57}_{-0.59}$	$^{+0.59}_{-0.61}$	$^{+0.60}_{-0.61}$	$^{+0.59}_{-0.60}$	$^{+0.65}_{-0.68}$
Muon trigger efficiency syst [%]	± 0.26	± 0.24	± 0.24	± 0.24	± 0.24	± 0.24	± 0.25	± 0.25	± 0.25	± 0.25	$^{+0.28}_{-0.27}$
Muon identification stat [%]	-	-	-	-	-	-	-	-	-	-	-
Muon identification syst [%]	± 0.15	± 0.14	± 0.15	± 0.17	± 0.19	± 0.21	± 0.24	± 0.26	± 0.29	± 0.32	± 0.41
Muon isolation efficiency stat [%]	-	-	-	-	-	-	-	-	-	-	-
Muon isolation efficiency syst [%]	± 0.11	± 0.10	± 0.10	± 0.10	± 0.10	± 0.11	± 0.11	± 0.11	± 0.12	± 0.12	± 0.15
Muon TTVA efficiency stat [%]	-	-	-	-	-	-	-	-	-	-	-
Muon TTVA efficiency syst [%]	-	-	-	-	-	-	-	-	-	-	-
$E_{\mathrm{T}}^{\mathrm{miss}}$ Soft jet resolution para [%]	± 0.59	± 0.27	-	-	-	-	∓ 0.10	-	± 0.13	∓ 0.23	± 0.26
$E_{\mathrm{T}}^{\mathrm{miss}}$ Soft jet resolution perp [%]	± 0.43	± 0.13	-	∓ 0.13	∓ 0.29	∓ 0.27	∓ 0.38	∓ 0.25	∓ 0.26	∓ 0.59	∓ 0.57
$E_{\mathrm{T}}^{\mathrm{miss}}$ Soft jet scale [%]	$^{+0.67}_{-0.49}$	$^{+0.17}_{-0.26}$	-	$^{-0.13}_{-}$	$^{-0.23}_{+0.16}$	$^{-0.17}_{+0.24}$	$^{-}_{-0.27}$	$^{-0.16}_{+0.27}$	$^{-0.26}_{+0.22}$	$^{-0.28}_{+0.11}$	$^{-0.37}_{+0.16}$
Luminosity [%]	∓ 2.06	∓ 2.06	∓ 2.06	∓ 2.06	∓ 2.06	∓ 2.06	∓ 2.06	∓ 2.06	∓ 2.06	∓ 2.06	∓ 2.06
Single top cross-section [%]	± 0.27	± 0.17	± 0.19	± 0.23	± 0.29	± 0.35	± 0.42	± 0.49	± 0.57	± 0.63	± 0.83
Z+jets cross-section [%]	± 1.40	± 0.48	± 0.44	± 0.48	± 0.62	± 0.46	± 0.51	± 0.93	± 1.16	± 0.92	± 2.32
Diboson cross-section [%]	± 0.19	-	-	± 0.10	± 0.13	± 0.19	± 0.24	± 0.30	± 0.39	± 0.44	± 0.65
$t\bar{t}V$ cross-section [%]	-	-	-	-	-	-	∓ 0.12	∓ 0.18	∓ 0.20	∓ 0.21	∓ 0.25
Monte Carlo sample statistics [%]	± 0.76	± 0.29	± 0.27	± 0.29	± 0.39	± 0.47	± 0.54	± 0.75	± 1.38	± 1.39	± 1.70
ISR/FSR + scale [%]	$^{-2.26}_{+1.69}$	$^{-2.31}_{+0.86}$	$^{-3.07}_{+2.75}$	$^{-3.17}_{+2.52}$	$^{-2.80}_{+2.22}$	$^{-2.03}_{+3.22}$	$^{-3.09}_{+2.50}$	$^{-2.42}_{+2.52}$	$^{-2.80}_{+2.24}$	$^{-5.25}_{+0.56}$	$^{-2.00}_{+1.66}$
Alternate hard-scattering model [%]	∓ 1.35	∓ 1.33	± 0.12	∓ 0.37	± 0.75	∓ 1.14	± 3.30	± 3.29	± 4.23	± 2.34	± 9.04
Alternate parton-shower model [%]	-	± 0.13	∓ 2.55	∓ 1.71	∓ 1.93	∓ 1.00	∓ 1.76	∓ 0.74	∓ 1.49	∓ 2.48	∓ 3.77
Inter PDF [%]	-	-	-	-	-	± 0.12	-	-	-	± 0.11	± 0.42
Intra PDF [%]	-	-	-	-	-	-	-	-	-	± 0.14	± 0.30
Real lepton efficiency stat [%]	∓ 0.10	$^{-0.11}_{+0.10}$	∓ 0.12	$^{-0.15}_{+0.14}$	$^{-0.18}_{+0.17}$	$^{-0.23}_{+0.20}$	$^{-0.25}_{+0.23}$	$^{-0.34}_{+0.28}$	$^{-0.39}_{+0.31}$	$^{-0.48}_{+0.36}$	$^{-0.64}_{+0.44}$
Fake lepton efficiency MC scale [%]	$^{+1.70}_{-1.85}$	$^{+0.53}_{-0.57}$	$^{+0.43}_{-0.48}$	$^{+0.39}_{-0.50}$	$^{+0.56}_{-0.74}$	$^{+0.65}_{-0.89}$	$^{+0.67}_{-0.86}$	$^{+0.89}_{-1.42}$	$^{+0.70}_{-1.78}$	$^{+0.17}_{-1.29}$	$^{+1.89}_{-2.07}$
Fake lepton efficiency alternate CR [%]	± 0.83	± 0.28	± 0.21	± 0.28	± 0.36	± 0.52	± 0.26	± 0.54	± 0.55	± 0.65	-
Fake overall normalisation [%]	± 8.86	± 2.97	± 2.30	± 2.46	± 3.23	± 3.35	± 3.88	± 4.84	± 5.87	± 5.60	± 10.5
W+jets CA_{4incl} stat error [%]	∓ 0.17	-	-	-	∓ 0.12	∓ 0.13	∓ 0.17	∓ 0.20	∓ 0.23	∓ 0.27	∓ 0.41
W+jets Fc stat error [%]	-	-	-	-	-	-	-	-	-	-	$^{+0.16}_{-0.15}$
W+jets Fcc stat error [%]	$^{+0.20}_{-}$	-	-	-	-	-	-	$^{-0.16}_{-}$	$^{-0.43}_{+0.21}$	$^{-0.41}_{+0.20}$	-
W+jets Flight stat error [%]	-	-	-	-	-	-	-	-	-	-	-

Table C.9: Table of systematic uncertainties for the absolute differential cross-section at particle level for the mass of the $t\bar{t}$ system in the resolved regime.

Bins [GeV]	0–25	25–50	50–75	75–105	105–135	135–165	165–195	195–230	230–265	265–300	300–350	350–400	400–450	450–500	500–1000.00
$1/\sigma \cdot d\sigma \,/\, dp_{\mathrm{T}}^{t}$	$1.32 \cdot 10^{-3}$	$3.82 \cdot 10^{-3}$	$5.68 \cdot 10^{-3}$	$6.28 \cdot 10^{-3}$	$5.61 \cdot 10^{-3}$	$4.02 \cdot 10^{-3}$	$2.74 \cdot 10^{-3}$	$1.79 \cdot 10^{-3}$	$1.10 \cdot 10^{-3}$	$7.52 \cdot 10^{-4}$	$3.99 \cdot 10^{-4}$	$2.18 \cdot 10^{-4}$	$1.08 \cdot 10^{-4}$	$5.13 \cdot 10^{-5}$	$7.14 \cdot 10^{-6}$
Total uncertainty [%]	$^{+4.08}_{-4.58}$	$^{+3.97}_{-3.74}$	$^{+2.81}_{-2.97}$	$^{+2.99}_{-1.88}$	$^{+1.51}_{-1.57}$	$^{+2.29}_{-1.88}$	$^{+2.88}_{-2.71}$	$^{+3.76}_{-4.36}$	$^{+5.21}_{-4.42}$	$^{+8.70}_{-7.06}$	$^{+6.83}_{-6.96}$	$^{+9.38}_{-8.54}$	$^{+9.44}_{-10.1}$	$^{+12.9}_{-20.4}$	$^{+13.5}_{-15.0}$
Statistical uncertainty [%]	± 2.0	± 1.1	± 0.9	± 0.7	± 0.8	± 0.9	± 1.1	± 1.3	± 1.7	± 2.1	± 2.5	± 3.5	± 5.2	± 8.2	± 7.3
Systematic uncertainty [%]	$^{+3.38}_{-3.97}$	$^{+3.46}_{-3.54}$	$^{+2.65}_{-2.80}$	$^{+1.84}_{-1.70}$	$^{+1.23}_{-1.31}$	$^{+2.04}_{-1.57}$	$^{+2.36}_{-2.40}$	$^{+3.51}_{-4.12}$	$^{+4.88}_{-4.03}$	$^{+6.35}_{-6.67}$	$^{+6.07}_{-5.77}$	$^{+8.61}_{-7.68}$	$^{+7.61}_{-8.47}$	$^{+18.0}_{-18.5}$	$^{+13.5}_{-13.0}$
b-Tagged jet energy scale (JES) [%]	$^{+0.92}_{-0.92}$	$^{+0.42}_{-0.42}$	$^{+0.28}_{-0.28}$	$^{+0.15}_{-0.15}$	$^{+0.19}_{-0.19}$	$^{+0.29}_{-0.29}$	$^{+0.27}_{-0.27}$	$^{+0.25}_{-0.25}$	$^{+0.24}_{-0.24}$	-	$^{+0.28}_{-0.28}$	-	-	$^{+0.85}_{-0.85}$	-
Effective detector NP set 1 (JES) [%]	$^{+0.61}_{-0.53}$	$^{+0.48}_{-0.23}$	$^{+0.30}_{-0.18}$	$^{+0.18}_{+0.53}$	$^{+0.33}_{+0.52}$	$^{+0.37}_{+0.39}$	$^{-0.10}_{-0.16}$	$^{-0.92}_{-1.10}$	$^{-0.17}_{-1.93}$	$^{-}_{-2.09}$	$^{-0.39}_{-1.53}$	$^{-}_{-1.25}$	$^{-}_{-2.46}$	$^{-0.75}_{-3.36}$	$^{-}_{-2.90}$
Effective detector NP set 2 (JES) [%]	$^{-0.93}_{-1.08}$	$^{-0.57}_{-1.30}$	$^{-0.74}_{\mp 1.09}$	$^{-0.30}_{-0.62}$	$^{-0.44}_{-0.28}$	$^{+0.37}_{+0.45}$	$^{+0.61}_{+0.73}$	$^{+1.88}_{+0.92}$	$^{+1.74}_{+1.93}$	$^{+1.95}_{+1.66}$	$^{+2.73}_{+2.26}$	$^{+3.78}_{+3.78}$	$^{+1.68}_{+2.53}$	$^{+1.46}_{+3.55}$	$^{+1.25}_{+6.36}$
Effective detector NP set 3 (JES) [%]	$^{+0.65}_{+0.41}$	$^{+1.18}_{\pm 0.76}$	$^{+0.81}_{+0.61}$	$^{+0.17}_{\pm 0.51}$	$^{-0.28}_{-}$	$^{-0.74}_{+0.32}$	$^{-1.24}_{+0.48}$	$^{-1.57}_{+0.57}$	$^{-2.09}_{+1.21}$	$^{-2.16}_{+0.97}$	$^{-3.40}_{+1.42}$	$^{-3.19}_{+1.64}$	$^{-3.78}_{-1.60}$	$^{-5.70}_{+1.12}$	$^{-2.19}_{+2.08}$
Effective detector NP set 4 (JES) [%]	$^{-0.59}_{+0.47}$	$^{-0.45}_{+0.46}$	$^{-0.56}_{+0.32}$	$^{-0.27}_{+0.30}$	$^{+0.11}_{-0.16}$	$^{+0.32}_{-0.26}$	$^{+0.48}_{-0.20}$	$^{+0.57}_{-0.49}$	$^{+1.21}_{\pm 0.45}$	$^{+0.97}_{-0.47}$	$^{+1.42}_{-0.42}$	$^{+1.57}_{-0.17}$	$^{+1.12}_{-0.32}$	$^{+2.08}_{-0.26}$	$^{+2.54}_{+0.45}$
Effective detector NP set 5 (JES) [%]	$^{+0.21}_{-}$	$^{+0.46}_{-}$	$^{+0.32}_{-}$	$^{+0.30}_{-}$	$^{-0.16}_{-0.12}$	$^{-0.26}_{-0.16}$	$^{-0.20}_{-}$	$^{-0.49}_{-}$	$^{-}_{-}$	$^{-0.47}_{-}$	$^{+0.32}_{-}$	$^{+0.35}_{-}$	$^{+0.78}_{-}$	$^{+0.78}_{-}$	$^{+0.29}_{-}$
Effective detector NP set 6 restTerm (JES) [%]	$^{-0.14}_{-}$	$^{-0.10}_{-}$	$^{-}_{-}$	$^{-}_{-}$	$^{-}_{-}$	$^{-}_{-}$	$^{-}_{-}$	$^{-}_{-}$	$^{+0.14}_{-}$	$^{-}_{-}$	$^{+0.28}_{-}$	$^{+0.36}_{-}$	$^{-0.53}_{-}$	$^{+0.77}_{-}$	$^{+0.61}_{-}$
η intercalibration model (JES) [%]	$^{-0.43}_{+0.14}$	$^{+0.17}_{-0.55}$	$^{-}_{-}$	$^{-}_{-}$	$^{+0.20}_{-0.21}$	$^{+0.42}_{-}$	$^{-}_{-0.23}$	$^{-0.16}_{-}$	$^{-}_{+0.57}$	$^{-}_{-0.33}$	$^{-0.33}_{-0.19}$	$^{-0.16}_{+0.42}$	$^{-0.30}_{-}$	$^{-0.67}_{-0.58}$	$^{-0.50}_{+0.69}$
η intercalibration total stat (JES) [%]	$^{+0.14}_{-0.74}$	$^{+0.29}_{-0.16}$	$^{-0.22}_{-}$	$^{-}_{-}$	$^{-0.21}_{-}$	$^{-}_{-}$	$^{-}_{-}$	$^{-}_{-0.25}$	$^{+0.26}_{-}$	$^{-0.33}_{-}$	$^{+0.10}_{+0.34}$	$^{-}_{+0.23}$	$^{-0.75}_{-}$	$^{+0.27}_{+0.40}$	$^{-0.53}_{+0.49}$
Flavour composition (JES) [%]	$^{+0.99}_{-1.22}$	$^{+0.23}_{-0.43}$	$^{+0.28}_{-0.32}$	$^{-}_{-}$	$^{-0.29}_{-0.28}$	$^{+0.32}_{-0.10}$	$^{-}_{-}$	$^{-0.27}_{+0.23}$	$^{-0.43}_{+1.35}$	$^{-0.36}_{+1.26}$	$^{-1.07}_{+1.23}$	$^{-0.42}_{+1.85}$	$^{-0.58}_{+1.58}$	$^{-2.36}_{+1.27}$	$^{-0.14}_{+0.76}$
Flavour response (JES) [%]	$^{-}_{-0.37}$	$^{+0.13}_{-0.12}$	$^{+0.31}_{-0.17}$	$^{+0.31}_{-0.17}$	$^{-0.23}_{+0.14}$	$^{-}_{+0.23}$	$^{-0.27}_{+0.21}$	$^{+0.17}_{-}$	$^{+0.39}_{-}$	$^{-}_{-0.29}$	$^{-}_{+0.20}$	$^{-}_{-}$	$^{-0.46}_{-0.71}$	$^{-}_{-}$	$^{+0.81}_{-0.57}$
Pile-up offset μ (JES) [%]	$^{-}_{-0.20}$	$^{-}_{-}$	$^{-}_{-}$	$^{-}_{-}$	$^{-}_{-}$	$^{-}_{-}$	$^{-}_{-}$	$^{-}_{-}$	$^{+0.11}_{-}$	$^{-}_{-}$	$^{-}_{-}$	$^{+0.21}_{-}$	$^{-}_{-0.40}$	$^{-}_{-}$	$^{+0.95}_{-0.93}$
Pile-up offset N_{PV} (JES) [%]	$^{-}_{-0.24}$	$^{-}_{-}$	$^{-}_{-}$	$^{-}_{-}$	$^{-}_{-}$	$^{-}_{-}$	$^{-}_{-}$	$^{-}_{-}$	$^{-}_{-}$	$^{-}_{-}$	$^{-}_{-}$	$^{-}_{-}$	$^{-}_{-0.51}$	$^{-0.26}_{-}$	$^{+0.79}_{-0.48}$
Pile-up offset p_{T} (JES) [%]	$^{-}_{+0.37}$	$^{-0.26}_{+0.23}$	$^{-0.13}_{+0.20}$	$^{-}_{-}$	$^{-}_{-}$	$^{+0.16}_{+0.27}$	$^{-}_{-}$	$^{-}_{-}$	$^{+0.27}_{-0.29}$	$^{+0.25}_{-0.49}$	$^{+0.15}_{-0.38}$	$^{+0.41}_{-}$	$^{+0.17}_{-0.46}$	$^{+0.16}_{-0.50}$	$^{+0.39}_{-}$
Pile-up offset ρ topology (JES) [%]	$^{-}_{-0.53}$	$^{-}_{-}$	$^{-}_{-0.25}$	$^{-}_{-}$	$^{+0.31}_{-0.27}$	$^{+0.27}_{-}$	$^{-}_{-}$	$^{-0.29}_{+0.14}$	$^{-0.41}_{+0.67}$	$^{-0.49}_{+0.26}$	$^{-0.57}_{+0.46}$	$^{-0.54}_{+0.95}$	$^{-0.81}_{+0.57}$	$^{-}_{-}$	$^{-0.84}_{+0.74}$
Punch-through (JES) [%]	$^{-}_{-}$	$^{-}_{-}$	$^{-}_{-}$	$^{-}_{-}$	$^{-}_{-}$	$^{-}_{-}$	$^{-}_{-}$	$^{-}_{-}$	$^{-}_{-}$	$^{-}_{-}$	$^{-}_{-}$	$^{-}_{-}$	$^{-}_{-}$	$^{-}_{-0.28}$	$^{-0.72}_{-}$
Single particle high-p_{T} (JES) [%]	-	-	-	-	-	-	-	-	-	-	-	-	-	-	-
Jet energy resolution [%]	∓ 0.53	∓ 0.85	∓ 0.60	∓ 0.24	-	± 0.66	± 0.71	-	± 1.42	-	± 0.33	± 1.62	∓ 0.63	∓ 1.17	∓ 0.57
Jet vertex fraction [%]	± 1.78	$^{+1.81}_{-1.86}$	$^{+1.43}_{-1.48}$	$^{+0.69}_{-0.72}$	-	∓ 0.68	$^{-1.19}_{+1.27}$	$^{-1.67}_{+1.53}$	$^{-1.93}_{+2.35}$	$^{-1.92}_{+1.98}$	$^{-2.33}_{+2.45}$	$^{-2.54}_{+2.95}$	$^{-2.96}_{+3.41}$	$^{-2.48}_{+2.56}$	$^{-3.07}_{+3.31}$
b-Quark tagging efficiency (eigenvector 0) [%]	$^{-0.68}_{\mp 0.65}$	$^{-1.05}_{\mp 0.59}$	$^{-1.48}_{\mp 0.31}$	$^{-0.72}_{-}$	$^{+0.10}_{-}$	$^{+0.21}_{-0.20}$	$^{+1.27}_{-0.45}$	$^{+1.53}_{-0.31}$	$^{+2.35}_{-0.33}$	$^{+1.98}_{-0.34}$	$^{+2.45}_{-0.31}$	$^{+2.95}_{-0.23}$	$^{+3.41}_{-0.49}$	$^{+2.56}_{-0.23}$	$^{-}_{-3.53}$
b-Quark tagging efficiency (eigenvector 1) [%]	$^{\mp 0.92}_{-0.79}$	$^{\mp 0.77}_{-0.74}$	$^{\mp 0.66}_{-0.65}$	$^{+0.50}_{-0.49}$	$^{\pm 0.28}_{-}$	$^{-}_{-}$	$^{-0.35}_{+0.42}$	$^{-1.30}_{+0.85}$	$^{-1.62}_{+1.37}$	$^{-1.62}_{+1.67}$	$^{-2.06}_{+2.04}$	$^{-2.64}_{+2.51}$	$^{-2.64}_{+2.62}$	$^{-2.58}_{+2.86}$	$^{-}_{+3.50}$
b-Quark tagging efficiency (eigenvector 2) [%]	$^{+0.39}_{-0.40}$	$^{+0.41}_{-0.42}$	$^{+0.38}_{-0.39}$	$^{+0.30}_{-0.31}$	$^{\pm 0.18}_{-}$	$^{-}_{-}$	$^{-0.25}_{+0.26}$	$^{\mp 0.52}_{-}$	$^{-0.81}_{+0.82}$	$^{-0.99}_{+1.01}$	$^{-1.20}_{+1.22}$	$^{-1.44}_{+1.47}$	$^{-1.60}_{+1.63}$	$^{-1.74}_{+1.77}$	$^{-1.96}_{+2.00}$
b-Quark tagging efficiency (eigenvector 3) [%]	∓ 0.14	∓ 0.12	-	-	-	± 0.12	± 0.11	-	-	∓ 0.14	∓ 0.25	$^{-}_{+0.36}$	$^{-0.35}_{\pm 0.42}$	$^{-}_{\pm 0.50}$	$^{-}_{\pm 0.64}$
b-Quark tagging efficiency (eigenvector 4) [%]	-	-	-	-	-	-	-	-	-	-	-	± 0.12	∓ 0.13	∓ 0.16	∓ 0.21
c-Quark tagging efficiency (eigenvector 0) [%]	$^{-0.26}_{+0.27}$	$^{-0.26}_{+0.25}$	$^{-0.33}_{+0.32}$	∓ 0.19	-	-	± 0.28	$^{+0.42}_{-0.41}$	± 0.42	$^{+0.50}_{-0.49}$	$^{+0.61}_{-0.60}$	$^{+0.61}_{-0.60}$	$^{+0.57}_{-0.59}$	± 0.43	$^{+0.13}_{-0.44}$
c-Quark tagging efficiency (eigenvector 1) [%]	± 0.20	± 0.19	± 0.16	-	-	-	∓ 0.13	∓ 0.18	∓ 0.22	∓ 0.29	∓ 0.33	∓ 0.30	$^{-}_{+0.30}$	∓ 0.36	$^{-}_{+0.43}$
c-Quark tagging efficiency (eigenvector 2) [%]	-	-	-	-	-	-	-	-	∓ 0.10	∓ 0.17	∓ 0.20	∓ 0.19	∓ 0.19	$^{-0.22}_{+0.23}$	∓ 0.25
c-Quark tagging efficiency (eigenvector 3) [%]	-	-	-	-	-	-	-	-	-	-	-	-	-	-	-
Light-jet tagging efficiency (eigenvector 0) [%]	$^{-0.53}_{+0.80}$	$^{-0.65}_{+0.70}$	-	$^{-}_{-0.11}$	$^{+0.19}_{-0.22}$	$^{+0.16}_{-0.20}$	-	$^{+0.27}_{-0.30}$	$^{+0.20}_{-0.23}$	-	$^{+0.12}_{-0.19}$	$^{-}_{\pm 0.37}$	$^{-1.03}_{+1.14}$	$^{-1.20}_{+1.10}$	$^{-2.33}_{+2.44}$
Light-jet tagging efficiency (eigenvector 1) [%]	-	-	-	-	-	-	-	-	-	-	-	-	$^{-0.15}_{-}$	∓ 0.12	$^{+0.15}_{-}$
Light-jet tagging efficiency (eigenvector 2) [%]	$^{+0.13}_{-0.12}$	$^{+0.12}_{-0.13}$	-	-	-	-	-	-	-	∓ 0.12	∓ 0.10	∓ 0.16	∓ 0.20	$^{-0.18}_{+0.19}$	∓ 0.23
Light-jet tagging efficiency (eigenvector 3) [%]	-	-	-	-	-	-	-	-	-	-	-	-	-	-	-
Light-jet tagging efficiency (eigenvector 4) [%]	-	-	-	-	-	-	-	-	-	-	-	-	-	-	∓ 0.21
Light-jet tagging efficiency (eigenvector 5) [%]	-	-	-	-	-	-	-	-	-	-	-	-	-	-	-
Light-jet tagging efficiency (eigenvector 6) [%]	-	-	-	-	-	-	-	-	-	-	-	-	-	-	-
Light-jet tagging efficiency (eigenvector 7) [%]	-	-	-	-	-	-	-	-	-	-	-	-	-	-	-
Light-jet tagging efficiency (eigenvector 8) [%]	-	-	-	-	-	-	-	-	-	-	-	-	-	-	-
Light-jet tagging efficiency (eigenvector 9) [%]	-	-	-	-	-	-	-	-	-	-	-	-	-	-	-
Light-jet tagging efficiency (eigenvector 10) [%]	-	-	-	-	-	-	-	-	-	-	-	-	-	-	-
Light-jet tagging efficiency (eigenvector 11) [%]	-	-	-	-	-	-	-	-	-	-	-	-	-	-	-
b-Quark tagging extrapolation [%]	∓ 0.31	$^{-0.31}_{+0.30}$	∓ 0.31	∓ 0.29	∓ 0.28	$^{-0.23}_{+0.22}$	$^{-0.13}_{+0.11}$	-	± 0.63	± 1.24	$^{+2.07}_{-2.06}$	$^{+3.10}_{-3.07}$	$^{+3.49}_{-3.44}$	$^{+4.20}_{-4.15}$	$^{+6.72}_{-6.62}$
b-Quark tagging extrapolation from c-Quark [%]	-	-	-	-	-	-	-	-	-	-	-	-	-	-	-
Electron energy resolution [%]	-	-	-	-	-	-	-	-	-	-	-	-	-	-	-
Electron energy scale [%]	-	-	-	-	-	-	-	-	-	-	-	-	-	-	$^{+0.13}_{-}$
Electron trigger efficiency [%]	-	-	-	-	-	-	-	-	-	-	-	-	-	-	± 0.10
Electron reconstruction efficiency [%]	-	-	-	-	-	-	-	-	-	-	-	-	-	-	± 0.12
Electron identification efficiency [%]	-	-	-	-	-	-	-	-	± 0.10	± 0.15	± 0.21	± 0.26	± 0.31	± 0.39	± 0.55
Electron isolation efficiency [%]	-	-	-	-	-	-	-	-	-	± 0.12	± 0.18	± 0.24	± 0.30	± 0.37	$^{+0.51}_{-0.52}$
Muon energy scale [%]	-	-	-	-	-	-	-	-	-	-	-	-	-	-	-
Muon (MS) momentum resolution [%]	-	-	-	-	-	-	-	-	-	-	-	-	-	-	-
Muon (ID) momentum resolution [%]	-	-	-	-	-	-	-	-	-	-	-	-	-	-	-
Muon trigger efficiency stat [%]	-	-	-	-	-	-	-	-	-	-	-	-	-	-	-
Muon trigger efficiency syst [%]	-	-	-	-	-	-	-	-	-	-	-	-	-	-	-
Muon identification stat [%]	-	-	-	-	-	-	-	-	-	-	-	-	-	-	-
Muon identification syst [%]	-	-	-	-	-	-	-	-	-	-	-	± 0.11	± 0.15	± 0.18	$^{+0.26}_{-0.25}$
Muon isolation efficiency stat [%]	-	-	-	-	-	-	-	-	-	-	-	-	-	-	-
Muon isolation efficiency syst [%]	-	-	-	-	-	-	-	-	-	-	-	-	-	-	-
Muon TTVA efficiency stat [%]	-	-	-	-	-	-	-	-	-	-	-	-	-	-	-
Muon TTVA efficiency syst [%]	-	-	-	-	-	-	-	-	-	-	-	-	-	-	-
$E_{\mathrm{T}}^{\mathrm{miss}}$ Soft jet resolution para [%]	-	-	-	-	-	-	-	-	-	-	-	-	-	-	-
$E_{\mathrm{T}}^{\mathrm{miss}}$ Soft jet resolution perp [%]	-	-	-	-	-	-	-	-	-	-	-	-	-	-	∓ 0.10
$E_{\mathrm{T}}^{\mathrm{miss}}$ Soft jet scale [%]	-	-	-	-	-	-	-	-	-	-	-	-	-	-	-
Luminosity [%]	-	-	-	-	-	-	-	-	-	-	-	-	-	-	-
Single top cross-section [%]	-	-	-	-	-	-	-	-	-	-	-	-	± 0.12	± 0.18	± 0.42
Z+jets cross-section [%]	-	± 0.11	± 0.29	-	-	∓ 0.15	∓ 0.13	∓ 0.20	∓ 0.18	∓ 0.20	∓ 0.25	∓ 0.19	∓ 0.29	± 0.15	± 0.35
Diboson cross-section [%]	-	-	-	-	-	-	-	-	-	-	± 0.10	-	± 0.24	± 0.32	± 0.68
$t\bar{t}V$ cross-section [%]	-	-	-	-	-	-	-	-	-	-	-	-	-	-	∓ 0.13
Monte Carlo sample statistics [%]	± 1.02	± 0.50	± 0.39	± 0.30	± 0.31	± 0.35	± 0.43	± 0.47	± 0.55	± 0.78	± 0.75	± 1.08	± 1.95	± 2.26	± 1.94
ISR/FSR + scale [%]	$^{-0.51}_{+0.36}$	$^{+0.25}_{-0.24}$	$^{+0.53}_{-}$	$^{+0.30}_{-0.54}$	$^{-0.31}_{+0.11}$	$^{+0.97}_{-}$	$^{-}_{-0.69}$	$^{-}_{-1.10}$	$^{-0.76}_{-0.64}$	$^{+0.69}_{-}$	$^{+0.53}_{-0.64}$	$^{+1.03}_{-0.53}$	$^{-1.94}_{+0.92}$	$^{-}_{-2.15}$	$^{+2.17}_{-1.05}$
Alternate hard-scattering model [%]	∓ 1.39	∓ 0.83	-	∓ 0.44	± 0.54	∓ 0.84	∓ 0.17	± 1.98	± 0.88	± 4.35	± 2.31	± 1.06	± 2.53	± 14.1	± 1.44
Alternate parton-shower model [%]	∓ 0.31	± 0.44	± 0.64	-	-	-	± 0.72	∓ 0.88	∓ 0.11	± 0.17	± 0.12	∓ 3.13	± 0.71	∓ 7.54	∓ 4.70
Inter PDF [%]	-	-	-	-	-	-	-	-	-	-	-	± 0.11	± 0.14	∓ 0.24	± 1.86
Intra PDF [%]	-	-	-	-	-	-	-	-	-	-	-	-	± 0.21	∓ 0.24	± 1.45
Real lepton efficiency stat [%]	-	-	-	-	-	-	-	-	-	-	$^{-0.14}_{+0.10}$	$^{-0.21}_{\mp 0.16}$	$^{-0.20}_{+0.16}$	$^{-0.38}_{+0.22}$	$^{-0.92}_{+0.47}$
Fake lepton efficiency MC scale [%]	-	$^{+0.21}_{-0.12}$	-	$^{+0.12}_{-0.10}$	-	-	$^{-0.12}_{+0.15}$	$^{-0.24}_{-}$	$^{-}_{+0.39}$	$^{-0.26}_{+0.39}$	$^{-}_{+0.34}$	$^{-}_{-0.34}$	$^{-}_{-0.37}$	± 0.45	$^{-}_{-0.50}$
Fake lepton efficiency alternate CR [%]	-	-	-	± 0.11	-	-	∓ 0.12	-	∓ 0.15	∓ 0.18	-	± 0.11	± 0.14	± 0.12	∓ 0.17
Fake overall normalisation [%]	± 1.21	± 1.49	± 0.96	± 0.60	∓ 0.49	∓ 0.50	∓ 1.04	∓ 1.12	∓ 0.99	∓ 1.38	∓ 0.89	∓ 1.58	± 0.32	± 0.55	± 2.64
W+jets CA_{simul} stat error [%]	-	-	-	-	-	-	-	-	-	-	-	-	-	-	-
W+jets Fc stat error [%]	-	-	-	-	-	-	-	-	-	-	-	-	-	-	-
W+jets Fcc stat error [%]	$^{+0.62}_{-0.30}$	$^{+0.20}_{-0.10}$	-	-	-	-	-	-	-	-	$^{-0.17}_{-}$	-	$^{+0.65}_{-0.31}$	-	$^{-0.42}_{+0.20}$
W+jets Flight stat error [%]	-	-	-	-	-	-	-	-	-	-	-	-	-	-	-

Table C.10: Table of systematic uncertainties for the relative differential cross-section at particle level for the top quark transverse momentum in the resolved regime.

Bins | Unit $\left\|y^{t}\right\|$	0–0.10	0.10–0.20	0.20–0.30	0.30–0.40	0.40–0.50	0.50–0.60	0.60–0.70	0.70–0.80	0.80–0.90	0.90–1	1–1.10	1.10–1.20	1.20–1.30	1.30–1.40	1.40–1.50	1.50–1.70	1.70–1.90	1.90–2.50
$1/\sigma \cdot \mathrm{d}\sigma / \mathrm{d}\left\|y^{t}\right\|$	$7.94 \cdot 10^{-1}$	$7.69 \cdot 10^{-1}$	$7.69 \cdot 10^{-1}$	$7.54 \cdot 10^{-1}$	$7.26 \cdot 10^{-1}$	$7.05 \cdot 10^{-1}$	$6.59 \cdot 10^{-1}$	$6.16 \cdot 10^{-1}$	$6.14 \cdot 10^{-1}$	$5.42 \cdot 10^{-1}$	$4.94 \cdot 10^{-1}$	$4.64 \cdot 10^{-1}$	$4.14 \cdot 10^{-1}$	$3.65 \cdot 10^{-1}$	$3.14 \cdot 10^{-1}$	$2.39 \cdot 10^{-1}$	$1.55 \cdot 10^{-1}$	$3.50 \cdot 10^{-2}$
Total uncertainty [%]	$^{+1.68}_{-2.41}$	$^{+1.99}_{-1.97}$	$^{+2.20}_{-1.77}$	$^{+2.86}_{-2.40}$	$^{+3.33}_{-3.05}$	$^{+1.93}_{-1.87}$	$^{+2.17}_{-2.27}$	$^{+2.09}_{-2.30}$	$^{+2.73}_{-2.08}$	$^{+1.86}_{-2.04}$	$^{+2.79}_{-2.81}$	$^{+1.98}_{-2.50}$	$^{+3.13}_{-3.19}$	$^{+3.32}_{-2.54}$	$^{+2.91}_{-2.93}$	$^{+2.56}_{-2.46}$	$^{+3.68}_{-3.34}$	$^{+5.12}_{-4.71}$
Statistical uncertainty σ [%]	± 1.1	± 1.2	± 1.2	± 1.2	± 1.2	± 1.3	± 1.3	± 1.4	± 1.3	± 1.5	± 1.6	± 1.6	± 1.7	± 1.8	± 2.0	± 1.5	± 1.9	± 2.1
Systematic uncertainty [%]	$^{+1.16}_{-2.07}$	$^{+1.47}_{-1.45}$	$^{+1.75}_{-1.19}$	$^{+2.06}_{-1.99}$	$^{+3.25}_{-3.22}$	$^{+1.34}_{-1.28}$	$^{+1.61}_{-1.75}$	$^{+1.42}_{-1.72}$	$^{+2.29}_{-1.46}$	$^{+0.86}_{-1.32}$	$^{+2.18}_{-2.23}$	$^{+0.94}_{-1.79}$	$^{+2.50}_{-2.58}$	$^{+2.65}_{-2.65}$	$^{+1.88}_{-1.91}$	$^{+2.02}_{-1.96}$	$^{+3.05}_{-2.63}$	$^{+4.55}_{-4.09}$
b-Tagged jet energy scale (JES) [%]	-	-	-	-	-	-	-	-	-	-	-	$^{+0.23}_{-0.23}$	-	-	-	$^{+0.19}_{-0.19}$	-	$^{+0.11}_{-0.11}$
Effective detector NP set 1 (JES) [%]	-	$^{+0.28}_{-0.23}$	$^{-0.15}_{+0.44}$	$^{-0.19}_{+0.44}$	-	$^{-0.34}$	$^{-0.39}$	$^{-0.26}_{+0.24}$	-	$^{+0.70}_{-0.26}$	$^{+0.20}$	$^{+0.59}$	$^{-0.41}$	$^{-0.32}$	$^{+0.72}$	-	$^{+0.34}$	$^{+0.34}$
Effective detector NP set 2 (JES) [%]	$^{-0.27}$	-	$^{-0.11}$	-	-	-	-	-	$^{-0.26}$	$^{+0.14}$	-	-	$^{-0.29}$	-	$^{+0.54}_{+0.22}$	-	-	$^{-0.22}$
Effective detector NP set 3 (JES) [%]	-	-	-	-	-	-	-	-	-	-	-	-	-	-	-	-	-	-
Effective detector NP set 4 (JES) [%]	-	-	-	-	-	-	-	-	-	-	-	-	-	-	-	-	-	-
Effective detector NP set 5 (JES) [%]	-	-	-	-	-	-	-	-	-	-	-	-	-	-	-	-	-	-
Effective detector NP set 6 resTerm (JES) [%]	-	-	-	-	-	-	-	-	-	-	-	-	-	-	-	-	-	-
η intercalibration model (JES) [%]	$^{-0.91}_{+0.64}$	$^{-0.62}_{+0.66}$	$^{-0.61}_{+0.79}$	$^{-0.90}_{+0.91}$	$^{-0.69}_{+0.45}$	$^{-0.49}_{+0.43}$	$^{-0.21}_{+0.10}$	$^{-0.40}_{+0.17}$	$^{+0.28}_{-0.23}$	$^{+0.30}_{-0.31}$	$^{+0.39}_{-0.15}$	$^{+0.56}_{-1.07}$	$^{+0.66}_{-0.67}$	$^{+1.33}_{-0.46}$	$^{+0.68}_{-1.15}$	$^{+1.54}_{-1.50}$	$^{+1.90}_{-1.47}$	$^{+2.04}_{-1.62}$
η intercalibration total stat (JES) [%]	-0.37	-	$^{-0.14}_{+0.36}$	-	-	-	-	$^{-0.25}$	-	$^{+0.23}$	-	$^{-0.28}$	$^{+0.12}_{-0.18}$	$^{+0.48}_{-0.12}$	-	$^{+0.22}$	$^{+0.37}_{-0.27}$	$^{+0.37}_{-0.24}$
Flavour composition (JES) [%]	$^{-0.41}$	$^{+0.21}$	$^{+0.33}$	-	$^{-0.71}$	$^{+0.17}_{-0.16}$	-	-	$^{+0.65}$	$^{+0.24}_{-0.34}$	$^{+0.28}$	$^{-0.20}$	$^{+0.24}$	$^{+0.22}_{-0.22}$	$^{-0.22}$	$^{+0.19}_{-0.28}$	$^{+0.20}_{-0.20}$	$^{+0.30}$
Flavour response (JES) [%]	$^{-0.51}$	-	$^{+0.58}_{+0.25}$	$^{+0.28}$	-	$^{-0.20}$	$^{+0.18}_{-0.24}$	$^{+0.19}_{-0.17}$	$^{+0.43}$	$^{-0.27}$	$^{+0.29}$	$^{-0.41}$	$^{-0.40}$	$^{+0.93}$	$^{+0.15}_{-0.29}$	-	$^{-0.22}$	$^{-0.26}$
Pile-up offset μ (JES) [%]	$^{-0.23}$	-	$^{-0.13}$	-	-	-	$^{-0.24}$	$^{-0.17}$	$^{+0.43}$	$^{-0.27}$	-	-	-	-	$^{-0.29}$	-	$^{+0.70}_{+0.24}$	$^{+0.36}_{+0.16}$
Pile-up offset N_{PV} (JES) [%]	-	-	-	-	-	-	-	$^{-0.12}$	-	-	-	-	-	$^{+0.21}$	-	-	-	$^{-0.21}_{+0.15}$
Pile-up offset p_{T} (JES) [%]	-	-	-	-	-	-	-	-	-	-	-	-	-	-	-	-	-	$^{-0.14}$
Pile-up offset ρ topology (JES) [%]	$^{-0.35}$	$^{-0.11}_{+0.13}$	$^{+0.24}$	-	-	-	-	-	$^{+0.42}_{-0.18}$	-	$^{+0.22}$	$^{-0.33}$	$^{+0.92}_{-0.34}$	$^{-0.28}$	$^{+0.25}$	$^{+0.32}$	-	-
Punch-through (JES) [%]	-	-	-	-	-	-	-	-	-	-	-	-	-	-	-	-	-	-
Single particle high-p_{T} (JES) [%]	-	-	-	-	-	-	-	-	-	-	-	-	-	-	-	-	-	-
Jet energy resolution [%]	∓ 0.57	∓ 0.27	-	± 1.48	∓ 1.34	∓ 0.32	± 0.17	∓ 0.64	± 1.25	± 0.53	∓ 0.58	± 0.18	-	± 0.46	± 0.54	∓ 0.15	∓ 0.18	± 0.38
Jet vertex fraction [%]	-	-	-	-	-	-	± 0.11	-	-	-	$^{+0.10}_{-0.11}$	-	-	-	-	-	∓ 0.11	∓ 0.43
b-Quark tagging efficiency (eigenvector 0) [%]	-	-	-	-	-	-	-	-	-	-	-	-	-	-	-	-	-	-
b-Quark tagging efficiency (eigenvector 1) [%]	-	-	-	-	-	-	-	-	-	-	-	-	-	-	-	-	-	-
b-Quark tagging efficiency (eigenvector 2) [%]	-	-	-	-	-	-	-	-	-	-	-	-	-	-	-	-	-	-
b-Quark tagging efficiency (eigenvector 3) [%]	-	-	-	-	-	-	-	-	-	-	-	-	-	-	-	-	-	-
b-Quark tagging efficiency (eigenvector 4) [%]	-	-	-	-	-	-	-	-	-	-	-	-	-	-	-	-	-	-
c-Quark tagging efficiency (eigenvector 0) [%]	∓ 0.13	-	-	-	-	-	-	-	-	-	-	-	-	$^{+0.17}_{-0.16}$	± 0.13	-	± 0.21	± 0.33
c-Quark tagging efficiency (eigenvector 1) [%]	-	-	-	-	-	-	-	-	-	-	-	-	-	-	-	-	-	-
c-Quark tagging efficiency (eigenvector 2) [%]	-	-	-	-	-	-	-	-	-	-	-	-	-	-	-	-	-	-
c-Quark tagging efficiency (eigenvector 3) [%]	-	-	-	-	-	-	-	-	-	-	-	-	-	-	-	-	-	-
Light-jet tagging efficiency (eigenvector 0) [%]	$^{+0.34}_{-0.20}$	$^{-0.21}_{+0.29}$	$^{+0.29}_{-0.24}$	$^{+0.12}_{-0.11}$	$^{-0.10}_{+0.15}$	$^{+0.24}_{-0.29}$	-	-	$^{+0.24}_{-0.32}$	-	$^{-0.17}_{+0.22}$	$^{+0.18}$	$^{+0.35}_{-0.25}$	-	$^{-0.16}$	-	$^{-0.64}_{+0.81}$	$^{+0.57}_{+0.48}$
Light-jet tagging efficiency (eigenvector 1) [%]	-	-	-	-	-	-	-	-	-	-	-	-	-	-	-	∓ 0.12	∓ 0.15	∓ 0.23
Light-jet tagging efficiency (eigenvector 2) [%]	-	-	-	-	-	-	-	-	-	-	-	-	-	-	-	-	-	-
Light-jet tagging efficiency (eigenvector 3) [%]	-	-	-	-	-	-	-	-	-	-	-	-	-	-	-	-	-	-
Light-jet tagging efficiency (eigenvector 4) [%]	-	-	-	-	-	-	-	-	-	-	-	-	-	-	-	-	-	-
Light-jet tagging efficiency (eigenvector 5) [%]	-	-	-	-	-	-	-	-	-	-	-	-	-	-	-	-	-	-
Light-jet tagging efficiency (eigenvector 6) [%]	-	-	-	-	-	-	-	-	-	-	-	-	-	-	-	-	-	-
Light-jet tagging efficiency (eigenvector 7) [%]	-	-	-	-	-	-	-	-	-	-	-	-	-	-	-	-	-	-
Light-jet tagging efficiency (eigenvector 8) [%]	-	-	-	-	-	-	-	-	-	-	-	-	-	-	-	-	-	-
Light-jet tagging efficiency (eigenvector 9) [%]	-	-	-	-	-	-	-	-	-	-	-	-	-	-	-	-	-	-
Light-jet tagging efficiency (eigenvector 10) [%]	-	-	-	-	-	-	-	-	-	-	-	-	-	-	-	-	-	-
Light-jet tagging efficiency (eigenvector 11) [%]	-	-	-	-	-	-	-	-	-	-	-	-	-	-	-	-	-	-
b-Quark tagging extrapolation [%]	-	-	-	-	-	-	-	-	-	-	-	-	-	-	-	-	-	-
b-Quark tagging extrapolation from c-Quark [%]	-	-	-	-	-	-	-	-	-	-	-	-	-	-	-	-	-	-
Electron energy resolution [%]	-	-	-	-	-	-	-	-	-	-	-	-	-	-	-	-	-	-
Electron energy scale [%]	-	-	-	-	-	-	-	-	-	-	-	-	-	-	-	-	-	-
Electron trigger efficiency [%]	-	-	-	-	-	-	-	-	-	-	-	-	-	-	-	-	-	-
Electron reconstruction efficiency [%]	-	-	-	-	-	-	-	-	-	-	-	-	-	-	-	-	-	-
Electron identification efficiency [%]	-	-	-	-	-	-	-	-	-	-	-	-	-	-	-	-	-	-
Electron isolation efficiency [%]	-	-	-	-	-	-	-	-	-	-	-	-	-	-	-	-	-	-
Muon energy scale [%]	-	-	-	-	-	-	-	-	-	-	-	-	-	-	-	-	-	-
Muon (MS) momentum resolution [%]	-	-	-	-	-	-	-	-	-	-	-	-	-	-	-	-	-	-
Muon (ID) momentum resolution [%]	-	-	-	-	-	-	-	-	-	-	-	-	-	-	-	-	-	-
Muon trigger efficiency stat [%]	-	-	-	-	-	-	-	-	-	-	-	-	-	-	-	-	-	-
Muon trigger efficiency syst [%]	-	-	-	-	-	-	-	-	-	-	-	-	-	-	-	-	-	-
Muon identification stat [%]	-	-	-	-	-	-	-	-	-	-	-	-	-	-	-	-	-	-
Muon identification syst [%]	-	-	-	-	-	-	-	-	-	-	-	-	-	-	-	-	-	-
Muon isolation efficiency stat [%]	-	-	-	-	-	-	-	-	-	-	-	-	-	-	-	-	-	-
Muon isolation efficiency syst [%]	-	-	-	-	-	-	-	-	-	-	-	-	-	-	-	-	-	-
Muon TTVA efficiency stat [%]	-	-	-	-	-	-	-	-	-	-	-	-	-	-	-	-	-	-
Muon TTVA efficiency syst [%]	-	-	-	-	-	-	-	-	-	-	-	-	-	-	-	-	-	-
$E_{\mathrm{T}}^{\mathrm{miss}}$ Soft jet resolution para [%]	-	-	-	-	-	-	-	-	-	-	-	-	-	-	-	-	-	-
$E_{\mathrm{T}}^{\mathrm{miss}}$ Soft jet resolution perp [%]	-	-	-	-	-	-	-	-	-	-	-	-	-	-	-	-	-	-
$E_{\mathrm{T}}^{\mathrm{miss}}$ Soft jet scale [%]	-	-	-	-	-	-	-	-	-	-	-	-	-	-	-	-	-	-
Luminosity [%]	-	-	-	-	-	-	-	-	-	-	-	-	-	-	-	-	-	-
Single top cross-section [%]	-	-	-	-	-	-	-	-	-	-	-	-	-	-	-	-	-	-
Z+jets cross-section [%]	-	-	-	-	-	-	-	-	-	± 0.23	-	-	∓ 0.11	∓ 0.22	± 0.15	∓ 0.23	-	∓ 0.18
Diboson cross-section [%]	-	-	-	-	-	-	-	-	-	-	-	-	-	-	-	-	-	-
$t\bar{t}V$ cross-section [%]	-	-	-	-	-	-	-	-	-	-	-	-	-	-	-	-	-	-
Monte Carlo sample statistics [%]	± 0.44	± 0.51	± 0.49	± 0.51	± 0.53	± 0.48	± 0.53	± 0.58	± 0.52	± 0.63	± 0.63	± 0.66	± 0.65	± 0.67	± 0.75	± 0.53	± 0.79	± 0.82
ISR/FSR + scale [%]	$^{-1.39}$	$^{+0.29}_{-0.44}$	$^{+0.98}$	$^{+0.29}_{-0.10}$	$^{-0.55}$	$^{+0.81}_{+0.18}$	$^{-0.67}_{+0.18}$	$^{-0.39}$	$^{+1.35}$	$^{-0.74}$	$^{-0.98}$	$^{+0.31}_{-0.69}$	$^{+0.59}$	$^{-0.66}$	$^{+0.92}$	$^{+0.47}$	$^{-0.70}$	$^{+1.18}$
Alternate hard-scattering model [%]	-	∓ 1.06	± 0.54	∓ 0.86	± 2.69	± 0.44	∓ 1.50	∓ 0.90	± 0.37	∓ 0.14	± 1.79	-	∓ 2.24	∓ 0.37	± 0.85	∓ 0.67	∓ 0.53	± 3.21
Alternate parton-shower model [%]	∓ 0.13	-	± 0.12	-	∓ 1.03	± 0.21	-	± 0.61	± 0.16	± 0.11	± 0.24	∓ 0.54	± 0.43	± 0.13	± 0.73	∓ 0.29	∓ 1.10	± 1.07
Inter PDF [%]	-	-	-	-	-	-	-	-	-	-	-	-	-	-	-	-	-	± 0.13
Intra PDF [%]	-	-	-	-	-	± 0.11	-	-	-	-	-	-	-	-	-	-	± 0.10	± 0.18
Real lepton efficiency stat [%]	-	-	-	-	-	-	-	-	-	-	-	-	-	-	-	-	-	-
Fake lepton efficiency MC scale [%]	-	$^{+0.18}_{-0.19}$	-	± 0.10	$^{+0.13}_{-0.19}$	-	-	-	-	-	$^{-0.17}$	-	$^{+0.12}_{-0.12}$	$^{-0.29}_{+0.34}$	-	$^{-0.13}$	$^{+0.17}_{-0.17}$	$^{+0.22}_{+0.30}$
Fake lepton efficiency alternate CR [%]	-	-	-	-	-	-	-	-	-	-	-	-	-	-	-	-	∓ 0.33	-
Fake overall normalisation [%]	± 0.29	± 0.34	± 0.41	-	± 0.26	± 0.27	± 0.12	± 0.26	-	± 0.20	∓ 0.48	∓ 0.20	∓ 0.20	∓ 0.99	∓ 0.63	∓ 0.24	∓ 1.22	∓ 1.13
W+jets CA_{fitted} stat error [%]	-	-	-	-	-	-	-	-	-	-	-	-	-	-	-	-	-	-
W+jets Fc stat error [%]	-	-	-	-	-	-	-	-	-	-	-	-	-	-	-	-	-	-
W+jets Fcc stat error [%]	-	-	$^{-0.18}$	-	-	-	-	-	-	-	$^{+0.18}$	-	-	$^{+0.15}$	-	-	$^{+0.14}$	-
W+jets Flight stat error [%]	-	-	-	-	-	-	-	-	-	-	-	-	-	-	-	-	-	-

Table C.11: Table of systematic uncertainties for the relative differential cross-section at particle level for the absolute value of the top quark rapidity in the resolved regime.

Bins [GeV]	0–35	35–75	75–125	125–170	170–225	225–800
$1/\sigma \cdot d\sigma / d p_T^{t\bar{t}}$	$1.00 \cdot 10^{-2}$	$7.89 \cdot 10^{-3}$	$3.34 \cdot 10^{-3}$	$1.63 \cdot 10^{-3}$	$8.14 \cdot 10^{-4}$	$8.37 \cdot 10^{-5}$
Total uncertainty [%]	$^{+10.1}_{-10.4}$	$^{+3.94}_{-4.03}$	$^{+11.0}_{-10.3}$	$^{+7.73}_{-6.90}$	$^{+5.67}_{-5.94}$	$^{+3.78}_{-3.82}$
Statistical uncertainty [%]	±0.4	±0.4	±0.7	±1.1	±1.6	±1.4
Systematic uncertainty [%]	$^{+10.1}_{-10.4}$	$^{+3.91}_{-4.00}$	$^{+10.9}_{-10.3}$	$^{+7.62}_{-6.79}$	$^{+5.40}_{-5.68}$	$^{+3.43}_{-3.48}$
b-Tagged jet energy scale (JES) [%]	-	-	-	-	-	$^{+0.19}_{-0.19}$
Effective detector NP set 1 (JES) [%]	$^{-4.61}_{+4.82}$	$^{+1.47}_{-1.74}$	$^{+5.17}_{-5.66}$	$^{+3.23}_{-3.64}$	$^{+1.72}_{-1.91}$	$^{+0.26}_{-0.16}$
Effective detector NP set 2 (JES) [%]	$^{-0.71}_{-0.16}$	$^{+0.77}_{+0.37}$	$^{+0.80}_{±0.21}$	$^{+0.22}_{-0.40}$	$^{-0.64}_{-0.54}$	$^{+1.77}_{-0.99}$
Effective detector NP set 3 (JES) [%]	$^{+0.17}_{-}$	$^{-0.17}_{+0.20}$	-	$^{+0.36}_{+0.27}$	$^{+0.39}_{+0.29}$	$^{+1.06}_{-}$
Effective detector NP set 4 (JES) [%]	-	-	$^{-0.11}_{+0.10}$	$^{-0.29}_{-}$	$^{-0.33}_{+0.10}$	$^{-}_{+0.28}$
Effective detector NP set 5 (JES) [%]	-	-	-	-	$^{-0.22}_{+0.12}$	$^{-0.21}_{+0.20}$
Effective detector NP set 6 restTerm (JES) [%]	-	-	-	-	$^{-0.13}_{+1.18}$	$^{-0.19}_{+0.72}$
η intercalibration model (JES) [%]	$^{-2.82}_{+2.72}$	$^{+1.02}_{-1.04}$	$^{+2.82}_{-2.56}$	$^{+1.65}_{-1.42}$	$^{-1.46}_{+0.63}$	$^{-0.86}_{+0.34}$
η intercalibration total stat (JES) [%]	$^{-0.90}_{+0.99}$	$^{+0.32}_{-0.35}$	$^{+0.80}_{-0.94}$	$^{+0.58}_{-0.44}$	$^{+0.80}_{+3.22}$	$^{+0.34}_{-0.33}$
Flavour composition (JES) [%]	$^{+5.06}_{+1.57}$	$^{+1.04}_{-1.39}$	$^{+5.66}_{-7.25}$	$^{+4.58}_{-4.27}$	$^{-3.14}_{-3.14}$	$^{+1.37}_{-0.78}$
Flavour response (JES) [%]	$^{+1.60}_{-1.60}$	$^{+0.44}_{-0.16}$	$^{+1.37}_{-0.37}$	$^{+1.37}_{-0.17}$	$^{+1.00}_{-0.28}$	$^{+0.70}_{-}$
Pile-up offset μ (JES) [%]	$^{-0.36}_{+0.18}$	$^{+0.13}_{-}$	$^{+0.40}_{-0.19}$	$^{+0.14}_{-}$	$^{+0.17}_{-}$	$^{-}_{-}$
Pile-up offset N_{PV} (JES) [%]	-	-	$^{+0.14}_{-}$	-	-	-
Pile-up offset p_T (JES) [%]	-	$^{-0.13}_{+0.12}$	-	$^{+0.17}_{-0.21}$	$^{+0.13}_{-0.29}$	$^{+0.18}_{-0.10}$
Pile-up offset ρ topology (JES) [%]	$^{-1.63}_{+1.50}$	$^{+0.69}_{-0.53}$	$^{+1.60}_{-1.47}$	$^{+1.17}_{-0.88}$	$^{+0.53}_{-1.20}$	$^{-}_{-0.23}$
Punch-through (JES) [%]	-	-	-	-	-	-
Single particle high-p_T (JES) [%]	-	-	-	-	-	-
Jet energy resolution [%]	∓1.56	±0.27	±1.70	±1.72	±1.66	-
Jet vertex fraction [%]	$^{-0.20}_{+0.19}$	$^{+0.15}_{-0.16}$	$^{+0.34}_{-0.32}$	$^{+0.15}_{+0.17}$	$^{-0.10}_{+0.11}$	$^{-0.83}_{+0.90}$
b-Quark tagging efficiency (eigenvector 0) [%]	$^{+0.25}_{+0.24}$	-	$^{+0.22}_{-0.21}$	$^{+0.33}_{-0.32}$	$^{+0.38}_{-0.37}$	$^{+0.45}_{-0.44}$
b-Quark tagging efficiency (eigenvector 1) [%]	-	-	-	-	-	$^{-0.74}_{+0.71}$
b-Quark tagging efficiency (eigenvector 2) [%]	±0.15	-	∓0.12	$^{-0.17}_{+0.18}$	∓0.16	∓0.59
b-Quark tagging efficiency (eigenvector 3) [%]	-	-	-	-	-	-
b-Quark tagging efficiency (eigenvector 4) [%]	-	-	-	-	-	-
c-Quark tagging efficiency (eigenvector 0) [%]	-	-	-	-	-	$^{+0.14}_{-0.15}$
c-Quark tagging efficiency (eigenvector 1) [%]	-	-	-	-	-	-
c-Quark tagging efficiency (eigenvector 2) [%]	-	-	-	-	-	-
c-Quark tagging efficiency (eigenvector 3) [%]	-	-	-	-	-	-
Light-jet tagging efficiency (eigenvector 0) [%]	$^{+0.19}_{-0.17}$	-	$^{-0.26}_{+0.24}$	-	-	$^{-0.12}_{-}$
Light-jet tagging efficiency (eigenvector 1) [%]	-	-	-	-	-	-
Light-jet tagging efficiency (eigenvector 2) [%]	-	-	-	-	-	-
Light-jet tagging efficiency (eigenvector 3) [%]	-	-	-	-	-	-
Light-jet tagging efficiency (eigenvector 4) [%]	-	-	-	-	-	-
Light-jet tagging efficiency (eigenvector 5) [%]	-	-	-	-	-	-
Light-jet tagging efficiency (eigenvector 6) [%]	-	-	-	-	-	-
Light-jet tagging efficiency (eigenvector 7) [%]	-	-	-	-	-	-
Light-jet tagging efficiency (eigenvector 8) [%]	-	-	-	-	-	-
Light-jet tagging efficiency (eigenvector 9) [%]	-	-	-	-	-	-
Light-jet tagging efficiency (eigenvector 10) [%]	-	-	-	-	-	-
Light-jet tagging efficiency (eigenvector 11) [%]	-	-	-	-	-	-
b-Quark tagging extrapolation [%]	-	-	-	$^{+0.11}_{-0.12}$	-	$^{+0.61}_{-0.63}$
b-Quark tagging extrapolation from c-Quark [%]	-	-	-	-	-	-
Electron energy resolution [%]	-	-	-	-	-	-
Electron energy scale [%]	-	-	-	-	-	-
Electron trigger efficiency [%]	-	-	-	-	-	-
Electron reconstruction efficiency [%]	-	-	-	-	-	-
Electron identification efficiency [%]	-	-	-	-	-	±0.16
Electron isolation efficiency [%]	-	-	-	-	-	±0.14
Muon energy scale [%]	-	-	-	-	-	-
Muon (MS) momentum resolution [%]	-	-	-	-	-	-
Muon (ID) momentum resolution [%]	-	-	-	-	-	-
Muon trigger efficiency stat [%]	-	-	-	-	-	-
Muon trigger efficiency syst [%]	-	-	-	-	-	-
Muon identification stat [%]	-	-	-	-	-	-
Muon identification syst [%]	-	-	-	-	-	-
Muon isolation efficiency stat [%]	-	-	-	-	-	-
Muon isolation efficiency syst [%]	-	-	-	-	-	-
Muon TTVA efficiency stat [%]	-	-	-	-	-	-
Muon TTVA efficiency syst [%]	-	-	-	-	-	-
E_T^{miss} Soft jet resolution para [%]	∓0.20	±0.14	±0.20	∓0.18	-	-
E_T^{miss} Soft jet resolution perp [%]	∓0.28	±0.23	±0.20	-	-	-
E_T^{miss} Soft jet scale [%]	-	-	-	-	-	-
Luminosity [%]	-	-	-	-	-	-
Single top cross-section [%]	-	-	-	-	-	-
Z+jets cross-section [%]	-	-	-	-	∓0.10	-
Diboson cross-section [%]	-	-	-	-	±0.10	±0.33
$t\bar{t}V$ cross-section [%]	-	-	-	-	-	-
Monte Carlo sample statistics [%]	±0.18	±0.17	±0.29	±0.44	±0.57	±0.48
ISR/FSR + scale [%]	$^{+0.75}_{-2.11}$	$^{-0.70}_{+1.13}$	$^{+1.23}_{-}$	$^{-0.43}_{+1.35}$	$^{-0.94}_{+1.31}$	$^{-0.22}_{+0.56}$
Alternate hard-scattering model [%]	∓1.14	-	±0.30	±3.46	±1.65	±0.75
Alternate parton-shower model [%]	∓6.03	±2.66	±6.37	±1.37	±2.06	±0.69
Inter PDF [%]	-	-	-	-	-	-
Intra PDF [%]	-	-	-	-	-	-
Real lepton efficiency stat [%]	-	-	-	-	-	$^{-0.19}_{+0.12}$
Fake lepton efficiency MC scale [%]	$^{-0.38}_{+0.50}$	$^{+0.31}_{-0.40}$	$^{+0.34}_{-0.48}$	$^{-0.13}_{+0.16}$	$^{-0.13}_{+0.17}$	$^{-0.16}_{+0.26}$
Fake lepton efficiency alternate CR [%]	-	±0.12	-	-	∓0.19	∓0.15
Fake overall normalisation [%]	∓0.75	±0.66	±0.61	∓0.39	∓0.44	-
W+jets CA_{direct} stat error [%]	-	-	-	-	-	-
W+jets Fc stat error [%]	-	-	-	-	-	-
W+jets Fcc stat error [%]	-	-	-	$^{-0.16}_{-}$	$^{-0.23}_{+0.11}$	$^{-0.28}_{+0.13}$
W+jets Flight stat error [%]	-	-	-	-	-	-

Table C.12: Table of systematic uncertainties for the relative differential cross-section at particle level for the $t\bar{t}$ system transverse momentum in the resolved regime.

Bins $\lvert$ Unit $\lvert y^{t\bar{t}} \rvert$	0–0.10	0.10–0.20	0.20–0.30	0.30–0.40	0.40–0.50	0.50–0.60	0.60–0.70	0.70–0.80	0.80–0.90	0.90–1	1–1.10	1.10–1.20	1.20–1.30	1.30–1.40	1.40–1.50	1.50–1.60	1.60–1.80	1.80–2.50
$1/\sigma \cdot d\sigma \cdot d\lvert y^{t\bar{t}} \rvert$	$1.02 \cdot 10^{0}$	$1.03 \cdot 10^{0}$	$9.97 \cdot 10^{-1}$	$9.58 \cdot 10^{-1}$	$9.34 \cdot 10^{-1}$	$8.41 \cdot 10^{-1}$	$7.53 \cdot 10^{-1}$	$6.91 \cdot 10^{-1}$	$5.99 \cdot 10^{-1}$	$5.05 \cdot 10^{-1}$	$4.17 \cdot 10^{-1}$	$3.46 \cdot 10^{-1}$	$2.71 \cdot 10^{-1}$	$2.19 \cdot 10^{-1}$	$1.50 \cdot 10^{-1}$	$1.09 \cdot 10^{-1}$	$6.05 \cdot 10^{-2}$	$6.17 \cdot 10^{-3}$
Total uncertainty [%]	$^{+1.54}_{-1.54}$	$^{+1.50}_{-1.50}$	$^{+1.76}_{-1.76}$	$^{+1.66}_{-1.66}$	$^{+1.72}_{-1.72}$	$^{+2.10}_{-2.10}$	$^{+1.92}_{-1.92}$	$^{+2.62}_{-2.62}$	$^{+1.91}_{-1.91}$	$^{+1.99}_{-1.99}$	$^{+1.95}_{-1.95}$	$^{+2.59}_{-2.59}$	$^{+3.01}_{-3.01}$	$^{+4.09}_{-4.09}$	$^{+5.12}_{-5.12}$	$^{+4.92}_{-4.92}$	$^{+5.43}_{-5.43}$	$^{+9.34}_{-9.34}$
Statistical uncertainty [%]	± 1.0	± 0.9	± 0.9	± 0.9	± 1.0	± 1.0	± 1.1	± 1.1	± 1.2	± 1.3	± 1.5	± 1.7	± 1.9	± 2.1	± 2.6	± 3.2	± 3.3	± 5.7
Systematic uncertainty [%]	$^{+1.10}_{-1.53}$	$^{+1.22}_{-1.31}$	$^{+1.41}_{-2.00}$	$^{+1.30}_{-1.30}$	$^{+1.30}_{-0.99}$	$^{+1.76}_{-1.66}$	$^{+1.50}_{-1.19}$	$^{+2.29}_{-2.22}$	$^{+1.19}_{-1.39}$	$^{+1.30}_{-1.43}$	$^{+1.08}_{-1.28}$	$^{+1.82}_{-1.98}$	$^{+2.16}_{-2.87}$	$^{+3.27}_{-2.73}$	$^{+4.60}_{-4.26}$	$^{+3.32}_{-2.80}$	$^{+4.17}_{-5.43}$	$^{+7.13}_{-6.76}$
b-Tagged jet energy scale (JES) [%]	-	-	-	-	$^{+0.19}_{-}$	-	-	-	-	-	-	$^{-0.26}_{+0.32}$	$^{+0.17}_{-}$	$^{+0.25}_{-}$	-	$^{-0.19}_{+0.93}$	$^{-0.29}_{-}$	-
Effective detector NP set 1 (JES) [%]	$^{-0.33}_{-}$	-	-	$^{+0.27}_{-0.20}$	$^{-}_{-0.25}$	$^{-0.12}_{+0.38}$	$^{+0.69}_{+0.21}$	$^{-}_{-0.28}$	$^{+0.20}_{-0.68}$	-	$^{-0.29}_{+0.10}$	$^{+0.31}_{+0.34}$	$^{-}_{-0.50}$	$^{+0.36}_{-}$	$^{+0.61}_{-}$	$^{+0.93}_{-}$	$^{-}_{-0.53}$	$^{+0.73}_{-}$
Effective detector NP set 2 (JES) [%]	-	-	-	-	-	-	-	-	-	-	$^{-0.35}_{+0.10}$	-	-	-	$^{+0.28}_{-}$	-	-	$^{+0.37}_{-0.18}$
Effective detector NP set 3 (JES) [%]	-	-	$^{-0.14}_{-}$	-	-	-	-	-	-	-	$^{+0.10}_{-}$	-	-	$^{-0.20}_{+0.21}$	-	$^{+0.76}_{+0.89}$	$^{-0.79}_{-}$	$^{-0.18}_{+0.18}$
Effective detector NP set 4 (JES) [%]	-	-	-	-	-	-	-	-	-	-	-	-	-	-	-	$^{+0.28}_{-}$	$^{-0.43}_{-}$	$^{+0.26}_{-0.27}$
Effective detector NP set 5 (JES) [%]	-	-	-	-	-	-	-	-	-	-	-	-	$^{-0.18}_{-}$	-	-	$^{+0.24}_{-}$	$^{-0.23}_{-}$	$^{-0.31}_{-}$
Effective detector NP set 6 restTerm (JES) [%]	-	-	-	-	-	-	-	-	-	-	-	-	-	-	-	$^{+0.29}_{-}$	-	-
η intercalibration model (JES) [%]	$^{-0.89}_{+0.28}$	$^{-0.24}_{+0.55}$	$^{-0.23}_{+0.35}$	$^{+0.38}_{-}$	$^{-0.27}_{-}$	$^{-0.36}_{+0.41}$	$^{+0.27}_{-}$	$^{-}_{-0.32}$	$^{+0.15}_{-0.59}$	$^{}_{\pm 0.30}$	$^{+0.59}_{-0.18}$	$^{+0.37}_{+0.23}$	$^{+0.45}_{-1.42}$	$^{+1.39}_{-1.04}$	$^{-0.16}_{+1.78}$	$^{+1.27}_{-1.35}$	$^{+1.62}_{-2.40}$	$^{+2.02}_{-1.50}$
η intercalibration total stat (JES) [%]	-	-	$^{+0.15}_{-}$	-	-	-	$^{+0.22}_{-}$	-	$^{-0.38}_{-}$	-	-	$^{-0.39}_{-}$	-	$^{-0.31}_{+0.42}$	$^{-0.89}_{+0.44}$	$^{+0.76}_{-}$	$^{-0.72}_{-}$	$^{-0.11}_{+0.97}$
Flavour composition (JES) [%]	$^{-0.38}_{+0.23}$	-	-	$^{-}_{-0.15}$	$^{}_{\pm 0.11}$	$^{-0.20}_{+0.20}$	$^{+0.31}_{-}$	$^{-0.25}_{-}$	$^{-0.44}_{-0.27}$	$^{-0.20}_{-}$	$^{+0.62}_{-}$	$^{-2.43}_{+0.36}$	$^{-1.01}_{-}$	$^{-0.75}_{-}$	$^{-}_{+0.41}$	$^{-}_{-}$	$^{-0.82}_{-}$	$^{-0.25}_{-}$
Flavour response (JES) [%]	-	-	$^{+0.12}_{-}$	$^{-}_{+0.13}$	-	$^{-}_{+0.10}$	-	-	-	$^{-}_{-0.17}$	-	-	-	$^{+0.19}_{-0.13}$	$^{-}_{+0.41}$	$^{+0.29}_{+0.61}$	$^{-1.12}_{-}$	$^{+0.61}_{-}$
Pile-up offset μ (JES) [%]	-	-	-	-	-	-	-	-	-	-	-	-	-	$^{+0.17}_{-}$	$^{+0.52}_{-0.30}$	-	$^{-0.39}_{-}$	-
Pile-up offset N_{PV} (JES) [%]	-	-	-	-	-	-	-	-	-	-	-	$^{+0.18}_{-0.12}$	-	-	$^{+0.69}_{-}$	-	$^{-0.37}_{-}$	$^{-0.23}_{+0.26}$
Pile-up offset p_T (JES) [%]	-	-	-	-	-	-	-	-	-	-	-	-	-	$^{+0.20}_{+0.21}$	$^{+0.14}_{+0.49}$	$^{+0.43}_{+0.56}$	$^{-0.24}_{-}$	$^{+0.33}_{+0.34}$
Pile-up offset ρ topology (JES) [%]	$^{-0.21}_{-}$	-	-	$^{+0.21}_{-0.14}$	$^{-}_{-0.23}$	$^{+0.25}_{-}$	-	-	$^{-}_{-0.32}$	-	-	$^{+0.21}_{-}$	-	-	$^{+0.49}_{-}$	-	$^{-0.56}_{-}$	-
Punch-through (JES) [%]	-	-	-	-	-	-	-	-	-	-	-	-	-	-	-	-	-	-
Single particle high-p_T (JES) [%]	-	-	-	-	-	-	-	-	-	-	-	-	-	-	-	-	-	-
Jet energy resolution [%]	∓ 0.20	± 0.15	∓ 0.38	± 0.80	-	-	± 0.83	∓ 0.22	-	∓ 0.18	-	± 0.11	∓ 1.36	∓ 0.93	∓ 0.54	± 0.11	∓ 0.53	∓ 1.67
Jet vertex fraction [%]	-	-	-	-	-	-	-	-	-	-	-	-	-	-	-	∓ 0.10	∓ 0.19	-0.35 $+0.37$
b-Quark tagging efficiency (eigenvector 0) [%]	-	-	-	-	-	-	-	-	-	-	-	-	-	± 0.12	$^{+0.15}_{-0.14}$	$^{+0.14}_{-0.13}$	$^{+0.20}_{-0.18}$	-
b-Quark tagging efficiency (eigenvector 1) [%]	-	-	-	-	-	-	-	-	-	-	-	-	-	-	-	-	-	∓ 0.15
b-Quark tagging efficiency (eigenvector 2) [%]	-	-	-	-	-	-	-	-	-	-	-	-	-	-	-	-	-	-
b-Quark tagging efficiency (eigenvector 3) [%]	-	-	-	-	-	-	-	-	-	-	-	-	-	-	-	-	-	-
b-Quark tagging efficiency (eigenvector 4) [%]	-	-	-	-	-	-	-	-	-	-	-	-	-	-	-	-	-	-
c-Quark tagging efficiency (eigenvector 0) [%]	-	-	-	-	-	-	-	-	-	-	-	-	-	-	-	± 0.15	$^{+0.18}_{-0.17}$	± 0.24
c-Quark tagging efficiency (eigenvector 1) [%]	-	-	-	-	-	-	-	-	-	-	-	-	-	-	-	-	-	-
c-Quark tagging efficiency (eigenvector 2) [%]	-	-	-	-	-	-	-	-	-	-	-	-	-	-	-	-	-	-
c-Quark tagging efficiency (eigenvector 3) [%]	-	-	-	-	-	-	-	-	-	-	-	-	-	-	-	-	-	-
Light-jet tagging efficiency (eigenvector 0) [%]	-	$^{+0.13}_{-0.14}$	$^{+0.25}_{-0.35}$	$^{+0.22}_{-0.27}$	-	-	$^{-0.13}_{+0.21}$	-	-	-	-	$^{-0.30}_{+0.36}$	$^{-0.62}_{+0.82}$	∓ 0.36	$^{-0.78}_{+0.84}$	$^{-0.62}_{+0.72}$	$^{+0.29}_{+0.18}$	$^{+0.35}_{-0.45}$
Light-jet tagging efficiency (eigenvector 1) [%]	-	-	-	-	-	-	-	-	-	-	-	-	∓ 0.12	∓ 0.13	∓ 0.14	∓ 0.19	∓ 0.20	∓ 0.19
Light-jet tagging efficiency (eigenvector 2) [%]	-	-	-	-	-	-	-	-	-	-	-	-	-	-	-	-	-	-
Light-jet tagging efficiency (eigenvector 3) [%]	-	-	-	-	-	-	-	-	-	-	-	-	-	-	-	-	-	-
Light-jet tagging efficiency (eigenvector 4) [%]	-	-	-	-	-	-	-	-	-	-	-	-	-	-	-	-	-	-
Light-jet tagging efficiency (eigenvector 5) [%]	-	-	-	-	-	-	-	-	-	-	-	-	-	-	-	-	-	-
Light-jet tagging efficiency (eigenvector 6) [%]	-	-	-	-	-	-	-	-	-	-	-	-	-	-	-	-	-	-
Light-jet tagging efficiency (eigenvector 7) [%]	-	-	-	-	-	-	-	-	-	-	-	-	-	-	-	-	-	-
Light-jet tagging efficiency (eigenvector 8) [%]	-	-	-	-	-	-	-	-	-	-	-	-	-	-	-	-	-	-
Light-jet tagging efficiency (eigenvector 9) [%]	-	-	-	-	-	-	-	-	-	-	-	-	-	-	-	-	-	-
Light-jet tagging efficiency (eigenvector 10) [%]	-	-	-	-	-	-	-	-	-	-	-	-	-	-	-	-	-	-
Light-jet tagging efficiency (eigenvector 11) [%]	-	-	-	-	-	-	-	-	-	-	-	-	-	-	-	-	-	-
b-Quark tagging extrapolation [%]	-	-	-	-	-	-	-	-	-	-	-	-	-	-	-	-	-	-
b-Quark tagging extrapolation from c-Quark [%]	-	-	-	-	-	-	-	-	-	-	-	-	-	-	-	-	-	-
Electron energy resolution [%]	-	-	-	-	-	-	-	-	-	-	-	$^{+0.23}_{-}$	-	$^{+0.21}_{-}$	$^{+0.21}_{-}$	$^{+0.26}_{-0.25}$	$^{-0.41}_{-}$	$^{+0.87}_{+1.00}$
Electron energy scale [%]	-	-	-	-	-	-	-	-	-	-	-	-	$^{-0.25}_{+0.30}$	$^{+0.28}_{-}$	$^{+0.20}_{-}$	$^{-0.25}_{+0.25}$	$^{-0.21}_{-}$	$^{-0.11}_{+0.11}$
Electron trigger efficiency [%]	-	-	-	-	-	-	-	-	-	-	-	-	-	± 0.12	± 0.18	± 0.23	± 0.28	± 0.39
Electron reconstruction efficiency [%]	-	-	-	-	-	-	-	-	-	-	-	-	-	-	-	-	-	-
Electron identification efficiency [%]	-	-	-	-	-	-	-	-	-	-	-	-	-	-	-	± 0.11	± 0.14	± 0.27
Electron isolation efficiency [%]	-	-	-	-	-	-	-	-	-	-	-	-	-	-	-	-	-	-
Muon energy scale [%]	-	-	-	-	-	-	-	-	-	-	-	-	-	-	-	-	-	-
Muon (MS) momentum resolution [%]	-	-	-	-	-	-	-	-	-	-	-	-	-	-	-	-	-	-0.24
Muon (ID) momentum resolution [%]	-	-	-	-	-	-	-	-	± 0.15	-	-	-	-	-	± 0.26	-	-	± 0.29
Muon trigger efficiency stat [%]	-	-	-	-	-	-	-	-	-	-	-	-	-0.40	-	-	-	-	-
Muon trigger efficiency syst [%]	-	-	-	-	-	-	-	-	-	-	-	-	-	-	-	-	-	-
Muon identification stat [%]	-	-	-	-	-	-	-	-	-	-	-	-	-	-	-	-	-	-
Muon identification syst [%]	-	-	-	-	-	-	-	-	-	-	-	-	-	-	-	-	-	-
Muon isolation efficiency stat [%]	-	-	-	-	-	-	-	-	-	-	-	-	-	-	-	-	-	-
Muon isolation efficiency syst [%]	-	-	-	-	-	-	-	-	-	-	-	-	-	-	-	-	-	-
Muon TTVA efficiency stat [%]	-	-	-	-	-	-	-	-	-	-	-	-	-	-	-	-	-	-
Muon TTVA efficiency syst [%]	-	-	-	-	-	-	-	-	-	-	-	-	-	-	-	-	-	-
E_T^{miss} Soft jet resolution para [%]	-	-	-	-	-	-	-	± 0.12	∓ 0.19	± 0.12	-	∓ 0.20	± 0.21	± 0.34	-	± 0.35	± 0.26	± 0.18
E_T^{miss} Soft jet resolution perp [%]	-	-	-	-	-	-	-	-	-	± 0.15	-	-	-	± 0.27	± 0.20	± 0.37	-	± 0.54
E_T^{miss} Soft jet scale [%]	-	-	-	-	-	-	-	-	-	-	-	-	-	$^{+0.11}_{-0.26}$	$^{+0.32}_{-}$	$^{+0.17}_{-0.11}$	$^{+0.24}_{-0.51}$	$^{+0.39}_{-}$
Luminosity [%]	-	-	-	-	-	-	-	-	-	-	-	-	-	-	-	-	-	-
Single top cross-section [%]	-	-	-	-	-	-	-	-	-	-	-	-	-	-	-	-	-	-
Z + jets cross-section [%]	-	-	-	-	± 0.10	-	-	-	-	-	-	-	± 1.12	∓ 0.15	-	-	∓ 0.15	∓ 0.70
Diboson cross-section [%]	-	-	-	-	-	-	-	-	-	-	-	-	-	-	-	-	-	± 0.13
$t\bar{t}V$ cross-section [%]	-	-	-	-	-	-	-	-	-	-	-	-	-	-	-	-	-	-
Monte Carlo sample statistics [%]	± 0.29	± 0.36	± 0.40	± 0.36	± 0.40	± 0.43	± 0.45	± 0.46	± 0.52	± 0.53	± 0.55	± 0.71	± 0.84	± 0.77	± 1.25	± 1.20	± 1.09	± 1.78
ISR/FSR + scale [%]	$^{-}_{-0.38}$	$^{+0.66}_{-0.88}$	$^{-}_{-1.35}$	$^{-}_{-}$	$^{+0.86}_{-}$	$^{+0.41}_{-0.10}$	$^{+0.39}_{-0.10}$	$^{+0.73}_{-0.22}$	$^{-}_{+0.30}$	$^{-0.58}_{+1.29}$	$^{-}_{-0.64}$	$^{+0.92}_{-}$	$^{-0.59}_{+0.31}$	$^{+1.65}_{-}$	$^{+0.46}_{-}$	$^{+1.03}_{-}$	$^{-1.68}_{-}$	$^{-0.66}_{+1.13}$
Alternate hard-scattering model [%]	∓ 0.44	± 0.29	± 0.78	∓ 0.55	± 0.65	± 1.46	∓ 0.67	∓ 2.11	-	∓ 1.03	-	± 0.95	∓ 1.77	± 0.13	± 3.79	-	∓ 3.19	± 5.68
Alternate parton-shower model [%]	∓ 0.87	± 0.56	∓ 0.88	-	± 0.36	± 0.50	± 0.21	-	± 0.16	∓ 0.40	∓ 0.46	± 0.15	± 0.56	± 0.78	∓ 0.18	± 0.90	∓ 0.44	± 0.91
Inter PDF [%]	-	-	-	-	-	-	-	-	-	-	-	-	∓ 0.12	± 0.27	-	-	± 0.12	∓ 0.51
Intra PDF [%]	-	-	-	-	-	-	-	-	-	-	-	-	± 0.23	-	-	± 0.14	± 0.36	± 0.49
Real lepton efficiency stat [%]	-	-	-	-	-	-	-	-	-	-	-	-	-	-	-	-	-	-
Fake lepton efficiency MC scale [%]	-	$^{+0.15}_{-0.16}$	-	-	-	-	-	-	-	-	-	$^{-0.11}_{+0.16}$	$^{-0.44}_{+0.32}$	$^{-0.35}_{+0.47}$	$^{-0.17}_{+0.13}$	$^{-0.66}_{+0.16}$	$^{-1.19}_{+0.55}$	$^{-0.70}_{+0.16}$
Fake lepton efficiency alternate CR [%]	-	-	-	± 0.13	-	-	-	-	∓ 0.15	-	-	-	∓ 1.21	∓ 0.13	∓ 0.31	∓ 0.32	-	± 0.21
Fake overall normalisation [%]	± 0.55	± 0.36	± 0.20	± 0.13	± 0.20	± 0.11	± 0.19	∓ 0.13	∓ 0.40	∓ 0.20	∓ 0.20	± 0.52	∓ 0.62	∓ 1.66	∓ 0.28	∓ 1.42	∓ 1.54	∓ 1.70
W+jets CA_{model} stat error [%]	-	-	-	-	-	-	-	-	-	-	-	-	-	-	-	-	-	-
W+jets Fc stat error [%]	-	-	$^{-}_{-0.14}$	-	-	-	-	-	-	-	-	-	-	-	$^{-}_{+0.40}$	$^{-}_{+0.16}$	$^{-}_{-0.17}$	-
W+jets Fcc stat error [%]	-	-	-	-	-	-	-	-	-	-	-	-	-	-	$^{+}_{-0.19}$	-	-	-
W+jets Flight stat error [%]	-	-	-	-	-	-	-	-	-	-	-	-	-	-	-	-	-	-

Table C.13: Table of systematic uncertainties for the relative differential cross-section at particle level for the absolute value of the $t\bar{t}$ system rapidity in the resolved regime.

Bins [GeV]	225–345	345–420	420–500	500–590	590–685	685–790	790–910	910–1040	1040–1175	1175–1320	1320–3000
$1/\sigma \cdot \mathrm{d}\sigma\ /\ \mathrm{d}m^{t\bar{t}}$	$4.83 \cdot 10^{-4}$	$2.82 \cdot 10^{-3}$	$2.83 \cdot 10^{-3}$	$2.07 \cdot 10^{-3}$	$1.26 \cdot 10^{-3}$	$7.62 \cdot 10^{-4}$	$4.23 \cdot 10^{-4}$	$2.28 \cdot 10^{-4}$	$1.17 \cdot 10^{-4}$	$6.44 \cdot 10^{-5}$	$7.16 \cdot 10^{-6}$
Total uncertainty [%]	$^{+13.2}_{-14.0}$	$^{+4.45}_{-4.73}$	$^{+3.02}_{-2.77}$	$^{+3.18}_{-2.98}$	$^{+3.01}_{-2.95}$	$^{+4.59}_{-3.95}$	$^{+5.35}_{-5.56}$	$^{+6.90}_{-7.15}$	$^{+8.25}_{-9.22}$	$^{+8.74}_{-9.07}$	$^{+16.9}_{-17.9}$
Statistical uncertainty [%]	± 1.6	± 0.6	± 0.6	± 0.7	± 0.9	± 1.1	± 1.5	± 1.9	± 2.7	± 3.9	± 3.4
Systematic uncertainty [%]	$^{+13.1}_{-13.9}$	$^{+4.39}_{-4.68}$	$^{+2.93}_{-2.67}$	$^{+3.08}_{-2.88}$	$^{+2.83}_{-2.77}$	$^{+4.41}_{-3.75}$	$^{+5.11}_{-5.32}$	$^{+6.57}_{-6.83}$	$^{+7.64}_{-8.68}$	$^{+7.70}_{-8.07}$	$^{+16.5}_{-17.5}$
b-Tagged jet energy scale (JES) [%]	$^{-3.38}_{+3.43}$	$^{-0.76}_{+0.62}$	$^{+0.36}_{-0.32}$	$^{+0.53}_{-0.54}$	$^{+0.57}_{-0.63}$	$^{+0.80}_{-0.48}$	$^{+0.30}_{-0.42}$	$^{+0.51}_{-0.41}$	$^{+0.29}_{-0.37}$	$^{+0.46}_{-0.29}$	$^{+0.35}_{-}$
Effective detector NP set 1 (JES) [%]	$^{-7.03}_{+6.00}$	$^{-0.59}_{+0.55}$	$^{+1.70}_{-1.41}$	$^{+1.61}_{-1.40}$	$^{+0.70}_{-0.48}$	$^{-0.14}_{+0.40}$	$^{-1.05}_{+1.20}$	$^{-1.71}_{+0.93}$	$^{-2.61}_{-}$	$^{-2.40}_{+1.90}$	$^{-4.98}_{+3.26}$
Effective detector NP set 2 (JES) [%]	$^{-2.72}_{+2.61}$	$^{-1.51}_{+1.44}$	$^{-0.39}_{+0.52}$	$^{+0.13}_{-0.24}$	$^{+1.03}_{-0.98}$	$^{+1.79}_{-1.35}$	$^{+1.23}_{-1.73}$	$^{+2.88}_{-2.83}$	$^{+2.83}_{-2.89}$	$^{+3.26}_{-3.09}$	$^{+4.52}_{-4.95}$
Effective detector NP set 3 (JES) [%]	$^{+2.21}_{-2.16}$	± 0.94	$^{+0.18}_{-0.14}$	$^{-0.30}_{+0.18}$	$^{-0.71}_{+0.69}$	$^{-0.85}_{+1.15}$	$^{-1.03}_{+0.71}$	$^{-1.39}_{+1.57}$	$^{-1.58}_{+1.66}$	$^{-1.69}_{+1.62}$	$^{-2.25}_{+2.16}$
Effective detector NP set 4 (JES) [%]	$^{-1.77}_{+1.74}$	$^{-0.56}_{+0.58}$	$^{-}_{-}$	$^{+0.26}_{-0.31}$	$^{+0.50}_{-0.43}$	$^{+0.61}_{-0.50}$	$^{+0.29}_{-0.56}$	$^{+0.53}_{-0.52}$	$^{+0.63}_{-0.70}$	$^{+0.42}_{-0.62}$	$^{+0.18}_{-0.45}$
Effective detector NP set 5 (JES) [%]	± 0.76	$^{-}_{-}$	$^{-0.11}_{+0.12}$	$^{-}_{-}$	$^{-0.12}_{+0.14}$	$^{-}_{-}$	$^{-}_{-}$	$^{+0.20}_{-0.11}$	$^{-}_{-}$	$^{+0.11}_{-0.19}$	$^{+0.25}_{-0.11}$
Effective detector NP set 6 restTerm (JES) [%]	$^{-0.50}_{+0.51}$	$^{-0.14}_{+0.10}$	$^{-}_{-}$	$^{-}_{-}$	$^{+0.13}_{-0.13}$	$^{+0.19}_{-0.14}$	$^{-}_{-}$	$^{+0.21}_{-0.23}$	$^{-}_{-}$	$^{+0.22}_{-0.28}$	$^{+0.20}_{-0.25}$
η intercalibration model (JES) [%]	$^{-3.67}_{+3.82}$	$^{-0.94}_{+0.87}$	$^{+0.27}_{-0.23}$	$^{+0.85}_{-0.59}$	$^{+0.75}_{-0.84}$	± 0.67	$^{+0.42}_{-0.50}$	$^{+0.58}_{-1.17}$	$^{+0.55}_{-1.03}$	$^{+0.51}_{-0.54}$	$^{-}_{-0.48}$
η intercalibration total stat (JES) [%]	$^{-2.22}_{+1.81}$	$^{-0.32}_{+0.25}$	$^{+0.28}_{-0.16}$	± 0.42	$^{+0.37}_{-0.29}$	$^{+0.49}_{-0.15}$	$^{-}_{-0.26}$	$^{-}_{-}$	$^{-}_{-0.30}$	$^{+0.23}_{-2.35}$	$^{-1.04}_{+0.79}$
Flavour composition (JES) [%]	$^{-4.34}_{+3.46}$	$^{-0.10}_{+0.19}$	$^{+0.99}_{-1.05}$	$^{+0.97}_{-1.00}$	$^{+0.47}_{-0.16}$	$^{-0.23}_{+0.70}$	$^{-0.70}_{+1.14}$	$^{-1.33}_{+0.86}$	$^{-2.35}_{+0.52}$	$^{-1.25}_{+2.15}$	$^{+4.12}_{+3.14}$
Flavour response (JES) [%]	$^{+1.72}_{-1.77}$	$^{+0.26}_{-0.11}$	$^{-0.21}_{+0.27}$	$^{-0.43}_{+0.46}$	$^{-0.29}_{+0.23}$	$^{+0.31}_{-}$	$^{-}_{-0.51}$	$^{-}_{-0.30}$	$^{-}_{-0.73}$	$^{-}_{-0.32}$	$^{+0.71}_{-2.14}$
Pile-up offset μ (JES) [%]	$^{+0.33}_{-0.47}$	$^{-}_{-}$	$^{-}_{-}$	$^{-0.14}_{+0.10}$	$^{-}_{-}$	$^{-}_{-}$	$^{-}_{-0.22}$	$^{+0.24}_{-}$	$^{-}_{-0.42}$	$^{+0.12}_{-0.17}$	$^{+0.57}_{-0.80}$
Pile-up offset N_{PV} (JES) [%]	$^{+0.17}_{-0.44}$	$^{-}_{-}$	$^{-}_{-}$	$^{-}_{-}$	$^{-}_{-}$	$^{-}_{-}$	$^{+0.13}_{-0.23}$	$^{-}_{-}$	$^{-}_{\pm 0.21}$	$^{+0.26}_{-0.22}$	$^{+0.57}_{-0.50}$
Pile-up offset p_{T} (JES) [%]	$^{-0.69}_{+0.75}$	$^{-0.22}_{+0.20}$	$^{-}_{-}$	$^{-}_{-0.15}$	$^{+0.20}_{-0.21}$	$^{+0.20}_{-}$	$^{+0.13}_{-0.20}$	$^{+0.28}_{-0.27}$	$^{+0.35}_{-0.16}$	$^{+0.21}_{-0.26}$	$^{-}_{-0.18}$
Pile-up offset ρ topology (JES) [%]	$^{-2.55}_{+2.51}$	$^{-0.10}_{+0.15}$	$^{+0.60}_{-0.38}$	$^{+0.71}_{-0.57}$	$^{+0.15}_{-0.36}$	$^{+0.31}_{-}$	$^{-0.94}_{+0.34}$	$^{-0.84}_{+0.18}$	$^{-1.61}_{+0.16}$	$^{-0.79}_{+0.20}$	$^{-3.01}_{+1.18}$
Punch-through (JES) [%]	$^{-}_{-}$	$^{-}_{-}$	$^{-}_{-}$	$^{-}_{-}$	$^{-}_{-}$	$^{-}_{-}$	$^{-}_{-}$	$^{-}_{-}$	$^{-}_{-}$	$^{-}_{-}$	$^{-}_{-}$
Single particle high-p_{T} (JES) [%]	$^{-}_{-}$	$^{-}_{-}$	$^{-}_{-}$	$^{-}_{-}$	$^{-}_{-}$	$^{-}_{-}$	$^{-}_{-}$	$^{-}_{-}$	$^{-}_{-}$	$^{-}_{-}$	$^{-}_{-}$
Jet energy resolution [%]	∓ 2.99	∓ 2.15	$^{-}_{-}$	± 1.25	± 1.15	± 2.05	± 0.88	± 1.47	± 0.63	∓ 0.76	∓ 0.74
Jet vertex fraction [%]	$^{+4.02}_{-4.05}$	$^{+1.77}_{-1.83}$	$^{+0.26}_{-0.30}$	$^{-0.59}_{+0.58}$	$^{-1.20}_{+1.22}$	$^{-1.67}_{+1.72}$	$^{-2.12}_{+2.24}$	$^{-2.39}_{+2.51}$	$^{-2.63}_{+2.85}$	$^{-2.76}_{+2.91}$	$^{-3.25}_{+3.51}$
b-Quark tagging efficiency (eigenvector 0) [%]	$^{-2.08}_{+1.99}$	$^{-0.44}_{+0.42}$	$^{+0.16}_{-0.15}$	$^{+0.31}_{-0.30}$	$^{+0.38}_{-0.36}$	$^{+0.43}_{-0.41}$	$^{+0.44}_{-0.42}$	$^{+0.34}_{-0.33}$	$^{+0.27}_{-0.26}$	± 0.32	$^{-}_{-}$
b-Quark tagging efficiency (eigenvector 1) [%]	$^{+1.48}_{-1.44}$	$^{+0.83}_{-0.82}$	$^{+0.37}_{-0.36}$	$^{-}_{-}$	$^{-0.52}_{+0.51}$	$^{-0.89}_{+0.88}$	$^{-1.30}_{+1.28}$	$^{-1.68}_{+1.64}$	$^{-1.99}_{+1.97}$	$^{-2.16}_{+2.13}$	$^{-2.81}_{+2.77}$
b-Quark tagging efficiency (eigenvector 2) [%]	± 0.39	$^{+0.45}_{-0.46}$	± 0.27	$^{-}_{-}$	∓ 0.27	∓ 0.50	$^{-0.72}_{+0.73}$	$^{-0.90}_{+0.91}$	$^{-1.08}_{+1.10}$	$^{-1.17}_{+1.19}$	$^{-1.45}_{+1.48}$
b-Quark tagging efficiency (eigenvector 3) [%]	∓ 0.44	$^{-}_{-}$	$^{-}_{-}$	± 0.14	$^{-}_{-}$	$^{-}_{-}$	$^{-}_{-}$	∓ 0.11	∓ 0.19	∓ 0.23	∓ 0.35
b-Quark tagging efficiency (eigenvector 4) [%]	$^{-}_{-}$	$^{-}_{-}$	$^{-}_{-}$	$^{-}_{-}$	$^{-}_{-}$	$^{-}_{-}$	$^{-}_{-}$	$^{-}_{-}$	$^{-}_{-}$	$^{-}_{-}$	∓ 0.13
c-Quark tagging efficiency (eigenvector 0) [%]	∓ 0.56	$^{-}_{-}$	± 0.21	$^{-}_{-}$	$^{-}_{-}$	$^{-}_{-}$	∓ 0.27	$^{-0.34}_{+0.33}$	$^{-0.43}_{+0.42}$	∓ 0.47	$^{-0.98}_{+0.97}$
c-Quark tagging efficiency (eigenvector 1) [%]	± 0.42	± 0.15	$^{-}_{-}$	$^{-}_{-}$	$^{-}_{-}$	∓ 0.16	∓ 0.24	∓ 0.33	∓ 0.43	∓ 0.46	∓ 0.71
c-Quark tagging efficiency (eigenvector 2) [%]	∓ 0.11	$^{-}_{-}$	$^{-}_{-}$	$^{-}_{-}$	$^{-}_{-}$	$^{-}_{-}$	$^{-}_{-}$	$^{-}_{-}$	$^{-}_{-}$	∓ 0.10	∓ 0.20
c-Quark tagging efficiency (eigenvector 3) [%]	∓ 0.17	$^{-}_{-}$	$^{-}_{-}$	$^{-}_{-}$	$^{-}_{-}$	$^{-}_{-}$	$^{-}_{-}$	$^{-}_{-}$	$^{-}_{-}$	$^{-}_{-}$	$^{-}_{-}$
Light-jet tagging efficiency (eigenvector 0) [%]	$^{-0.44}_{+0.50}$	$^{+0.53}_{-0.55}$	$^{+0.40}_{-0.42}$	$^{+0.33}_{-0.34}$	$^{-0.12}_{+0.16}$	$^{-0.50}_{+0.55}$	$^{+0.69}_{+0.63}$	$^{-1.18}_{+1.11}$	$^{-1.90}_{+1.91}$	$^{-1.92}_{+1.89}$	$^{-5.50}_{+5.89}$
Light-jet tagging efficiency (eigenvector 1) [%]	$^{-}_{-}$	$^{-}_{-}$	$^{-}_{-}$	$^{-}_{-}$	$^{-}_{-}$	$^{-}_{-}$	$^{-}_{-}$	$^{-}_{-}$	$^{-}_{-}$	$^{-}_{\mp 0.14}$	$^{-0.41}_{+0.42}$
Light-jet tagging efficiency (eigenvector 2) [%]	± 0.14	$^{-}_{-}$	$^{-}_{-}$	$^{-}_{-}$	$^{-}_{-}$	$^{-}_{-}$	$^{-}_{-}$	$^{-}_{-}$	$^{-0.11}_{+0.10}$	∓ 0.19	∓ 0.38
Light-jet tagging efficiency (eigenvector 3) [%]	∓ 0.10	$^{-}_{-}$	$^{-}_{-}$	$^{-}_{-}$	$^{-}_{-}$	$^{-}_{-}$	$^{-}_{-}$	$^{-}_{-}$	$^{+0.12}_{-0.11}$	$^{-}_{-}$	$^{-}_{-}$
Light-jet tagging efficiency (eigenvector 4) [%]	$^{-}_{-}$	$^{-}_{-}$	$^{-}_{-}$	$^{-}_{-}$	$^{-}_{-}$	$^{-}_{-}$	$^{-}_{-}$	$^{-}_{-}$	$^{-}_{-}$	$^{-}_{-}$	$^{-}_{-}$
Light-jet tagging efficiency (eigenvector 5) [%]	$^{-}_{-}$	$^{-}_{-}$	$^{-}_{-}$	$^{-}_{-}$	$^{-}_{-}$	$^{-}_{-}$	$^{-}_{-}$	$^{-}_{-}$	$^{-}_{-}$	$^{-}_{-}$	$^{-}_{-}$
Light-jet tagging efficiency (eigenvector 6) [%]	$^{-}_{-}$	$^{-}_{-}$	$^{-}_{-}$	$^{-}_{-}$	$^{-}_{-}$	$^{-}_{-}$	$^{-}_{-}$	$^{-}_{-}$	$^{-}_{-}$	$^{-}_{-}$	$^{-}_{-}$
Light-jet tagging efficiency (eigenvector 7) [%]	$^{-}_{-}$	$^{-}_{-}$	$^{-}_{-}$	$^{-}_{-}$	$^{-}_{-}$	$^{-}_{-}$	$^{-}_{-}$	$^{-}_{-}$	$^{-}_{-}$	$^{-}_{-}$	$^{-}_{-}$
Light-jet tagging efficiency (eigenvector 8) [%]	$^{-}_{-}$	$^{-}_{-}$	$^{-}_{-}$	$^{-}_{-}$	$^{-}_{-}$	$^{-}_{-}$	$^{-}_{-}$	$^{-}_{-}$	$^{-}_{-}$	$^{-}_{-}$	$^{-}_{-}$
Light-jet tagging efficiency (eigenvector 9) [%]	$^{-}_{-}$	$^{-}_{-}$	$^{-}_{-}$	$^{-}_{-}$	$^{-}_{-}$	$^{-}_{-}$	$^{-}_{-}$	$^{-}_{-}$	$^{-}_{-}$	$^{-}_{-}$	$^{-}_{-}$
Light-jet tagging efficiency (eigenvector 10) [%]	$^{-}_{-}$	$^{-}_{-}$	$^{-}_{-}$	$^{-}_{-}$	$^{-}_{-}$	$^{-}_{-}$	$^{-}_{-}$	$^{-}_{-}$	$^{-}_{-}$	$^{-}_{-}$	$^{-}_{-}$
Light-jet tagging efficiency (eigenvector 11) [%]	$^{-}_{-}$	$^{-}_{-}$	$^{-}_{-}$	$^{-}_{-}$	$^{-}_{-}$	$^{-}_{-}$	$^{-}_{-}$	$^{-}_{-}$	$^{-}_{-}$	$^{-}_{-}$	$^{-}_{-}$
b-Quark tagging extrapolation [%]	$^{-0.31}_{+0.32}$	∓ 0.31	∓ 0.31	∓ 0.27	$^{-}_{-}$	$^{+0.33}_{-0.32}$	$^{+0.89}_{-0.88}$	± 1.45	$^{+1.96}_{-1.95}$	$^{+2.30}_{-2.29}$	$^{+3.98}_{-3.95}$
b-Quark tagging extrapolation from c-Quark [%]	$^{-}_{-}$	$^{-}_{-}$	$^{-}_{-}$	$^{-}_{-}$	$^{-}_{-}$	$^{-}_{-}$	$^{-}_{-}$	$^{-}_{-}$	$^{-}_{-}$	$^{-}_{-}$	$^{-}_{\pm 0.10}$
Electron energy resolution [%]	$^{-}_{-}$	$^{-}_{-}$	$^{-}_{-}$	$^{-}_{-}$	$^{-}_{-}$	$^{-}_{-}$	$^{-}_{-}$	$^{-}_{-}$	$^{-0.16}_{+0.14}$	$^{-}_{-0.32}$	$^{-0.26}_{+0.10}$
Electron energy scale [%]	$^{-0.24}_{+0.22}$	$^{-}_{-}$	$^{-}_{-}$	$^{-}_{-}$	$^{-}_{-}$	$^{+0.20}_{-}$	$^{-}_{-}$	$^{+0.23}_{-0.11}$	$^{+0.16}_{-}$	$^{-}_{-}$	$^{+0.23}_{-0.13}$
Electron trigger efficiency [%]	$^{-}_{-}$	$^{-}_{-}$	$^{-}_{-}$	$^{-}_{-}$	$^{-}_{-}$	$^{-}_{-}$	$^{-}_{-}$	$^{-}_{-}$	± 0.12	± 0.14	± 0.25
Electron reconstruction efficiency [%]	$^{-}_{-}$	$^{-}_{-}$	$^{-}_{-}$	$^{-}_{-}$	$^{-}_{-}$	$^{-}_{-}$	$^{-}_{-}$	$^{-}_{-}$	$^{-}_{-}$	$^{-}_{-}$	$^{+0.13}_{-0.14}$
Electron identification efficiency [%]	$^{-}_{-}$	$^{-}_{-}$	$^{-}_{-}$	$^{-}_{-}$	$^{-}_{-}$	$^{-}_{-}$	± 0.14	± 0.20	± 0.27	± 0.30	± 0.48
Electron isolation efficiency [%]	$^{-}_{-}$	$^{-}_{-}$	$^{-}_{-}$	$^{-}_{-}$	$^{-}_{-}$	$^{-}_{-}$	± 0.11	± 0.15	± 0.20	± 0.23	± 0.35
Muon energy scale [%]	$^{-}_{-}$	$^{-}_{-}$	$^{-}_{-}$	$^{-}_{-}$	$^{-}_{-}$	$^{-}_{-}$	$^{-}_{-}$	$^{-}_{-}$	$^{-}_{-}$	$^{-}_{-}$	$^{-}_{-}$
Muon (MS) momentum resolution [%]	$^{-}_{-}$	$^{-}_{-}$	$^{-}_{-}$	$^{-}_{-}$	$^{-}_{-}$	$^{-}_{-}$	$^{-}_{-}$	$^{-}_{-}$	$^{-}_{-}$	$^{-}_{-}$	$^{-}_{-}$
Muon (ID) momentum resolution [%]	$^{-}_{-}$	$^{-}_{-}$	$^{-}_{-}$	$^{-}_{-}$	$^{-}_{-}$	$^{-}_{-}$	$^{-}_{-}$	$^{-}_{-}$	$^{-}_{-}$	$^{-}_{-}$	$^{-}_{-}$
Muon trigger efficiency stat [%]	$^{-}_{-}$	$^{-}_{-}$	$^{-}_{-}$	$^{-}_{-}$	$^{-}_{-}$	$^{-}_{-}$	$^{-}_{-}$	$^{-}_{-}$	$^{-}_{-}$	$^{-}_{-}$	$^{-}_{-}$
Muon trigger efficiency syst [%]	$^{-}_{-}$	$^{-}_{-}$	$^{-}_{-}$	$^{-}_{-}$	$^{-}_{-}$	$^{-}_{-}$	$^{-}_{-}$	$^{-}_{-}$	$^{-}_{-}$	$^{-}_{-}$	$^{-}_{-}$
Muon identification stat [%]	$^{-}_{-}$	$^{-}_{-}$	$^{-}_{-}$	$^{-}_{-}$	$^{-}_{-}$	$^{-}_{-}$	$^{-}_{-}$	$^{-}_{-}$	$^{-}_{-}$	$^{-}_{-}$	$^{-}_{-}$
Muon identification syst [%]	$^{-}_{-}$	$^{-}_{-}$	$^{-}_{-}$	$^{-}_{-}$	$^{-}_{-}$	$^{-}_{-}$	$^{-}_{-}$	$^{-}_{-}$	± 0.11	± 0.14	± 0.23
Muon isolation efficiency stat [%]	$^{-}_{-}$	$^{-}_{-}$	$^{-}_{-}$	$^{-}_{-}$	$^{-}_{-}$	$^{-}_{-}$	$^{-}_{-}$	$^{-}_{-}$	$^{-}_{-}$	$^{-}_{-}$	$^{-}_{-}$
Muon isolation efficiency syst [%]	$^{-}_{-}$	$^{-}_{-}$	$^{-}_{-}$	$^{-}_{-}$	$^{-}_{-}$	$^{-}_{-}$	$^{-}_{-}$	$^{-}_{-}$	$^{-}_{-}$	$^{-}_{-}$	$^{-}_{-}$
Muon TTVA efficiency stat [%]	$^{-}_{-}$	$^{-}_{-}$	$^{-}_{-}$	$^{-}_{-}$	$^{-}_{-}$	$^{-}_{-}$	$^{-}_{-}$	$^{-}_{-}$	$^{-}_{-}$	$^{-}_{-}$	$^{-}_{-}$
Muon TTVA efficiency syst [%]	$^{-}_{-}$	$^{-}_{-}$	$^{-}_{-}$	$^{-}_{-}$	$^{-}_{-}$	$^{-}_{-}$	$^{-}_{-}$	$^{-}_{-}$	$^{-}_{-}$	$^{-}_{-}$	$^{-}_{-}$
$E_{\mathrm{T}}^{\mathrm{miss}}$ Soft jet resolution para [%]	± 0.50	± 0.18	$^{-}_{-}$	∓ 0.15	∓ 0.10	∓ 0.17	∓ 0.18	$^{-}_{-}$	$^{-}_{-}$	∓ 0.31	± 0.17
$E_{\mathrm{T}}^{\mathrm{miss}}$ Soft jet resolution perp [%]	± 0.51	± 0.21	$^{-}_{-}$	$^{-}_{-}$	∓ 0.21	∓ 0.18	∓ 0.30	∓ 0.17	∓ 0.18	∓ 0.51	∓ 0.49
$E_{\mathrm{T}}^{\mathrm{miss}}$ Soft jet scale [%]	$^{+0.70}_{-0.47}$	$^{+0.19}_{-0.24}$	$^{-}_{-}$	$^{-}_{-}$	$^{-0.21}_{+0.18}$	$^{-0.15}_{+0.25}$	$^{-0.25}_{-}$	$^{-0.14}_{+0.29}$	$^{-0.23}_{+0.24}$	$^{-0.26}_{+0.13}$	$^{-0.35}_{+0.17}$
Luminosity [%]	$^{-}_{-}$	$^{-}_{-}$	$^{-}_{-}$	$^{-}_{-}$	$^{-}_{-}$	$^{-}_{-}$	$^{-}_{-}$	$^{-}_{-}$	$^{-}_{-}$	$^{-}_{-}$	$^{-}_{-}$
Single top cross-section [%]	$^{-}_{-}$	$^{-}_{-}$	$^{-}_{-}$	$^{-}_{-}$	$^{-}_{-}$	$^{-}_{-}$	± 0.15	± 0.23	± 0.31	± 0.36	± 0.56
Z+jets cross-section [%]	± 0.79	∓ 0.11	∓ 0.15	∓ 0.11	$^{-}_{-}$	∓ 0.13	$^{-}_{-}$	± 0.33	± 0.56	± 0.32	± 1.71
Diboson cross-section [%]	$^{-}_{-}$	$^{-}_{-}$	$^{-}_{-}$	$^{-}_{-}$	$^{-}_{-}$	$^{-}_{-}$	± 0.10	± 0.16	± 0.25	± 0.30	± 0.51
$t\bar{t}V$ cross-section [%]	$^{-}_{-}$	$^{-}_{-}$	$^{-}_{-}$	$^{-}_{-}$	$^{-}_{-}$	$^{-}_{-}$	$^{-}_{-}$	∓ 0.10	∓ 0.12	∓ 0.13	∓ 0.17
Monte Carlo sample statistics [%]	± 0.74	± 0.26	± 0.25	± 0.28	± 0.37	± 0.46	± 0.54	± 0.74	± 1.37	± 1.38	± 1.68
ISR/FSR + scale [%]	$^{+0.50}_{-0.45}$	$^{+0.45}_{-1.26}$	$^{-0.33}_{+0.57}$	$^{-0.42}_{+0.35}$	$^{-}_{-}$	$^{+1.04}_{-}$	$^{-0.34}_{+0.33}$	± 0.35	$^{-}_{-}$	$^{-}_{-2.57}$	$^{+0.76}_{-0.48}$
Alternate hard-scattering model [%]	∓ 1.41	∓ 1.40	$^{-}_{-}$	∓ 0.44	± 0.68	∓ 1.20	± 3.23	± 3.22	± 4.16	± 2.27	± 8.97
Alternate parton-shower model [%]	± 1.36	± 1.55	∓ 1.18	∓ 0.32	∓ 0.54	± 0.39	∓ 0.37	± 0.66	$^{-}_{-}$	∓ 1.10	∓ 2.41
Inter PDF [%]	$^{-}_{-}$	$^{-}_{-}$	$^{-}_{-}$	$^{-}_{-}$	$^{-}_{-}$	$^{-}_{-}$	$^{-}_{-}$	$^{-}_{-}$	$^{-}_{-}$	$^{-}_{-}$	± 0.34
Intra PDF [%]	$^{-}_{-}$	$^{-}_{-}$	$^{-}_{-}$	$^{-}_{-}$	$^{-}_{-}$	$^{-}_{-}$	$^{-}_{-}$	$^{-}_{-}$	$^{-}_{-}$	$^{-}_{-}$	± 0.24
Real lepton efficiency stat [%]	$^{-}_{-}$	$^{-}_{-}$	$^{-}_{-}$	$^{-}_{-}$	$^{-}_{-}$	$^{-}_{-}$	$^{-}_{-}$	$^{-0.17}_{+0.12}$	$^{-0.22}_{+0.15}$	$^{-0.31}_{+0.21}$	$^{-0.47}_{+0.29}$
Fake lepton efficiency MC scale [%]	$^{+1.10}_{-1.11}$	$^{-}_{+0.16}$	$^{-0.16}_{+0.26}$	$^{-0.20}_{+0.24}$	$^{-}_{-}$	$^{-}_{-}$	$^{-}_{-}$	$^{+0.29}_{-0.67}$	$^{+0.10}_{-1.04}$	$^{-}_{-0.55}$	$^{+1.28}_{-1.34}$
Fake lepton efficiency alternate CR [%]	± 0.50	$^{-}_{-}$	∓ 0.12	$^{-}_{-}$	$^{-}_{-}$	± 0.18	$^{-}_{-}$	± 0.20	± 0.21	± 0.32	∓ 0.34
Fake overall normalisation [%]	± 5.28	∓ 0.40	∓ 1.05	∓ 0.90	∓ 0.15	$^{-}_{-}$	± 0.47	± 1.40	± 2.40	± 2.14	± 6.96
W+jets CA_{4incl} stat error [%]	$^{-}_{-}$	$^{-}_{-}$	$^{-}_{-}$	$^{-}_{-}$	$^{-}_{-}$	$^{-}_{-}$	$^{-}_{-}$	$^{-}_{-}$	∓ 0.12	∓ 0.16	∓ 0.30
W+jets Fc stat error [%]	$^{-}_{-}$	$^{-}_{-}$	$^{-}_{-}$	$^{-}_{-}$	$^{-}_{-}$	$^{-}_{-}$	$^{-}_{-}$	$^{-}_{-}$	$^{-}_{-}$	$^{-}_{-}$	$^{+0.16}_{-0.15}$
W+jets Fcc stat error [%]	$^{+0.20}_{-}$	$^{-}_{-}$	$^{-}_{-}$	$^{-}_{-}$	$^{-}_{-}$	$^{-}_{-}$	$^{-}_{-}$	$^{-0.16}_{-}$	$^{-0.44}_{+0.21}$	$^{-0.41}_{+0.20}$	$^{-}_{-}$
W+jets Flight stat error [%]	$^{-}_{-}$	$^{-}_{-}$	$^{-}_{-}$	$^{-}_{-}$	$^{-}_{-}$	$^{-}_{-}$	$^{-}_{-}$	$^{-}_{-}$	$^{-}_{-}$	$^{-}_{-}$	$^{-}_{-}$

Table C.14: Table of systematic uncertainties for the relative differential cross-section at particle level for the mass of the $t\bar{t}$ system in the resolved regime.

Appendix D

Covariance Matrices

In this appendix are shown the covariance matrices for all the measured variables, obtained as described in Chapter 7. The covariance matrices for the particle level $p_T^{t,had}$, absolute and relative, are shown in Tables D.1, D.2 for the *resolved* topology and in Tables D.3, D.4 for the *boosted* one. The covariance matrices for the particle level $|y^{t,had}|$ distribution, absolute and relative, are shown in Tables D.5, D.6 for the *resolved* topology and in Tables D.7, D.8 for the *boosted* one. Tables D.9- D.14 show the covariance matrices for the particle level $m^{t\bar{t}}$, $p_T^{t\bar{t}}$ and $|y^{t\bar{t}}|$ in the resolved topology, for absolute and relative spectra.

bin [GeV]	0-25	25-50	50-75	75-105	105-135	135-165	165-195	195-230	230-265	265-300	300-350	350-400	400-450	450-500	500-1000
0-25	3.05e-04	8.25e-04	1.17e-03	1.22e-03	1.04e-03	6.95e-04	4.26e-04	2.74e-04	1.49e-04	9.81e-05	5.13e-05	2.62e-05	1.47e-05	8.74e-06	1.17e-06
25-50	8.25e-04	2.38e-03	3.33e-03	3.46e-03	2.91e-03	1.94e-03	1.18e-03	7.47e-04	4.05e-04	2.64e-04	1.40e-04	6.87e-05	3.94e-05	2.18e-05	3.17e-06
50-75	1.17e-03	3.33e-03	4.79e-03	4.94e-03	4.18e-03	2.79e-03	1.71e-03	1.09e-03	5.87e-04	3.83e-04	2.03e-04	9.94e-05	5.63e-05	3.15e-05	4.42e-06
75-105	1.22e-03	3.46e-03	4.94e-03	5.25e-03	4.43e-03	2.98e-03	1.83e-03	1.16e-03	6.35e-04	4.05e-04	2.19e-04	1.14e-04	6.08e-05	3.41e-05	5.02e-06
105-135	1.04e-03	2.91e-03	4.18e-03	4.43e-03	3.92e-03	2.63e-03	1.64e-03	1.05e-03	5.77e-04	3.68e-04	1.98e-04	1.05e-04	5.55e-05	3.10e-05	4.42e-06
135-165	6.95e-04	1.94e-03	2.79e-03	2.98e-03	2.63e-03	1.83e-03	1.13e-03	7.29e-04	4.12e-04	2.64e-04	1.43e-04	7.80e-05	4.04e-05	2.33e-05	3.29e-06
165-195	4.26e-04	1.18e-03	1.71e-03	1.83e-03	1.64e-03	1.13e-03	7.35e-04	4.64e-04	2.63e-04	1.72e-04	9.31e-05	5.04e-05	2.65e-05	1.49e-05	2.13e-06
195-230	2.74e-04	7.47e-04	1.09e-03	1.16e-03	1.05e-03	7.29e-04	4.64e-04	3.40e-04	1.82e-04	1.31e-04	6.80e-05	3.78e-05	2.01e-05	1.47e-05	1.64e-06
230-265	1.49e-04	4.05e-04	5.87e-04	6.35e-04	5.77e-04	4.12e-04	2.63e-04	1.82e-04	1.13e-04	7.31e-05	3.91e-05	2.29e-05	1.19e-05	7.65e-06	1.01e-06
265-300	9.81e-05	2.64e-04	3.83e-04	4.05e-04	3.68e-04	2.64e-04	1.72e-04	1.31e-04	7.31e-05	6.33e-05	2.97e-05	1.60e-05	9.20e-06	7.41e-06	7.48e-07
300-350	5.13e-05	1.40e-04	2.03e-04	2.19e-04	1.98e-04	1.43e-04	9.31e-05	6.80e-05	3.91e-05	2.97e-05	1.73e-05	9.03e-06	4.81e-06	3.51e-06	4.36e-07
350-400	2.62e-05	6.87e-05	9.94e-05	1.14e-04	1.05e-04	7.80e-05	5.04e-05	3.78e-05	2.29e-05	1.60e-05	9.03e-06	6.91e-06	2.81e-06	2.04e-06	2.87e-07
400-450	1.47e-05	3.94e-05	5.63e-05	6.08e-05	5.55e-05	4.04e-05	2.65e-05	2.01e-05	1.19e-05	9.20e-06	4.81e-06	2.81e-06	2.05e-06	1.13e-06	1.42e-07
450-500	8.74e-06	2.18e-05	3.15e-05	3.41e-05	3.10e-05	2.33e-05	1.49e-05	1.47e-05	7.65e-06	7.41e-06	3.51e-06	2.04e-06	1.13e-06	1.45e-06	9.93e-08
500-1000	1.17e-06	3.17e-06	4.42e-06	5.02e-06	4.42e-06	3.29e-06	2.13e-06	1.64e-06	1.01e-06	7.48e-07	4.36e-07	2.87e-07	1.42e-07	9.93e-08	1.99e-08

Table D.1: Covariance matrix of the absolute cross-section as function of the top quark p_T, accounting for the statistical and systematic uncertainties in the resolved topology.

Bin [GeV]	0-25	25-50	50-75	75-105	105-135	135-165	165-195	195-230	230-265	265-300	300-350	350-400	400-450	450-500	500-1000
0-25	3.25e-09	5.52e-09	5.68e-09	3.97e-09	3.79e-10	-1.18e-09	-2.21e-09	-1.29e-09	-1.67e-09	-6.67e-10	-5.91e-10	-4.89e-10	-1.38e-10	4.26e-11	-1.11e-11
25-50	5.52e-09	1.90e-08	1.72e-08	1.12e-08	-1.28e-10	-4.83e-09	-7.02e-09	-4.66e-09	-5.13e-09	-2.59e-09	-1.87e-09	-1.51e-09	-4.57e-10	-1.30e-11	-3.32e-11
50-75	5.68e-09	1.72e-08	2.62e-08	1.28e-08	-1.45e-10	-5.84e-09	-7.42e-09	-5.62e-09	-6.38e-09	-4.20e-09	-2.61e-09	-1.85e-09	-7.18e-10	-2.02e-10	-5.22e-11
75-105	3.97e-09	1.12e-08	1.28e-08	1.39e-08	6.17e-10	-2.21e-09	-4.95e-09	-3.40e-09	-3.76e-09	-2.17e-09	-1.59e-09	-1.27e-09	-4.72e-10	-9.56e-11	-4.43e-11
105-135	3.79e-10	-1.28e-10	-1.45e-10	6.17e-10	7.57e-09	2.77e-09	6.11e-10	9.98e-10	-6.14e-10	2.15e-10	-2.74e-10	-2.95e-10	-1.78e-10	1.00e-10	-2.77e-11
135-165	-1.18e-09	-4.83e-09	-5.84e-09	-2.21e-09	2.77e-09	8.28e-09	4.05e-09	3.73e-09	2.57e-09	2.27e-09	9.70e-10	6.91e-10	2.40e-10	3.37e-10	1.31e-11
165-195	-2.21e-09	-7.02e-09	-7.42e-09	-4.95e-09	6.11e-10	4.05e-09	6.19e-09	3.93e-09	2.86e-09	2.08e-09	1.12e-09	9.91e-10	3.22e-10	2.74e-10	2.68e-11
195-230	-1.29e-09	-4.66e-09	-5.62e-09	-3.40e-09	9.98e-10	3.73e-09	3.93e-09	5.71e-09	2.88e-09	3.04e-09	1.44e-09	9.67e-10	4.52e-10	5.21e-10	3.45e-11
230-265	-1.67e-09	-5.13e-09	-6.38e-09	-3.76e-09	-6.14e-10	2.57e-09	2.86e-09	2.88e-09	3.20e-09	2.04e-09	1.11e-09	8.55e-10	3.50e-10	2.46e-10	2.94e-11
265-300	-6.67e-10	-2.59e-09	-4.20e-09	-2.17e-09	2.15e-10	2.27e-09	2.08e-09	3.04e-09	2.04e-09	2.80e-09	1.10e-09	6.58e-10	3.70e-10	3.94e-10	2.79e-11
300-350	-5.91e-10	-1.87e-09	-2.61e-09	-1.59e-09	-2.74e-10	9.70e-10	1.12e-09	1.44e-09	1.11e-09	1.10e-09	7.25e-10	3.92e-10	1.91e-10	1.66e-10	1.79e-11
350-400	-4.89e-10	-1.51e-09	-1.85e-09	-1.27e-09	-2.95e-10	6.91e-10	9.91e-10	9.67e-10	8.55e-10	6.58e-10	3.92e-10	4.23e-10	1.31e-10	1.06e-10	1.49e-11
400-450	-1.38e-10	-4.57e-10	-7.18e-10	-4.72e-10	-1.78e-10	2.40e-10	3.22e-10	4.52e-10	3.50e-10	3.70e-10	1.91e-10	1.31e-10	1.15e-10	6.03e-11	7.12e-12
450-500	4.26e-11	-1.30e-11	-2.02e-10	-9.56e-11	1.00e-10	3.37e-10	2.74e-10	5.21e-10	2.46e-10	3.94e-10	1.66e-10	1.06e-10	6.03e-11	1.10e-10	5.59e-12
500-1000	-1.11e-11	-3.32e-11	-5.22e-11	-4.43e-11	-2.77e-11	1.31e-11	2.68e-11	3.45e-11	2.94e-11	2.79e-11	1.79e-11	1.49e-11	7.12e-12	5.59e-12	1.35e-12

Table D.2: Covariance matrix of the relative cross-section as function of the top quark p_T, accounting for the statistical and systematic uncertainties in the resolved topology.

Bin [GeV]	300-350	350-400	400-450	450-500	500-550	550-650	650-750	750-1500
300-350	1.49e-05	8.83e-06	4.86e-06	3.12e-06	2.04e-06	1.25e-06	4.46e-07	7.02e-08
350-400	8.83e-06	6.27e-06	3.34e-06	2.21e-06	1.52e-06	9.70e-07	3.29e-07	5.88e-08
400-450	4.86e-06	3.34e-06	2.18e-06	1.36e-06	9.56e-07	6.15e-07	2.08e-07	3.65e-08
450-500	3.12e-06	2.21e-06	1.36e-06	1.00e-06	6.79e-07	4.20e-07	1.45e-07	2.57e-08
500-550	2.04e-06	1.52e-06	9.56e-07	6.79e-07	5.89e-07	3.25e-07	1.04e-07	1.99e-08
550-650	1.25e-06	9.70e-07	6.15e-07	4.20e-07	3.25e-07	2.42e-07	6.42e-08	1.27e-08
650-750	4.46e-07	3.29e-07	2.08e-07	1.45e-07	1.04e-07	6.42e-08	3.41e-08	3.84e-09
750-1500	7.02e-08	5.88e-08	3.65e-08	2.57e-08	1.99e-08	1.27e-08	3.84e-09	1.08e-09

Table D.3: Covariance matrix for the absolute cross-section as function of the hadronic top-quark top quark p_T, accounting for the statistic and systematic uncertainties in the boosted topology.

Bin [GeV]	300-350	350-400	400-450	450-500	500-550	550-650	650-750	750-1500
300-350	3.59e-07	6.24e-08	-4.84e-08	-5.53e-08	-4.82e-08	-3.43e-08	-1.79e-08	-3.44e-09
350-400	6.24e-08	8.14e-08	-7.38e-10	-1.03e-08	-1.62e-09	1.28e-09	-3.70e-09	-3.52e-10
400-450	-4.84e-08	-7.38e-10	3.70e-08	1.07e-08	1.01e-08	1.15e-08	2.98e-09	7.79e-10
450-500	-5.53e-08	-1.03e-08	1.07e-08	2.61e-08	1.44e-08	8.77e-09	4.37e-09	8.65e-10
500-550	-4.82e-08	-1.62e-09	1.01e-08	1.44e-08	3.10e-08	1.24e-08	4.36e-09	9.80e-10
550-650	-3.43e-08	1.28e-09	1.15e-08	8.77e-09	1.24e-08	1.45e-08	2.93e-09	7.11e-10
650-750	-1.79e-08	-3.70e-09	2.98e-09	4.37e-09	4.36e-09	2.93e-09	3.20e-09	2.72e-10
750-1500	-3.44e-09	-3.52e-10	7.79e-10	8.65e-10	9.80e-10	7.11e-10	2.72e-10	1.19e-10

Table D.4: Covariance matrix for the relative cross-section as function of the hadronic top-quark top quark p_T, accounting for the statistic and systematic uncertainties in the boosted topology.

bin	0.0-0.1	0.1-0.2	0.2-0.3	0.3-0.4	0.4-0.5	0.5-0.6	0.6-0.7	0.7-0.8	0.8-0.9	0.9-1.0	1.0-1.1	1.1-1.2	1.2-1.3	1.3-1.4	1.4-1.5	1.5-1.7	1.7-1.9	1.9-2.5
0.0-0.1	7.55e+01	7.08e+01	6.88e+01	6.61e+01	7.15e+01	6.46e+01	6.22e+01	5.70e+01	5.74e+01	5.09e+01	4.52e+01	4.29e+01	3.83e+01	3.34e+01	2.78e+01	2.25e+01	1.43e+01	3.00e+00
0.1-0.2	7.08e+01	7.01e+01	6.63e+01	6.37e+01	6.91e+01	6.21e+01	6.00e+01	5.50e+01	5.56e+01	4.93e+01	4.38e+01	4.16e+01	3.70e+01	3.25e+01	2.70e+01	2.17e+01	1.38e+01	2.93e+00
0.2-0.3	6.88e+01	6.63e+01	6.60e+01	6.17e+01	6.72e+01	6.03e+01	5.83e+01	5.32e+01	5.39e+01	4.76e+01	4.26e+01	4.01e+01	3.60e+01	3.12e+01	2.61e+01	2.09e+01	1.32e+01	2.86e+00
0.3-0.4	6.61e+01	6.37e+01	6.17e+01	6.24e+01	6.29e+01	5.76e+01	5.62e+01	5.07e+01	5.29e+01	4.63e+01	4.04e+01	3.88e+01	3.45e+01	3.05e+01	2.53e+01	2.03e+01	1.28e+01	2.72e+00
0.4-0.5	7.15e+01	6.91e+01	6.72e+01	6.29e+01	7.55e+01	6.28e+01	6.05e+01	5.50e+01	5.55e+01	4.90e+01	4.58e+01	4.19e+01	3.81e+01	3.22e+01	2.74e+01	2.17e+01	1.39e+01	3.14e+00
0.5-0.6	6.46e+01	6.21e+01	6.03e+01	5.76e+01	6.28e+01	5.79e+01	5.44e+01	4.97e+01	5.06e+01	4.46e+01	4.00e+01	3.76e+01	3.38e+01	2.94e+01	2.45e+01	1.97e+01	1.25e+01	2.70e+00
0.6-0.7	6.22e+01	6.00e+01	5.83e+01	5.62e+01	6.05e+01	5.44e+01	5.41e+01	4.81e+01	4.92e+01	4.34e+01	3.88e+01	3.66e+01	3.29e+01	2.88e+01	2.40e+01	1.92e+01	1.22e+01	2.64e+00
0.7-0.8	5.70e+01	5.50e+01	5.32e+01	5.07e+01	5.50e+01	4.97e+01	4.81e+01	4.56e+01	4.43e+01	3.95e+01	3.52e+01	3.33e+01	2.99e+01	2.61e+01	2.17e+01	1.75e+01	1.10e+01	2.35e+00
0.8-0.9	5.74e+01	5.56e+01	5.39e+01	5.29e+01	5.55e+01	5.06e+01	4.92e+01	4.43e+01	4.78e+01	4.06e+01	3.58e+01	3.42e+01	3.07e+01	2.72e+01	2.24e+01	1.80e+01	1.14e+01	2.48e+00
0.9-1.0	5.09e+01	4.93e+01	4.76e+01	4.63e+01	4.90e+01	4.46e+01	4.34e+01	3.95e+01	4.06e+01	3.69e+01	3.14e+01	3.02e+01	2.70e+01	2.39e+01	1.97e+01	1.59e+01	1.01e+01	2.15e+00
1.0-1.1	4.52e+01	4.38e+01	4.26e+01	4.04e+01	4.58e+01	4.00e+01	3.88e+01	3.52e+01	3.58e+01	3.14e+01	3.01e+01	2.67e+01	2.44e+01	2.11e+01	1.77e+01	1.41e+01	9.00e+00	2.04e+00
1.1-1.2	4.29e+01	4.16e+01	4.01e+01	3.88e+01	4.19e+01	3.76e+01	3.66e+01	3.33e+01	3.42e+01	3.02e+01	2.67e+01	2.67e+01	2.28e+01	2.02e+01	1.67e+01	1.35e+01	8.73e+00	1.84e+00
1.2-1.3	3.83e+01	3.70e+01	3.60e+01	3.45e+01	3.81e+01	3.38e+01	3.29e+01	2.99e+01	3.07e+01	2.70e+01	2.44e+01	2.28e+01	2.15e+01	1.79e+01	1.50e+01	1.20e+01	7.65e+00	1.71e+00
1.3-1.4	3.34e+01	3.25e+01	3.12e+01	3.05e+01	3.22e+01	2.94e+01	2.88e+01	2.61e+01	2.72e+01	2.39e+01	2.11e+01	2.02e+01	1.79e+01	1.70e+01	1.31e+01	1.07e+01	6.96e+00	1.46e+00
1.4-1.5	2.78e+01	2.70e+01	2.61e+01	2.53e+01	2.74e+01	2.45e+01	2.40e+01	2.17e+01	2.24e+01	1.97e+01	1.77e+01	1.67e+01	1.50e+01	1.31e+01	1.17e+01	8.77e+00	5.62e+00	1.25e+00
1.5-1.7	2.25e+01	2.17e+01	2.09e+01	2.03e+01	2.17e+01	1.97e+01	1.92e+01	1.75e+01	1.80e+01	1.59e+01	1.41e+01	1.35e+01	1.20e+01	1.07e+01	8.77e+00	7.43e+00	4.63e+00	9.76e-01
1.7-1.9	1.43e+01	1.38e+01	1.32e+01	1.28e+01	1.39e+01	1.25e+01	1.22e+01	1.10e+01	1.14e+01	1.01e+01	9.00e+00	8.73e+00	7.65e+00	6.96e+00	5.62e+00	4.63e+00	3.18e+00	6.24e-01
1.9-2.5	3.00e+00	2.93e+00	2.86e+00	2.72e+00	3.14e+00	2.70e+00	2.64e+00	2.35e+00	2.48e+00	2.15e+00	2.04e+00	1.84e+00	1.71e+00	1.46e+00	1.25e+00	9.76e-01	6.24e-01	1.60e-01

Table D.5: Covariance matrix of the absolute cross-section as function of the absolute value of the rapidity of the top quark, accounting for the statistical and systematic uncertainties in the resolved topology.

bin	0.0-0.1	0.1-0.2	0.2-0.3	0.3-0.4	0.4-0.5	0.5-0.6	0.6-0.7	0.7-0.8	0.8-0.9	0.9-1.0	1.0-1.1	1.1-1.2	1.2-1.3	1.3-1.4	1.4-1.5	1.5-1.7	1.7-1.9	1.9-2.5
0.0-0.1	3.30e-04	5.03e-05	1.24e-04	1.86e-05	1.14e-04	1.14e-04	3.47e-05	5.96e-05	4.40e-05	1.43e-05	4.21e-05	-1.23e-05	1.13e-05	-3.44e-05	5.27e-06	-9.81e-06	-1.22e-05	-1.32e-06
0.1-0.2	5.03e-05	2.38e-04	8.47e-05	5.18e-05	2.12e-04	5.90e-05	9.29e-05	7.89e-05	1.28e-05	1.93e-06	8.02e-05	-1.80e-05	5.99e-05	-1.75e-05	8.05e-06	-6.33e-06	-7.28e-06	5.93e-06
0.2-0.3	1.24e-04	8.47e-05	2.80e-04	6.62e-05	1.07e-04	9.16e-05	6.94e-05	6.95e-05	4.63e-05	1.62e-05	6.10e-05	-1.67e-05	2.88e-05	-2.34e-05	7.14e-06	-1.51e-05	-1.75e-05	1.77e-06
0.3-0.4	1.86e-05	5.18e-05	6.62e-05	3.42e-04	3.14e-05	1.60e-05	8.51e-05	-6.78e-06	1.01e-04	1.85e-05	2.44e-05	-2.81e-05	3.54e-05	-5.56e-07	1.65e-05	-1.59e-05	-1.70e-05	4.47e-06
0.4-0.5	1.14e-04	2.12e-04	1.07e-04	3.14e-05	6.78e-04	1.05e-04	1.87e-04	1.93e-04	-1.21e-05	-6.40e-07	1.99e-04	7.97e-06	1.90e-04	-5.03e-06	4.59e-05	2.47e-05	1.79e-05	2.03e-05
0.5-0.6	1.14e-04	5.90e-05	9.16e-05	1.60e-05	1.05e-04	1.98e-04	2.89e-05	3.26e-05	3.38e-05	4.58e-06	4.60e-05	-5.25e-06	3.17e-05	-1.45e-05	7.30e-06	-1.29e-06	-4.42e-06	2.60e-06
0.6-0.7	3.47e-05	9.29e-05	6.94e-05	8.51e-05	1.87e-04	2.89e-05	2.15e-04	5.65e-05	3.73e-05	2.39e-05	9.20e-05	1.91e-06	9.16e-05	1.20e-05	3.29e-05	1.31e-05	4.52e-06	1.07e-05
0.7-0.8	5.96e-05	7.89e-05	6.95e-05	-6.78e-06	1.93e-04	3.26e-05	5.65e-05	1.93e-04	-2.07e-05	6.21e-07	6.95e-05	8.83e-06	5.87e-05	-1.26e-05	1.34e-05	2.89e-07	-1.92e-07	5.08e-06
0.8-0.9	4.40e-05	1.28e-05	4.63e-05	1.01e-04	-1.21e-05	3.38e-05	3.73e-05	-2.07e-05	2.56e-04	4.61e-05	2.45e-05	2.80e-05	4.43e-05	4.81e-05	4.11e-05	1.71e-05	1.25e-05	7.94e-06
0.9-1.0	1.43e-05	1.93e-06	1.62e-05	1.85e-05	-6.40e-07	4.58e-06	2.39e-05	6.21e-07	4.61e-05	1.25e-04	3.97e-06	1.30e-05	2.40e-05	1.74e-05	2.20e-05	8.02e-06	6.18e-06	3.34e-06
1.0-1.1	4.21e-05	8.02e-05	6.10e-05	2.44e-05	1.99e-04	4.60e-05	9.20e-05	6.95e-05	2.45e-05	3.97e-06	2.10e-04	7.44e-06	9.26e-05	3.59e-05	4.33e-05	2.55e-05	2.49e-05	1.44e-05
1.1-1.2	-1.23e-05	-1.80e-05	-1.67e-05	-2.81e-05	7.97e-06	-5.25e-06	1.91e-06	8.83e-06	2.80e-05	1.30e-05	7.44e-06	1.12e-04	2.03e-05	1.71e-05	2.55e-05	1.47e-05	1.76e-05	4.53e-06
1.2-1.3	1.13e-05	5.99e-05	2.88e-05	3.54e-05	1.90e-04	3.17e-05	9.16e-05	5.87e-05	4.43e-05	2.40e-05	9.26e-05	2.03e-05	1.75e-04	2.45e-05	3.91e-05	3.01e-05	2.17e-05	1.42e-05
1.3-1.4	-3.44e-05	-1.75e-05	-2.34e-05	-5.56e-07	-5.03e-06	-1.45e-05	1.20e-05	-1.26e-05	4.81e-05	1.74e-05	3.59e-05	1.71e-05	2.45e-05	1.17e-04	1.89e-05	1.96e-05	2.59e-05	7.31e-06
1.4-1.5	5.27e-06	8.05e-06	7.14e-06	1.65e-05	4.59e-05	7.30e-06	3.29e-05	1.34e-05	4.11e-05	2.20e-05	4.33e-05	2.55e-05	3.91e-05	1.89e-05	9.03e-05	1.55e-05	1.96e-05	7.72e-06
1.5-1.7	-9.81e-06	-6.33e-06	-1.51e-05	-1.59e-05	2.47e-05	-1.29e-06	1.31e-05	2.89e-07	1.71e-05	8.02e-06	2.55e-05	1.47e-05	3.01e-05	1.96e-05	1.55e-05	3.85e-05	1.42e-05	5.54e-06
1.7-1.9	-1.22e-05	-7.28e-06	-1.75e-05	-1.70e-05	1.79e-05	-4.42e-06	4.52e-06	-1.92e-07	1.25e-05	6.18e-06	2.49e-05	1.76e-05	2.17e-05	2.59e-05	1.96e-05	1.42e-05	3.11e-05	4.91e-06
1.9-2.5	-1.32e-06	5.93e-06	1.77e-06	4.47e-06	2.03e-05	2.60e-06	1.07e-05	5.08e-06	7.94e-06	3.34e-06	1.44e-05	4.53e-06	1.42e-05	7.31e-06	7.72e-06	5.54e-06	4.91e-06	3.13e-06

Table D.6: Covariance matrix of the relative cross-section as function of the absolute value of the rapidity of the top quark, accounting for the statistical and systematic uncertainties in the resolved topology.

bin	0.0-0.2	0.2-0.4	0.4-0.6	0.6-0.8	0.8-1.0	1.0-1.2	1.2-1.4	1.4-1.6	1.6-1.8	1.8-2.0
0.0-0.2	1.65e-01	1.48e-01	1.44e-01	1.28e-01	1.11e-01	1.09e-01	8.73e-02	6.73e-02	4.94e-02	3.21e-02
0.2-0.4	1.48e-01	1.49e-01	1.35e-01	1.21e-01	1.06e-01	1.02e-01	8.00e-02	6.32e-02	4.69e-02	3.03e-02
0.4-0.6	1.44e-01	1.35e-01	1.40e-01	1.14e-01	1.02e-01	9.83e-02	7.87e-02	5.96e-02	4.47e-02	2.91e-02
0.6-0.8	1.28e-01	1.21e-01	1.14e-01	1.15e-01	9.00e-02	8.92e-02	7.43e-02	5.70e-02	4.15e-02	2.66e-02
0.8-1.0	1.11e-01	1.06e-01	1.02e-01	9.00e-02	8.66e-02	7.71e-02	6.31e-02	4.85e-02	3.60e-02	2.33e-02
1.0-1.2	1.09e-01	1.02e-01	9.83e-02	8.92e-02	7.71e-02	8.16e-02	6.15e-02	4.81e-02	3.48e-02	2.26e-02
1.2-1.4	8.73e-02	8.00e-02	7.87e-02	7.43e-02	6.31e-02	6.15e-02	6.42e-02	4.04e-02	2.89e-02	1.86e-02
1.4-1.6	6.73e-02	6.32e-02	5.96e-02	5.70e-02	4.85e-02	4.81e-02	4.04e-02	3.54e-02	2.24e-02	1.44e-02
1.6-1.8	4.94e-02	4.69e-02	4.47e-02	4.15e-02	3.60e-02	3.48e-02	2.89e-02	2.24e-02	1.89e-02	1.03e-02
1.8-2.0	3.21e-02	3.03e-02	2.91e-02	2.66e-02	2.33e-02	2.26e-02	1.86e-02	1.44e-02	1.03e-02	8.03e-03

Table D.7: Covariance matrix for the absolute cross-section as function of the absolute value of the rapidity of the top quark, accounting for the statistic and systematic uncertainties in the boosted topology.

bin	0.0-0.2	0.2-0.4	0.4-0.6	0.6-0.8	0.8-1.0	1.0-1.2	1.2-1.4	1.4-1.6	1.6-1.8	1.8-2.0
0.0-0.2	1.71e-03	1.60e-04	6.31e-04	3.77e-05	1.46e-04	1.06e-04	1.24e-04	2.52e-05	-1.17e-04	8.75e-05
0.2-0.4	1.60e-04	1.82e-03	2.26e-04	-7.75e-06	-7.06e-05	-2.11e-05	-1.32e-05	-6.38e-05	-2.47e-04	-3.52e-05
0.4-0.6	6.31e-04	2.26e-04	2.32e-03	1.08e-04	5.74e-04	1.72e-04	8.59e-04	3.71e-04	4.06e-05	2.02e-04
0.6-0.8	3.77e-05	-7.75e-06	1.08e-04	1.40e-03	7.38e-05	-6.42e-05	3.30e-04	8.43e-05	6.23e-05	1.01e-04
0.8-1.0	1.46e-04	-7.06e-05	5.74e-04	7.38e-05	1.73e-03	-1.40e-05	7.26e-04	2.41e-04	1.54e-04	2.02e-04
1.0-1.2	1.06e-04	-2.11e-05	1.72e-04	-6.42e-05	-1.40e-05	1.09e-03	9.89e-05	1.22e-04	-4.75e-05	9.35e-05
1.2-1.4	1.24e-04	-1.32e-05	8.59e-04	3.30e-04	7.26e-04	9.89e-05	2.03e-03	5.30e-04	2.96e-04	2.52e-04
1.4-1.6	2.52e-05	-6.38e-05	3.71e-04	8.43e-05	2.41e-04	1.22e-04	5.30e-04	9.45e-04	9.27e-05	1.10e-04
1.6-1.8	-1.17e-04	-2.47e-04	4.06e-05	6.23e-05	1.54e-04	-4.75e-05	2.96e-04	9.27e-05	6.05e-04	4.88e-05
1.8-2.0	8.75e-05	-3.52e-05	2.02e-04	1.01e-04	2.02e-04	9.35e-05	2.52e-04	1.10e-04	4.88e-05	3.00e-04

Table D.8: Covariance matrix for the relative cross-section as function of the absolute value of the rapidity of the top quark, accounting for the statistic and systematic uncertainties in the boosted topology.

bin [GeV]	225-345	345-420	420-500	500-590	590-685	685-790	790-910	910-1040	1040-1175	1175-1320	1320-3000
225-345	6.45e-05	1.87e-04	1.16e-04	6.61e-05	4.10e-05	2.19e-05	1.53e-05	8.10e-06	5.03e-06	2.72e-06	5.52e-07
345-420	1.87e-04	1.07e-03	9.92e-04	6.54e-04	3.65e-04	1.87e-04	1.04e-04	5.31e-05	2.87e-05	1.52e-05	1.83e-06
420-500	1.16e-04	9.92e-04	1.17e-03	8.06e-04	4.51e-04	2.35e-04	1.23e-04	6.32e-05	3.34e-05	1.79e-05	1.79e-06
500-590	6.61e-05	6.54e-04	8.06e-04	5.79e-04	3.26e-04	1.74e-04	9.05e-05	4.84e-05	2.53e-05	1.32e-05	1.38e-06
590-685	4.10e-05	3.65e-04	4.51e-04	3.26e-04	1.93e-04	1.04e-04	5.58e-05	3.09e-05	1.66e-05	8.75e-06	1.07e-06
685-790	2.19e-05	1.87e-04	2.35e-04	1.74e-04	1.04e-04	6.07e-05	3.21e-05	1.83e-05	9.94e-06	5.15e-06	6.84e-07
790-910	1.53e-05	1.04e-04	1.23e-04	9.05e-05	5.58e-05	3.21e-05	1.97e-05	1.09e-05	6.11e-06	3.17e-06	4.95e-07
910-1040	8.10e-06	5.31e-05	6.32e-05	4.84e-05	3.09e-05	1.83e-05	1.09e-05	6.80e-06	3.67e-06	1.86e-06	3.05e-07
1040-1175	5.03e-06	2.87e-05	3.34e-05	2.53e-05	1.66e-05	9.94e-06	6.11e-06	3.67e-06	2.28e-06	1.09e-06	1.87e-07
1175-1320	2.72e-06	1.52e-05	1.79e-05	1.32e-05	8.75e-06	5.15e-06	3.17e-06	1.86e-06	1.09e-06	6.81e-07	9.56e-08
1320-3000	5.52e-07	1.83e-06	1.79e-06	1.38e-06	1.07e-06	6.84e-07	4.95e-07	3.05e-07	1.87e-07	9.56e-08	2.16e-08

Table D.9: Covariance matrix of the absolute cross-section as function of the mass of the $t\bar{t}$ system, accounting for the statistical and systematic uncertainties in the resolved topology.

bin [GeV]	225-345	345-420	420-500	500-590	590-685	685-790	790-910	910-1040	1040-1175	1175-1320	1320-3000
225-345	4.41e-09	5.25e-09	-2.89e-09	-3.55e-09	-1.69e-09	-8.63e-10	-9.50e-11	-7.97e-11	1.40e-11	2.58e-11	2.57e-11
345-420	5.25e-09	1.73e-08	2.21e-09	-3.26e-09	-2.98e-09	-2.47e-09	-8.18e-10	-8.11e-10	-4.22e-10	-1.58e-10	-1.25e-11
420-500	-2.89e-09	2.21e-09	6.88e-09	3.55e-09	5.65e-10	-3.53e-10	-6.43e-10	-5.21e-10	-3.69e-10	-1.94e-10	-5.39e-11
500-590	-3.55e-09	-3.26e-09	3.55e-09	4.15e-09	1.60e-09	8.52e-10	1.39e-10	7.45e-11	-2.53e-11	-4.56e-11	-2.22e-11
590-685	-1.69e-09	-2.98e-09	5.65e-10	1.60e-09	1.45e-09	9.60e-10	4.70e-10	3.66e-10	1.78e-10	8.28e-11	1.28e-11
685-790	-8.63e-10	-2.47e-09	-3.53e-10	8.52e-10	9.60e-10	1.15e-09	5.71e-10	4.05e-10	2.13e-10	1.16e-10	2.00e-11
790-910	-9.50e-11	-8.18e-10	-6.43e-10	1.39e-10	4.70e-10	5.71e-10	5.31e-10	3.18e-10	1.86e-10	9.36e-11	2.19e-11
910-1040	-7.97e-11	-8.11e-10	-5.21e-10	7.45e-11	3.66e-10	4.05e-10	3.18e-10	2.61e-10	1.38e-10	6.76e-11	1.61e-11
1040-1175	1.40e-11	-4.22e-10	-3.69e-10	-2.53e-11	1.78e-10	2.13e-10	1.86e-10	1.38e-10	1.03e-10	4.27e-11	1.04e-11
1175-1320	2.58e-11	-1.58e-10	-1.94e-10	-4.56e-11	8.28e-11	1.16e-10	9.36e-11	6.76e-11	4.27e-11	3.49e-11	5.28e-12
1320-3000	2.57e-11	-1.25e-11	-5.39e-11	-2.22e-11	1.28e-11	2.00e-11	2.19e-11	1.61e-11	1.04e-11	5.28e-12	1.59e-12

Table D.10: Covariance matrix of the relative cross-section as function of the mass of the $t\bar{t}$ system, accounting for the statistical and systematic uncertainties in the resolved topology.

bin [GeV]	0-35	35-75	75-125	125-170	170-225	225-800
0-35	1.33e-02	4.50e-03	2.42e-03	7.19e-04	3.14e-04	4.66e-05
35-75	4.50e-03	1.03e-02	5.73e-03	2.36e-03	1.07e-03	9.25e-05
75-125	2.42e-03	5.73e-03	3.62e-03	1.42e-03	6.26e-04	5.36e-05
125-170	7.19e-04	2.36e-03	1.42e-03	6.29e-04	2.72e-04	2.26e-05
170-225	3.14e-04	1.07e-03	6.26e-04	2.72e-04	1.24e-04	1.02e-05
225-800	4.66e-05	9.25e-05	5.36e-05	2.26e-05	1.02e-05	9.55e-07

Table D.11: Covariance matrix of the absolute cross-section as function of the $t\bar{t}$ system p_T, accounting for the statistical and systematic uncertainties in the resolved topology.

bin [GeV]	0-35	35-75	75-125	125-170	170-225	225-800
0-35	1.10e-06	-3.36e-08	-1.04e-07	-5.63e-08	-1.61e-08	-5.22e-10
35-75	-3.36e-08	1.00e-07	1.06e-07	2.23e-08	1.00e-08	2.32e-10
75-125	-1.04e-07	1.06e-07	1.30e-07	3.30e-08	1.39e-08	4.62e-10
125-170	-5.63e-08	2.23e-08	3.30e-08	1.41e-08	4.95e-09	1.97e-10
170-225	-1.61e-08	1.00e-08	1.39e-08	4.95e-09	2.24e-09	8.37e-11
225-800	-5.22e-10	2.32e-10	4.62e-10	1.97e-10	8.37e-11	1.06e-11

Table D.12: Covariance matrix of the relative cross-section as function of the $t\bar{t}$ system p_T, accounting for the statistical and systematic uncertainties in the resolved topology.

bin	0.0-0.1	0.1-0.2	0.2-0.3	0.3-0.4	0.4-0.5	0.5-0.6	0.6-0.7	0.7-0.8	0.8-0.9	0.9-1.0	1.0-1.1	1.1-1.2	1.2-1.3	1.3-1.4	1.4-1.5	1.5-1.6	1.6-1.8	1.8-2.5
0.0-0.1	1.25e+02	1.19e+02	1.23e+02	1.15e+02	1.12e+02	9.68e+01	8.65e+01	8.21e+01	7.25e+01	6.08e+01	4.90e+01	3.90e+01	3.31e+01	2.58e+01	1.84e+01	1.26e+01	7.24e+00	7.20e-01
0.1-0.2	1.19e+02	1.19e+02	1.21e+02	1.12e+02	1.10e+02	9.60e+01	8.50e+01	8.11e+01	7.10e+01	5.91e+01	4.77e+01	3.85e+01	3.23e+01	2.55e+01	1.84e+01	1.25e+01	7.12e+00	7.37e-01
0.2-0.3	1.23e+02	1.21e+02	1.28e+02	1.16e+02	1.14e+02	9.95e+01	8.71e+01	8.42e+01	7.36e+01	6.19e+01	4.98e+01	4.00e+01	3.36e+01	2.66e+01	1.94e+01	1.28e+01	7.59e+00	7.88e-01
0.3-0.4	1.15e+02	1.12e+02	1.16e+02	1.11e+02	1.06e+02	9.11e+01	8.23e+01	7.75e+01	6.91e+01	5.74e+01	4.61e+01	3.70e+01	3.13e+01	2.47e+01	1.73e+01	1.21e+01	6.90e+00	6.86e-01
0.4-0.5	1.12e+02	1.10e+02	1.14e+02	1.06e+02	1.06e+02	9.12e+01	7.97e+01	7.68e+01	6.77e+01	5.63e+01	4.51e+01	3.66e+01	3.09e+01	2.44e+01	1.76e+01	1.19e+01	6.94e+00	7.19e-01
0.5-0.6	9.68e+01	9.60e+01	9.95e+01	9.11e+01	9.12e+01	8.11e+01	6.93e+01	6.67e+01	5.81e+01	4.87e+01	3.91e+01	3.19e+01	2.66e+01	2.11e+01	1.57e+01	1.03e+01	6.03e+00	6.47e-01
0.6-0.7	8.65e+01	8.50e+01	8.71e+01	8.23e+01	7.97e+01	6.93e+01	6.33e+01	5.86e+01	5.15e+01	4.32e+01	3.48e+01	2.80e+01	2.36e+01	1.86e+01	1.32e+01	9.16e+00	5.17e+00	5.18e-01
0.7-0.8	8.21e+01	8.11e+01	8.42e+01	7.75e+01	7.68e+01	6.67e+01	5.86e+01	5.79e+01	4.97e+01	4.12e+01	3.32e+01	2.71e+01	2.28e+01	1.80e+01	1.32e+01	8.77e+00	5.17e+00	5.43e-01
0.8-0.9	7.25e+01	7.10e+01	7.36e+01	6.91e+01	6.77e+01	5.81e+01	5.15e+01	4.97e+01	4.51e+01	3.67e+01	2.92e+01	2.36e+01	2.04e+01	1.61e+01	1.12e+01	7.83e+00	4.55e+00	4.61e-01
0.9-1.0	6.08e+01	5.91e+01	6.19e+01	5.74e+01	5.63e+01	4.87e+01	4.32e+01	4.12e+01	3.67e+01	3.14e+01	2.47e+01	1.96e+01	1.68e+01	1.34e+01	9.49e+00	6.51e+00	3.78e+00	3.84e-01
1.0-1.1	4.90e+01	4.77e+01	4.98e+01	4.61e+01	4.51e+01	3.91e+01	3.48e+01	3.32e+01	2.92e+01	2.47e+01	2.04e+01	1.59e+01	1.33e+01	1.07e+01	7.63e+00	5.18e+00	3.02e+00	3.05e-01
1.1-1.2	3.90e+01	3.85e+01	4.00e+01	3.70e+01	3.66e+01	3.19e+01	2.80e+01	2.71e+01	2.36e+01	1.96e+01	1.59e+01	1.35e+01	1.09e+01	8.57e+00	6.32e+00	4.24e+00	2.48e+00	2.59e-01
1.2-1.3	3.31e+01	3.23e+01	3.36e+01	3.13e+01	3.09e+01	2.66e+01	2.36e+01	2.28e+01	2.04e+01	1.68e+01	1.33e+01	1.09e+01	9.98e+00	7.60e+00	5.13e+00	3.65e+00	2.14e+00	2.16e-01
1.3-1.4	2.58e+01	2.55e+01	2.66e+01	2.47e+01	2.44e+01	2.11e+01	1.86e+01	1.80e+01	1.61e+01	1.34e+01	1.07e+01	8.57e+00	7.60e+00	6.48e+00	4.26e+00	2.91e+00	1.71e+00	1.80e-01
1.4-1.5	1.84e+01	1.84e+01	1.94e+01	1.73e+01	1.76e+01	1.57e+01	1.32e+01	1.32e+01	1.12e+01	9.49e+00	7.63e+00	6.32e+00	5.13e+00	4.26e+00	3.59e+00	2.08e+00	1.24e+00	1.42e-01
1.5-1.6	1.26e+01	1.25e+01	1.28e+01	1.21e+01	1.19e+01	1.03e+01	9.16e+00	8.77e+00	7.83e+00	6.51e+00	5.18e+00	4.24e+00	3.65e+00	2.91e+00	2.08e+00	1.63e+00	8.20e-01	8.39e-02
1.6-1.8	7.24e+00	7.12e+00	7.59e+00	6.90e+00	6.94e+00	6.03e+00	5.17e+00	5.17e+00	4.55e+00	3.78e+00	3.02e+00	2.48e+00	2.14e+00	1.71e+00	1.24e+00	8.20e-01	5.62e-01	5.35e-02
1.8-2.5	7.20e-01	7.37e-01	7.88e-01	6.86e-01	7.19e-01	6.47e-01	5.18e-01	5.43e-01	4.61e-01	3.84e-01	3.05e-01	2.59e-01	2.16e-01	1.80e-01	1.42e-01	8.39e-02	5.35e-02	8.25e-03

Table D.13: Covariance matrix of the absolute cross-section as function of the absolute value of the rapidity of the $t\bar{t}$ system, accounting for the statistical and systematic uncertainties in the resolved topology.

bin	0.0-0.1	0.1-0.2	0.2-0.3	0.3-0.4	0.4-0.5	0.5-0.6	0.6-0.7	0.7-0.8	0.8-0.9	0.9-1.0	1.0-1.1	1.1-1.2	1.2-1.3	1.3-1.4	1.4-1.5	1.5-1.6	1.6-1.8	1.8-2.5
0.0-0.1	3.19e-04	1.06e-04	1.51e-04	1.26e-05	9.64e-05	1.26e-04	3.84e-05	6.55e-05	-3.43e-05	2.38e-05	1.11e-05	1.09e-05	-1.12e-06	-1.75e-05	1.44e-05	-1.15e-05	-9.25e-07	8.06e-07
0.1-0.2	1.06e-04	2.79e-04	2.23e-04	1.55e-05	9.46e-05	1.07e-04	5.95e-05	5.13e-05	-2.71e-05	2.47e-05	2.55e-05	2.08e-05	-1.40e-05	4.40e-06	1.21e-05	-1.90e-06	-2.19e-06	5.60e-07
0.2-0.3	1.51e-04	2.23e-04	5.08e-04	3.93e-05	1.53e-04	1.83e-04	5.57e-05	1.54e-04	-6.71e-06	7.50e-05	5.20e-05	5.18e-05	2.98e-05	5.16e-05	4.93e-05	7.44e-06	1.62e-05	3.63e-06
0.3-0.4	1.26e-05	1.55e-05	3.93e-05	2.37e-04	6.82e-05	3.34e-05	6.03e-05	6.19e-05	5.92e-06	8.42e-06	-1.39e-05	9.98e-06	-2.33e-05	-2.47e-05	9.08e-06	-3.76e-06	4.42e-06	7.72e-07
0.4-0.5	9.64e-05	9.46e-05	1.53e-04	6.82e-05	2.53e-04	1.16e-04	1.19e-05	1.05e-04	2.56e-05	4.61e-05	1.41e-05	3.25e-05	2.29e-05	1.93e-05	2.80e-05	4.17e-06	1.48e-05	2.20e-06
0.5-0.6	1.26e-04	1.07e-04	1.83e-04	3.34e-05	1.16e-04	3.16e-04	1.08e-04	1.54e-04	-3.33e-05	7.26e-05	1.72e-05	5.21e-05	1.26e-05	4.47e-06	7.00e-05	2.16e-06	1.73e-05	4.10e-06
0.6-0.7	3.84e-05	5.95e-05	5.57e-05	6.03e-05	1.19e-05	1.08e-04	1.96e-04	7.15e-05	-4.99e-05	1.87e-05	6.98e-06	3.01e-05	-1.71e-05	-1.37e-05	2.65e-05	3.24e-06	2.81e-06	9.41e-07
0.7-0.8	6.55e-05	5.13e-05	1.54e-04	6.19e-05	1.05e-04	1.54e-04	7.15e-05	3.21e-04	2.55e-05	6.98e-05	5.83e-06	5.85e-05	5.13e-05	2.74e-05	8.63e-05	8.52e-06	3.38e-05	5.74e-06
0.8-0.9	-3.43e-05	-2.71e-05	-6.71e-06	5.92e-06	2.56e-05	-3.33e-05	-4.99e-05	2.55e-05	1.28e-04	1.81e-05	-1.71e-05	-1.00e-06	3.01e-05	2.30e-05	-3.10e-07	8.83e-06	1.10e-05	8.27e-07
0.9-1.0	2.38e-05	2.47e-05	7.50e-05	8.42e-06	4.61e-05	7.26e-05	1.87e-05	6.98e-05	1.81e-05	1.07e-04	2.18e-05	1.69e-05	2.53e-05	2.75e-05	3.76e-05	1.07e-05	1.60e-05	2.58e-06
1.0-1.1	1.11e-05	2.55e-05	5.20e-05	-1.39e-05	1.41e-05	1.72e-05	6.98e-06	5.83e-06	-1.71e-05	2.18e-05	7.42e-05	2.01e-05	-4.08e-06	1.86e-05	1.06e-05	6.35e-06	4.17e-06	6.09e-07
1.1-1.2	1.09e-05	2.08e-05	5.18e-05	9.98e-06	3.25e-05	5.21e-05	3.01e-05	5.85e-05	-1.00e-06	1.69e-05	2.01e-05	8.17e-05	2.14e-05	1.34e-05	2.40e-05	1.12e-05	1.04e-05	1.61e-06
1.2-1.3	-1.12e-06	-1.40e-05	2.98e-05	-2.33e-05	2.29e-05	1.26e-05	-1.71e-05	5.13e-05	3.01e-05	2.53e-05	-4.08e-06	2.14e-05	8.14e-05	3.57e-05	1.41e-05	1.05e-05	1.54e-05	1.76e-06
1.3-1.4	-1.75e-05	4.40e-06	5.16e-05	-2.47e-05	1.93e-05	4.47e-06	-1.37e-05	2.74e-05	2.30e-05	2.75e-05	1.86e-05	1.34e-05	3.57e-05	8.07e-05	2.03e-05	1.35e-05	1.18e-05	1.62e-06
1.4-1.5	1.44e-05	1.21e-05	4.93e-05	9.08e-06	2.80e-05	7.00e-05	2.65e-05	8.63e-05	-3.10e-07	3.76e-05	1.06e-05	2.40e-05	1.41e-05	2.03e-05	6.64e-05	9.29e-06	1.24e-05	2.44e-06
1.5-1.6	-1.15e-05	-1.90e-06	7.44e-06	-3.76e-06	4.17e-06	2.16e-06	3.24e-06	8.52e-06	8.83e-06	1.07e-05	6.35e-06	1.12e-05	1.05e-05	1.35e-05	9.29e-06	2.71e-05	3.94e-06	4.07e-07
1.6-1.8	-9.25e-07	-2.19e-06	1.62e-05	4.42e-06	1.48e-05	1.73e-05	2.81e-06	3.38e-05	1.10e-05	1.60e-05	4.17e-06	1.04e-05	1.54e-05	1.18e-05	1.24e-05	3.94e-06	1.25e-05	9.47e-07
1.8-2.5	8.06e-07	5.60e-07	3.63e-06	7.72e-07	2.20e-06	4.10e-06	9.41e-07	5.74e-06	8.27e-07	2.58e-06	6.09e-07	1.61e-06	1.76e-06	1.62e-06	2.44e-06	4.07e-07	9.47e-07	3.39e-07

Table D.14: Covariance matrix of the relative cross-section as function of the absolute value of the rapidity of the $t\bar{t}$ system, accounting for the statistical and systematic uncertainties in the resolved topology.

Appendix E

Stress Test of the Unfolding Procedure

In this appendix are shown the stress test results, used to check the absence of bias introduced by the unfolding procedure. The stress tests are performed as described in Section 5.3.2. Figures E.1-E.4 show the stress test results obtained reweighting the distributions with $f(p_T^{t,had}, p_T^{t,lep})$, $f(m^{t\bar{t}})$, $f(p_T^{t\bar{t}})$ and $f(y^{t\bar{t}})$ in resolved topology, while Figure E.5-E.6 shows stress test results obtained reweighting the distributions with $f(p_T^{t,had}, p_T^{t,lep})$, $f(y^{t\bar{t}})$ in the boosted topology. In general, the unfolding procedure correctly recovers the reweighted shape as indicated by the green line in plots which compares the stressed and unfolded distribution to the expected reweighted particle-level spectrum. The red line in the plots represents the ratio between the un-reweighted truth and the stressed unfolded distributions. A few per-cent non-closure has been observed in regions where the reweighting function is characterized by high derivatives and is mostly contained within MC statistics band.

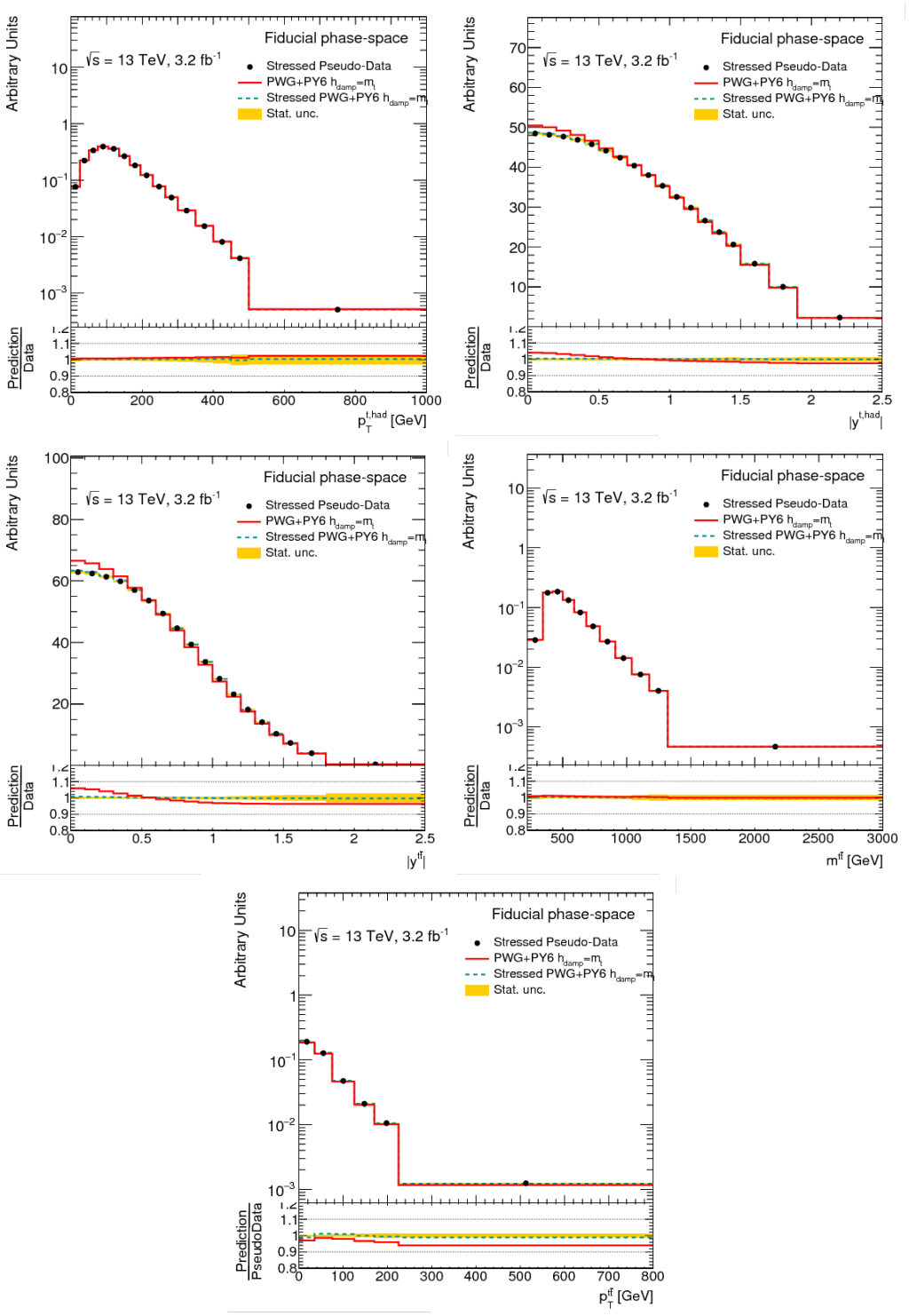

Figure E.1: Stress test plots in the ℓ+jets channel performed by reweighting the absolute spectra in the resolved topology with $f(y_{t\bar{t}})$. The y-axis is the number of events divided by the bin width, i.e. the efficiency correction has not been applied.

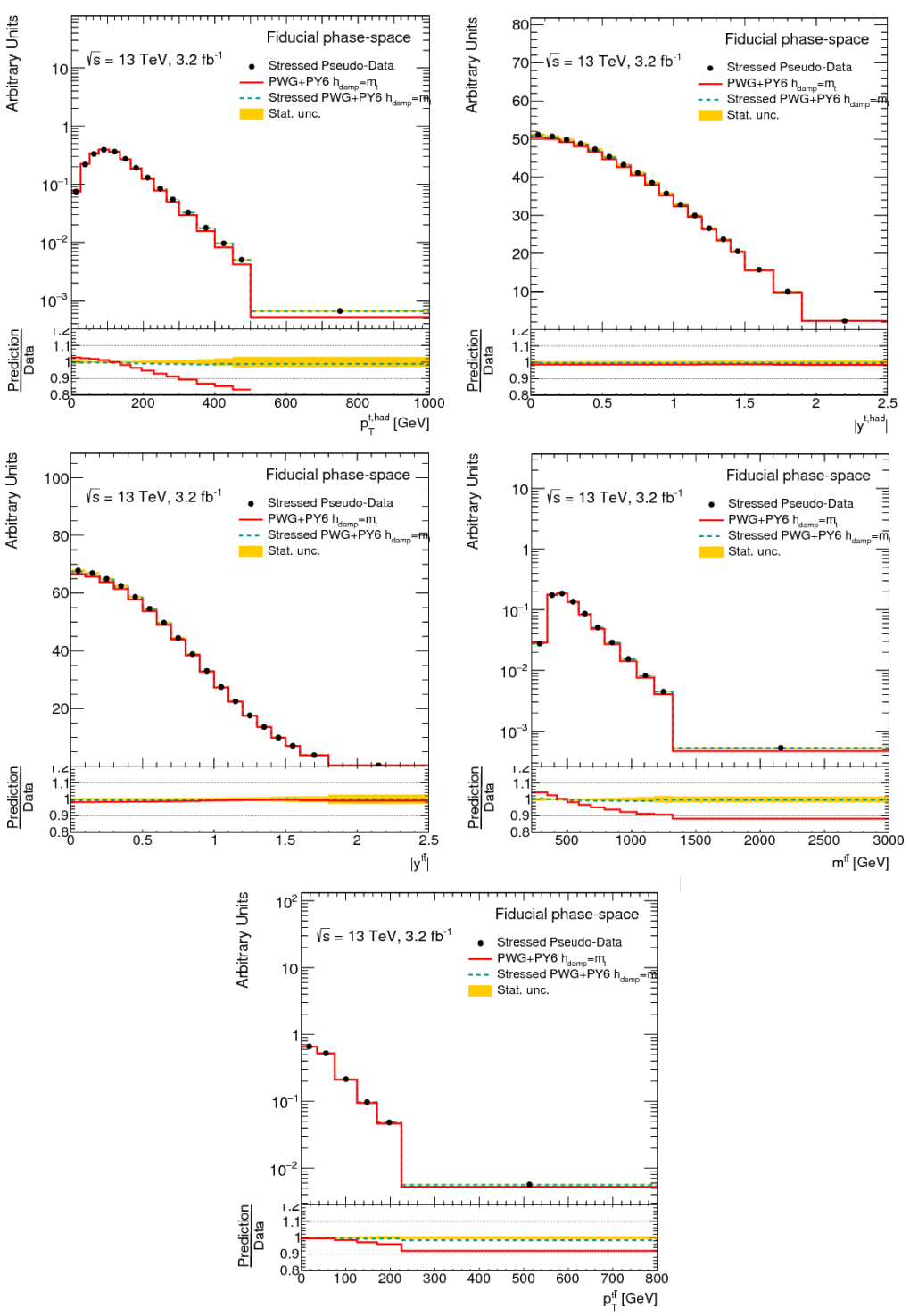

Figure E.2: Stress test plots in the ℓ+jets channel performed by reweighting the absolute spectra in the resolved topology with $f(p_T^{t,had}, p_T^{t,lep})$. The y-axis is the number of events divided by the bin width, i.e. the efficiency correction has not been applied.

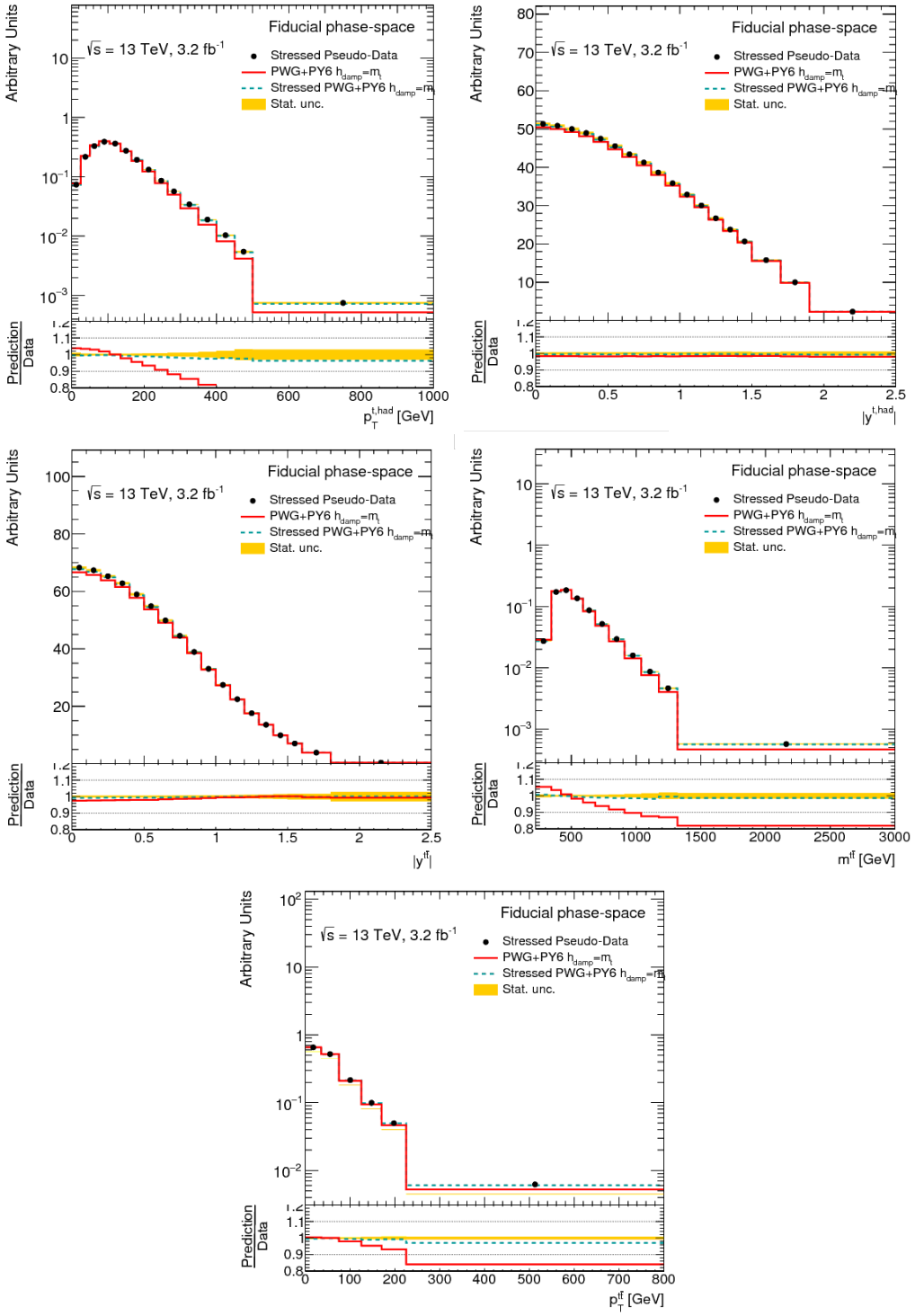

Figure E.3: Stress test plots in the ℓ+jets channel performed by reweighting the absolute spectra in the resolved topology with $f(p_T^{t\bar{t}})$. The y-axis is the number of events divided by the bin width, i.e. the efficiency correction has not been applied.

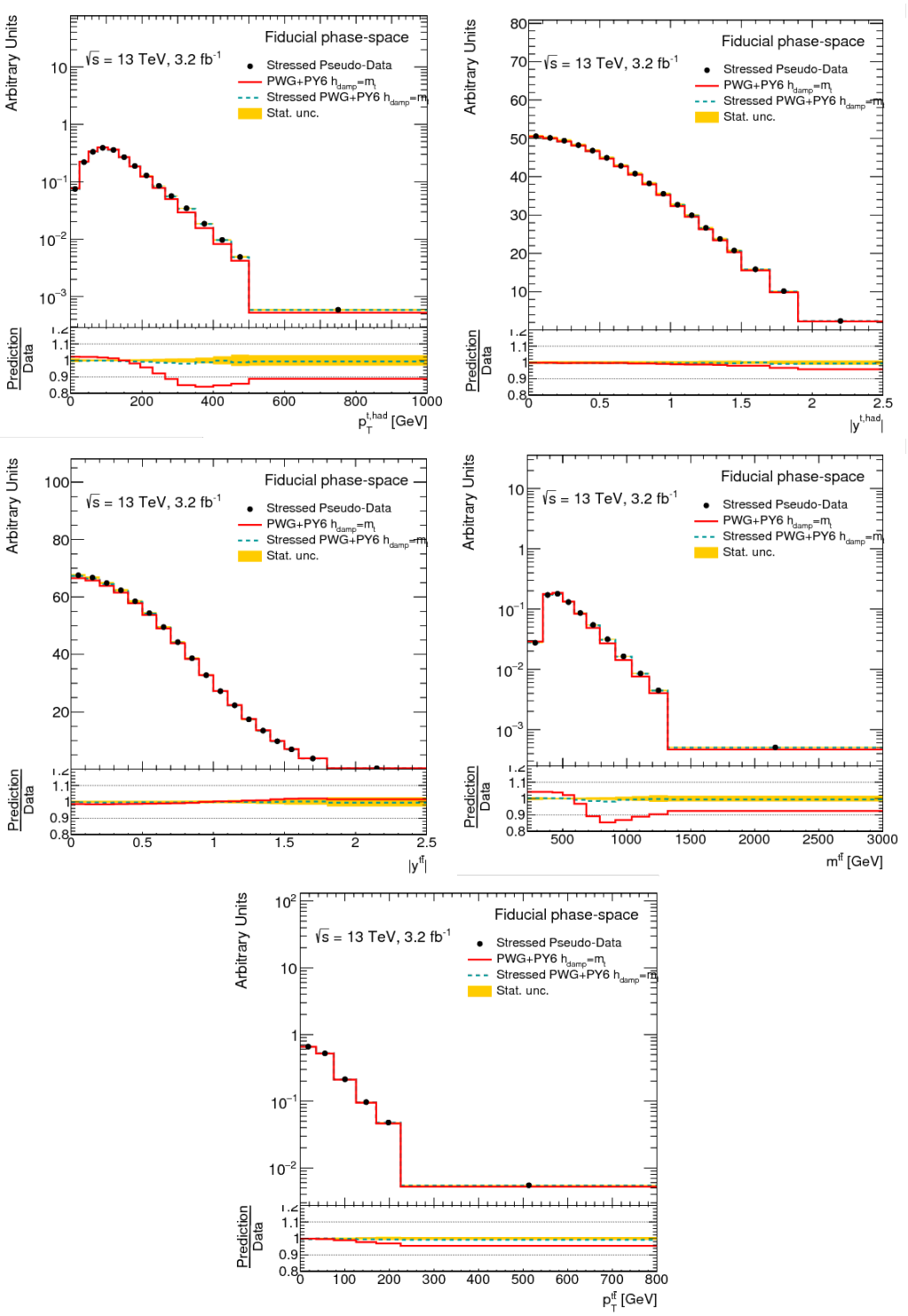

Figure E.4: Stress test plots in the ℓ+jets channel performed by reweighting the absolute spectra in the resolved topology with $f(m_{t\bar{t}})$. The y-axis is the number of events divided by the bin width, i.e. the efficiency correction has not been applied.

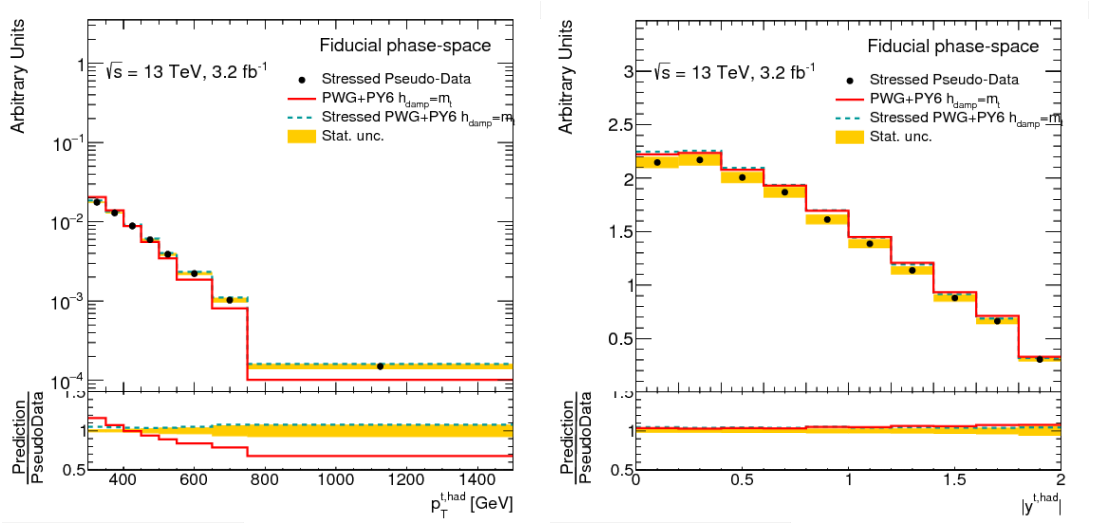

Figure E.5: Stress test plots in the ℓ+jets channel performed by reweighting the absolute spectra in the boosted topology with $f(p_T^{t,had}, p_T^{t,lep})$. The y-axis is the number of events divided by the bin width, i.e. the efficiency correction has not been applied.

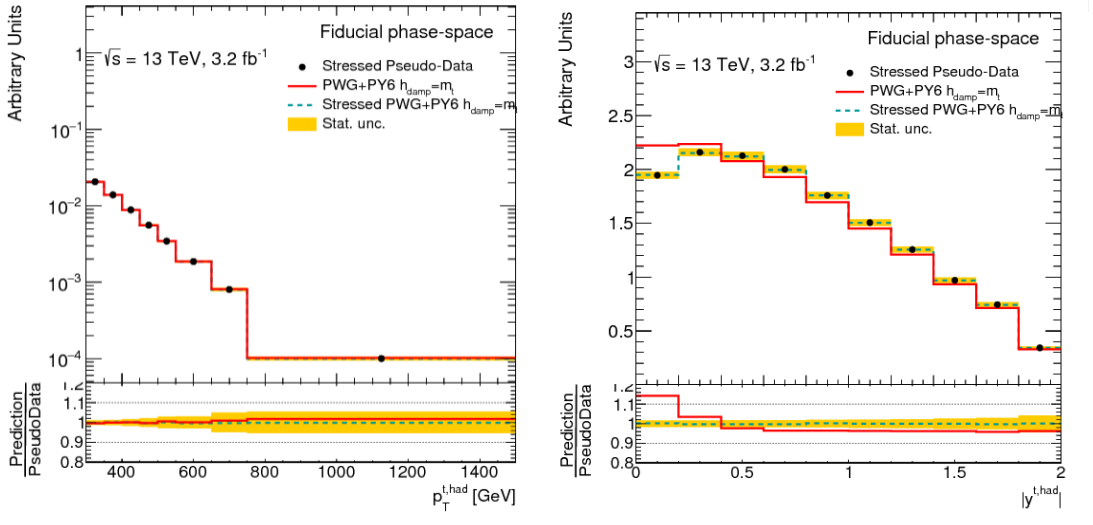

Figure E.6: Stress test plots in the ℓ+jets channel performed by reweighting the absolute spectra in the boosted topology with $f(y_{t\bar{t}})$. The y-axis is the number of events divided by the bin width, i.e. the efficiency correction has not been applied.

Bibliography

[1] ATLAS Collaboration. "Measurements of top-quark pair differential cross-sections in the lepton+jets channel in pp collisions at $\sqrt{s} = 13$ TeV using the ATLAS detector". In: *JHEP* 11 (2017), p. 191. DOI: 10.1007/JHEP11(2017)191.

[2] CDF Collaboration. "Observation of Top Quark Production in $\overline{p}p$ Collisions with the Collider Detector at Fermilab". In: *Phys. Rev. Lett.* 74 (14 1995), 2626–2631. DOI: 10.1103/PhysRevLett.74.2626.

[3] D0 Collaboration. "Observation of the Top Quark". In: *Phys. Rev. Lett.* 74 (14 1995), pp. 2632–2637. DOI: 10.1103/PhysRevLett.74.2632.

[4] M. Gell-Mann. "A schematic model of baryons and mesons". In: *Physics Letters* 8.3 (1964), pp. 214–215. DOI: http://dx.doi.org/10.1016/S0031-9163(64)92001-3.

[5] G. Zweig. "An SU_3 model for strong interaction symmetry and its breaking". In: CERN-TH-401 (1964).

[6] J. -E. Augustin et al. "Discovery of a Narrow Resonance in e^+e^- Annihilation". In: *Phys. Rev. Lett.* 33 (23 1974), pp. 1406–1408. DOI: 10.1103/PhysRevLett.33.1406.

[7] J. J. Aubert et al. "Experimental Observation of a Heavy Particle J". In: *Phys. Rev. Lett.* 33 (23 1974), pp. 1404–1406. DOI: 10.1103/PhysRevLett.33.1404.

[8] S. W. Herb et al. "Observation of a Dimuon Resonance at 9.5 GeV in 400-GeV Proton-Nucleus Collisions". In: *Phys. Rev. Lett.* 39 (5 1977), pp. 252–255. DOI: 10.1103/PhysRevLett.39.252.

[9] W. R. Innes et al. "Observation of Structure in the Υ Region". In: *Phys. Rev. Lett.* 39 (20 1977), pp. 1240–1242. DOI: 10.1103/PhysRevLett.39.1240.

[10] K. Ueno et al. "Evidence for the Υ'' and a Search for New Narrow Resonances". In: *Phys. Rev. Lett.* 42 (8 1979), pp. 486–489. DOI: 10.1103/PhysRevLett.42.486.

[11] S. H. Neddermeyer and C. D. Anderson. "Note on the Nature of Cosmic-Ray Particles". In: *Phys. Rev.* 51 (10 1937), pp. 884–886. DOI: 10.1103/PhysRev.51.884.

[12] M. L. Perl et al. "Evidence for Anomalous Lepton Production in $e^+ - e^-$ Annihilation". In: *Phys. Rev. Lett.* 35 (22 1975), pp. 1489–1492. DOI: 10.1103/PhysRevLett.35.1489.

[13] P. A. M. Dirac. "The Quantum Theory of the Electron". In: *Proceedings of the Royal Society of London A: Mathematical, Physical and Engineering Sciences* 117.778 (1928), pp. 610–624. DOI: 10.1098/rspa.1928.0023.

[14] S. Weinberg. "A Model of Leptons". In: *Phys. Rev. Lett.* 19 (21 1967), pp. 1264–1266. DOI: 10.1103/PhysRevLett.19.1264.

[15] A. Salam. "Weak and Electromagnetic Interactions". In: *Conf. Proc. 8th Nobel Symposium Lerum, Sweden,* C680519 (1968).

[16] G.'t Hooft. "Renormalizable Lagrangians for massive Yang-Mills fields". In: *Nuclear Physics B* 35.1 (1971), pp. 167–188. DOI: http://dx.doi.org/10.1016/0550-3213(71)90139-8.

[17] S. Braibant, G. Giacomelli, and M. Spurio. *Particles and fundamental interactions: an introduction to particle physics*. Dordrecht, 2012.

[18] Particle Data Group. "Review of Particle Physics". In: *Chin. Phys.* C40.10 (2016), p. 100001. DOI: 10.1088/1674-1137/40/10/100001.

[19] N. Cabibbo. "Unitary Symmetry and Leptonic Decays". In: *Phys. Rev. Lett.* 10 (12 1963), pp. 531–533. DOI: 10.1103/PhysRevLett.10.531.

[20] M Kobayashi and T. Maskawa. "CP-Violation in the Renormalizable Theory of Weak Interaction". In: *Progress of Theoretical Physics* 49.2 (1973), p. 652. DOI: 10.1143/PTP.49.652.

[21] J. Ellis. "Proceedings, 2013 European School of High-Energy Physics (ESHEP 2013): Paradfurdo, Hungary, June 5-18, 2013". In: 2015, pp. 117–168. DOI: 10.5170/CERN-2015-004.117.

[22] P. W. Higgs. "Broken Symmetries and the Masses of Gauge Bosons". In: *Phys. Rev. Lett.* 13 (16 1964), pp. 508–509. DOI: 10.1103/PhysRevLett.13.508.

[23] F. Englert and R. Brout. "Broken Symmetry and the Mass of Gauge Vector Mesons". In: *Phys. Rev. Lett.* 13 (9 1964), pp. 321–323. DOI: 10.1103/PhysRevLett.13.321.

[24] ATLAS Collaboration. "Observation of a new particle in the search for the Standard Model Higgs boson with the ATLAS detector at the LHC". In: *Phys. Lett.* B716 (2012), pp. 1–29. DOI: 10.1016/j.physletb.2012.08.020.

[25] CMS Collaboration. "Observation of a new boson at a mass of 125 GeV with the CMS experiment at the LHC". In: *Phys. Lett.* B716 (2012), pp. 30–61. DOI: 10.1016/j.physletb.2012.08.021.

[26] ATLAS and CMS Collaborations. "Combined Measurement of the Higgs Boson Mass in pp Collisions at $\sqrt{s} = 7$ and 8 TeV with the ATLAS and CMS Experiments". In: *Phys. Rev. Lett.* 114 (2015), p. 191803. DOI: 10.1103/PhysRevLett.114.191803.

[27] CDF Collaboration. "Top quark mass measurement using the template method in the lepton + jets channel at CDF II". In: *Phys. Rev. D* 73 (3 2006), p. 032003. DOI: 10.1103/PhysRevD.73.032003.

[28] *Top LHC Summery plots*. URL: https://twiki.cern.ch/twiki/bin/view/LHCPhysics/LHCTopWGSummaryPlots.

[29] P. Haefner F. Fiedler A. Grohsjean and P. Schieferdecker. "The matrix element method and its application to measurements of the top quark mass". In: *Nuclear Instruments and Methods in Physics Research Section A: Accelerators, Spectrometers, Detectors and Associated Equipment* 624.1 (2010), pp. 203–218. DOI: http://dx.doi.org/10.1016/j.nima.2010.09.024.

[30] J. Abdallah el alt. "Measurement of the mass and width of the W boson in e+e- collisions at $\sqrt{s} = 161$–209 GeV". In: *The European Physical Journal C* 55.1 (2008), p. 1. DOI: 10.1140/epjc/s10052-008-0585-7.

[31] A. H. Hoang. "The Top Mass: Interpretation and Theoretical Uncertainties". In: *Proceedings, 7th International Workshop on Top Quark Physics (TOP2014): Cannes, France, September 28-October 3, 2014*. 2014. arXiv: 1412.3649 [hep-ph].

[32] S. Moch et al. "High precision fundamental constants at the TeV scale". In: (2014). arXiv: 1405.4781 [hep-ph].

[33] A. Buckley et al. "General-purpose event generators for LHC physics". In: *Physics Reports* 504.5 (2011), pp. 145–233. DOI: http://dx.doi.org/10.1016/j.physrep.2011.03.005.

[34] ATLAS Collaboration. "Measurement of lepton differential distributions and the top quark mass in $t\bar{t}$ production in pp collisions at $\sqrt{s} = 8$ TeV with the ATLAS detector". In: *Eur. Phys. J.* C77.11 (2017), p. 804. DOI: 10.1140/epjc/s10052-017-5349-9.

[35] K. Kröninger, A. B. Meyer, and P. Uwer. "The Large Hadron Collider: Harvest of Run 1,Top-Quark Physics at the LHC". In: ed. by Thomas Schörner-Sadenius. 2015, pp. 259–300. DOI: 10.1007/978-3-319-15001-7_7.

[36] F. Schilling. "Top Quark Physics at the LHC: A Review of the First Two Years". In: *Int. J. Mod. Phys.* A27 (2012), p. 1230016. DOI: 10.1142/S0217751X12300165.

[37] S. Dulat et al. "New parton distribution functions from a global analysis of quantum chromodynamics". In: *Phys. Rev. D* 93 (3 2016), p. 033006. DOI: 0.1103/PhysRevD.93.033006.

[38] M. Czakon and A. Mitov. "Top++: A Program for the Calculation of the Top-Pair Cross-Section at Hadron Colliders". In: *Comput. Phys. Commun.* 185 (2014), p. 2930. DOI: 10.1016/j.cpc.2014.06.021.

[39] M. Botje et al. "The PDF4LHC Working Group Interim Recommendations". In: (2011). arXiv: 1101.0538 [hep-ph].

[40] J. Gao et al. "CT10 next-to-next-to-leading order global analysis of QCD". In: *Phys. Rev.* D89.3 (2014), p. 033009. DOI: 10.1103/PhysRevD.89.033009.

[41] R. D. Ball et al. "Parton distributions with LHC data". In: *Nucl. Phys.* B867 (2013), pp. 244–289. DOI: 10.1016/j.nuclphysb.2012.10.003.

[42] A. D. Martin et al. "Uncertainties on alpha(S) in global PDF analyses and implications for predicted hadronic cross sections". In: *Eur. Phys. J.* C64 (2009), pp. 653–680. DOI: 10.1140/epjc/s10052-009-1164-2.

[43] J. H. Kuhn, A. Scharf, and P. Uwer. "Electroweak effects in top-quark pair production at hadron colliders". In: *Eur. Phys. J.* C51 (2007), pp. 37–53. DOI: 10.1140/epjc/s10052-007-0275-x.

[44] M. Czakon, D. Heymes, and A. Mitov. "High-Precision Differential Predictions for Top-Quark Pairs at the LHC". In: *Phys. Rev. Lett.* 116 (8 2016), p. 082003. DOI: 10.1103/PhysRevLett.116.082003.

[45] CMS Collaboration. "Measurement of the differential cross section for top quark pair production in pp collisions at $\sqrt{s} = 8$ TeV". In: *Eur. Phys. J.* C75.11 (2015), p. 542. DOI: 10.1140/epjc/s10052-015-3709-x.

[46] B. D. Pecjak, D.J. Scott, and L. Wang X. Yang. "Resummed Differential Cross Sections for Top-Quark Pairs at the LHC". In: *Phys. Rev. Lett.* 116 (20 2016), p. 202001. DOI: 10.1103/PhysRevLett.116.202001.

[47] A. Ferroglia, Ben D. Pecjak, and L. Yang. "Soft-gluon resummation for boosted top-quark production at hadron colliders". In: *Phys. Rev. D* 86 (3 2012), p. 034010. DOI: 10.1103/PhysRevD.86.034010.

[48] ATLAS Collaboration. "Measurements of top-quark pair differential cross-sections in the lepton+jets channel in pp collisions at $\sqrt{s} = 8$ TeV using the ATLAS detector". In: *The European Physical Journal C* 76.10 (2016), p. 538. DOI: 10.1140/epjc/s10052-016-4366-4.

[49] ATLAS Collaboration. "Measurement of the differential cross-section of highly boosted top quarks as a function of their transverse momentum in $\sqrt{s} = 8$ TeV proton-proton collisions using the ATLAS detector". In: *Phys. Rev. D* 93 (3 2016), p. 032009. DOI: 10.1103/PhysRevD.93.032009.

[50] M. Czakon, D. Heymes, and A. Mitov. "Dynamical scales for multi-TeV top-pair production at the LHC". In: (2016). arXiv: 1606.03350 [hep-ph].

[51] M. Aliev et al. "HATHOR: HAdronic Top and Heavy quarks crOss section calculatoR". In: *Comput. Phys. Commun.* 182 (2011), pp. 1034–1046. DOI: 10.1016/j.cpc.2010.12.040.

[52] P. Kant et al. "HATHOR for single top-quark production: Updated predictions and uncertainty estimates for single top-quark production in hadronic collisions". In: *Comput. Phys. Commun.* 191 (2015), pp. 74–89. DOI: 10.1016/j.cpc.2015.02.001.

[53] S. Frixione et al. "Single-top hadroproduction in association with a W boson". In: *JHEP* 07 (2008), p. 029. DOI: 10.1088/1126-6708/2008/07/029.

[54] ATLAS Collaboration. "Studies on top-quark Monte Carlo modelling for Top2016". In: ATL-PHYS-PUB-2016-020 (2016).

[55] CMS Collaboration. "Measurement of the integrated and differential $t\bar{t}$ production cross sections for high-p_{T} top quarks in pp collisions at $\sqrt{s} = 8$ TeV". In: *Phys. Rev. D* 94 (7 2016), p. 072002. DOI: 10.1103/PhysRevD.94.072002.

[56] CMS Collaboration. "Measurement of differential cross sections for top quark pair production using the lepton+jets final state in proton-proton collisions at 13 TeV". In: *Submitted to: Phys. Rev. D* (2016). arXiv: 1610.04191 [hep-ex].

[57] ATLAS Collaboration. "A search for $t\bar{t}$ resonances using lepton-plus-jets events in proton-proton collisions at $\sqrt{s} = 8$ TeV with the ATLAS detector". In: *Journal of High Energy Physics* 2015.8 (Aug. 2015), p. 148. DOI: 10.1007/JHEP08(2015)148.

[58] CMS Collaboration. "Searches for new physics using the $t\bar{t}$ invariant mass distribution in pp collisions at $\sqrt{s}$=8TeV". In: *Phys. Rev. Lett.* 111.21 (2013), p. 211804. DOI: 10.1103/PhysRevLett.111.211804.

[59] CMS Collaboration. "Search for resonant $t\bar{t}$ production in proton-proton collisions at $\sqrt{s} = 8$ TeV". In: *Phys. Rev. D* 93 (1 2016), p. 012001. DOI: 10.1103/PhysRevD.93.012001.

[60] Diogo Buarque F., F. Fabbri, and S. Schumann. "Constraining scalar resonances with top-quark pair production at the LHC". In: (2017). arXiv: 1711.00102 [hep-ph].

[61] J. Wenninger. "Approaching the Nominal Performance at the LHC". In: *Proc. of International Particle Accelerator Conference (IPAC'17), Copenhagen, Denmark, 14â19 May, 2017.* (Copenhagen, Denmark). International Particle Accelerator Conference 8. Geneva, Switzerland, 2017, pp. 13–18. DOI: https://doi.org/10.18429/JACoW-IPAC2017-MOYAA1.

[62] ATLAS Collaboration. "The ATLAS Experiment at the CERN Large Hadron Collider". In: *JINST* 3 (2008), S08003. DOI: 10.1088/1748-0221/3/08/S08003.

[63] ATLAS Collaboration. "Track Reconstruction Performance of the ATLAS Inner Detector at $\sqrt{s} = 13$ TeV". In: ATL-PHYS-PUB-2015-018 (2015).

[64] ATLAS Collaboration. "Tracking Studies for b-tagging with 7 TeV Collision Data with the ATLAS Detector". In: ATLAS-CONF-2010-070 (2010).

[65] ATLAS Collaboration. "ATLAS pixel detector electronics and sensors". In: *JINST* 3 (2008), P07007. DOI: 10.1088/1748-0221/3/07/P07007.

[66] ATLAS Collaboration. "ATLAS Insertable B-Layer Technical Design Report". In: CERN-LHCC-2010-013. ATLAS-TDR-19 (2010).

[67] ATLAS Collaboration. "ATLAS Insertable B-Layer Technical Design Report Addendum". In: CERN-LHCC-2012-009. ATLAS-TDR-19-ADD-1 (2012).

[68] ATLAS Collaboration. "ATLAS Pixel Detector: Operational Experience and Run-1 to Run-2 Transition". In: *PoS* Vertex2014 (2015), p. 001. arXiv: 1410.6347 [physics.ins-det].

[69] ATLAS Collaboration. *ATLAS magnet system: Technical Design Report, 1.* Technical Design Report ATLAS. 1997.

[70] ATLAS Collaboration. "Drift Time Measurement in the ATLAS Liquid Argon Electromagnetic Calorimeter using Cosmic Muons". In: *Eur. Phys. J.* C70 (2010), pp. 755–785. DOI: 10.1140/epjc/s10052-010-1403-6.

[71] ATLAS Collaboration. "Commissioning of the ATLAS Muon Spectrometer with Cosmic Rays". In: *Eur. Phys. J.* C70 (2010), pp. 875–916. DOI: 10.1140/epjc/s10052-010-1415-2.

[72] ATLAS Collaboration. *Electron Trigger Public Plots.* URL: https://twiki.cern.ch/twiki/bin/view/AtlasPublic/EgammaTriggerPublicResults#Electron_trigger_performance_in.

[73] The ATLAS Collaboration. *Muon Trigger Public Plots.* URL: https://twiki.cern.ch/twiki/bin/view/AtlasPublic/MuonTriggerPublicResults#Muon_trigger_performances_in_AN3.

[74] G.L. Alberghi et al. "Choice and characterization of photomultipliers for the new ATLAS LUCID detector". In: *Journal of Instrumentation* 11.05 (2016), P05014.

[75] M. Bruschi. "The new ATLAS/LUCID detector". In: ATL-FWD-PROC-2015-002 (2015).

[76] H. Pernegger. "First test results of a high-speed beam conditions monitor for the atlas experiment". In: *IEEE Transactions on Nuclear Science* 52.5 (2005), pp. 1590–1594. DOI: 10.1109/TNS.2005.856748.

[77] S. Agostinelli et al. "GEANT4: A Simulation toolkit". In: *Nucl. Instrum. Meth.* A506 (2003), pp. 250–303. DOI: 10.1016/S0168-9002(03)01368-8.

[78] J. Allison et al. "Geant4 developments and applications". In: *IEEE Transactions on Nuclear Science* 53.1 (2006), pp. 270–278. DOI: 10.1109/TNS.2006.869826.

[79] J. Allison et al. "Recent developments in Geant4". In: *Nuclear Instruments and Methods in Physics Research Section A: Accelerators, Spectrometers, Detectors and Associated Equipment* 835 (2016), pp. 186–225. DOI: https://doi.org/10.1016/j.nima.2016.06.125.

[80] *ATLAS Luminosity public results*. URL: https://twiki.cern.ch/twiki/bin/view/AtlasPublic/LuminosityPublicResultsRun2.

[81] M. A. Dobbs et al. "Physics at TeV colliders, Les Houches guidebook to Monte Carlo generators for hadron collider physics". In: 2004, pp. 411–459. arXiv: hep-ph/0403045 [hep-ph].

[82] P. Z. Skands. "Proceedings, High-energy Physics, QCD for Collider Physics". In: 2011. arXiv: 1104.2863 [hep-ph].

[83] CDF Collaboration. "Proceedings, APS / DPF / DPB Summer Study on the Future of Particle Physics, The Underlying event in hard scattering processes". In: *eConf* C010630 (2001), P501.

[84] B. R. Webber. "A QCD Model for Jet Fragmentation Including Soft Gluon Interference". In: *Nucl. Phys.* B238 (1984), pp. 492–528. DOI: 10.1016/0550-3213(84)90333-X.

[85] D. Amati and G. Veneziano. "Preconfinement as a Property of Perturbative QCD". In: *Phys. Lett.* 83B (1979), pp. 87–92. DOI: 10.1016/0370-2693(79)90896-7.

[86] X. Artru and G. Mennessier. "String model and multiproduction". In: *Nucl. Phys.* B70 (1974), pp. 93–115. DOI: 10.1016/0550-3213(74)90360-5.

[87] T. Sjostrand. "Jet Fragmentation of Nearby Partons". In: *Nucl. Phys.* B248 (1984), pp. 469–502. DOI: 10.1016/0550-3213(84)90607-2.

[88] B. Andersson et al. "Parton Fragmentation and String Dynamics". In: *Phys. Rept.* 97 (1983), pp. 31–145. DOI: 10.1016/0370-1573(83)90080-7.

[89] P. Nason. "A New method for combining NLO QCD with shower Monte Carlo algorithms". In: *JHEP* 11 (2004), p. 040. DOI: 10.1088/1126-6708/2004/11/040.

[90] S. Frixione, P. Nason, and C. Oleari. "Matching NLO QCD computations with Parton Shower simulations: the POWHEG method". In: *JHEP* 11 (2007), p. 070. DOI: 10.1088/1126-6708/2007/11/070.

[91] S. Alioli et al. "A general framework for implementing NLO calculations in shower Monte Carlo programs: the POWHEG BOX". In: *JHEP* 06 (2010), p. 043. DOI: 10.1007/JHEP06(2010)043.

[92] S. Frixione and B.R. Webber. "Matching NLO QCD computations and parton shower simulations". In: *JHEP* 06 (2002), p. 029. DOI: 10.1088/1126-6708/2002/06/029.

[93] T. Sjöstrand et al. "An Introduction to PYTHIA 8.2". In: *Comput. Phys. Commun.* 191 (2015), pp. 159–177. DOI: 10.1016/j.cpc.2015.01.024.

[94] ATLAS Collaboration. "Summary of ATLAS Pythia 8 tunes". In: ATL-PHYS-PUB-2012-003 (2012).

[95] J. Bellm et al. In: *Eur. Phys. J.* C76.4 (2016), p. 196. DOI: 10.1140/epjc/s10052-016-4018-8.

[96] D. Stump et al. "Inclusive jet production, parton distributions, and the search for new physics". In: *JHEP* 10 (2003), p. 046. DOI: 10.1088/1126-6708/2003/10/046.

[97] ATLAS Collaboration. "The ATLAS Simulation Infrastructure". In: *Eur. Phys. J.* C70 (2010), pp. 823–874. DOI: 10.1140/epjc/s10052-010-1429-9.

[98] Matt Do. and J. B. Hansen. "The HepMC C++ Monte Carlo event record for High Energy Physics". In: *Computer Physics Communications* 134.1 (2001), pp. 41–46. DOI: https://doi.org/10.1016/S0010-4655(00)00189-2.

[99] K. Edmonds et al. "The Fast ATLAS Track Simulation (FATRAS)". In: ATL-SOFT-PUB-2008-001. ATL-COM-SOFT-2008-002 (2008).

[100] ATLAS Collaboration. "The simulation principle and performance of the ATLAS fast calorimeter simulation FastCaloSim". In: ATL-PHYS-PUB-2010-013 (2010).

[101] T. Cornelissen et al. "The new ATLAS track reconstruction (NEWT)". In: *Journal of Physics: Conference Series* 119.3 (2008), p. 032014.

[102] R. Frühwirth. "Application of Kalman filtering to track and vertex fitting". In: *Nuclear Instruments and Methods in Physics Research Section A: Accelerators, Spectrometers, Detectors and Associated Equipment* 262.2 (1987), pp. 444–450. DOI: http://dx.doi.org/10.1016/0168-9002(87)90887-4.

[103] ATLAS Collaboration. "Performance of the ATLAS Track Reconstruction Algorithms in Dense Environments in LHC run 2". In: (2017). arXiv: 1704.07983 [hep-ex].

[104] ATLAS Collaboration. "Early Inner Detector Tracking Performance in the 2015 data at $\sqrt{s} = 13$ TeV". In: ATL-PHYS-PUB-2015-051 (2015).

[105] W. Lampl et al. "Calorimeter Clustering Algorithms: Description and Performance". In: ATL-LARG-PUB-2008-002. ATL-COM-LARG-2008-003 (2008).

[106] ATLAS Collaboration. "Improved electron reconstruction in ATLAS using the Gaussian Sum Filter-based model for bremsstrahlung". In: ATLAS-CONF-2012-047 (2012).

[107] ATLAS Collaboration. "Electron efficiency measurements with the ATLAS detector using the 2015 LHC proton-proton collision data". In: ATLAS-CONF-2016-024 (2016).

[108] J. Illingworth and J. Kittler. "A survey of the hough transform". In: *Computer Vision, Graphics, and Image Processing* 44.1 (1988), pp. 87–116. DOI: http://dx.doi.org/10.1016/S0734-189X(88)80033-1.

[109] ATLAS Collaboration. "Muon reconstruction performance of the ATLAS detector in proton–proton collision data at $\sqrt{s}$ =13 TeV". In: *Eur. Phys. J.* C76.5 (2016), p. 292. DOI: 10.1140/epjc/s10052-016-4120-y.

[110] M. Cacciari, G. P. Salam, and G. Soyez. "The anti-kt jet clustering algorithm". In: *Journal of High Energy Physics* 2008.04 (2008), p. 063.

[111] G. P. Salam. "Towards Jetography". In: *Eur. Phys. J.* C67 (2010), pp. 637–686. DOI: 10.1140/epjc/s10052-010-1314-6.

[112] ATLAS Collaboration. "Jet energy scale measurements and their systematic uncertainties in proton-proton collisions at $\sqrt{s} = 13$ TeV with the ATLAS detector". In: (2017). arXiv: 1703.09665 [hep-ex].

[113] Matteo Cacciari and Gavin P. Salam. "Pileup subtraction using jet areas". In: *Physics Letters B* 659.1 (2008), pp. 119–126. DOI: http://dx.doi.org/10.1016/j.physletb.2007.09.077.

[114] ATLAS Collaboration. "Expected performance of the ATLAS b-tagging algorithms in Run-2". In: ATL-PHYS-PUB-2015-022 (2015).

[115] ATLAS Collaboration. "Performance of jet substructure techniques for large-R jets in proton-proton collisions at $\sqrt{s} = 7$ TeV using the ATLAS detector". In: *JHEP* 09 (2013), p. 076. DOI: 10.1007/JHEP09(2013)076.

[116] D. Krohn, J. Thaler, and L. Wang. "Jet trimming". In: *Journal of High Energy Physics* 2010.2 (2010), p. 84. DOI: 10.1007/JHEP02(2010)084.

[117] J. Thaler and K. V. Tilburg. "Identifying boosted objects with N-subjettiness". In: *Journal of High Energy Physics* 2011.3 (2011), p. 15. DOI: 10.1007/JHEP03(2011)015.

[118] J. Thaler and K. V. Tilburg. "Maximizing Boosted Top Identification by Minimizing N-subjettiness". In: *JHEP* 02 (2012), p. 093. DOI: 10.1007/JHEP02(2012)093.

[119] A. J. Larkoski, D. Neill, and J. Thaler. "Jet Shapes with the Broadening Axis". In: *JHEP* 04 (2014), p. 017. DOI: 10.1007/JHEP04(2014)017.

[120] ATLAS Collaboration. "Boosted hadronic top identification at ATLAS for early 13 TeV data". In: ATL-PHYS-PUB-2015-053 (2015).

[121] ATLAS Collaboration. "Expected performance of missing transverse momentum reconstruction for the ATLAS detector at $\sqrt{s} = 13$ TeV". In: ATL-PHYS-PUB-2015-023 (2015).

[122] ATLAS Collaboration. ""Performance of pile-up mitigation techniques for jets in pp collisions at $\sqrt{s} = 8$ TeV using the ATLAS detector"". In: *The European Physical Journal C* 76.11 (2016), p. 581. DOI: 10.1140/epjc/s10052-016-4395-z.

[123] ATLAS Collaboration. "Differential top-antitop cross-section measurements as a function of observables constructed from final-state particles using pp collisions at $\sqrt{s} = 7$ TeV in the ATLAS detector". In: *JHEP* 06 (2015), p. 100. DOI: 10.1007/JHEP06(2015)100.

[124] F. Halzen, Y. S. Jeong, and C. S. Kim. "Charge Asymmetry of Weak Boson Production at the LHC and the Charm Content of the Proton". In: *Phys. Rev.* D88 (2013), p. 073013. DOI: 10.1103/PhysRevD.88.073013.

[125] ATLAS Collaboration. "Estimation of non-prompt and fake lepton backgrounds in final states with top quarks produced in proton-proton collisions at $\sqrt{s} = 8$ TeV with the ATLAS detector". In: ATLAS-CONF-2014-058 (2014).

[126] V. Blobel. "An Unfolding method for high-energy physics experiments". In: *Advanced Statistical Techniques in Particle Physics. Proceedings, Conference, Durham, UK, March 18-22, 2002*. 2002, pp. 258–267. arXiv: hep-ex/0208022 [hep-ex].

[127] G. D'Agostini. "A multidimensional unfolding method based on Bayes' theorem". In: *Nuclear Instruments and Methods in Physics Research Section A: Accelerators, Spectrometers, Detectors and Associated Equipment* 362.2 (1995), pp. 487–498. DOI: http://dx.doi.org/10.1016/0168-9002(95)00274-X.

[128] T. Adye. "Unfolding algorithms and tests using RooUnfold". In: 2011, pp. 313–318. DOI: 10.5170/CERN-2011-006.313.

[129] A. Hocker and V. Kartvelishvili. "SVD approach to data unfolding". In: *Nucl. Instrum. Meth.* A372 (1996), pp. 469–481. DOI: 10.1016/0168-9002(95)01478-0.

[130] ATLAS Collaboration. "Jet energy measurement with the ATLAS detector in proton-proton collisions at $\sqrt{s} = 7$ TeV". In: *Eur. Phys. J.* C73.3 (2013), p. 2304. DOI: 10.1140/epjc/s10052-013-2304-2.

[131] ATLAS Collaboration. "Single hadron response measurement and calorimeter jet energy scale uncertainty with the ATLAS detector at the LHC". In: *Eur. Phys. J.* C73.3 (2013), p. 2305. DOI: 10.1140/epjc/s10052-013-2305-1.

[132] ATLAS Collaboration. "Jet energy measurement and its systematic uncertainty in proton-proton collisions at $\sqrt{s} = 7$ TeV with the ATLAS detector". In: *Eur. Phys. J.* C75 (2015), p. 17. DOI: 10.1140/epjc/s10052-014-3190-y.

[133] ATLAS Collaboration. "Jet energy resolution in proton-proton collisions at $\sqrt{s} = 7$ TeV recorded in 2010 with the ATLAS detector". In: *The European Physical Journal C* 73.3 (2013), p. 2306. DOI: 10.1140/epjc/s10052-013-2306-0.

[134] ATLAS Collaboration. "Performance of Missing Transverse Momentum Reconstruction in Proton-Proton Collisions at 7 TeV with ATLAS". In: *Eur. Phys. J.* C72 (2012), p. 1844. DOI: 10.1140/epjc/s10052-011-1844-6.

[135] N. Kidonakis. "Next to next to leading order collinear and soft gluon corrections for $t-$channel single top quark production". In: *Phys. Rev.* D83 (2011), p. 091503. DOI: 10.1103/PhysRevD.83.091503.

[136] N. Kidonakis. "Next to next to leading logarithm resummation for s channel single top quark production". In: *Phys. Rev. D* 81 (5 2010), p. 054028. DOI: 10.1103/PhysRevD.81.054028.

[137] N. Kidonakis. "Two-loop soft anomalous dimensions for single top quark associated production with a W^- or H^-". In: *Phys. Rev. D* 82 (5 2010), p. 054018. DOI: 10.1103/PhysRevD.82.054018.

[138] J. Butterworth et al. "PDF4LHC recommendations for LHC Run II". In: *J. Phys.* G43 (2016), p. 023001. DOI: 10.1088/0954-3899/43/2/023001.

[139] M. Cacciari et al. "Top-pair production at hadron colliders with next-to-next-to-leading logarithmic soft-gluon resummation". In: *Physics Letters B* 710.4 (2012), pp. 612–622. DOI: https://doi.org/10.1016/j.physletb.2012.03.013.

[140] M. Beneke et al. "Hadronic top-quark pair production with NNLL threshold resummation". In: *Nucl. Phys.* B855 (2012), pp. 695–741. DOI: 10.1016/j.nuclphysb.2011.10.021.

[141] P. Bärnreuther, M. Czakon, and A. Mitov. "Percent Level Precision Physics at the Tevatron: First Genuine NNLO QCD Corrections to $q\bar{q}$ to $t\bar{t}+X$". In: *Phys. Rev. Lett.* 109 (2012), p. 132001. DOI: 10.1103/PhysRevLett.109.132001.

[142] M. Czakon and A. Mitov. "NNLO corrections to top-pair production at hadron colliders: the all-fermionic scattering channels". In: *JHEP* 12 (2012), p. 054. DOI: 10.1007/JHEP12(2012)054.

[143] M. Czakon and A. Mitov. "NNLO corrections to top pair production at hadron colliders: the quark-gluon reaction". In: *JHEP* 01 (2013), p. 080. DOI: 10.1007/JHEP01(2013)080.

[144] M. Czakon, P. Fiedler, and A. Mitov. "Total Top-Quark Pair-Production Cross Section at Hadron Colliders Through $O(\alpha_S^4)$". In: *Phys. Rev. Lett.* 110 (2013), p. 252004. DOI: 10.1103/PhysRevLett.110.252004.

[145] A. Buckley et al. "Rivet user manual". In: *Comput. Phys. Commun.* 184 (2013), pp. 2803–2819. DOI: 10.1016/j.cpc.2013.05.021.

[146] ATLAS Collaboration. "In-situ measurements of the ATLAS large-radius jet response in 13 TeV pp collisions". In: ATLAS-CONF-2017-063 (2017).

[147] B. Nachman et al. "Jets from Jets: Re-clustering as a tool for large radius jet reconstruction and grooming at the LHC". In: *JHEP* 02 (2015), p. 075. DOI: 10.1007/JHEP02(2015)075.

[148] ATLAS Collaboration. "Search for direct pair production of the top squark in all-hadronic final states in proton-proton collisions at $\sqrt{s} = 8$ TeV with the ATLAS detector". In: *JHEP* 09 (2014), p. 015. DOI: 10.1007/JHEP09(2014)015.

[149] ATLAS Collaboration. "Search for new phenomena in final states with large jet multiplicities and missing transverse momentum at $\sqrt{s}$=8 TeV proton-proton collisions using the ATLAS experiment". In: *JHEP* 10 (2013), p. 130. DOI: 10.1007/JHEP10(2013)130,10.1007/JHEP01(2014)109.

[150] ATLAS Collaboration. "Jet reclustering and close-by effects in ATLAS run II". In: ATLAS-CONF-2017-062 (2017).

[151] CMS Collaboration. "Measurement of double-differential cross sections for top quark pair production in pp collisions at $\sqrt{s} = 8$ TeV and impact on parton distribution functions". In: *Eur. Phys. J.* C77.7 (2017), p. 459. DOI: 10.1140/epjc/s10052-017-4984-5.

[152] T. Gleisberg et al. "Event generation with SHERPA 1.1". In: *JHEP* 02 (2009), p. 007. DOI: 10.1088/1126-6708/2009/02/007.

[153] T. Gleisberg et al. "SHERPA 1. alpha: A Proof of concept version". In: *JHEP* 02 (2004), p. 056. DOI: 10.1088/1126-6708/2004/02/056.

[154] J. Alwall et al. "The automated computation of tree-level and next-to-leading order differential cross sections, and their matching to parton shower simulations". In: *JHEP* 07 (2014), p. 079. DOI: 10.1007/JHEP07(2014)079.

[155] K. J. F. Gaemers and F. Hoogeveen. "Higgs Production and Decay Into Heavy Flavors With the Gluon Fusion Mechanism". In: *Phys. Lett.* B146 (1984), p. 347. DOI: 10.1016/0370-2693(84)91711-8.

[156] D. Dicus, A. Stange, and S. Willenbrock. "Higgs decay to top quarks at hadron colliders". In: *Phys. Lett.* B333 (1994), pp. 126–131. DOI: 10.1016/0370-2693(94)91017-0.

[157] R. Frederix and F. Maltoni. "Top pair invariant mass distribution: A Window on new physics". In: *JHEP* 01 (2009), p. 047. DOI: 10.1088/1126-6708/2009/01/047.

[158] S. Gori et al. "Closing the Wedge: Search Strategies for Extended Higgs Sectors with Heavy Flavor Final States". In: *Phys. Rev.* D93.7 (2016), p. 075038. DOI: 10.1103/PhysRevD.93.075038.

[159] S. Jung, J. Song, and Y. Yoon. "Dip or nothingness of a Higgs resonance from the interference with a complex phase". In: *Phys. Rev.* D92.5 (2015), p. 055009. DOI: 10.1103/PhysRevD.92.055009.

[160] A. Djouadi, J. Ellis, and J. Quevillon. "Interference effects in the decays of spin-zero resonances into $\gamma\gamma$ and $t\bar{t}$". In: *JHEP* 07 (2016), p. 105. DOI: 10.1007/JHEP07(2016)105.

[161] *ATLAS Computing public plots*. URL: https://twiki.cern.ch/twiki/bin/view/AtlasPublic/ComputingandSoftwarePublicResults.

[162] ATLAS Collaboration. "The Fast Simulation Chain for ATLAS". In: ATL-SOFT-SLIDE-2016-617 (2016).

[163] ATLAS collaboration. "Concepts and Plans towards fast large scale Monte Carlo production for the ATLAS Experiment". In: ATL-SOFT-PROC-2013-004 (2013).

[164] ATLAS Collaboration. "FATRAS-the ATLAS Fast Track Simulation project". In: *Journal of Physics: Conference Series* 331.3 (2011), p. 032046.